



THERMOPOLIS 2009 Campaign

ESA Contract No.22693/09/I-EC

FINAL REPORT (FR)

24th November, 2010

LIST OF PARTICIPANTS

European Space Agency (ESA)

Remo Bianchi, Marc Paganini, Timothy Pearson

Centre for Research and Technology Hellas (GR)

S. Rapsomanikis, K. Kourtidis, G. Loupa, I. Kosmadakis, E. Karageorgos, C. Polyzou, D. Karali, A. Georgoulas

National Observatory of Athens, Institute for Space Applications and Remote Sensing (GR)

I. Daglis, V. Amiridis, E. Gerasopoulos, I. Keramitsoglou, G. Petropoulos, N. Kouremeti, P. Kokkalis, D. Kaskaoutis, M. Gratsea

World Radiation Center (CH)

J. Groebner, Stefan Wacker

National Technical University of Athens (GR)

A. Papayiannis, G. Tsaknakis, R.E. Mamouri, and P. Kokkalis

Aerophoto Ltd. (GR)

P. Boutsoukis, G. Noitsis

INTA (ES)

Alix Fernandez-Renau, Jose Antonio Gomez, Eduardo de Miguel, Óscar Gutiérrez de la Cámara, Marcos Jiménez, Elena Prado

CECAF - Cartographic and Photographic Center of Spanish Air Force (ES)

Col. Fulgencio Saura, Tenant Ricardo Puente, Tenant Christian Fernandez, Tenant Miguel Angel Arevalo

University of Valencia -- Global Change Unit (ES)

J. A. Sobrino, G. Sòria, R. Oltra-Carrió, J. C. Jiménez-Muñoz, C. Mattar

DRAXIS Environmental S.A. (GR)

E. Kosmidis, P. Symeonidis, Vaso Somataridou

FR Table of Contents

Executive Summary of FR.....	14
1. Introduction.....	16
1.1 General Background	16
1.2 Overview	17
1.3. Executed Work Plan	18
2. Description of the Study Area	20
2.1 Athens and Attica.....	20
2.2 The Project Team and Allocated Tasks	23
3. Satellite Data Acquisitions and Analyses.....	27
3.1 Data Acquisitions	27
3.1.1 LANDSAT	27
3.1.2 ASTER.....	28
3.1.3 ATSR and AATSR	30
3.1.4 MODIS.....	31
3.1.5 CERES	35
3.1.6 CALIPSO	36
3.1.7 AVHRR.....	39
3.1.8 SEVIRI.....	40
3.2 Satellite data analyses	42
3.2.1 Satellite data validation by looking at Marathon Lake and bare soil cases for each image (NOA)	42
3.2.2 Check Landsat processing algorithm to resolve the ~20°C difference issue NOA with contribution from UVEG-GCU.....	47
3.2.3 Analysis of variations in LST w.r.t. land use (NOA)	50
3.2.4 Finalised quality assessment of each UHI product using mainly ground (and airborne) data as appropriate (NOA-AUTH-VITO).....	69
3.2.5 Characterise the temporal evolution of UHI phenomena using the MODIS dataset (question of how to define threshold); compare with equivalent results from airborne data (NOA& UVEG- CGU)	100
4. Airborne Data Acquisitions, Processing and Analyses	113
4.1 AHS system.....	113
4.2 INTA-AHS data acquisition and processing	115
4.3 Campaign Planning And Execution.....	116
4.3.1 Survey Plan Flights Performed	117
4.4 Pre-Processing AHS Images	128
4.5 Evaluation of AHS Data Quality	130
4.6 AHS Geolocation	132
4.8 Radiometric Calibration	137
4.9 Spectral Calibration	139
4.10 AHS L1B Images in the Thermopolis Data Base.....	141
4.11 AHS Data Analysis Constraints.....	143
4.13 The AEROPHOTO data acquisition system	144
4.14 AEROPHOTO Data Acquiring Flights	148
4.15 Analyses of Results	151

4.15.1 “The use of the variances similarity method to calculate heat fluxes above Athens from aircraft measurements” (CERTH).....	151
4.15.2 “Determination of aerosol chemical and optical properties, for the validation of the lidar data used in atmospheric optical corrections” (CERTH)	155
5. Ground-based and in-situ measurements	156
5.1 Atmospheric measurements	159
5.1.1 Vertical profile soundings of meteorological parameters.....	159
5.1.2 Sun photometric measurements of total aerosol load in ultraviolet, visible and infrared spectral regions and ceilometer measurements of boundary layer structures (NOA).....	160
5.1.3 Lidar measurements of aerosol and water vapour vertical profiles in the free troposphere	175
5.1.4 Calibration and validation.....	177
5.2 Reference Meteorological data	179
5.3 Multiwavelength Raman lidar, sunphotometric and airborne measurements for the estimation of the vertical profiles of the aerosol optical and microphysical properties over Athens, Greece (NTUA-LIDAR)	197
5.3.1 Aerosol optical properties	198
5.3.2 Microphysical aerosol properties.....	199
5.3.3 Aerosol concentration measurements	199
5.3.4 Aerosol load measurements	200
5.3.5 Aerosol lidar measurements.....	201
5.3.6 Anthropogenic and biomass burning aerosols (14-20 July and 21-23 July, 2009).....	202
5.3.7 Saharan dust particles (24-26 July 2009).....	207
5.3.8 Correlated ground-based and space-borne aerosol lidar measurements	211
5.4 Radiometric cal/val ground measurements (UVEG-GCU).....	218
5.5. Ground measurements (UVEG-GCU).....	222
6. HEAT FLUXES MEASUREMENTS AND MODELING (CERTH).	260
6.1 Overview	260
6.2. Introduction.	260
6.3. Methods.....	263
6.3.1. Measurement site and instrumentation	263
6.3.2. Calibration, validation, data acquisition	266
6.3.3. Protocol of measurements, results and discussion.....	266
6.3.4. Data Processing.....	267
6.4. Results	267
6.4.1. Some indicative graphs from the EC tower data.	267
6.4.2. Aerodynamic parameters at the observation site.	270
6.4.3. Heat fluxes calculations	272
6.4.5. Heat fluxes modeling	272
6.4.6. The ARM application for the whole city (INTA aircraft swath)	280
6.4.7. Statistical analysis	283
6.5. References	285
7. Validation and Exploitation of AHS Data	286

7.1 Introduction.....	286
7.2. Atmospheric Correction in the Solar Range	286
7.2.1 Surface Reflectance Retrieval.....	288
7.3 Validation.....	289
7.4 Atmospheric Correction in the Thermal Infrared Range	293
7.5 Land Surface Temperature and Emissivity Retrieval.....	293
7.5.1 Split-Window technique and emissivity from NDVI	293
7.5.2 Temperature and Emissivity Separation (TES) algorithm.....	298
7.5.3 Vicarious Calibration	304
7.6 Validation.....	309
7.7 Generation of Examples of Simulated Uhi Products at Different Spatial Sampling Distances	311
7.8. Suhi Characterization By Means Of AHS Images	311
7.9 Conclusions	315
8. Thermopolis 2009 data base	317
9. Conclusions.....	319
10. Relevant Documents and References	321

List of Figures

Figure 1. Map of greater Athens area.....	20
Figure 18: Histogram of the differences between AHS and LST PK.	47
Figure 19: Image of the LST difference between AHS and LST PK. The values are appropriately grouped for easier interpretation.....	48
Figure 20: Histogram of the differences between AHS and LST GCU.	49
Figure 21: Image of the LST difference between AHS and LST GCU. The values are appropriately grouped for easier interpretation. The colour scale is the same as in Figure 19.....	50
Figure 22 : Exaggerated 3D anaglyph of Athens study area overlaid with a pseudocolour ASTER image (light blue is the urban area and red is vegetation).	54
Figure 23: CORINE Land Cover map of Athens study area. The three morning Hot-Spots (HSM) and the night urban heat island (HSN1) are defined. The legend is attached in Annex II.....	54
Figure 24: The industrial zone that creates the morning hot-spot of Aspropyrgos and Elefsis (HSM2). It must be noted that the area has (among other industrial activities) refineries consisting of steel tanks. Steel's specific heat is very low ($\sim 500 \text{ J / (kg K)}$) so the area warms up very easily. Steel is also expected to exhibit the small diurnal temperature variations...56	56
Figure 25: of Landsat TM LST map of Athens using Landsat TM image of 24.07.2009.....	58
Figure 26: Detail of Landsat TM LST map to focus on the dominant morning hot spot of Aspropyrgos-Elefsis. The map is accompanied by the corresponding CLC2000 map for visual interpretation of the thermal distribution and its relation to land cover type.	59
Figure 27: Detail of of Landsat TM LST map to focus on the dominant morning hot spot of Megara. The map is accompanied by the corresponding CLC2000 map for visual interpretation of the thermal distribution and its relation to land cover type.....	60
Figure 29: The effect of urban parks in the city centre. The thermal information is derived from a Landsat image of the morning of 24.07.2009.....	65
Figure 30: The thermal distribution at and around a complex sports centre. Thermal information is derived from a Landsat image of the morning of 24.07.2009.....	66
Figure 31: hourly data revealing some aspects of the model's behaviour.	73
Figure 32: Trivial model for the air temperatures based upon an hourly climatology expressed as a function of urban land cover.	76
Figure 41: Comparison of the aircraft AHS LST with the LST-PK.....	90
Figure 43: Frequency histogram of the calculated model biases for the entire validation dataset. 70% of the calculated model biases fall in the [-1,1] bin.....	97
Figure 44: Correlation plot between the R2.9-AT and GB-AT for the entire validation dataset. The mean correlation coefficient was found to be equal to 0.83.....	97
Figure 45: The evolution of Maximum LST temperatures in the areas of interest.....	106
Figure 46: Plot of the results of table 40 Approach 3: "A third analysis can be done making a delimitation of what can be considered as the urban area of the city of Athens and selecting an area near to the city to be considered as a reference rural area. This rural area should be similar to the city in terms of altitude, no densely urbanized and without landforms between them (e.g. the area near to the north-east airport of Athens or the one considered after a qualitative reconnaissance of the image).	109
Approach 3: "A third analysis can be done making a delimitation of what can be considered as the urban area of the city of Athens and selecting an area near to the city to be considered as a reference rural area. This rural area should be similar to the city in terms of altitude, no densely urbanized and without landforms between them (e.g. the area near to the north-east airport of Athens or the one considered after a qualitative reconnaissance of the image).....	110
Figure 47: The magnitude of the Surface Urban Heat Island in Kelvin	110
Figure 48: The SUHI Phenomenon using AHS overpass 2	111
Figure 49: Linear correlation between rural and urban SUHI (both day and night).....	112
Figure 50. INTA C-212 Series 200 aircraft and AHS system.....	114
Figure 51: Initial flight plan	117
Figure 52: AHS flight pattern 01	121
Figure 53: AHS flight pattern 02	122
Figure 54: AHS flight pattern 03	123

Figure 55: AHS flight pattern 04	124
Figure 56: AHS quick-looks of visible and	125
Infrared surveys	125
Figure 57: AHS pictures of Acropolis and Piraeus Harbour	126
Figure 58: Flight patterns of July 18 th -20 th -21 st and 24 th	127
Figure 59 : Overall view of the AHS data preprocessing chain for L1b products (georeferenceable at-sensor radiance)	129
Figure 60 : SNR plots for all day time AHS flights.	131
Figure 61: Noise equivalent temperature for all MIR & TIR bands and for all flight sessions. .	132
Figure 62 : Effect of height error as a function of angle from nadir ($\Delta L = \Delta Z \tan \theta$)	134
Figure 63: A mosaic of two images (P03 - P04) on the Olympic Port area. The match between the two images is satisfactory.	135
Figure 64: difference between the expected emission spectrum of water (Lake Marathonos) for different spectral shifts and different atmospheric situations and the observed value. The minimum difference is located at +60 nm shift.	140
Figure 65 : The AEROPHOTO Cessna 310 Q.	145
Figure 66 : AEROPHOTO Instrumentation rack.....	146
Figure 67 : AEROPHOTO rack and onboard data acquisition computer.....	146
Figure 68 : AEROPHOTO Cessna during instrument installation.	147
Figure 69 : AEROPHOTO Cessna instrument diagram.....	147
Figure 70 : AEROPHOTO Cessna during deployment	148
Figure 71 : Flight path (NE-SE) of the AEROPHOTO aircraft.	149
Figure 72: A time series of the three aerosol sizes	151
Figure 75. Ground-based experimental sites (see text below for station identifiers based on operator)	157
Figure 77. NOA's CIMEL CE318-NEDPS9 sunphotometer and radiometric station in the Academy of Athens site.	162
Figure 78. NOA's UV-MFR multifilter radiometer	162
Figure 79. Aerosol Optical Depths at 8 wavelengths retrieved by AERONET for Athens CIMEL for July 2009, along with UV-MFR retrievals for the UV wavelength.....	163
Figure 80: Extinction-related Angstrom exponents (440/870nm) for July 2009.....	164
Figure 81: Fine mode aerosol fraction for July 2009.....	164
Figure 82: Water vapour content for July 2009	165
Figure 83: PGS-100 spectrophotometer (left), and the instrument installed at NOA's Penteli station (right).....	166
Figure 84. Selected spectra on 17 of July 2009 at 08:00, 09:00, 10:00 and 12:00 LT, measured with the PGS-100 spectrophotometer	166
Figure 85: Scattering and absorption coefficients by nephelometer and particle soot absorption photometer for the time period between 14 and 17 of July 2009	167
Figure 86: Example of Microtops recordings performed in NOA's Penteli station.....	168
Figure 87: View to SouthWest (left) and view to Hymetos mountain, from NOA's cameras.....	168
Figure 88. Vaisala CL31 ceilometer (left), and NOA's station at Thissio (right)	171
Figure 89. Quick-look of the aerosol backscatter coefficient at 900nm for the 15th of July 2009	171
Figure 90: WRC's pyrgeometers during deployment in Athens	172
Figure 91: Broadband downwelling longwave radiation at all sites	173
Figure 93: Relative humidity and precipitable water derived from pyrgeometer measurements	174
Figure 94: Aerosol optical depth and angstrom coefficients for 16th of July 2009 retrieved from PFR direct irradiance measurements at NOA's Academy of Athens station	175
Figure 95. MICROTOPS II.....	175
Figure 97. NTUA's instruments	177
Figure 98 : Example of Raman lidar measurements.....	178
Figure 99: Example of the hourly variability of PM _{2.5} aerosol concentration	178
Figure 100: DUTH T/RH measurements	182
Figure 101: DUTH T/RH measurements	182
Figure 102: DUTH T/RH measurements	183
Figure 103: Map of measuring sites used for urban canopy air temperature (T_{air}) analyses in the Greater Athens Area.	183

Figure 104: Results of the interpolation for 00, 06, 12 and 18 hrs using different station data as input.....	185
Figure 105: Timeseries of T_{air} and concurrent satellite acquisition data for the pixels corresponding to the T_{air} ground stations.....	187
Figure 106: LST from all satellite sensors and concurrent AT data from all ground stations within the respective satellite pixels.....	188
Figure 107: Aerial map (approx. 2 km X 2 km)	191
Figure 108: Aerial map (approx. 200m X 200 m).....	192
Figure 109: Diurnal variation at DUTH Thaleias St station.....	193
Figure 110: Example of mean diurnal variation of T_{air} during the THERMOPOLIS 2009 campaign. Data and plots for all stations can be found in the campaign database (see above).....	193
Figure 111: Mean diurnal variation of spatial T_{air} features for the Athens area during the THERMOPOLIS 2009 campaign. All stations (29) with available data were used. Time is 00 hrs at the upper left panel. Time proceeds with 1-hr step from left to right and from top to bottom.....	194
Figure 112. The NTUA Raman lidar system.	198
Figure 113. AOD and Ångström exponent from Cimel over Athens (top) from 15-27 July, 2009. AOD below and above 2 km from Raman lidar measurements (bottom).....	200
Figure 114. Range-corrected lidar signals at 1064 nm (upper graphs) obtained during the time period 20-21 July, 2009 (anthropogenic origin of aerosols) over the city of Athens, together with the aerosol $PM_{2.5}$ concentration measured 15 m above ground level (215 m above mean sea level: asl.).....	203
Figure 115. Air mass back trajectory analysis based on the HYSPLIT model for July 20, 2009 (arrival time 19:00 UTC over Athens).....	204
Figure 116. Retrieved aerosol backscatter coefficients for 20 July 2009 at 355-532-1064 nm, as well as the Ångström backscatter-related exponent obtained by the NTUA lidar between 10:01 and 12:00 UTC.....	205
Figure 117. Retrieved nighttime aerosol optical properties (extinction, backscatter, lidar ratio, Ångström backscatter-related exponent) at 355-532-1064 nm, obtained by the NTUA lidar on 21 July 2009 between 01:00 and 02:42 UTC.....	206
Figure 118. Retrieved aerosol effective radius (μm), refractive index and single scattering albedo (SSA) based on the aerosol optical properties derived by the NTUA Raman lidar on 21 July 2009.	207
Figure 119. Range-corrected lidar signals at 1064 nm obtained by the NTUA lidar during the time period of 24 July, 2009 (Saharan dust intrusion) over the city of Athens.....	208
Figure 120: Range-corrected lidar signals at 1064 nm (upper graphs) obtained during the time period 25-26 July, 2009 (Saharan dust intrusion) over the city of Athens, together with the aerosol $PM_{2.5}$ concentration measured 15 m above ground level (215 m above mean sea level: asl.).....	208
Figure 121. <i>Left</i> : HYSPLIT back-trajectory code (lower graph) and output of the DREAM dust model (upper graph) for air masses arriving over Athens on 24 July (19:00 UTC) and 25 July (00:00 UTC) 2009, respectively. <i>Right</i> : SeaWiFS satellite image obtained for 24 July, 2009.	209
Figure 122. Retrieved aerosol backscatter coefficients for 24 July 2009 at 355-532-1064 nm, as well as the Ångström backscatter-related exponent obtained by the NTUA lidar between 09:01 and 11:00 UTC.....	210
Figure 123. Retrieved nighttime aerosol optical properties (extinction, backscatter, lidar ratio, Ångström backscatter-related exponent) at 355-532-1064 nm, obtained by the NTUA lidar on 24 July 2009 between 20:00 and 21:59 UTC.....	210
Figure 124. Typical ground-track of the CALIPSO satellite over Greece. The corresponding aerosol attenuated backscatter profile along the satellite's path is also presented on the left side of the image.	211
Figure 125. CALIPSO level 2 data comparison with the ground based retrievals of the aerosol optical properties. The minimum horizontal distance between NTUA Raman lidar and the CALIPSO ground track during the nighttime measurements on 26-27 July, 2009 was of the order of 12 km.	213
Figure 126. Radiometric response of the CIMEL CE312-2.....	219
Figure 127. Instruments for thermal radiometric measurements	220

Figure 128. a) HOBO TMC6 HB air temperature sensor and b) AHLBORN FHA464-E1 sensor used for air temperature and relative humidity measurements.	221
Figure 129. GER 1500 spectroradiometer	222
Figure 130.- Surface temperature of the green grass of Panathinaikos Stadium measured with CIMEL radiometer on 16 th July 2009.	223
Figure 131.- Surface temperature of water of the Marathonos Lake (day and night), and an urban surface from the Syntagma Square measured with CIMEL radiometer on 18 th July 2009.	224
Figure 132.- Surface temperature of a) the Metal Grid and b) the Black Glass from the roof of the Akropolis Museum measured with CIMEL radiometer on 20 th July 2009.	225
Figure 133.- Surface temperature of Water from Marathonos Lake in different day times a) at sunset and b) at night measured with RAYTEK radiometer on 21 st July 2009.....	226
Figure 134.- Surface temperature of Gravel and Rocks from the Akropolis measured with RAYTEK and CIMEL radiometers on 24 st July 2009.....	227
Figure 135.- Maximum, minimum and mean value of the reflectance spectra measured during transects on a) Syntagma Square (18 th July 2010) and b) Black Glass and c) Metal Grid of the roof of the Akropolis museum (20 th July 2010) measured with GER spectroradiometer.	228
Figure 136.- Air temperature and Relative Humidity measured during transects on the roof of the Akropolis museum (20 th July 2010) measured with AHLBORN sensor.	229
Figure 137.- Route defined for the transects with car	230
Figure 138.- Air temperature and height of the transect on 16 th of July at night.	231
Figure 139.- Air temperature and height of the transect on 18 th of July at noon.....	232
Figure 140.- Air temperature and height of the transect on 18 th of July at night.	232
Figure 141.- Air temperature and height of the transect on 21 st of July at sunset.	232
Figure 142.- Air temperature and height of the transect on 21 st of July at night.....	233
Figure 143.- Air temperature and height of the transect on 24 th of July at night.	233
Figure 144.- Fixed masts in the Thermopolis field campaign.....	234
Figure 145.- Surface and Air Temperature measurements: (a) in the bare soil mast of NTUA and (b) in the green grass mast of Panathinaikos Stadium.....	235
Figure 146.- Maximum and minimum values of Air temperature and Surface Temperature registered for every day of measurement in Bare Soil and Green grass masts. Spectral characterization of urban surfaces	236
Spectral characterization of urban surfaces.....	237
Figure 147.- Panoramic view and detail of the urban surfaces characterized with reflectivity and emissivity during the Thermopolis campaign.	239
Figure 148.- Emissivity and reflectance of natural and urban surfaces.	243
Figure 149.- Example of reflectance spectra of different surfaces measured with the GER 1500 spectroradiometer	243
Figure 150.- Example of the some emissivity spectra for different urban surfaces measured with CIMEL thermal radiometer	243
Figure 151. Overview.....	260
Figure 152: Sketch of the urban boundary layer structure indicating the various (sub) layers and their names (from Rotach et al., 2004a; modified after Oke, 1987).....	262
Picture 153. Aerial photograph of the study area. EC tower is shown in yellow.	263
Figure 154. Ten-meter flux tower in the roof of a 7-storey building and the respective fetch.....	264
Figure 155. Wind velocities from sonic anemometer	268
Figure 156. Temperature from sonic anemometer.....	268
Figure 157. Atm. Pressure.....	268
Figure 158. Wind speed at 4 heights	269
Figure 159. Wind direction at 9m	269
Figure 160. Temperature at 3 heights.....	269
Figure 161. Relative humidity and temperature at 2 heights.....	270
Figure 162. The height of EC tower lied above the roughness sub-layer.	270
Figure 163. Wind profile and aerodynamic parameters.	271
Figure 164. Flow chart of the structure of LUMPS. Quantities in parentheses are needed only if net all-wave radiation Q^* or incoming shortwave radiation K_{\downarrow} are not measured: T_a is air temperature, e_a is actual vapor pressure, c_f is cloud fraction, P is pressure, U is wind speed, ΔQ_s is storage heat flux, Q_H is turbulent sensible heat flux density, Q_E is latent heat flux density, L is Obukhov length, and u^* is friction velocity.	273

Figure 165. Definition of layers involved in the study of urban climates at the local scale (modified after Oke 1997) relative to the box modeled by LUMPS. The lateral (or third) dimension of the box (not shown) is 10^2 – 10^4 m. Within the roughness sublayer (RSL) there is greater spatial variability of temporally averaged fluxes than within the inertial sublayer; i.e., these fluxes are chaotic in the urban canopy layer and RSL but become invariant in the inertial sublayer. The top of the box is within the inertial sublayer, and the bottom is at the depth at which there is no net heat exchange over the time period of interest.	274
Figure 166. Radiometers source area and heat fluxes source area at the EC tower.	275
Figure 167. Average modelled energy fluxes around the EC tower.	277
Figure 168. An example of friction velocity calculations.....	278
Figure 169. An example of R_i and r_{ah} calculation results	279
Figure 170. Sensible heat flux comparisons.	279
Figure 171. Latent heat flux comparisons.	280
Figure 172. Bowen ratio.	280
Figure 173. Sensible heat flux over Athens (daytime flight)	281
Figure 174. Sensible heat flux over Athens (night time flight).....	282
Figure 175. Latent heat flux over Athens (daytime flight).....	282
Figure 176. Latent heat flux over Athens (night time flight)	283
Figure 177. Mean energy flux densities (\pm SD) at the EC tower footprints.....	284
Figure 178. Heat flux as percentages of net all wave radiation.....	284
Figure 179. Different contributions of the atmosphere and the surface to the top of the atmosphere signal.	287
Figure 180: Spectrum in the VNIR spectral range measured in situ and estimated from AHS of a) a bare soil and b) a green grass.....	290
Figure 181. Band 9 and band 12 test over every flight.....	291
Figure 182. Comparison between every flight's surface reflectance.	291
Figure 183. Atmospheric correction of AHS band 12.	292
Figure 184. LST image retrieved from SW algorithm using emissivity from TES algorithm. P01I2 AHS overpass from 18 th July 2009 at 20:52 UTC.....	295
Figure 185. (a) Atmospheric water vapor content versus the altitude for different standard atmospheres and (b) ratio between atmospheric water vapor content at a certain altitude and the total content.....	296
Figure 186. LST image retrieved from TES algorithm using 9 TIR bands. P01I2 AHS overpass from 18 th July 2009 at 20:52 UTC.....	300
Figure 187. LST image retrieved from TES algorithm using 9 TIR bands. P02I2 AHS overpass from 18 th July 2009 at 21:09 UTC.....	300
Figure 188. LST image retrieved from TES algorithm using 9 TIR bands. P03I2 AHS overpass from 18 th July 2009 at 20:30 UTC.....	301
Figure 189. LST image retrieved from TES algorithm using 9 TIR bands. P03I2 AHS overpass from 18 th July 2009 at 20:11 UTC.....	302
Figure 190. AHS emissivity image obtained with the TES algorithm on July 21 st at 20:52, for the overpass number 3.....	303
Figure 191. Difference on emissivity in AHS band 77 obtained with TES algorithm on July 18 th at 09:21 and on July 18 th at 20:07. And histogram of the difference image.	303
Figure 192. Vicarious calibration of AHS TIR bands for the green grass plot.	306
Figure 193. Vicarious calibration of AHS TIR bands for the water plot.	307
Figure 194. Comparison between the at-sensor brightness temperatures reproduced from ground-based measurements (Tsensor In-Situ) and the ones extracted from the AHS images (Tsensor AHS).....	308
Figure 195. Validation of TES algorithm using 9 AHS TIR bands (LST AHS) with in situ measurements (LST In-Situ) using (a) only water points, (b) only green grass points and (c) water and green grass points.....	309
Figure 196. Validation of SW algorithm using 9 AHS TIR bands (LST AHS) with in situ measurements (LST In-Situ) using (a) only water points, (b) only green grass points and (c) water and green grass points.....	310
Figure 197. Resampling of the LST AHS image of July 18 th at 20:11 UTC. Detail of the 4 th AHS overpass.	311
Figure 198. LST image with the urban zone considered delimited with a black line.....	312
Figure 199. SUHI effect obtained using LST images from AHS overpass 2.	313

Figure 200. AHS image with a line indicating the profile. Numbers corresponds to the position indicated in next figure.....	313
Figure 201. LST profiles in the AHS overpass 2 at night time. Position indicates number of pixels	314

List of Tables

Table 1. Thermopolis 2009 experimental campaign executed work plan.....	18
Table 2. Main ASTER technical characteristics.....	29
Table 3. TIR Aster bands	29
Table 4. Ceres and MODIS overpasses over Athens	35
Table 5. Calipso overpasses over Athens	37
Table 6. Summary of the satellite observations collected during the THERMOPOLIS campaign. However, the final evaluation of the data to be used in the processing that will follow is subject to quality control (checking of presence of clouds, noise, view angle, etc) that is in progress.....	41
Table 7. Summary of the Aerosol and Flux satellite observations collected from DUTH during the THERMOPOLIS campaign.....	42
Table 21: Morning Hot Spots for the Athens study area	55
Table 22: Night-time Hot Spots for the Athens study area	57
Table 23: List of UHI Products supported by Thermopolis2009	69
Table 24: Mean differences between R2.2 AT and GB measured AT along with the standard deviations and correlation coefficients between the two datasets.....	72
Table 25: Initial guesses for OHM parameters in the uhiflux model.	74
Table 26: Results from the comparison over Bare Soil, NTUA (37° 58.886' N , 23° 46.993' E), for the surface temperature:	85
Table 27: Comparisons of LST (LST has been produced by applying the TES algorithm to the CIMEL instrument measurements).....	85
Table 28: Standard Deviation in the estimation of the above ground measurements was reported to be:	85
Table 29: Comparisons of LST (LST has been computed here from the RAYTEK ST6 broadband radiometer)	86
Table 30: Mean absolute differences and standard deviations for each NRT AT retrieval during THERMOPOLIS 2009, for the total of 22 GB stations. Analysis PER AT PRODUCT	92
Table 31: Mean differences between NRT AT and GB measured AT along with the standard deviations. Analysis PER STATION.	93
Table 32: Mean differences for each forecasted AT retrieval during THERMOPOLIS for the total of 16 GB stations selected.	94
Table 33: Mean differences between R2.9-AT and GB-AT along with the standard deviations, correlation coefficients between the two datasets and root mean squared errors. Values in parentheses correspond to the magnitude of the presented statistics prior to the downscaling of the forecasts.	95
Table 34: Mean differences between daily maximum, minimum and average R2.9-AT and GB-AT along with the standard deviations, correlation coefficients between the two datasets and root mean squared errors.	96
Table 35: Mean absolute differences and standard deviations for each NRT DI retrieval during THERMOPOLIS 2009, for the total of 13 GB stations. Analysis PER MAP PRODUCT ...	97
Table 36: Mean differences between NRT DI and GB computed DI along with the standard deviations. Analysis PER STATION	98
Table 37: Comparisons versus emissivity Band 2 of ground instrument (emissivity computed using the CIMEL instrument)	99

Table 38: Comparisons versus emissivity Band 3 of ground instrument (emissivity computed using the CIMEL instrument):	99
Table 39: Comparisons versus the broadband emissivity values (emissivity computed using the CIMEL instrument):	99
Table 40 : The dynamic thresholds and the diurnal LST variability	108
Table 41. AHS Technical specification	114
Table 42. AHS operating modes, flight parameters and pixel size at nadir	115
Table 43. AHS spectral configuration †Full Width Half Maximum (updated Feb.2008).....	115
Table 44: AHS spectral configuration	116
Table 45: Flight data and sensor settings.....	126
Table 46: Summary of flight lines. Start time is reported when a difference > 1 hour from the nominal overflight time is detected.....	128
Table 47: The taxonomy for AHS products.....	129
Table 48: Position and orientation error	132
Table 49: Image to image ground control points for two image pairs.....	136
Table 50: configuration of the illumination/atmospheric correction performed.	138
Table 52:Aquired Data Report- Up To 22/7/2009	149
Table 53: Calibration and validation.....	150
Table 54: Variance similarities method	154
Table 55: Aerosol Chemical and Optical Properties	156
Table 56: Experimental sites	158
Table 57: Radiometric stations and measurements.....	160
Table 58: CERTH T/RH Stations	179
Table 59: LOCAL SCALE	189
Table 60: MICROSCALE	189
Table 62: MICROSCALE	191
Table 63:. CERTH T _{air} /RH Stations. Stations with bold site id# have provided valid data.	195
Table 64: T _{air} stations by other providers. Stations with bold site id# have provided valid data.	195
Table 65: Dates when daytime (yellow colour) and nighttime (blue colour) aerosol lidar measurements were performed.....	201
Table 66. Aerosol microphysical properties derived by inverse modeling (from NTUA Raman lidar data) and in situ measurements performed by the Democritus University of Thrace (DUTH).	212
Table 66. Technical specifications of the thermal instruments	219
Table 67. Technical specifications of air temperature and humidity sensors	220
Table 68. Technical specifications of GER 1500 spectroradiometer	221
Table 69.- Fixed Masts description.	234
Table70.- Emissivity for the 6 bands of the CIMEL radiometer and effective reflectance for the AVHRR bands 1 and 2 of different natural and urban surfaces of the spectral characterization measurements database.....	244
Table 71: Summary of the thermal images taken for every day of the campaign:	245
Table 72.- Work Plan carried out by GCU in the framework of Thermopolis 2009.	256
Table 73 Measurement site description	264
Table 74: Parameters and frequency of measurements	265
Table 75. Empirical parameters α and β estimated for Athens.	276
Table 76. Parameters in the OHM model (For <i>hourly</i> average heat fluxes).....	277
Table 77: Water vapor content and aerosol optical thickness values considered.	288
Table 78. Errors on the Land Surface Temperature retrieved from Split-Window algorithms according to the sensitivity analysis and using different AHS bands combinations. ‘Std. Dev’ is the standard error of estimation, ‘r’ is the correlation coefficient, ‘e_noise’ is the error due to the NE \square T, e’emis’ is the error due to the emissivity uncertainty, e’vapor’ is the error due to the total water vapour content uncertainty and ‘e_total’ is the total error. Bands combinations providing total errors higher than 2 K have not been included.	294
Table 79. Values of ratio between atmospheric water vapor content at a certain altitude and the total content for different standard atmospheres. The mean ratio value is also given.	297
Table 80. Date, time, instrument, sample and statistical values from calibration measurements.	305

List of acronyms and abbreviations

AATSR	Advanced Along-Track Scanning Radiometer
AHS	Airborne Hyperspectral Scanner
ARM	Atmospheric Resistance Model
ASTER	Advanced Spaceborne Thermal Emission and Reflection Radiometer
AT	Air Temperature
AVHRR	Advanced Very High Resolution Radiometer
CASA	Construcciones Aeronáuticas Sociedad Anónima
DEM	Digital Elevation Model
DESIREX	Dual-use European Security IR EXperiment
DUE	Data User Element
EC	Eddy Covariance
ESA	European Space Agency
EUFAR	EUropean Fleet for Airborne Research
FOV	Field Of View
FTP	File Transfer Protocol
FWHM	Full Width Half Maximum
GCU	Global Change Unit (University of Valencia)
GIFOV	Ground Instantaneous Field Of View
GMES	Global Monitoring of Environment and Security
GMT	Greenwich Mean Time
GPS	Global Positioning System
IFOV	Instantaneous Field Of View
INS	Inertial Navigation System
INTA	Instituto Nacional de Técnica Aeroespacial
LIDAR	LIght Detection And Ranging
LST	Land Surface Temperature
LST	Land Surface Temperature
LUMPS	Local-scale Urban Meteorological Parameterization Scheme
LUZ	Larger Urban Zone
LWIR	Long Wavelength Infra-Red
MAS	MODIS Airborne Simulator
MODIS	Moderate Resolution Imaging Spectroradiometer
MOST	Monin-Obuckov Similarity Theory
MSL	Mean Sea Level

MWIR	Medium Wavelength Infra-Red
NIR	Near Infra-Red
OHM	Objective Hysteresis Model
PAR	Photosynthetic Active Radiation
PI	Principal Investigator
RADAR	RAdio Detection And Ranging
SEB	Surface Energy Balance
SEVIRI	Spinning Enhanced Visible and InfraRed Imager
SNR	Signal to Noise Ratio
SUHI	Surface Urban Heat Island
T/RH	Temperature/Relative Humidity
TES	Temperature and Emissivity Separation Method
TIR	Thermal InfraRed
UHI	Urban Heat Island
UT	Urban Thermography

Executive Summary of FR

□ *The present document reports, in each chapter, the timeframe and instrumentation used to acquire the data of the Thermopolis 2009 campaign in Athens, Greece. Examples of data acquired are then presented. Data analyses and conclusions follow and complete each chapter. Each “scientific domain” of data acquisition and analysis is presented in turn. Firstly, the satellite data acquired, analysed, and compared with aircraft data as far as land surface temperatures (LSTs) are concerned, is presented. Then aircraft LSTs and aircraft optical and chemical properties are presented and analysed. Ground based acquired measurements, concerning air temperatures (ATs), reflectivity, thermal radiometric temperatures, emissivities, atmospheric radiances and atmospheric dynamic and optical properties are discussed and analysed. Heat fluxes obtained from a micrometeorological tower, validated by the DUTH-AEROPHOTO aircraft and extended to the INTA-AHS swath of LSTs is presented. Finally the link between the LSTs acquired by satellite, aircraft and confirmed and validated by ground measurements and the evolution of the Athens UHI phenomenon, is confirmed.*

□ *The THERMOPOLIS campaign was performed as planned in and over Athens, during the summer 2009. Aircraft flights were performed within the contingency limits set out in the Experiment Plan. Satellite acquisitions were also within the contingency limits. The core measurement period for the ground-based instrumentation was carried out between 15-31 July 2009. Some of the ground-based instrumentation was operated for 1 full month (15 July - 15 August 2009). This was the case for the T/RH stations, allowing 1-month of UHI measurements. Cal/Val activities were also performed as described in the Experiment Plan. All critical data were uploaded by the responsible partners to the project database. Overall, all airborne and ground-based instrumentation was deployed successfully with only minor exceptions (mentioned where relevant in the DAR) not impacting the overall aims of the campaign; satellite acquisitions were also, to a large degree, successful. Hence the project consortium can here declare that the Experiment*

Plan has been executed as planned. Data acquired during the Thermopolis campaign were successfully analysed and proven suitable to support the UHI project. The reported work carried out by CERTH, NOA, NTUA, INTA and UVEG during the ATHENS THERMOPOLIS 2009 Campaign, resulted in data that support the UHI project objectives, via the analysis of comprehensive validation data sets, together with the data from the urban weather stations, for the quality assessment of the UHI information products. Data from the INTA-AHS were compared with satellite derived LSTs, validated and differences with std deviations and RMSEs recorded and commented upon. The magnitude of the UHI phenomenon was also recorded via the intercomparison of LSTs for rural and urban areas in the Attica region. The ATs recorded at the weather stations run by CERTH across the conurbation of Athens for the period of the campaign, were interpolated to give spatial AT variability maps to match the satellite LST coverage. Hence, LST and AT retrieval of urban and surrounding rural areas, at a high spatial resolution (5 to 90m,) was achieved, in order to study in details the spatial variability of UHI Athens. The feasibility of time series retrievals of AT and LST for the Athenian conurbation, together with weather forecasting, will, via the use of stochastic modeling, help us to take prognostic and forecasting actions for Urban Heat Waves. The secondary objective of providing additional datasets to perform a preliminary mission analysis for a dedicated TIR sensor that would feature the necessary higher spatial resolution and revisiting time for a more adequate provision of LST retrievals in the metropolitan areas of European cities was also achieved. The study of energy balance of the cities for a better response to the energy efficiency policies was achieved by determining heat fluxes from a micrometeorological tower, calibrating the heat flux measurements of the overflying DUTH-AEROPHOTO airplane and extrapolating the heat flux calculations to the swaths of the LST given by the INTA-AHS data. Hence, in the future we should be able to obtain daily or half daily heat fluxes of the conurbation, provided that we have satellite LSTs in situ ATs and occasional calibration of heat fluxes by aircraft measurements at very high spatial resolution. Again, stochastic and numerical modeling will support the forecast of heat fluxes.

Done on the 24th of November of A.D. 2010
in Xanthi, GREECE,

by the Scientifically Responsible for the project,

Prof. Dr. S. Rapsomanikis

1. Introduction

In the framework of its Earth Observation Programmes the European Space Agency (ESA) carries out a number of ground-based and airborne campaigns to support geophysical algorithm development, calibration/validation and the simulation of future space-borne earth observation missions for applications development related to land, oceans and atmosphere.

The THERMOPOLIS 2009 campaign was part of the framework of proposed activities for the UHI project for Athens, GREECE.

The experimental plan provides insights into the planning philosophy, the participants, their tasks, instrumentation needed and actual deployment, aircraft operations in harmony with satellite overpasses, data acquisition and data treatment. All measurements were constrained into the time frame of 15 July - 2nd August 2009 for the experiment in Athens, GREECE (although some measurements continued up to the 15th of August).

1.1 General Background

The THERMOPOLIS 2009 campaign mainly served the DUE “Urban Heat islands (UHI) and Urban Thermography (UT) Project” [RD2] and also played part of the framework of proposed activities for the Reorientation of the Fuegosat Consolidation Phase of the Earth Watch Programme [RD1].

A consultation of internal and external infrared EO application experts was initiated by the Agency (this included a one-day workshop at ESRIN on 17 October 2006) with the goal of verifying the impact of IR data at higher resolution than the traditional AVHRR and AATSR on a number of applications relevant for GMES. A high resolution Thermal Infra-Red capability is recognized as necessary for Europe in the medium/long term and, in addition to applications that are fire related, additional applications of infrared observations of potential relevance to GMES were identified and considered during the initial requirement consolidation exercise. The applications addressed at the workshop included:

- fire monitoring for climate studies and ecology
- coal mine fires monitoring for ecology
- volcano monitoring
- irrigation water management
- urban climate
- security and surveillance

Taking into account the complementary data and applications supported by other missions such as MSG and MTG for monitoring of large fires (and in the future also medium-size fires) and the Sentinel-2 and -3 for forest fire prevention and post-damage assessment, the following new applications have been preliminary identified as of relevance to GMES services, either initiated or planned, in particular because of their clear relevance to EC policies:

-Urban Heat Islands for micro-climate, energy conservation, carbon emission limitation;

-Security: various kinds of human and industrial activities, including several of interest to law enforcement authorities, may be detected during day or night using high resolution infrared sensors, such as motion of means of transport, detection of ships and their routes, industrial operations causing thermal anomalies, waste management, landfill monitoring, energy security, etc.

The reorientation was recently discussed (October 2007 and February 2008) and endorsed by the Participants to the Fuegosat element (Consolidation phase). The reorientation planned the identification of activities to support establishing requirements reconsidering previous studies and through Data User Element (DUE) projects relevant to the infrared element development. Tasks will be added to these DUE projects to prototype products and services using airborne and space sensors and to assess the related operational usefulness and the scope of use in Europe.

A Data User Element (DUE) workshop took place March 2009 and the on going DUE activities produced relevant inputs before the end of 2008, covering in particular the user requirements for urban heat islands for micro-climate and energy conservation.

Therefore, the aim of THERMOPOLIS 2009 airborne campaign was to anticipate generation of thermal datasets to address coming trade-off studies supporting both DUE projects for products prototyping and mission requirements analysis. The "Urban Heat Islands (UHI) and Urban Thermography (UT)" [RD2] is an Earth Observation Application project funded by DUE within the 3rd Earth Observation Envelope Programme started July 2008 that includes studies to demonstrate the integration of remote sensing observations, with special focus on NIR/TIR observations, in support to UHI mitigation and Urban Energy Efficiency policies.

In the framework of the DUE, UHI and UT project, ESA organized dedicated airborne campaigns (baseline: Madrid 2008 [DESIREX2008] and Athens 2009 [THERMOPOLIS2009]) on a limited number of cities to generate thermal datasets to be used principally as input to the TIR sensor trade-off study.

1.2 Overview

The THERMOPOLIS 2009 campaign combined the collection of quality and coordinated airborne hyper-spectral, space-borne and in-situ measurements to generate spectrally, geometrically and radiometrically representative datasets to address observational requirements of Urban Heat Islands (UHI) for the assessment of an operational system. The period 15th July to 2nd August 2009 was an optimal time window for good weather conditions in ATHENS (GREECE), where the campaign was carried out. During this period, the CERTH (Center for Research and Technology Hellas) and INTA (Spain) airborne optical systems, as well as the ground instruments of CERTH, National Observatory of Athens, National Technical University of Athens, World Radiation Center (CH) and Global Change Unit of the University of Valencia, were deployed to cope with the campaign objectives.

The datasets that were produced during the THERMOPOLIS 2009 campaign served the following main objectives of the "Urban Heat Islands and Urban

Thermography" project:

- ☐ I. Analysis of comprehensive validation data sets – together with the data from the urban weather stations and from ad-hoc field campaigns - for the quality assessment of the UHI information products.
- ☐ II. Prognostic and forecasting actions for Urban Heat Waves.
- ☐ III. Land Surface Temperature and Air Temperature retrieval of urban and surrounding rural areas, at a high spatial resolution (5 to 90m) in order to study in details the spatial variability of UHI in metropolitan areas.

Secondary objectives of the project were:

- ☐ V. Provision of additional datasets to perform a preliminary mission analysis for a dedicated TIR sensor that would feature the necessary higher spatial resolution and revisiting time for a more adequate provision of LST retrievals in the metropolitan areas of European cities.
- ☐ IV. Study of energy balance of the cities for a better response to the energy efficiency policies.
- ☐

1.3. Executed Work Plan

Table 1. Thermopolis 2009 experimental campaign executed work plan

JULY 2009	Ground** measurements	Aircraft	Satellite
12	Setting up ground equipment	ground testing and calibration	MODIS/CERES, AVHRR, SEVIRI, CALIPSO ⁺
13	Setting up ground equipment	ground testing and calibration	MODIS/CERES, AVHRR, SEVIRI, AATSR*
14	Setting up ground equipment	ground testing and calibration	MODIS/CERES, AVHRR, SEVIRI, AATSR
15	radiosoundings, atmospheric measurements, radiometric measurements, Heat fluxes	ground testing and calibration	MODIS/CERES, AVHRR, SEVIRI, AATSR, CALIPSO ⁺
16	radiosoundings, atmospheric measurements, radiometric measurements, Heat fluxes		MODIS/CERES, AVHRR, SEVIRI, ASTER
17	radiosoundings, atmospheric measurements, radiometric measurements, Heat fluxes.		MODIS/CERES, AVHRR, SEVIRI, Landsat-5 TM, CALIPSO ^{+,++}
18	radiosoundings, atmospheric measurements, radiometric measurements, Heat fluxes.	INTA-AHS flights morning and evening AEROPHOTO flights at three heights midday	MODIS/CERES, AVHRR, SEVIRI, AATSR
19	radiosoundings, atmospheric measurements, radiometric measurements, Heat fluxes.		MODIS/CERES, AVHRR, SEVIRI, CALIPSO ^{+,++}

20	radiosoundings, atmospheric measurements, radiometric measurements, Heat fluxes.	INTA-AHS flights morning AEROPHOTO flights at three heights midday	MODIS/CERES, AVHRR, SEVIRI,
21	radiosoundings, atmospheric measurements, radiometric measurements, Heat fluxes.	INTA-AHS flights morning and evening AEROPHOTO flights at three heights morning and evening	MODIS/CERES, AVHRR, SEVIRI, AATSR
22	radiosoundings, atmospheric measurements, radiometric measurements, Heat fluxes.		MODIS/CERES, AVHRR, SEVIRI,
23	radiosoundings, atmospheric measurements, radiometric measurements, Heat fluxes		MODIS/CERES, AVHRR, SEVIRI, ASTER
24	radiosoundings, atmospheric measurements, radiometric measurements, Heat fluxes	INTA-AHS flights morning and evening	MODIS/CERES, AVHRR, SEVIRI, Landsat-5 TM, AATSR, CALIPSO ^{+,++}
25	radiosoundings, atmospheric measurements, radiometric measurements, Heat fluxes		MODIS/CERES, AVHRR, SEVIRI
26	radiosoundings, atmospheric measurements, radiometric measurements		MODIS/CERES, AVHRR, SEVIRI, CALIPSO ^{+,++}
27****	radiosoundings, atmospheric measurements		
28	radiosoundings, atmospheric measurements		
29	radiosoundings, atmospheric measurements,		
30	radiosoundings, atmospheric measurements,		
31	atmospheric measurements		
AUG 1-15	atmospheric measurements		ASTER (on 1.8.09)

NOTES:

* means that Athens is at the edge of the image, therefore oblique viewing effects should be accounted for. [Landsat-7 ETM+] image quality is questionable due to known problem of the sensor

**means daily acquisitions. Time set at UTC (not GMT) for all data loggers.

**** Measurements and flights after the 27th of July were foreseen in the Experiment Plan only as contingency.

⁺ Details on CALIPSO acquisitions are given in Table 5.

⁺⁺CALIPSO overpasses within 250 km from Athens.

2. Description of the Study Area

2.1 Athens and Attica

The chosen area for THERMOPOLIS 2009 campaign is Athens, the capital and largest city of Greece. The urban area of Athens extends beyond the administrative city limits with a population of 3,130,841 (National Statistical Service of Greece, 2001) and a land area of 412 km² basin (Hellenic Interior Ministry). According to the recent census paper of Eurostat (2004), the Athens Larger Urban Zone (LUZ) is the 7th most populated LUZ in the European Union with a population of 4,013,368.

The area, with its particularities, presents characteristics which makes it especially interesting for urban heat island studies. Under given synoptic conditions there are three interacting sets of climatic controls, each operating on different space and time scales. These controls are topography, urban morphology and proximity to the sea.

Athens sprawls across the central plain of Attica, often referred to as the Attica Basin, and bound by Mount Egaleo to the west, Mount Parnitha in the north, Mount Penteli in the northeast, Mount Hymettus in the east, and the Saronic Gulf in the southwest (Figure 1). The basin is bisected by a series of small hills.



Figure 1. Map of greater Athens area

Athens enjoys a typical Mediterranean climate, with the mountainous northern suburbs, for their part, experience a somewhat differentiated climatic pattern, with generally lower temperatures. Summers can be particularly hot and at times prone to smog and pollution related conditions (however, much less so than in the past). The average daytime maximum temperature for the month of July is 33.5 °C and heat waves are relatively common, occurring generally during the months of July and/or August, when hot air masses sweep across Greece from the south or the southwest. On such days temperatures soar over 37.8 °C. The all-time high temperature for the metropolitan area of Athens of the order of 48.0 °C was recorded in Elefsina, a suburb industrial zone of Athens in 1987.

Based on a 105-year (1887-2001) surface air temperature record of the National Observatory of Athens, Founda et al., (2004), showed that the annual maximum of the record is from 34.7 to 44.1⁰C. Considering these values as thresholds, Founda et al., (2004), calculated the frequency of occurrence of daily maximum temperatures exceeding these values. The results are illustrated in Figure 2:

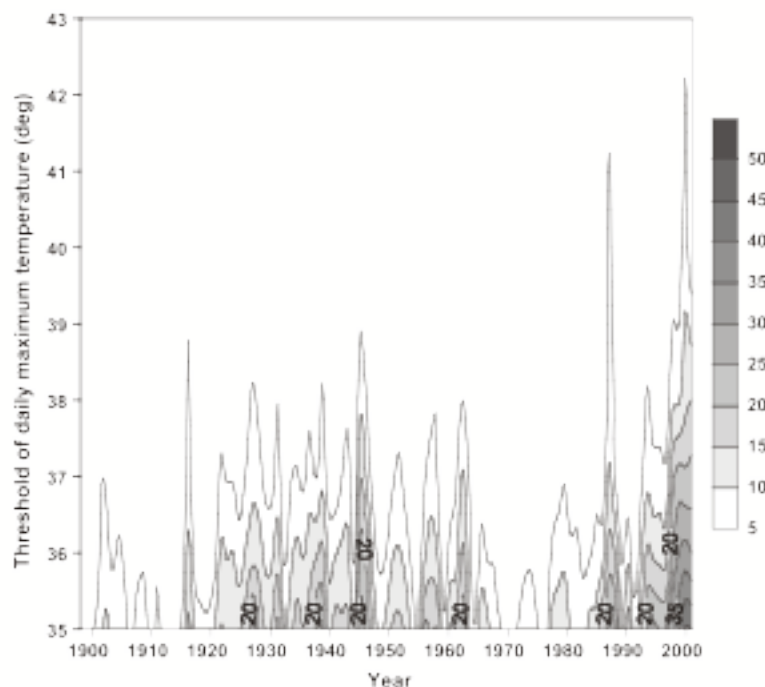


Figure 2. Contours of number of days per year with maximum temperature above the threshold value of the y-axis

What is notable in this figure is the significant increase of the number of days exceeding all threshold values during the last decade and particularly the last 5 years of the record. It was calculated that the total number of days exceeding the threshold of 37.8 ⁰C during the decade 1992–2001 is 113 days, with the same parameter being 435 days for the whole record. This means that 25% of the days exceeding 37.8 ⁰C for a 105-year period occurred during the last 10 years.

It is true that the city of Athens is characterized by a strong heat island effect, mainly caused by the accelerated industrialization and urbanization during recent years. The Municipality of Athens is a densely built city with a narrow street network. In summertime the city suffers from severe heat waves events that create high discomfort to residents and visitors alike. The appearance of Urban Heat Islands in the city is strongly linked to the long-standing problem of high air pollution due to dense traffic and the nearby industries, as well as to intense air conditioning. Limited green and open space areas, lack of water evaporation as well as the conductivity of building and surface materials contribute to the magnitude and the duration of the heat wave events. Athens has a well known, long-standing problem of limited green and open spaces. It is a densely built city suffering a number of heat waves every summer. During the summer of 2007, Athens suffered a severe heat wave that lasted for seven days reaching temperatures as high as 46 ⁰C. A visual inspection of the spatial distribution of the land surface temperature for the heat wave of June 2007, taken from MODIS, is presented in Figure 3.

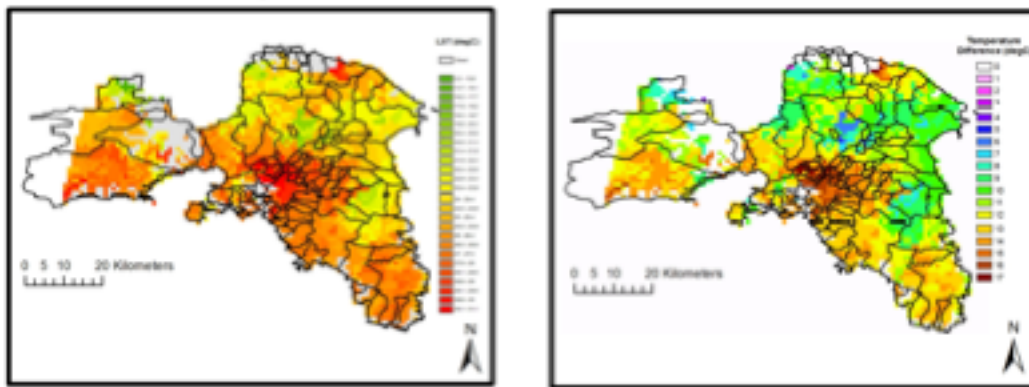


Figure 3. Land surface temperature map (left panel) and urban heat island map (right panel) for Athens on 26 June 2007, at 21:05 UTC

The spatial distribution of land surface temperatures for the Athens basin for the heat wave case study of Figure 3 indicates that southwestern suburbs such as Petroupoli, Nikaia and Kallithea obtain higher surface temperatures than northeastern suburbs such as Kifissia, Chalandri, Zografos etc. This can be explained by the fact that in these suburbs the vegetation cover and density is very low. In addition, the industrial area located in between Nikaia, Kallithea and the centre of Athens appears to exhibit high surface temperatures. Most of the industrial activities are gathered to this area consisting of textile, cement, chemical, fertilizer, paint and paper factories.

To visualize land cover variability in greater Athens area, a land cover / land use map is presented in Figure 4, based on Corine Land Cover (CLC) European database of the European Environmental Agency.

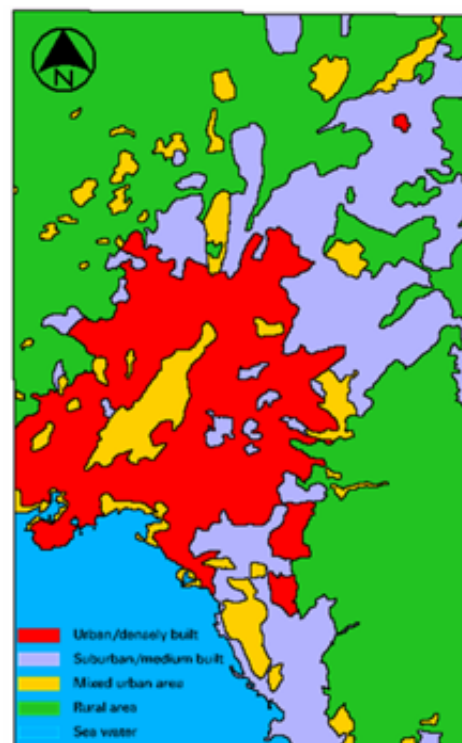


Figure 4. Land cover map of Athens

The land cover presented here is based on a re-classification of the 44 classes of Corine into 5 “urban heat island” related classes, namely: “urban/densely built”, “suburban/medium built”, “mixed urban area”, “rural area” and “water surface”, firstly introduced by Stathopoulou et al. (2007).

Beyond the land use variability, the intensity of the urban heat island in Athens is attributed also in the population growth and industrial development of the city, its topography, physical layout, regional climate and meteorological conditions. Athens is characterized by very strong heat island effects. We mention here a 10-day heat-wave in Athens in 1987, which was resulted in 926 deaths classified as heat-related. However, the attributable excess mortality was estimated to be more than 2000 (Katsouyanni et al., 1988). The severity of heat waves in the metropolitan area of Athens requires accurate monitoring of land surface and air temperatures on a daily basis for the summer period.

2.2 The Project Team and Allocated Tasks

Center for Research and Technology Hellas via the associated Laboratory of Atmospheric Pollution and of Pollution Control Engineering of Atmospheric Pollutants of the Department of Environmental Engineering, DUTH, P.O. Box 447, Vas. Sofias 12, Xanthi 67100, Greece. Tel:+3025410793-79, -80, -83,-84,-86. url:<http://www.env.duth.gr/APL>. Hereafter referred to as CERTH.

National Observatory of Athens, Institute for Space Applications and Remote Sensing (ISARS) Vas. Pavlou & I. Metaxa, Penteli 15236, Greece. Tel: +30-2108109182, Fax:+30-2106138343. url: <http://www.space.noa.gr> Hereafter referred to as NOA.

World Radiation Center, Infrared Radiometry Section, Switzerland. Hereafter referred to as WRC.

The Infrared Radiometry Section of the World Radiation Centre (WRC-IRS) was established in January 2004 at the PMOD/WRC following the recommendation of the Commission for instruments and methods of observation (CIMO) at its thirteenth session in Bratislava, 25 September to 3 October 2002 (Recommendation 1, CIMO-XIII). The WRC-IRS establishes an interim WMO Pyrgeometer Infrared Reference using the procedures and instrumentation that make up the World Infrared Standard Group of Pyrgeometers (WISG). The WRC-IRS holds the global infrared radiation reference and as such defines the longwave infrared scale to which all longwave infrared radiation measurements should be traced. The role of the WRC-IRS is to disseminate this scale to the worldwide community either by individual instrument calibrations at the PMOD/WRC, or preferably through the creation of regional calibration centers which are themselves traceable to the WRC-IRS.

WRC participated in THERMOPOLIS with two separate systems (CG4 and PIR pyrgeometers), measuring longwave downwelling and upwelling radiation. In addition, WRC operated a pyranometer for global SW radiation and a special pyrgeometer only sensitive to the 8-14 micrometer band. With the latter instrument it

is possible to determine the temperature of the boundary layer.

National Technical University of Athens, Laboratory of Laser Development and Applications, Laser Remote Sensing Unit (LRSU), Department of Physics School of Applied Mathematical and Physical Sciences Zografou Campus GR-157 80 Zografou, Greece Tel:+30 210772 2992/2933, Fax:+30 210772 2928, url: <http://www.physics.ntua.gr/~papayannis/> . Hereafter referred to as NTUA.

Aerophoto Ltd., Vas. Olgas 156, Thessaloniki 54645, tel +302310-857242, -865664, Fax -888459, url: <http://www.aerophoto.gr/en/index.asp>. Hereafter referred to as Aerophoto.

Instituto Nacional de Técnica Aeroespacial, Departamento de Observación de la Tierra, Teledetección y Atmósfera, Carretera de Ajalvir, km. 4; 28850 Torrejón de Ardoz, Madrid, Spain. Hereafter referred to as INTA.

Universidad de Valencia-Estudi General, Facultad de Física, Departamento de Física de la Tierra y Termodinámica C/Dr. Moliner, 50, E-46100 Burjassot, Valencia, Spain. Hereafter referred to as UVEG.

Draxis Ltd, Mitropoleos 63, Thessaloniki 54623, Greece Tel: +302310-274566 Fax: +302310-253819 url: <http://www.draxis.gr>. Hereafter referred to as Draxis.

The proposed work share is as follows:

Center for Research and Technology Hellas(CERTH)–Greece for the following tasks:

- ☐ Contractor
- ☐ Ground atmospheric field measurements
- ☐ Airborne campaign design and planning for in situ data acquisition
- ☐ Data processing
- ☐ Data modeling with LUMPS

National observatory of Athens-Greece for the following tasks:

- ☐ Contractor
- ☐ Ground atmospheric field measurements acquisition
- ☐ Satellite acquisitions
- ☐ Data processing
- ☐ Data processing for comparing ground determined LST's with satellite retrieved LST's

☐ Provision to the project of data and measurements collected with **WRC** pyrgeometers and pyranometers

☐ Data processing for atmospheric corrections

NTUA –Greece for the following tasks:

☐ Sub-Contractor

☐ Field measurements LIDAR

☐ Data processing for atmospheric corrections

University of Valencia (UVEG) –Spain for the following tasks:

☐ Contractor

☐ Field measurements

☐ Design and planning for in situ data acquisition and airborne instrument calibration

☐ Data processing

INTA – Madrid, Spain for the following tasks:

☐ Sub-Contractor

☐ Airborne platform (CASA 212) operations

☐ Airborne campaign design and planning for AHS data acquisition

☐ Survey performance

☐ AHS data process up to level B

Aerophoto-Greece for the following tasks:

☐ Sub-Contractor

☐ Airborne platform (Cessna 310Q) operations

☐ Airborne campaign design and planning for meteorological and flux data acquisition

☐ Survey performance

Draxis-Greece for the following tasks:

☐ Data processing

☐ Database design

☐ Georeferenced data base maintenance.

Institution	Investigator	email	Task
ESRIN	R. Bianchi	Remo.Bianchi@esa.int	P.O
ESRIN	M. Paganini	Marc.Paganini@esa.int	P.O
ESRIN	T. Pearson	tim@rsacl.co.uk	Office Support
CERTH	S. Rapsomanikis	rapso@env.duth.gr	Campaign coord airborne heat fluxes
CERTH	I. Kosmadakis	ikosmada@env.duth.gr	Aircraft electronics and data acquisition
CERTH	E. Karageorgos	vkarageo@env.duth.gr	Aerosol Instruments
CERTH	C. Polyzou	cpolyzou@env.duth.gr	Sonic heat fluxes
CERTH	K. Kourtidis	kourtidi@env.duth.gr	Ground measurements coord/ Heat fluxes
CERTH	G. Loupa	gloupa@env.duth.gr	LUMP/ARM/heat fluxes -TES
CERTH	D. Karali	dkarali@env.duth.gr	Aerosol analyses
CERTH	A. Georgoulas	argeor@env.duth.gr	MODIS/ CALIPSO/ CERES acquisitions
NOA	I. Daglis	daglis@space.noa.gr	Satellite acquisitions
NOA	V. Amiridis	vamoir@space.noa.gr	CIMEL-UVMFR radiation and aerosol data
NOA	E. Gerasopoulos	egeraso@env.noa.gr	Kipp&Zonen PGS 100 sunphotometer
NOA	I. Keramitsoglou	ik@space.noa.gr	Satellite acquisitions
AEROPHOTO	P. Boutsoukis	boutsoukis@otenet.gr	Aircraft operations
AEROPHOTO	G. Noitsis	info@aerophoto.gr	Aircraft operations
NTUA	A. Papayiannis	apdlidar@central.ntua.gr	LIDAR meas.
DRAXIS	E. Kosmidis	kosmidis@draxis.gr	Data base
DRAXIS	P. Symeonidis	symeonidis@draxis.gr	Data base
UVEG-UCG	J. A. Sobrino	sobrino@uv.es	Ground measur. in

			the TIR/VIS/NIR.
UVEG-UCG	G. Soria	guillem.soria@uv.es	Ground measur. in the TIR/VIS/NIR.
UVEG-UCG	J.C. Jimenez	jcjm@uv.es	Ground measur in the TIR/VIS/NIR.
UVEG-UCG	Rosa Oltra	Rosa.oltra@uv.es	Ground measur. in the TIR/VIS/NIR.
UVEG-UCG	Cristian Mattar	Cristian.mattar@uv.es	Ground measur. in the TIR/VIS/NIR.
UVEG-UCG	J. Cuenca	Juan.cuenca@uv.es	Ground data processing
UVEG-UCG	Yves Julien	Yves.julien@uv.es	Ground data processing
UVEG-UCG	V. Hidalgo	M.victoria.hidalgo@uv.es	Ground data processing
UVEG-UCG	B. Franch	Belen.franch@uv.es	Ground data processing

3. Satellite Data Acquisitions and Analyses

3.1 Data Acquisitions

3.1.1 LANDSAT

Landsat acquires thermal infrared images over Athens every 16 days with very high spatial resolution. Landsat-5 TM with a spatial resolution of 120 m and Landsat-7 ETM+ with a resolution of 60 m. This is considered to be suitable for capturing the complex intra-urban surface temperature differences allowing thus, an effective and detailed analysis of the urban thermal environment. Both TM and ETM+ have a single spectral channel (although ETM+ differentiates between low and high gain modes) in the spectral range of 10.40-12.50 μm . In theory, Landsat may acquire images during night-time, in practice though these images are very hard to find. Therefore, only daytime images (of around 09:00 UTC) are available.

Special attention needs to be drawn that since May 31, 2003, the Scan Line Corrector (SLC), which compensates for the forward motion of Landsat-7, failed. Subsequent efforts to recover the SLC were not successful, and the failure appears to be permanent. Without an operating SLC, ETM+ line of sight now traces a zig-zag pattern along the satellite ground track.

Therefore, during the period of the THERMOPOLIS campaign in Athens only LANDSAT TM images were acquired. An example of one collected LANDSAT TM imagery over Athens is shown in Fig. 5:



Figure 5. LANDSAT TM imagery acquired on July 24th (08:53 UTC) over the Athens during the THERMOPOLIS campaign. The sensor records information in 7 spectral bands and it has a spatial resolution 30 m in the reflective bands (visible to shortwave infrared) and 120 m in the thermal infrared band.

3.1.2 ASTER

The ASTER (Advanced Spaceborne Thermal Emission and Reflection Radiometer) instrument is on board the Terra platform, which was launched into sun-synchronous Earth orbit on December 18, 1999, and started sending data back to earth in February 2000. The ASTER instrument (<http://asterweb.jpl.nasa.gov>) consists of three separate instrument subsystems. Each subsystem operates in a different spectral region, has its own telescope(s), and was built by a different Japanese company. ASTER's three subsystems are: the Visible and Near Infrared (VNIR), the Shortwave Infrared (SWIR), and the Thermal Infrared (TIR).

VNIR: The VNIR subsystem operates in three spectral bands at visible and near-IR wavelengths, with a resolution of 15 m. It consists of two telescopes--one nadir-looking with a three-spectral-band detector, and the other backward-looking with a single-band detector. The backward-looking telescope provides a second view of the target area in Band 3 for stereo observations.

SWIR: The SWIR subsystem operates in six spectral bands in the near-IR region through a single, nadir-pointing telescope that provides 30 m resolution.

TIR: The TIR subsystem operates in five bands in the thermal infrared region using a single, fixed-position, nadir-looking telescope with a resolution of 90 m. Table 2 summarizes the main ASTER technical characteristics.

Table 2. Main ASTER technical characteristics

VNIR		SWIR TIR	
Ground resolution (m)	15	30	90
Data Rate (Mbps)	62	23	4
Cross-track Pointing (°)	±24	±8.55	±8.55
Cross-track Pointing (km)	±318	±116	±116
Swath Width (km)	60	60	60
Detector Type	Si	PtSi-Si	HgCdTe
Quantization (bits)	8	8	12
Stereo	Yes	No	No
Spectral Region	Band	Band Width (µm)	
VNIR	1	0.52-0.60	
	2	0.63-0.69	
	3	0.76-0.86	
SWIR	4	1.60-1.70	
	5	2.145-2.185	
	6	2.185-2.225	
	7	2.235-2.285	
	8	2.295-2.365	
	9	2.360-2.430	
TIR	10	8.125-8.475	
	11	8.475-8.825	
	12	8.925-9.275	
	13	10.25-10.95	
	14	10.95-11.65	

ASTER has five TIR spectral bands in the range of 8.0-12.0 µm (see Table below) and a spatial resolution of 90 m, offering the best available spatial resolution (commercially), given the known problem of ETM+ onboard Landsat (see section above). The orbit of TERRA and the geometry of acquisition of ASTER allow a temporal resolution of 16 days.

Table 3. TIR Aster bands

ASTER Band	Central Wavelength (µm)
10	8.274
11	8.626

12	9.072
13	10.654

A snapshot of one of the ASTER imagery acquired during the THERMOPOLIS expedition is shown in Fig 6. The image is not useful as it is rather cloudy over critical areas of the Athens urban net.



Figure 6. ASTER imagery acquired during over Athens on July 16th (09:22 UTC), during the THERMOPOLIS campaign. This is a false colour composite image produced from the raw visible and near infrared channels of the sensor (R3G2B1). The sensor records information in 15 spectral channels whereas its spatial resolution varies from 15 m (visible to near infrared channels) to 30 m (shortwave infrared channels) and 90 m (thermal infrared channels).

3.1.3 ATSR and AATSR

The Along-Track Scanning Radiometer (ATSR) and the Advanced ATSR (AATSR) are onboard ESA's ERS-2 and ENVISAT satellites respectively. They both have two TIR spectral bands, centred at 10.8 and 12.0 μm and provide TIR observations as a spatial resolution of 1.1 km at nadir. The first ATSR instrument was launched by ESA in 1991, followed by the launch of ATSR-2 (an enhanced version of ATSR instrument) in 1995. The ATSR channels are at wavelengths of 1.6 μm (visible) and three thermal bands at 3.7 μm , 11 μm , and 12 μm . The major differences of the ATSR-2 instrument from its predecessor include the inclusion of 3 additional spectral bands in the visible part of electromagnetic radiation and of an on-board visible calibration system. The AATSR instrument is largely the same to ATSR-2, with the major advantage of AATSR over ATSR-2 being the telemetry bandwidth available on Envisat, which significantly simplifies the ground processing required for

AATSR data. One of the key characteristics of these instruments includes the application of the along track scanning technique from the instrument's conical scanning mechanism, which allows making two observations of the same point on the Earth's surface from different observation angles. This dual view design is an important characteristic as it permits accounting for the direct measurement of the effect of the atmosphere to the observations acquired, resulting to accurate atmospheric correction of the data. A snapshot of one AATSR imagery acquired during the THERMOPOLIS expedition is presented in Fig 7.



Figure 7. AATSR imagery acquired over Athens on July 24th (08:47 UTC), during the THERMOPOLIS campaign. Nominal pixel size of the sensor is 1 km and it records information at 7 spectral bands from the visible to the thermal infrared part of the electromagnetic radiation.

3.1.4 MODIS

MODIS (or Moderate Resolution Imaging Spectroradiometer) is a key instrument on board the Terra (EOS AM) and Aqua (EOS PM) satellites. Terra's orbit around the Earth is timed so that it passes from north south across the equator in the morning, while Aqua passes south to north over the equator in the afternoon. MODIS has twenty infrared bands; however, two of them are suitable for LST retrievals, namely, band 31 and 32 at 11.0 and 12.0 μm , respectively. The spatial resolution of TIR bands is approximately 1 km. MODIS may also provide information on aerosols and especially aerosol optical depth (using band 4 at 553.6 nm) and Angstrom Exponent (using also spectral information from 860 nm). Aerosol Optical Depth (AOD) at 0.55 μm along with Angstrom Exponent (\AA E) data for both land and ocean from the Moderate Resolution Imaging Spectroradiometer (MODIS) instrument aboard EOS-TERRA satellite will be analyzed for the purposes of the THERMOPOLIS campaign 12-26/7/2009. AOD and \AA E data from MODIS are available on a daily basis spanning from February 2000 and can be coupled with other MODIS products concerning the quality of the measurements, the fraction of fine mode aerosols and the cloud

coverage during the retrieval. Aerosol retrievals from MODIS measurements are performed over land and ocean with two separate algorithms comprehensively described in Kaufman and Tanré (1998). EOS-TERRA passes from north to south across the equator in the morning. The overpass time for Athens is around 10:30 UTC. The whole of the aforementioned MODIS data were available from NASA's Level 1 Atmosphere Archive and Distribution System (LAADS) web site. The spatial resolution of the available collection 5 (C005) data is (10kmx10km) for Level 2 data and (1°x1°) for Level 3 data.

The MODIS instrument provides high radiometric sensitivity (12 bit) in 36 spectral bands ranging in wavelength from 0.4 μm to 14.4 μm . Two bands are imaged at a nominal resolution of 250 m at nadir, with five bands at 500 m, and the remaining 29 bands at 1 km. A ± 55 -degree scanning pattern at the EOS orbit of 705 km achieves a 2,330-km swath and provides global coverage every one to two days. The Scan Mirror Assembly uses a continuously rotating double-sided scan mirror to scan ± 55 -degrees and is driven by a motor encoder built to operate at 100 percent duty cycle throughout the 6-year instrument design life. The optical system consists of a two-mirror off-axis afocal telescope, which directs energy to four refractive objective assemblies; one for each of the VIS, NIR, SWIR/MWIR and LWIR spectral regions to cover a total spectral range of 0.4 to 14.4 μm . A highperformance passive radiative cooler provides cooling to 83K for the 20 infrared spectral bands on two HgCdTe Focal Plane Assemblies (FPAs). Novel photodiode-silicon readout technology for the visible and near infrared provide unsurpassed quantum efficiency and low-noise readout with exceptional dynamic range. Analog programmable gain and offset and FPA clock and bias electronics are located near the FPAs in two dedicated electronics modules, the Space-viewing Analog Module (SAM) and the Forward-viewing Analog Module (FAM). A third module, the Main Electronics Module (MEM) provides power, control systems, command and telemetry, and calibration electronics. The system also includes four on-board calibrators as well as a view to space: a Solar Diffuser (SD), a v-groove Blackbody (BB), a Spectroradiometric calibration assembly (SRCA), and a Solar Diffuser Stability Monitor (SDSM). Fig 8 presents a snapshot of one of the MODIS images collected over Athens during the period of the THERMOPOLIS campaign.

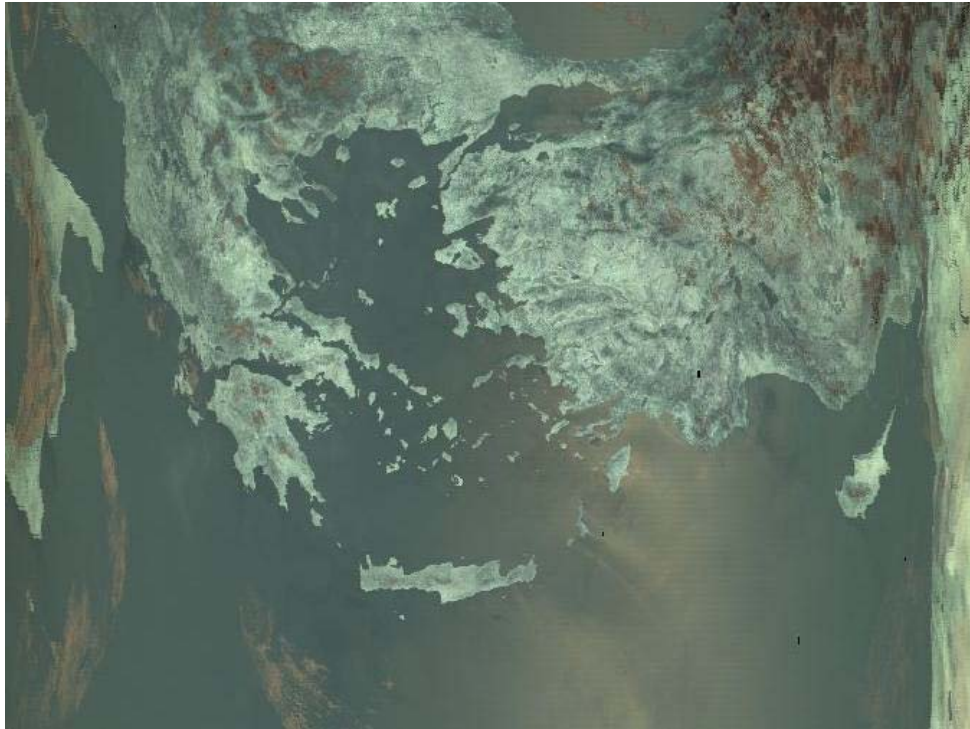


Figure 8. MODIS Terra imagery acquired over Athens on July 18th (09:09 UTC) during the period of the THERMOPOLIS campaign. MODIS radiometer is on-board both the Terra and Aqua NASA platforms and is able to record information in 36 spectral channels from the visible to the thermal parts of the electromagnetic spectrum and at a variable spatial resolution ranging from 250 m to 1 km.

Aerosol Optical Depth (AOD) at $0.55\mu\text{m}$ along with Ångström Exponent (\AA E) data for both land and ocean from the Moderate Resolution Imaging Spectroradiometer (MODIS) instrument aboard EOS-TERRA satellite were obtained through NASA's Level 1 Atmosphere Archive and Distribution System (LAADS) web site (<http://ladsweb.nascom.nasa.gov/>) for the purposes of the THERMOPOLIS campaign (12-26/7/2009). The data consist of collection 5 (C005) Level 3 daily Joint Aerosol/Water vapour/Cloud files (MOD04_L2) and Level2 Aerosol files (MOD04_L2). Concerning the Level 3 data, a total of 15 files were obtained, one for each day, with a spatial resolution of 1×1 degrees. On the other hand, since Level 2 data have a finer resolution of $10\times 10\text{ km}^2$, a total of 103 files were obtained for the greater area of Mediterranean area [30° - 50°N , 0° - 40°E]. Except for the 15-days period of the campaign, Level 3 data for the greater area of Athens are also available for the whole MODIS operation period 2/2000-7/2009. Aerosol retrievals from MODIS measurements are performed over land and ocean with two separate algorithms. EOS-TERRA passes from north to south across the equator in the morning. The morning overpass time for Athens is around 10:30UTC.

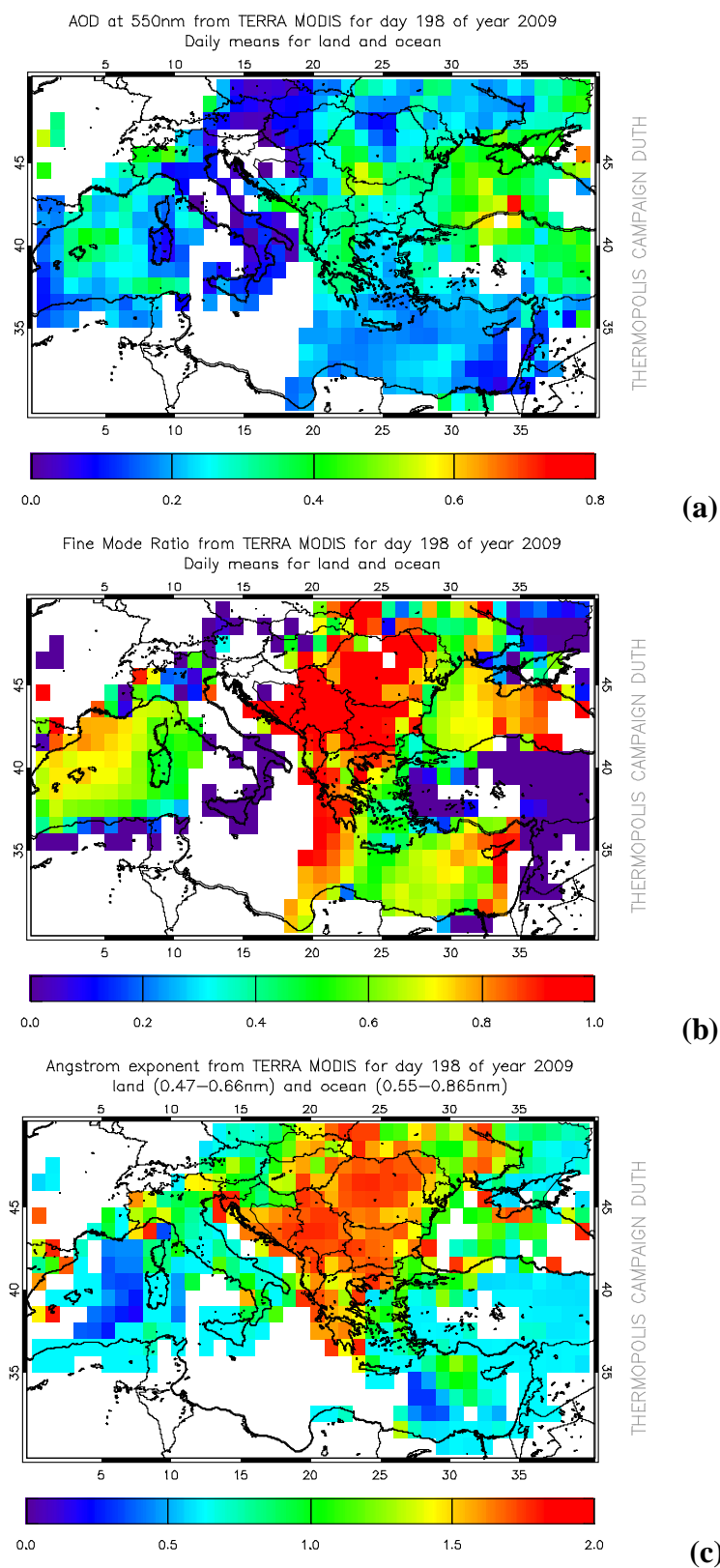


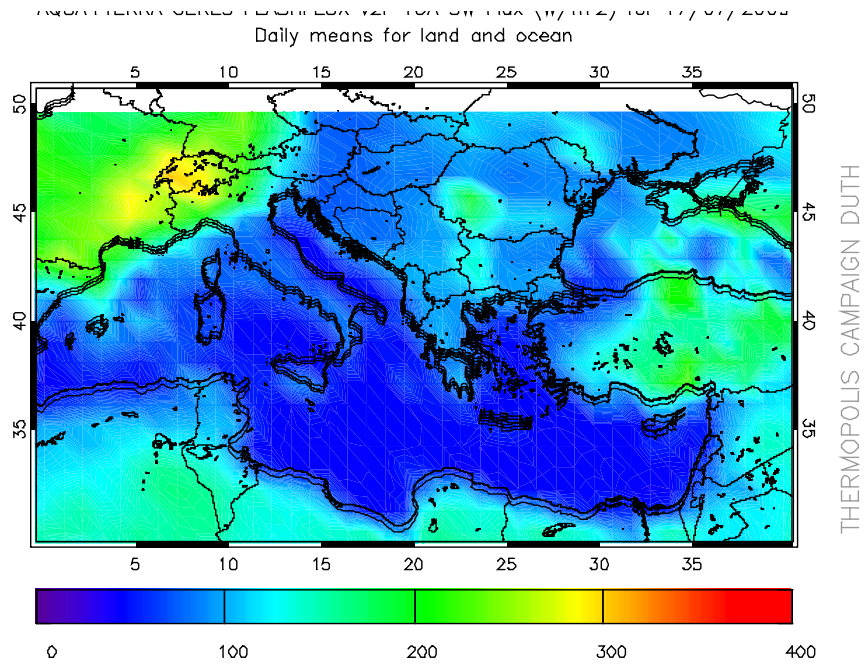
Figure 9. Maps with Level 3 MODIS (C005) AOD550 data (a), Fine mode ratio (b) and Ångström exponent (c) data for 17/7/2009.

3.1.5 CERES

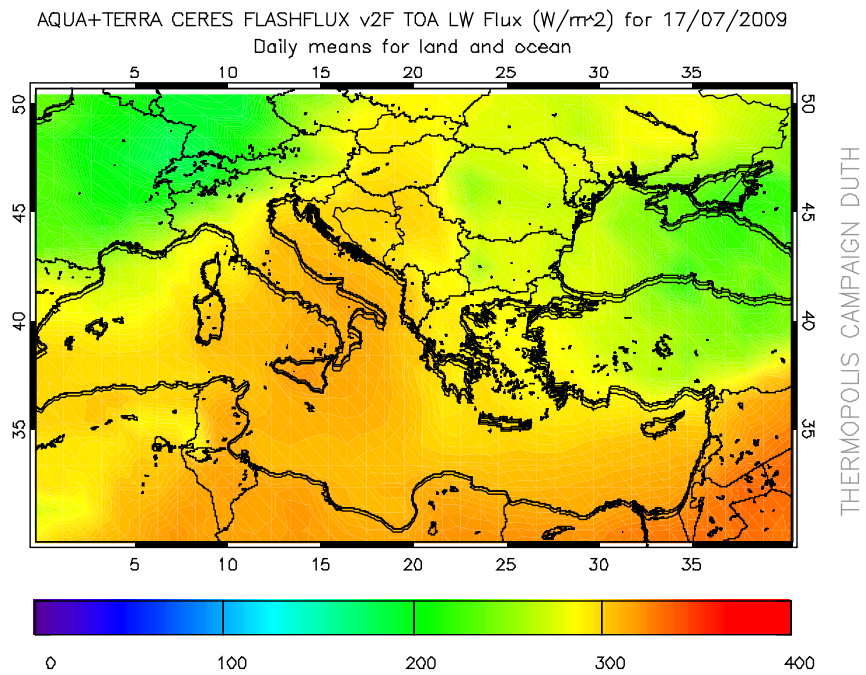
Clouds and the Earth's Radiant Energy System (CERES) aboard EOS-TERRA and EOS-AQUA satellite instruments share the same morning/noon overpass times with MODIS (TERRA ~10:30p.m. and AQUA ~13:30p.m.). CERES provides radiometric measurements of the Earth's atmosphere from 3 broadband channels: a shortwave (0.3-5 μ m), a total (0.3-200 μ m) and an infrared window channel (8-12 μ m). There are two identical instruments aboard EOS-TERRA, one operating in a cross-track scan mode and the other in a biaxial scan mode with a nadir FOV of 20km (FM1 and FM2). The same stands for EOS-AQUA with CERES FM3 and FM4. The data that lie within the scopes of our campaign include measurements of the top of atmosphere radiances along with a set of other parameters that enable the calculation of the corresponding fluxes in W/m². The dataset denoted as FLASH_TISA_Terra+Aqua_Version2F includes synergistic TERRA FM1 and AQUA FM3 daily and hourly gridded (1deg) measurement files, while, the dataset denoted as FLASH_SSF_Terra-FM1-MODIS_Version2F includes TERRA FM1 hourly single scanner footprint measurement files with a spatial resolution of 20km. Both datasets are available from NASA's Langley Atmospheric Science Data Center (ASDC). 15 files from the first dataset and 357 files from the second dataset were obtained through (http://eosweb.larc.nasa.gov/PRODOCS/flashflux/table_flashflux.html) for the period of the campaign (12-26/7/2009).

Table 4. Ceres and MODIS overpasses over Athens

Day	Date	MODIS	CERES
Sun	12	•	•
Mon	13	•	•
Tue	14	•	•
Wed	15	•	•
Thu	16	•	•
Fri	17	•	•
Sat	18	•	•
Sun	19	•	•
Mon	20	•	•
Tue	21	•	•
Wed	22	•	•
Thu	23	•	•
Fri	24	•	•
Sat	25	•	•
Sun	26	•	•



(a)



(b)

Figure 10. Map with daily TERRA+AQUA (FLASHFLUX v2F) Shortwave TOA Flux (W/m²) (a), and Longwave TOA Flux (W/m²) (b) data for 17/7/2009.

3.1.6 CALIPSO

Cloud Aerosol Lidar and Infrared Pathfinder Satellite observations (CALIPSO) combines a polarization lidar instrument (532nm and 1064nm) with passive infrared and visible imagers to probe the vertical structure and properties of thin clouds and aerosols. CALIPSO data set starts from June 2006. The Level1 aerosol data include

Lidar attenuated backscatter while Level2 data parameters such as integrated attenuated backscatter aerosol profiles, aerosol optical thickness, etc. For the THERMOPOLIS campaign either Level 1B profile data or Level2 aerosol data are going to be used depending on the analysis applied on the aerosol data from the rest instruments. A table follows with the CALIPSO closest daytime and nighttime overpass times and the corresponding distances from Athens [37.5N, 23.8E] for the days of the campaign. CALIPSO's overpass distance from Athens center is varying between 4-90 km. It is true that CALIPSO's profiles can be used for the Greater Athens area only under horizontal homogeneity of aerosol distribution. There is not a clear threshold for the selection of an appropriate CALIPSO profile which will be representative for all of the city. Satellite aerosol profiles are used in conjunction with ground-based lidar data and after validation of their accuracy and representativeness using synergistic sunphotometric and airborne aerosol measurements in parallel with air mass back-trajectories calculations.

Table 5. Calipso overpasses over Athens

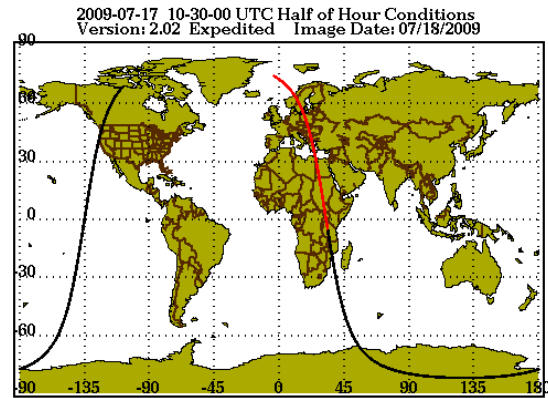
Day	Date	Daytime	Distance	Nighttime	Distance
Sun	12	11:26	371km	00:23	249km
Mon	13	12:09	583km	01:06	705km
Tue	14	11:13	644km	00:10	521km
Wed	15	11:56	311km	00:54	433km
Thu	16	11:01	916km	00:02	794km
Fri	17*	11:45	38km	00:41	160km
Sat	18	12:28	992km	23:45	1066km
Sun	19*	11:33	235km	00:29	112km
Mon	20	12:16	719km	01:11	842km
Tue	21	11:20	507km	00:17	385km
Wed	22	12:03	447km	01:00	569km
Thu	23	11:07	780km	00:04	658km
Fri	24*	11:50	174km	00:47	297km
Sat	25	10:54	1052km	00:08	930km
Sun	26*	11:39	98km	00:35	24km

NOTES:

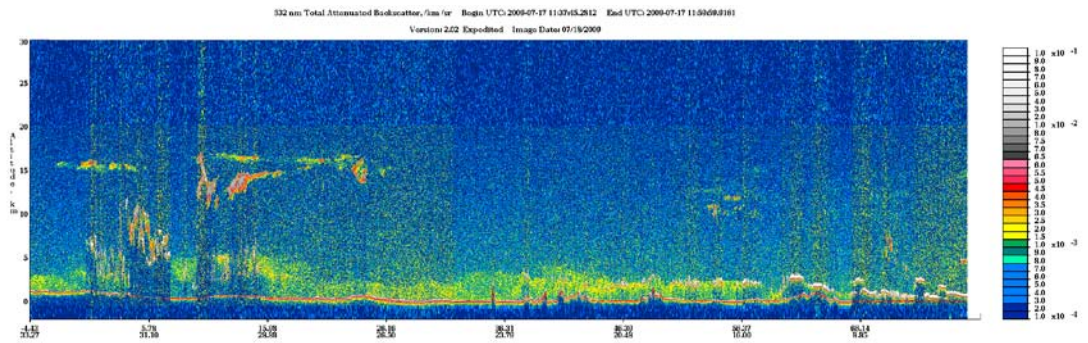
* means that the satellite nearest overpass point is relatively close to Athens

For the scopes of the THERMOPOLIS campaign we have obtained CALIPSO images with the total attenuated backscatter coefficient at 532nm which gives us an indication of the altitude and the concentration of aerosol plumes. The images were downloaded from (http://www.calipso.larc.nasa.gov/products/lidar/browse_images/show_calendar.php) and are part of the Lidar browse images for expedited release dataset (v2.02). As it is discussed on the website, these expedited CALIPSO browse images have a processing latency of about 12 hours. These products use degraded attitude information, a simple calibration scheme based on climatology and are made available to support operational forecasting activities. When available, the standard products should be used for detailed science analysis. However, the standard product is available only until 16/2/2009. We will work with the expedited images and when available we will also use the standard images. We have obtained images with a

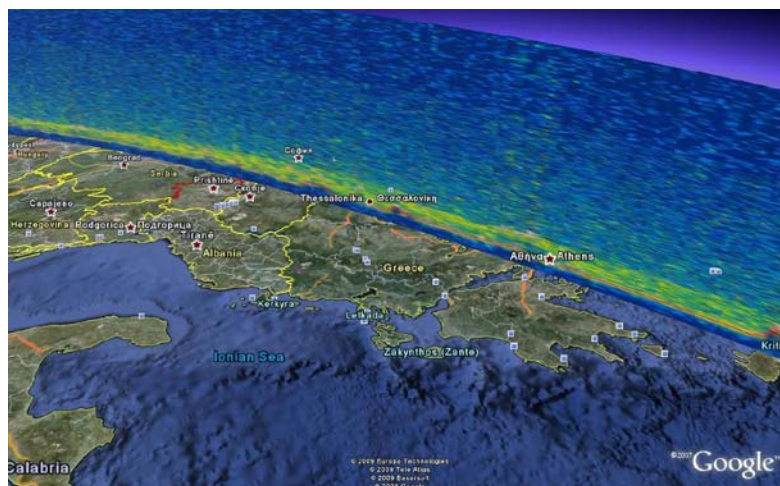
moderate orbit distance from Athens [37.5°N, 23.8°E] for the days (17/7, 19/7, 24/7 and 26/7) of the campaign. Images were also downloaded for 12/7 and 15/7 even though the distance was bigger.



(a)



(b)



(c)

Figure 11. Morning CALIPSO Lidar browse images from expedited release dataset (v2.02). An orbit picture (a), an attenuated backscatter coefficient at 532nm profile picture (b) and an attenuated backscatter coefficient at 532nm profile google earth picture for 17/7/2009. The estimated overpass time is ~11:45UTC and the minimum distance is ~38km.

3.1.7 AVHRR

The Advanced Very High Resolution Radiometer (AVHRR) sensor is carried on NOAA's Polar Orbiting Environmental Satellites (POES) starting with TIROS-N in 1978. AVHRR provides four- to six-band multispectral data from the NOAA polar-orbiting satellite series. Onboard the TIROS-N, NOAA-6, 8 and 10 POES Satellites, the AVHRR Sensor measures in four spectral bands, while on the NOAA-7, 9, 11, 12 and 14 POES Satellites, the sensor measures in five bands. The AVHRR/3 sensor on NOAA-15-19 measures in six bands though only five are transmitted to the ground at any time. One of the key advantages of AVHRR is that it provides a fairly continuous global coverage since June 1979, at a spatial resolution of 1.1 kilometer at nadir. The orbits for each satellite are timed to allow complete global coverage twice per day, per satellite (normally daytime and a night-time view of the earth) in swaths of about 2,600 km in width. The number of daily acquisitions over an area of interest depends on the number of operational NOAA satellites. Generally speaking, POES satellites operate in relatively low orbits, ranging from 830 to 870 km above the Earth. Currently 5 NOAA satellites are operational providing an average 12 images per day, whereas the most recent NOAA AVHRR satellite (i.e. NOAA-19) was launched on 6 February 2009. A snapshot of one NOAA AVHRR imagery acquired over Athens during the THERMOPOLIS expedition is shown in Fig 12. The image was acquired in real time from the AVHRR station of the National Observatory of Athens (Institute for Space Applications and Remote Sensing).



Figure 12. NOAA-19 AVHRR imagery acquired on July 19th (12:10 UTC) over Athens during the THERMOPOLIS expedition. NOAA-19 imagery during the period of the campaign was acquired in real time from the NOA/ISARS receiving station. AVHRR has a nominal spatial resolution of 1 km and it records spectral information in 5 bands from the visible to the thermal infrared parts of the electromagnetic spectrum.

3.1.8 SEVIRI

The main limitation of polar satellite systems like the ones listed above, with regard to the needs of a continuous and real-time monitoring, is their low temporal resolution (revisiting capability), which varies inversely with the spatial resolution of the sensor. To this respect only a geostationary system, such as MSG, can be useful. MSG carries the SEVIRI sensor, the only Earth observation sensor allowing for every 15 minutes observations of Europe, and every 5 minutes in the Rapid Scanning Service mode at the expense of coverage. SEVIRI has 12 spectral bands, five of which are operative in the infrared wavelengths. Two bands centered at 10.8 μm and 12.0 μm are sensitive to Earth's surface radiative temperature. For the purposes of THERMOPOLIS 2009, the required LST products were downloaded from the Land Surface Analysis Satellite Applications Facility (LSA SAF). The following Table 6 indicates that 96 images are available daily, however, only the ones necessary for the purposes of the project were included in the THERMOPOLIS database.

An example of one LST imagery acquired for a selected day during the period of the THERMOPOLIS campaign is shown in Fig 13.

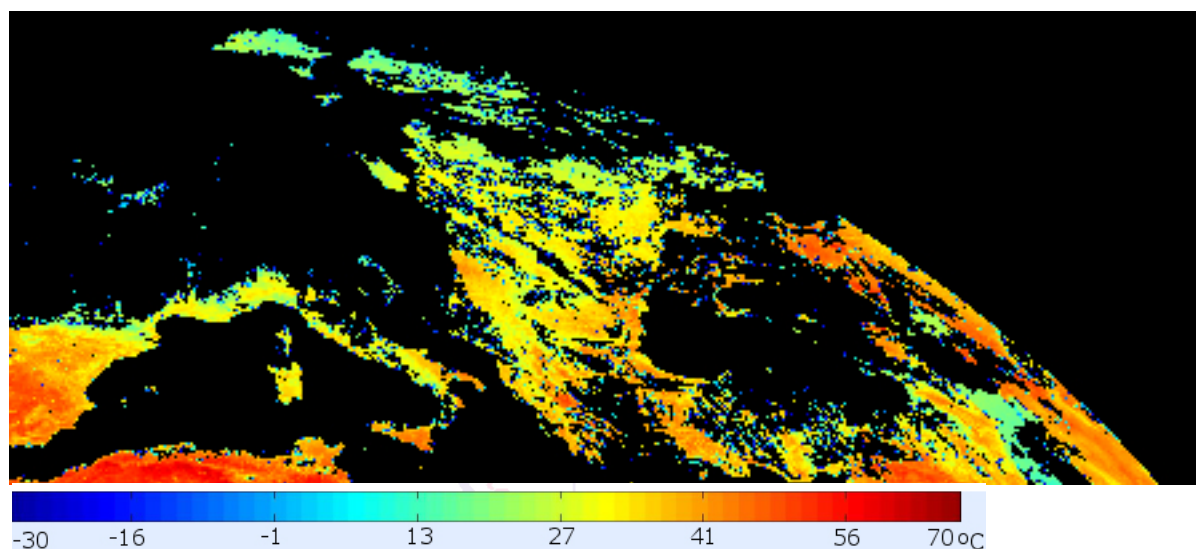


Figure 13. Land Surface Temperature (LST) map for July 18th, one of the days of the THERMOPOLIS expedition, computed from the METEOSAT-2 SEVIRI radiometer.

Table 6. Summary of the satellite observations collected during the THERMOPOLIS campaign. However, the final evaluation of the data to be used in the processing that will follow is subject to quality control (checking of presence of clouds, noise, view angle, etc) that is in progress

<i>Images acquired (including acquisition date)</i>	<i>Spectral Bands</i>	<i>Instrument/Platform</i>
30/06/09 (09:23 UTC) 16/07/09 (09:22 UTC) 23/07/09 (09:28 UTC) 01/08/09 (09:22 UTC)	15	ASTER
17/07/09 (08:47 UTC) 24/07/09 (08:53 UTC) * coincident a/c measurements	7	LANDSAT TM
14/07/09 (09:01 UTC) 15/07/09 (19:46 UTC) 18/07/09 (19:51 UTC) 21/07/09 (08:42 UTC) 21/07/09 (19:57 UTC) 24/07/09 (08:47 UTC) 24/07/09 (20:03 UTC)	7	AATSR ENVISAT
No acquired data have been found for the THERMOPOLIS period (based on a search in EOLISA archive)		ATSR ERS

Continuous, 4 scenes per day (2 daytime, 2 nighttime)	36	MODIS (Terra & Aqua)
Continuous, 3 scenes per day (2 daytime, 1 nighttime)	5	AVHRR NOAA
Continuous, 96 scenes per day (one scene every 15 minutes, not all scenes were used)	LST PRODUCT (from LAND SAF)	SEVIRI METEOSAT

Table 7. Summary of the Aerosol and Flux satellite observations collected from DUTH during the THERMOPOLIS campaign

<i>Acquisition period</i>	<i>Instrument</i>	<i>Data Type/Region</i>
12/7/2009-26/7/2009	MODIS (EOS-Terra)	Level 3 (C005)
12/7/2009-26/7/2009	MODIS (EOS-Terra)	Level 2 (C005) (Mediterranean) [30°-50°N, 0°-40°E]
2/2000-7/2009	MODIS (EOS-Terra)	Level 3 (C005)
12/7/2009-26/7/2009	CERES (Terra/Aqua)	daily and hourly gridded (1deg)
12/7/2009-26/7/2009	CERES (Terra)	single scanner footprint (20km)
17, 19, 24, 26/7/2009 (12, 15/7/2009)	CALIPSO	Attenuated backscatter coefficient images v2.02

3.2 Satellite data analyses

3.2.1 Satellite data validation by looking at Marathon Lake and bare soil cases for each image (NOA)

MODIS, AATSR and AVHRR 1-km LST products have been validated against ground-truth data for the THERMOPOLIS campaign period. Specifically, LST in-situ measurements from 2 ground-based (GB) stations have been used to assess the ability of the 1km sensors to evaluate the UHI over cities by using homogeneous areas as targets. LST measurements over bare soil performed with fixed mast instrumentation were used in the first stage. The in-situ measurements were performed at the NTUA's University campus and specifically at the football field (latitude: 37.9814, longitude: 23.7832) for the THERMOPOLIS time frame and they are presented along with the satellite retrievals in the following figure.

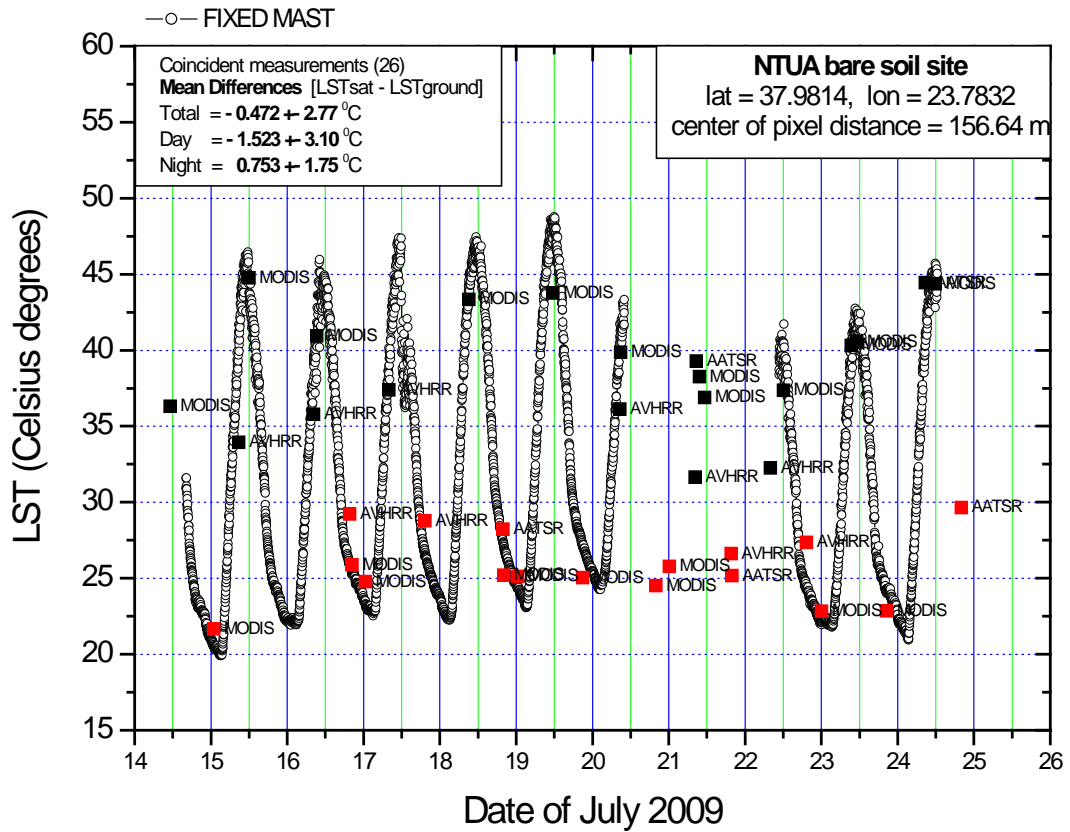


Figure 14. In-situ LST measurements over NTUA's bare soil site along with 1-km satellite retrievals of LST (MODIS, AVHRR, AATSR) during THERMOPOLIS

The minimum distance of the pixel centre from the ground-based station was found equal to 156.64m. The ground-based time-series are presented with open circles, while the satellite products with black or red squares for daytime and night-time retrievals, respectively, along with a satellite label. As it is evident from the figure, the LST satellite products follow the LST diurnal variation recorded with the fixed mast over NTUA's bare soil site.

To quantify the ability of 1-km satellite retrievals to represent LST, the coincident satellite/ground-truth pair of data sets were identified and the mean differences [LST_{satellite} - LST_{ground}] were calculated. For the 26 coincident measurements, a difference of -0.472 ± 2.77 °C was found, indicating less than half a degree underestimation of satellite LSTs.

By separating the coincident measurements in daytime and night-time observations, the mean differences were found equal to -1.523 ± 3.10 °C for 14 **daytime** data pairs and 0.753 ± 1.75 °C for the remaining 12 **night-time** datasets. **These results indicate more accurate satellite retrievals during night-time.** It is stressed that only satellite data with flag equal to 0 were used in this study. To further illustrate the comparison results, a correlation between the satellite and ground-based

retrievals is presented in the following figure for NTUA's bare soil site:

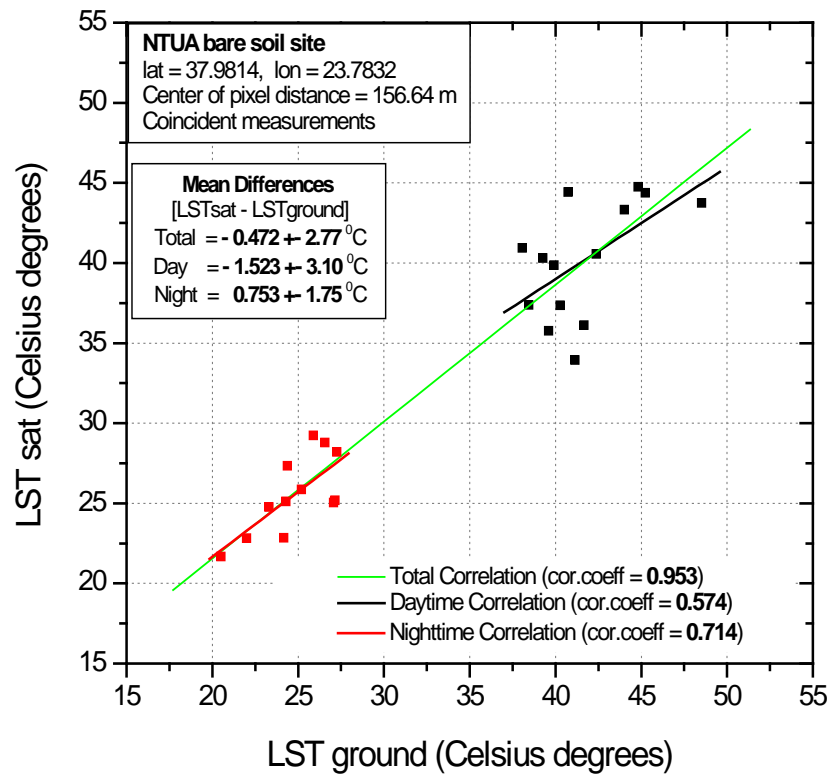


Figure 15. 1-km satellite retrievals of LST versus in-situ LST mast measurements over NTUA's bare soil site during THERMOPOLIS

Again, night-time retrievals are in better agreement with ground-truth data, giving a correlation coefficient of 0.714. The correlation coefficient for daytime measurements was found equal to 0.574. As far as the satellite sensor is concerned, the analysis showed comparable performances as shown in the following figure, the best acquired by MODIS (less than half degree difference) which nevertheless has the largest sample. AVHRR gives a mean difference of approximately -1 degree, but with large standard deviation. AATSR observations are too limited in number for concrete conclusions to be drawn.

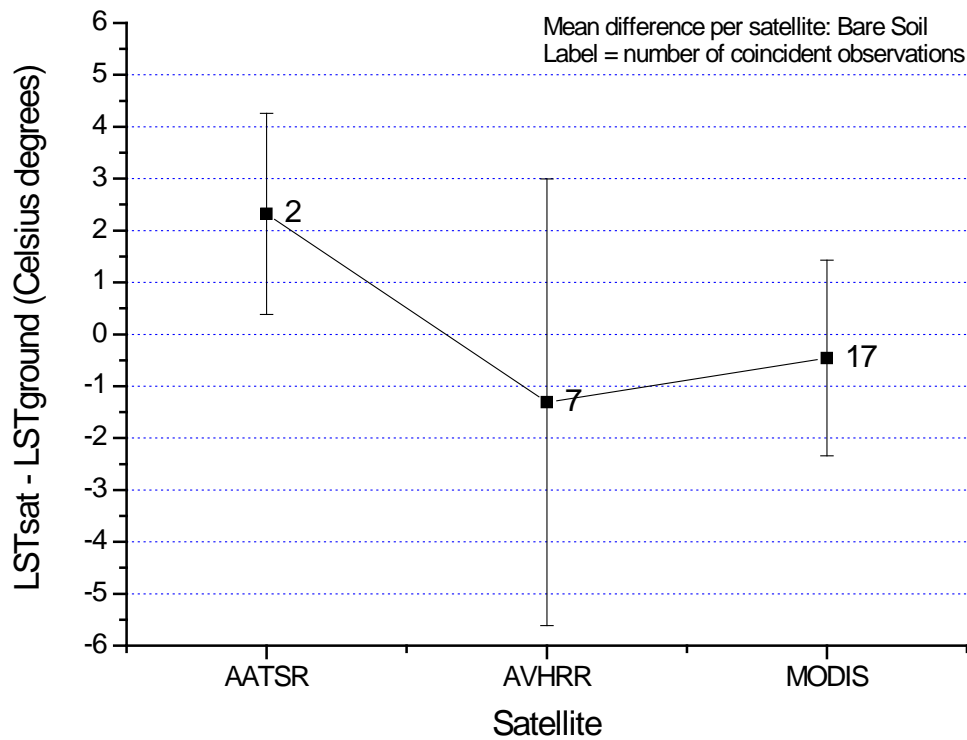


Figure 16. Diference between LST sat and LST ground

Following the same approach, 1-km satellite retrievals were compared with ground-based LST measurements carried out for Calibration/Validation activities over the water surface of Marathon lake (latitude: 38.1676, longitude: 23.9059). The measurements were performed by two instruments, the RAYTEK ST6 broadband radiometer and the 6-band CIMEL ce312. The surface temperature T_s for RAYTEK instrument were obtained from measurements carried out with the broad band radiometer (8-14 μ m) assuming the emissivity obtained for the broad band of the CIMEL 6 by applying TES to the CIMEL 6 data, and downward radiation is the downward radiation measured by the broad band of the CIMEL 6. These retrievals are presented in the following figure with open circles for CIMEL and open squares for RAYTEK, along with the satellite products which are denoted with black or red squares for daytime and night-time retrievals respectively (along with a satellite label).

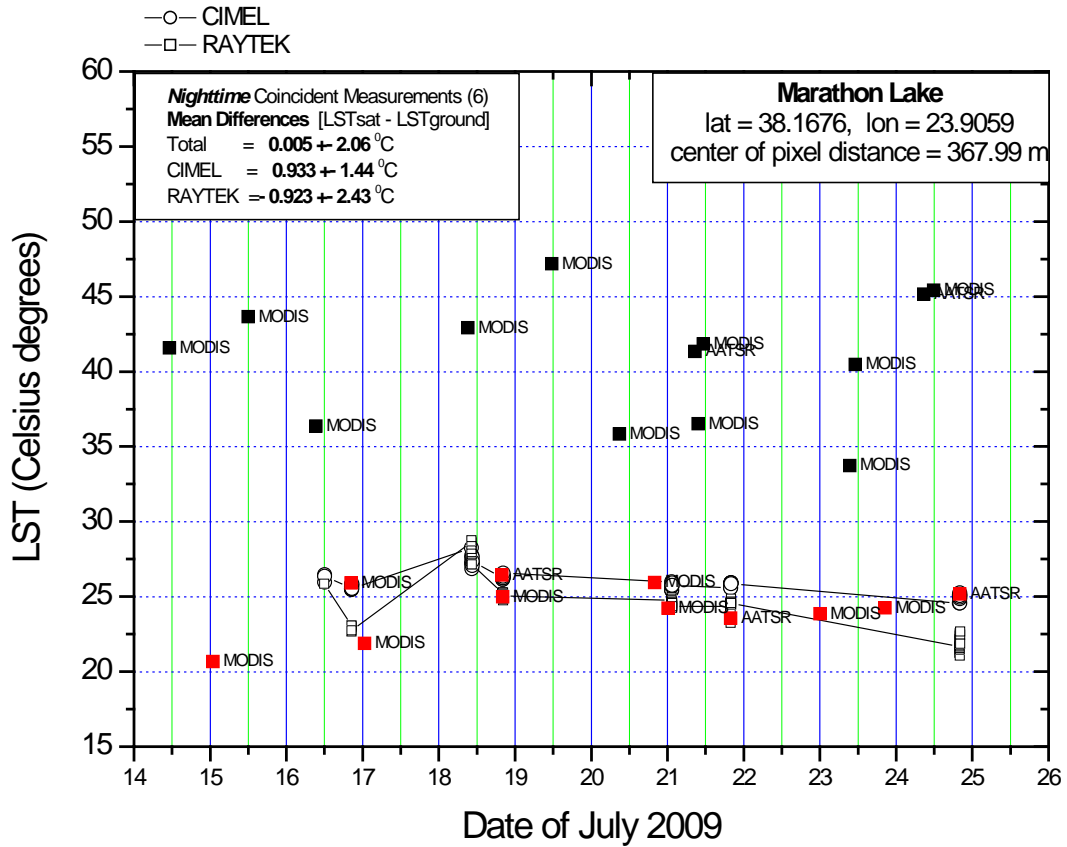


Figure 17. In-situ LST measurements over Marathon lake along with 1-km satellite retrievals of LST (MODIS, AVHRR, AATSR) during THERMOPOLIS

The minimum distance of the pixel centre from the ground-based station was found equal to 367.99m. As it is evident from the figure, the LST satellite products during daytime do not follow the ground-truth measurements. This is attributed to the fact that the satellite pixel includes land, and in the morning the difference between land and water is maximum. For **night-time observations**, 6 coincident satellite/ground-truth pair of data sets were found and the mean differences [LSTsatellite - LSTground] was calculated equal to 0.005 ± 2.06 °C, indicating a perfect match albeit with a 2-degrees standard deviation. By separating the coincident measurements for the different ground-based instruments, a mean difference of 0.933 ± 1.44 °C was found for 3 coincident CIMEL measurements, while for the 3 remaining cases of RAYTEK LSTs, the average difference was found equal to 0.923 ± 2.43 °C, showing a similar response. Again, as in the case of bare soil, only satellite data flagged with 0 were used in this study. Due to the limited time coincidences of data, no correlation plots were produced for Marathon lake observation site.

3.2.2 Check Landsat processing algorithm to resolve the ~20°C difference issue NOA with contribution from UVEG-GCU

The aim of the present action is to present the main finding from the LST comparisons performed between the AHS airborne imagery and the LANDSAT TM sensor (let us call it LST PK, as the algorithm was implemented by Planetek Italia in the framework of UHI project), both acquired on the campaign day July 24th 2009. Initial analysis between the two datasets revealed a bias of the order of 2 °C, the aircraft measuring higher LST than the satellite. This finding together with a number of pixels presenting discrepancies as high as 20 °C, initiated a discussion and experience exchanges among the partners of the consortium. GCU kindly provided their output of LST (let us call it LST CGU) and corresponding differences with the AHS, showing that in their case the mean difference was very close to 0 °C. In addition the number of outlying points was not as high. This is appropriately illustrated below.

The histogram of the differences between AHS and LST PK (Figure 1), as well as the accompanying statistics show that LST PK systematically underestimates LSTs by a mean of 2.3 °C (standard deviation 2.4 °C).

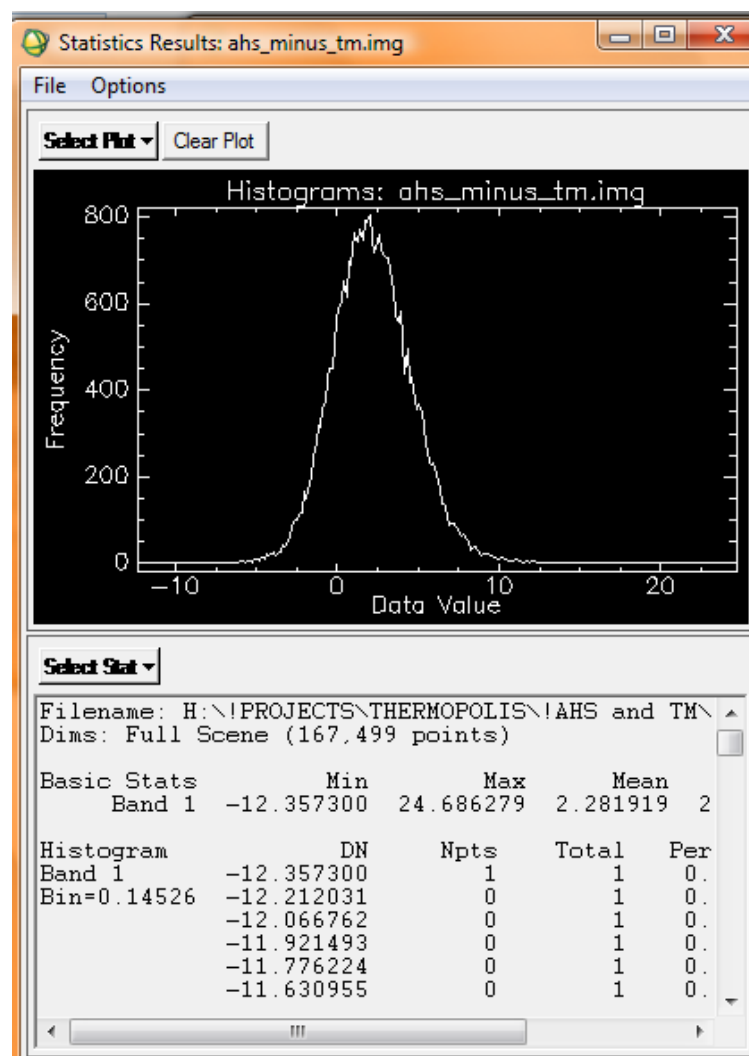


Figure 18: Histogram of the differences between AHS and LST PK.

Analysis of the differences showed that ~0.5% of the pixels fall in the range (-12, -4) °C, whilst ~20% of the pixels fall in the range (+4, +20) °C. It is worth noting that only 1% of the exhibit differences larger than 8.5 °C. The trend of the differences can be also seen in Figure 2, which attributes specific difference ranges to colours to facilitate interpretation. It is suggested to adopt a user-defined colour scale, as the one automatically created by ENVI software may be misleading.

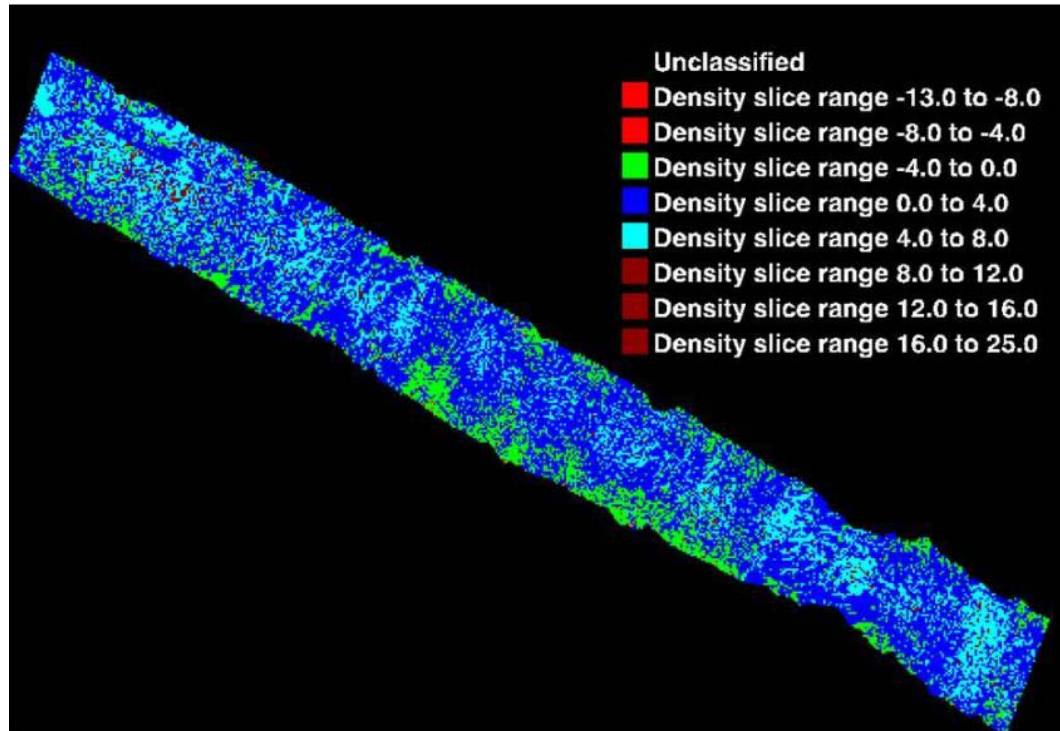


Figure 19: Image of the LST difference between AHS and LST PK. The values are appropriately grouped for easier interpretation.

For consistency, the same methodology was applied to the differences between AHS and LST GCU. Figure 3 shows the histogram of the differences between AHS and LST GCU. In this case the bias of Figure 1 is not observed, as the mean value is -0.09 °C (standard deviation= 2.37 °C). The standard deviation is almost the same as the one of Figure 1, indicating the same spread of values.

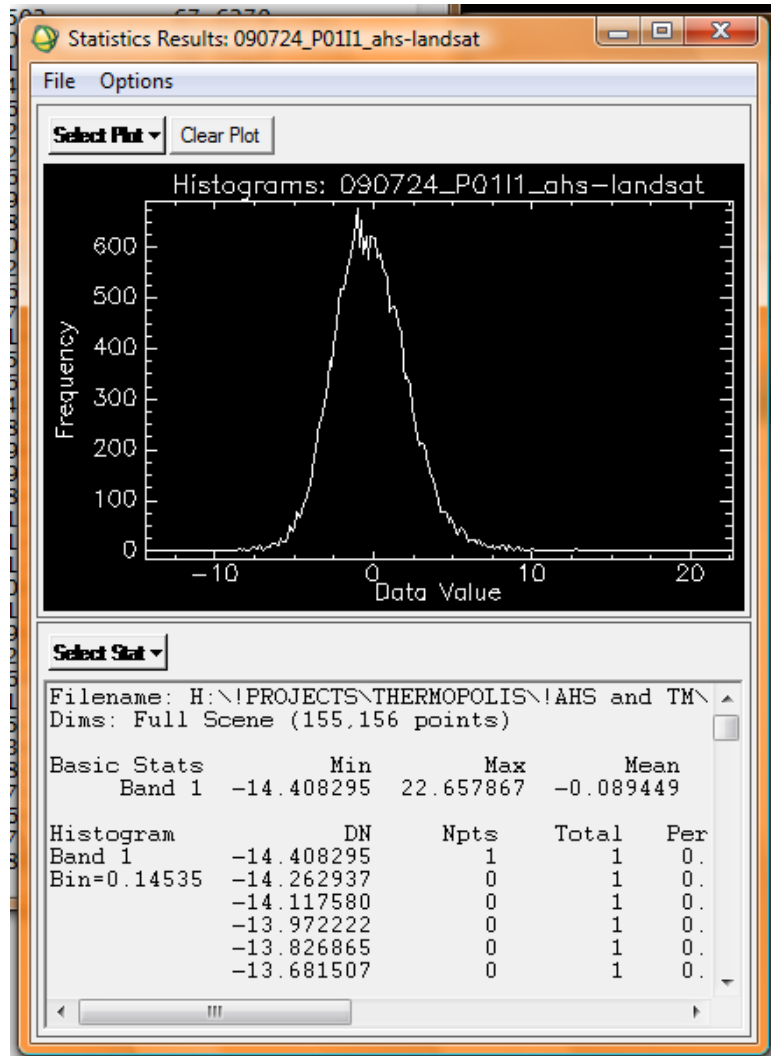


Figure 20: Histogram of the differences between AHS and LST GCU.

Analysis of the differences between AHS and LST GCU showed that ~3.6% of the pixels fall in the range (-14, -4) °C, whilst ~4% of the pixels fall in the range (+4, +20) °C. Only 1% exhibits differences larger than 6 °C. The trend of the differences can be also seen in Figure 4 which attributes specific difference ranges to colours to facilitate interpretation. The colour scale is the same as in Figure 2, so that the results of the different groups can be directly compared.

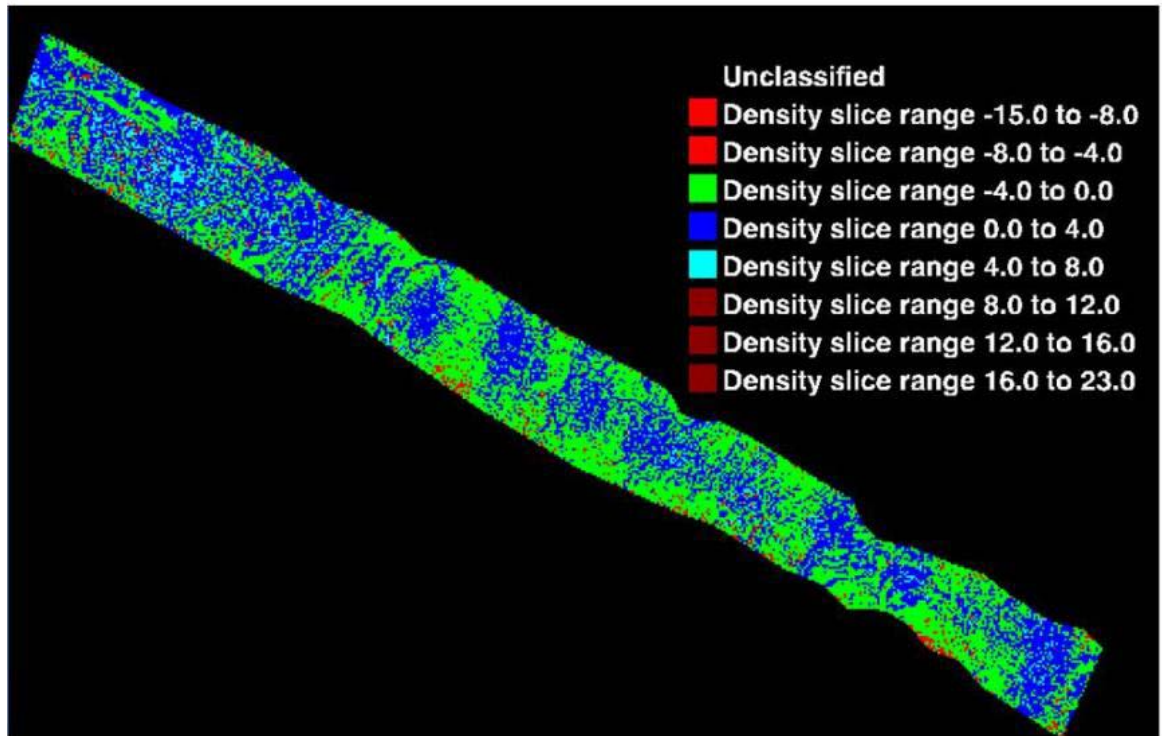


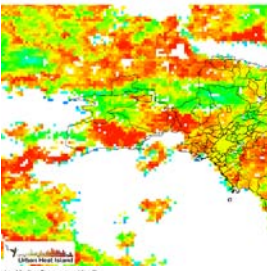
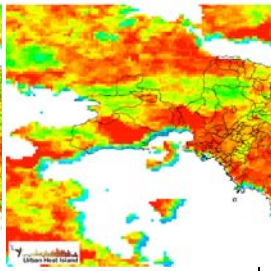
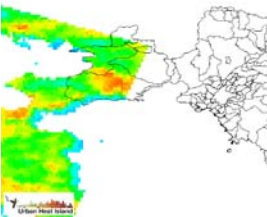
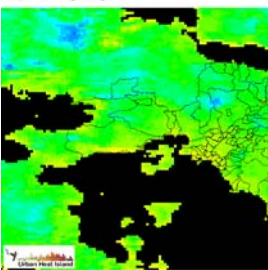
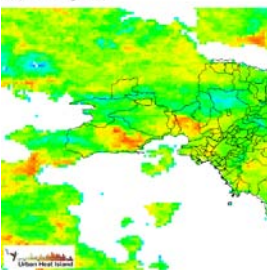
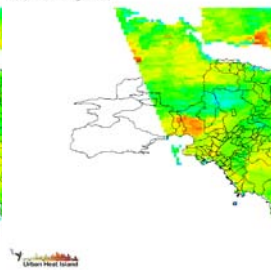
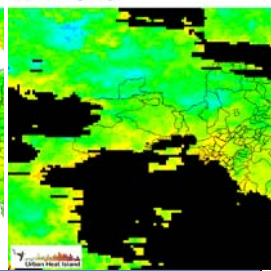
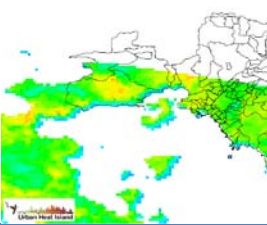
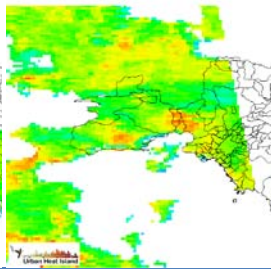
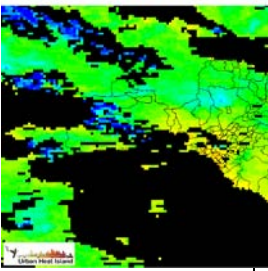
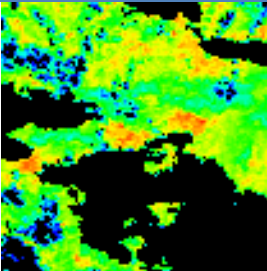
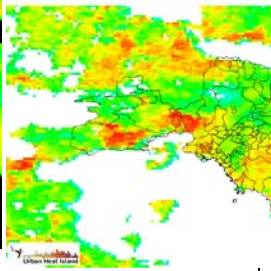
Figure 21: Image of the LST difference between AHS and LST GCU. The values are appropriately grouped for easier interpretation. The colour scale is the same as in Figure 19

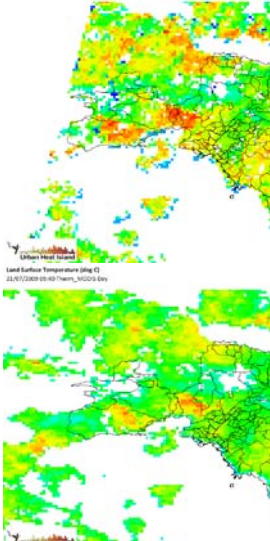
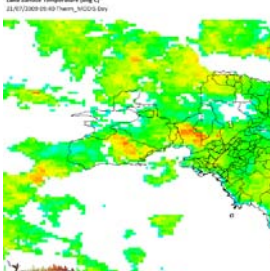
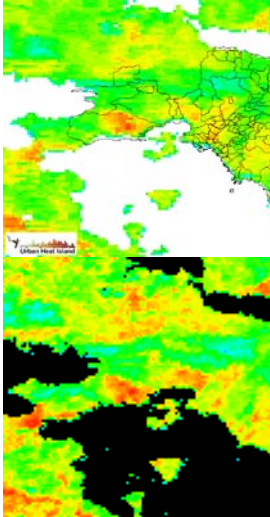
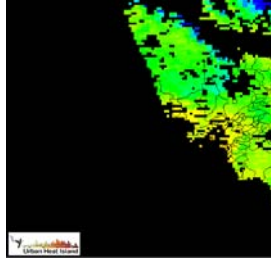
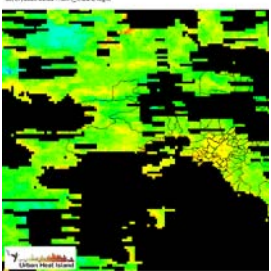
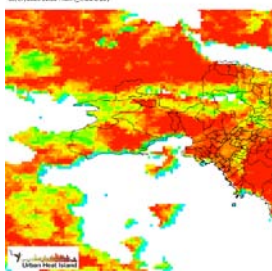
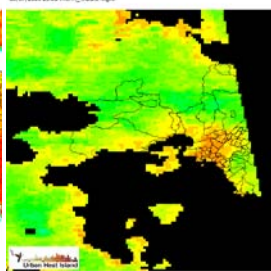
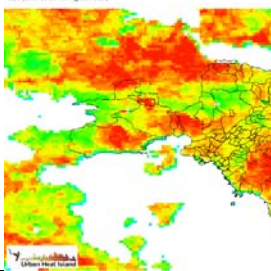
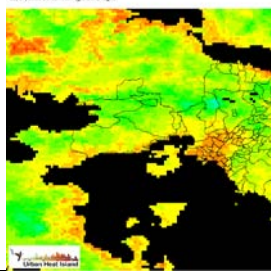
The recognition of this disagreement can be probably attributed to the parameterization of the algorithm for Landsat LST retrieval (R2.5) and requires further investigation.

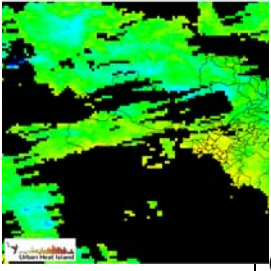
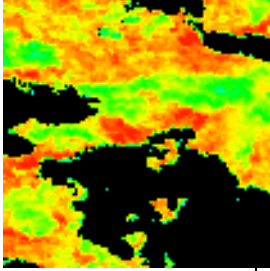
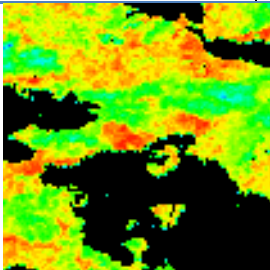
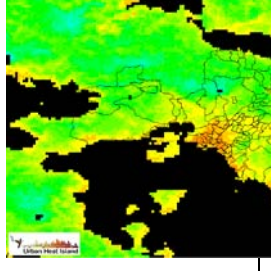
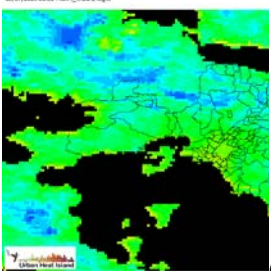
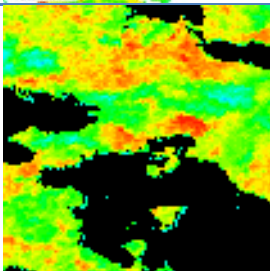
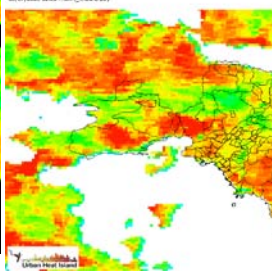
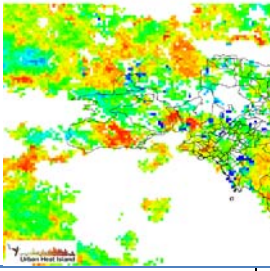
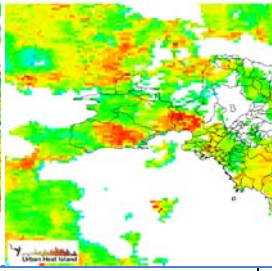
3.2.3 Analysis of variations in LST w.r.t. land use (NOA)

The purpose of this report is to illustrate the thermal patterns of Athens Greater Area and to investigate on the possible causes of regional and local scale hot spots by looking at the relevant land cover/land use. The latter is derived appropriately from CORINE Land Cover 2000 database as well as the optical images of the aircraft acquired during the Thermopolis 2009 campaign. A top down approach is adopted, namely starting from regional to local scale.

The following is a calendar of all the useful 1km images present in the Thermopolis 2009 database (MODIS Terra & AQUA, AATSR, AVHRR) which cover different moments of the day.

	0-1	8-10	10-13	19-21
2 5				
2 4		<div>Land Surface Temperature (Jing CI) 20/07/2009 08:47 (AVHRR Day)</div>  <div>Land Surface Temperature (Jing CI) 20/07/2009 11:30 (Therm_MQDS Day)</div>  <div>Land Surface Temperature (Jing CI) 20/07/2009 08:17 (AVHRR Day)</div> 		
2 3	<div>Land Surface Temperature (Jing CI) 21/07/2009 06:03 (Therm_MQDS Night)</div> 	<div>Land Surface Temperature (Jing CI) 21/07/2009 09:23 (Therm_MQDS Day)</div> 	<div>Land Surface Temperature (Jing CI) 21/07/2009 11:30 (Therm_MQDS Day)</div> 	<div>Land Surface Temperature (Jing CI) 21/07/2009 10:20 (Therm_MQDS Night)</div> 
2 2		<div>Land Surface Temperature (Jing CI) 21/07/2009 07:58 (AVHRR Day)</div> 	<div>Land Surface Temperature (Jing CI) 21/07/2009 11:30 (Therm_MQDS Day)</div> 	
2 1	<div>Land Surface Temperature (Jing CI) 21/07/2009 06:13 (Therm_MQDS Night)</div> 	<div>Land Surface Temperature (Jing CI) 21/07/2009 07:58 (AVHRR Day)</div> 	<div>Land Surface Temperature (Jing CI) 21/07/2009 11:30 (Therm_MQDS Day)</div> 	
		0819_AVHRR		

	0-1	8-10	10-13	19-21
		<p>Land Surface Temperature (img C) 23/07/2009 08:42 AVHRR Day</p>  <p>Land Surface Temperature (img C) 23/07/2009 09:40 Therm_MODIS Day</p> 		
20		<p>Land Surface Temperature (img C) 20/07/2009 08:53 Therm_MODIS Day</p>  <p>0839_AVHRR</p>		<p>Land Surface Temperature (img C) 20/07/2009 20:00 Therm_MODIS Night</p> 
19	<p>Land Surface Temperature (img C) 20/07/2009 00:30 Therm_MODIS Night</p> 		<p>Land Surface Temperature (img C) 20/07/2009 12:30 Therm_MODIS Day</p> 	<p>Land Surface Temperature (img C) 20/07/2009 20:00 Therm_MODIS Night</p> 
18		<p>Land Surface Temperature (img C) 20/07/2009 00:30 Therm_MODIS Night</p> 		<p>Land Surface Temperature (img C) 20/07/2009 20:00 Therm_MODIS Night</p> 

	0-1	8-10	10-13	19-21
1 7		 0802_AVHRR		
1 6		 0822_AVHRR		
1 5		 0843_AVHRR		
1 4				
1 3				

In order to investigate in the possible sources of the high LSTs the topography and land cover of Athens Metropolitan area is discussed. The area of interest is characterised by a complex rugged terrain, as shown below.

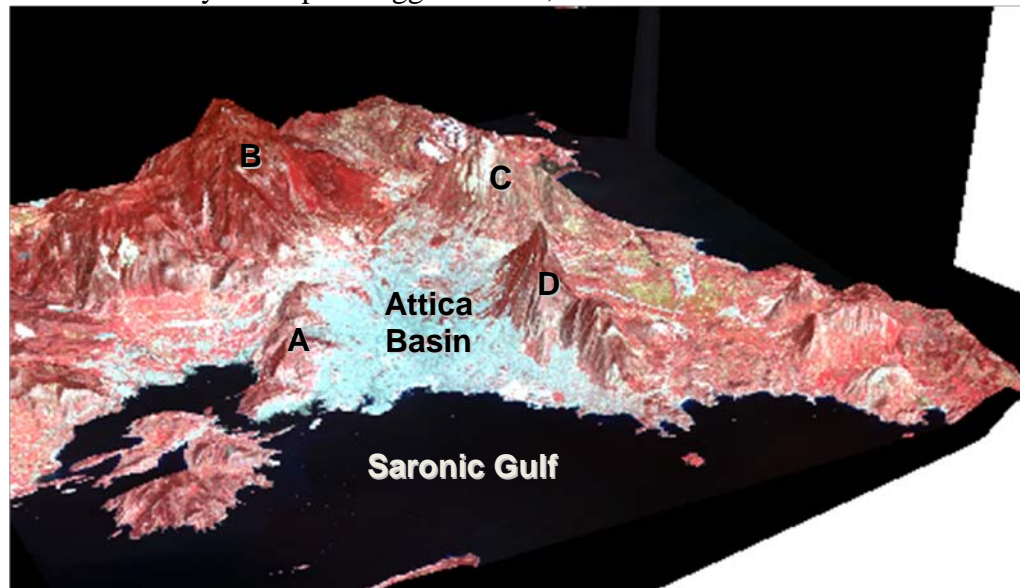


Figure 22 : Exaggerated 3D anaglyph of Athens study area overlaid with a pseudocolour ASTER image (light blue is the urban area and red is vegetation).

Athens sprawls across the central plain of Attica, often referred to as the Attica Basin, and bound by Mount Egaleo (Figure 1, A) to the west, Mount Parnitha (B) in the north, Mount Penteli (C) in the northeast, Mount Hymettus (D) in the east, and the Saronic Gulf in the southwest. The basin is bisected by a series of small hills.

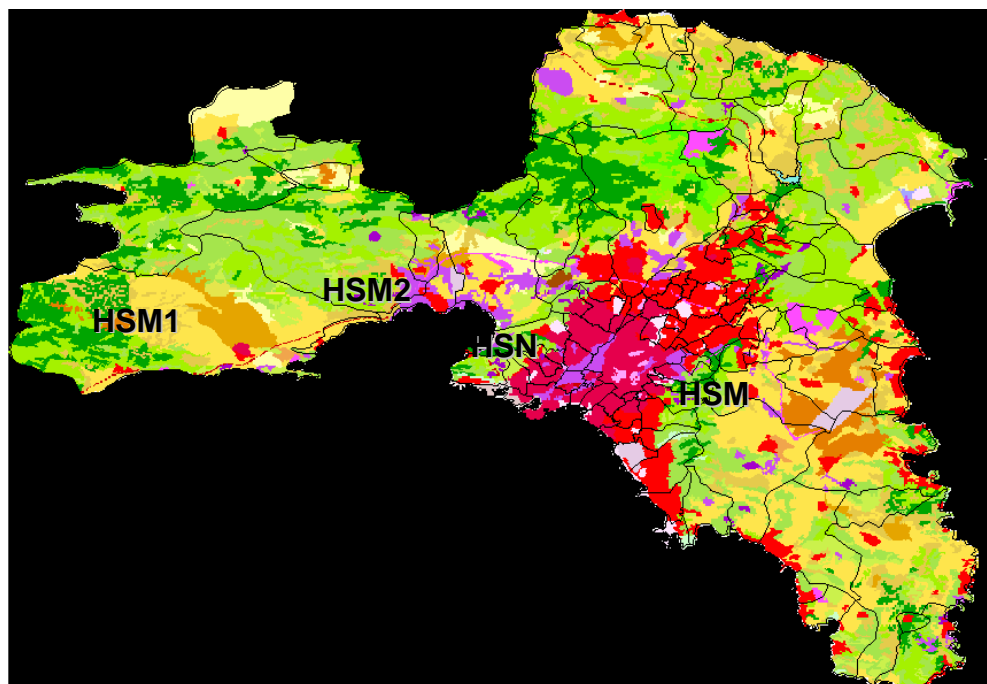


Figure 23: CORINE Land Cover map of Athens study area. The three morning Hot-Spots (HSM) and the night urban heat island (HSN) are defined. The legend is attached in Annex II

On the daytime images (most of which are acquired before 11:00 Local time), surface temperature spatial patterns reveal that the centre of Athens does not exhibit the highest LST. On the contrary, the LST pattern yields the presence of two dominant and one weaker hot spot, as described in Table 21.

Table 21: Morning Hot Spots for the Athens study area

Hot Spot No.	Hot Spot characterisation	Municipalities	Municipalities ID on Map of Annex I	CORINE Land Cover	CORINE Land Cover Code
HSM1	Dominant	Megara	88	Agricultural land	2.2.3, 2.4.2, 2.3.1
HSM2	Dominant	South part of Aspropyrgos and Elefsis	83 and 85	Industrial zone (Fig.3), Discontinuous urban fabric, Airport and Agricultural land	1.2.1, 1.1.2, 1.2.4, 2.4.2
HSM3	Weaker	At and around Koropion, Paiania, Spata-Loutsas	35, 40, 42	Agricultural land, Airport	2.4.2, 2.2.1, 1.2.4



Figure 24: The industrial zone that creates the morning hot-spot of Aspropyrgos and Elefsis (HSM2). It must be noted that the area has (among other industrial activities) refineries consisting of steel tanks. Steel's specific heat is very low ($\sim 500 \text{ J / (kg K)}$) so the area warms up very easily. Steel is also expected to exhibit the small diurnal temperature variations¹.

The hot spots (especially the two dominant ones) exhibit a LST discrepancy of at least 6 degrees from the suburban areas. They all appear in almost every morning image of the campaign.

In general, it can be concluded that the thermal environment of Athens during daytime depends on the combined influence of the area topography and surface cover characteristics. The open plain of Mesogia (HSM3) is mainly covered with sparse low vegetation (particularly olive trees and vineyards) and bare soil (Athens International Airport "El. Venizelos" is also located at this area) and Thriassion (HSM2) is mainly an industrial zone (Figure 3 and comments in the caption). These plains become warm faster than urban areas which are extensively covered by building materials of high thermal inertia such as concrete and asphalt. The influence of topography is also evident in the thermal pattern of the study area, as higher altitudes exhibit lower LST. In addition, one can observe a distinct differential warming during daytime along the

¹ Nicholas M. Short, Remote Sensing Online Tutorial
http://rst.gsfc.nasa.gov/Sect9/Sect9_3.html

East-West direction (Eastern side being warmer) of the mountain slope of Mount Hymettus.

During night-time, the thermal pattern of Athens is inverted as higher surface temperatures are related with the residential urban zones rather than the different urban use zones and rural areas. There is one dominant hot-spot as described in Table 22.

Table 22: Night-time Hot Spots for the Athens study area

Hot Spot No.	Hot Spot characterisation	Municipalities	CORINE Land Cover	CORINE Land Cover Code
N1	Dominant	City of Athens (Athinai), Ilion, Ag. Anargyroi, Nea Halkidona, Peristerion, Egaleo, Kamatero, Nikaia, Keratsinion, Tavros, Ag. Ioanni Renti, Peiraiefs, Moshaton, Kallithea, N. Smyrni, Drapetsona	Urban areas (mainly continuous urban fabric)	Mainly 1.1.1

At that time of day, cooling or warming of a surface is determined by its thermal characteristics. Thus, during night hours, the continuous urban fabric is at least 4 degC warmer than rural areas, due to the lower thermal inertia of the soil compared to concrete. In contrast, the morning hot-spots (Table 1) of the city have faded out in the night and appear to be cooler than the continuous urban fabric owing to the fact that in industrial and agricultural areas usually extended open spaces of bare soil cover most of the area.

The thermal environment of Athens metropolitan area can be better studied using a higher spatial resolution thermal image of Landat TM. This image was acquired on the 24th July 2009 during the Thermopolis campaign. It is the satellite image with the highest spatial resolution, therefore it will be used for studying several thermal patterns at regional and local scale.

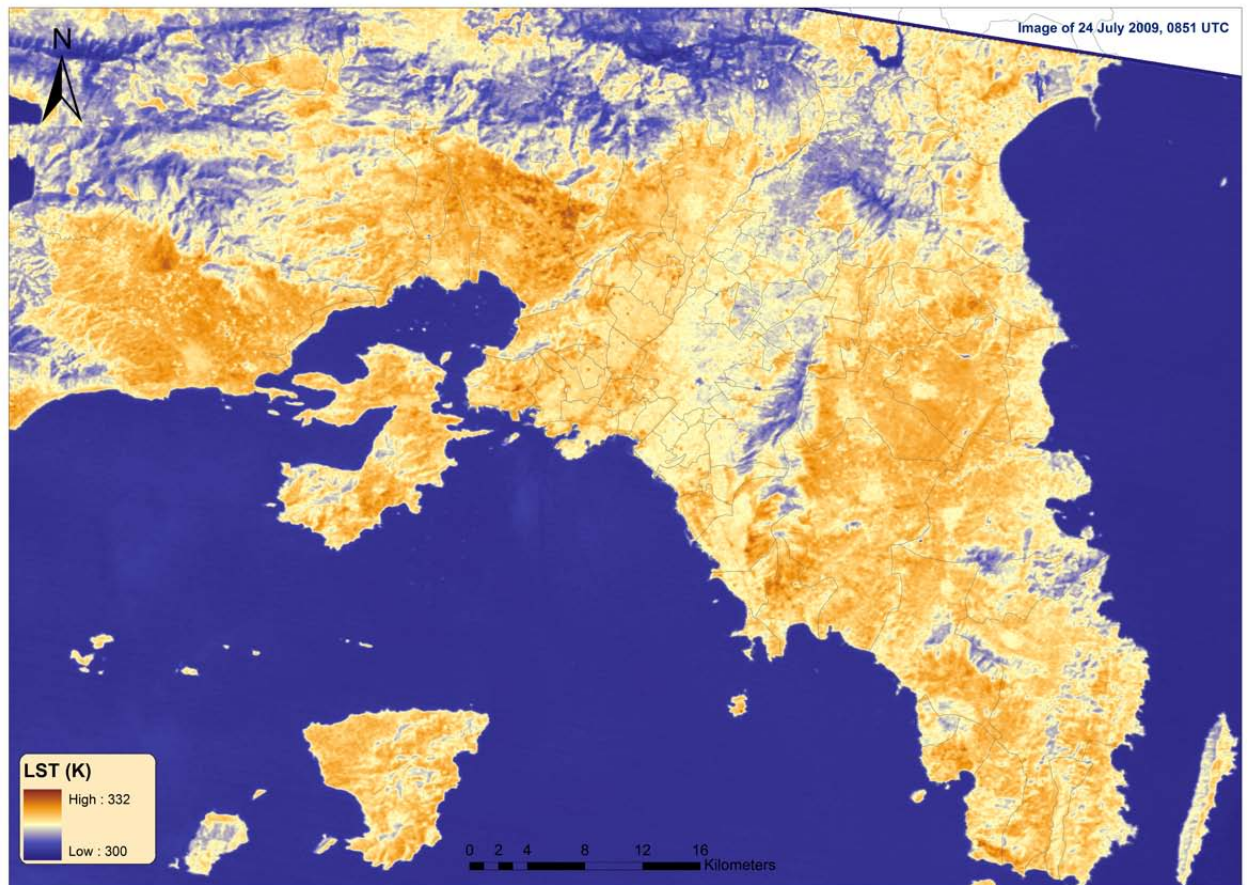


Figure 25: of Landsat TM LST map of Athens using Landsat TM image of 24.07.2009.

Figure 25 shows that there are thermal features at and around the two dominant morning hot spots which are not identifiable in the 1km resolution products (see Calendar of MODIS images of the campaign). Two figures are given to illustrate this point. In particular, Figure 5 illustrates the hot spot of the industrial zone of Aspropyrgos and Elefsis. The image shows that different land cover has a visible effect in the LST distribution, for instance the LST is lower in vegetation areas and urban areas (it is reminded that this is a morning pass). Furthermore, in Figure 6, which is focused at and around the hot spot of Megara, one can clearly see the patterns of agricultural land and forest, which have distinctively different temperatures (the temperatures corresponding to forest-vegetation being lower). The temperature-associated patterns match exactly the CLC2000 patterns.

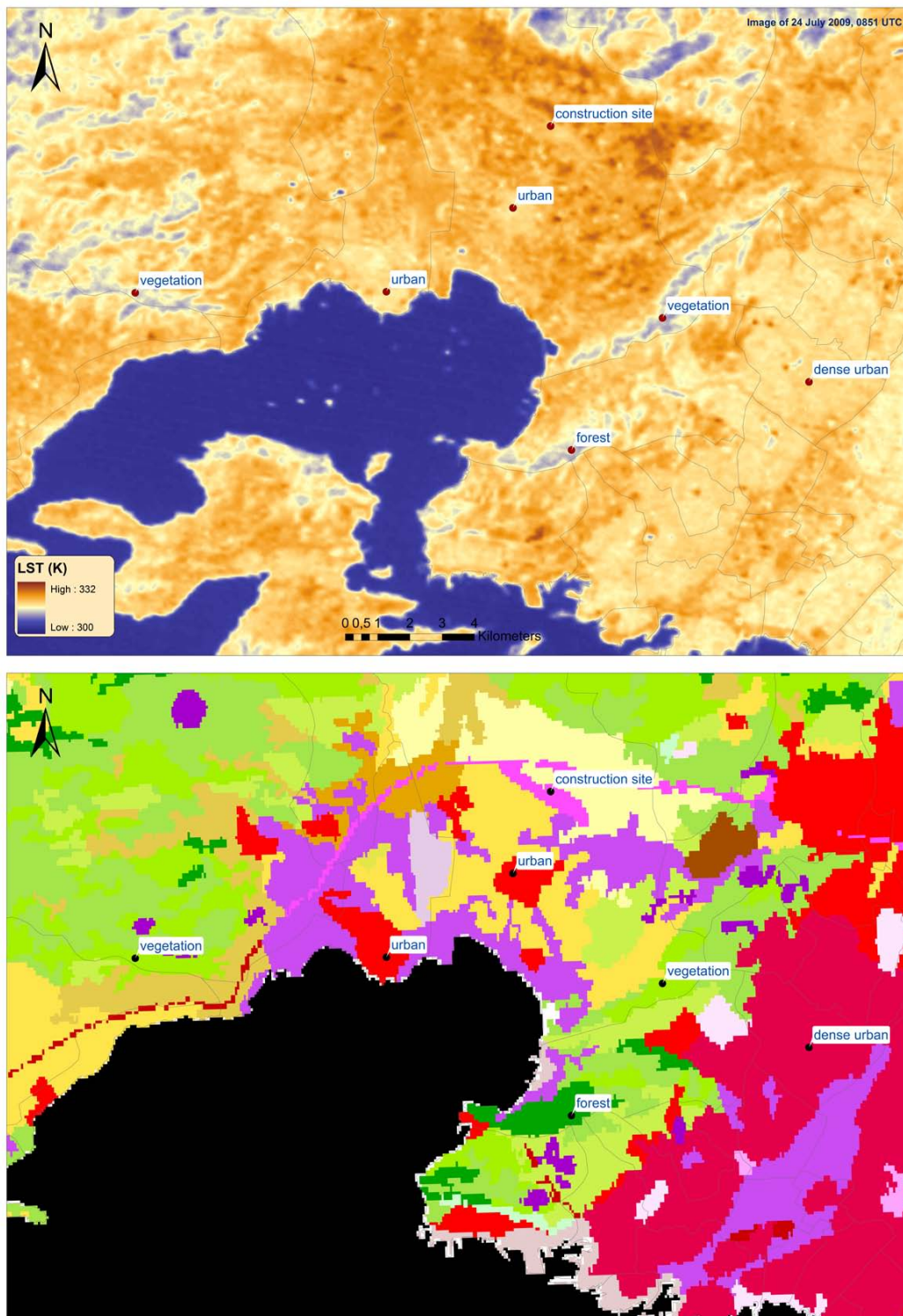


Figure 26: Detail of Landsat TM LST map to focus on the dominant morning hot spot of Aspropyrgos-Elefsis. The map is accompanied by the corresponding CLC2000 map for visual interpretation of the thermal distribution and its relation to land cover type.

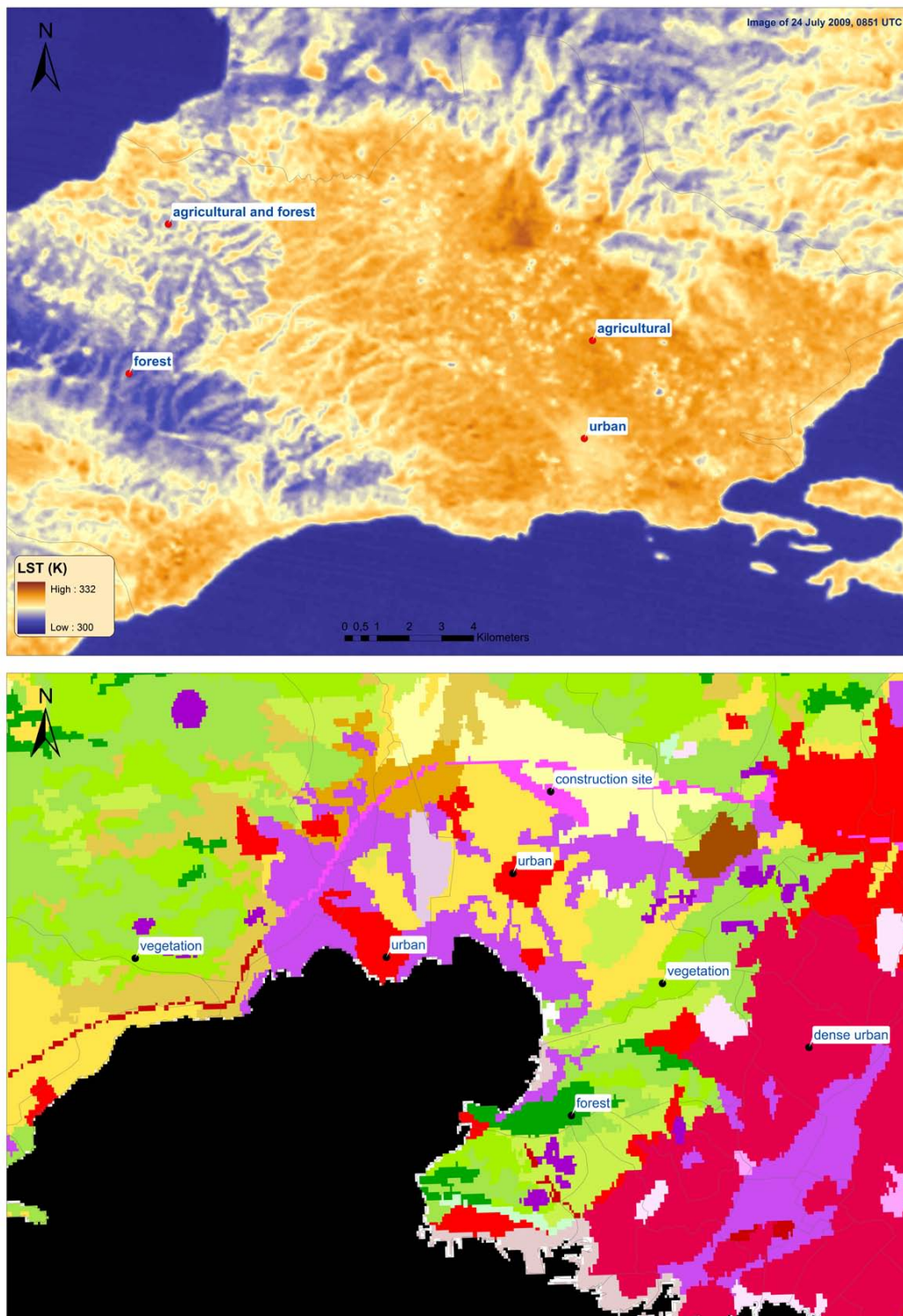


Figure 27: Detail of of Landsat TM LST map to focus on the dominant morning hot spot of Megara. The map is accompanied by the corresponding CLC2000 map for visual interpretation of the thermal distribution and its relation to land cover type.

It is of great interest to investigate the local thermal patterns of the city centre by overlaying the Landsat TM LST map with the aircraft optical images of Athens.

Below is sample of such screenshots presenting the Landsat TM itself followed by the composed map (temperature from Landsat and land use from aircraft). The image used is the one provided of 24 July 2009, processed by CGU.

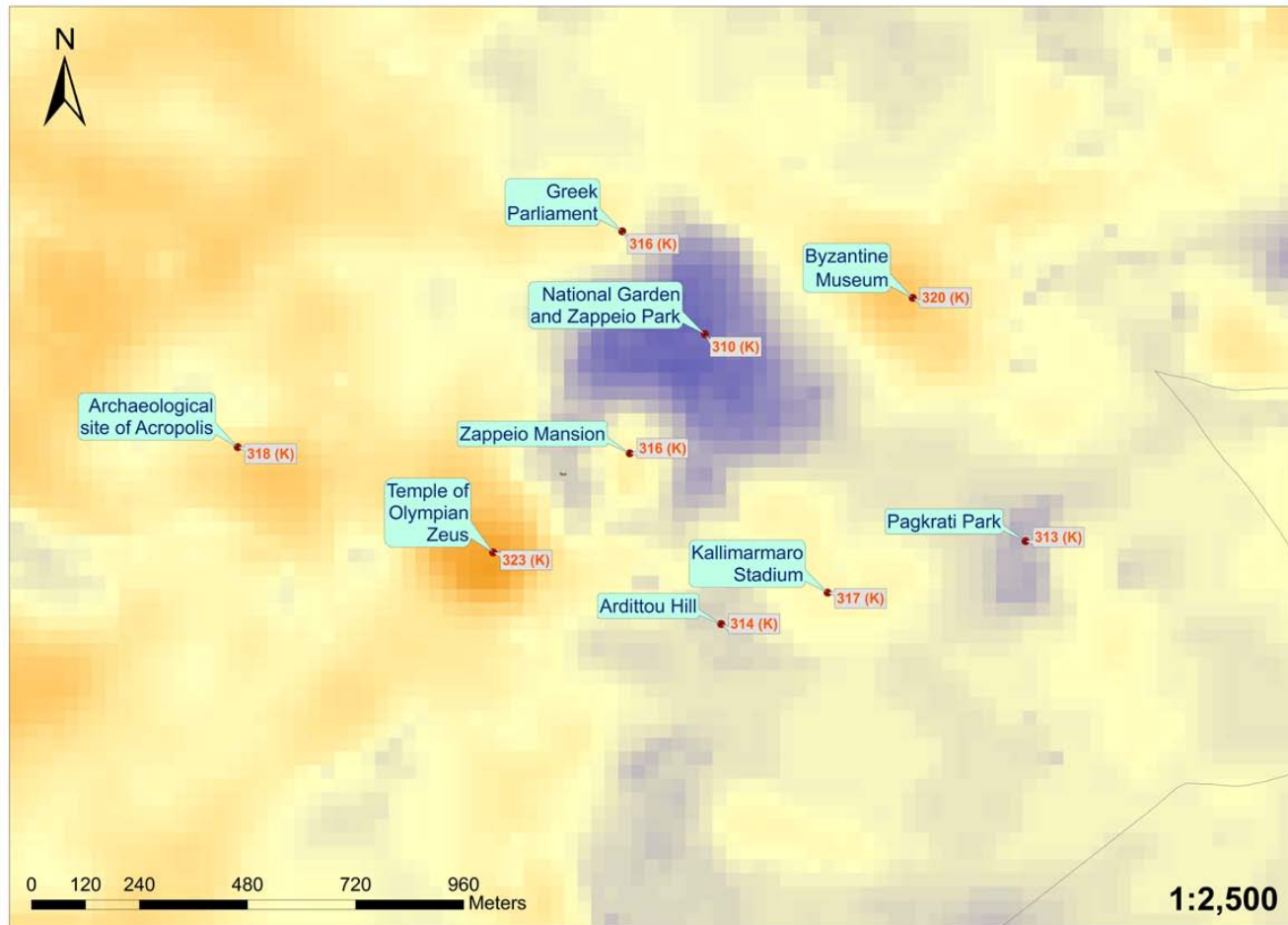




Figure 28: The thermal environment of the city centre of Athens, as acquired by Landsat image of the morning of 24.07.2009.

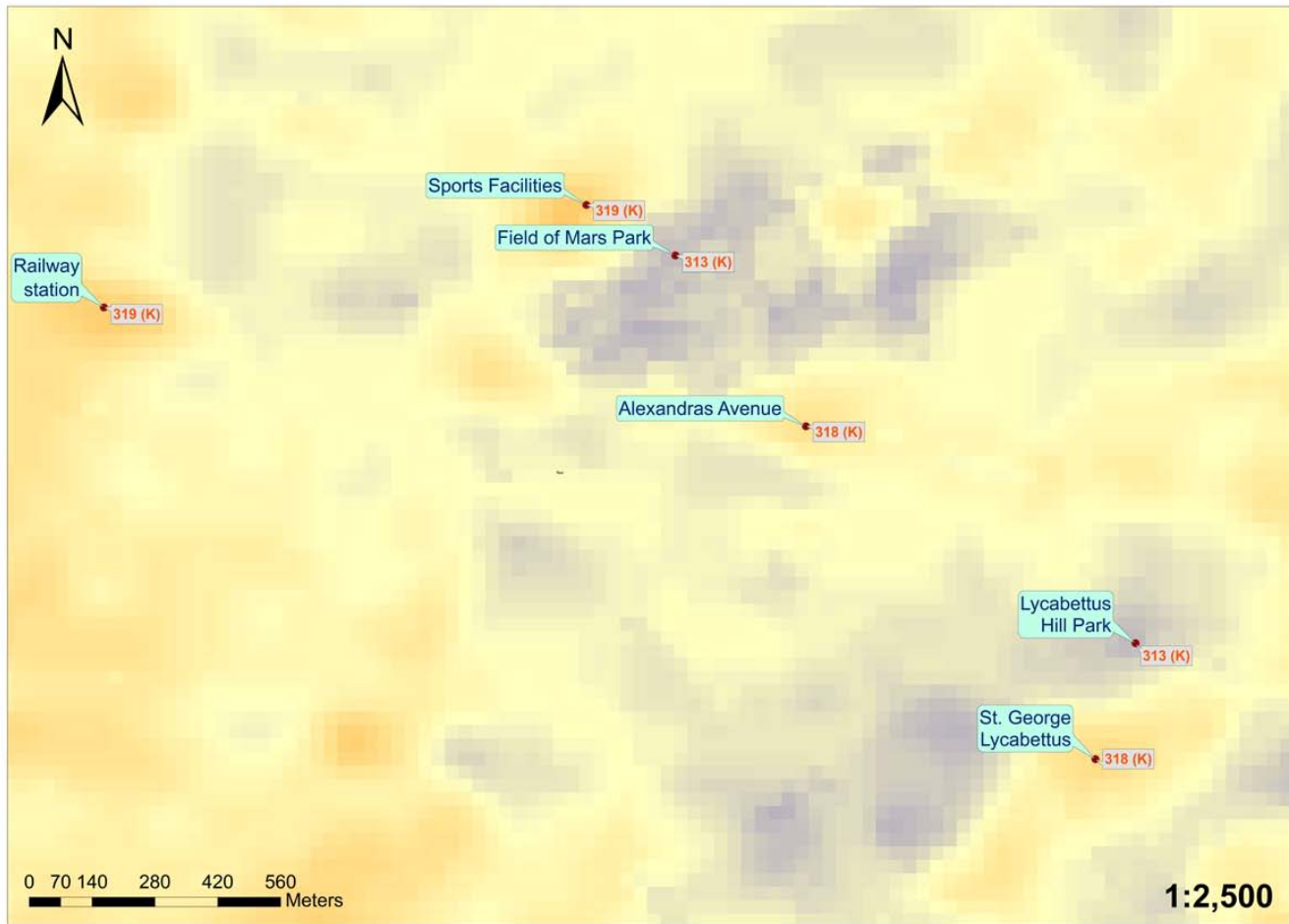




Figure 29: The effect of urban parks in the city centre. The thermal information is derived from a Landsat image of the morning of 24.07.2009.

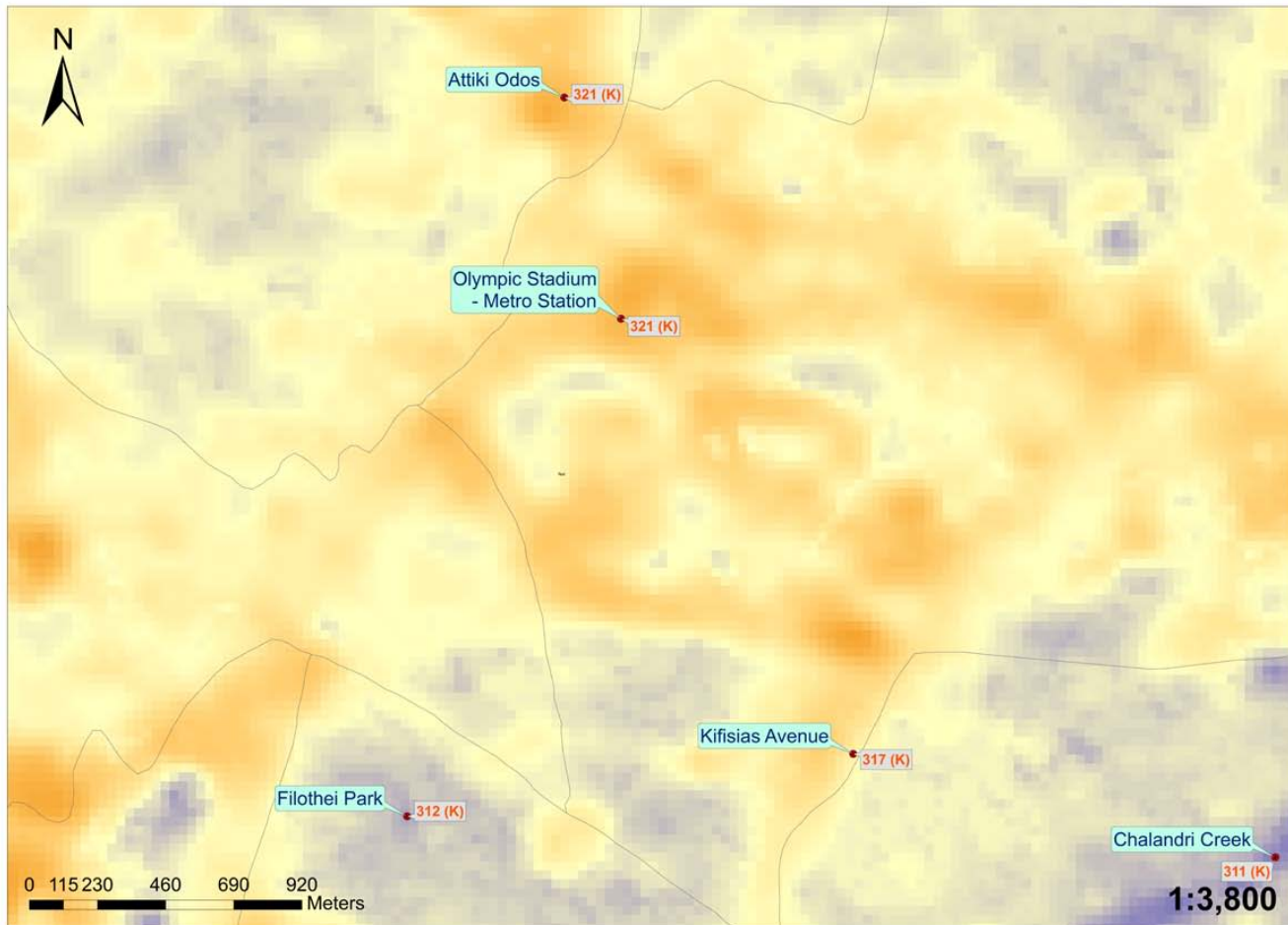
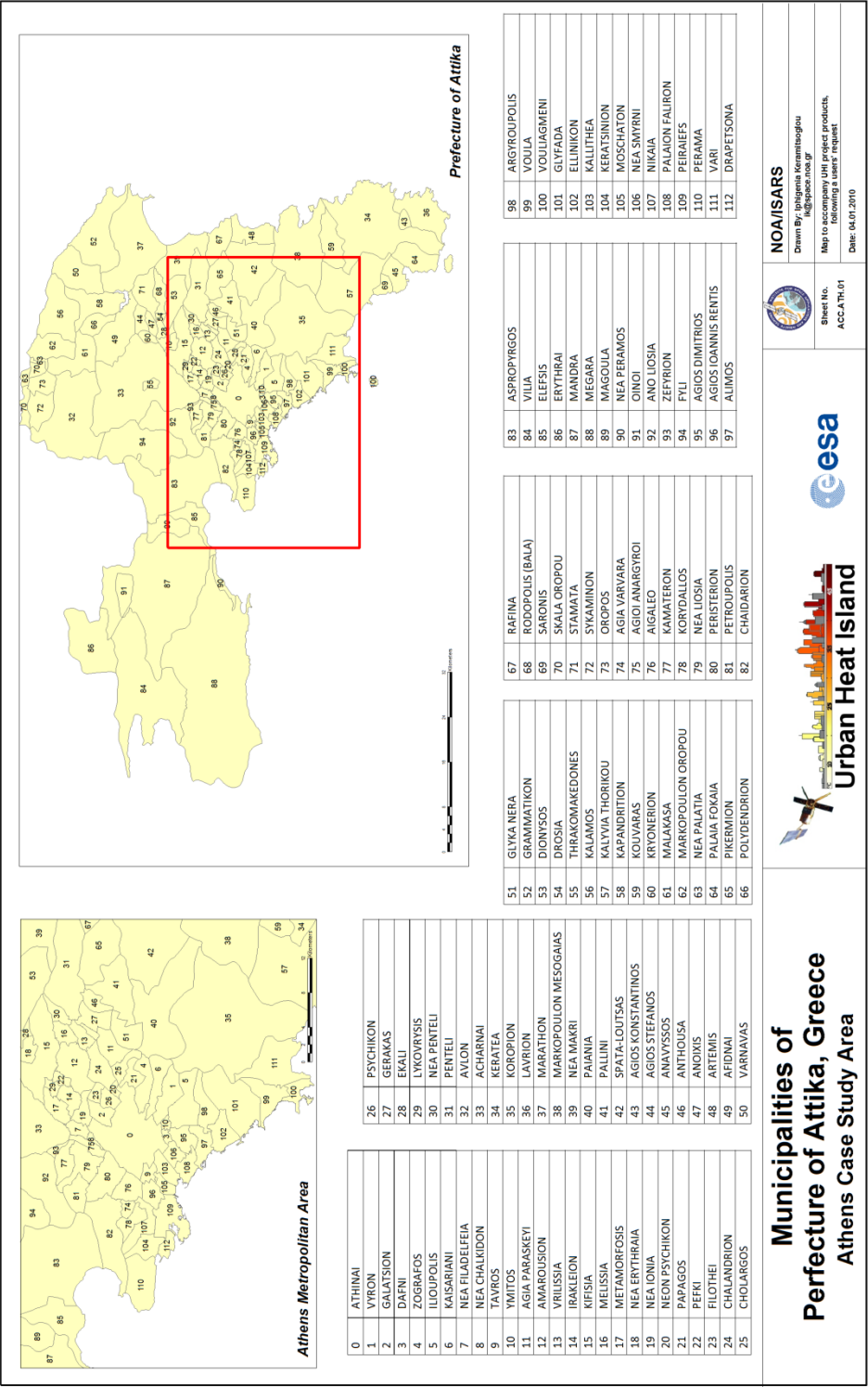




Figure 30: The thermal distribution at and around a complex sports centre. Thermal information is derived from a Landsat image of the morning of 24.07.2009.

In Figure 30 which illustrates the thermal distribution of the centre of Athens, we have labelled some points of interest together with their LST. The images show the high temperatures of archaeological sites (e.g. 318K at Acropolis and 323K at Temple of Olympian Zeus) and buildings (316K at the Parliament) with the much cooler temperatures of urban parks (e.g. 310K at the National Garden). Figure 8 shows the effect of urban parks in the thermal environment of the city centre. One can clearly identify the LST temperatures of the park being 5-6 degrees lower than the urban area around it. Alexandras Avenue is one of the arterial roads at the fringe of the city centre. Figure 8 contributes further to the previous findings on the presence of urban parks (e.g. Filothei Park and Chalandri Creek) and illustrates clearly the thermal load imposed by motorways, such as Attiki Odos. Attiki Odos is a modern urban-periurban motorway, constituting the ring road of the greater metropolitan area of Athens and the backbone of the road network of the entire Attica region. It has three traffic lanes in either direction and an emergency lane. The size of the motorway makes the thermal footprint of Attiki Odos clearly identifiable on the Landsat image (LST= 321K).

ANNEX I: Municipalities of Athens study area



ANNEX II: CORINE Land Cover Legend

	1.1.1. - Continuous Urban Fabric		3.1.1. - Broad-leaved Forest
	1.1.2. - Discontinuous Urban Fabric		3.1.2. - Coniferous Forest
	1.2.1. - Industrial or Commercial Units		3.1.3. - Mixed Forest
	1.2.2. - Road & Rail Networks		3.2.1. - Natural Grasslands
	1.2.3. - Port Area		3.2.2. - Moors & Heathland
	1.2.4. - Airports		3.2.3. - Sclerophyllus Vegetation
	1.3.1. - Mineral Extraction Sites		3.2.4. - Transitional Wood-land Shrubs
	1.3.2. - Dump Sites		3.3.1. - Beaches, Dunes & Sand Plains
	1.3.3. - Construction Sites		3.3.2. - Bare Rock
	1.4.1. - Green Urban Areas		3.3.3. - Sparsely Vegetated Areas
	1.4.2. - Sports & Leisure Facilities		3.3.4. - Burnt Areas
	2.1.1. - Non-irrigated Arable Land		3.3.5. - Glaciers & Perpetual Snow
	2.1.2. - Permanently Irrigated Land		4.1.1. - Inland Marshes
	2.1.3. - Rice Fields		4.1.2. - Peat Bogs
	2.2.1. - Vineyards		4.2.1. - Salt Marshes
	2.2.2. - Fruit Tree & Berry Plantations		4.2.2. - Salines
	2.2.3. - Olive Trees		4.2.3. - Intertidal Flats
	2.3.1. - Pastures		5.1.1. - Water Courses
	2.4.1. - Annual Crops Associated with Permanent Crops		5.1.2. - Water Bodies
	2.4.2. - Complex Cultivation Patterns		5.2.1. - Coastal Lagoons
	2.4.3. - Principally Agriculture, with Natural vegetation		5.2.2. - Estuaries
	2.4.4. - Agro-forestry Areas		5.2.3. - Seas & Oceans

3.2.4 Finalised quality assessment of each UHI product using mainly ground (and airborne) data as appropriate (NOA-AUTH-VITO)

Purpose

The purpose of the present section is to summarise the activities performed during the course of Thermopolis 2009 project regarding the support to UHI products. It will also be delivered to the UHI project consortium for further improvement of the products, where applicable.

List of Acronyms

AATSR	Advanced Along-Track Scanning Radiometer
AT	Air Temperature
AVHRR	Advanced Very High Resolution Radiometer
CORINE	Coordination of information on the environment
CGU	Global Change Unit
DI	Discomfort Index
ECMWF	European Centre for Medium-Range Weather Forecasts
FOR	Forecasted
GB	Ground Based
HNMS	Hellenic National Meteorological Service
ISARS	Institute for Space Applications and Remote Sensing
LAP_AUTH	Laboratory of Atmospheric Physics, Aristotle University of Thessaloniki
LST	Land Surface Temperature
MODIS	Moderate Resolution Imaging Spectroradiometer
MSG	Meteosat Second Generation
NDVI	Normalized Difference Vegetation Index
NOA	National Observatory of Athens
NRT	Near Real Time
PK	Planetek SA
RT	Real Time
SEVIRI	Spinning Enhanced Visible and Infrared Imager
TM	Thematic Mapper
UHI	Urban Heat Island
UTM	Universal Transverse Mercator
VITO	Vlaamse Instelling Voor Technologisch Onderzoek (Flemish Institute for Technological Research)
WV	Water Vapour

Table 23: List of UHI Products supported by Thermopolis2009

UHI Product Code	Name of Product	Thermopolis dataset used	Activity	Result
------------------	-----------------	--------------------------	----------	--------

UHI Product Code	Name of Product	Thermopolis dataset used	Activity	Result
R2.2	AT based on MSG-SEVIRI and an Urban Climate Model	GB AT flux measurements	Validation Model Tuning	Confirmation of independent validation activity Improvement of the R2.2 Model, which will also affect the performance of R2.4
R2.3	LST at 1km	GB LST	Pixel Comparisons to assess the ability of the 1km sensors to evaluate the UHI over cities by using homogeneous areas as targets (water and bare soil)	Assessment of R2.3 LST retrieval by MODIS, AATSR and AVHRR sensors
R2.5	LST at 60m	GB LST Aircraft LST Atmospheric data	Pixel and Pattern Comparisons to assess the ability of Landsat TM sensor to depict the UHI over cities Sensitivity analysis of the algorithm used to produce LST maps from Landsat TM	Debugging of R2.5 code Better understanding of R2.5 behavior Investigation of areas prone to high differences between datasets
R2.9 NRT	AT calculated by NRT satellite image of 1km spatial resolution and RT GD	AVHRR from NOAA station at Near-Real Time GB AT	Validation of the product Revalidation after improvement by Edisoft, based on a series of Products and a series of GB	Assessment of R2.9 NRT product quality and confidence level

UHI Product Code	Name of Product	Thermopolis dataset used	Activity	Result
			stations	
R2.9 Forecast	3-day Forecasted AT at 250m	GB AT	<p>Validation of initial R2.9 Forecasted product</p> <p>Downscaling of Forecast Model using Thermopolis 2009 GB AT for training</p> <p>Re-validation of R2.9 Forecasted product</p>	<p>Validation of the R2.9 FOR product</p> <p>Improvement of the forecast model regarding spatial resolution and precision</p>
R2.10 NRT	Discomfort Index calculated by NRT satellite image of 1km spatial resolution and RT GD	AVHRR from NOAA station at Near-Real Time GB AT GB Relative Humidity	Validation of the product based on a series of Products and a series of GB stations	Assessment of R2.10 NRT product quality and confidence level
R2.17	Emissivity at 60m	GB Emissivity	Comparison between Landsat-derived emissivity and ground measurement	<p>Debugging of R2.17 emissivity from Landsat TM code</p> <p>Assessment of the satellite derived value</p>

Input

- UHI Products R2.2, R2.3, R2.5, R2.9 NRT, R2.9 Forecast, R2.10 NRT, R2.17. City: Athens
- Thermopolis 2009 dataset

Supporting actions and relevant Results

R2.2 AT

Validation

R2.2 AT product has been further validated independently against ground-truth data for the THERMOPOLIS campaign period. This has been done in order to increase confidence to the product using an independent set of measurements not available for other time periods. AT in-situ measurements from 26 ground-based (GB) stations have been used.

For each pair of data sets (R2.2 and GB), the absolute difference in AT [R2.2 AT – GB AT] is calculated. Validation analysis has been concentrated to each of the 26 stations. Averaging of AT absolute differences has been performed for each station separately. Mean values of the absolute difference for each station examined along with the standard deviations of the averaging are presented in Table 2 for the THERMOPOLIS campaign period. Additionally, the correlation coefficients between R2.2 ATs and GB ATs for each station are given.

Table 24: Mean differences between R2.2 AT and GB measured AT along with the standard deviations and correlation coefficients between the two datasets

	Station Name	Latitude (°N)	Longitude (°E)	Mean Difference (°C)	Standard Deviation	Correlation Coefficient
1	Kountouriotou	37.9260	23.7124	0.25	1.89	0.899
2	Serifou	37.9569	23.6575	0.02	2.31	0.806
3	Seirionon1	37.9627	23.7564	0.26	1.92	0.898
4	Seirionon2	37.9627	23.7564	0.44	1.80	0.915
5	Anaximenous	37.9698	23.7488	1.17	1.70	0.906
6	Dorms	37.9816	23.7810	1.47	1.67	0.911
7	Pipinou	37.9965	23.7330	-0.83	1.98	0.882
8	Thaleias	38.0226	23.8334	0.67	2.02	0.886
9	Pellis	38.0279	23.8174	1.03	1.65	0.925
10	Papayannis	38.0553	23.8129	2.13	1.96	0.878
11	Hellenikon	37.8997	23.7433	0.76	1.99	0.865
12	NeaFiladelfia	38.0497	23.6600	1.25	1.81	0.913
13	Elefsina	38.0669	23.5500	1.25	1.66	0.915
14	Thiseio	37.9720	23.7180	0.26	2.09	0.850
15	Academy	37.9914	23.7810	1.22	1.85	0.892
16	Penteli1	38.0473	23.8650	3.05	2.42	0.811
17	Elliniko	37.8988	23.7234	1.10	2.59	0.752
18	Ilioupoli	37.9183	23.7610	0.61	1.78	0.903
19	Psytaleia	37.9419	23.5871	0.74	2.34	0.818
20	Zografou	37.9771	23.7869	1.56	2.98	0.806

21	Pikermi	38.0011	23.9287	0.83	2.39	0.853
22	Galatsi	38.0294	23.7574	1.37	2.12	0.852
23	Anolosia	38.0752	23.6707	0.32	1.73	0.915
24	Penteli2	38.0865	23.8636	3.10	2.37	0.830
25	Menidi	38.1066	23.7339	-1.36	2.07	0.881
26	Mandra	38.1229	23.5637	1.71	1.94	0.894
	ENTIRE DATASET			0.938	2.04	0.8714

R2.2 AT product overestimates ground-based temperatures by 1°C (± 2 °C). The mean difference ranges between -1.36°C and 3.10°C. Mean correlation coefficient for the entire dataset found to be equal to 0.8714.

However, of more interest is the in-depth investigation of the behaviour of R2.2 compared to the diurnal variation recorded by GB thermometers. This is appropriately depicted in the following figure for the period of the Thermopolis 2009 campaign.

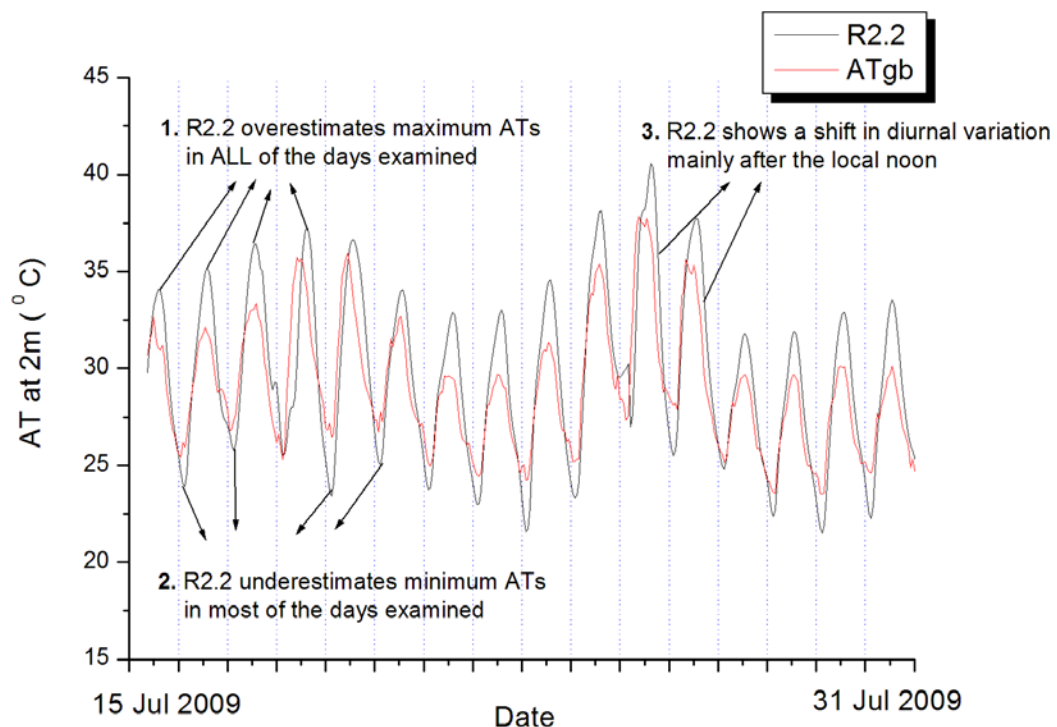


Figure 31: hourly data revealing some aspects of the model's behaviour.

Model's behaviour is:

- R2.2 fails to retrieve minimum ATs in the diurnal variation.
- The R2.2 overestimation of AT during night-time. Maximum differences are

observed after 00:00 UTC

- R2.2 overestimates maximum ATs in most of the days examined
- R2.2 shows a shift in diurnal variation mainly after the local noon.
- Absolute differences show a diurnal variation as well.

Model Improvement (by Bino Maiheu, VITO, contact: bino.maiheu@vito.be)

The THERMOPOLIS measurement campaign has provided **important feedback** for the Urban Heat Island project's air temperature (AT) model. This experimental model was developed by VITO, the Flemish Institute for Technological Research in Belgium. The AT model consists of a surface part, which calculates the turbulent sensible heat flux into the atmosphere for urban environments. An atmospheric heat dispersion model subsequently takes care of heat dispersion and couples to large scale meteorological parameters derived from ECMWF. The surface flux model is constrained and part of its parameters estimated by a sequential Monte Carlo (SMC) data assimilation scheme, which is fed by satellite observed land surface temperature fields (LST).

Comparison of OHM parameters

A key ingredient in the surface flux model is the Objective Hysteresis Model (OHM) (Grimmond, C. S. B., Oke, T. R., 2002)², which expresses the storage heat flux G as a function of the surface net radiation balance R_N at the surface and it's time derivative:

$$G = a_1 R_N + a_2 \frac{dR_N}{dt} + a_3$$

where the coefficients a_1, a_2 and a_3 are depending on the surface material and more specifically it's thermal properties. Even though these parameters are partly estimated in the SMC scheme, it is quite important to have good estimates in order to represent the correct forcing cycle in the urban canopy. Since this data is not readily available, surface flux measurements, as performed in the THERMOPOLIS campaign are very valuable.

The a_i parameters in the surface flux model were defined for 4 different surface classes as given in the table below.

Table 25: Initial guesses for OHM parameters in the uhiflux model.

Land Cover	a1	a2	a3
<i>Urban</i>	0.70	0.25	-80.0
<i>Vegetation</i>	0.15	0.15	-15.0
<i>Bare Soil</i>	0.35	0.30	-40.0
<i>Water</i>	0.50	0.20	-40.0

² Grimmond, C. S. B., Oke, T. R. (2002). Turbulent heat fluxes in urban areas: Observations and a local-scale urban meteorological parameterization scheme (lumps). Journal of Applied Meteorology, 41: p. 792-810.

In the THERMOPOLIS measurement campaign, the storage heat flux was derived from the flux measurements and modelled using the same OHM model. The values derived for urban land cover materials ranged roughly for a_1 between 0.65 – 0.68, a_2 : 0.20 – 0.30 and a_3 : 54.0 – 57.0. These values were kindly provided by Dr. Rea Loupa of the Democritus University of Thrace. One can see that the a_1 and a_2 coefficients that are used in the model for the pure Urban land cover type agree quite well with THERMOPOLIS OHM coefficients. The last a_3 parameter does differ somewhat, but on the other hand this parameter is dynamically estimated in the flux model via the SMC data assimilation scheme.

Detailed validation using in-situ air temperature measurements

The validation results performed in the frame of the UHI project using the THERMOPOLIS data learnt the existence of a phase shift between the modelled values and the measurements. Understanding this shift is essential to improving the AT model performance. However, one must note here that a direct comparison was made between the in-situ measurement and a rather coarse pixel, without any regard for possible local effects of representativity and experimental uncertainty. VITO proposes therefore a methodology which attempts to correct for these effects before performing a model validation.

This methodology is based upon the well known data assimilation technique called **optimal interpolation**. Using this technique, experimental data and a model are fused together taking into account the background error variances of both model (background) and observations. The optimal interpolation technique is among others described in detail in (Daley, R., 1991)³. The idea behind the approach is that we try to express the measured in-situ temperature for the THERMOPOLIS campaign as a function of land cover derived from the CORINE dataset. For each hour of the day, we calculate the climatology (i.e. long term average) over the full THERMOPOLIS campaign dataset and model it as a function of urban land cover fraction. This can be seen in the below.

³ Daley, R. (1991). Atmospheric data analysis, Cambridge University Press 1991.

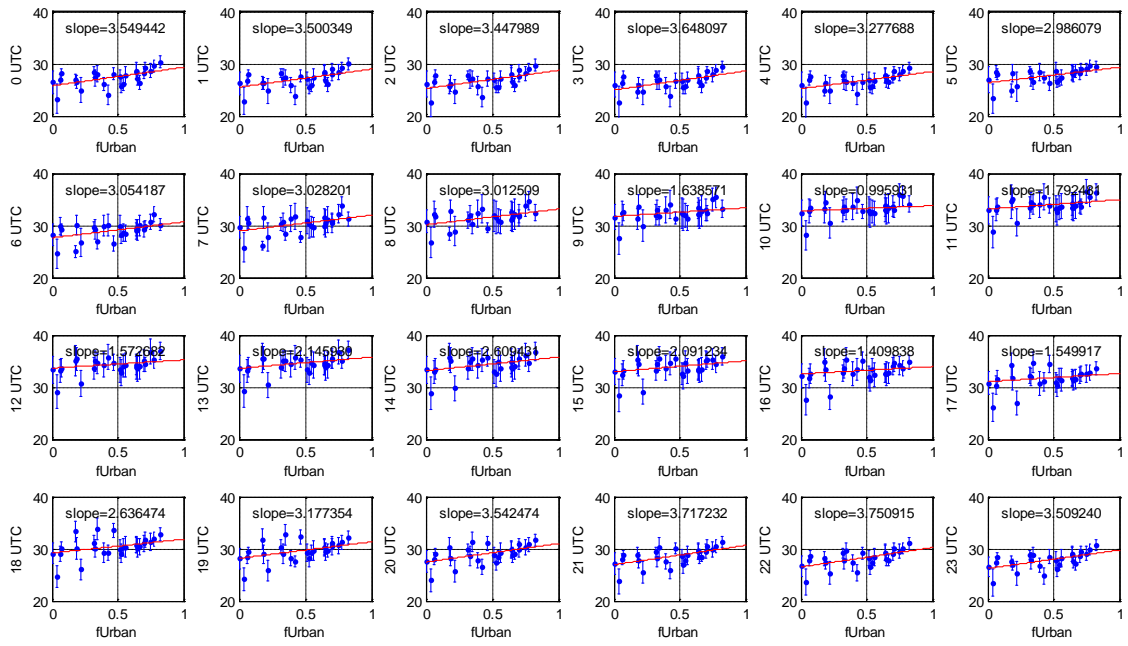


Figure 32: Trivial model for the air temperatures based upon an hourly climatology expressed as a function of urban land cover.

The fraction of urban land cover for each measurement location is derived using the same catchment area as the UHI air temperature spatial resolution. One interesting feature of this trivial model is that the slope of the regression fits directly gives an estimate for the temperature difference between a fully urban location and a fully rural location. So inherently it provides one means to estimate the UHI effect.

Using this simple land use regression model - which is in fact directly based on the THERMOPOLIS measurement themselves- one can produce an initial estimate for the air temperature field in the vicinity of the air temperature measurements, using information of urban land cover in each UHI AT model pixel. In each time step both the regression model prediction (background) and the current measurement set are combined using optimal interpolation. For this one needs to model the background error covariance and observation error covariance. Assuming the observation errors are uncorrelated, we can estimate these quantities from the background departure covariances. A first estimate of this quantity is given as a function of distance in the following figure.

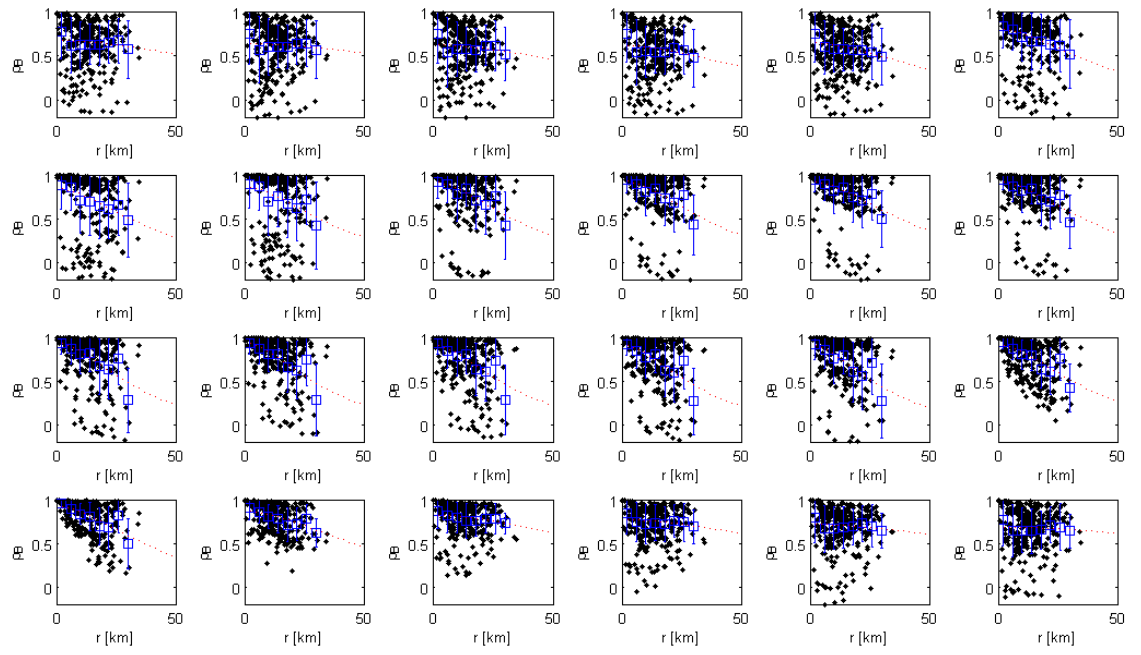
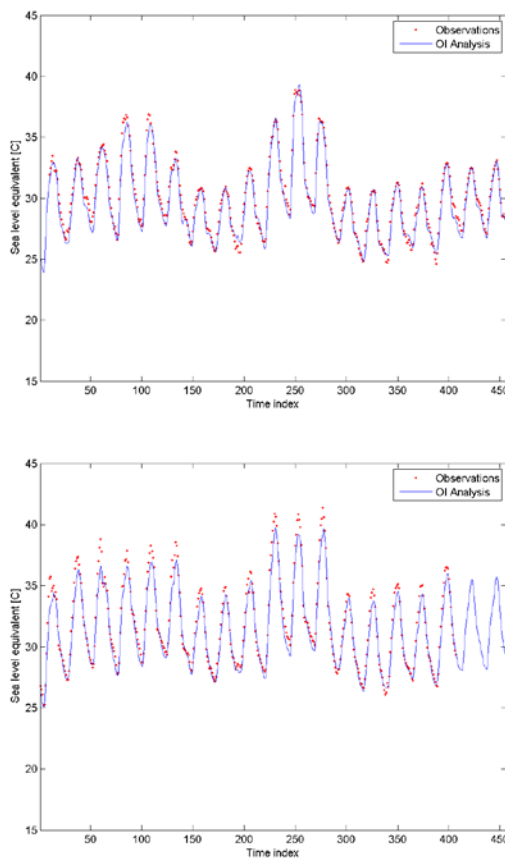


Figure 33: First estimate of the background departure covariance versus distance for each hour of the day UTC.

From the intercept at $r = 0$, one can derive the fraction for background error variance to observation error variance and thus disentangle both contributions from the background departure covariances. Using these error covariances, interpolation weights can be obtained for the experimental data to be interpolated to the UHI AT model grid taking into account the land use information in the full pixel (via the CORINE parametrisation) as well as microscale effects such as representativity and experimental uncertainty via the background and observation error covariances. Unlike most other interpolation techniques one therefore does not obtain the exact same values at the measurement locations, but an optimal estimate of the true AT value taking into account the catchment area of the full pixel. Indeed, when we compare the optimal interpolation time series and the in-situ experimental data, in some stations, we can see quite large differences



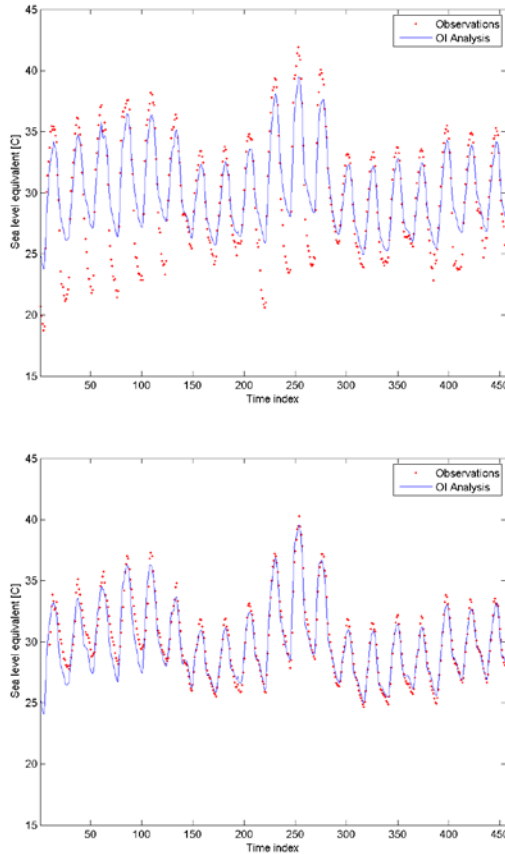
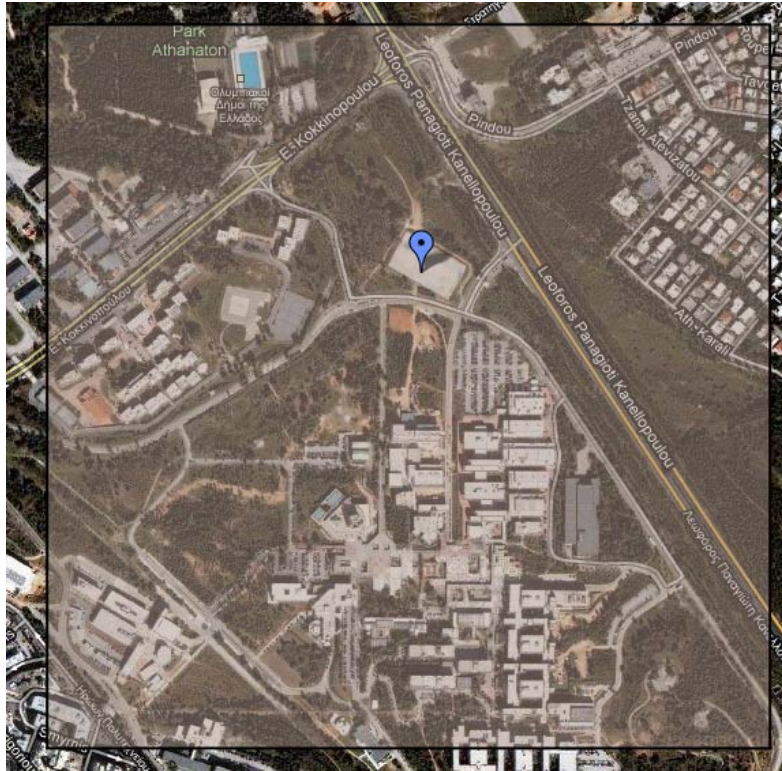


Figure 34: Example comparison between in-situ time-series and the optimal interpolation analyses at the exact same location. Top row: Thaleias and Thiseio stations, bottom row: Zografou and Pellis stations.

Note finally, that the optimal interpolation technique is fairly similar to the Kriging interpolation technique, with the difference that the experimental uncertainty (and thus also representativity) are naturally taken into account. At the time of writing this technique is currently implemented and tested, during the next phase the model comparison and improvement will take place.

R2.3

MODIS, AATSR and AVHRR 1-km LST products have been validated against ground-truth data for the THERMOPOLIS campaign period. Specifically, LST in-situ measurements from 2 ground-based (GB) stations have been used to assess the ability of the 1km sensors to evaluate the UHI over cities by using homogeneous areas as targets.



**Figure 35: The area of the Bare Soil measurement is shown with the blue point.
The corresponding satellite pixel is overlaid for comparison.**

LST measurements over bare soil performed with fixed mast instrumentation were used in the first stage. The in-situ measurements were performed at the NTUA's University campus and specifically at the football field (latitude: 37.9814, longitude: 23.7832) for the THERMOPOLIS time frame and they are presented along with the satellite retrievals in the following figure.

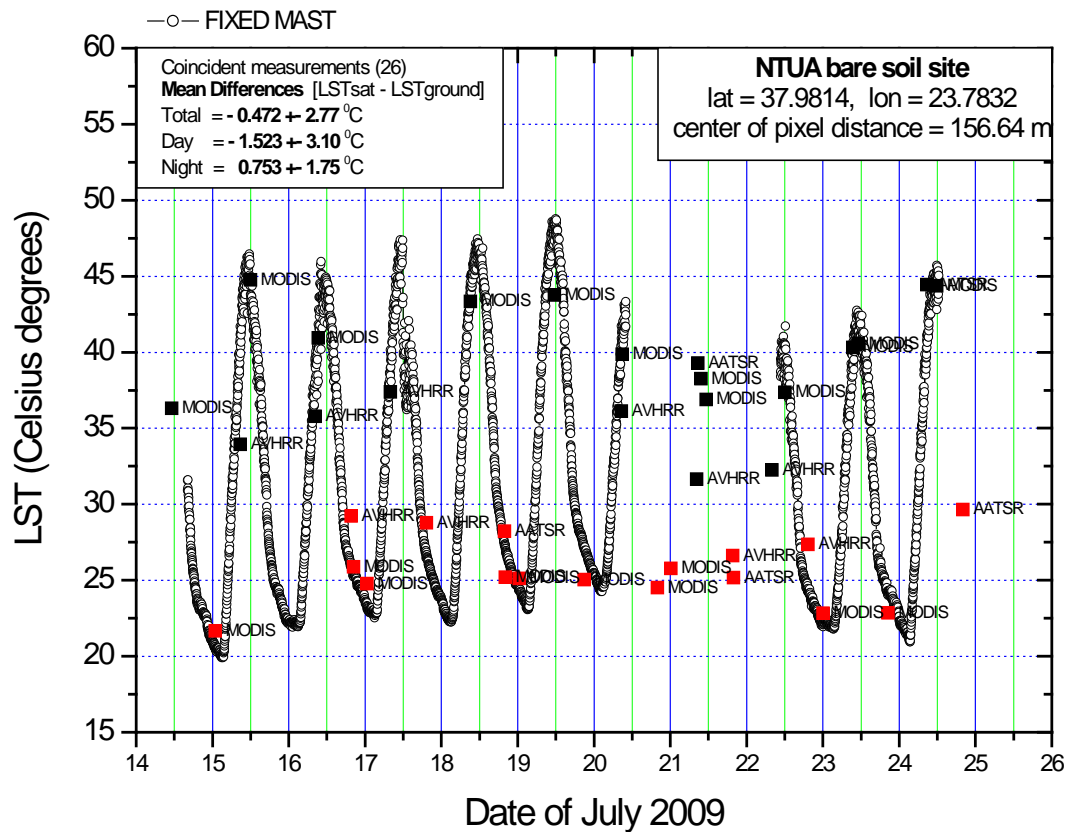


Figure 36: In-situ LST measurements over NTUA's bare soil site along with 1-km satellite retrievals of LST (MODIS, AVHRR, AATSR) during THERMOPOLIS

The minimum distance of the pixel centre from the ground-based station was found equal to 156.64m. The ground-based time-series are presented with open circles, while the satellite products with black or red squares for daytime and night-time retrievals, respectively, along with a satellite label. As it is evident from the figure, the LST satellite products are following the LST diurnal variation recorded with the fixed mast over NTUA's bare soil site.

To quantify the ability of 1-km satellite retrievals to represent LST, the coincident satellite/ground-truth pair of data sets were identified and the mean differences [LST_{satellite} - LST_{ground}] were calculated. For the 26 coincident measurements, a difference of -0.472 ± 2.77 °C was found, indicating less than half a degree underestimation of satellite LSTs.

By separating the coincident measurements in daytime and night-time observations, the mean differences were found equal to -1.523 ± 3.10 °C for 14 **daytime** data pairs and 0.753 ± 1.75 °C for the remaining 12 **night-time** datasets. **These results indicate more accurate satellite retrievals during night-time.** It is stressed that only satellite data with flag equal to 0 were used in this study. To further illustrate the comparison

results, a correlation between the satellite and ground-based retrievals is presented in the following figure for NTUA's bare soil site:

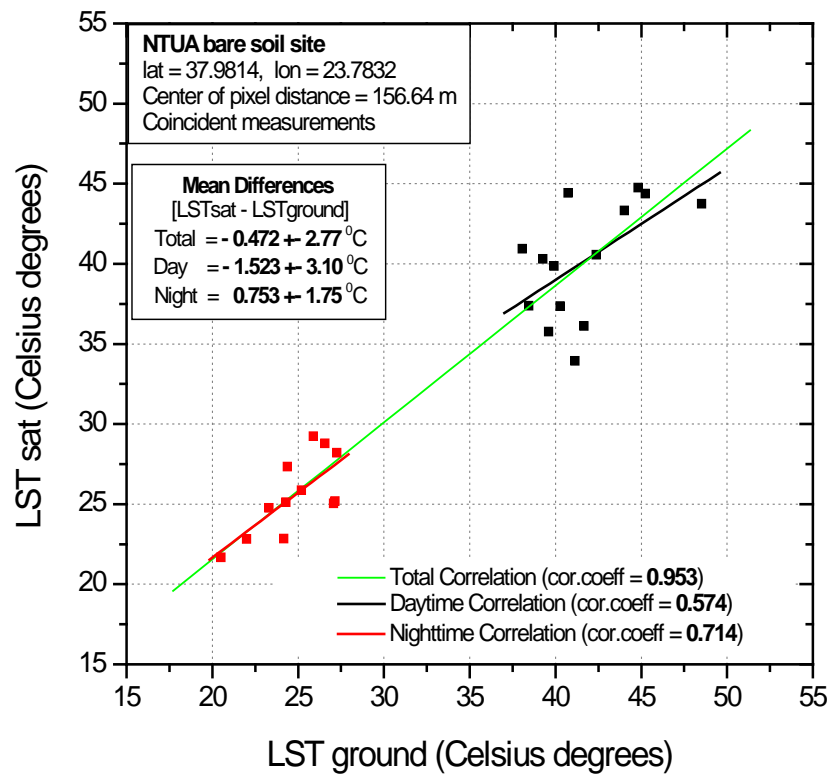


Figure 37: 1-km satellite retrievals of LST versus in-situ LST mast measurements over NTUA's bare soil site during THERMOPOLIS

Again, night-time retrievals are in better agreement with ground-truth data, giving a correlation coefficient of 0.714. The correlation coefficient for daytime measurements was found equal to 0.574.



Figure 38: The Marathon Lake measurement is shown with the blue point. The corresponding satellite pixel is overlaid for comparison.

Following the same approach, 1-km satellite retrievals were compared with ground-based LST measurements carried out for Calibration/Validation activities over the water surface of Marathon lake (latitude: 38.1676, longitude: 23.9059). The measurements were performed with two instruments, the RAYTEK ST6 broadband radiometer and the 6-band CIMEL ce312. The surface temperature T_s for RAYTEK instrument were obtained from measurements carried out with the broad band radiometer (8-14 μ m) assuming the emissivity obtained for the broad band of the CIMEL 6 by applying TES to the CIMEL 6 data, and downward radiation is the downward radiation measured by the broad band of the CIMEL 6. These retrievals are presented in the following figure with open circles for CIMEL and open squares for RAYTEK, along with the satellite products which are denoted with black or red squares for daytime and night-time retrievals respectively (along with a satellite label).

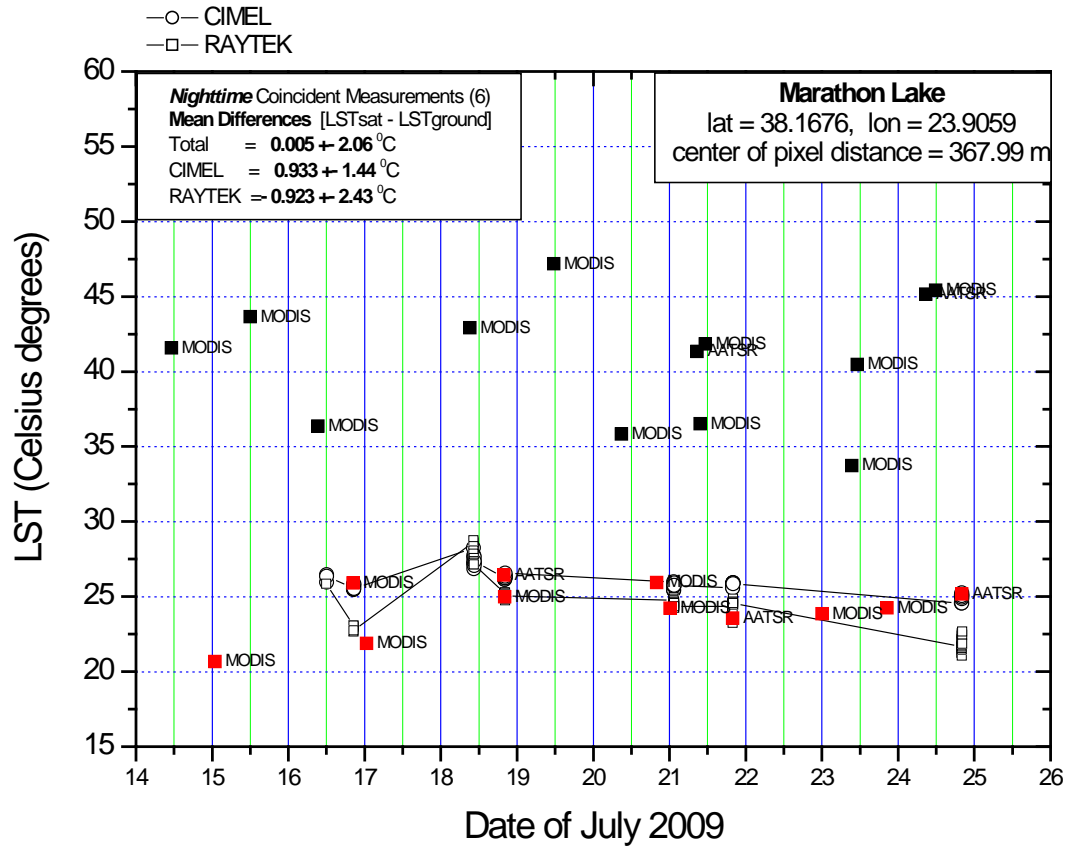


Figure 39: In-situ LST measurements over Marathon lake along with 1-km satellite retrievals of LST (MODIS, AVHRR, AATSR) during THERMOPOLIS

The minimum distance of the pixel centre from the ground-based station was found equal to 367.99m. As it is evident from the figure, the LST satellite products during daytime are not following the ground-truth measurements. This is attributed to the fact that the satellite pixel includes land, and in the morning the difference between land and water is maximum. For **night-time observations**, 6 coincident satellite/ground-truth pair of data sets were found and the mean differences [LSTsatellite - LSTground] was calculated equal to 0.005 ± 2.06 °C, indicating a perfect match albeit a 2-degrees standard deviation. By separating the coincident measurements for the different ground-based instruments, a mean difference of 0.933 ± 1.44 °C was found for 3 coincident CIMEL measurements, while for the 3 remaining cases of RAYTEK LSTs, the average difference was found equal to 0.933 ± 2.43 °C, showing a similar response. Again, as in the case of bare soil, only satellite data flagged with 0 were used in this study. Due to the limited time coincidences of data, no correlation plots were produced for Marathon lake observation site.

R2.5

A series of actions have been taken to examine the accuracy of LST product R2.5 calculated from Landsat TM satellite as well as to investigate the sensitivity of the Jiménez-Muñoz et al. (2009⁴) used for the calculations. These actions are presented next:

Comparisons between LST R2.5 and Ground Measurements

1. Fixed masts:

Table 26: Results from the comparison over Bare Soil, NTUA (37° 58.886' N , 23° 46.993' E), for the surface temperature:

Site name	Measurement Time (UTC)	Latitude	Longitude	Ground LST measurement (K)	Landsat TM LST measurement (K)	Difference in LST estimation (K)
NTUA (bare soil)	08:54	37° 58.886'	23° 46.993'	314.13	316.28	2.15

2. Spectral characterization of urban surfaces: spectral library

Table 27: Comparisons of LST (LST has been produced by applying the TES algorithm to the CIMEL instrument measurements)

Site name	Measurement Time (UTC)	Latitude	Longitude	Ground LST measurement (K)	LANDSAT TM LST measurement (K)	Difference in LST estimate (K)
Acropolis (Floor-Rocks)	09:23:11	37° 58.171'	23° 43.699'	325.19	315.60	8.69
Acropolis (Dry grass)	09:37:19	37° 58.208'	23° 43.711'	338.39	315.98	22.41
Acropolis (Rock-1)	09:57:06	37° 58.312'	23° 43.629'	313.80	315.03	1.23

Table 28: Standard Deviation in the estimation of the above ground measurements was reported to be:

⁴ Jiménez-Muñoz, J. C., Cristóbal, J. Sobrino, J. A., Soria, G., Ninyerola, M., and X. Pons (2009): Revision of the Single-Channel Algorithm for Land Surface Temperature Retrieval From Landsat Thermal-Infrared Data. IEEE Transactions on Geoscience and Remote Sensing, 47 (1), 339-349.

Site name	Measurement Time (UTC)	Latitude	Longitude	St. Dev. in Ground LST measurement (K)	St. Dev. in Emissivity band 3 measurement (10.57 μm)	St. Dev. in Emissivity band 2 measurement (11.29 μm)
Acropolis (Floor-Rocks)	09:23:11	37° 58.171'	23° 43.699'	1.17	0.010	0.002
Acropolis (Dry grass)	09:37:19	37° 58.208'	23° 43.711'	0.69	0.010	0.019
Acropolis (Rock-1)	09:57:06	37° 58.312'	23° 43.629'	0.26	0.002	0.003

3. Calibration/Validation Activities

Table 29: Comparisons of LST (LST has been computed here from the RAYTEK ST6 broadband radiometer)

Site name	Measurement Time (UTC)	Latitude	Longitude	Ground LST measurement (K)	LANDSAT TM LST measurement (K)	Difference in LST estimate (K)
Acropolis (Dry grass)	09:40	37° 58.208'	23° 43.711'	338.1	315.98	22.12
Acropolis (Rock-1)	09:55	37° 58.312'	23° 43.629'	313.4	315.04	1.64

Sensitivity Analysis of R2.5 procedure

Here we report the results from our study carried out to appreciate the algorithm's sensitivity to input parameterization conditions. Being able to identify the most critical algorithm inputs to the LST computation from this specific algorithm is rather important, given its use as the core method for the LST computation from the TM sensor in the framework of the Urban Heat Island (UHI) project.

The key datasets which were used for the implementation of the present study can be grouped into three main categories namely: satellite data, ground measurements, and algorithms.

In terms of the satellite datasets, in the present study it was used the Landsat TM imagery which was acquired during the period of the Thermopolis campaign, on July 24th 2009 at 08.54 UTC. The latter imagery was obtained directly from the USGS GLOVIS archive with some pre-processing applied, including terrain correction and georeferencing to a UTM datum Zone 34N projection system. In addition to the at-sensor radiance TM imagery, a water vapour (WV) map of the studied region, close as possible to the TM overpass was obtained from Planetek S.A., as part of a product that is made available in UHI project.

Ground measurements collected during the Thermopolis campaign in Athens were used in the present study to either parameterise or validate the examined here LST algorithm. These measurements, which were collected at a time nearly concurrent to the TM image overpass, included essentially the water vapour (WV) column and the ground-measured LST. The WV column ground measurement was collected from a CIMEL channel 940nm instrument which had been installed at Akadimias station. From this instrument, the WV value of 1.804367 gr/cm^2 recorded at 08:49 UTC was the measurement that was used in this study. The LST ground measurement was obtained over a bare soil site located at NTUA site (located close to Akadimia station), on which a fixed mast station had been installed during Thermopolis campaign and operated by the GCU group of the University of Valencia Spain. According to GCU team, the coordinates of this site were $37^\circ 58.886$ Latitude and $23^\circ 46.993$ Longitude. As these coordinates were not configured as UTM but as geographical coordinates (lat/lon degrees) with WGS84 datum those were needed to be converted to match the TM image projection in order to be able subsequently to identify the location of this point in the TM scene and perform analysis of comparisons between the point and pixel-derived LSTs. Thus, the point coordinates representing the location of the NTUA fixed mast station in the TM scene were $37^\circ 58' 53.25''\text{N}$, $23^\circ 46' 59.55''\text{E}$.

Concerning the algorithms used, computation of the LST maps from the TM image data was based on the Jiménez-Muñoz et al. (2009) algorithm which was implemented by Planetek S.A and executed in ERDAS Modeler tool and was subsequently provided to ISARS/NOA. At this point it should be noted that a few bugs concerning the model code were identified and fixed. These mainly included a correction in the equation describing the computation of the apparent reflectance and of the ESUN Irradiance for band 3 instead of band 4 in the same equation. The present study was carried out using this updated version of the LST algorithm. Generally, key input parameters in the Jiménez-Muñoz et al. (2009) algorithm implementation for computing LST maps include the Distance Earth-Sun (units: UA), the Sun elevation at the time of image acquisition (units: radians), the NDVI threshold values over bare soil (NDVI₀) and full vegetation cover (NDVI_s), the total atmospheric water vapour content “w” (units: g/cm^2) and, finally, the coefficients set for the atmospheric functions selected from various databases described in Jiménez-Muñoz et al. (2009). Implementation of the LST algorithm for all scenarios that were executed using ERDAS Modeller tool, whereas any pre- or post- processing that was carried out in the TM image using ENVI image processing platform. Statistical analysis was performed using mainly MS Office Excel and SPSS statistical packages.

The approach adopted for the sensitivity analysis is schematically represented in the following figure.

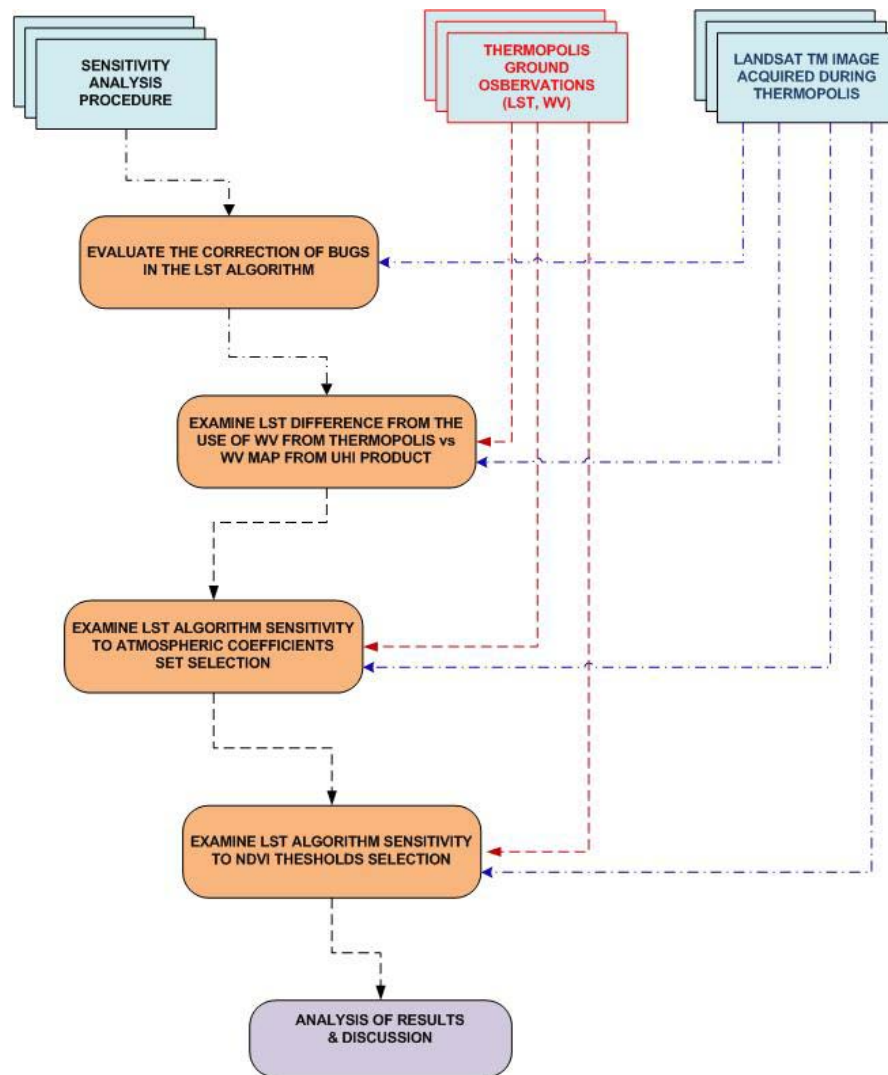


Figure 40: Flowchart of the overall methodology followed in performing the present study

The results are presented in detail elsewhere, however, the most important conclusions drawn from the analysis are summarised here:

- Correction of **geometric parameters** in the LST algorithm showed a noticeable difference in the computation of LST from the previous version of the algorithm, varying from 0 to ~1.8 K. However, LST differences over the urban area of Athens city were mostly below 0.6 K, whereas the highest LST differences were observed in the sub-urban/rural areas.
- Use of the ground-measured **water vapour** which was available at the time of the TM overpass did not seem to improve the LST computation from the algorithm. The results showed that the LST algorithm generally performs better when a spatial WV map is used as input during its parameterisation stage. What is more, results obtained from the present study also illustrated the significant effect of the correct WV parameterisation to the accurate LST computation by the specific algorithm with TM data. This is to some extent reasonable to expect, given that this parameter is of key importance in describing the local atmospheric conditions during the sensor overpass (along with the selection of the atmospheric coefficients also required during algorithm parameterisation).

- Examination of the LST computation sensitivity to the **set of atmospheric coefficients** for each case of WV input (either from Thermopolis or from the MODIS product) indicated generally a very small effect to the LST retrieval, at least for the comparisons performed here over the bare soil site located at NTUA premises. Generally, the TIGR2311 dB for both WV retrieval scenarios provided the closest agreement to the ground-measured LST, at least for the NDVI threshold values for which the comparisons here were performed.
- Concerning the sensitivity of the LST algorithm to the **NDVI threshold** values selection, results from this study generally indicated that the precise selection of these threshold values does not have a very important effect in the LST computation, either when the WV input is acquired from the ground measurement of Thermopolis or from the UHI product. Nevertheless, in comparison to the dB of atmospheric functions effect, the NDVI threshold selection has slightly more appreciable effect in the LST computation.

Comparison with the aircraft LST dataset

During the Thermopolis campaign in Athens (July 14th – 24th, 2009), a number of data from different sources (i.e. ground measurements, airborne and satellite observations) were simultaneously acquired over the wider studied area and at a large range of spatial scales. The aim of the present action is to present the main finding from the LST comparisons performed between the AHS airborne imagery and the LANDSAT TM sensor (let us call it LST PK, as the algorithm was implemented by Planetek Italia in the framework of UHI project), both acquired on the campaign day July 24th 2009. Initial analysis between the two datasets revealed a bias of the order of 2 °C the aircraft measuring higher LST than the satellite. This finding together with a number of pixels presenting discrepancies as high as 20 °C, initiated a discussion and experience exchanges between the partners of the consortium. GCU kindly provided their output of LST (let us call it LST CGU) and corresponding differences with the AHS, showing that in their case the mean difference was very close to 0 °C. In addition the number of outlying points was not as high. This is appropriately illustrated in the next Table (with appropriate figures).

The recognition of this disagreement will most probably lead to an updated algorithm for Landsat LST retrieval by Planetek.

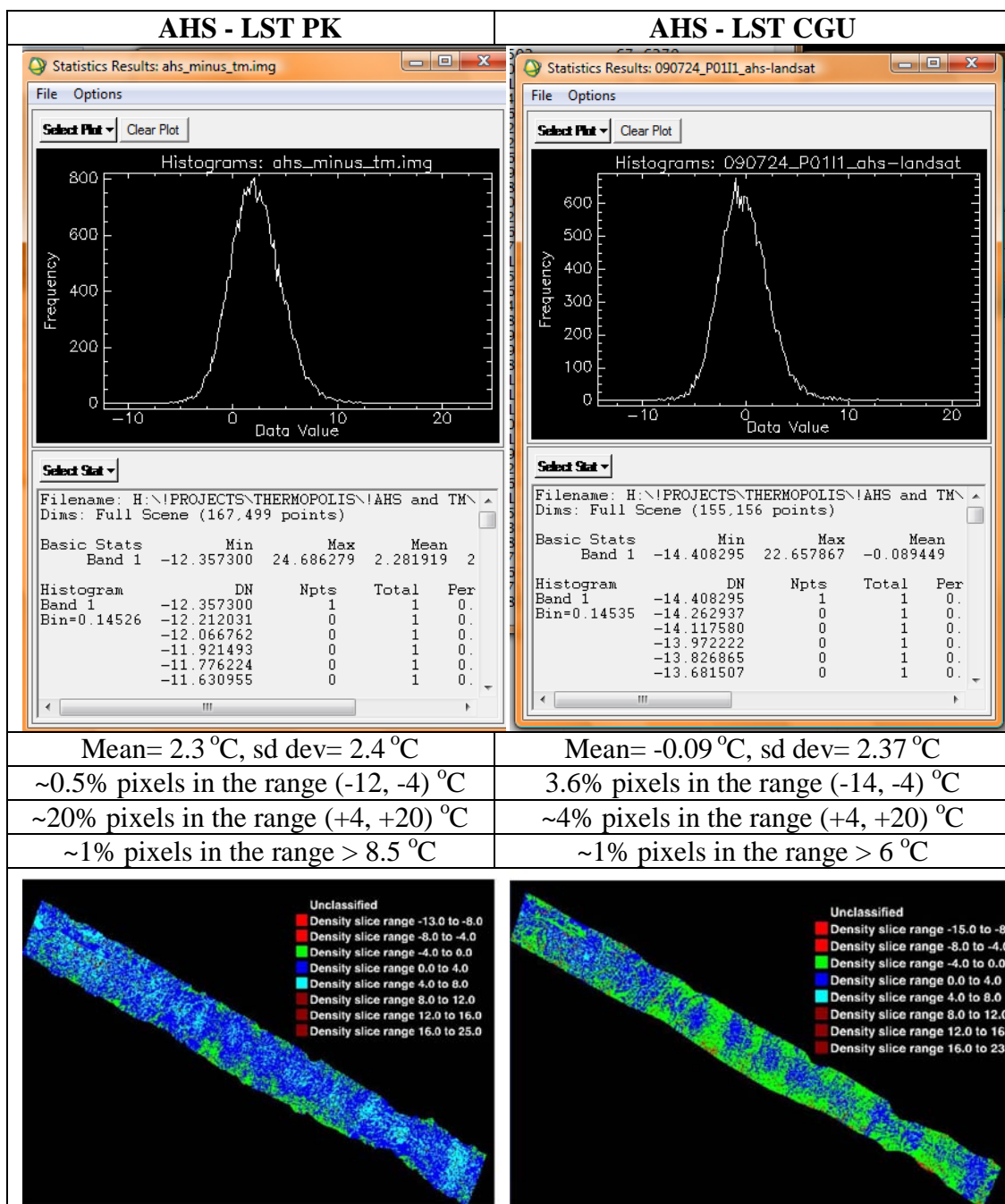


Figure 41: Comparison of the aircraft AHS LST with the LST-PK

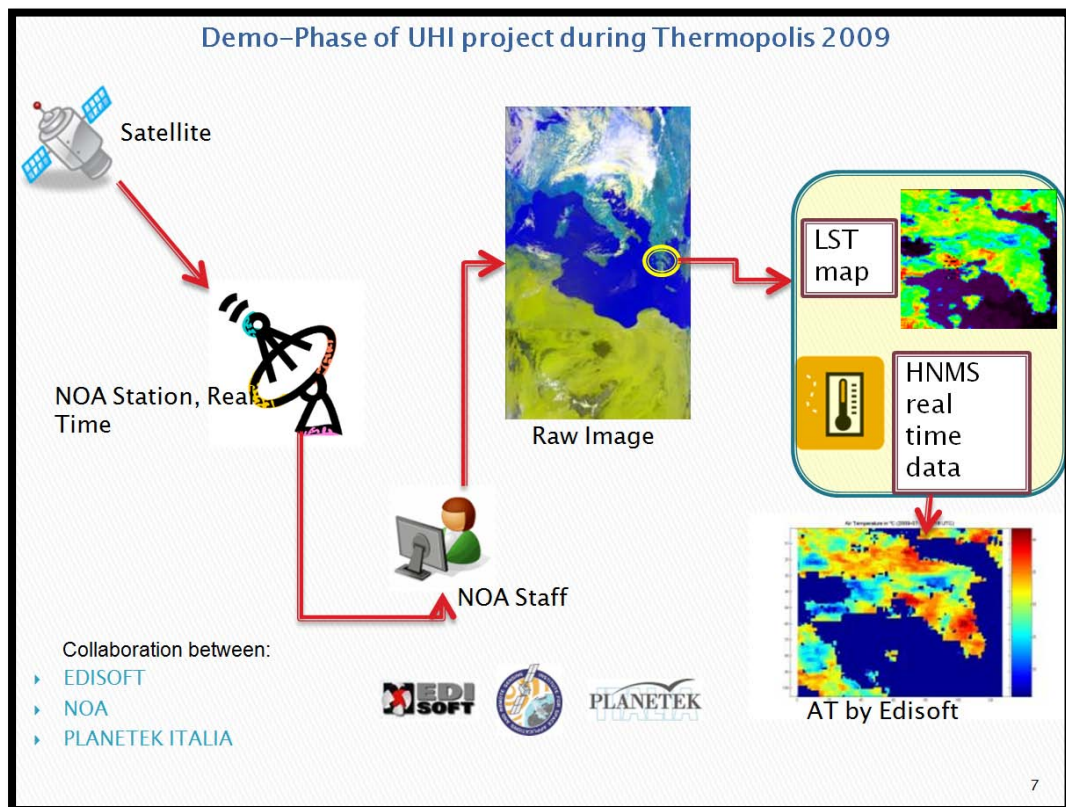
R2.9 NRT

R2.9 NRT AT product has been supported by Thermopolis in a two-fold manner:

- Firstly, by providing in near real time the LST maps from NOAA/AVHRR as received by NOAA's station operated at the National Observatory of Athens.
- Secondly, in post-campaign, by using the GB measurements to validate

the R2.9 NRT product. The validation took place twice: one for the initial product and another one for the improved product provided by Edisoft.

The workflow for **activity (i)** is illustrated in the following diagram. This shows how the data flow during the operational demo phase of UHI project. The satellite data is received by NOAA satellite station in Real Time and is subsequently processed by NOAA staff. Once the quality of the image is assured, the image undergoes specific processing to produce the LST product. The LST map is then uploaded to a dedicated ftp site and a notification email is sent to Edisoft for further processing. The subsequent calculation of AT is also combined with coincident GB data provided at Real Time from the HNMS in an email.





Activity (ii) is to validate the R2.9 product against ground-truth data for 6 days during the project Summer 2009 Demo Phase which coincided with the ESA THERMOPOLIS 2009 campaign. As mentioned before, this was done twice (before and after product improvement), however here we will include only the final validation exercise. AT in-situ measurements were collected from 22 ground-based (GB) stations. The validation is done **per AT product** and **per station**.

Table 30: Mean absolute differences and standard deviations for each NRT AT retrieval during THERMOPOLIS 2009, for the total of 22 GB stations. Analysis PER AT PRODUCT

The calculated mean absolute AT difference from the entire dataset is -0.34 with a standard deviation of 2.39. According to the validation results, R2.9 NRT AT product underestimates ground-based temperatures.

Additionally, validation analysis has also been carried out **per station** for each of the 22 stations. Averaging of AT absolute differences has been performed on the 6 dates of NRT AT products available for each station separately. Results for each station concerning the absolute difference between the R2.9 NRT AT and the measured AT at ground are presented in the following Table along with the standard deviations.

Table 31: Mean differences between NRT AT and GB measured AT along with the standard deviations. Analysis PER STATION.

	Station Name	Latitude (°N)	Longitude (°E)	Mean Difference (°C)	Standard Deviation
1	Kountouriotou	37.9260	23.7124	-2.2162	2.9590
2	Serifou	37.9569	23.6575	-4.2546	4.4231
3	Seirion1	37.9627	23.7564	-1.9538	2.5711
4	Seirion2	37.9627	23.7564	-1.1858	2.4496
5	Anaximenous	37.9698	23.7488	-0.9862	2.7124
6	Dorms	37.9816	23.7810	-0.4500	1.8832
7	Pipinou	37.9965	23.7330	-0.3442	2.4166
8	Thaleias	38.0226	23.8334	-1.3695	1.8134
9	Pellis	38.0279	23.8174	-0.6270	2.5176
10	Papayannis	38.0553	23.8129	-0.2575	1.8637
11	Thiseio	37.9720	23.7180	-2.4033	3.4982
12	Academy	37.9914	23.7810	-0.1079	2.2282
13	Penteli1	38.0473	23.8650	3.4000	2.7981
14	Elliniko	37.8988	23.7234	-7.2525	2.3246
15	Ilioupoli	37.9183	23.7610	-1.9017	4.0478
16	Zografou	37.9771	23.7869	-2.5533	1.9272
17	Pikermi	38.0011	23.9287	2.7117	2.2347
18	Galatsi	38.0294	23.7574	-0.2133	2.2437
19	Anolosia	38.0752	23.6707	2.7833	3.1984
20	Penteli2	38.0865	23.8636	2.1083	1.6195
21	Menidi	38.1066	23.7339	0.9950	4.1631

22	Mandra	38.1229	23.5637	3.8983	5.4715
----	--------	---------	---------	--------	--------

Again, R2.9 NRT AT product underestimates ground-based temperatures in all stations examined by -0.55°C ($\pm 2.59^{\circ}\text{C}$). The mean difference ranges between -7.25 and 3.90°C .

R2.9 Forecasted

Thermopolis 2009 campaign dataset has supported the validation as well as the improvement of the forecast model of LAP_AUTH and has, therefore, increased the accuracy of the produced AT forecast maps for Athens. The product was first validated against the Thermopolis dataset and showed that the model underestimates the ATs. Following that LAP_AUTH (Th. Giannaros and D. Melas) **improved the accuracy** of the model by proposing a downscaling procedure (see below). Finally the improved (downscaled) product was re-validated.

1. Initial Validation

For each pair of data sets, the relative difference in AT [$100 * ((\text{GB AT}) - (\text{R2.9 forecasted AT})) / \text{GB AT}$] is calculated along with the absolute difference [$(\text{GB AT}) - (\text{R2.9 forecasted AT})$] and the corresponding standard deviations. Final results for the urban area of Athens are presented in the following table for each forecasted AT retrieval during the THERMOPOLIS campaign and for the total of 16 stations selected.

Table 32: Mean differences for each forecasted AT retrieval during THERMOPOLIS for the total of 16 GB stations selected.

Date (yyyymmddhhmm)	Mean relative difference (%)	Standard Deviation	Absolute Difference	Standard Deviation
200907221147	8.08	3.79	2.52	1.29
200907231137	13.44	2.71	4.27	0.98
200907241126	20.71	2.99	7.37	1.16
200907281226	11.12	3.18	3.37	1.09
200907291216	12.22	3.10	3.79	1.08
200907301205	8.81	3.52	2.74	1.20
200907311200	9.89	3.31	3.22	1.17

The calculated mean absolute AT difference is 2.90°C with a standard deviation of 1.64°C . According to the validation results, R2.9 forecasted AT product underestimates ground-based temperatures. The correlation coefficient between forecasted and GB ATs was found to be of the order of 0.8.

2. Model Improvement (Downscaling)

The purpose of the improvement was to downscale the primary 2-km AT forecasts to 250-m spatial resolution. This was developed on the basis of artificial neural networks (ANNs), implementing off-line a predictive modelling software (i.e.

Tiberius v.6.1.9, <http://www.tiberius.biz/>). For Athens the following steps were accomplished:

- Implementation of UHI-FS off-line for a 2-months period (i.e. July – August 2009)
- Collection of GB data corresponding to the time period of interest
- Generation of pairs of datasets (i.e. model / observations)
- Definition of training/testing and validation datasets (i.e. 90% and 10% of the entire datasets respectively)
- Implementation of Tiberius for deriving the statistical, non-linear, downscaling equation:

$$AT(i_c) = f(lu_{i_c}, MAT(i_n, j_n), hr)$$

where i_c = index of CORINE-250m grid point, to which AT will be downscaled; (i_n, j_n) = indices of WRF model grid points that are nearest to the i_c CORINE-250m grid point; MAT = model AT and; hr = hour

3. Re-validation

For each pair of datasets, the absolute difference in AT (i.e. R2.9-AT – GB-AT) was calculated for to re-validate the R2.9 AT forecasted product. The validation exercise was focused on each of the 5 GB stations. Averaging of AT absolute differences was has been performed for each station separately. Mean values of the absolute difference for each station examined along with the standard deviations of the averaging are presented in the following table. Additionally, the correlation coefficients between R2.9-ATs and GB-ATs for each station are given, as well as the root mean squared error (RMSE). The table also shows the corresponding comparisons BEFORE the improvements implemented in the previous step.

Table 33: Mean differences between R2.9-AT and GB-AT along with the standard deviations, correlation coefficients between the two datasets and root mean squared errors. Values in parentheses correspond to the magnitude of the presented statistics prior to the downscaling of the forecasts.

	Station Name	Latitude (°N)	Longitude (°E)	Mean Difference (°C)	Standard Deviation	Cor. Coef.	RMSE
1	Serifou	37.9569	23.6575	-0.88 (-2.97)	0.81 (0.87)	0.95 (0.94)	1.19 (3.10)
2	Anaximenous	37.9698	23.7488	-0.19 (-2.86)	1.32 (1.20)	0.92 (0.92)	1.33 (3.10)
3	Dorms	37.9816	23.7810	-1.10 (-3.88)	2.74 (2.78)	0.45 (0.47)	2.93 (4.76)

4	Thaleias	38.0279	23.8174	-0.18 (-2.81)	1.18 (1.10)	0.89 (0.89)	1.19 (3.01)
5	Papayannis	38.0553	23.8129	-0.94 (-3.97)	2.09 (2.02)	0.70 (0.71)	2.29 (4.45)
ENTIRE DATASET				-0.53 (-3.22)	1.65 (1.63)	0.83 (0.83)	1.73 (3.61)

As it can be seen in the above Table, product R2.9 AT underestimates ground-based temperatures by 0.53 (± 1.65). The mean difference ranges between -1.10 and -0.18. The mean correlation coefficient for the entire dataset was found to be equal to 0.83, while RMSE for the entire dataset was found to be equal to 1.73. **The results are much improved for all stations.**

The next Table presents the mean differences between daily maximum, minimum and average R2.9-AT and GB AT, along with the corresponding standard deviations, correlation coefficients and root mean squared errors for the entire dataset.

Table 34: Mean differences between daily maximum, minimum and average R2.9-AT and GB-AT along with the standard deviations, correlation coefficients between the two datasets and root mean squared errors.

	Station Name	Mean Difference	Standard Deviation	Correlation Coefficient	RMSE
M A X	ENTIRE DATASET	-1.82	1.64	0.66	2.44
M I N	ENTIRE DATASET	0.74	1.49	0.63	1.65
A V G	ENTIRE DATASET	-0.54	0.83	0.84	0.99

The improved results are further supported by the frequency histogram of the calculated model biases (i.e. absolute differences between R2.9-AT and GB-AT) for the entire validation dataset as well as the relevant scatter plot with a correlation coefficient of 0.83, as shown below.

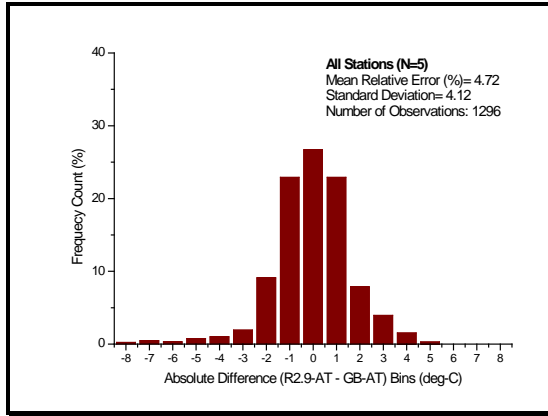


Figure 43: Frequency histogram of the calculated model biases for the entire validation dataset. 70% of the calculated model biases fall in the [-1,1] bin.

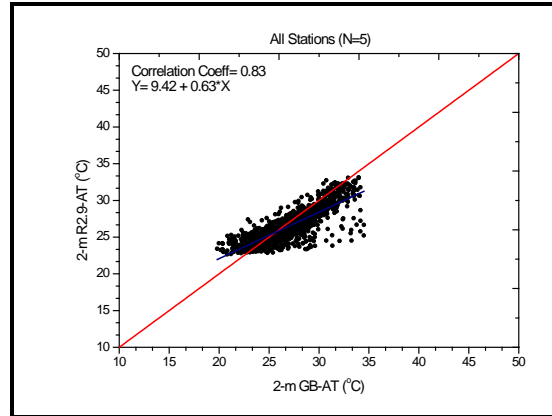


Figure 44: Correlation plot between the R2.9-AT and GB-AT for the entire validation dataset. The mean correlation coefficient was found to be equal to 0.83.

R2.10

R2.10 NRT Discomfort Index (DI) product has been validated against ground-truth data for 6 days during THERMOPOLIS 2009 campaign. AT and Relative Humidity (RH - %) in-situ measurements were collected from 13 ground-based (GB) stations.

Discomfort Index (DI) has been computed from in-situ AT and RH data at 2 m a.s.l., following the formula provided by Giles et al., (1990):

$$DI = AT - 0.55 (1 - 0.01 RH) (AT - 14.5)$$

For each pair of data sets, the absolute difference in DI [R2.10 NRT DI – GB DI] is calculated for validation purposes. Mean values of the absolute difference for each station examined along with the standard deviations of the averaging are presented in the following table for each NRT DI retrieval during the THERMOPOLIS campaign. The validation is done **per DI product** and **per station**.

Table 35: Mean absolute differences and standard deviations for each NRT DI retrieval during THERMOPOLIS 2009, for the total of 13 GB stations. Analysis PER MAP PRODUCT

Date (yyyymmddhhmm)	Absolute Difference (°C)	Standard Deviation
200907180910	1.5843	1.0899
200907190950	-1.3999	1.3731
200907210940	-0.5662	0.6940

200907220845	0.8441	0.7812
200907230925	-0.5188	0.8221
200907240830	-2.0663	1.4367
ENTIRE DATASET	-0.35	1.36

The calculated mean absolute DI difference from the entire dataset is -0.35 °C with a standard deviation of 1.36 °C. According to the validation results, R2.10 NRT DI product slightly underestimates ground-based temperatures.

Validation analysis has been concentrated additionally to each of the 13 stations. Averaging of DI absolute differences has been performed on the 6 dates of NRT DI products available for each station separately. Results for each station concerning the absolute difference between the R2.10 NRT DI and the computed DI from GB measurements are presented in the following Table along with the standard deviations.

Table 36: Mean differences between NRT DI and GB computed DI along with the standard deviations. Analysis PER STATION

	Station Name	Latitude (°N)	Longitude (°E)	Mean Difference (°C)	Standard Deviation
1	Kountouriotou	37.9260	23.7124	-1.7135	1.5991
2	Serifou	37.9569	23.6575	-1.6469	2.3924
3	Seirion1	37.9627	23.7564	-1.3622	1.4510
4	Seirion2	37.9627	23.7564	-0.5816	1.3592
5	Anaximenous	37.9698	23.7488	-0.2284	1.6801
6	Dorms	37.9816	23.7810	-0.3568	1.0661
7	Pipinou	37.9965	23.7330	0.3028	1.4287
8	Thaleias	38.0226	23.8334	-0.5216	0.9021
9	Pellis	38.0279	23.8174	-0.3257	1.4002
10	Papayannis	38.0553	23.8129	0.2239	1.0826
11	Thiseio	37.9720	23.7180	-1.3296	2.0787
12	Academy	37.9914	23.7810	0.3478	1.2675
13	Penteli	38.0473	23.8650	1.5597	1.5227

Again, R2.10 NRT DI product underestimates ground-based DIs in all stations examined by -0.4332°C (± 0.932 °C). The mean difference ranges between -1.71 °C and 1.56 °C.

R2.17

Emissivity was calculated using the Landsat TM image. The following tables include comparisons between R2.17 emissivity and ground based measurements.

**Table 37: Comparisons versus emissivity Band 2 of ground instrument
(emissivity computed using the CIMEL instrument)**

Site name	Measurement Time (UTC)	Latitude	Longitude	Emissivity band 2 measurement (11.29 μm)	LANDSAT TM emissivity (10.4-12.5 μm)	Difference in emissivity
Acropolis (Floor-Rocks)	09:23:11	37° 58.171'	23° 43.699'	0.965	0.970	0.005
Acropolis (Dry grass)	09:37:19	37° 58.208'	23° 43.711'	0.927	0.970	0.043
Acropolis (Rock-1)	09:57:06	37° 58.312'	23° 43.629'	0.924	0.972	0.048

**Table 38: Comparisons versus emissivity Band 3 of ground instrument
(emissivity computed using the CIMEL instrument):**

Site name	Measurement Time (UTC)	Latitude	Longitude	Emissivity band 3 measurement (10.57 μm)	LANDSAT TM emissivity (10.4-12.5 μm)	Difference in emissivity
Acropolis (Floor-Rocks)	09:23:11	37° 58.171'	23° 43.699'	0.949	0.970	0.021
Acropolis (Dry grass)	09:37:19	37° 58.208'	23° 43.711'	0.926	0.970	0.044
Acropolis (Rock-1)	09:57:06	37° 58.312'	23° 43.629'	0.950	0.972	0.022

Table 39: Comparisons versus the broadband emissivity values (emissivity computed using the CIMEL instrument):

Site name	Measurement Time (UTC)	Latitude	Longitude	Broadband emissivity from measurement (11.29 μm)	Emissivity from Landsat TM (10.4-12.5 μm)	Difference
Acropolis (Floor-Rocks)	09:23:11	37° 58.171'	23° 43.699'	0.965	0.970	0.005
Acropolis	09:37:19	37°	23°	0.927	0.970	0.043

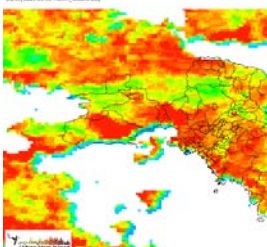
(Dry grass)		58.208'	43.711'			
Acropolis (Rock-1)	09:57:06	37° 58.312'	23° 43.629'	0.924	0.972	0.046

Output

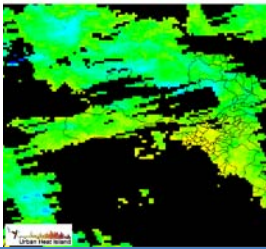
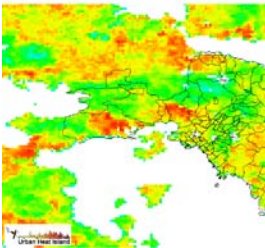
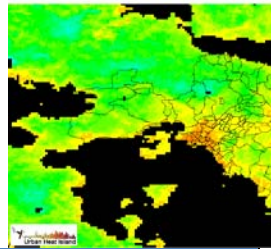
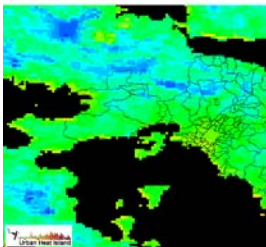
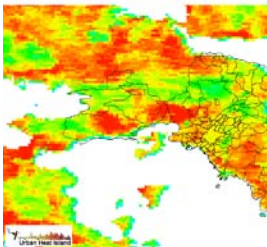
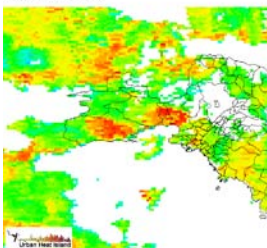
The results presented in this report illustrate the supportive actions of Thermopolis for **in depth validation** of UHI products R2.2, R2.3, **R2.4**, R2.5, R2.9 NRT, R2.9 Forecast, R2.10 NRT, R2.17 and for the improvement of the quality of several UHI products (R2.2, R2.4, R2.5, R2.9 Forecast) by **substantially upgrading the relevant procedures and models** used in the UHI project.

3.2.5 Characterise the temporal evolution of UHI phenomena using the MODIS dataset (question of how to define threshold); compare with equivalent results from airborne data (NOA& UVEG- CGU)

The following Table is a calendar of the useful MODIS images present in the Thermopolis 2009 database which cover different moments of the day. The first step on the characterization of temporal evolution of UHI is to obtain an LST map of every image using a common temperature scale for day images and another scale for night images. The daytime scale ranges from 20-49 °C whilst the nighttime LST scale ranges from 10-29 °C. It has to be noted that several images had flagged pixels and therefore they are not taken into consideration in the analysis.

Date	Time Window UTC			
	Midnight	8-10	Midday	19-21
25				
24				

Date	Time Window UTC			
	Midnight	8-10	Midday	19-21
23				
22				
21				
20				
19				
18				

Date	Time Window UTC			
	Midnight	8-10	Midday	19-21
17				
16				
15				
14				
13				

In order to characterize the UHI phenomena in Athens during the campaign, three approaches are adopted, following Prof. J.A. Sobrino recommendations.

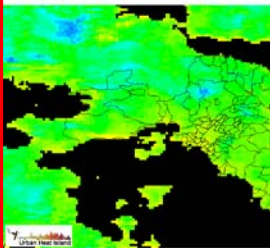
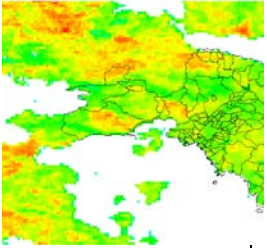
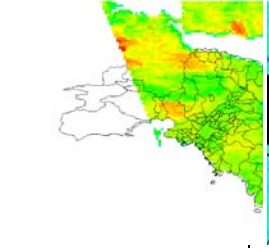
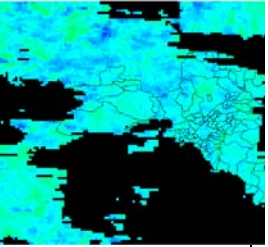
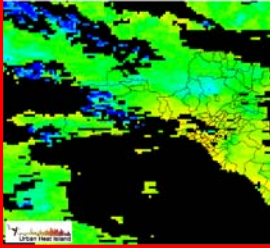
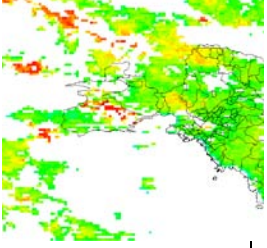
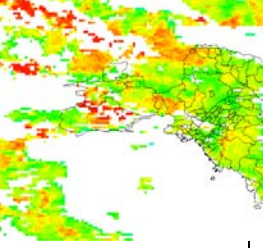
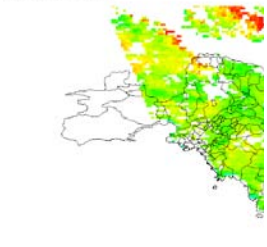
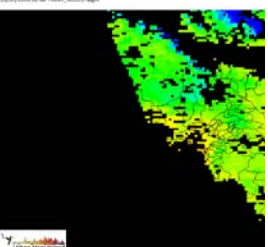
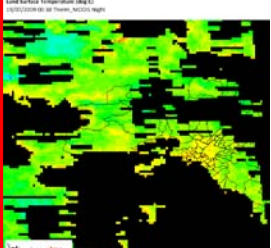
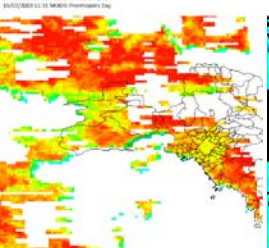
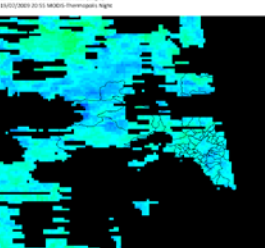
Approach 1: “Takes the coldest image of every day and subtract this image from the rest of the same day (example, assume the coldest of day 17 is the MODIS image of 1h UTC, then you must calculate 5 image difference between this MODIS and the other 5 images of the same day (see Figure). Then an analysis could be done looking for the areas with the highest differences and following the evolution of these differences in terms of area and also in the difference value.”

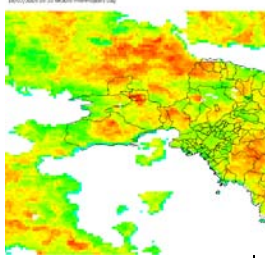
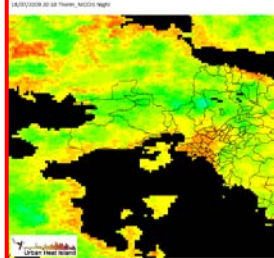
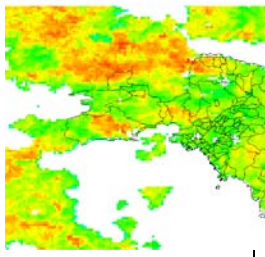
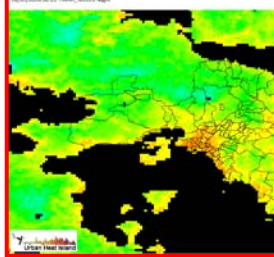
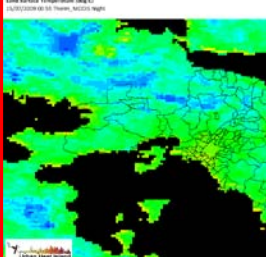
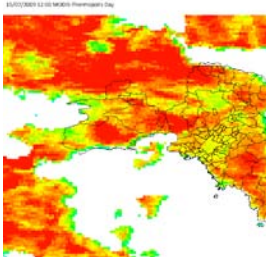
The above was implemented in the following way. Firstly, the images were clustered in dates. Subsequently, the images that would be used as input in the calculations had to be determined. The selection was made based on the following criteria:

1. A single date must have more than one images (to be able to define the ‘coldest’)

2. The city centre has more than 75% valid pixels (flags != 0)
3. The coldest image is defined by the mean temperature of the wider city centre area
4. Two pixels are subtracted if both their flags are equal to 0 (valid pixels)
5. LST differences are plotted using the same scale (from -10 to 29 °C).

The result is presented in the following Table (following the previous one), marking clearly the reference image by a red border.

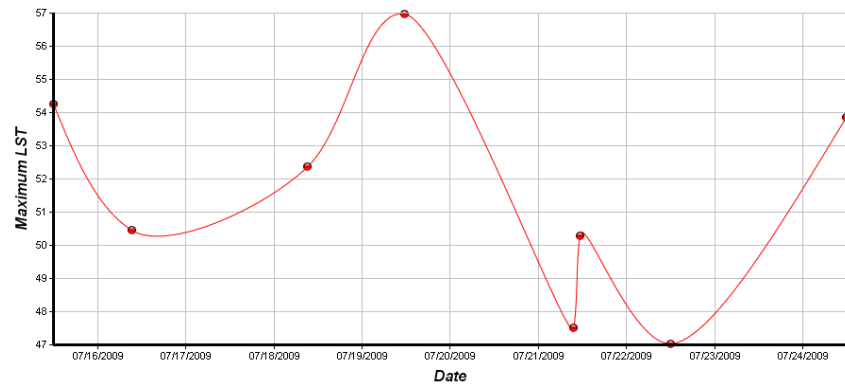
Date	Time Window UTC			
	Midnight	8-10	Midday	19-21
25				
24				
23				
22				
21				
20				
19				

Date	Time Window UTC			
	Midnight	8-10	Midday	19-21
18				
17				
16				
15				
14				
13				

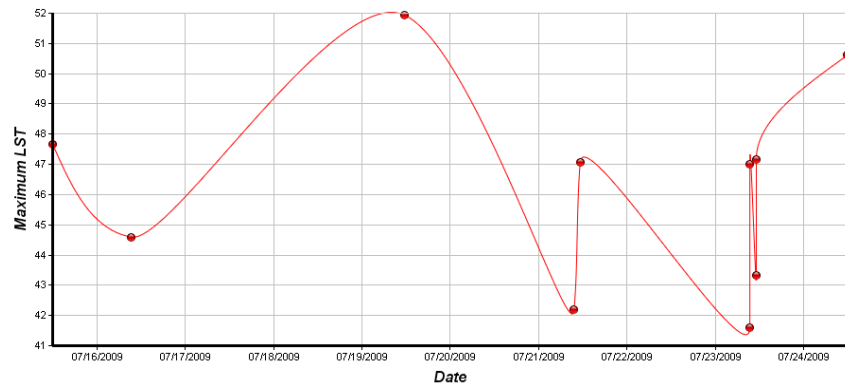
This approach shows the patterns of the hot spots compared with the coldest image of the day. The above analysis shows that the midnight UTC is the coldest image (when present). Otherwise the evening one (19-21 UTC) is used as reference. Due to data gaps it is difficult to conclude, however, it seems that the city centre is approximately 10-20 °C warmer than the coldest image. The difference varies depending on the overall thermal situation of the day. On a particularly warm day (e.g. 15/7/2009 and 19/7/2009) the city centre was ~20 °C warmer at midday (UTC) than it was at midnight (UTC). The two dominant morning hot spots of Megara and Elefsis-Aspropyrgos and – to a lesser extent - the weaker hot spot of Mesogeia exhibited the largest LST diurnal variations, in some cases reaching 30 °C. As expected the largest discrepancies (highest temperatures) are exhibited in the time window 10-13 UTC (13-16 local time).

The evolution of Maximum LST temperatures of these areas of interest are shown in the flowing plots:

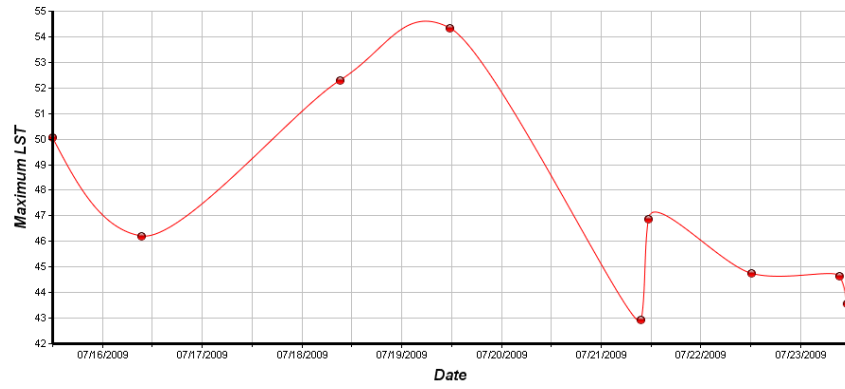
Maximum LST, Elefsina, Daytime



Maximum LST, Urban Center, Daytime



Maximum LST, Mesogeia, Daytime



Maximum LST, Urban Center, Nighttime

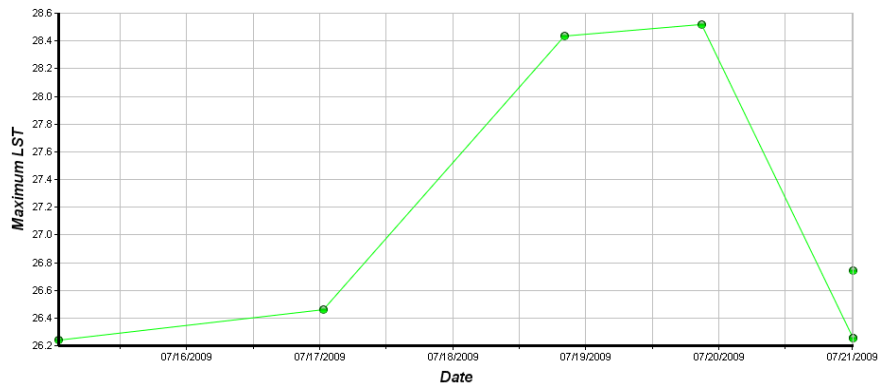
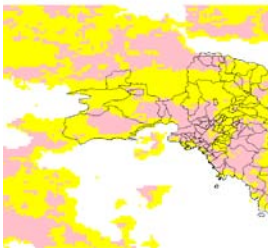

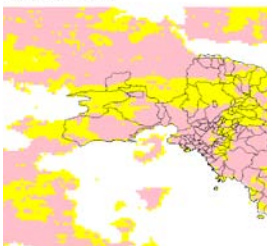
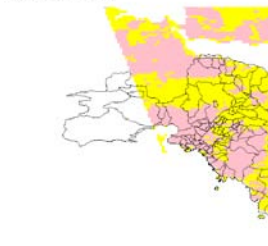
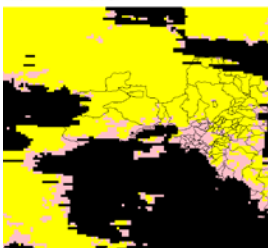


Figure 45: The evolution of Maximum LST temperatures in the areas of interest

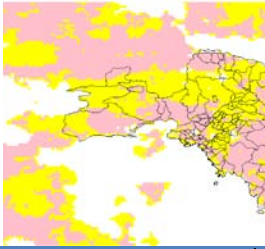
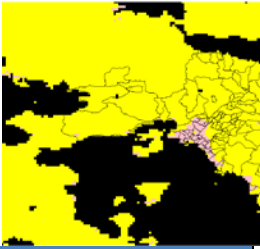
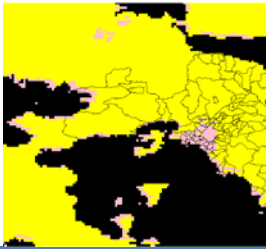
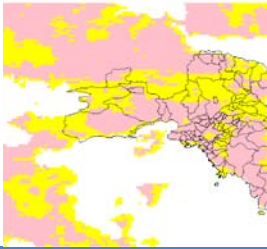
Approach 2: “Another analysis can be done considering all the LST images. Select a threshold value for the temperature (the threshold can be obtained from the maximum of the histogram of the city area) and make a distinction between pixels with LST higher than this threshold value and the pixels with a lower value (i.e. make an isotherm for the threshold temperature).”

This was implemented taking into consideration the images for which at least the 75% of the city centre had valid LST values (flag=0). Subsequently, for the city centre the histogram of the LSTs is calculated from the minimum to the maximum LST using a 1-degree bin. The LST value where the frequency of occurrence is maximum (histogram peak) is defined as a dynamic threshold. We use the term dynamic here as this threshold differs from image to image.

The results are presented in the following table. The pink pixels are the ones with $LST > \text{dynamic threshold}$ and the yellow ones with $LST < \text{dynamic threshold}$.

Date	Time Window UTC			
	Midnight	8-10	Midday	19-21
25				
24				
23				

Date	Time Window UTC			
	Midnight	8-10	Midday	19-21
22				
21				
20				
19				
18				
17				

Date	Time Window UTC			
	Midnight	8-10	Midday	19-21
16				
15				
14				
13				

The patterns of the dynamic LST threshold isotherm (border between pink and yellow pixels) are difficult to be evaluated especially during daytime as the city centre is surrounded by mountains (lower LSTs) and away from the centre there exist three hot spots, namely Megara, Elefsis-Aspropyrgos and Mesogeia. It is more interesting to concentrate on the night-time patterns which are mainly at the city centre (UHI phenomenon). These show that in the 20 UTC images the included area of high LSTs is larger for the warm day of 19.07.

The dynamic thresholds (where city centre LST histogram peaks) are given in the following table together with the diurnal variability (where it can be defined, i.e. for dates that more than one images are usable) and with the mean and standard deviation per time window. The results show that for the time period of Thermopolis, the coldest images are (as expected) the night ones, i.e. at midnight UTC where the LST dynamic threshold is 24 °C and at around 20 UTC where the relevant value is 26.3 °C. Both night images have a small standard deviation of ~ 1 °C indicating minimum variations. The highest differences are observed in the daytime images, at around 8 and 12 UTC where the dynamic LST threshold is 40.8 and 42.7 °C, respectively, albeit with higher standard deviations of 2.2 and 3.7 °C, respectively. The highest LST variability within the same day is exhibited in 19.07 (a particularly warm day) and was found to be equal to 22 °C.

Table 40 : The dynamic thresholds and the diurnal LST variability

Date/Time (UTC)	Midnight	8	Midday	20	Max-Min
24			47		
23	24	38	39	25	15

22	39				17
21	24	39	41		
20	42				
19	25		47	26	22
18	43				16
17	25				
16	42				15
15	22	43			21
Mean (Stdev)	24 (1.2)	40.8 (2.2)	42.7 (3.7)	26.3 (1.0)	

A plot of selected dates (where three images of the same date were available) can be seen next, illustrating the above results.

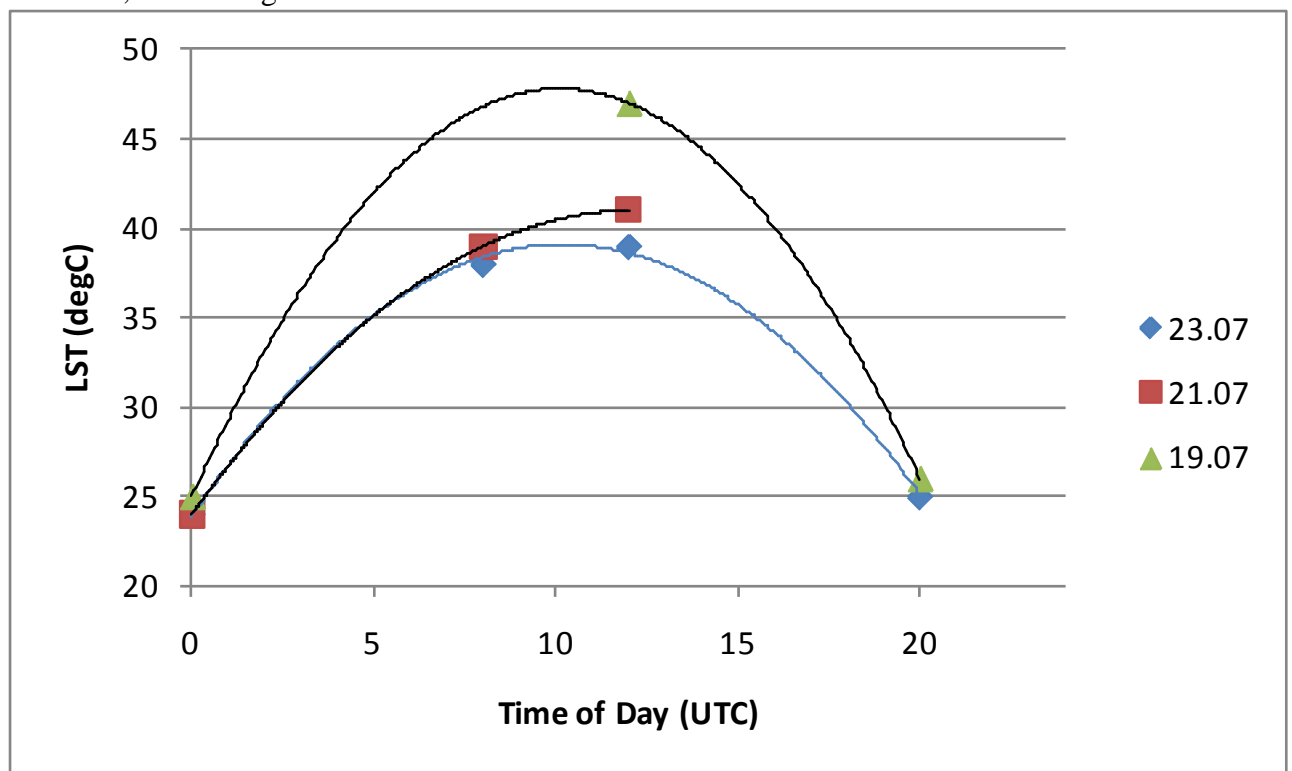


Figure 46: Plot of the results of table 40

Approach 3: "A third analysis can be done making a delimitation of what can be considered as the urban area of the city of Athens and selecting an area near to the city to be considered as a reference rural area. This rural area should be similar to the city in terms of altitude, no densely urbanized and without landforms between them (e.g. the area near to the north-east airport of Athens or the one considered after a qualitative reconnaissance of the image).

A comparison between the urban area and the reference area can be done obtaining the Median value and also the standard deviation of the every area and later on making the differences between the Median of the urban area minus the Median of the rural area. The evolution of these differences and also the magnitude of the standard deviation can provide a characterization of the daily evolution of the UHI phenomena during all the days of the campaign."

First two areas were selected:

- Urban area is in the city centre, covering only dense urban land use with an altitude not exceeding 200m, and
- Rural area is the reference area selected at the vicinity of but not including the Athens airport, covering non dense urban fabric and other rural land cover. For consistency with the urban area the reference area is also below 200m of altitude.

Within this approach, we are only interested in the two areas, not in the whole image. The mean and standard deviation of the LST_U and LST_R pixels are calculated and the difference between them gives the magnitude of the Surface Urban Heat Island. The results are shown in the following Figure.

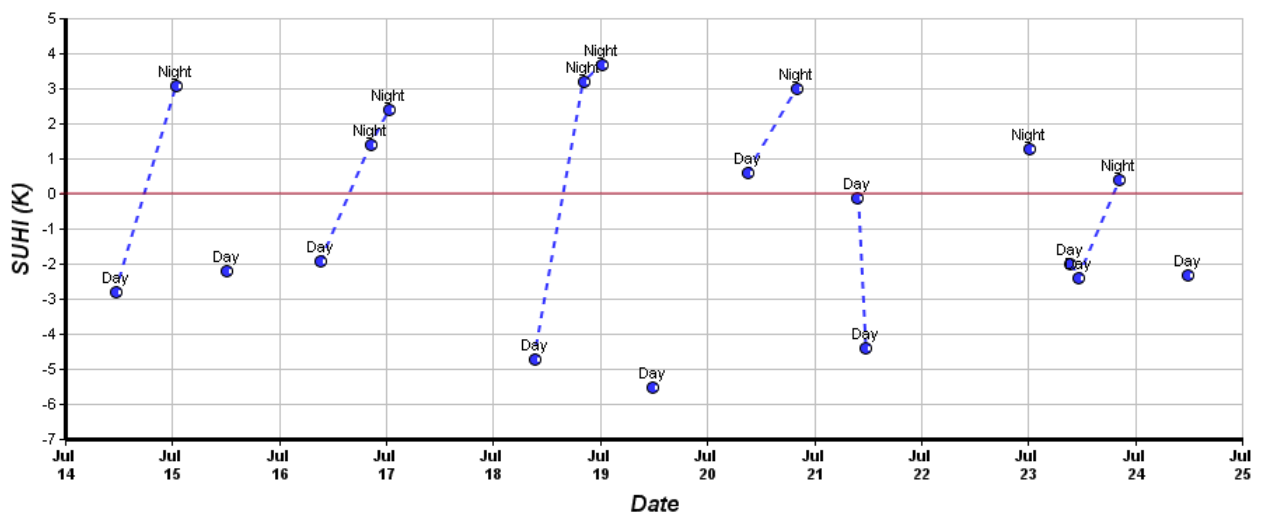


Figure 47: The magnitude of the Surface Urban Heat Island in Kelvin

It is worth comparing this figure with the one derived by CGU group using AHS data (from aircraft) and presented during the Thermopolis final meeting. In any case, the

figures cannot be compared one-to-one as the time of data acquisition is different and the aircraft rural areas are identical to the ones used for the MODIS comparisons.

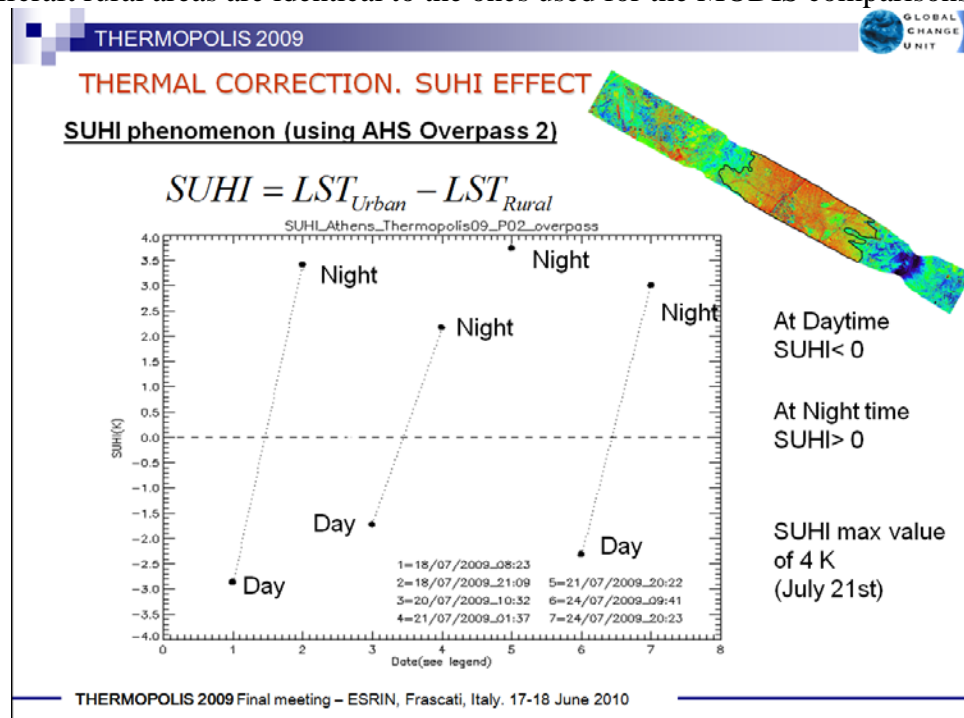


Figure 48: The SUHI Phenomenon using AHS overpass 2

The difference

$$SUHI = LST_U - LST_R$$

takes negative values during daytime where the rural areas are warmer than urban areas. The standard deviation of LST_U and LST_R is less than 1-degC. The situation is reversed at night-time. It is worth noting that free of cost, daily MODIS imagery depicts satisfactorily the SUHI phenomenon and – through proper processing- can be used to monitor its evolution with time. On the particularly warm day of 19 July 2009, $LST_R=52.6$ °C and $LST_U=47.1$ °C making SUHI equal to -5.5 °C during the day, which was the highest SUHI observed in this dataset. It is worth noting the very high linear correlation of 0.98 between urban and rural LST as shown in the following plot (the linear model applies both for day and night images):

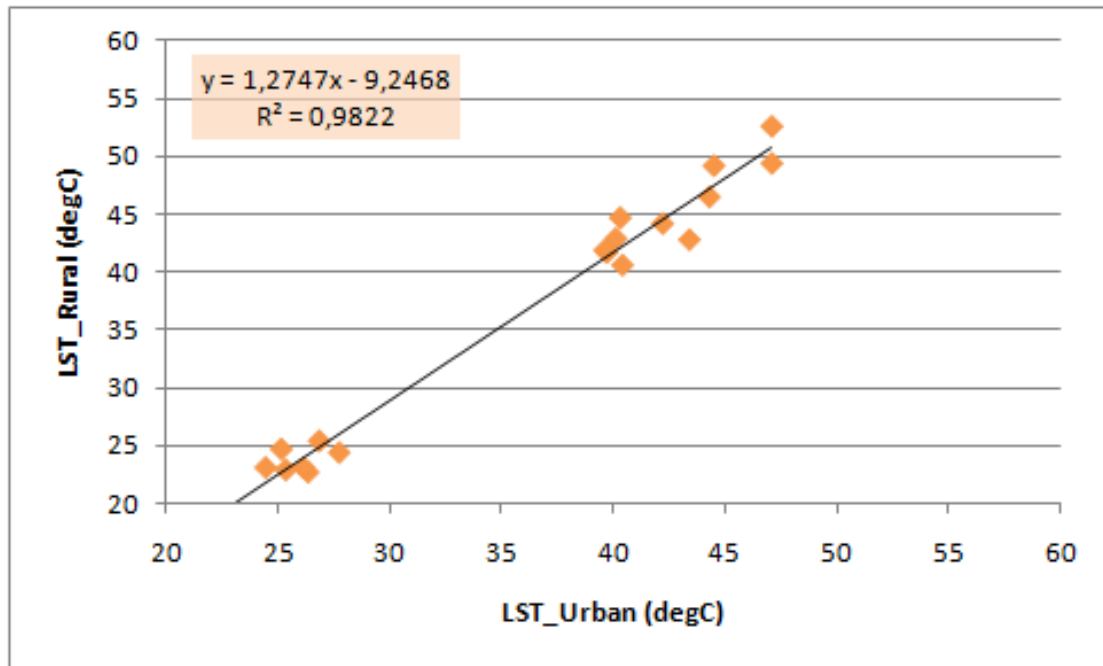


Figure 49: Linear correlation between rural and urban SUHI (both day and night).

4. Airborne Data Acquisitions, Processing and Analyses

CENTER FOR RESEARCH AND TECHNOLOGY HELLAS(CERTH) and the company AEROPHOTO, + the company INTA of Spain deployed the aircraft + imaging instruments + technical staff at the ELEFSINA airport of ATHENS, Greece for the minimization of handling costs. The details of the deployment have been agreed with the CIVIL AVIATION AUTHORITY OF GREECE due to flight restrictions over Athens and with the campaign coordinators.

There were three flight heights (see below), whereby UHI-1 at around 6250 ft was performed at two passes each pass for all radiation data collection by the INTA aircraft. The AEROPHOTO aircraft operated at UHI-1 at around 8000 ft, and additionally at a higher UHI-2 at around 11000 ft (except the last flight) and a lower height UHI-3 at around 2000-4000 ft at one pass so that heat fluxes and net radiation can be obtained.

After a successful data acquisition survey, a set of quick-looks was prepared for each daily acquisition by the INTA cameras, shortly after landing, and was forwarded to the campaign coordinators for review. TWO OPERATIONS CENTRES were established, one at the airport and a second at NOA.

4.1 AHS system

The AHS is an imaging 80-band line-scanner radiometer, built by SensyTech Inc. (currently Argon ST, and formerly Daedalus Ent. Inc.), delivered to INTA late in 2003. It is based on previous airborne hyperspectral scanners as MIVIS (Multispectral Infrared and Visible Imaging Spectrometer) and MAS (MODIS Airborne Simulator). The AHS has been installed in a CASA-212 200 Series aircraft owned and operated by INTA's technicians and CECAF's crews, and integrated with a GPS/INS POS-AV 410 from Applanix (Figure 14). The AHS was first flown by INTA on September 2003. During 2004 the instrument was validated during a number of flight campaigns which included extensive ground surveys (SPARC-2004 and others), and is fully operational since early 2005. The AHS spectrometer has been configured with very distinct spectral performances depending on the spectral region considered. It contains four types of detectors organized in five optical ports. Port 1 covers the VIS/NIR range. Its bands are relatively broad (28-30 nm). The spectral coverage is continuous from 442nm up to 1026 nm. In the SWIR range, port 2a has an isolated band centred at 1.6 μm and 90 nm width, used to simulate the corresponding spectral channel found in a number of satellite missions. Next, port 2, has a set of continuous, fairly narrow bands (18-19 nm) laying between 1909 nm and 2558 nm, well suited for soil/geologic studies. In the MWIR region, port 3 with 7 bands operating from 3.1 to 5.4 μm , gathers the energy through an Indium Antimonide – InSb 7-elements detector array, cooled with liquid nitrogen. The mean bandwidth is 350 nm. Instead the LWIR photons, from 8.3 to 13.4 μm are collected by optical port 4, with a 10-element Mercury Cadmium Telluride – MCT detector array that needs as well to be kept at cryogenic temperature to optimize its performance. The average bandwidth is now of 480 nm. Electronic signals coming from the detectors, pre-amplifiers and amplifiers are digitized at 12 bits, and sampled every 2.1 mrad along the FOV (90° -1.57rad), that results 750 pixels-samples per scanline. AHS IFOV is 2.5 mrad determined by an square field-stop placed in the middle of its optical path.

Radiometric calibration is achieved by at-lab measurements looking at an integrating

sphere for the reflective channels (port 1, port 2a and port 2). Instead the radiometric response of the emissive detectors, port 3 and port 4, is calibrated comparing the signal gathered by the detectors when looking to the known reference thermal sources integrated in the scan head frame: two black bodies the sensor looks at every scan line, before and after each scanline is completed. Two more features have been implemented to enlarge the dynamic range of the emissive infrared detectors: a bi-linear amplification curve that provides lower gain at high radiance levels, and a set of thermal attenuating filters that can be placed at the entrance of the thermal infrared ports to prevent detector saturation when looking at high temperature targets.

These spectral features allow to state that AHS is best suited for multipurpose studies/campaigns, in which a wide range of spectral regions have to be covered simultaneously, specially if no detailed spectroscopy is required. In particular, AHS is a very powerful instrument for thermal remote sensing. The resulting system is available to the International Remote Sensing Community through specific agreements (contractual or based on joint collaborations).



Figure 50. INTA C-212 Series 200 aircraft and AHS system.

The spectral bands in the VNIR and SWIR have a gaussian distribution with FWHM equal to bandpeak-to-bandpeak spacing, as assumed by processing tools such as ENVI. Bands in the thermal ports (MWIR and LWIR) are also well approximated by the gaussian curve, but their broader size would require the use of the spectral responsivity for detailed analysis. Band AHS-21 (port 2A) is less regular, and band centre, peak response and FWHM have a singular relation.

The instrument has been installed in the cabin of the INTA's aircraft, EC-DUQ, and integrated with an Applanix POS/AV 410 GPS/INS. This module will provide proper positioning and attitude measurements to geo-reference image data accurately.

Table 41. AHS Technical specification

Imaging technique	whisk-broom line scanning
Spectral coverage	VNIR+SWIR+MWIR+LWIR (80 bands)
FOV/IFOV	1.571rad (90°)/ 2.5mrad
Ground sampling	2.1mrad (0.12°)

distance	
Scanning rates	12.5, 18.7, 25, 31.2 and 35rps providing ground sampling distance from 2.5 to 7 m @ GS 72ms-1
Pixels per scanline	750 samples per line (16% side overlapping)
Spatial resolution range	from 2.5 to 7 m @ 72ms ⁻¹
Swath	2000m to 5500m
Core architecture	2 INTEL Pentium 4/W2K processors 12 bits data recorded in a removable SCSI magnetic hard disk

Table 42. AHS operating modes, flight parameters and pixel size at nadir

Scan rate (rps)	Ground Speed (Kts)	Altitude (m)	GIFOV (m)	Swath (m)
6.25	140	2751	6.88	5502
12.5		1839	4.560	3678
18.7		1376	3.44	2751
25		1102	2.76	2204
31.2		983	2.46	1965
35		2751	6.88	5502

Table 43. AHS spectral configuration †Full Width Half Maximum (updated Feb.2008)

Spectral range	Spectral region	No. of bands	Bandwidth $\Delta\lambda$ @FWHM†	$\lambda/\Delta\lambda$ minimum
442-1026nm	VNIR	20	28-30nm	≈ 17
1556-1643nm	SWIR	1	90nm	≈ 18
1909-2558nm	SWIR	42(34)	18-19nm	≈ 100
3055-5448nm	MIR	7	289-428nm	≈ 9
8111-13361nm	TIR	10	418-542nm	≈ 19

4.2 INTA-AHS data acquisition and processing

The INTA role within Thermopolis was to deploy a hyperspectral sensor to gather TIR data sets of the test site (the urban area of Athens), synchronised with acquisitions from satellite sensors and in coordination with the collection of in situ measurements in order to meet the requirements of the project. Reflective data from the VIS to the MIR regions would be used to support the main TIR measurements.

Table 44: AHS spectral configuration

Optical Port	Detector	Number of Bands	Spectral Range (nm)	Band Width $\Delta\lambda$ (FWHM, nm)
Port 1 - VNIR	Si - not cooled	20	457 to 1009	27 to 30
Port 2A - SWIR	InGaAs - cooled	1	1590	90
Port 2 - SWIR	InSb - cooled	42	1916 to 2549	16 to 19
Port 3 - MWIR	InSb - cooled	7	3233 to 5311	280 to 440
Port 4 - LWIR	HgCdTe - cooled	10	8374 to 13103	420 to 560

The spectral bands in the narrower ports (Port 1 and Port 2) have a gaussian distribution with FWHM equal to bandpeak-to-bandpeak spacing, as assumed by processing tools (typically ENVI). Bands in the thermal ports (3 and 4) are also well approximated by the gaussian curve, but their broader size would require the use of the spectral responsivity for detailed analysis. Band AHS-21 (port 2A) is the less regular one, and band center, peak response and FWHM have a singular relation.

4.3 Campaign Planning And Execution.

The AHS campaign was fully described in the Thermopolis progress report. A summary is given below.

Preparation of the surveys was started at the preparation meeting on Athens, March 6th, with the support of Democritus University of Thrace, European Space Agency, University of Valencia, Aerophoto and CECAF.

The AHS instrument was radiometrically and spectrally calibrated at INTA facilities April 2009. To complete the instrument check-out, a radiometric validation and geometric calibration (boresight) survey was performed over the Tirez test site (Toledo, Spain) on May 22th.

Through different iterations with the project partners, the initial flight plan was established (see figure).

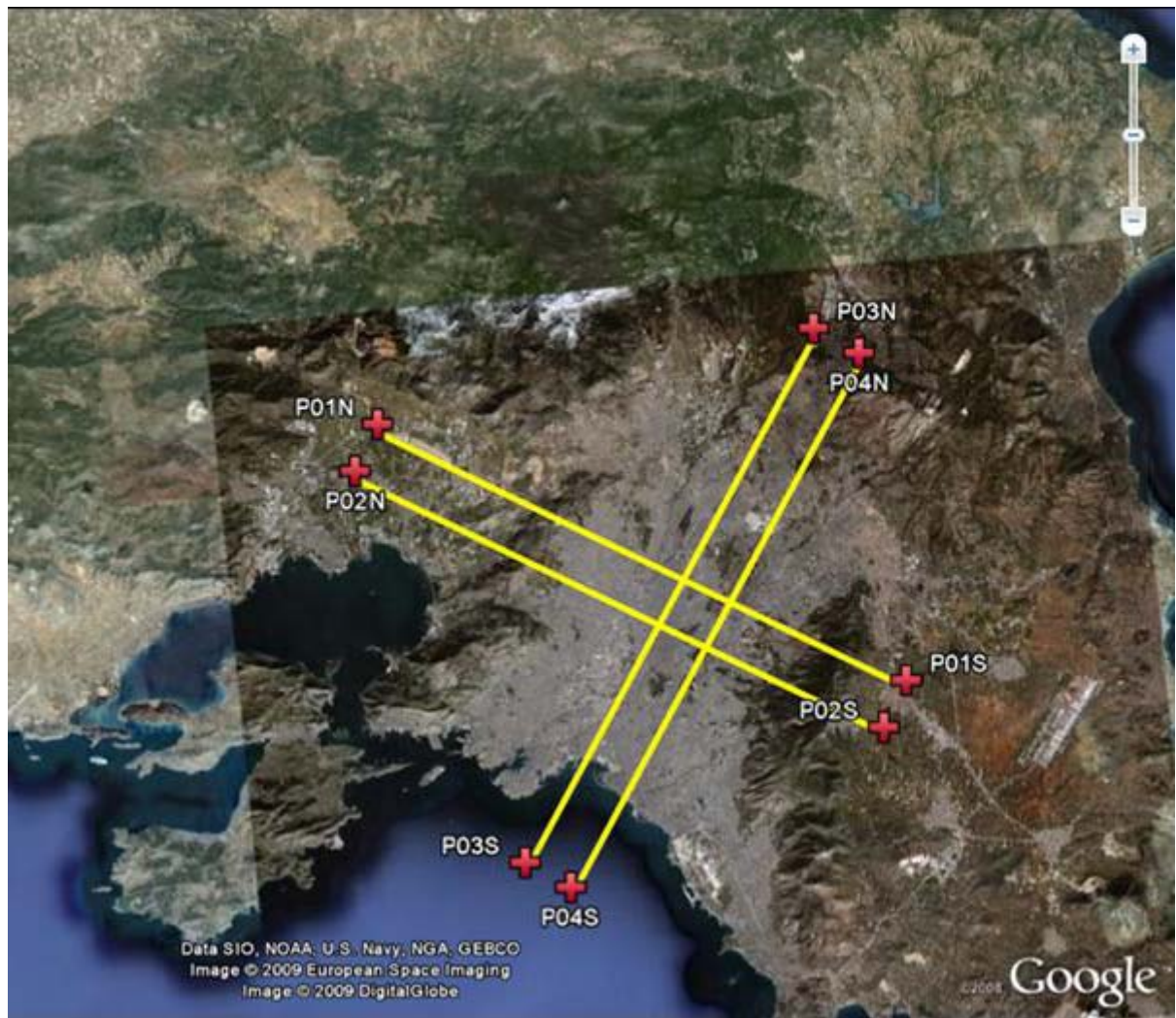


Figure 51: Initial flight plan

4.3.1 Survey Plan Flights Performed

TEST SITE: ATHENS URBAN AREA

FLIGHT 01. July 18, 2009 starting at UTC08:00. UHI survey (UHI ALT MSL6250FT)

FLIGHT 02. July 18, 2009 starting at UTC20:00. UHI survey (UHI ALT MSL6250FT)

FLIGHT 03. July 20, 2009 starting at UTC10:00. UHI survey (UHI ALT MSL6250FT)

FLIGHT 04. July 21, 2009 starting at UTC01:00. UHI survey (UHI ALT MSL6250FT)

FLIGHT 05. July 21, 2009 starting at UTC20:00. UHI survey (UHI ALT MSL6250FT)

FLIGHT 06. July 24, 2009 starting at UTC09:00. UHI survey (UHI ALT MSL6250FT)

FLIGHT 07. July 24, 2009 starting at UTC20:00. UHI survey (UHI ALT MSL6250FT)

Flight 01 UHI survey (UHI FLIGHT ALT MSL6250FT)

Date: Saturday, July 18, 2009, starting at 08:00UTC (11:00LT)

Flight pattern #02 (P03 and P04 enlarged towards N to cover Marathónos Lake)

Weather conditions: Clear sky SKC (0/8). Mid-intensity wind from the NE. Hazy atmosphere.

FLIGHT LINE ID.	REC.ID. HARD DISK&FILE	TIME (UTC)	ALTITUDE (MSL)	TRUE HDG	LENGTH/DUR. (GS 72ms ⁻¹ /140KTS)	AHS SCAN-RATE	REMARKS
AHS P01A Elefsina → Koropi 200907180800-18.7-P01A	HD08 F01	08:05	6250FT (1905m)	121°	29.1km/8m44s	18.7 rps	TBB1=283K,TBB2=328K Haze. Turbulence. High XTE in the beginning.
AHS P02 Koropi → Elefsina 200907180800-18.7-P02	HD08 F02	08:19	6250FT (1905m)	301°	29.1km/8m44s	18.7 rps	TBB1=283K,TBB2=331K
AHS P04 Saronikos → Penteli 200907180800-18.7-P04	HD08 F03	08:39	6250FT (1905m)	034°	42.1km/9min44s	18.7 rps	
AHS P03 Penteli → Saronikos 200907180800-18.7-P03	HD08 F04	08:55	6250FT (1905m)	214°	42.1km/9min44s	18.7 rps	
AHS P01B Elefsina → Koropi 200907180800-18.7-P01B	HD08 F05	09:16	6250FT (1905m)	121°	29.1km/8m44s	18.7 rps	Strong crossed wind at the end.

Flight 02 UHI survey (UHI FLIGHT ALT MSL6250FT)

Date: Saturday, July 18, 2009, starting at 20:00UTC (23:00LT)

Flight pattern #02 (P03 and P04 enlarged towards N to cover Marathónos Lake)

Weather conditions: Clear sky SKC (0/8).

FLIGHT LINE ID.	REC.ID. HARD DISK&FILE	TIME (UTC)	ALTITUDE (MSL)	TRUE HDG	LENGTH/DUR. (GS 72ms ⁻¹ /140KTS)	AHS SCAN-RATE	REMARKS
AHS P04 Saronikos → Penteli 200907182000-18.7-P04	HD08 F06	20:05	6250FT (1905m)	034°	42.1km/9min44s	18.7 rps	TBB1=282K,TBB2=323K
AHS P03 Penteli → Saronikos 200907182000-18.7-P03	HD08 F07	20:24	6250FT (1905m)	214°	42.1km/9min44s	18.7 rps	
AHS P01 Elefsina → Koropi 200907182000-18.7-P01	HD08 F08	20:48	6250FT (1905m)	121°	29.1km/8m44s	18.7 rps	
AHS P02 Koropi → Elefsina 200907182000-18.7-P02	HD08 F09	21:05	6250FT (1905m)	301°	29.1km/8m44s	18.7 rps	

Flight 03 UHI survey (UHI FLIGHT ALT MSL6250FT)

Date: Monday, July 20, 2009, starting at 10:00UTC (13:00LT)

Flight pattern #03 (P04 covering Marathónos Lake, P03&P04 shortened in the South side).

Weather conditions: Clear sky SKC (0/8). Some sparse clouds appear over the study area at the end of the survey at the flight level (North ending of P04). Weak wind blowing for the North that decreases during the survey. Thick haze. Temperature reported at the cabin before starting is 306K (33C).

FLIGHT LINE ID.	REC.ID. HARD DISK&FILE	TIME (UTC)	ALTITUDE (MSL)	TRUE HDG	LENGTH/DUR. (GS 72ms ⁻¹ /140KTS)	AHS SCAN-RATE	REMARKS
AHS P01 Elefsina → Koropi 200907201000-18.7-P01	HD08 F10	10:12	6250FT (1905m)	121°	29.1km/8m44s	18.7 rps	TBB1=281K,TBB2=333K Haze. Turbulence. High XTE in the beginning.
AHS P02 Koropi → Elefsina 200907201000-18.7-P02	HD08 F11	10:28	6250FT (1905m)	301°	29.1km/8m44s	18.7 rps	
AHS P04 Saronikos → Penteli 200907201000-18.7-P04	HD08 F12	10:47	6250FT (1905m)	034°	36.0km/8min20s	18.7 rps	
AHS P03 Penteli → Saronikos 200907201000-18.7-P03	HD08 F13	10:56	6250FT (1905m)	214°	24.0km/5min33s	18.7 rps	

Flight 04 UHI survey (UHI FLIGHT ALT MSL6250FT)

Date: Tuesday, July 21, 2009, starting at 01:00UTC (04:00LT)

Flight pattern #03 (P04 covering Marathónos Lake, P03&P04 shortened in the South side).

Weather conditions: Some sparse high clouds over the study area (less than 1/8). Mid intensity wind blowing from the North at the flight level. Temperature reported at the cabin before starting is 301K (28C).

FLIGHT LINE ID.	REC.ID. HARD DISK&FILE	TIME (UTC)	ALTITUDE (MSL)	TRUE HDG	LENGTH/DUR. (GS 72ms ⁻¹ /140KTS)	AHS SCAN-RATE	REMARKS
AHS P01 Elefsina → Koropi 200907210100-18.7-P01	HD06 F14	01:20	6250FT (1905m)	121°	29.1km/8m44s	18.7 rps	TBB1=281K,TBB2=323K
AHS P02 Koropi → Elefsina 200907210100-18.7-P02	HD06 F15	01:33	6250FT (1905m)	301°	29.1km/8m44s	18.7 rps	
AHS P04 Saronikos → Penteli 200907210100-18.7-P04	HD06 F16	01:49	6250FT (1905m)	034°	36.0km/8min20s	18.7 rps	
AHS P03 Penteli → Saronikos 200907210100-18.7-P03	HD06 F17	02:00	6250FT (1905m)	214°	24.0km/5min33s	18.7 rps	

Flight 05 UHI survey (UHI FLIGHT ALT MSL6250FT)

Date: Tuesday, July 21, 2009, starting at 20:00UTC (23:00LT)

Flight pattern #03 (P04 covering Marathónos Lake, P03&P04 shortened in the South side).

Weather conditions: Clear sky. Strong wind blowing from the N-NE at the flight level up to ca. 30KTS that creates some turbulence and requires to extent 25% flaps to keep the nominal GS of 140KTS along P03 (tail wind).

FLIGHT LINE ID.	REC.ID. HARD DISK&FILE	TIME (UTC)	ALTITUDE (MSL)	TRUE HDG	LENGTH/DUR. (GS 72ms ⁻¹ /140KTS)	AHS SCAN-RATE	REMARKS
AHS P01 Elefsina → Koropi 200907212000-18.7-P01	HD06 F18	20:03	6250FT (1905m)	121°	29.1km/8m44s	18.7 rps	TBB1=281K,TBB2=323K
AHS P02 Koropi → Elefsina 200907212000-18.7-P02	HD06 F19	20:18	6250FT (1905m)	301°	29.1km/8m44s	18.7 rps	Delay due to air traffic over Athens Intl. Airport
AHS P04 Saronikos → Penteli 200907212000-18.7-P04	HD06 F20	20:35	6250FT (1905m)	034°	36.0km/8min20s	18.7 rps	Strong wind from N-NE
AHS P03 Penteli → Saronikos 200907212000-18.7-P03	HD06 F21	20:48	6250FT (1905m)	214°	24.0km/5min33s	18.7 rps	Strong tail wind. Flaps at 25%

Flight 06 UHI survey (UHI FLIGHT ALT MSL6250FT)

Date: Friday, July 24, 2009, starting at 09:00UTC (12:00LT)

Flight pattern #03 (P04 covering Marathónos Lake, P03&P04 shortened in the South side).

Weather conditions: Clear sky. Strong wind blowing from the N-NW at the flight level up to about 30KTS. It makes necessary to use the flaps to keep the nominal GS of 72ms⁻¹ along P03 (strong tail wind). Temperature at the cabin is 310K (37C) before starting the engines.

FLIGHT LINE ID.	REC.ID. HARD DISK&FILE	TIME (UTC)	ALTITUDE (MSL)	TRUE HDG	LENGTH/DUR. (GS 72ms ⁻¹ /140KTS)	AHS SCAN-RATE	REMARKS
AHS P01 Elefsina → Koropi 200907240900-18.7-P01	HD06 F22	09:24	6250FT (1905m)	121°	29.1km/8m44s	18.7 rps	TBB1=279K,TBB2=338K Delay due to a failure of navigation computer. Probably caused by the high temperature 310K (37C).
AHS P02 Koropi → Elefsina 200907240900-18.7-P02	HD06 F23	09:36	6250FT (1905m)	301°	29.1km/8m44s	18.7 rps	Strong wind coming from the NW. Some turbulence over the mountains surrounding the city.
AHS P04 Saronikos → Penteli 200907240900-18.7-P04	HD06 F24	09:52	6250FT (1905m)	034°	36.0km/8min20s	18.7 rps	Ídem
AHS P03 Penteli → Saronikos 200907240900-18.7-P03	HD06 F25	10:04	6250FT (1905m)	214°	24.0km/5min33s	18.7 rps	Strong tail wind (gust higher than 30Kts) Flaps at 37.5% (15 degrees deflection).

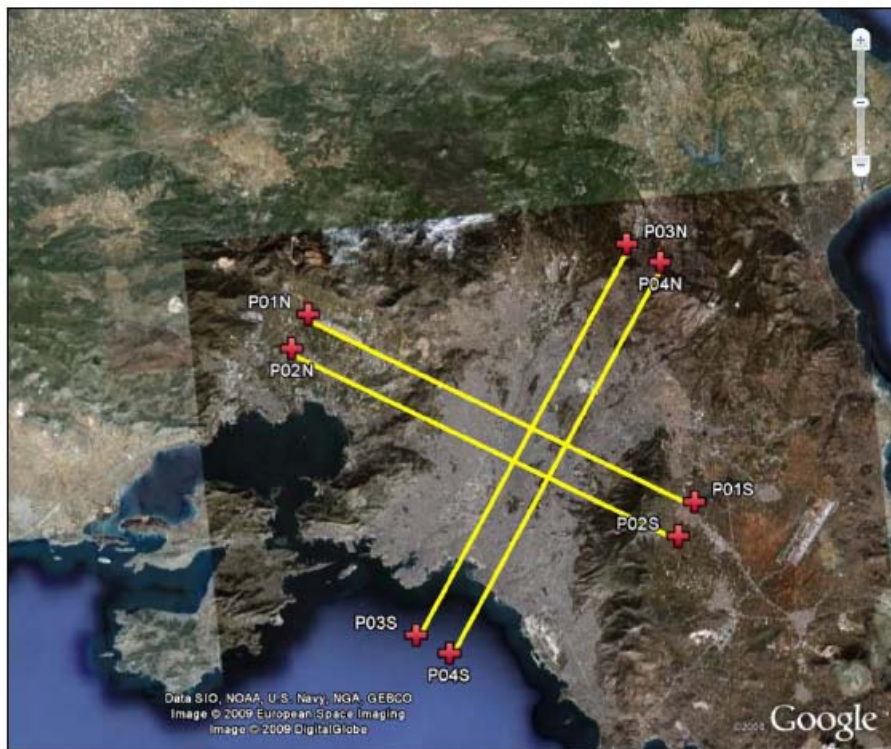
Flight 07 UHI survey (UHI FLIGHT ALT MSL6250FT)

Date: Friday, July 24, 2009, starting at 20:00UTC (23:00LT)

Flight pattern #03 (P04 covering Marathónos Lake, P03&P04 shortened in the South side).

Weather conditions: Clear sky. Strong wind blowing from the N-NE at the flight level up to ca. 37Kts. Temperature at the cabin is 306K (33C) before starting the engines.

FLIGHT LINE ID.	REC.ID. HARD DISK&FILE	TIME (UTC)	ALTITUDE (MSL)	TRUE HDG	LENGTH/DUR. (GS 72ms ⁻¹ /140KTS)	AHS SCAN-RATE	REMARKS
AHS P01 Elefsina → Koropi 200907242000-18.7-P01	HD08 F26	20:06	6250FT (1905m)	121°	29.1km/8m44s	18.7 rps	TBB1=278K, TBB2=328K
AHS P02 Koropi → Elefsina 200907242000-18.7-P02	HD08 F27	20:17	6250FT (1905m)	301°	29.1km/8m44s	18.7 rps	
AHS P04A Saronikos → Penteli 200907242000-18.7- P04A	HD08 F28	20:36	6250FT (1905m)	034°	36.0km/8min20s	18.7 rps	TBB1=281K, TBB2=328K Strong wind blowing from the front. Power is increased to keep constant the GS, it causes that auto- pilot be disconnected. Flight level is lost. The line is aborted. Later on, in the second attempt, AHS fails and has to be re-started (File 29 is a test file).
AHS P04B Saronikos → Penteli 200907242000-18.7- P04B	HD08 F30	20:58	6250FT (1905m)	034°	36.0km/8min20s	18.7 rps	AHS problem is solved and P04 line is completed.
AHS P03 Penteli → Saronikos 200907242000-18.7-P03	HD08 F31	21:10	6250FT (1905m)	214°	24.0km/5min33s	18.7 rps	Strong tail wind with an intensity of up to 37Kts. Flaps are extended.



THERMOPOLIS 2009. AHS FLIGHT PATTERN #01
Flight pattern according to THERMOPOLIS 2009 Experimental Plan.

Waypoint	UTM WGS84/ETRS89 DMX	
	Latitude	Longitude
P01N	N38° 05.313'	E23° 34.530'
P01S	N37° 57.128'	E23° 51.531'
P02N	N38° 04.122'	E23° 33.617'
P02S	N37° 55.937'	E23° 50.621'
P03N	N38° 06.746'	E23° 49.561'
P03S	N37° 53.266'	E23° 38.089'
P04N	N38° 05.968'	E23° 51.021'
P04S	N37° 52.487'	E23° 39.545'

THERMOPOLIS 2009 AHS FLIGHT PATTERN #01
UTM WGS84/ETRS89 flight line waypoints coordinates (P01-P04).

Figure 52: AHS flight pattern 01



THERMOPOLIS 2009. AHS FLIGHT PATTERN #02

Flight pattern according to the THERMOPOLIS 2009 Experimental Plan and modified by the decisions made in the coordination meeting hold at Physics building of NTUA on July 20. P03 and P04 lines extended to cover Marathónos Lake.

Waypoint	UTM WGS84/ETRS89 DMX	
	Latitude	Longitude
P01N	N38° 05.313'	E23° 34.530'
P01S	N37° 57.128'	E23° 51.531'
P02N	N38° 04.122'	E23° 33.617'
P02S	N37° 55.937'	E23° 50.621'
P03N	N38° 12.126'	E23° 54.159'
P03S	N37° 53.266'	E23° 38.089'
P04N	N38° 11.347'	E23° 55.619'
P04S	N37° 52.487'	E23° 39.545'

THERMOPOLIS 2009 AHS FLIGHT PATTERN #02

UTM WGS84/ETRS89 flight line waypoints coordinates P01-P04, P03 and P04 extended towards the North ending to cover Marathónos Lake.

Figure 53: AHS flight pattern 02



THERMOPOLIS 2009. AHS FLIGHT PATTERN #03

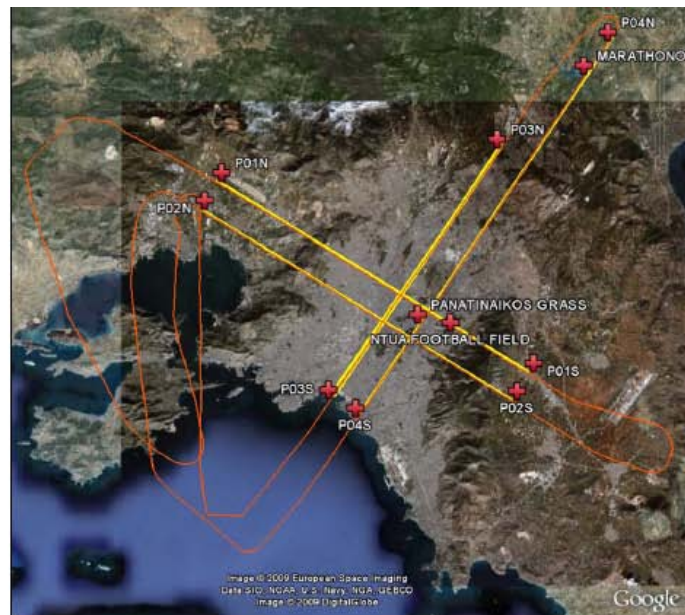
term according to the THERMOPOLIS 2009 Experimental Plan and the decisions made in the coordination meeting hold Physics building on July 29. P03 and P04 lines are shortened to reduce the flight time required to complete the survey. Study zone limits in yellow, flight lines in blue and swath in light green color.

Waypoint	UTM WGS84/ETRS89 DMX	
	Latitude	Longitude
P01N	N38° 05.313'	E23° 34.530'
P01S	N37° 57.128'	E23° 51.531'
P02N	N38° 04.122'	E23° 33.617'
P02S	N37° 55.937'	E23° 50.621'
P03N	N38° 06.750'	E23° 49.554'
P03S	N37° 55.996'	E23° 40.365'
P04N	N38° 11.347'	E23° 55.619'
P04S	N37° 55.211'	E23° 41.839'

THERMOPOLIS 2009 AHS FLIGHT PATTERN #03

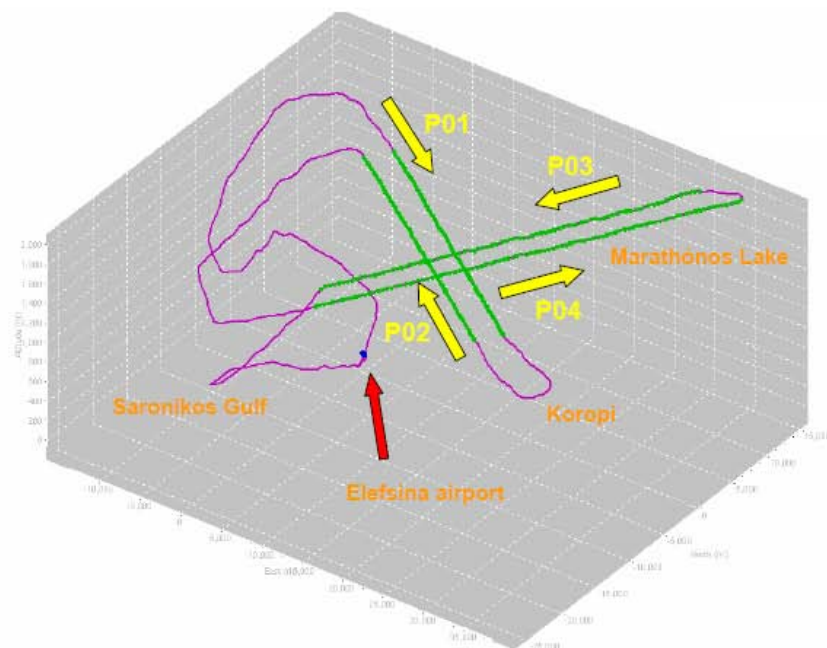
UTM WGS84/ETRS89 flight line waypoints coordinates P01-P04, P03 and P04 shortened in their Southern endings to optimize the flight time.

Figure 54: AHS flight pattern 03



THERMOPOLIS 2009. FLIGHT #04

The image shows in orange color the track followed during the Thermopolis AHS Flight #04 of July 21.



THERMOPOLIS 2009. FLIGHT #04.
3D flight track. Image events in fuchsia color.

Figure 55: AHS flight pattern 04



THERMOPOLIS 2009. AHS surveys.
Mosaic of AHS real color AHS quick-look's.



THERMOPOLIS 2009. AHS surveys.
Mosaic of thermal infrared AHS-75 (thermal infrared) quick-look's.

Figure 56: AHS quick-looks of visible and Infrared surveys

Table 45: Flight data and sensor settings

FLIGHT DATA & SENSORS SETTINGS

AIRCRAFT	CASA 212-200 S/N270, "Paternina"
Nominal aircraft ground speed	GS 72ms ⁻¹ (140KTS)
Altitude above ground level	UHI AGL1839m (6033FT)
Mean elevation @ Omonia Square	70m (230FT)
Positioning	Autonomous GPS
AHS (S/N 001)	
Installation	on the main cabin floor front window
Positioning & orientation	Applanix POS/AV 410 V5 - Autonomous GPS (PCS S/N 2336 IMU LN200 S/N 402296)
IMU installation	On AHS scan head. ACTIVE
Set up lever arms	See note 1 below
Boresight calibration flight	May 22, 2009. Tirez 2009 geometric cal flight
Scan rate	18.7rps @ 1839m (AGL6033FT)
IFOV/FOV	2.5mrad / 1.571rad (90degrees)
Number of pixels per scan-line	750 pixels
Pixel size @ nadir	4.60m @ 1839m&72ms ⁻¹ (AGL6033FT&GS140KTS)
GSD @ nadir	3.86m @ 1839m&72ms ⁻¹ (AGL6033FT&GS140KTS)
Swath	3678m @ 1839m(AGL6033FT)
Along-track scan-line overlap	16% @ 72ms ⁻¹ (GS140KTS)
Internal thermal reference sources	See tables of each flight.
Spectral configuration	80 spectral channels (VNIR, SWIR, MWIR & LWIR) Port 1+ Port 2A + Port 2 + Port 3 + Port 4
Calibration date	See note 2 March 2009

(Further information about AHS can be found at www.inta.es and www.crepad.rcanaria.es/info/npoc/indexlab.html)

Note 1. "Lever Arms" for AHS scan head mounted on the front nadir-looking window.

Ref. to IMU lever arm

X(m) = -0.2981

Y(m) = +0.2309

Z(m) = -0.2720

Ref. to primary GPS lever arm

X(m) = -0.200

Y(m) = -0.008

Z(m) = -2.253

Note 2. AHS spectral configuration characterized on March 2009 after system spectral characterisation.

e



THERMOPOLIS 2009. AHS surveys.
Pictures of Acropolis and Piraeus harbor taken during the flights.

Figure 57: AHS pictures of Acropolis and Piraeus Harbour

GPS data from ground stations where gathered by DRAXIS, provided from the Geodynamics Institute (National Observatory of Athens) for the geocorrection of the images to the INTA Remote Sensing team. Data came from the NOA1 ground station situated in Attica (mountain Penteli). The station operates since 2006 and is part of the EUREF network. The frequency of the data was 1s for the days: 18, 19, 20, 21 and 24th of July 2009. Data were provided in Rinex format and daily archive duration.

The AHS configuration selected is the same one for all flight lines, and it is described below.

scan rate	ground speed	Altitude above terrain	Across-track Ground Sampling Distance	Along-track Ground Sampling Distance	Swath
18.75 Hz	72 m/s	1835 m	4.6 m at nadir	4.6 m	3700 m

Following an analysis of weather forecasts, "GO to proceed" was given on July 10th. The aircraft transit to Athens was performed, with a two days delay in Sicily because a failure of left engine. Arrival to Athens was on July 16th.

During the first on-site meeting, the flight plan was reviewed and modified (see figure below, left side picture). Accordingly, the first and second flights were performed on July 18th (morning / evening).

The flight plan was again reviewed considering the feedback from the first and second flight, and the so-called flight pattern #3 (figure below, right side) was established as the final pattern for all subsequent flights.

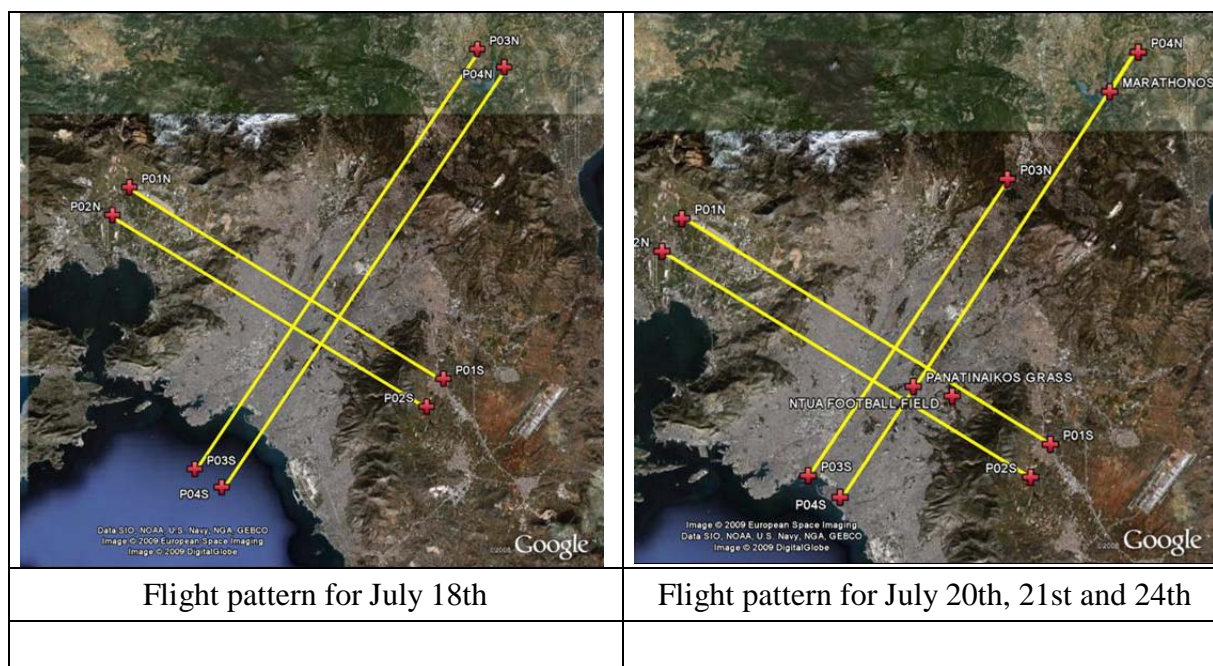


Figure 58: Flight patterns of July 18th-20th-21st and 24th

Campaign is declared officially finished on July 24th, after 30 flight lines and more than 1000 km of data recorded over the study area. The flights performed are summarised in the table below.

Table 46: Summary of flight lines. Start time is reported when a difference > 1 hour from the nominal overflight time is detected

Flight#	01	02	03	04	05	06	07
<i>Date & Start time</i>	18th 08 UTC	18th 20 UTC	20th 10 UTC	21st 01 UTC	21st 20 UTC	24th 09 UTC	24th 20 UTC
P01	P01IX P01II: 09:15	OK	OK	OK	OK	OK	OK
P02	OK	21:05	OK	OK	OK	OK	OK
P03	OK	OK	OK	02:00	OK	10:04	21:10
P04	OK	OK	OK	OK	OK	OK	21:00

4.4 Pre-Processing AHS Images

BACKGROUND

The preprocessing of AHS data includes three different steps:

1. importing the raw instrument files to a generic binary (ENVI-like) format,
2. quality checks
3. spectral, radiometric and geometric calibration.

These tasks are performed by a semi-automated chain at INTA facilities, providing repeatability and reliability while giving room to flexibility. This semi-automated chain is based on IDL and MATLAB scripts. The figure below shows the basic concept of this chain.

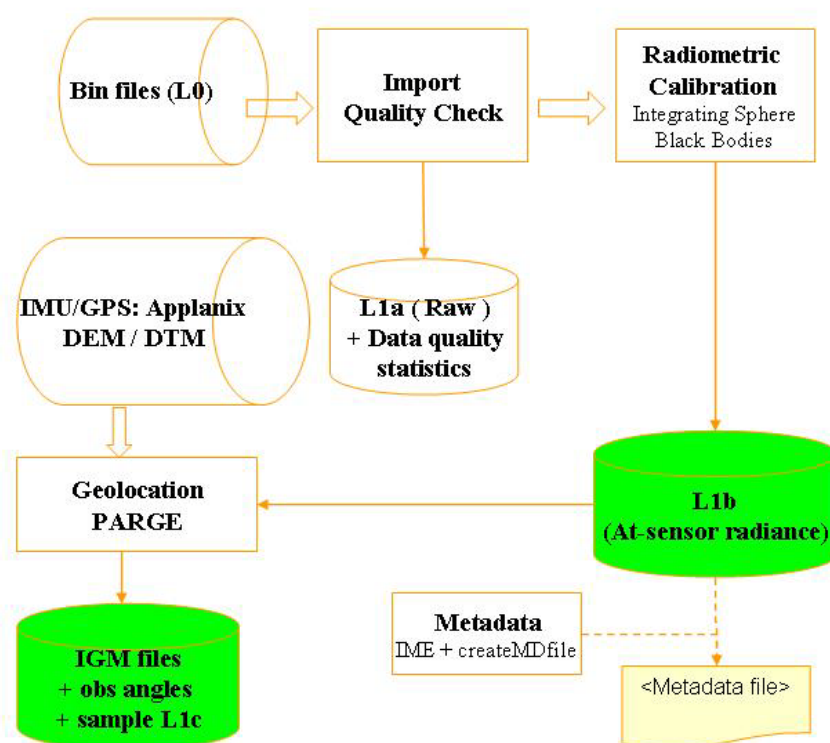


Figure 59 : Overall view of the AHS data preprocessing chain for L1b products (georeferenceable at-sensor radiance)

The processing of the Applanix data, although not shown in the figure, is a critical point in the chain. It is performed with POSPAC, a commercial tool furnished by Applanix, and it requires master GPS data and some other ancillary information.

The figure above and this report use the taxonomy for AHS products described in the table below.

Table 47: The taxonomy for AHS products

Generic level	Bands	Description	Code in the filename
L1a	1:80	raw data in ENVI format	L0R00_PTT
L1b	1:63	georeferenceable at-sensor radiance in image geometry + igm (Input Geometry) file.	L10020_PT12
	64:80	georeferenceable at-sensor radiance in image geometry + igm (Input Geometry) file.	L00120_PT34
L1c	1:63	georeferenced at-sensor radiance, UTM grid.	L10022_PT12
	64:80	georeferenced at-sensor radiance, UTM grid.	L00122_PT34

All products from the INTA system have a ENVI-compatible header with the basic metadata information. In addition, complete metadata is provided in XML files, following (as much as possible) International Standards ISO19115 (Geographic information: Metadata) and ISO19139 (Geographic information: XML schema implementation).

The next section details methodology and results for:

- quality checks,
- geolocation,
- spectral and radiometric calibration.

4.5 Evaluation of AHS Data Quality

METHODS

Image quality is evaluated by visual inspection and by analysis of the L1a image statistics. There is a single statistics file per image acquired; the name of the file is the same of the parent image plus the suffix "_stats" and the extension ".csv". The statistics file includes, for each spectral band:

- maximum value, useful to check for saturated pixels,
- minimum value, useful to check for missing data (=0) or low values,
- mean value, useful to estimate signal to noise ratio,
- standard deviation, useful to detect anomalous bands (low information content),
- for each of the two onboard reference blackbodies, minimum, maximum, mean and standard deviation,
- noise figures: NEdL computed as the standard deviation of blackbodies transformed to radiance units ($\text{uw}/[\text{cm}^2 \text{ sr nm}]$), NEdT computed as standard deviation of blackbodies for MIR/TIR bands transformed to temperature, and SNR computed as mean image signal to NEdL and NEdT.

These statistics are delivered to the project database along with the calibrated images.

The quality check was performed on all scenes acquired for Thermopolis. Note that for nighttime imagery the quality parameters for VNIR/SWIR bands (min, max, mean signal, stdev, SNR...) are not applicable.

RESULTS

The following is a summary of the quality check results:

1. Presence of clouds is negligible.
2. No missing lines / pixels are detected.
3. All bands are recorded properly except for:
 - a. AHS 44 and AHS46: appears randomly anomalous, with lower SNR than adjacent bands.
 - b. AHS66: defective
4. Noise in VNIR/SWIR bands is within specifications.
5. SNR in the VNIR bands is excellent (see figure below).

6. SNR in the SWIR region ranges from 90 in the short edge of the SWIR region to hardly 10 above 2.3 microns (see figure below).
7. Noise in MIR and TIR bands is within specifications. As an exception, band AHS80 is usually above specifications, and sometimes AHS78 (see figure below).

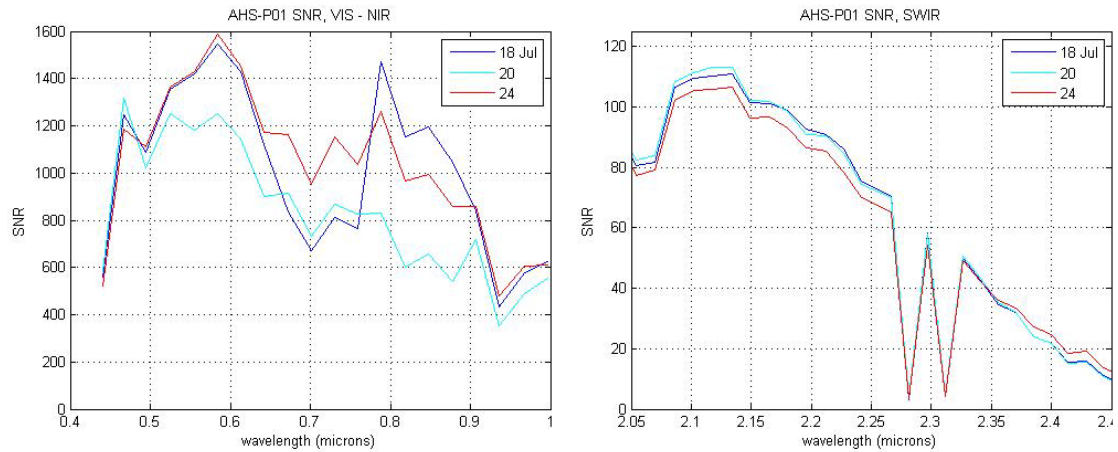


Figure 60 : SNR plots for all day time AHS flights.

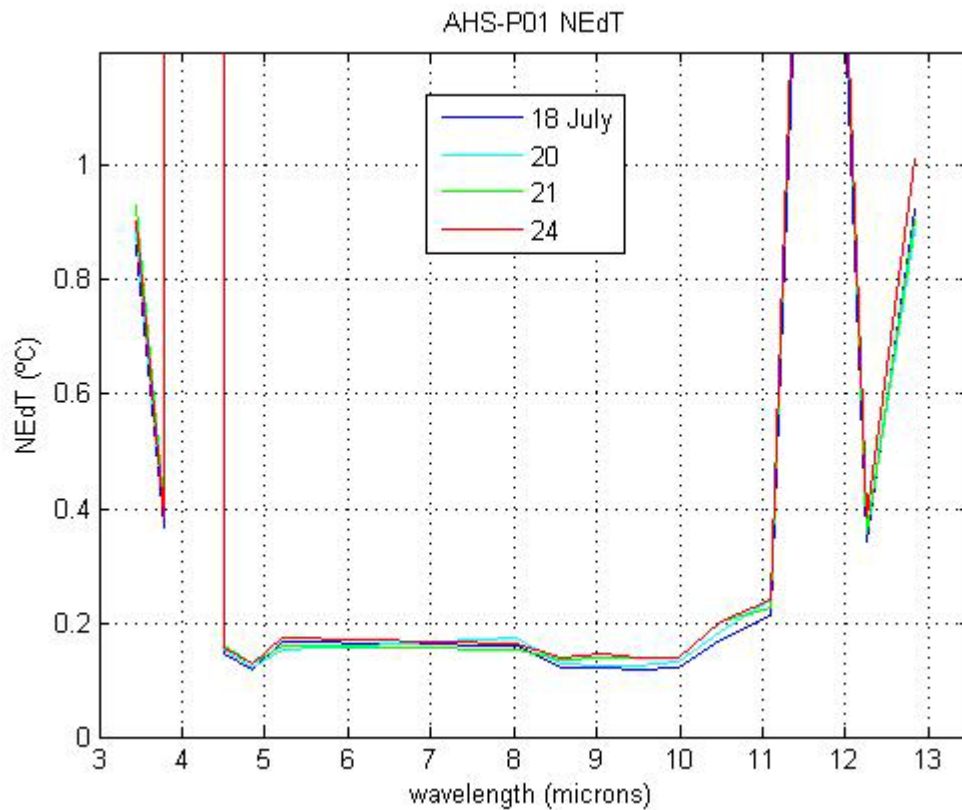


Figure 61: Noise equivalent temperature for all MIR & TIR bands and for all flight sessions.

Concerning auxiliar data, Applanix POS /AV records are processed and a quality check implemented. In this check, the expected error in position and orientation (angular) is estimated from the data processing results. The position error is reported as % of records in different error classes (see table). The orientation error is reported as the estimated uncertainty of each record. The check shows that the quality of Applanix data is very good.

Table 48: Position and orientation error

Position St. Dev. Percentage s	25/0 6/ - D1	25/0 6/ - N1	26/0 6/ - N1	28/0 6/ - D1	28/0 6/ - N1	01/0 7/ - D1	01/0 7/ - N1	02/0 7/ - N1	04/0 7/ - D1	04/0 7/ - N1
0.00 - 0.10 m	100 %	99.6 %	100 %	99.6 %	100 %	100 %	100 %	90.4 %	99.6 %	100 %
0.10 - 0.30 m	0.0%	0.4%	0.0%	0.4%	0.0%	0.0%	0.0%	9.4%	0.4%	0.0%
0.30 - 1.00 m	0.0%	0.0%	0.0%	0.0%	0.0%	0.0%	0.0%	0.0%	0.0%	0.0%
1.00 - 5.00 m	0.0%	0.0%	0.0%	0.0%	0.0%	0.0%	0.0%	0.1%	0.0%	0.0%

4.6 AHS Geolocation

METHODS

The AHS position and orientation for each image is computed from Applanix POSAV-410 data using the POSPAC Software. The version used was POSPAC 4.4. The master GPS data was obtained from the EUREF network of GPS stations. The boresight angles (angles between Applanix IMU axis and AHS image axis) were computed during the June 2009 geometric calibration campaign. The values obtained and the expected uncertainty in each angle is shown in the table below. UTM grid convergence and geoid undulation, required for adapting POSPAC output to PARGE requirements, were computed nominally.

The geolocation of each image pixel is performed using PARGE, a commercial tool available from Rese Applications (www.rese.ch). All imagery is georeferenced to UTM grid, ellipsoid WGS84, zone 34. The georeferencing information is stored in the so-called Image Geometry Maps (IGM files), where the UTM position of each raw image pixel is written. PARGE also creates images describing the observation geometry (azimuth and zenith observation angles, and distance to terrain at nadir for each geolocated pixel).

The IGM files can be used to geolocate any AHS image. We have produced with ENVI sample geolocated images This is called L1c data. These images have been delivered to the data base as samples of the geolocation output. They are in UTM (zone 34), datum WGS84, in ENVI BSQ format:

1-AHS data, three reflective bands:

AHS_YYMMDD_HHMMZ_PXXHD_L10022.bsq / .hdr

2-AHS data, one thermal band: AHS_YYMMDD_HHMMZ_PXXHD_L00122.bsq / .hdr

Sample georeferenced bands are provided in a 4 m spatial grid and have been resampled with a nearest neighbour rule.

DEM

A DEM was provided by Draxis. This DEM is the Global ASTER DEM. The grid size of this DEM is 0.000278 degrees, corresponding to roughly 30 m x 30 m. The height resolution is 1 meter. The reported accuracy is 30 m (90% confidence) for UTMx-UTMy position and 20 m (90% confidence) for the Z values.

The DEM was processed with the following procedure

1-Convert data type from integer to float

2-Transform from geographic coordinates to UTM (zone 34) keeping the datum WGS84: output grid size set to 28 m, resampling bilinear.

3-Subset and resample the MDT. The subset is defined by the imaged area for each flight line: the imaged area is determined projecting the recorded airplane position over a flat terrain with mean altitude 0 meters: A subset (and therefore two different files) was defined for P01 and P02, and a second one for P03 and P04.

The resampling was done with a bilinear interpolation. The output grid size was 4 m, and this grid size determine the future georeferencing resolution.

flight line	DEM filename	upper left	lower right
P01I	MDT_TPLIS_4m_P01I1_ele	721200, 4221600	754600, 4199500
P02I	MDT_TPLIS_4m_P02I1_ele	"	"
P03I	MDT_TPLIS_4m_P03I1_ele	728500, 4235550	759800, 4192800
P04I	MDT_TPLIS_4m_P04I1_ele	"	"

RESULTS

The high quality of the POSPAC solution, as shown in the table tal above, and the low uncertainty in the geometric calibration (boresight) performed by INTA (a fraction of a pixel) guarantees the best possible geolocation accuracy. The only source of error is the low DEM resolution (20 m standard uncertainty). However, altitude errors are relevant only away from the image nadir (see figure below), and therefore the DEM low accuracy has a limited impact on the image accuracy.

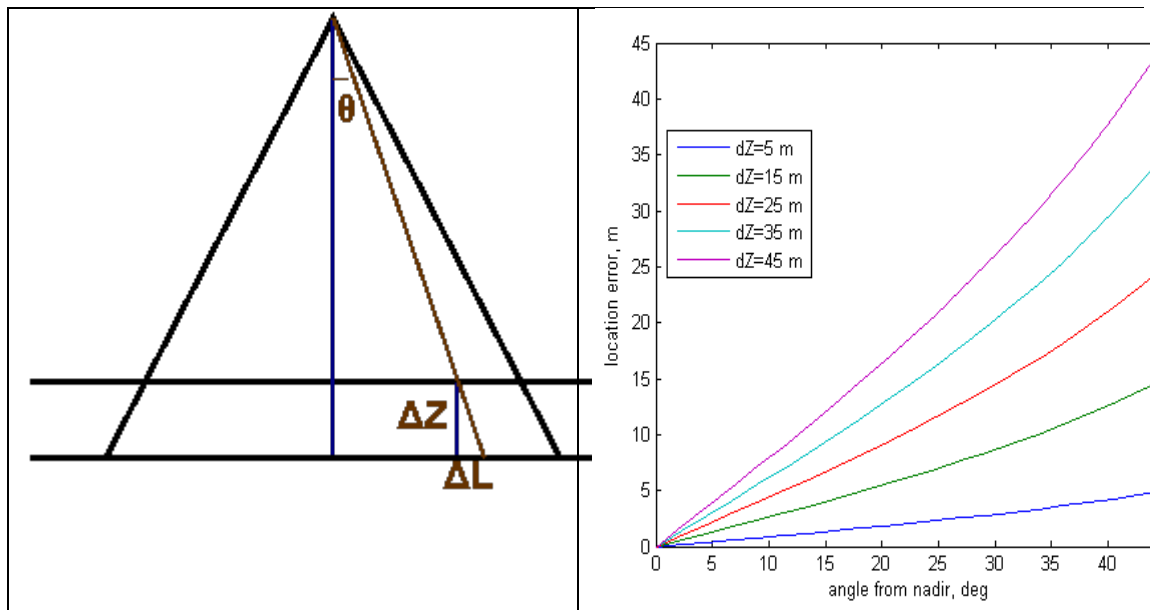


Figure 62 : Effect of height error as a function of angle from nadir ($\Delta L = \Delta Z \tan \theta$)

No absolute evaluation of accuracy has been produced, because as explained above the use of high resolution and accuracy navigation data is assumed to give the best possible geolocation.

On the other hand relative accuracy is important to assess the limitations of pixel-level temporal analysis (for example day to night temperature evolution). A first, qualitative check of the relative accuracy of the geolocation is done by visual inspection of overlapping areas. A sample is shown in the figure below.



Figure 63: A mosaic of two images (P03 - P04) on the Olympic Port area. The match between the two images is satisfactory.

Image to image ground control points for two image pairs are used to evaluate quantitative the relative accuracy. The tables below show the result of the analysis. A half-pixel bias is detected, which is considered acceptable. Note that a significant spread of the GCPs error is possible due to the fact that each image samples the terrain in a different, randomly distributed grid. But if the GCPs sample is large enough and no outliers are present, the average error should be 0. Therefore, a possible explanation of the observed bias is that the sample is not big enough.

Table 49: Image to image ground control points for two image pairs

P01I1 vs P01I2

	x	y	x	y	ΔX	ΔY	$\Delta X2$	$\Delta Y2$
1	732330.90	4216054.08	732327.72	4216052.02	3.18	2.06	10.12	4.24
2	729636.31	4217246.48	729639.72	4217252.02	-3.42	-5.54	11.69	30.70
3	729119.31	4217741.15	729119.72	4217744.02	-0.42	-2.87	0.18	8.26
4	728319.70	4216723.68	728319.72	4216720.02	-0.02	3.66	0.00	13.39
5	727601.88	4217138.77	727599.72	4217140.02	2.15	-1.26	4.63	1.58
6	726931.97	4217609.82	726927.72	4217612.02	4.25	-2.21	18.04	4.87
7	725753.31	4218575.82	725751.72	4218576.02	1.58	-0.21	2.50	0.04
8	733998.10	4214310.88	733995.72	4214312.02	2.38	-1.14	5.67	1.30
9	735528.51	4213938.08	735527.72	4213940.02	0.78	-1.94	0.61	3.77
10	734565.31	4212384.48	734567.72	4212388.02	-2.42	-3.54	5.85	12.54
11	736890.10	4212417.28	736887.72	4212420.02	2.38	-2.74	5.67	7.51
12	742217.31	4210267.48	742215.72	4210264.02	1.58	3.46	2.50	11.96
13	740908.31	4208928.48	740907.72	4208928.02	0.58	0.46	0.34	0.21
14	745950.64	4207030.48	745947.72	4207028.02	2.92	2.46	8.50	6.05

RMS error (m)
= 2.33 2.76

P03I1 vs P03I2

	x	y	x	y	ΔX	ΔY	$\Delta X2$	$\Delta Y2$
1	741755.94	4212307.26	741754.91	4212308.38	1.02	-1.12	1.05	1.26
2	735609.71	4202517.48	735610.91	4202520.38	-1.20	-2.90	1.44	8.40
3	734313.94	4202329.26	734310.91	4202332.38	3.02	-3.12	9.14	9.74
4	735019.94	4204549.92	735018.91	4204552.38	1.02	-2.46	1.05	6.03
5	736262.34	4204783.26	736266.91	4204788.38	-4.58	-5.12	20.94	26.23
6	737464.74	4204393.66	737462.91	4204396.38	1.82	-2.72	3.33	7.40
7	737717.27	4206414.59	737714.91	4206416.38	2.36	-1.79	5.56	3.19
8	738481.27	4206755.26	738478.91	4206752.38	2.36	2.88	5.56	8.29
9	737905.27	4207260.59	737902.91	4207260.38	2.36	0.21	5.56	0.05
10	739856.94	4208390.26	739854.91	4208392.38	2.02	-2.12	4.10	4.50
11	740394.22	4208773.54	740394.21	4208780.38	0.01	-6.84	0.00	46.73
12	740663.37	4211602.11	740662.91	4211604.38	0.45	-2.26	0.21	5.12
13	740555.14	4212558.45	740554.91	4212556.38	0.22	2.08	0.05	4.32
14	743678.34	4215497.66	743678.91	4215500.38	-0.58	-2.72	0.33	7.40

RMS error (m)
= 2.04 3.15

4.8 Radiometric Calibration

METHODS

The initial radiometric calibration is performed using a linear model for all VNIR/SWIR bands:

$$Ls(i,j,k) = fd \cdot fe(k) \cdot sc(k)/g(k) \cdot (DN(i,j,k) - DNbb(i,k)) \quad [\text{eq. 1}]$$

where

$sc(k)$: slope of the laboratory calibration for band k

$g(k)$: gain setting for band k during the flight. Note that slope and gain for each image are reported in the statistics file.

$DN(i,j,k)$: Digital Number for pixel (i,j) for band k

$DNbb(i,k)$: DN for the onboard blackbodies for line i (average of BB1 and BB2)

fd = a factor to account for optic transmittance degradation between the calibration date and the flight date. For the Thermopolis dataset it was set to 1.05.

fe = an eventual empirical correction factor derived from the analysis of the calibration/validation campaign performed in June 2009. For the Thermopolis data set, fe was 1 for all bands except for the factors reported in the table below.

Band	AHS1	AHS2	AHS3	AHS4	AHS5	AHS6	AHS7	AHS8	AHSx
Fe	1.622	1.262	1.173	1.108	1.065	1.052	1.042	1.030	1.000

The radiometric calibration for TIR bands is based on the onboard blackbodies. BB1 ("cold" blackbody) is set to a temperature lower than the expected scene minimum, and BB2 ("hot" blackbody) to a temperature higher than scene maximum. A digital number to at-sensor radiance transformation is then computed using the AHS records of the blackbodies:

$$Ls(i,j,k) = (DN(i,j,k) - DNbb1) / (DNbb2 - DNbb1) \cdot (Lbb2 - Lbb1) + Lbb1 \quad [\text{eq. 2}]$$

where the blackbodies radiance is computed from their temperature and the spectral responsivity functions ("resp") using the Planck function:

$$Lbb1 = c1 / (\lambda.^5 \cdot (\exp(c2 / (\lambda \cdot (Tbb1)))) - 1) \cdot (\text{resp}) / \text{sum}(\text{resp}); \quad [\text{eq. 3}]$$

$$Lbb2 = c1 / (\lambda.^5 \cdot (\exp(c2 / (\lambda \cdot (Tbb2)))) - 1) \cdot (\text{resp}) / \text{sum}(\text{resp}); \quad [\text{eq. 4}]$$

VNIR & SWIR bands in night time imagery are calibrated to at-sensor radiance in the same way as day time imagery. These calibrated images could be useful for studies on city illumination.

RESULTS

To evaluate the calibration we have applied a quick illumination/atmospheric correction to one of the images, namely AHS_090718_P03I1. The configuration of this correction is detailed in the table below.

Table 50: configuration of the illumination/atmospheric correction performed.

parameter	value	source
sun zenith/azimuth	from date/time/scene center coordinates	time of flight
observation zenith/azimuth	variable	sensor model
terrain height	70 m	average scene height according to flight plan
flight height	1800 m	platform navigation data
aerosol model	rural	standard choice
visibility	50 km	ATCOR estimation from image data
water vapour content	initial value: 2 gr/cm2 reviewed per pixel using the spectral signature	ATCOR estimation from image data

The following criteria have been used to check the calibration:

- reflectance of DDV must be between 1% and 4% in the blue.
 - reflectance of ocean water must be between 1% and 3% in NIR wavelengths
 - reflectance of bare soil must be smoothly increasing from blue to SWIR.
- No major anomalies were found, so that the initial calibration was accepted.

A more detailed calibration check and validation of AHS radiometry was performed by the GCU team and is reported in its section. The procedure and the results obtained are summarised here:

1) VNIR

- Ground truth targets: bare soil at the NTUA soccer field and green grass at the Panathinaikos stadium.
- Instrument: GER field spectroradiometer, providing surface nadir reflectance measurements.
- AHS data from L1b_PT1, 3 x 3 pixels average centered in the expected ground measurement position.
- comparison with AHS data.

The results show a minor underestimation of surface reflectance by AHS. Note that this error could be explained by the adjacency effect (which tends to lower the observed signal in bright targets), which is not considered in the validation and is certainly quite significant for AHS flying at 1.8 km above urban areas.

2) TIR

- Ground truth targets: lake Marathonos water and green grass at the Panathinaikos stadium. A total of 16 +14 samples are used, coming for one instrument on the grass and two on the water.
- Instrument: On the green grass the instrument is CT-LT15 installed on a fixed mast (continuous temporal sampling of surface radiance) combined with CIMEL for emissivity and downwelling radiance. On the water test surface the instruments are Raytek and Cimel.
- AHS data from L1b "updated". Two flight lines from each of the 5 flights.

-first test: propagation of radiance to at sensor level and comparison with AHS data

The results show that the bias in the split window case is negligible, while in the TES case could be caused by the errors in the emissivity result from TES in water and grass. In both cases, the spread could be explained by the dynamic nature of temperature, by small differences in the grass target and by minor adjacency effect.

4.9 Spectral Calibration

As reported during the Sen3Exp and Thermopolis progress meetings, there is an uncertainty in the actual spectral position of AHS bands for Sen3Exp and Thermopolis campaigns. This is due to the fact that the spectral calibration performed on September 2009, short after the campaigns, gave different results (shift of 25% of the bandwidth) to the spectral calibration performed on March 2009, which was the one applied for calibration and atmospheric correction of the Sen3Exp and Thermopolis campaigns.

The actual shift, if any, could be different to that computed from the comparison of September and March calibrations, due to the specific behaviour of the AHS under flight conditions and the time elapsed between the flights and the pre- and post-campaign calibrations.

To assess the situation in terms of the AHS image quality, we have considered two problems.

- 1) Which is the actual shift in the AHS datasets?
- 2) Which is the effect of such spectral shift in terms of surface parameters (reflectance, emissivity, temperature)?

The work performed is summarised in the following section.

METHODS

In the VNIR, two different procedures were tested:

- adjusting the AHS VNIR spectral curve to a FieldSpec curve obtained simultaneously.
- searching for the shift that best predict the observed location of the water absorption maximum at 935 nm in the AHS data.

The TIR analysis is based in comparing the expected signal from a water body with the actual signal. The expected signal was computed with MODTRAN from the lake Marathonos in-situ temperature measurements plus observed atmospheric conditions: a small range of water temperatures and water vapour contents around the nominal values was used to watch the effect of parameter uncertainty. Next, the signal is convolved with different bands positions, from the nominal to ± 150 nm, and compared with the AHS-measured at sensor radiance.

RESULTS

A shift of around 10% of the FWHM "redwards" is likely from the analysis of VNIR and TIR features.

The shift in the VNIR is around 3 nm. The effect of such shift in the retrieval of surface temperature was considered minor and no reprocessing was performed. In the TIR, for all cases tested, the minimum difference between the observed at-sensor radiance and the expected curve is found when band centers are shifted 60 nm to the long-wave end (see figure).

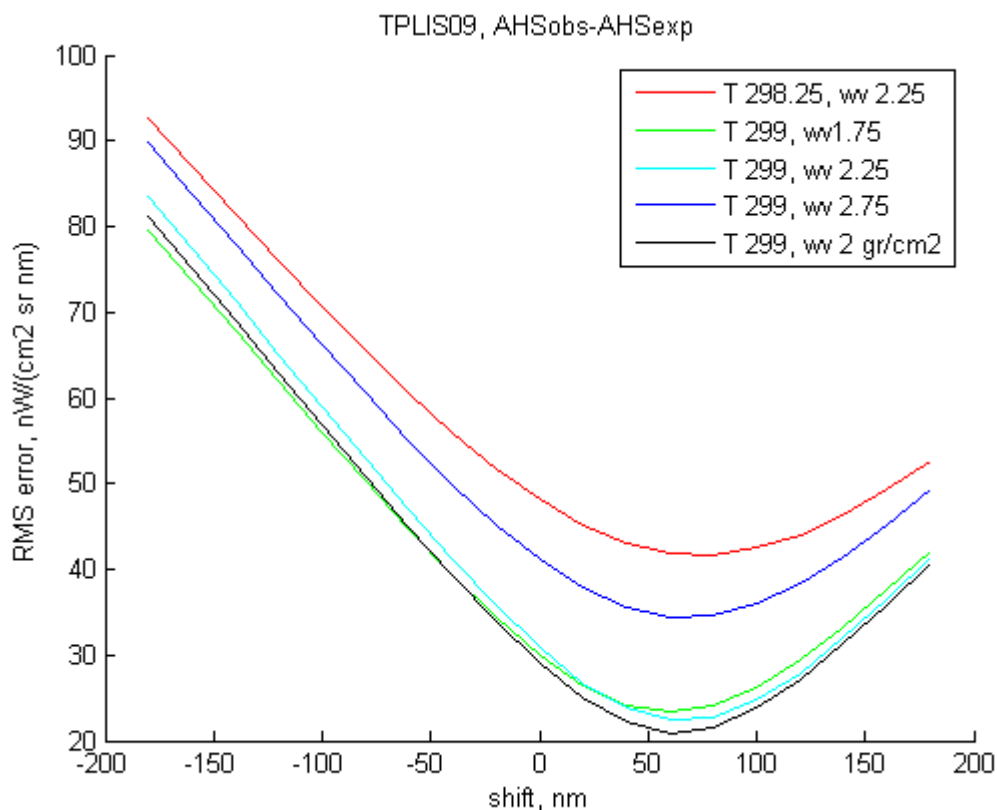


Figure 64: difference between the expected emission spectrum of water (Lake Marathonos) for different spectral shifts and different atmospheric situations and the observed value. The minimum difference is located at +60 nm shift.

Different tests were carried to check the effect of such shift in the retrieval of surface emissivity and temperature. Tests performed at INTA with ATCOR4 and the ANEM procedure (see annex) showed very little significance of the shift either in temperature or emissivity. However, tests performed with TES by the UCG showed a significant effect. Therefore, it was decided to reprocess all Thermopolis AHS data with the new spectral configuration. This was done in two steps:

1. Computation of new spectral responsivity curves with the band centers shifted 60 nm to the long-wavelength end and the nominal FWHM.
2. New calibration by applying the new responsivity to equations [2] to [4] above.

The L1b data obtained with this reprocessing was delivered to the project partners for the computation of improved surface emissivity and temperature values.

4.10 AHS L1B Images in the Thermopolis Data Base

The calibrated AHS images (level 1b in the INTA taxonomy) were delivered to the project data base. In addition, geolocation information (IGM files) are attached to each image file. A specific readme file is available to summarise the main features of this images. This readme file is shown here for quick reference.

I-CONTENTS

These folders contains AHS images acquired for the THERMOPOLIS 2009 campaign. The details of the flight campaign are reported in a separate document.

There is one folder per flight date, named as AHS_YYMMDD (YearMonthDay, two digits each).

In the next level, there is a folder for the at-sensor radiance data, named L1b, and a folder for the georeferenced images, named L1c.

Within the L1b/L1c folders there is a separate sub-folder for each flightline, named as YYMMDD_PXXHR. In this sub-folders you will find:

L1b

>AHS at-sensor radiance, in nW/(cm² sr nm), in ENVI BSQ format:

1-AHS data, reflective bands:
AHS_YYMMDD_HHMMZ_PXXHD_L10020_PT12.raw / .hdr (only in daytime flights)

2-AHS data, thermal bands:
AHS_YYMMDD_HHMMZ_PXXHD_L00120_PT34.raw / .hdr

3-Image Geometry Map (IGM) files, for georeferencing (reference system: UTM 34, WGS84).

4-AHS data, VNIR bands: AHS_YYMMDD_HHMMZ_PXXHD_L10020_PT1.raw / .hdr (only in night-time flights)

>Metadata for 1) and 2): MD_*.xml

L1c

>Sample georeferenced AHS bands (reference system: UTM 34, WGS84) in ENVI BSQ format:

1-AHS data, three reflective bands:
AHS_YYMMDD_HHMMZ_PXXHD_L10022.bsq / .hdr (only in daytime flights)

2-AHS data, one thermal band: AHS_YYMMDD_HHMMZ_PXXHD_L00122.bsq / .hdr

All georeferenced images are provided in a 4 m spatial grid and have been resampled with a nearest neighbour rule.

The code for identifying scenes with the filename is as follows:

P.....fixed value, standing for "Pass"

XX.....scene number according to flight plan
H.....a single code to identify the flight height. For Thermopolis it is I ("Intermedio", 1850 m).
R.....an ordinal to identify the scene instance for that flight height and date.

II-DATA QUALITY

RADIOMETRIC ACCURACY. The L1b radiance is computed as follows:

$$Ls(i,j,k) = [scale(k) * (ND0(i,j,k) - NDbb(i,k))/gain(k)]$$

The scale factor has been computed at INTA laboratory in March 2009. An empirical correction factor has been applied to bands AHS1 to AHS8.

NDbb is the onboard blackbodies digital value averaged over a small neighbourhood for each scanline.

Gain is the electronic gain value reported in the *flight.csv file, corrected according to laboratory test.

Band AHS21 has been calibrated with a specific non-linear model based also in laboratory tests.

The L1b radiance for MIR and TIR bands is computed from the onboard blackbodies records.

NOISE. Noise level is within specifications except for bands AHS44, AHS46, AHS78 and AHS80.

SPECTRAL ACCURACY

The spectral responsivity (and therefore band center and FWHM) was measured on March 2009 at INTA facilities with a 0.2 nm resolution monochrometer.

A dedicated study on the Thermopolis imagery shows a possible shift of 3 nm towards the longer wavelengths in the VNIR range (PT1), i.e. actual bandcenter might be +3 nm than reported in the image file headers. However, this shift has not been applied to the images stored in this database.

A shift of +60 nm was detected in the TIR range (PT4), i.e. actual bandcenter might be +3 nm than reported in the March 2009 calibration. The images stored in this database has been reprocessed according to this shift and the corresponding file headers and Metadata Files corrected.

GEOMETRIC QUALITY

The IMU/GPS quality was satisfactory. The georeferencing algorithm renders an accuracy better than one pixel when the provided terrain altitude is correct. The image-to-image misregistration is <1 pixel.

III-CONTACT

For any question on the characteristics of these images, please contact:

INTA

Area de Teledeteccion - Remote Sensing Laboratory

Cta Ajalvir s/n

Torrejon de Ardoz

28850 Madrid

SPAIN

phone: 34-91 5201990, 34-91 5201992

email:

Eduardo de Miguel (processing responsible): demiguel@inta.es

Jose Antonio Gomez (project responsible): gomezs@inta.es

4.11 AHS Data Analysis Constraints

Finally, some points concerning the interpretation of AHS images are summarised below.

1) Each AHS pixel represents the surface observed by a 2.5 x 2.5 mrad Instantaneous Field of View (IFOV) determined by a field stop. In the Thermopolis campaign this field stop scans the Earth surface with a scan rate of 18.75 hertz across the AHS Field of View (FOV). The platform motion is set to a specific speed and altitude to achieve a complete terrain coverage with a line-to-line overlap of 18% of the IFOV.

2) The AHS field of view is 90°. It is centered in the nadir, so that 750 samples are acquired with an angular separation from nadir ranging from -45° to +45°.

The corresponding ground pixel size or GIFOV (ground IFOV) is:

$$\text{GIFOV} = \text{Height} \cdot \tan(\text{IFOV}) \cdot \sec^2(\text{ON}),$$

where ON is the angular Off-Nadir distance (from 0° and 45°).

In the Thermopolis data set GIFOV ranges from 4.5 m at nadir to nearly 9 m at both edges (+/- 45°). This range of sizes corresponds to the nominal flight height; when the terrain-to-sensor distance changes, the GIFOV also changes. In the Thermopolis scenes, this altitude dependence is relevant for the hilly areas around Athens city, where GIFOV is smaller to the nominal one and the swath width is narrower.

3) Georeferenced images (Level "c" in our taxonomy) have to be created with a regular grid size. This grid size has been set to 4 m, which is slightly below the original nadir GIFOV, as recommended in the PARGE User Manual (PARGE is the geocoding tool used by INTA, see www.rese.ch).

4) The actual looking angle for each pixel depends not only in the position of the pixel within the FOV, but also on the platform attitude, i.e. its orientation wrt to a plane tangent to the local surface. This angle is reported in the sca files delivered to the data base (they are found in the L1c folders). These files report the azimuth and zenith components of the looking direction for each pixel of the orthorectified image.

They also report the ground-to-sensor altitude for each flight line. All this information is useful for detailed atmospheric or BRDF corrections.

5) The following points has to be considered carefully for data analysis:

i) The changing ground pixel size, as reported above.

ii) The increased path length from nadir to the edges. It is responsible for a larger atmospheric interference in the image borders. Even with a dedicated treatment of atmospheric interference, this increased atmospheric interference might be observed in the image borders.

iii) The variable observation angle. If the terrain reflection (and therefore emission) is not lambertian, the radiance measured by the AHS depends on the observation angle. The magnitude of this effect depends on the surface BRDF, which is rarely well known, but should be limited to less than 1 degree in most surfaces.

4.13 The AEROPHOTO data acquisition system

The Cessna 310 Q shown below (Figure 15) will carry the components of AIMMS-20, an airborne Air Turbulence Temperature Pressure and Relative Humidity system coupled to INS and GPS systems, all operating at 40 Hz. Data were acquired at 10 Hz. The specifications are given below:

AIR DATA PROBE (ADP)

Internal Sampling Rate: 200 Hz

Anti-Alias Filter: 50 Hz

Digital Low Pass Frequency Range: 1 Hz - 40 Hz

Maximum Data Output Rate: 40 Hz

Pressure

Pressures Barometric (Static): Pitot-Static

Differential: Range 0 - 110000 Pa 0 - 14000 Pa

Accuracy + % of Reading 100 Pa + 0.05% 20 Pa + 0.05%

Angle-of-Attack / Sideslip Differentials: +/-7000 Pa 20 Pa + 0.05%

Three-Axis (X,Y,Z) Acceleration +/-5 g 0.005 g

Temperature

Temperature Resolution: 0.01 K

Calibrated Accuracy: 0.05 K

Including Dynamic Heating Error Uncertainties: 0.30 K

Time Constant (63% Step Response Time): 5 sec

Relative Humidity

Resolution: 0.1 %RH

Accuracy 2% RH (0-100% RH)

INERTIAL MEASUREMENT UNIT (IMU)

Internal Sampling Rate: 200 Hz

Digital Low Pass Frequency Range: 1 Hz - 40 Hz

Maximum Data Output Rate: 40 Hz

Range Accuracy

Three-Axis (X,Y,Z) Acceleration: $\pm 5 \text{ g}$ 0.005 g

Three-Axis (P,Q,R) Rates: $\pm 60 \text{ deg/sec}$ 0.03 deg/sec

CENTRAL PROCESSING MODULE (CPM)

Processor: Motorola DSP56F807

Internal FLASH Memory: 16 Mbit

Wind Speed Accuracy:

Horizontal North and East Components: 0.50 m/s (1.0 knot) @ 150 knot TAS

Vertical: 0.50 m/s (1.0 knot) @ 150 knot TAS

Broadcast / Log Update Rate: 1 - 10 Hz

Log Capacity: 45000 Records (12.5 hours @ 1 Hz)



Figure 65 : The AEROPHOTO Cessna 310 Q.



Figure 66 : AEROPHOTO Instrumentation rack.



Figure 67 : AEROPHOTO rack and onboard data acquisition computer.



Figure 68 : AEROPHOTO Cessna during instrument installation.

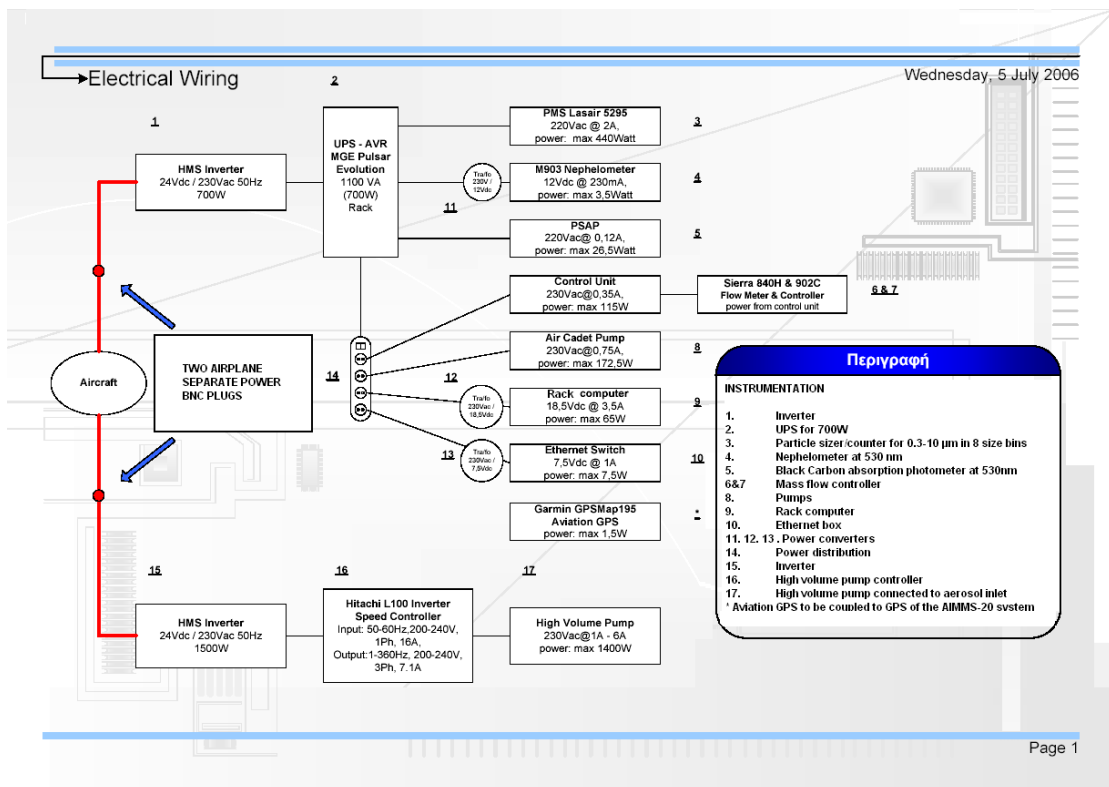


Figure 69 : AEROPHOTO Cessna instrument diagram.



Figure 70 : AEROPHOTO Cessna during deployment

Aircraft measurements of: (I) aerosol optical and physico-chemical properties, for atmospheric correction of ground based and satellite derived optical parameters (II) sensible and latent heat fluxes within the boundary layer

4.14 AEROPHOTO Data Acquiring Flights

Table 51: Waypoints coordinates for DUTH-AEROPHOTO flights

NORTH-SOUTH	Starting Point North Penteli		Ending Point Saronikos	
	Lat-N	Long-E	Lat-N	Long-E
Northing	38° 07' 18"	23° 48' 12"	37° 53' 37"	23° 37' 05"
Southing	38° 05' 25"	23° 52' 23"	37° 52' 08"	23° 40' 33"

Test site	Athens urban area
Mean ground elevation	70 m (200FT) @ Omonia square
Flight altitude UHI-1	2497 m MSL (8200FT MSL) GIFOV=4.6m. INTA (@6250FT MSL) and AEROPHOTO
Flight altitude UHI-2	3409 m MSL (11200FT MSL) GIFOV=6.9m. AEROPHOTO
Flight altitude UHI-3	577 m MSL (1894 FT MSL) Only total radiation and met data AEROPHOTO
Aircraft velocity	72 ms ⁻¹ (140 KTS) for CASA and 50 ms ⁻¹ for Cessna

	310Q
Flight pattern	One flight line along the NW-SE urban axis.
Flight schedule	Flights schedule is shown in table A



Figure 71 : Flight path (NE-SE) of the AEROPHOTO aircraft.

Table 52: Aquired Data Report- Up To 22/7/2009

Flight No 1 midday 18/7/2009 take off 11:05 landing 13:34

Height FT	Temp	Aeros	bext	bscat	CO ₂	Filter pack
10500	√	-	√	√	√	Teflon-nylon
8000	√	-	√	√	√	GF-nylon
2000	√	-	√	√	√	Teflon-nylon

Flight No 2 midday 20/7/2009 take off 13:45 landing 15:45

Height FT	Temp	Aeros	bext	bscat	CO ₂	Filter pack
11200	√	√	√	√	√	Teflon-nylon 1
8200	√	√	√	√	√	Teflon-nylon 2
2000	√	√	√	√	√	GF-nylon

Flight No 3 morning 21/7/2009 take off 04:15 landing 6:20

Height FT	Temp	Aeros	bext	bscat	CO ₂	Filter pack
11200	√	√	√	√	√	Teflon-nylon
8200	√	√	√	√	√	GF-nylon
3000	√	√	√	√	√	Teflon-nylon

Flight No 4 evening 21/7/2009 take off 23:09 landing 22/7/2009 00:42

Height FT	Temp	Aeros	bext	bscat	CO ₂	Filter pack
8200	√	√	√	√	√	GF-nylon
4000	√	√	√	√	√	Teflon-nylon

Temp= outside temp at 10 Hz for use for method of variances

Aeros= aerosol number concentration at size bins 0.5-0.7, 0.7-1.0, 1.0-2.5

bext= extinction coefficient at 0.1 Hz

bscat= scattering coefficient at 0.1 Hz

CO₂= carbon dioxide concentration in ppmv at 0.1 Hz

Filter pack= Teflon filter for collection of particles < 2.5 µm; analysis for soluble ions and all elements; Glass fiber (GF) filter for collection of particles < 2.5 µm; analysis for OC/EC; Nylon filter for collection and analysis of gaseous inorganic and organic acids

Ancillary measurements= pressure, position, height, true wind speed and direction

Table 53: Calibration and validation

PARAMETER	METHOD OF CALIBRATION	VALIDATION
Temp	New Thies Ltd Calibrated	Factory calibrated
Aerosol	Mono-disperse aerosol	Certified factory annual calibration
CO ₂	Standard concentration gases	NIST traceable Messr. Griesheim standards
Bscat *	N2 and CO2 zeroed	NIST traceable Messr. Griesheim gases
Bext *	Machine zero and light scattering inter-comparison with our FGH 2000	Machine zero and light scattering standardisation
Filter pack	Mass flow meter calibration	Sierra Instruments certified calibration
Glass fiber filters analysis	Dessert Research Institute analysis for total, inorganic and organic carbon analysis	ISO method
Teflon filter analysis	XRF for elemental analysis, Ion chromatography for soluble ions	Bruker factory analysis, DUTH laboratory analysis**

Protocol of measurements, results and discussion

All measurements were collected on the central data acquisition computer in one common spread sheet, but also in separate spreadsheets. The common time recording

and ease of data treatment was the aim of the exercise. A time series of the three aerosol size bins follows.

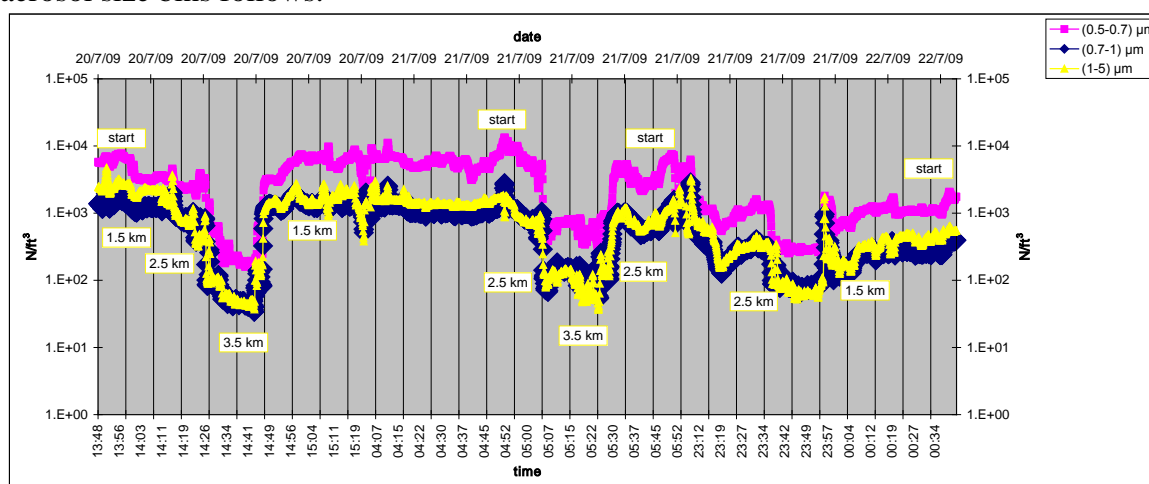


Figure 72: A time series of the three aerosol sizes

References

1. “Optical properties of aerosol over a South European urban environment”, K.Kelektoglou, S. Rapsomanikis, E.T.karageorgos and I. Kosmadakis. Int J. Remote Sensing, In Press (2009).
2. “Estimation of the microphysical aerosol properties over Thessaloniki, Greece, during the SCOUT-O3 campaign with the synergy of Raman lidar and sunphotometer data” D. Balis, E. Giannakaki, D. Müller, V. Amiridis, K. Kelektoglou, S. Rapsomanikis and A. Bais. J. G. R. (Atmospheres) Accepted 2009.

4.15 Analyses of Results

4.15.1 “The use of the variances similarity method to calculate heat fluxes above Athens from aircraft measurements” (CERTH)

Footprint models

By using appropriate footprint models, it will be possible to compare simultaneous fluxes calculations from aircraft and the tower.

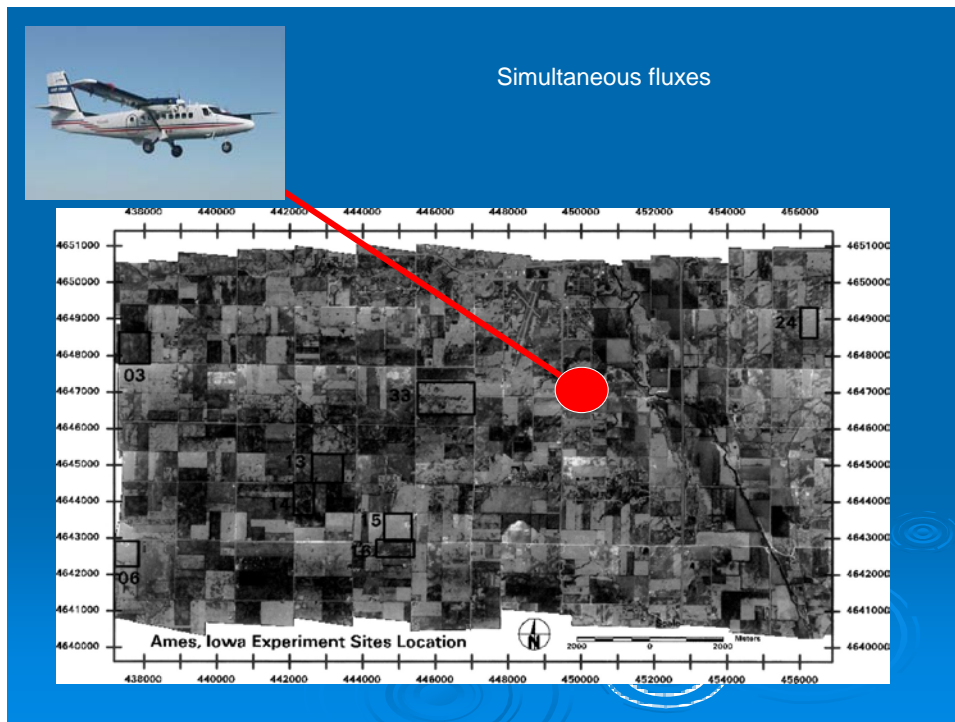


Figure 73. Aircraft passes over the EC tower

A technique to properly integrate the remote sensing heat flux pixels is needed for the comparisons with ground-measured fluxes in order to validate the use of remote sensing methodologies for accurate fluxes estimates.

Footprint models have been developed to determine what area (upwind of micrometeorological-flux stations) is contributing the heat fluxes to the sensors as well as the relative weight of each particular cell inside the footprint limits. The footprint tool developed by Neftel et al., 2008 was applied. Fig. 67 summarises the measured parameters and the parameters that will result through calculations from aircraft measurements.

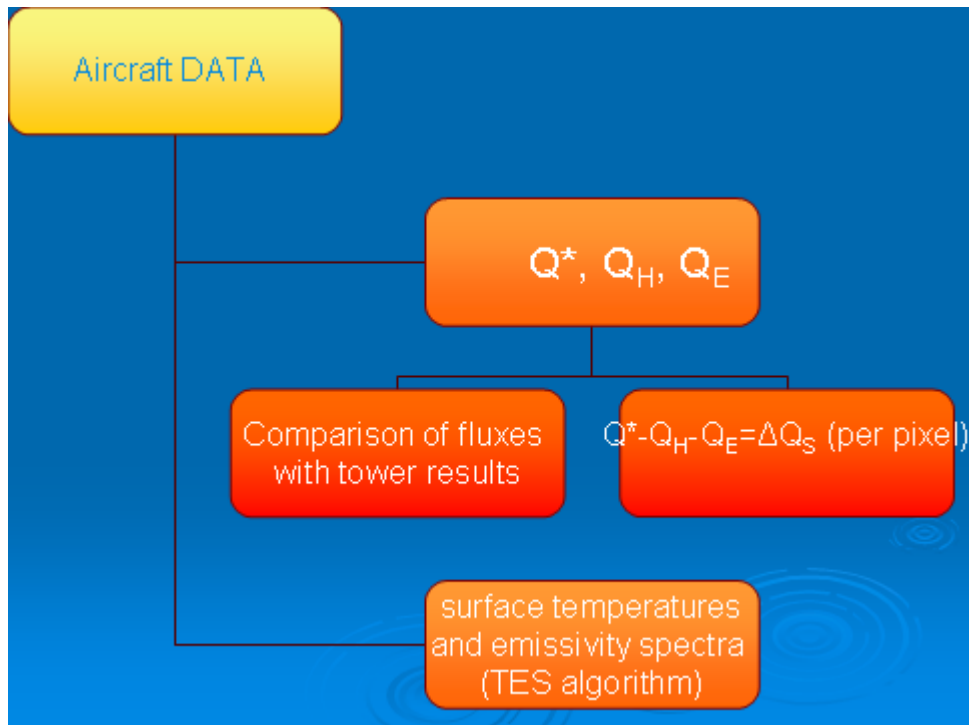


Figure 74. Aircraft results

The combination of several model calculation and data treatment techniques will provide valuable information about the parameters that affect Athens UHI and how the UHI can be monitored through remote sensing data

We have used the aircraft as a sensor platform to measure T at high frequencies. In principle the σ^2 of T aircraft measurements in a convective boundary layer is related to the σ^2 of T and hence to the $\langle w'\theta' \rangle$ at ground level via the MOST.

Simply: $|F_0| = |F_h| \cdot \sigma_h/\sigma$, where $|F| = \langle w'\theta' \rangle$ (relevant theory and its applications in references 1-5) Only in the convective BL whereby $16 < |\mu| < 550$ and $|\mu| = h_i/L$ where h_i = the height of the convective layer and L = Obukhov length.

The limitation of the method indicates the dominance of buoyant convection.

Also, it uses a non directly determined parameter the h_i . Difficulties also arise if measurements are carried out above the CBL. Parameterisation of the entrainment and detrainment of the flux is then needed. Ground calibration of the aircraft measurements is also needed. Aircraft measurements of temperature (x2), pressure, and positioning and flight height were recorded. Two temperature measurements one inside and one outside the aircraft were recorded for the calculation of the virtual potential Temperature. For the variance of T inside the aircraft, a fast response thermometer was used.

The formulation of reference [3] was used to obtain surface flux:

$\langle w'\theta' \rangle = \sigma_\theta^{3/2} [g \cdot z/\theta]^{1/2} \alpha^{-3/4} \{1\}$. Whereby z = height of (sensor) aircraft, avoiding formulations with h_i . For calibration of the α parameter above:

$\langle w'\theta' \rangle = \sigma_\theta^{3/2} [g \cdot z/\theta]^{1/2} [b_1 \xi^{-2/3} + b_2(b_3 - \xi)^{b_4}]^{-3/4} \{2\}$. The parameter σ was determined for the time of flying above the central axis of Athens. Then z determined from the aircraft GPS. The parameter θ was determined from in situ T and pressure

measurements. The constant α was given the value of 1.8 from reference [3] and references therein.

Values of L already established at ground and the condition for $\mu = h_i/L$, from the h_i given by NTUA (lidar) and NOA ceillometer was also determined for each flight.

It was also found that the condition $z/h_i < 0.8$ held. Formulation {2} was not needed since the value of $\alpha = 1.8$ was sufficient to give matched results of $\langle w'\theta' \rangle$ from both aircraft and the ground EC tower. In the cases of the flights above the convective boundary layer, the use of formula {2} resulted in values of β_1 - β_4 and ξ entrainment parameterisation factors that matched both (ground and airborne) sigmas (σ), as shown in the table below.

Table 54: Variance similarities method

Date	Time (local)	Altitude (m)	σ (aircraft)	$w'\theta' \pm 0.005$ K.m.s ⁻¹ (aircraft)	$w'\theta' \pm 0.005$ K.m.s ⁻¹ (ground)
20-7-2009	14:30	2620	0.02340	0.580	0.520
20-7-2010	15:15	960	0.01170	0.150	0.160
21-7-2009	05:05	2810	0.00512	0.030	0.030
21-7-2009	05:30	3370	0.00782	0.09	0.110
21-7-2009	23:55	2630	0.00872	0.080	0.070
22-7-2009	00:20	1380	0.01832	0.012	0.010

The caveats of the method are that for night time measurements difficult to achieve $|\mu|$ condition. Secondly, similarity of variances held for formulation {1} only for aircraft measurements within CBL and for the $z/h_i < 0.8$. The rest of the data were treated using the entrainment parameterisation of reference [3] and references therein.

Conclusions

We do have a method to determine regional sensible heat fluxes from an aircraft platform, given the fact that this time the aircraft measurements were calibrated using an eddy-covariance tower. If the aircraft flies within the convective boundary layer, calculations are relatively simple. More complicated iterations are necessary for flights above the CBL.

References

1. T. Foken “Micrometeorology”, Springer, (2008).
2. M.L. Wesely “Use of variance techniques to measure dry air surface exchange rates”. Bound. Layer Meteorol.44, 13-31, (1988).
3. A. Kotani & M. Sugita “Variance methods to estimate regional heat fluxes with aircraft measurements in the CBL”. J. Hydrol. 333, 68-85, (2007).
4. G. Katul et.al. “Latent and sensible heat flux predictions from a uniform pine forest using surface renewal and flux variance methods”. Bound. Layer Meteorol., 80, 249-282, (1996).
5. M. Sugita & N. Kawakubo . “Surface and mixed layer variance methods to estimate regional sensible heat flux at the surface”. Bound. Layer Meteorol., 80, 249-282, (1996).

4.15.2 “Determination of aerosol chemical and optical properties, for the validation of the lidar data used in atmospheric optical corrections” (CERTH)

Retrieved data from lidar ground measurements using inversion model are in the table below. An initial assumption for sea-salt being the major origin of aerosols during the flights was not verified by the chemical composition data, excluding one case where marine influence was evident: 21/7, at 8600 ft. Secondary aerosol and secondary organic aerosol, seem to play a fundamental role in the other cases. All calculations have been made on the assumption of homogeneity of the atmosphere over short periods of time.

Table 55: Aerosol Chemical and Optical Properties

Date	Time (local)	Alt (ft)	Alt (km)	Mean radius (μm) (reff) NTUA Fine/Total	Mean radius (μm) (reff) DUTH Fine/Total	SSA (ω) NTUA (532 nm)	SSA (ω) DUTH (532 nm)	Refractive index NTUA Real part	Refractive index NTUA Imag. part	Refractive index DUTH Real part	Refractive index DUTH Imag. part	Remarks
21/7/2009	11:54 PM	8612	2.63	0.11±0.043/0.35±0.2	0.25/0.3695	0.61±0.1	N/A	1.376±0.05	0.065±0.01	1.299	0.01	NW Flow-clear
22/7/2009	12:16 AM	4539	1.38	N/A	0.25/0.391	N/A	0.513	N/A	N/A	1.205	0.01	NW Flow-clear
20/7/2009	2:23 PM	8592	2.62	N/A	0.25/0.357	N/A	0.654	N/A	N/A	1.436	0.01	Fires/ photoch
20/7/2009	3:07 PM	3167	0.96	N/A	0.25/0.379	N/A	0.965	N/A	N/A	N/A	N/A	Fires/ photoch
21/7/2009	5:05 AM	9228	2.81	0.19±0.04/0.4±0.14	0.25/ 0.370	0.63±0.11	0.698	1.56±0.13	0.051±0.03	N/A	N/A	Haze/ Photoc-USA
21/7/2009	5:18 AM	11055	3.37	0.14±0.03/0.14±0.03	0.25/0.337	0.87±0.08	N/A	1.43±0.07	0.028±0.02	1.391	0.01	Haze/ Photoc-USA
24/7/2009					N/A		N/A			N/A	N/A	Sahara
25/7/2009					N/A		N/A			N/A	N/A	Sahara

Further explanation of the above data is also presented in table 66 and in section 5.3.

5. Ground-based and in-situ measurements

Quality assured ground-based measurements were provided for the greatest Athens area by a number of Greek Agencies and Institutes/Universities. Three different kind of ground-based measurements were carried out during the two weeks of the intensive period of the THERMOPOLIS 2009 campaign:

- Atmospheric columnar and vertical profile measurements of aerosol, clouds, and water vapor to be used for atmospheric corrections of satellite imagery.
- Measurements for characterizing the Athens urban heat island (UHI), such as the air temperature among others, which are used to analyze the effect and the evolution of the UHI during the experiment.
- Radiometric measurements, which are used for calibration/validation of parameters extracted from the airborne data.

Figure 16 shows the selected experimental sites. Different symbols refer to different kind of ground based measurements and different colors refer to different Institutes/Universities or Greek Agencies that participate to the campaign.

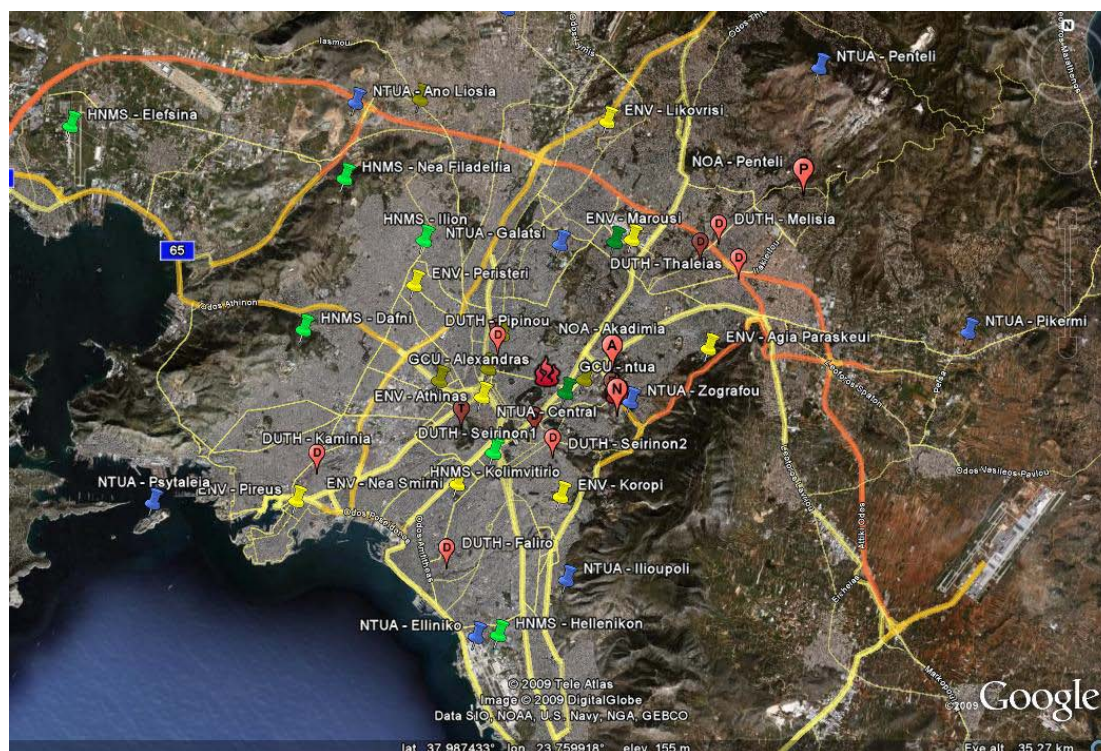


Table 56: Experimental sites

α/α	Station name	Operator	Latitude ⁰N	Longitude ⁰E
1.	Patision	ENV	37.99917	23.73306
2.	Athinas	ENV	37.97833	23.725
3.	Pireus	ENV	37.94333	23.6475
4.	Geoponiki	ENV	37.98361	23.70694
5.	Nea Smirni	ENV	37.94944	23.715
6.	Peristeri	ENV	38.01528	23.69611
7.	Liosia	ENV	38.07667	23.69778
8.	Marousi	ENV	38.03083	23.78722
9.	Likovrisi	ENV	38.06972	23.77639
10.	Aristotelous	ENV	37.98778	23.7275
11.	Agia Paraskevi	ENV	37.995	23.81944
12.	Thrakomakedones	ENV	38.14361	23.75806
13.	Koropi	ENV	37.94583	23.75833
14.	Goudi	ENV	37.98444	23.76778
15.	Zografou 200m ASL	NTUA	37.9771	23.7869
16.	Menidi	NTUA	38.1066	23.7339
17.	Psytaleia	NTUA	37.9419	23.5870
18.	Elliniko	NTUA	37.8988	23.7234
19.	Ilioupoli	NTUA	37.9183	23.7610
20.	Mandra	NTUA	38.1229	23.5637
21.	Galatsi	NTUA	38.0293	23.7574
22.	Penteli	NTUA	38.0865	23.8635
23.	Pikermi	NTUA	38.0011	23.9286
24.	Ano Liosia	NTUA	38.0752	23.6707
25.	Central	NTUA	37.99	23.78
26.	Thissio	NOA	37.972	23.718
27.	Penteli	NOA	38.050	23.861
28.	Akadimia	NOA	37.988	23.775
29.	Hellenikon	HNMS	37.89972	23.73278
30.	Elefsina	HNMS	38.06694	23.55
31.	Nea Filadelfia	HNMS	38.04972	23.66694
32.	Goudi	HNMS	37.98	23.76
33.	Dafni	HNMS	38.00	23.65
34.	Kolimviti	HNMS	37.96	23.73
35.	Ilion	HNMS	38.03	23.70
36.	Kotroni	HNMS	38.13	23.95
37.	Oaka	HNMS	38.03	23.78
38.	Dekeleia	HNMS	38.11	23.76

39.	Estia-ATH1#042 185 m ASL 1 st floor ⁺	CERTH	37.981636	23.780973
40.	Seirion1-ATH2#040 2 nd floor ⁺	CERTH	37.962698	23.756444
41.	Seirion2-ATH3#879 2 nd floor (backyard) ⁺	CERTH	37.962698	23.756444
42.	Thaleias 12-D1 217 m ASL 2 nd floor ⁺	CERTH	38.02262	23.833454
43.	Pipinou-D2 101 m ASL 3 rd floor ⁺	CERTH	37.99652	23.733013
44.	Pellis-D3 211 m ASL 2 nd floor ⁺	CERTH	38.027869	23.817457
45.	Konsoula-D4 5 th floor	CERTH	37.969848	23.748767
46.	Kaminia	CERTH	37.956885	23.657529
47.	Faliro	CERTH	37.925999	23.712448
48.	Melissia	CERTH	38.0338	23.8251
49.	Panathinaikos stadium	UVEG*	37.9871	23.7536
50.	NTUA soccer field	UVEG*	37.98143	23.78322
51.	Syntagma square	UVEG*	37.975667	23.734383
52.	Acropolis Museum	UVEG*	37.9687	23.728867
53.	Acropolis	UVEG*	37.971867	23.72715
54.	Transects	UVEG*	See 5.3	See 5.3
55.	Lake Maratnonos	UVEG*	See 5.3	See 5.3

⁺ Street name and sensor identifier/height asl, floor

*Reported in detail under Section 5.3 of the present DAR.

In the next, the ground-based measurements will be presented in more detail.

5.1 Atmospheric measurements

Temperature, water vapor, wind and aerosols columnar/vertical profile measurements were performed at Athens during the THERMOPOLIS 2009 campaign. Knowledge of the atmospheric conditions, mainly the aerosol optical depth, its vertical profile and the water content, is required to perform accurate atmospheric correction of satellite imagery.

In the next, the three types of performed measurements are analyzed in the following order:

- Vertical profile soundings of meteorological parameters
- Sunphotometric measurements of total aerosol load in ultraviolet, visible and infrared spectral regions and ceilometer measurements of boundary layer structures.
- Lidar measurements of aerosol and water vapor vertical profiles in the free troposphere

5.1.1 Vertical profile soundings of meteorological parameters

One balloon was released each day at midnight (00:00 UTC) by the Hellenic National Meteorological Agency (HNMS) at the old airport of Hellenikon, instead of the two foreseen in the Experiment Plan (HNMS did not perform nighttime soundings during the experiment). The coordinates of the ground station (station identifier: HNMS Hellenikon) are presented in Table 11. The soundings provide the vertical distribution of Temperature, Relative Humidity and wind speed/direction for the whole period of THERMOPOLIS2009. An example is presented below.

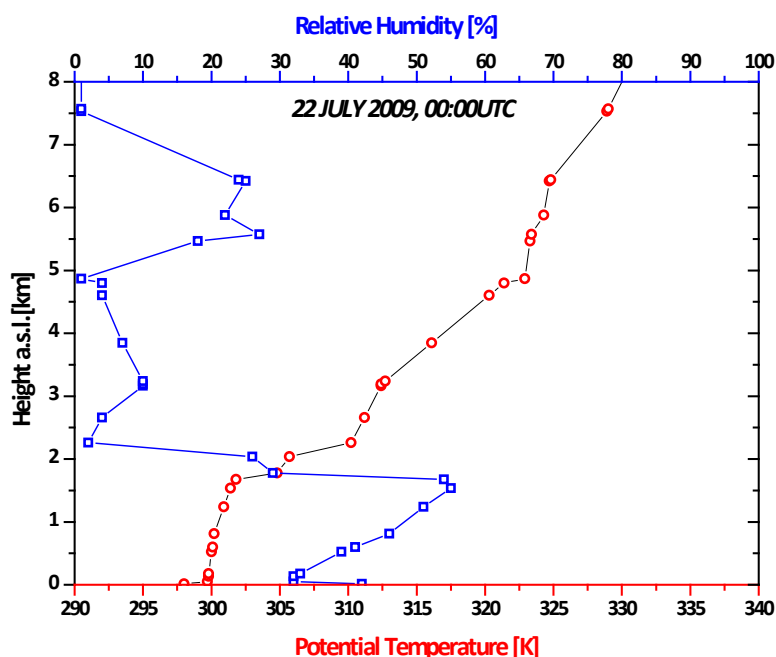


Figure 76. Vertical profiles of the Potential Temperature (OK) and Relative Humidity (%) for the 22nd of July 2009 at Hellenikon HNMS station.

5.1.2 Sun photometric measurements of total aerosol load in ultraviolet, visible and infrared spectral regions and ceilometer measurements of boundary layer structures (NOA)

Sunphotometric measurements of the aerosol load over the study area were performed continuously by the radiometric stations of the National Observatory of Athens (NOA). NOA performs aerosol measurements with passive remote sensing ground based instruments continuously in 3 sites within the Greater Athens area (Fig. 16), one at Penteli rural site and two at Athens centre (Academy of Athens and Thissio). Station coordinates are presented in following Table (station identifiers: NOA Penteli, Akadimia, Thissio). Additionally to these 3 stations, NOA was responsible for the Hellenikon HNMS radiosonde data collection. WRC instrumentation was installed also at the Patision flux tower site.

Table 57: Radiometric stations and measurements

Site	N	E	Height ASL	Comments
Academy	37.988	23.775	130	15-31.7.2009
Penteli	38.050	23.861	527	15-31.7.2009

Thissio	37.972	23.718	94	15-31.7.2009
Patision	38.000	23.733	110	15-31.7.2009
Hellenikon	37.899	23.733	10	15-31.7.2009

Period and type of measurement (e.g. continuous with 5-min resolution, etc)	Measured parameter	Instrument
Continuous, 15-min res.	AOD at visible and IR spectral regions	CIMEL
Continuous, 15-min res.	Water Vapor column	CIMEL
Continuous, 15-min res.	Angstroem exponent, Aerosol size distribution, Columnar Aerosol Absorption	CIMEL
Continuous, 5-min res.	Aerosol Optical Depth at UV wavelengths	UV-MFR
Continuous, 5-min res.	Radiation at UV, visible and IR spectral regions	PGS-100
Continuous, 1-min res.	Backscatter coefficient profiles at 900 nm	Ceilometer CL31
Continuous, 1-min res.	downwelling SW irradiance	pyranometer CM21
Continuous, 1-min res.	downwelling LW irradiance	pyrgeometer CG4
Continuous, 1-min res.	upwelling LW irradiance	EppleyPIR
Continuous, 1-min res.	upwelling LW irradiance	pyranometer CM21
Continuous, 1-min res.	downwelling LW irradiance @ 8-14 um	modified pyrgeometer CGR3
Continuous, 1-min res.	AOD@ 368, 412, 500, 862 nm	Precision Filter Radiometer (PFR)
Continuous, 1/15-min res.	Meteorological parameters	Automatic MET stations

The station of NOA – Akadimia is equipped with a CIMEL CE318-NEDPS9 sunphotometer for the retrieval of aerosol optical depth at 8 wavelengths from 340 to 1640 nm, including polarization measurements. The CIMEL instrument is a part of NASA's AERONET (Aerosol Robotic Network) network (<http://aeronet.gsfc.nasa.gov>). The data are level 2.0 Quality Assured and aerosol inversion retrievals are additionally available for complete aerosol characterization (e.g. Saharan dust events, smoke cases etc). The instrument is located on the roof of the Research Center for Atmospheric Physics and Climatology of the Academy of Athens with an elevation of 130 m from mean sea level. The campus is located in the city center and 10 km from the sea.



Figure 77. NOA's CIMEL CE318-NEDPS9 sunphotometer and radiometric station in the Academy of Athens site.

The station is additionally equipped with a Yanke UV-MFR multifilter radiometer for the retrieval of aerosol optical properties in the ultraviolet region. The UVMFR-7 Ultraviolet Multi-Filter Rotating Shadowband Radiometer is an instrument that measures diffuse and total global irradiance, and computes direct irradiance at seven narrow-bandwidth wavelengths in the UV-B and UV-A regions (300, 305.5, 311.4, 317.6, 325.4, 332.4 and 368 nm, @2nm FWHM). Pointing the head at the surface provides spectral measurements of reflected irradiance. This instrument provides ozone columnar measurements for aerosol optical depth corrections in all operated wavelength bands of NOA's sunphotometers in Athens.



Figure 78. NOA's UV-MFR multifilter radiometer

AOD at 8 wavelengths retrieved by AERONET's algorithms from CIMEL measurements in this NOA station are presented in the next Figures for July 2009, along with UV AOD retrievals from UV-MFR and a number of other parameters.

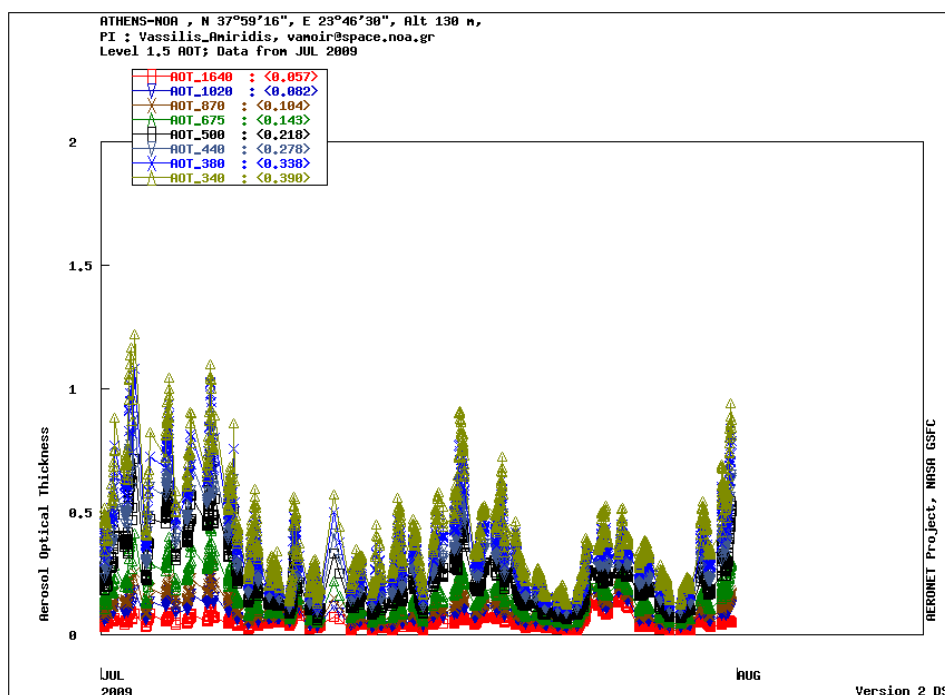


Figure 79. Aerosol Optical Depths at 8 wavelengths retrieved by AERONET for Athens CIMEL for July 2009, along with UV-MFR retrievals for the UV wavelength.

In Figures 21, 22 and 23 the Angström exponents, the fine mode aerosol fraction and the water vapour content in the atmospheric column are presented correspondingly for July 2009.

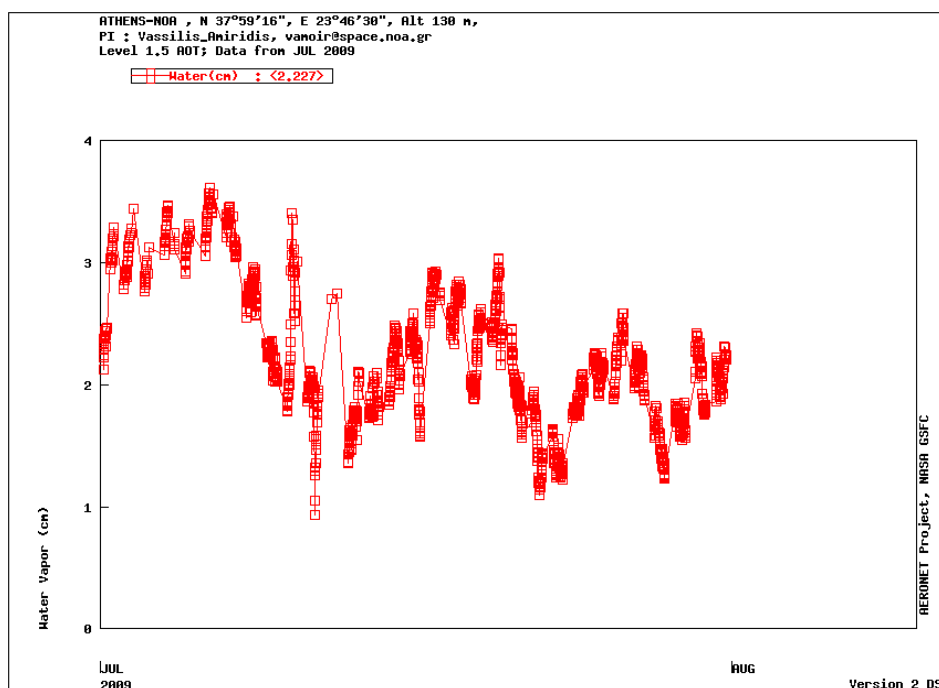


Figure 80: Extinction-related Angstroem exponents (440/870nm) for July 2009

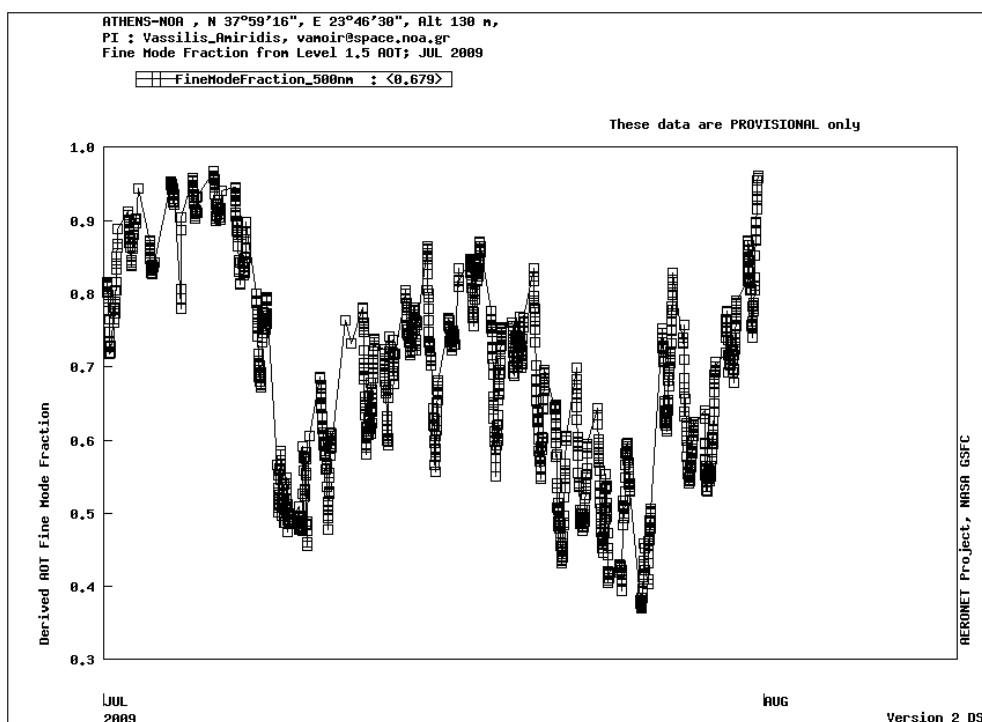


Figure 81: Fine mode aerosol fraction for July 2009

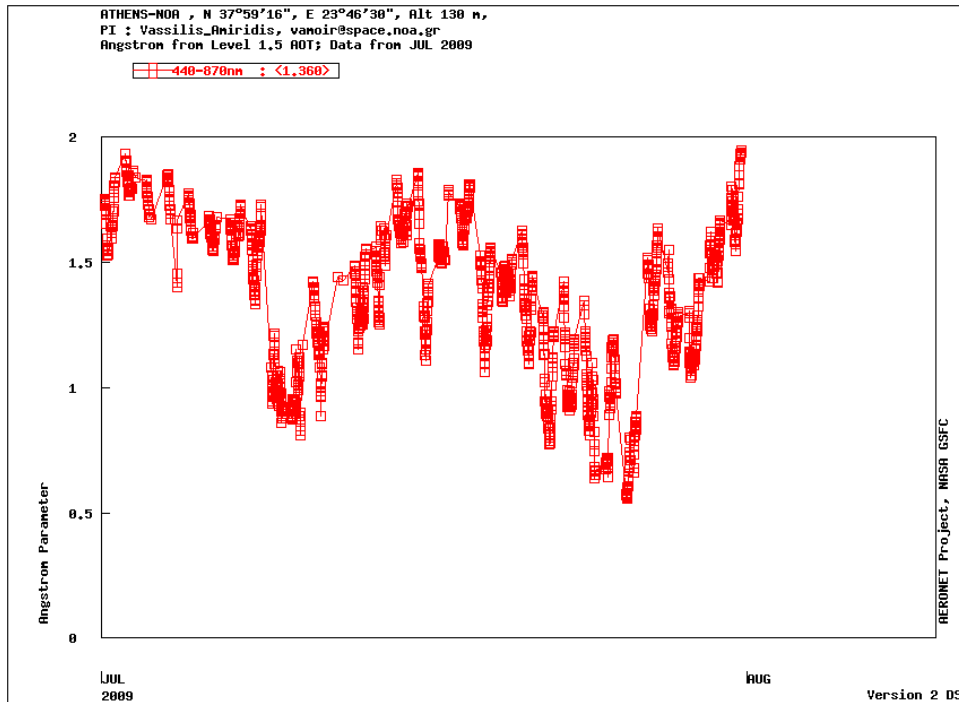


Figure 82: Water vapour content for July 2009

The station of NOA Penteli is equipped with a Kipp&Zonen PGS 100 spectrophotometer, with no moving parts, for routine measurement of solar radiation. This instrument is especially designed for:

- Direct solar measurements using an integrated solar tracker with active sun sensor correction
- Diffuse and scattered measurements by programmed sky scans
- Programmable measurement

PGS-100 provides spectral data that can be post-processed by the user to derive a variety of parameters, including:

- Optical depth
- Scattering coefficients
- Aerosol distribution
- Energy distribution
- Absorption by atmospheric gasses



Figure 83: PGS-100 spectrophotometer (left), and the instrument installed at NOA's Penteli station (right)

The instrument was located on Penteli's station of NOA. The elevation of this station is at 550 m ASL.

Selected spectra on 17 of July 2009 at 08:00, 09:00, 10:00 and 12:00 LT, measured with the PGS-100 spectrophotometer at NOA's Penteli station for THERMOPOLIS are presented below.

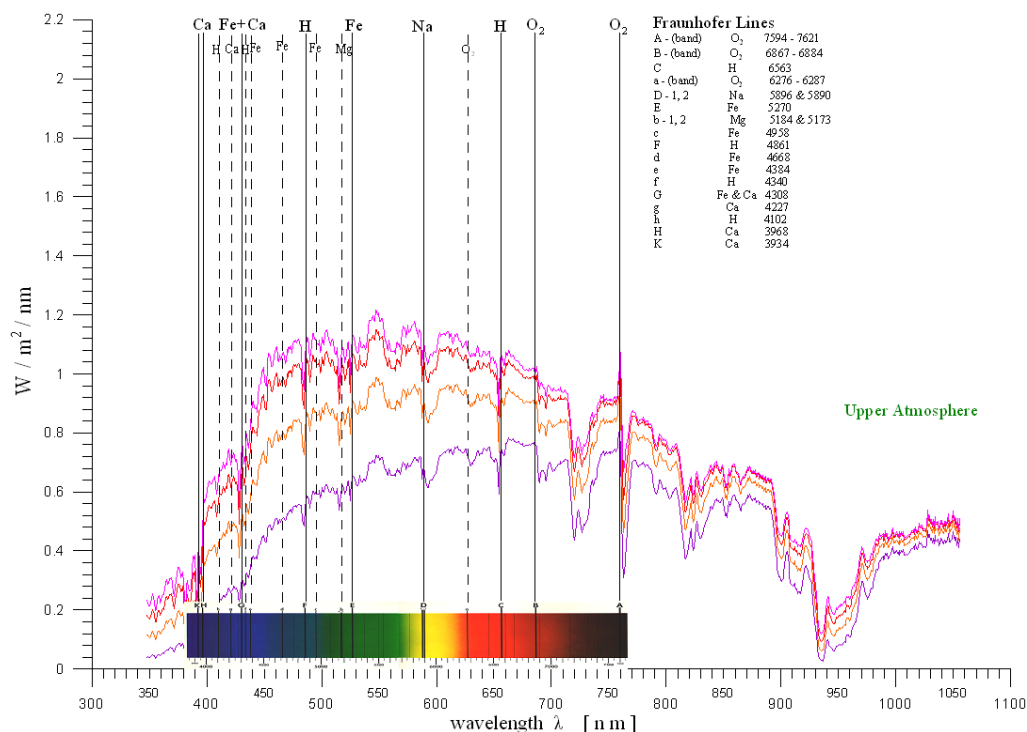


Figure 84. Selected spectra on 17 of July 2009 at 08:00, 09:00, 10:00 and 12:00 LT, measured with the PGS-100 spectrophotometer
NOA's Penteli station is additionally equipped with a nephelometer and a particle soot absorption photometer for aerosol in-situ measurements of scattering and

absorption (not mentioned in the Experiment Plan). An example of the retrievals for the time period between 14 and 17 of July 2009 is presented in the next Figure.

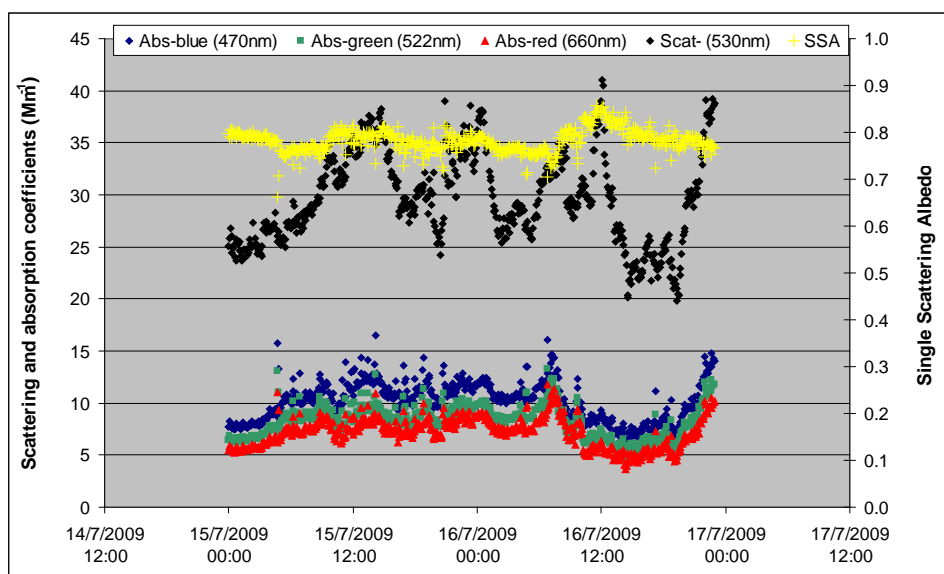


Figure 85: Scattering and absorption coefficients by nephelometer and particle soot absorption photometer for the time period between 14 and 17 of July 2009

Additionally, the DUTH 5-channel MicroTOPS II for the measurement of total ozone, water vapour column (at 936 nm) and aerosol optical thickness (AOT) at 1020 nanometers has been used during THERMOPOLIS 2009 at NOA's Penteli station. Direct solar ultraviolet radiation at 3 discrete wavelengths within the UV-B range was also measured and stored. The instrument was operated at 11:30, 13:30 and 15:30 local time (UTC+3). An example of the Microtops recordings performed is presented below.

THERMOPOLIS CAMPAIGN - JULY 2009										
NOA - PENTELI										
Date	15/7/2007	Altitude	527 m a.s.l.							
		Coordinates	38°03' N , 23°52' E							
Time	03 (corr)	03 (1/2)	03 (2/3)	Water	AOT 1020	SZA	305 (W/m²)	312 (W/m²)	320 (W/m²)	936 (W/m²)
11.28	337,7 DU	326,8 DU	311,5 DU	1,35 cm	0.082	31.032	5.22E-02	1.90E-01	3.45E-01	2.54
11.35	334,0 DU	324,6 DU	311,5 DU	1,33 cm	0.096	29.847	5.43E-02	1.93E-01	3.49E-01	2.54
11.39	329,7 DU	323,6 DU	315,0 DU	1,37 cm	0.104	29.125	5.45E-02	1.92E-01	3.47E-01	2.48
average	331,8 DU	325,0 DU	312,7 DU	1,35 cm	0.094	30.001	5.37E-02	1.92E-01	3.47E-01	2.52
	305nm	312nm	320nm	936nm	1020nm	305/312	312/320	Pressure	Temperature	
	376,59 mv	690,41 mv	352,56 mv	454,70 mv	952,02 mv	0.54546	1.95828	960 mb		
	391,48 mv	702,97 mv	366,72 mv	453,52 mv	937,57 mv	0.55696	1.9706	960 mb		
	393,07 mv	697,92 mv	354,50 mv	443,59 mv	930,36 mv	0.56328	1.96861	960 mb		
average	387,05 mv	697,10 mv	354,59 mv	450,60 mv	939,98 mv	0.55523	1.96583	960 mb		
Time	03 (corr)	03 (1/2)	03 (2/3)	Water	AOT 1020	SZA	305 (W/m²)	312 (W/m²)	320 (W/m²)	936 (W/m²)
13.30	330,5 DU	327,6 DU	323,6 DU	1,52 cm	0.088	16.58	6.65E-02	2.15E-01	3.75E-01	2.54
13.35	323,3 DU	326,3 DU	330,4 DU	1,61 cm	0.071	16.619	6.67E-02	2.14E-01	3.78E-01	2.51
13.39	332,1 DU	328,3 DU	322,9 DU	1,52 cm	0.065	16.698	6.78E-02	2.19E-01	3.83E-01	2.61
average	328,6 DU	327,4 DU	325,6 DU	1,55 cm	0.075	16.632	6.70E-02	2.16E-01	3.79E-01	2.55
	305nm	312nm	320nm	936nm	1020nm	305/312	312/320	Pressure	Temperature	
	479,73 mv	780,90 mv	383,11 mv	454,56 mv	956,39 mv	0.61452	2.03833	959 mb		
	480,88 mv	779,58 mv	385,58 mv	449,14 mv	973,98 mv	0.61687	2.0218	958 mb		
	488,81 mv	797,43 mv	390,99 mv	467,01 mv	979,74 mv	0.61299	2.03949	958 mb		
average	483,14 mv	785,97 mv	386,56 mv	456,90 mv	970,04 mv	0.61479	2.03321	958,3 mb		
Time	03 (corr)	03 (1/2)	03 (2/3)	Water	AOT 1020	SZA	305 (W/m²)	312 (W/m²)	320 (W/m²)	936 (W/m²)
15.24	338,8 DU	330,7 DU	319,2 DU	1,43 cm	0.094	29.509	4.93E-02	1.78E-01	3.25E-01	2.44
15.30	328,0 DU	327,1 DU	325,8 DU	1,44 cm	0.097	30.632	4.72E-02	1.71E-01	3.16E-01	2.41
15.35	328,7 DU	327,1 DU	324,9 DU	1,44 cm	0.123	32.267	4.26E-02	1.57E-01	2.93E-01	2.29
average	331,8 DU	328,3 DU	323,3 DU	1,44 cm	0.105	30.803	4.64E-02	1.69E-01	3.11E-01	2.38
	305nm	312nm	320nm	936nm	1020nm	305/312	312/320	Pressure	Temperature	
	355,66 mv	648,38 mv	331,78 mv	437,03 mv	940,79 mv	0.54858	1.95447	958 mb		
	340,25 mv	621,36 mv	322,57 mv	430,02 mv	936,42 mv	0.54778	1.92608	957 mb		
	307,22 mv	572,45 mv	299,54 mv	408,90 mv	905,32 mv	0.53681	1.91075	957 mb		
average	334,38 mv	614,06 mv	317,96 mv	425,32 mv	927,51 mv	0.54439	1.93043	957,3 mb		

Figure 86: Example of Microtops recordings performed in NOA's Penteli station

Also, photos and videos of the Athens Greater Area were taken from NOA's Penteli station at 11:30, 13:30 and 15:30 local time (UTC+3) of each day (not mentioned in the Experiment Plan). Photos and short video sequences were taken by DUTH's Panasonic Lumix DMC-FZ8 Camera for 7 days, while everyday photographs for the whole measurement period were taken by NOA's automatic camera system. An example is presented in the next Figure.

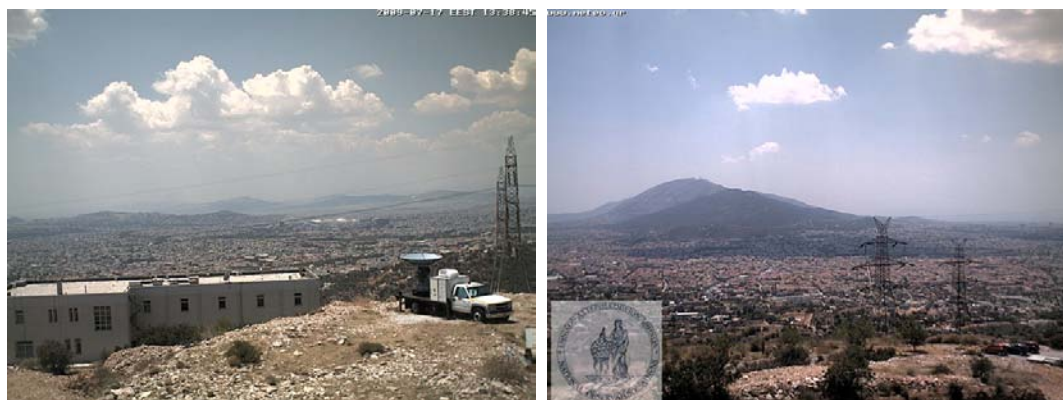
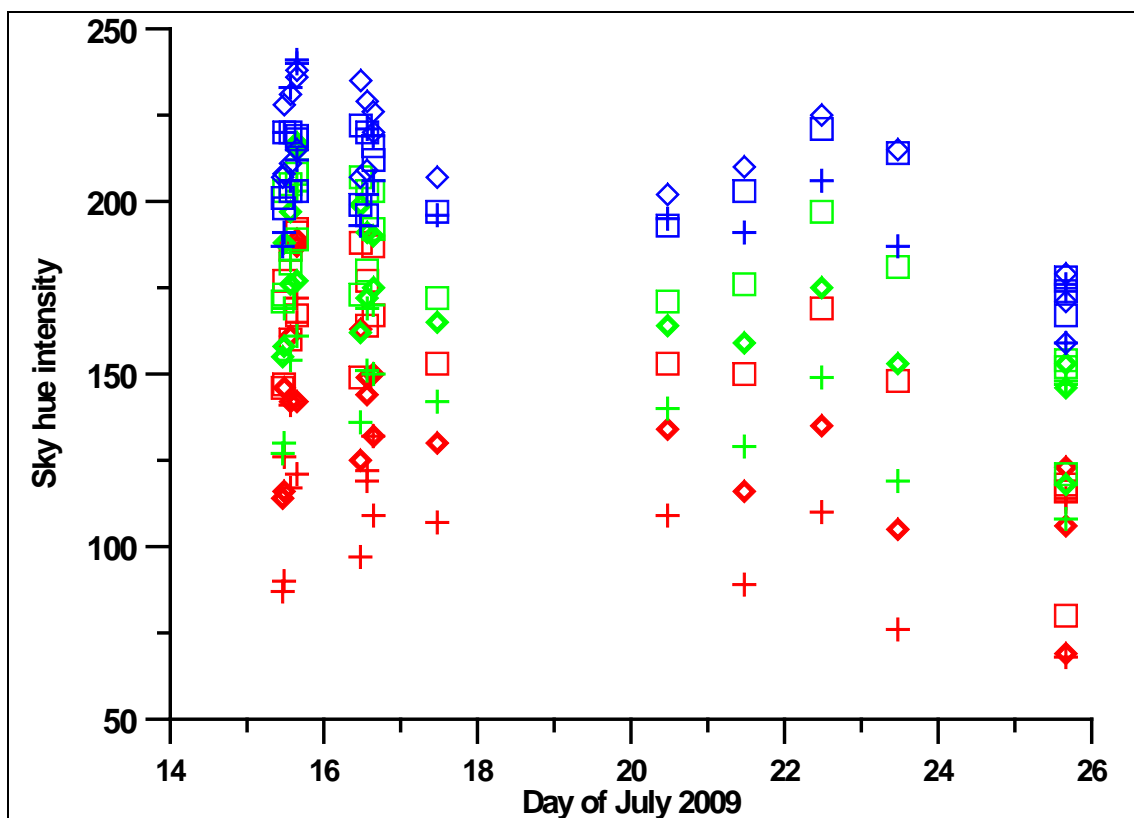
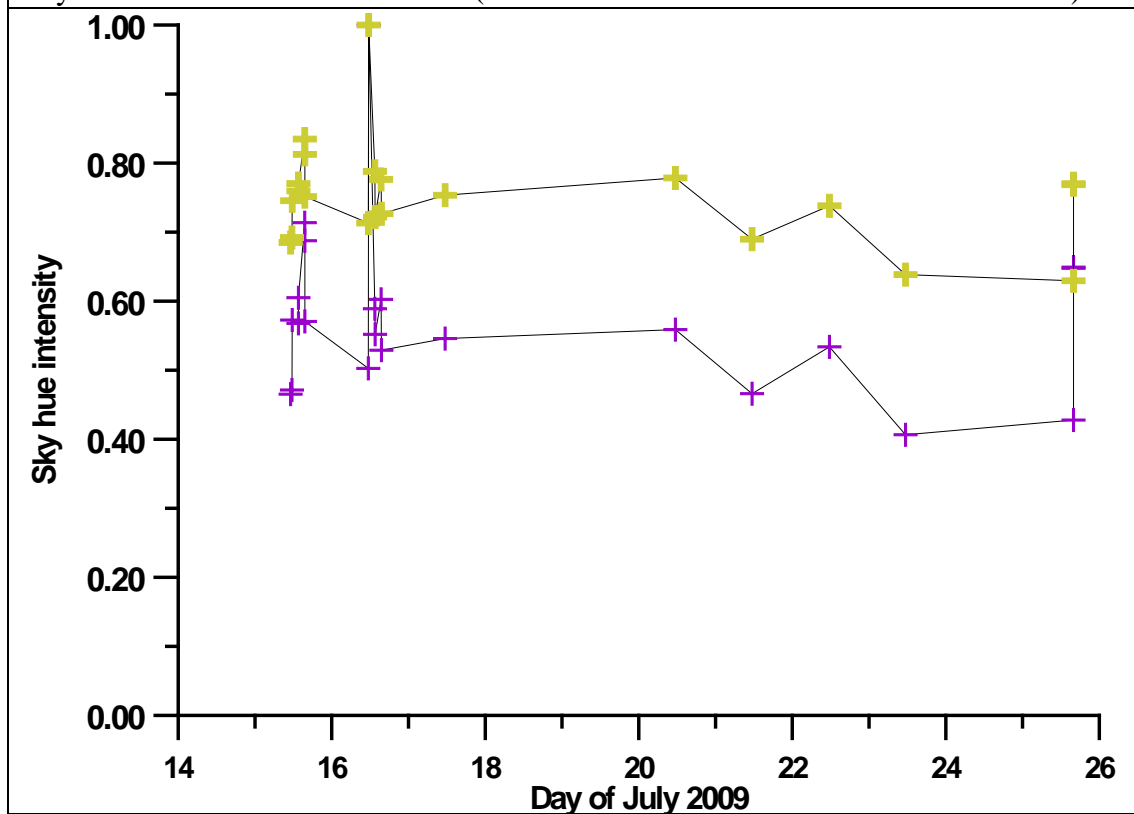


Figure 87: View to SouthWest (left) and view to Hymettos mountain, from NOA's cameras

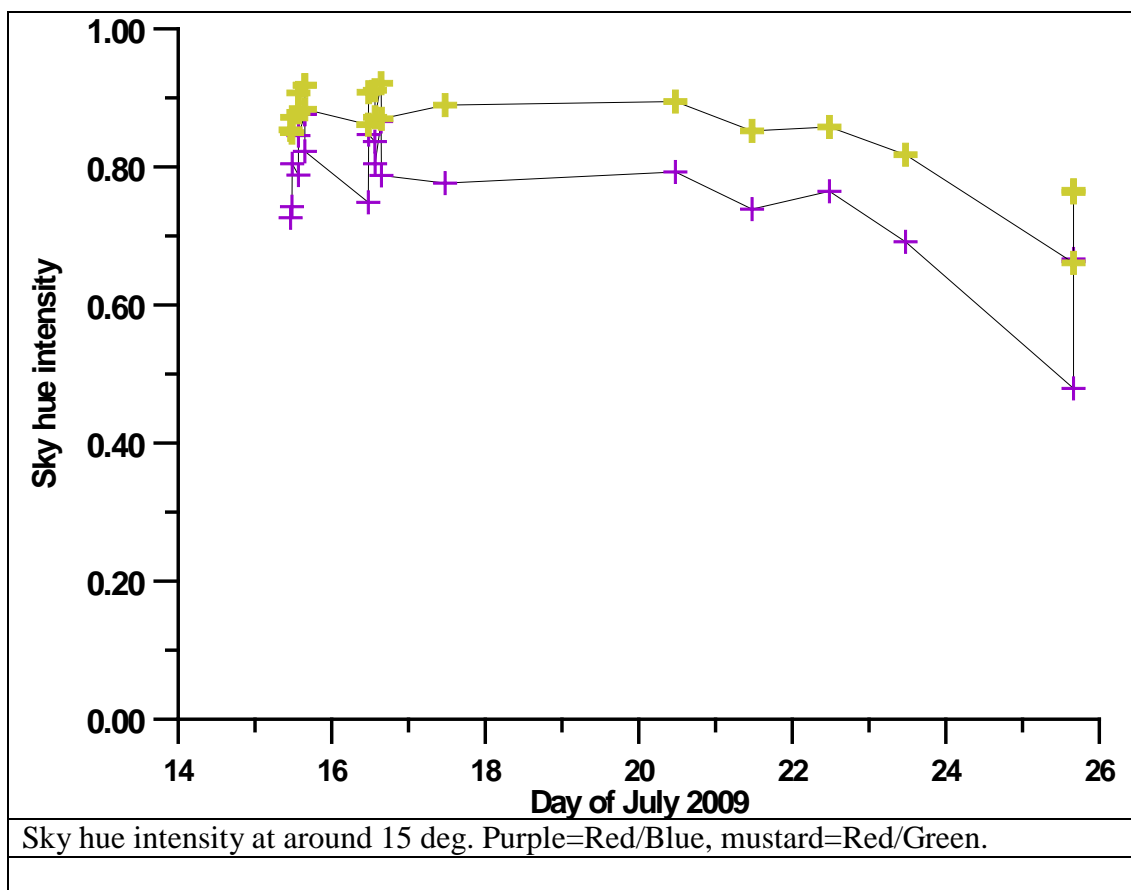
Sky colour measurements (not mentioned in the Experiment Plan) by the Panasonic Lumix DMC-FZ8 digital camera preliminary data as retrieved from the digital images are presented below.



Sky color in RGB at various SZAs (measured with a Panasonic Lumix DMC-FZ8).



Sky hue intensity at 45 deg. Purple=Red/Blue, mustard=Red/Green.



The station of NOA at Thissio is equipped with the latest Vaisala ceilometer CL31. This ceilometer is an eye-safe single lens lidar system reporting attenuated backscatter profiles. The instrument operates 24 h a day in fully automated, hands-off operation mode. The profiles provided can be used for more than just cloud-base height determination. In dryweather situations, there is a fairly good correlation between the ceilometer near-range backscatter and in situ PM10 concentration readings. The comparison of mixing height values based on soundings and on ceilometers backscattering profiles indicates that ceilometers are suitable instruments for determining the convective mixing height. Its enhanced optics and electronics enables the CL31 ceilometer to detect fine boundary-layer structures whose counterparts are seen in temperature profiles. Station's coordinates are presented in last Table under station identifier NOA – Thissio.

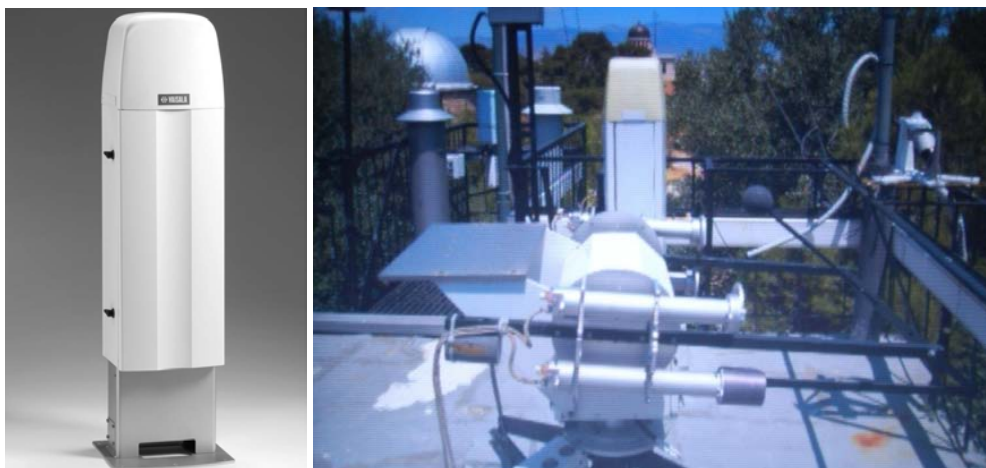


Figure 88. Vaisala CL31 ceilometer (left), and NOA's station at Thissio (right)

In the next Figure, an example of timeseries of the aerosol backscatter profiles at 900nm is presented for the 15th of July 2009. These measurements, obtained with the CL31 ceilometer, show the evolution of the boundary layer for that day, using aerosol as a tracer.

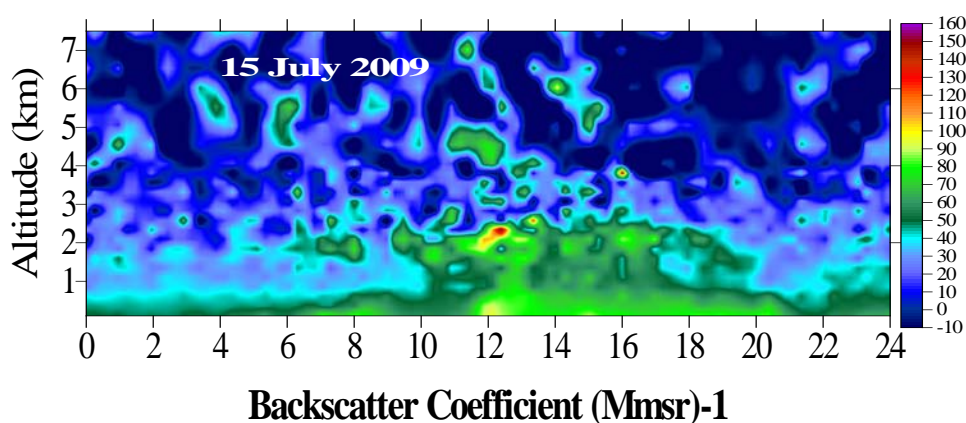


Figure 89. Quick-look of the aerosol backscatter coefficient at 900nm for the 15th of July 2009

The Physikalisch-Meteorologisches Observatorium Davos (PMOD) group of the World Radiation Center (WRC) deployed additionally a PIR pyrgeometer at the premises of the Academy of Athens Institute of Biological Sciences to measure LW downwelling and upwelling radiation from 14 to 19 of July 2009. This instrument was moved then to the Patision str. flux tower station of DUTH, measuring there from 20 to 24 of July 2009. The system features also a special pyrgeometer only sensitive to the 8-14 μm band. With the latter instrument it is possible to determine the temperature of the boundary layer.

Additionally, WRC deployed a CG4 pyrgeometer and SW pyranometer for downwelling and upwelling LW and SW radiation at the premises of NTUA for the time period between 13 and 24 of July 2009.

WRC instruments were calibrated prior and after deployment at PMOD against World Radiation Center reference standards. Pyranometers against the World standard group of absolute pyrheliometers, pyrgeometers against the world infrared standard group of pyrgeometers (WISG).

From the measurements of PMOD the following quantities can be derived:

- 1) Downwelling and upwelling longwave irradiance
- 2) Downwelling and upwelling shortwave irradiance
- 3) Shortwave albedo (combining upwelling and downwelling SW radiation)
- 4) Surface emissivity (if surface temperature is available from ancillary measurements)
- 5) Effective boundary layer temperature (see publication in press, Gröbner et al., JGR, 2009)



Figure 90: WRC's pyrgeometers during deployment in Athens

Measurement examples of the downwelling and upwelling longwave and sortwave radiation performed with WRC instruments at the NTUA University campus, the Academy of Athens NOA's station and the Patision downtown station are presented in the next Figures.

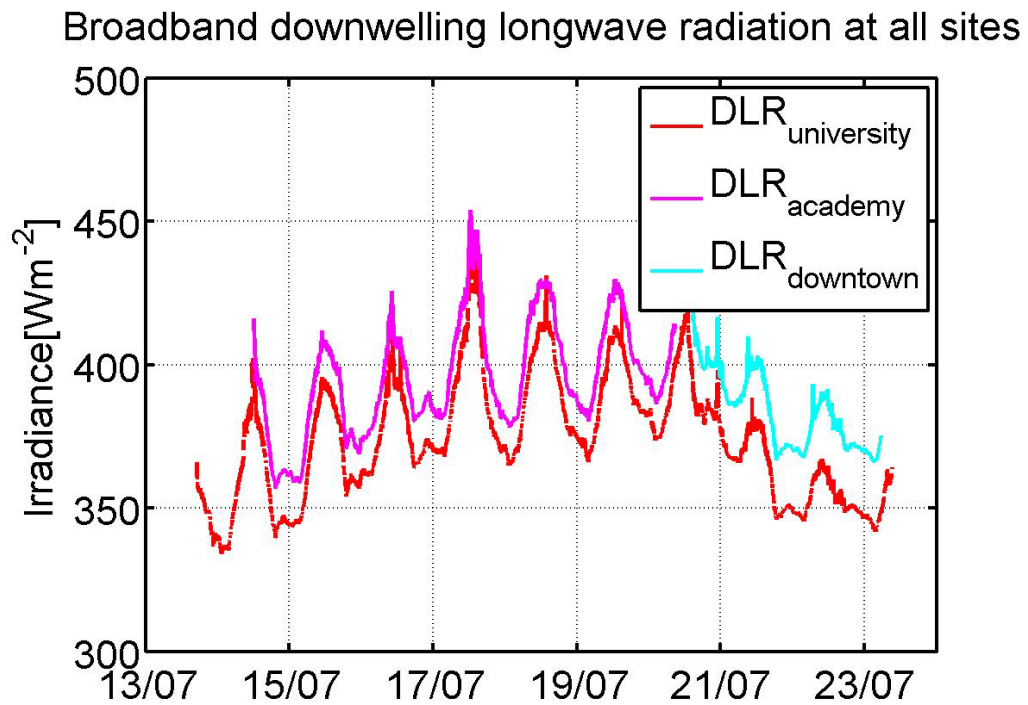


Figure 91: Broadband downwelling longwave radiation at all sites

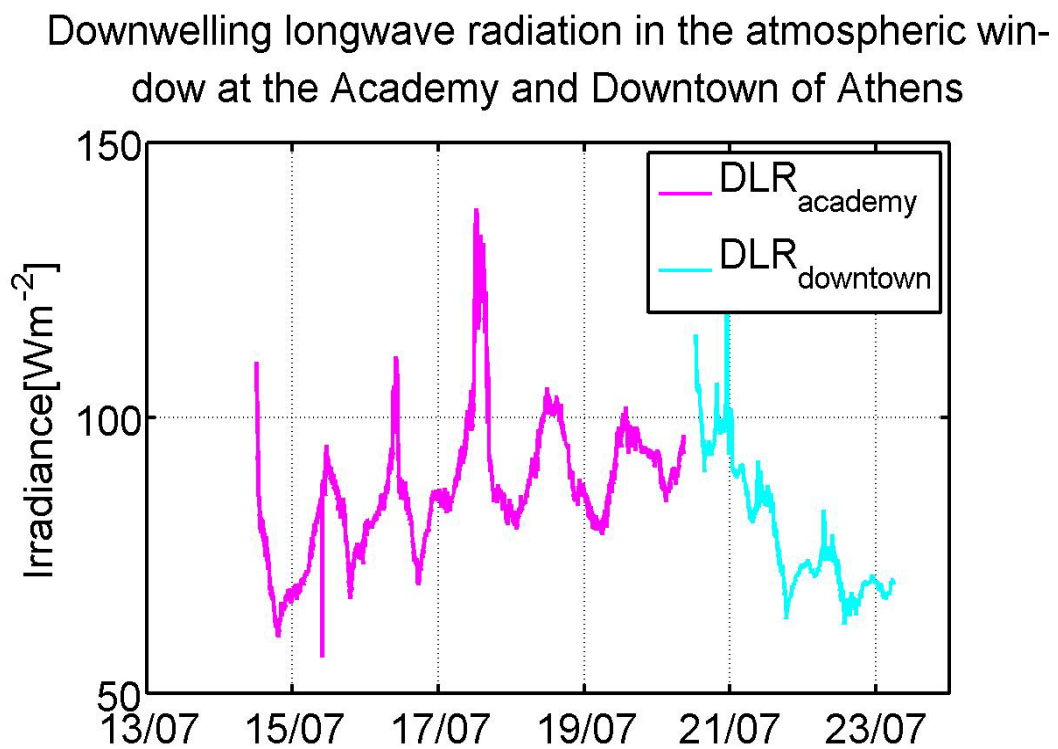


Figure 92: Downwelling longwave radiation in the atmospheric window at the Academy of Athens and at Patision downtown of Athens

In Figure 93, an example of the humidity conditions and precipitable water is presented, retrieved by pyrgeometer measurements at the Academy of Athens.

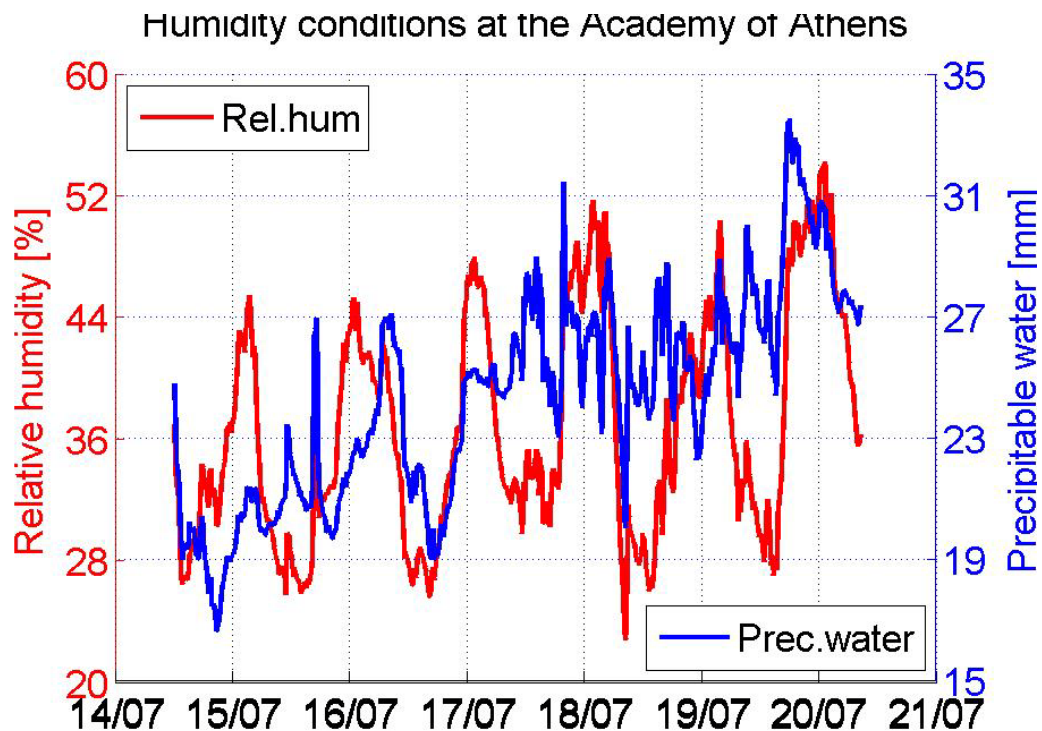


Figure 93: Relative humidity and precipitable water derived from pyrgeometer measurements

Finally, PMOD/WRC participated in THERMOPOLIS with an additional photometer, the Precision Filter Radiometer (PFR) for direct solar irradiance measurements in 4 narrow spectral bands centered at wavelengths recommended by the World Meteorological Organization (WMO) (368, 412, 500 and 862 nm). The instrument was operated during THEMOPOLIS at NOA's station of Academy of Athens from 15-21 July of 2009 and moved at NOA's Penteli station from 22 to 25 of July 2009 (not mentioned in the Experiment Plan). An example of PFR retrievals is presented in Figure 94.

Station NOA, PFR-N52, 16 Jul 2009

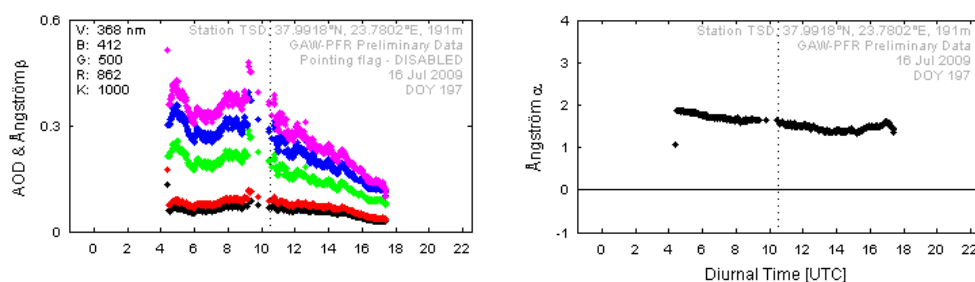


Figure 94: Aerosol optical depth and angström coefficients for 16th of July 2009 retrieved from PFR direct irradiance measurements at NOA's Academy of Athens station

Finally, two 5-channel MicroTOPS II for the measurement of total ozone, water vapour column (at 936 nm) and aerosol optical thickness (AOT) at 1020 nanometers were used during THERMOPOLIS 2009. Direct solar ultraviolet radiation at 3 discrete wavelengths within the UV-B range is measured and stored with these instruments. The instruments were measuring at 11:30, 13:30 and 15:30 local time (UTC+3) at NTUA (Zografou) and NOA (Penteli) premises.



Figure 95. MICROTOS II

5.1.3 Lidar measurements of aerosol and water vapour vertical profiles in the free troposphere

Lidar measurements are a tool to determine the diurnal evolution of the aerosols vertical structure. Changes in this structure can have some importance for the detailed atmospheric corrections of hyperspectral/multiangular data. With these measurements

an evaluation of the impact of the aerosol vertical structure on radiative transfer computations of atmospheric transmittance and radiance will be performed. These studies will be concentrated in the infrared spectral region by the use of 1064 nm lidar channel.

Lidar measurements were performed continuously during THERMOPOLIS 2009 at NTUA station (station identifier: NTUA - Zografou). NTUA provided its Lidars and support instrumentation, which consisted of:

- A 6-wavelength (elastic and Raman) aerosol lidar system operating at 355-387-407-532-607-1064 nm,
- An aerosol counter based on laser-diffraction.

Period and type of measurement	Measured parameter	Instrument
Continuous with 10-min resolution	Pressure, temperature, rainfall, total solar irradiance, UVB solar irradiance and wind (direction and speed) in situ measurements	Meteorological station (Davis Instruments Inc.)
Continuous with 1.5 min-3hr temporal resolution (for selected periods during daytime and/or nighttime)	Vertical profile of aerosol volume extinction coefficient (@ 355 nm and 532 nm) (nighttime conditions), Vertical profile of the aerosol volume backscatter coefficient (@ 355 nm, 532 nm, 1064 nm) (daytime/nighttime conditions), Vertical profile of the water vapour mixing ratio (nighttime conditions)	NTUA Raman lidar
Every 1 hour between 11:00 and 14:00 LT.	Total ozone and aerosol optical depth (1020 nm)	Sun photometer (Solar Light Inc.)
Acquired continuously with 10-min resolution, provided 1-hr averaged values	Absolute concentration measurements of aerosols at ground level (PM _{2.5})	Aerosol monitor (DustTrak II, TSI Inc.)



Figure 96. NTUA's 6 wavelength lidar Raman system




		
NTUA meteorological station	NTUA dust concentration instrument (TSI Inc.)	NTUA sun photometer (Solar Light Inc.)

Figure 97. NTUA's instruments

5.1.4 Calibration and validation

The NTUA Raman lidar system has been calibrated and validated through a series of intercomparison campaigns, both in hardware and software levels (Bockmann et al., 2004; Matthias et al., 2004; Pappalardo et al., 2004).

The TSI DustTrak II aerosol monitor (model 8530) has been factory calibrated and validated (october 2008).

The sun photometer has been factory calibrated and validated (September 2006).

The Raman lidar measurements were performed on alert basis and covered several days of semi-continuous measurements. An example is given in the following figure

(18 July 2009) where aerosols are lifted from ground up to nearly 3000 m height during noon hours (11:00-15:00 UTC). During the whole period of measurements aerosols are found up to nearly 4000 m height.

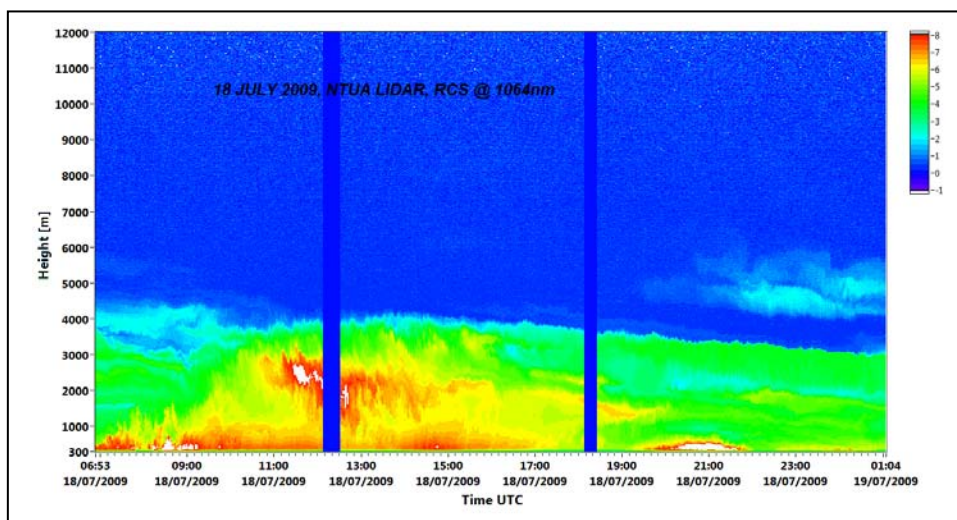


Figure 98 : Example of Raman lidar measurements

In the following figure the hourly variability of PM_{2.5} aerosol concentration is shown. We can see the arrival of a big dust load between 10:00-17:00 LT, which coincides very well with the lidar aerosol data shown above.

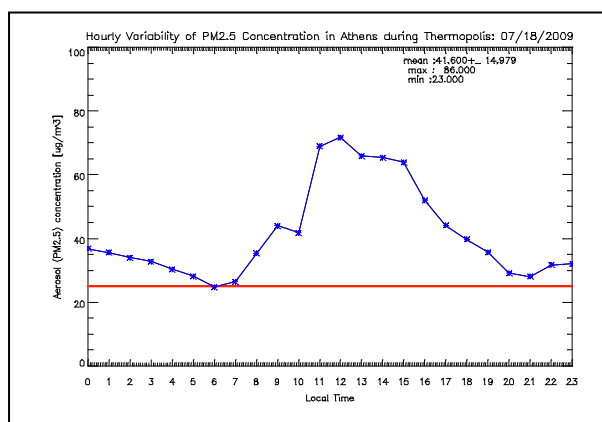


Figure 99: Example of the hourly variability of PM_{2.5} aerosol concentration

NTUA's team will provide the following products from post-processing of the retrieved data:

- Vertical profile of the aerosol volume extinction (@ 355 nm and 532 nm) coefficient (only under nighttime conditions),
- Vertical profile of the aerosol volume backscatter (@ 355 nm, 532 nm, 1064 nm) coefficient,
- Vertical profile of the water vapour mixing ratio (only under nighttime conditions),
- Total ozone content,

- Aerosol optical depth at 355 nm and 532 nm (daytime and nighttime conditions),
- Determination of the presence of clouds and cloud heights
- Retrieval of cloud and dust properties (base height, thickness, top) in the troposphere.

5.2 Reference Meteorological data

The meteorological stations that participated in THERMOPOLIS 2009 are listed in table 11. The in-situ meteorological data are quality assured and were provided for the greatest Athens area by the following Greek Agencies and Institutes/Universities:

The Ministry of the Environment (ENV), Directorate for Air and Noise Pollution has developed his own air pollution network, where, alongside with the air pollution measurements meteorological measurements are performed (T, RH, pressure, wind, solar radiation in most stations). The measurement points have been located so that they cover the whole Municipality of Athens and be the most representative possible, with this objective 14 stations (Table 11).

The Hellenic National Meteorological Agency (HNMS), participated with 10 stations. Meteorological data from three HNMS stations located within the Greater Athens Area were obtained during the measurement period. These stations will provide air temperature, precipitation, wind speed/direction, relative humidity, visibility, insolation, cloudiness.

The National Technical University of Athens (NTUA), has installed in the wider area of Athens, 10 fully automatic telemetric hydrometeorological stations that are continuously operating in the framework of the METEONET network. This network was developed by members of the Laboratory of Hydrology and Water Resources Management of the National Technical University of Athens. The selection of the sites and the products provided are following the WMO guidelines.

The National Observatory of Athens (NOA), will provide meteorological data from its historical 110-year records of the well known meteorological station of Thissio. Additionally, meteorological data were provided by the new meteorological stations of NOA at Penteli and Akadimia.

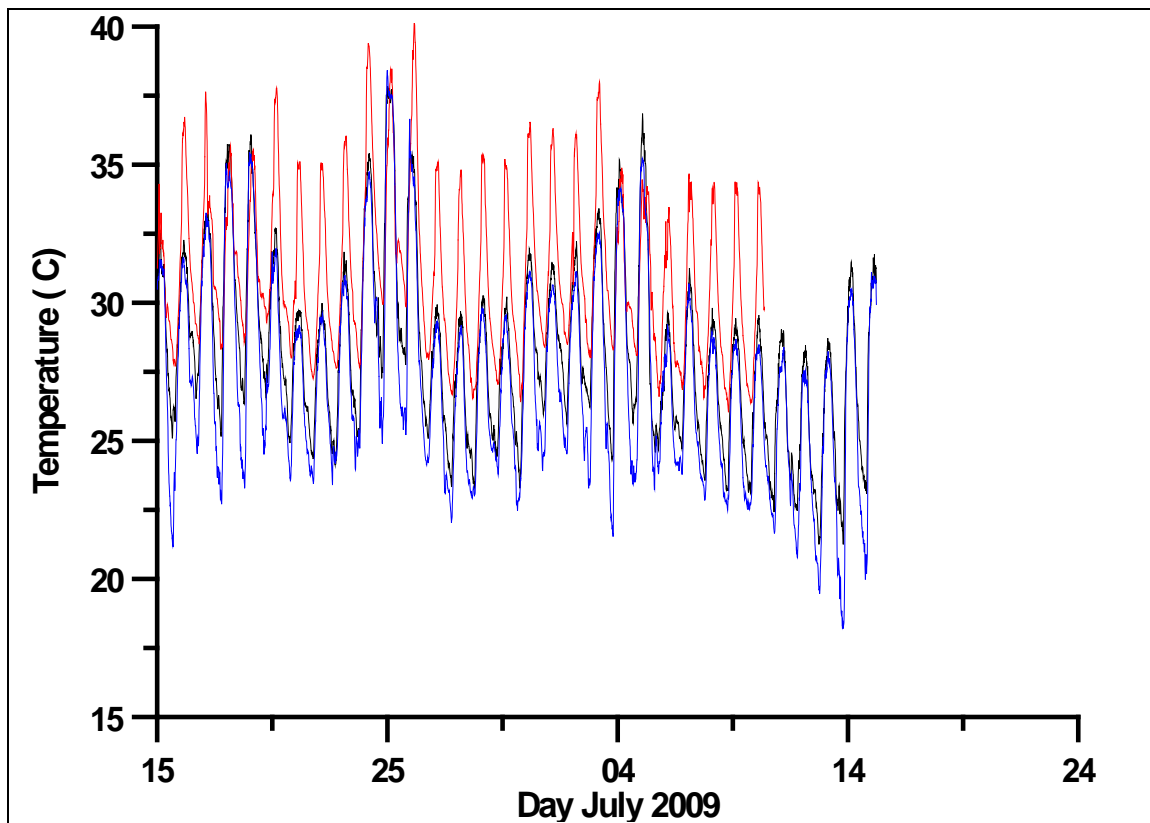
Center for Research and Technology Hellas(CERTH), installed 10 T/RH meteorological stations in the Greater Athens Area, in the selected sites presented in Table 11 (and the Table below) and Figure 16. The locations of the stations were chosen to maximize spatial coverage.

Table 58: CERTH T/RH Stations

Site ID #	Location	Height	Latitude (deg N)	Longitude (deg E)
ATH1	Dorms	185 m ASL 2 st floor	37.981636	23.780973
ATH2	Seirion1	158 m ASL 2 nd floor	37.962698	23.756444
ATH3	Seirion2	158 m ASL	37.962698	23.756444

		2 nd floor (backyard)		
1	Thaleias 12	217 m ASL 2 nd floor	38.02262	23.833454
2	Pipinou	101 m ASL 5 th floor	37.99652	23.733013
3	Pellis	211 m ASL 2 nd floor	38.027869	23.817457
4	Konsulas Anaximenous	125 m ASL 5 th floor	37.969848	23.748767
6	Themelis Parodos Serifou 6 Kaminia	8 m ASL 1 st floor	37.956885	23.657529
5	Founda Kountouriotou 2A/Terpsitheas Faliro	29 m ASL 3 rd floor	37.925999	23.712448
7	Papayannis	235 m ASL 1 st floor	38.055285	23.812929

Some preliminary data from the DUTH T/RH measurements are presented below.



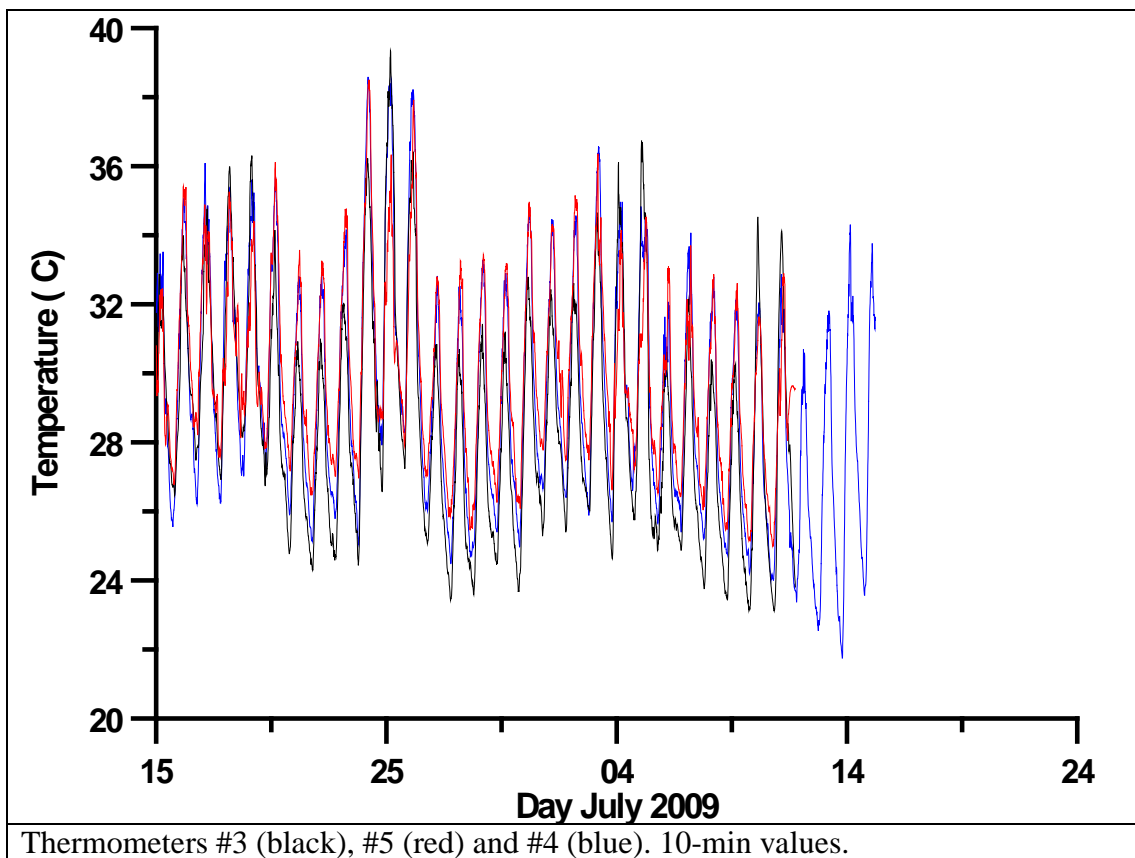
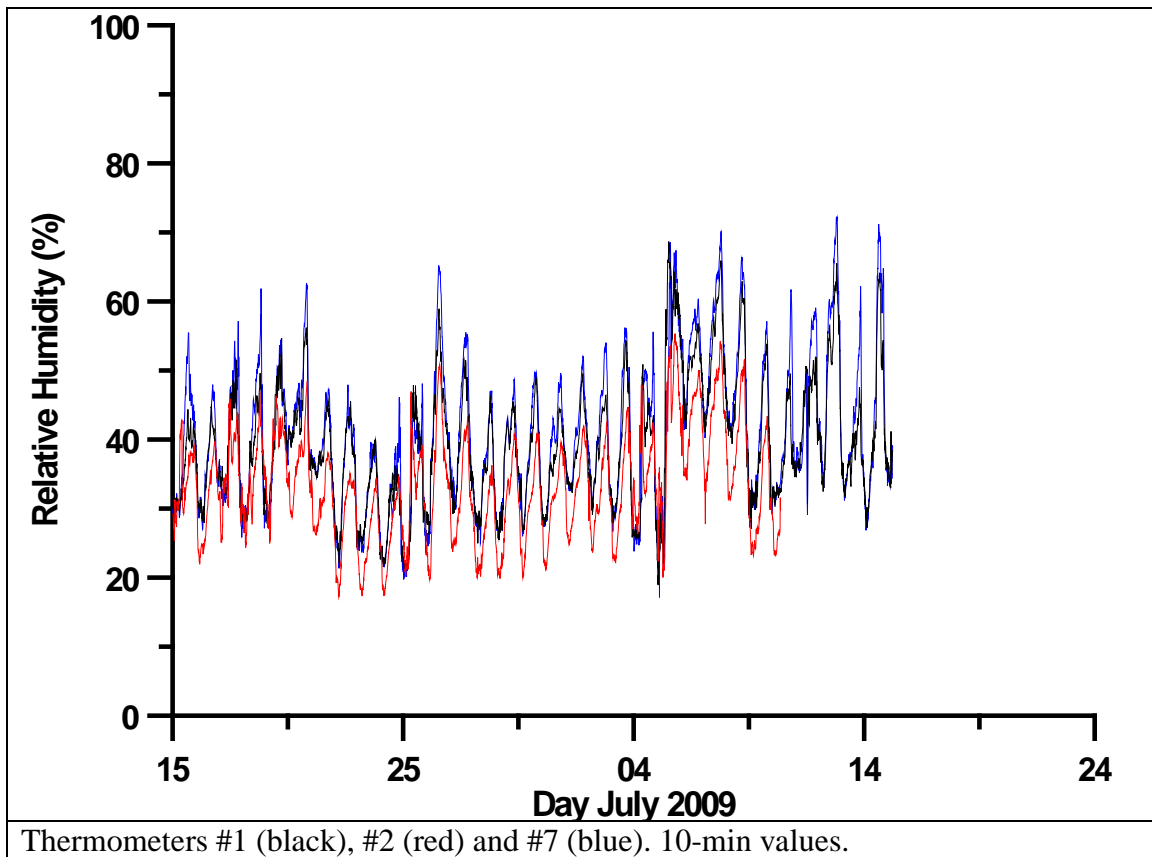


Figure 100: DUTH T/RH measurements

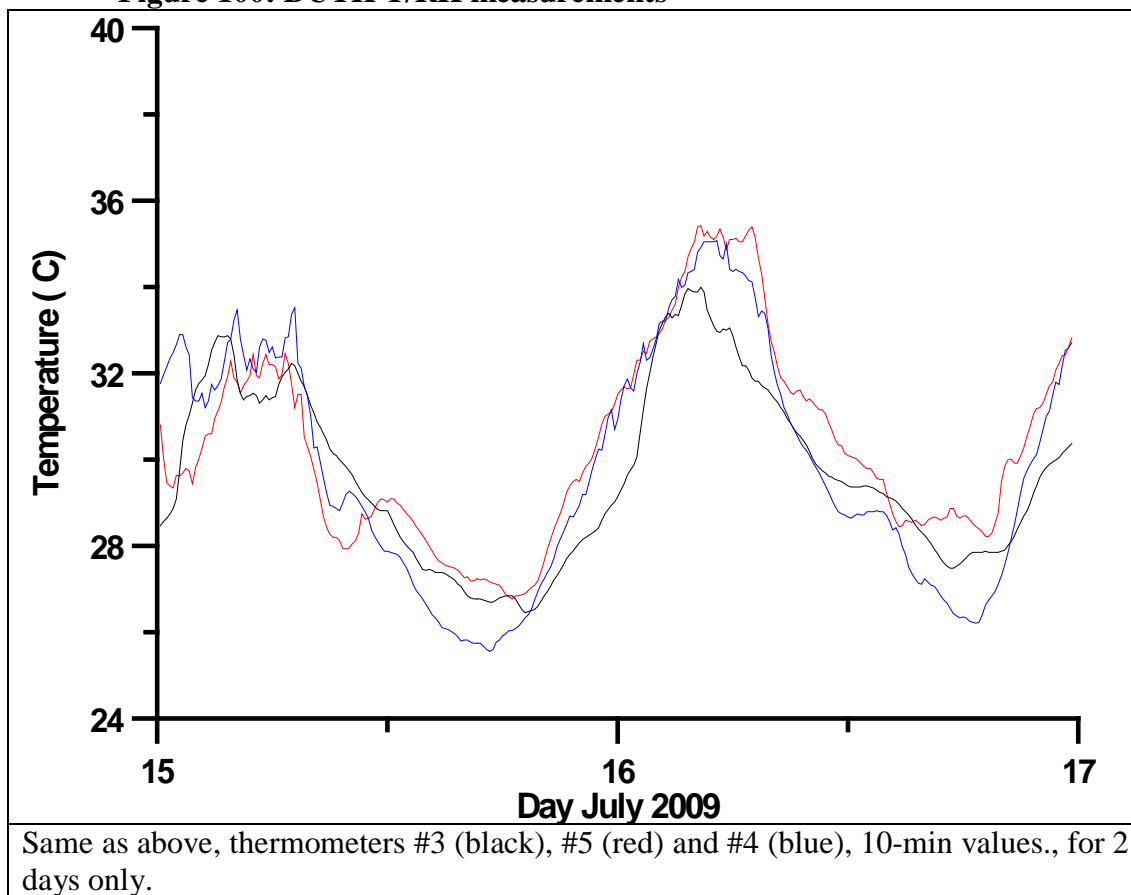
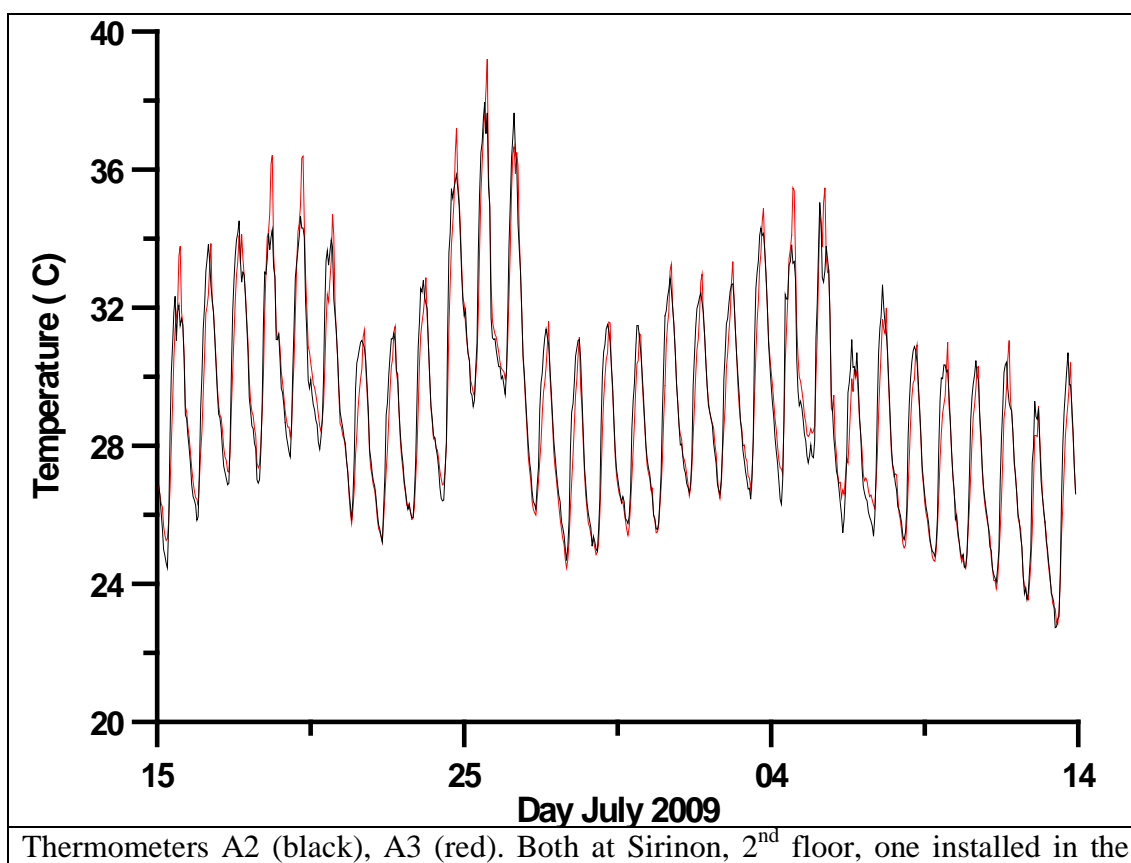


Figure 101: DUTH T/RH measurements



façade (black) and one in the backyard (red) of the same house. 1-hr values.

Figure 102: DUTH T/RH measurements

Validation of the interpolation of in-situ AT measurements



Figure 103: Map of measuring sites used for urban canopy air temperature (T_{air}) analyses in the Greater Athens Area.

The spatial interpolation was performed using the *Delaunay triangulation*.

In mathematics, and computational geometry, a Delaunay triangulation for a set \mathbf{P} of points in the plane is a triangulation $\text{DT}(\mathbf{P})$ such that no point in \mathbf{P} is inside the circumcircle of any triangle in $\text{DT}(\mathbf{P})$. Delaunay triangulations maximize the minimum angle of all the angles of the triangles in the triangulation; they tend to avoid skinny triangles (*Delaunay*, 1934). Compared to any other triangulation of the points, the smallest angle in the Delaunay triangulation is at least as large as the smallest angle in any other.

It had been observed for some time that triangulations that lead to good interpolations avoid long and skinny triangles. The result that there is—if we ignore degenerate cases—only one locally optimal triangulation with respect to the angle-vector, namely the Delaunay triangulation, is due to *Sibson* (1981). A further property of this triangulation is that the resulting interpolation has lower roughness when compared to other triangulations (Rippa, 1990).

Hence, the interpolation performed is the best possible.

Further, a test was performed in which the mean spatial Tair was computed using the Delauney triangulation for each hour of the day for three cases: 1. using measurements at all 29 available stations listed in Tables 1 and 2 below. 2. Using only the 10 DUTH/CERTH stations (Table 1) and finally 3. using only the NTUA and HNMS stations (16 stations) of Table 2. Cases 1 and 3 gave almost identical results. Case 2 gives results only for the central; part, since this is where these stations were located, and despite the fact that in this Case much more stations are located in the center, the results for this part of Athens are almost identical with Case 3 where very few stations are located in the center. This gives further credibility to the assumption of a very good interpolation. In the figure below, results of this exercise for 00, 06, 12, and 18 hrs are presented.

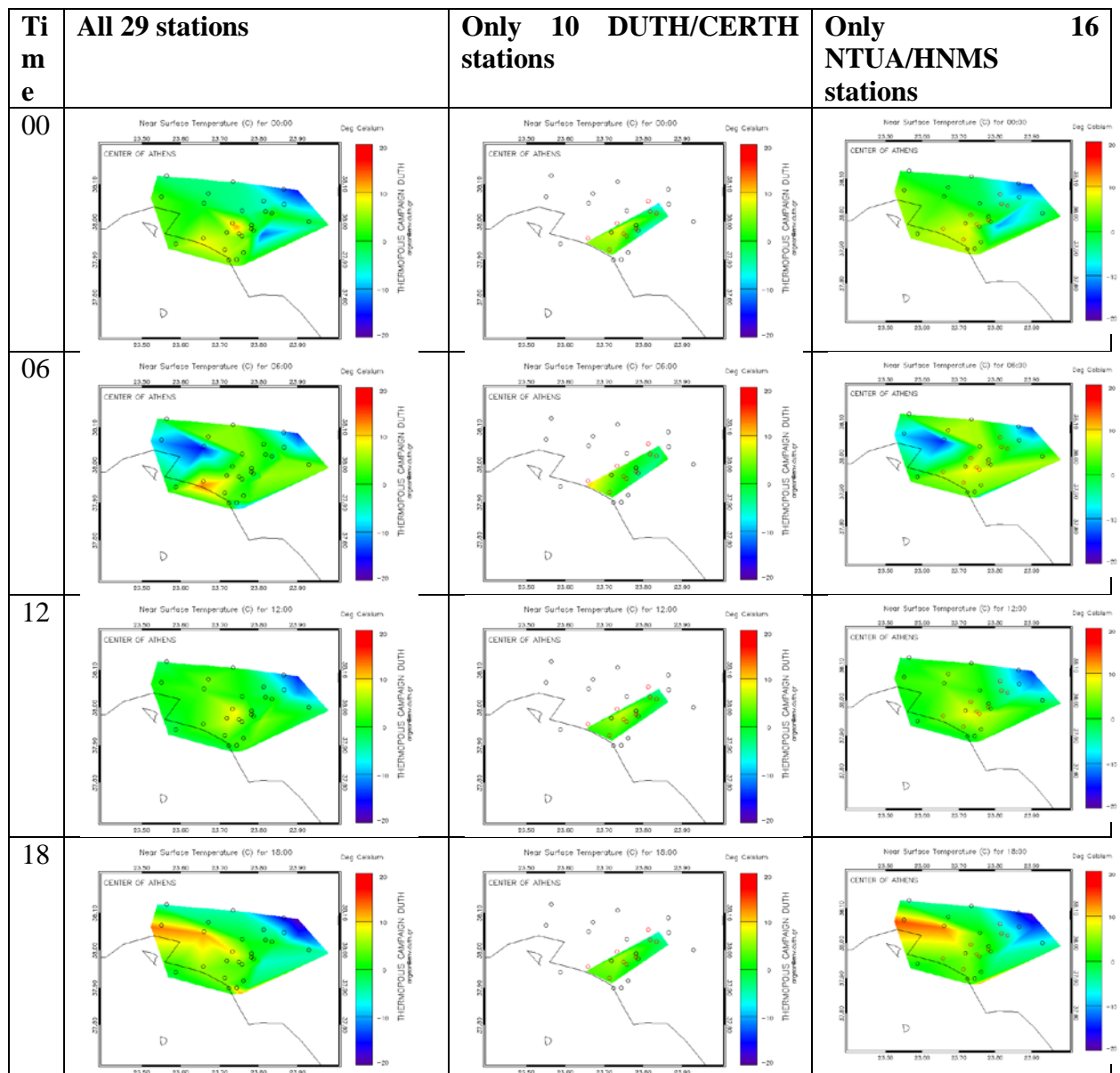


Figure 104: Results of the interpolation for 00, 06, 12 and 18 hrs using different station data as input.

References

Delaunay B., Sur la sphère vide, *Izvestia Akademii Nauk SSSR, Otdelenie Matematicheskikh i Estestvennykh Nauk*, 7:793–800, 1934.

Rippa S., Minimal roughness property of the Delaunay triangulation, *Computer Aided Geometric Design*, 7, 6, 489-497, 1990.

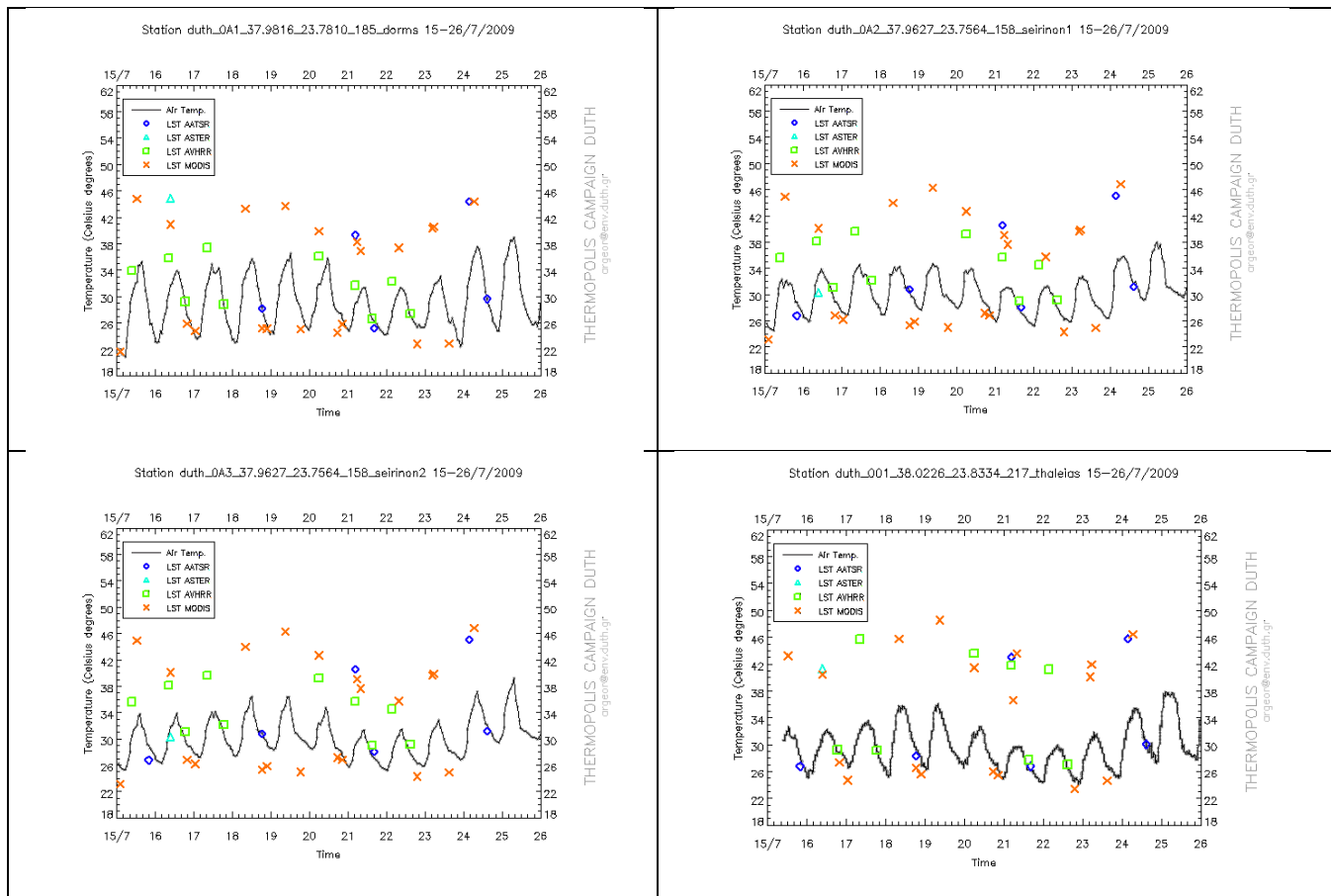
Sibson, R., A brief description of natural neighbor interpolations, In *Interpreting Multivariate Data*, Ed. V. Barnett, Chichester, 21-36, John Wiley, 1981.

Generation of AT-LST difference maps from in-situ and satellite data

Satellite acquisition data for the pixels corresponding to the T_{air} ground stations deployed by DUTH/CERTH during the campaign were provided by NOAA as requested. For each station, timeseries of T_{air} and the corresponding LST timeseries (i.e. the LST for the satellite pixel where each station lies within) were plotted (see Figure below). Generally, it can be said that

1. Late afternoon AATSR LST acquisitions agree very well with T_{air} for all stations and all days, i.e. for Athens the AATSR LST afternoon retrieval is a very good approximation of T_{air} .
2. The same holds for the AVHRR LST late afternoon acquisitions.
3. The MODIS late afternoon/early morning data agree also fairly well (although not as good as AATSR and AVHRR) with T_{air} for most stations and most days, in all cases the discrepancy being < 4 K.

It follows from the above that it might be possible to reconstruct the spatial evolution of the daily course of the T_{air} in Athens from afternoon AVHRR observations (or AATSR, although at this case there is no daily coverage) IN THE CASE that a robust statistical relationship exists between afternoon T_{air} and T_{air} in other times of the day.



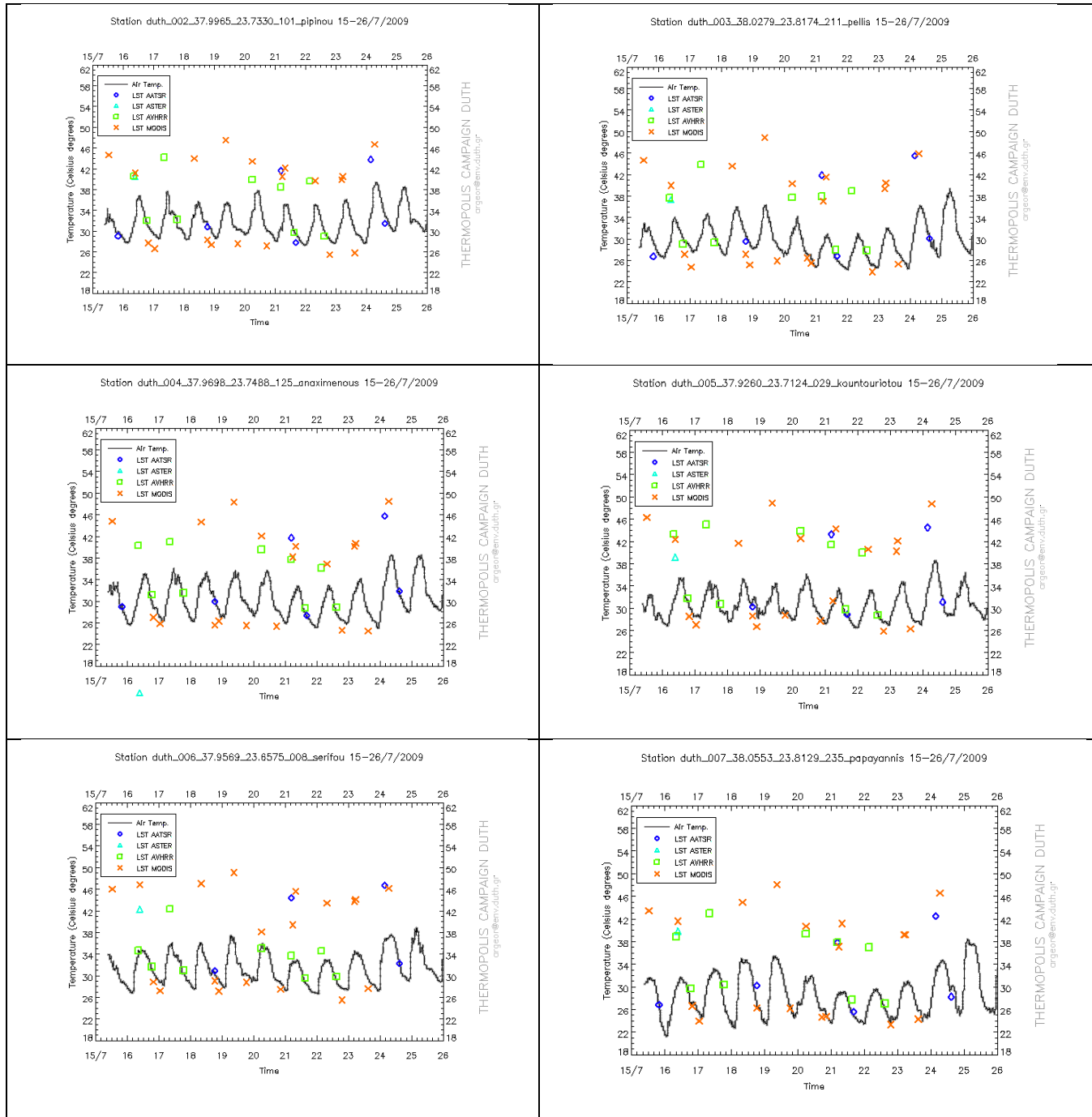


Figure 105: Timeseries of T_{air} and concurrent satellite acquisition data for the pixels corresponding to the T_{air} ground stations.

Below, a figure with all data is presented. It is apparent from the figure that in the LST- T_{air} phase space LST would trace an “8”, if LST measurements were available for each hour of the day (which is not the case). LST can be 5 K at most lower than the respective T_{air} (during late afternoon/nighttime), while it can be up to 15 K higher (during the rest of the day).

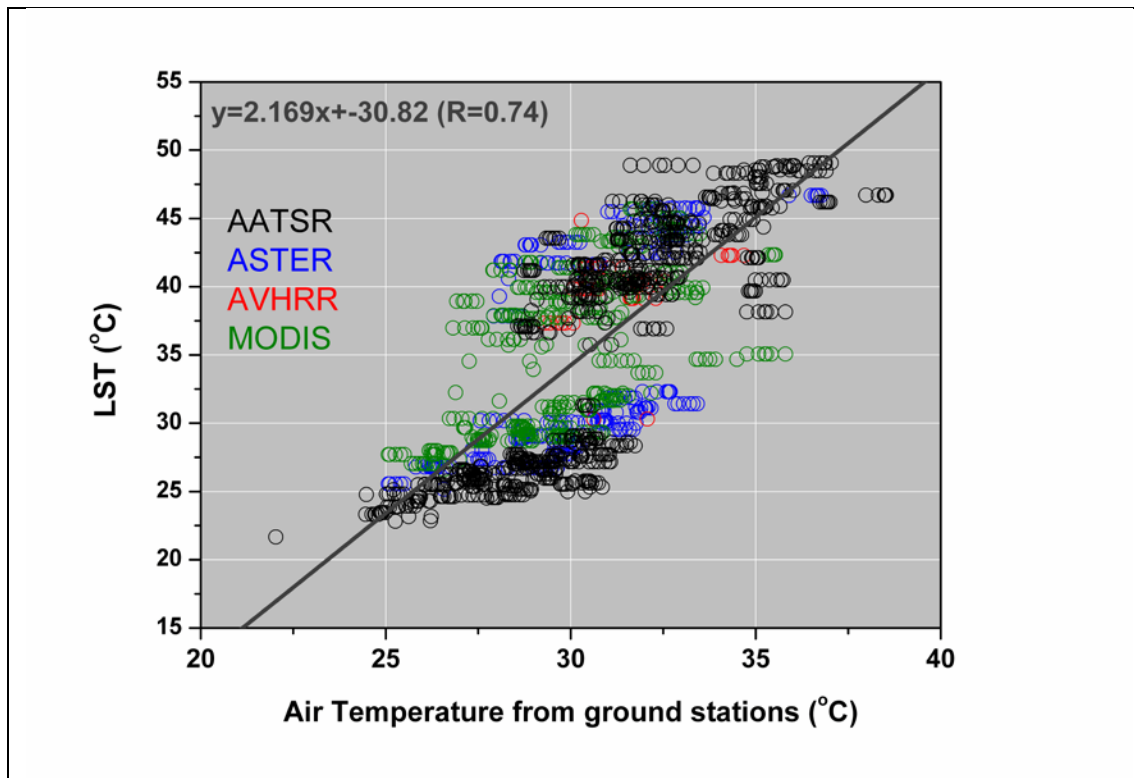


Figure 106: LST from all satellite sensors and concurrent AT data from all ground stations within the respective satellite pixels.

Animation of wind measurements

For this purpose, DUTH/CERTH requested wind direction and velocity measurements from METEONET stations. Data from 9 stations have been given. While some patterns might be evident from the produced animation of T_{air} /Wind, it is also apparent that the quality of the wind data might not be optimal. For two very closely located stations, divergent flows can be observed from the animation. Hence, not being in the position to have a control on the data quality, no further analysis has been attempted with these data. The produced movie is placed in the folder

THERMO

/

/3_ATMOSPHERIC MEASUREMENTS

/3.4_METEOROLOGICAL DATA

/CERTH_DUTH/ windairt.wmv.

Correction of T_{air} for station orientation and station metadata

The files in the folder THERMO

/

/3_ATMOSPHERIC MEASUREMENTS

/3.4_METEOROLOGICAL DATA

/STATIONS_METADATA

contain 1 file per station with metadata for this station. The metadata are according to the template below.

Station id: XXXX_YYY¹

Address: *Street address or location*

Date of update: 30.7.2009

¹**XXXX_YYY:** *Station identifier, where YYY=001 to 010 (station number) and XXXX=DUTH, NOAX, HNMS or NTUA (station operator). See map at the end of this document.*

Table 59: LOCAL SCALE

Urban Climate Zone (UCZ)	<i>According to the simplified scheme of Oke (2006)</i>
Dominant Land Use	
Topographic relief	
Davenport roughness class upstream from enclosure	<i>To each direction (N, E, S, W), according to Davenport et al. (2000) and Wieringa (1992)</i>
Land cover	<i>% vegetated, % built over, % water, % open</i>
Typical tree height	
Typical building height (m or storeys)	
Lawn/Garden Irrigation	
Typical wall materials	
Typical roof	<i>Material, flat or pitched</i>
Space heating/cooling	
Traffic density	
Aerial map (2 km X 2 km)	

Table 60: MICROSCALE

Latitude	<i>Decimal latitude</i>
Longitude	<i>Decimal longitude</i>
Ground Elevation (m ASL)	
Sensor	
Sensor placement	
Sensor orientation	
Building type	
Building materials	
Roof type	
UCZ	<i>According to the simplified scheme of Oke (2006)</i>
Davenport roughness class upstream from enclosure	<i>To each direction (N, E, S, W), according to Davenport et al. (2000) and Wieringa (1992)</i>
Traffic density	

Heat/moisture vents:	
Aerial map (approx. 200 m X 200 m)	

Here a figure with the mean diurnal variation of air temperature for the period of the campaign is displayed

Diurnal variation

An example of the station DUTH_001 is given below.

Station id: DUTH_001

Address: 12 Thaleias str.

Date of update: 30.7.2009

Table 61: LOCAL SCALE

Urban Climate Zone (UCZ)	3
Dominant Land Use	Suburban residential
Topographic relief	Almost flat
Davenport roughness class upstream from enclosure	To N: 7 To E: 5-6 To S: 7 To W: 7
Land cover	10% vegetated, 75% built over, 0% water, 15% open
Typical tree height	Not known
Typical building height (m or storeys)	3 storeys
Lawn/Garden Irrigation	No
Typical wall materials	Concrete
Typical roof	flat concrete or inclined with tiles
Space heating/cooling	No/some
Traffic density	High on the highways, low on the residential roads

Figure 107:
Aerial map
(approx. 2 km
X 2 km)



Table 62: MICROSCALE

Latitude	38.02262
Longitude	23.833454
Ground Elevation (m ASL)	217
Sensor	HOBO Pro v2 T/RH U23-001
Sensor placement	2 nd floor
Sensor orientation	Street NW-SE, sensor on building façade facing NE
Building type	Residence
Building materials	Concrete
Roof type	Flat
UCZ	3
Davenport roughness class upstream from enclosure	To N: 5 To E: 4 To S: 6 To W: 7
Traffic density	Low
Heat/moisture vents:	No

Figure 108:
Aerial map
(approx. 200m
X 200 m)

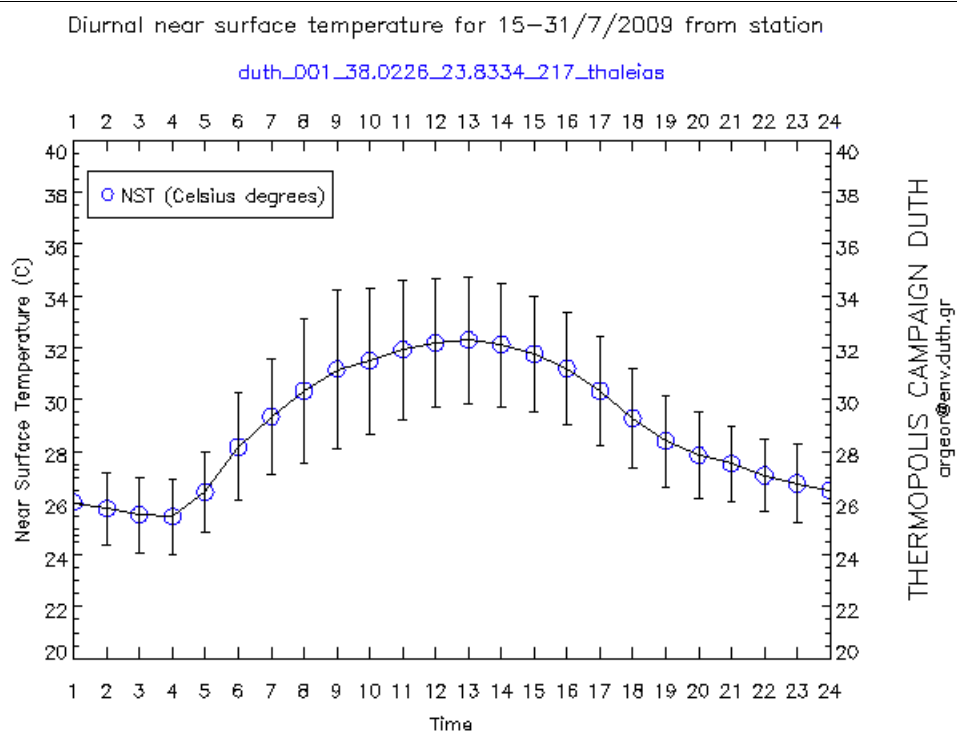
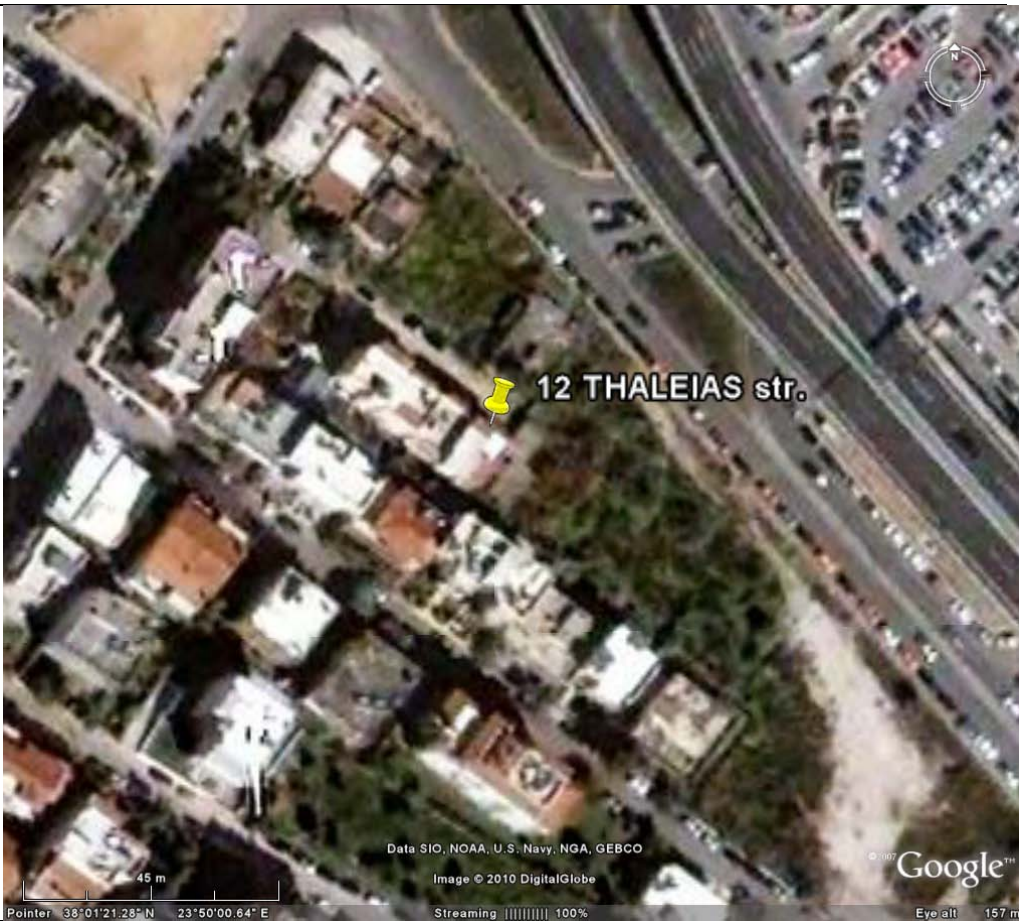


Figure 109: Diurnal variation at DUTH Thaleias St station

For the stations where information on sensor orientation was available, this information has been included in the station metadata files.

From the study of the data from stations with different orientations, no apparent orientation bias was detected.

References

Davenport A.G., C.S.B. Grimmond, T.R. Oke and J. Wieringa (2000), Estimating the roughness of cities and sheltered country, Proc. 12th Conf. on Applied Climatology, Asheville, NC, American Meteorological Society, Boston, pp. 96-99.

Oke T.R. (2006), Initial Guidance to obtain representative meteorological observations at urban sites, Instruments and observing methods Report No. 81, WMO/TD-No. 1250, World Meteorological Organisation, Geneva.

Wieringa J. (1992), Updating the Davenport roughness classification, Journal of Wind Engineering and Industrial Aerodynamics, 41-44, pp. 357-368.

Mean diurnal variation of Tair

For all the campaign stations, mean diurnal variation plots (and the corresponding data) for the campaign period (15-31/7/2009) have been put in the folder

THERMO

/

/3_ATMOSPHERIC MEASUREMENTS

/3.4_METEOROLOGICAL DATA

/STATIONS_METADATA

/MEAN_DIURNAL_OF_AT

of the campaign database. Only an example of two stations is presented below.

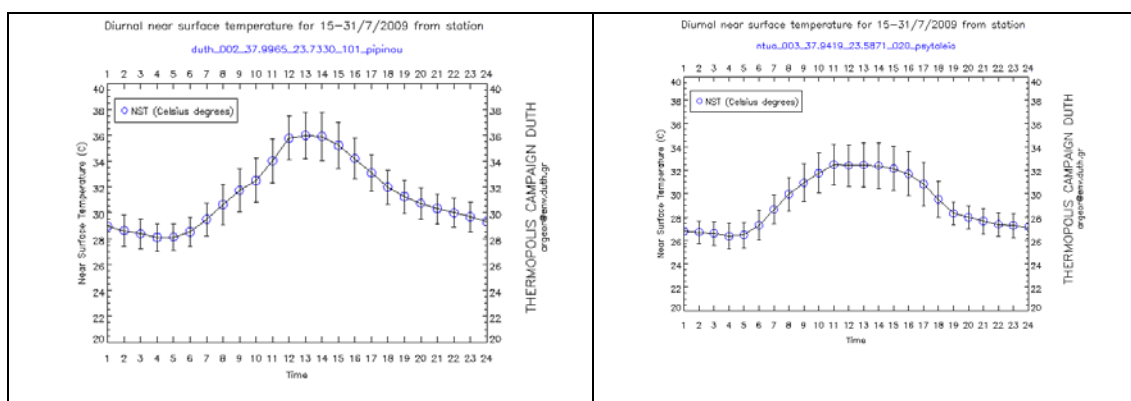


Figure 110: Example of mean diurnal variation of Tair during the THERMOPOLIS 2009 campaign. Data and plots for all stations can be found in the campaign database (see above).

Regarding the mean diurnal evolution of the spatial Tair features, these are presented in the figure below.

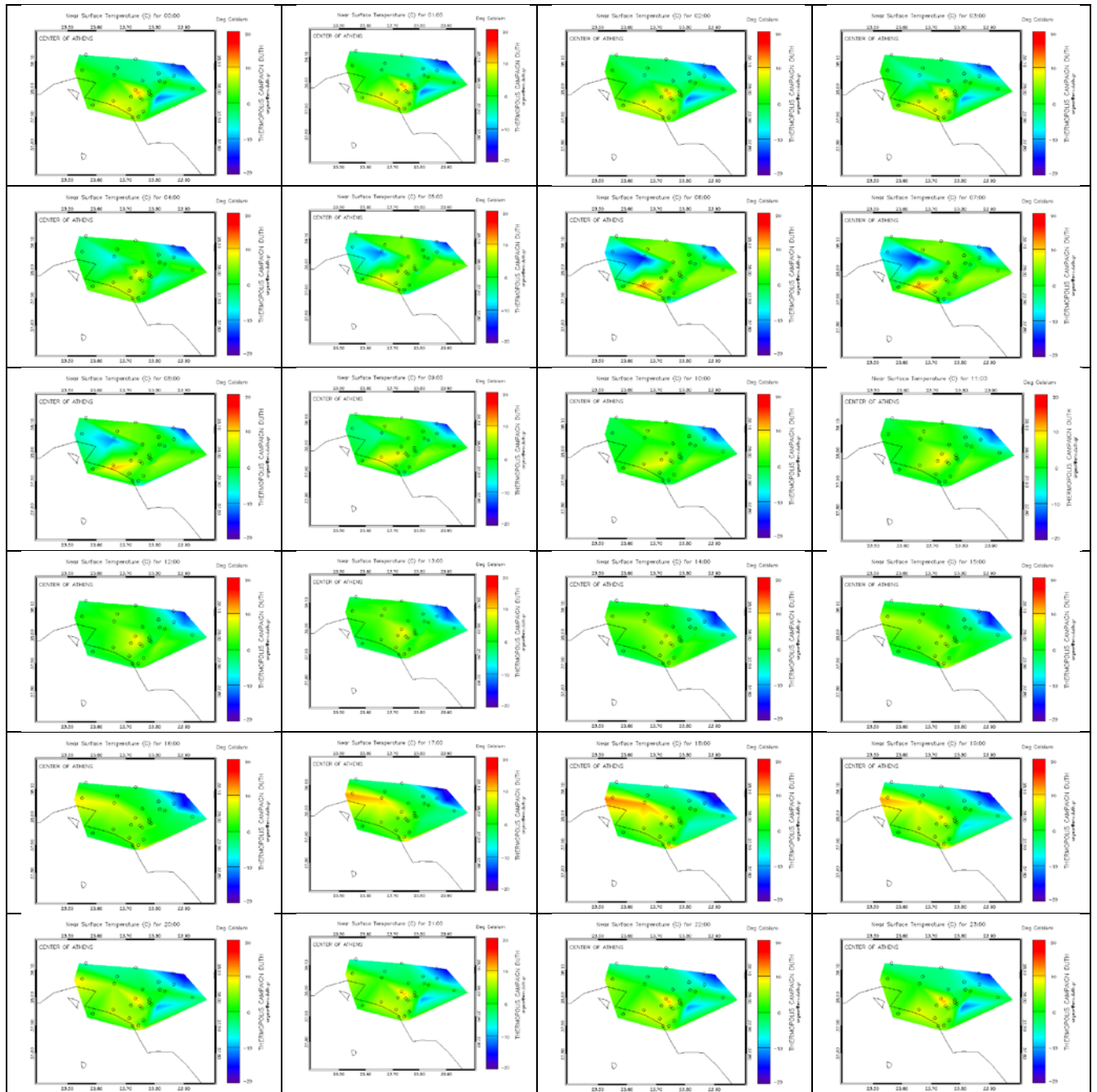


Figure 111: Mean diurnal variation of spatial Tair features for the Athens area during the THERMOPOLIS 2009 campaign. All stations (29) with available data were used. Time is 00 hrs at the upper left panel. Time proceeds with 1-hr step from left to right and from top to bottom.

Site coordinates and map locations

Table 63: CERTH T_{air}/RH Stations. Stations with bold site id# have provided valid data.

Site ID #	Location	Height (m ASL, floor)	Decimal latitude (deg N)	Decimal longitude (deg E)	Latitude	Longitude
DUTH_OA1	Dorms	185 m, 2 st floor	37.981636	23.780973	37° 58' 53.8896"	23° 46' 51.5022"
DUTH_OA2	Seirion1	158 m, 2 nd floor	37.962698	23.756444	37° 57' 45.7128"	23° 45' 23.1978"
DUTH_OA3	Seirion2	158 m, 2 nd floor (backyard)	37.962698	23.756444	37° 57' 45.7128"	23° 45' 23.1978"
DUTH_001	Thaleias 12	217 m, 2 nd floor	38.02262	23.833454	38° 1' 21.432"	23° 50' 0.4338"
DUTH_002	Pipinou	101 m, 5 th floor	37.99652	23.733013	37° 59' 47.4714"	23° 43' 58.8462"
DUTH_003	Pellis	211 m, 2 nd floor	38.027869	23.817457	38° 1' 40.3284"	23° 49' 2.8452"
DUTH_004	Konsulas Anaximenous	125 m, 5 th floor	37.969848	23.748767	37° 58' 11.4522"	23° 44' 55.5612"
DUTH_005	Founda Kountouriotou 2A/Terpsitheas Faliro	29 m, 3 rd floor	37.925999	23.712448	37° 55' 33.5958"	23° 42' 44.8122"
DUTH_006	Themelis Parodos Serifou 6 Kaminia	8 m, 1 st floor	37.956885	23.657529	37° 57' 24.7854"	23° 39' 27.1044"
DUTH_007	Papayannis	235 m, 1 st floor	38.055285	23.812929	38° 3' 19.0254"	23° 48' 46.5444"

Table 64: T_{air} stations by other providers. Stations with bold site id# have provided valid data.

Site ID #	Location	Operator	Decimal latitude (deg N)	Decimal longitude (deg E)	Latitude	Longitude
	Patision	ENV	37.99917	23.73306	37° 59' 57.0114"	23° 43' 59.0154"
	Athinas	ENV	37.97833	23.725	37° 58' 41.9874"	23° 43' 30"
	Pireus	ENV	37.94333	23.6475	37° 56' 35.988"	23° 38' 51"

	Geoponiki	ENV	37.98361	23.70694	37° 59' 0.9954"	23° 42' 24.9834"
	Nea Smirni	ENV	37.94944	23.715	37° 56' 57.984"	23° 42' 53.9994"
	Peristeri	ENV	38.01528	23.69611	38° 0' 55.0074"	23° 41' 45.996"
	Liosia	ENV	38.07667	23.69778	38° 4' 36.012"	23° 41' 52.008"
	Marousi	ENV	38.03083	23.78722	38° 1' 50.988"	23° 47' 13.992"
	Likovrisi	ENV	38.06972	23.77639	38° 4' 10.9914"	23° 46' 35.0034"
	Aristotelous	ENV	37.98778	23.7275	37° 59' 16.008"	23° 43' 38.9994"
	Agia Paraskevi	ENV	37.995	23.81944	37° 59' 41.9994"	23° 49' 9.984"
	Thrakomakedones	ENV	38.14361	23.75806	38° 8' 36.996"	23° 45' 29.016"
	Koropi	ENV	37.94583	23.75833	37° 56' 44.988"	23° 45' 29.988"
	Goudi	ENV	37.98444	23.76778	37° 59' 3.9834"	23° 46' 4.0074"
NTUA_001	Zografou 200m ASL	NTUA	37.9771	23.7869	37° 58' 37.56"	23° 47' 12.8394"
NTUA_002	Menidi	NTUA	38.1066	23.7339	38° 6' 23.76"	23° 44' 2.0394"
NTUA_003	Psytaleia	NTUA	37.9419	23.5870	37° 56' 30.8394"	23° 35' 13.1994"
NTUA_004	Elliniko	NTUA	37.8988	23.7234	37° 53' 55.68"	23° 43' 24.24"
NTUA_005	Ilioupoli	NTUA	37.9183	23.7610	37° 55' 5.88"	23° 45' 39.5994"
NTUA_006	Mandra	NTUA	38.1229	23.5637	38° 7' 22.44"	23° 33' 49.32"
NTUA_007	Galatsi	NTUA	38.0293	23.7574	38° 1' 45.4794"	23° 45' 26.64"
NTUA_008	Penteli	NTUA	38.0865	23.8635	38° 5' 11.4"	23° 51' 48.5994"
NTUA_009	Pikermi	NTUA	38.0011	23.9286	38° 0' 3.96"	23° 55' 42.9594"
NTUA_010	Ano Liosia	NTUA	38.0752	23.6707	38° 4' 30.72"	23° 40' 14.52"
	Central	NTUA	37.99	23.78	37° 59' 24"	23° 46' 48"
NOA1_001	Thissio	NOA	37.972	23.718	37° 58' 19.2"	23° 43' 4.7994"
NOA2_002	Penteli	NOA	38.050	23.861	38° 2' 59.9994"	23° 51' 39.6"
NOA3_003	Akadimia	NOA	37.988	23.775	37° 59'	23° 46'

					16.7994"	29.9994"
HNMS_001	Nea Filadelfia	HNMS	38.04972	23.66694	38° 2' 58.992"	23° 40' 0.984"
HNMS_002	Hellenikon	HNMS	37.89972	23.73278	37° 53' 58.992"	23° 43' 58.008"
HNMS_003	Elefsina	HNMS	38.06694	23.55	38° 4' 0.984"	23° 33' 0"
	Goudi	HNMS	37.98	23.76	37° 58' 47.9994"	23° 45' 36"
	Dafni	HNMS	38.00	23.65	38° 0' 0"	23° 38' 59.9994"
	Kolimvitorio	HNMS	37.96	23.73	37° 57' 36"	23° 43' 48"
	Ilion	HNMS	38.03	23.70	38° 1' 48"	23° 41' 59.9994"
	Kotroni	HNMS	38.13	23.95	38° 7' 48"	23° 56' 59.9994"
	Oaka	HNMS	38.03	23.78	38° 1' 48"	23° 46' 48"
	Dekeleia	HNMS	38.11	23.76	38° 6' 35.9994"	23° 45' 36"

5.3 Multiwavelength Raman lidar, sunphotometric and airborne measurements for the estimation of the vertical profiles of the aerosol optical and microphysical properties over Athens, Greece (NTUA-LIDAR)

INTRODUCTION

Atmospheric aerosols have large influence on Earth's radiation budget. Recent estimations on the possible impact of aerosols (both direct and indirect effects) on the radiative forcing (cooling effect) in a global average show that they are of the same order of magnitude as the CO₂ effect (warming effect). However, medium to high uncertainties still exist concerning the indirect and direct effects, which are connected with the aerosol influence on climate. According to (Forster et al., 2007) the total direct aerosol radiative forcing combined across all aerosol types is $-0.5 \pm 0.4 \text{ W/m}^2$, with a medium-low level of scientific understanding.

The laser remote sensing (lidar) technique using the Raman channels is a unique tool able to provide the vertical distribution of the aerosol optical properties (aerosol backscattering and extinction coefficients, lidar ratio-LR) and the water vapor content, expressed in terms of mixing ratio of water vapor in dry air (in g/kg).

This report presents the retrieved vertical profiles of the optical and microphysical properties of aerosol particles - mixed with locally produced ones - in the troposphere over the city of Athens (Greece), obtained during the European Space Agency (ESA) THERMOPOLIS field campaign which was carried out between 15 and 31 July, 2009. This period was an optimal time window for good weather conditions over Athens.

METHODOLOGY

5.3.1 Aerosol optical properties

At the National Technical University (NTUA) (37.93°N, 23.8°E, altitude 200m) a compact 6-wavelength NTUA Raman lidar system is used to perform continuous measurements of suspended aerosols particles in the Planetary Boundary Layer and the lower troposphere. The system is based on a pulsed Nd:YAG laser emitting simultaneously at 355, 532 and 1064 nm. The respective emitted output energies per pulse are 75, 130 and 140 mJ, with a 10 Hz repetition rate. The optical receiver is a Cassegrainian reflecting telescope with a primary mirror of 300 mm diameter and a focal length of $f=600$ mm, directly coupled, through an optical fiber, to the lidar signal six-channel filter spectrometer.

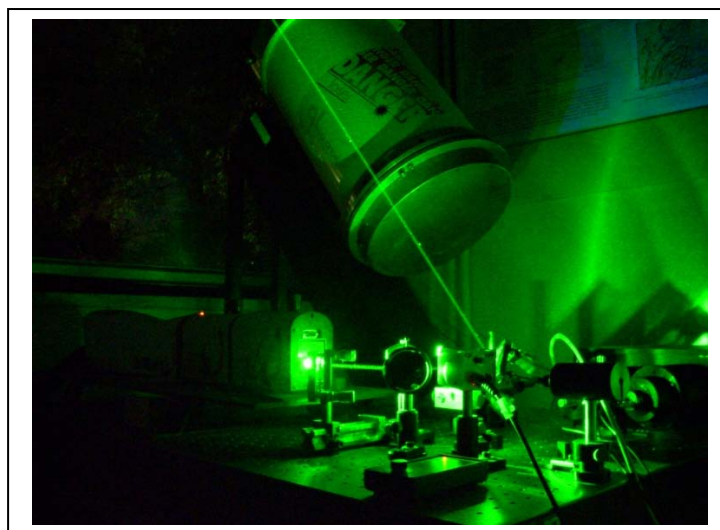


Figure 112. The NTUA Raman lidar system.

The elastically backscattered lidar signals (at 355, 532 and 1064 nm), as well as those generated by Raman scattering by atmospheric N₂ and H₂O (at 387, 607 and 407 nm, respectively) are simultaneously recorded by photomultipliers (PMTs) and avalanche photodiode systems (APD), after the spectral separation of the returned lidar signals. The lidar signals detected at 355, 387, 532, 607 and 1064 nm were used to derive the aerosol backscatter (at 355, 532 and 1064 nm) and the extinction (at 355 and 532 nm) coefficient profiles (Ansmann *et al.*, 2002), while the 407 nm channel was used to derive the water vapor mixing ratio. Since the year 2000 the NTUA Raman lidar system is member of the European Aerosol Research Lidar Network-EARLINET (Bösenberg *et al.*, 2003) (<http://www.earlinet.org>).

5.3.2 Microphysical aerosol properties

The microphysical particle properties of spheroid aerosols inside various layers during Saharan dust events in the lower free troposphere, were retrieved using the hybrid regularization technique developed by Veselovskii *et al.* (2010), while the non dust aerosol microphysical properties were retrieved by the code provided by Müller *et al.* (1999). A detailed description of the original version of the algorithm which assumes spherical shape of the investigated particles in the retrieval procedures given by Müller *et al.* (1999). Modifications concerning the optimum solution space were made by Veselovskii *et al.* (2002), while changes concerning the minimum number of the needed measured wavelengths can be found in Müller *et al.* (2001). These models use as input the mean values of the optical properties of the aerosols calculated from the vertical profiles of elastic and Raman backscattered lidar signals (obtained at 5 different wavelengths: 355-387-532-607-1064 nm). The aerosol microphysical properties which were derived are the effective radius (r_{eff}), the surface-area concentration (α_t) and the volume concentration (v_t), as well as the single-scattering albedo (ω) and the mean complex refractive index (m).

5.3.3 Aerosol concentration measurements

PM_{2.5} continuous concentration monitoring was performed from 15 to 27 July 2009 (every 10 min in the range between 0.001-100 mg/m³, with a resolution of the order of 0.001 mg/m³) by a TSI Dustrak 8520 instrument (Chan *et al.*, 2002).

PRESENTATION AND ANALYSIS OF EXPERIMENTAL RESULTS

5.3.4 Aerosol load measurements

The NTUA Raman lidar system, in synergy with the National Observatory of Athens (NOA) sun photometer (CIMEL) was used to retrieve the aerosol optical depth (AOD) over the city of Athens. During the campaign the aerosol load presented a large variation due to the prevailing different meteorological conditions, thus advecting air masses from different origins. Variations of the AOD between 0.07 and 0.35 at 500 nm and of the Ångström exponent (440/870 nm) between 0.75 and 1.75 were recorded. Figure 2 (top) shows the average AOD at 500 nm, as well as the mean value of the Ångström exponent for each day of the reported period.

In order to estimate the free tropospheric contribution of the aerosol particles, the AODs at 532 nm from the Raman lidar extinction profiles, were calculated in the height range below and above 2 km, which is the mean PBL height for July over Athens. The results presented in Figure 2 (bottom) show that the free tropospheric contribution was quite variable. Variations of the columnar Ångström exponent are mainly attributed to the different aerosol types mixed over Athens.

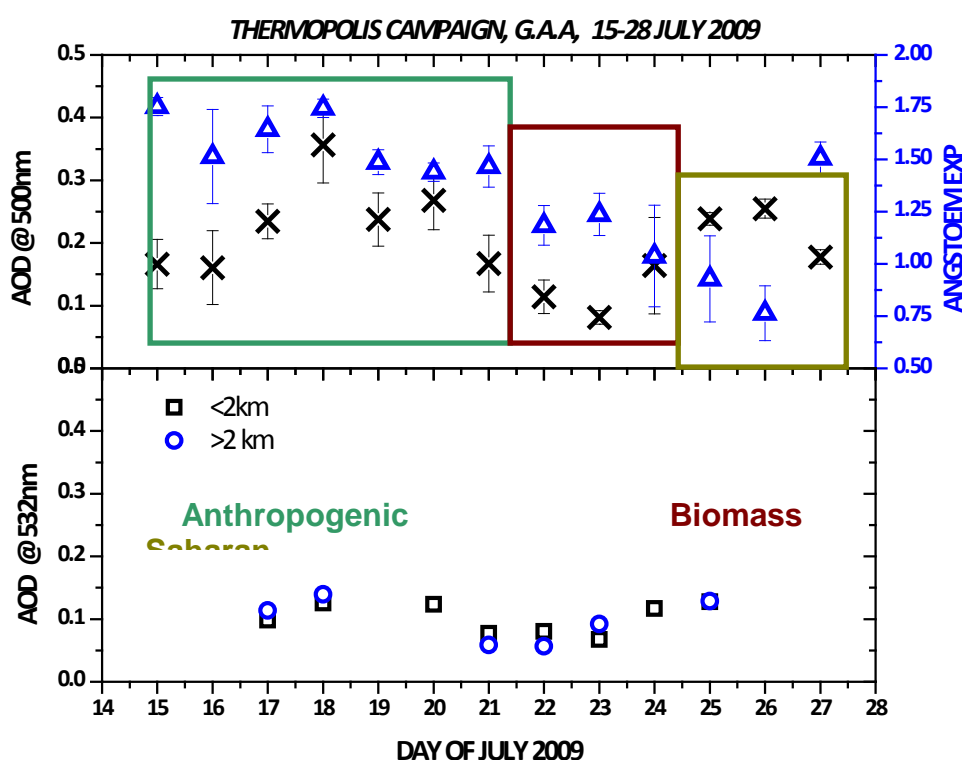


Figure 113. AOD and Ångström exponent from Cimel over Athens (top) from 15-27 July, 2009. AOD below and above 2 km from Raman lidar measurements (bottom).

Thus, from the backward trajectories (not shown here) variable aerosol sources have been identified for each day. For instance, Saharan dust particles were

observed over Athens on 24-26 July, whereas in the period 20-22 July a mixture of anthropogenic and smoke aerosols is most likely to occur. Between 14 and 20 July 2009, anthropogenically produced particles were found over Athens.

5.3.5 Aerosol lidar measurements

During non cloudy days nearly continuous aerosol measurements were performed by NTUA Raman lidar system. Table 65 shows the summary of the dates when daytime (yellow colour) and nighttime (blue colour) aerosol lidar measurements were performed. No measurements were performed during system failure.

Table 65: Dates when daytime (yellow colour) and nighttime (blue colour) aerosol lidar measurements were performed.

	Hour of the Day (in UTC)																							
July 2009	1	2	3	4	5	6	7	8	9	10	11	12	13	14	15	16	17	18	19	20	21	22	23	24
15																								
16																								
17																								
18																								
19																								
20																								
21																								
22																								
23																								
24																								
25																								
26																								
27																								

In the following sections we will present a synopsis of the lidar measurements performed for each characteristic time period of the origin of the sampled aerosols particles: anthropogenic, biomass burning and Saharan desert origin (see Fig. 2).

5.3.6 Anthropogenic and biomass burning aerosols (14-20 July and 21-23 July, 2009)

In Fig. 3 we present a sample of the range-corrected lidar signals at 1064 nm (upper graphs) obtained during the time period 20-21 July, 2009 (anthropogenic origin of aerosols) over the city of Athens, together with the aerosol $\text{PM}_{2.5}$ concentration measured 15 m above ground level (215 m above mean sea level: asl.).

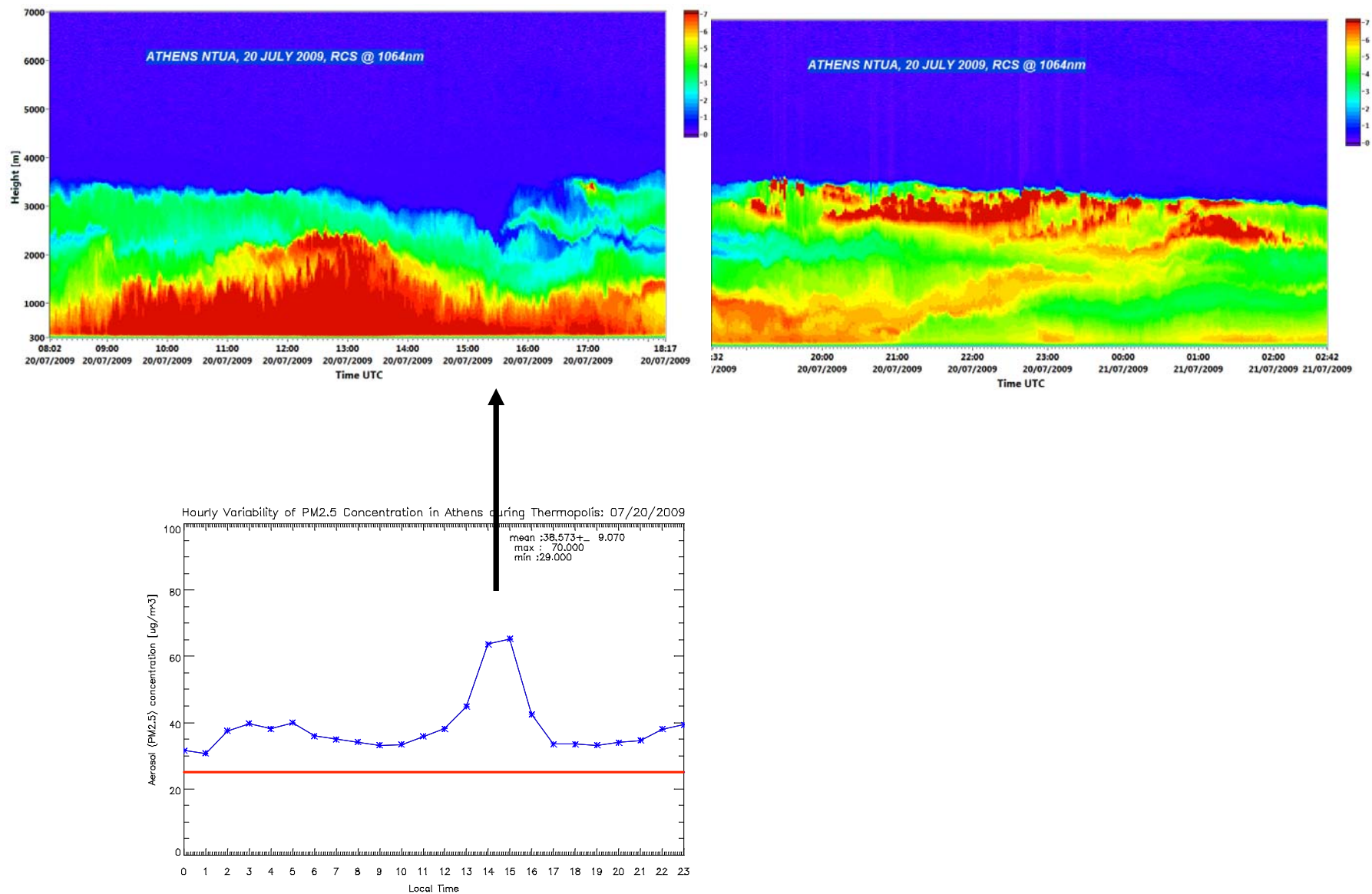


Figure 114. Range-corrected lidar signals at 1064 nm (upper graphs) obtained during the time period 20-21 July, 2009 (anthropogenic origin of aerosols) over the city of Athens, together with the aerosol PM_{2.5} concentration measured 15 m above ground level (215 m above mean sea level: asl.).

From Fig. 114 we can see that the PBL growth reaches its full development around 12:30 UTC (PBL height around 2 km), which coincides with time with the maximum of the aerosol PM_{2.5} concentration measured at that time (around 62 µg/m³). The red line in Fig 3 delineates the European Union (EU) reference concentration level not to be exceeded by the PM_{2.5} particles. This means that the EU reference levels were exceeded during all day of 20 July 2009. Later that day an elevated aerosol layer is formed over the PBL at the entrainment zone (between 2.2 and 3.2 km).

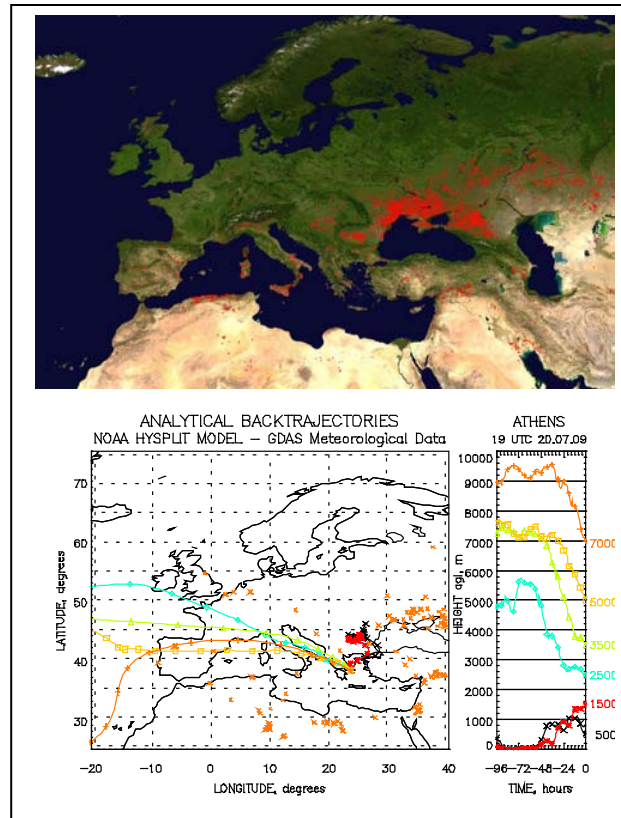


Figure 115. Air mass back trajectory analysis based on the HYSPLIT model for July 20, 2009 (arrival time 19:00 UTC over Athens).

The air mass back trajectory analysis based on the HYSPLIT model for July 20, 2009 (arrival time 19:00 UTC over Athens) indicated that the aerosol-rich air masses sampled between ground and 2 km height stagnated over the Greek territory for the last 3 days prior to our observations (Fig. 4), where they were probably enriched by locally produced and biomass burning aerosols. On the other hand the air masses arriving at 3 km height around 22:00 UTC (20 July 2009) (see Fig. 3) originated from the USA continent where they were

probably enriched with biomass burning aerosols and other anthropogenic emissions (not shown). Figure 5 shows the retrieved daytime aerosol backscatter coefficients for 20 July 2009 at 355-532-1064 nm, as well as the Ångström backscatter-related exponent obtained by the NTUA lidar between 10:01 and 12:00 UTC. The appearance of the aerosol layer around 3 km is clearly visible.

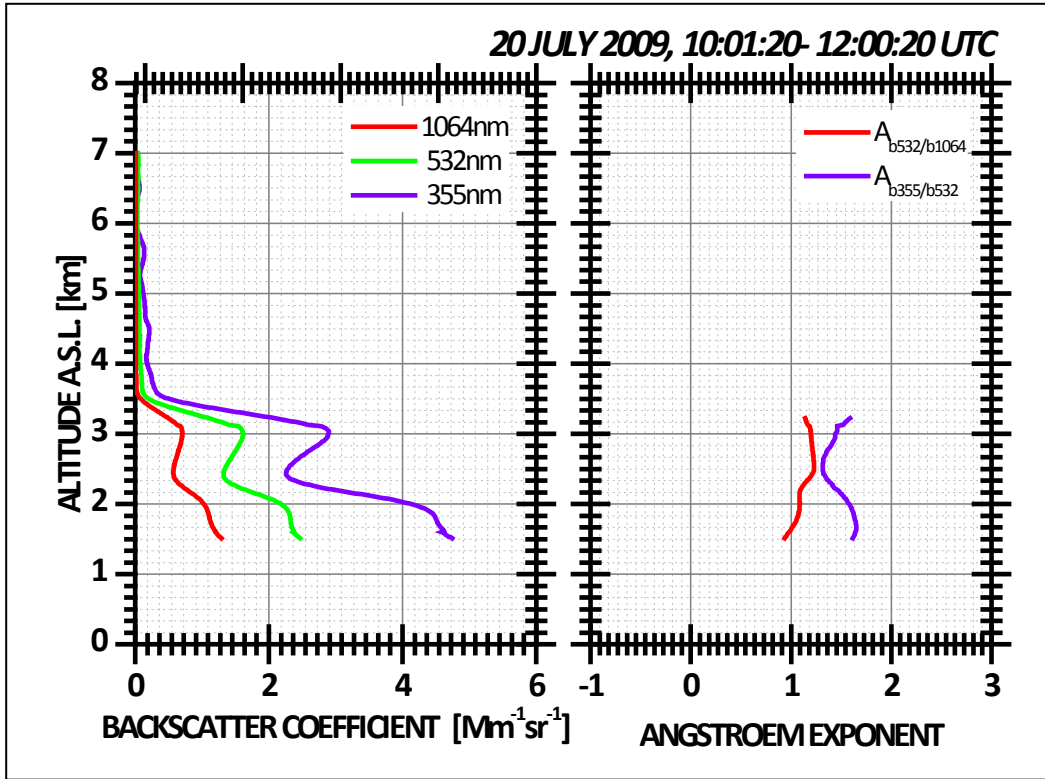


Figure 116. Retrieved aerosol backscatter coefficients for 20 July 2009 at 355-532-1064 nm, as well as the Ångström backscatter-related exponent obtained by the NTUA lidar between 10:01 and 12:00 UTC.

Figure 117 shows the retrieved nighttime aerosol optical properties (extinction, backscatter, lidar ratio, Ångström backscatter-related exponent) at 355-532-1064 nm, obtained by the NTUA lidar on 21 July 2009, between 01:00 and 02:42 UTC. We see the persistent aerosol layer located around 3 km height. The high LR (60-80 sr) and Ångström exponent values (between 1 and 1.7), indicate the presence of rather polluted and small urban-like particles in the height region between 2 and 3 km. The calculated AOD at 355 nm and 532 nm were 0.82 and 0.43, respectively, according to the Raman lidar extinction measurements.

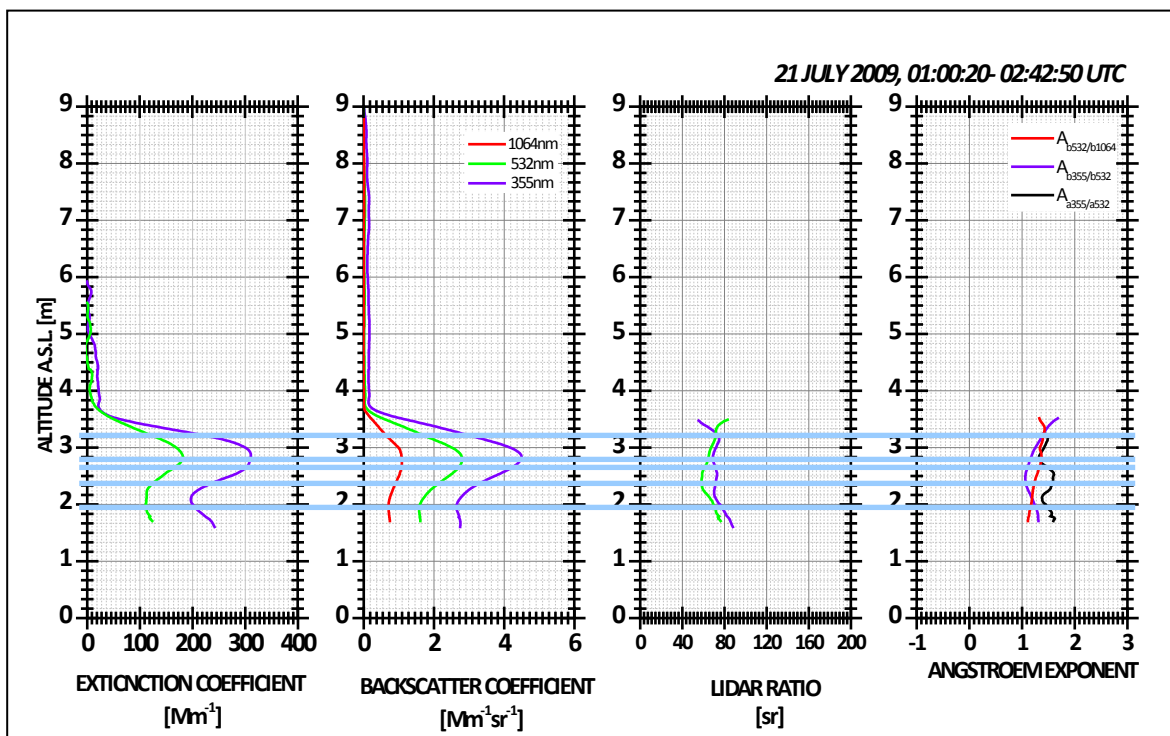


Figure 117. Retrieved nighttime aerosol optical properties (extinction, backscatter, lidar ratio, Ångström backscatter-related exponent) at 355-532-1064 nm, obtained by the NTUA lidar on 21 July 2009 between 01:00 and 02:42 UTC.

To derive the microphysical properties at different altitudes, the lidar profiles were separated to 5 layers as is represented by the light blue lines in Fig. 6. The segregation of the lidar profiles was based on the concept that each layer should be characterized by relatively stable optical properties. The required homogeneity of the aerosol layer is hypothesized from the stability of the lidar ratio and the Ångström exponent within each layer.

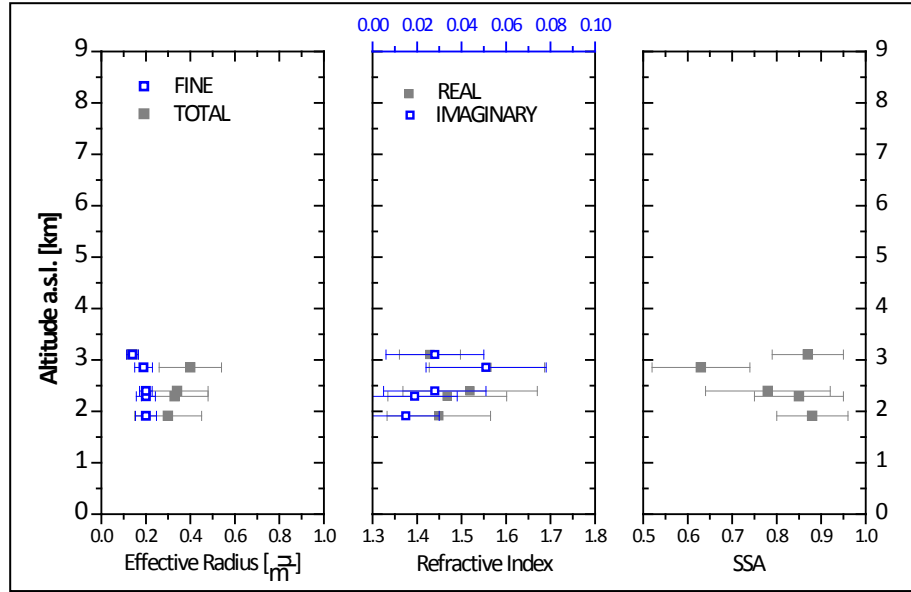


Figure 118. Retrieved aerosol effective radius (μm), refractive index and single scattering albedo (SSA) based on the aerosol optical properties derived by the NTUA Raman lidar on 21 July 2009.

Using the mathematical code provided by Müller et al. (1999) we retrieved the microphysical properties of aerosols for 21 July 2009 and plotted in Fig. 7 the aerosol effective radius (μm), the refractive index and the single scattering albedo (SSA). In this figure we see that the aerosol effective radius remains lower than 0.4 ± 0.15 , the refractive index ranges between 1.35-1.55 (indicating the mixture of various types of aerosols) and the SSA shows strongly to moderate absorbing aerosols ranging between 0.88 (at 3 km height) and 0.62 (at 2.9 km height). When we focus on the aerosol microphysical properties derived around 3 km height, we have strong indications of mixing of anthropogenic with biomass burning aerosols (coming from the USA continent as mentioned previously) (Müller et al., 2005).

5.3.7 Saharan dust particles (24-26 July 2009)

In Figs. 8 and 9 (upper graph), we present a sample of the range-corrected lidar signals at 1064 nm obtained during the time period of 24 and 25-26 July, 2009 (Saharan dust intrusion) over the city of Athens. The lower graph of Fig. 9 shows also the aerosol $\text{PM}_{2.5}$ concentration measured 15 m above ground level (215 m above mean sea level: asl.) for 26 July 2009. The Saharan dust layer is clearly visible up to 4.5 km height (24 July, 2009) and up to 3.2 km height the following days (25-26 July, 2009).

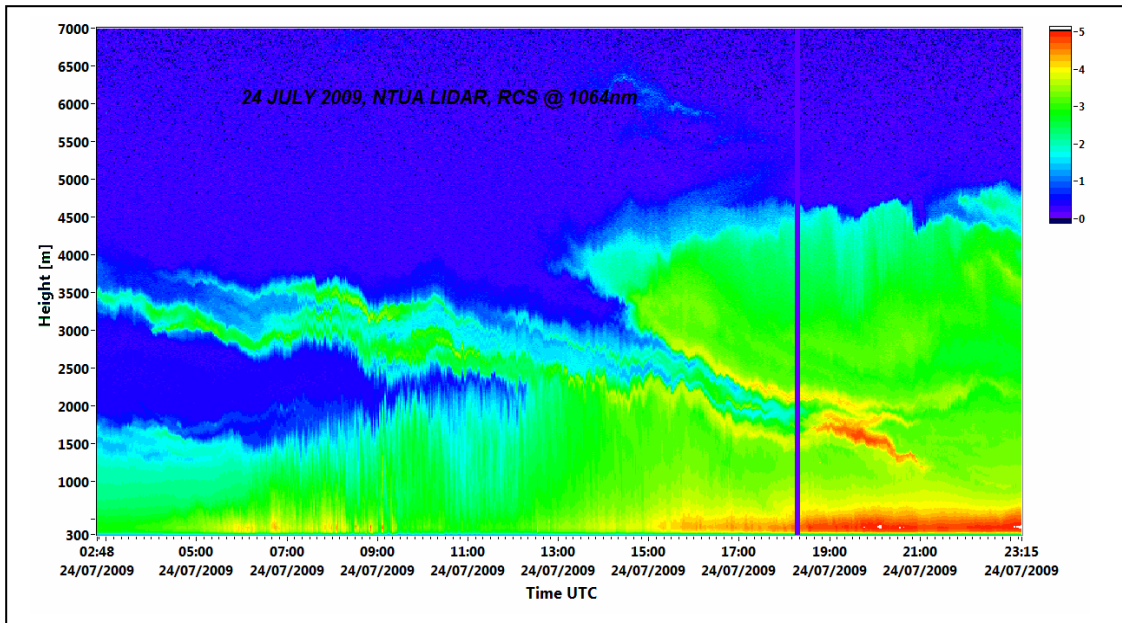


Figure 119. Range-corrected lidar signals at 1064 nm obtained by the NTUA lidar during the time period of 24 July, 2009 (Saharan dust intrusion) over the city of Athens.

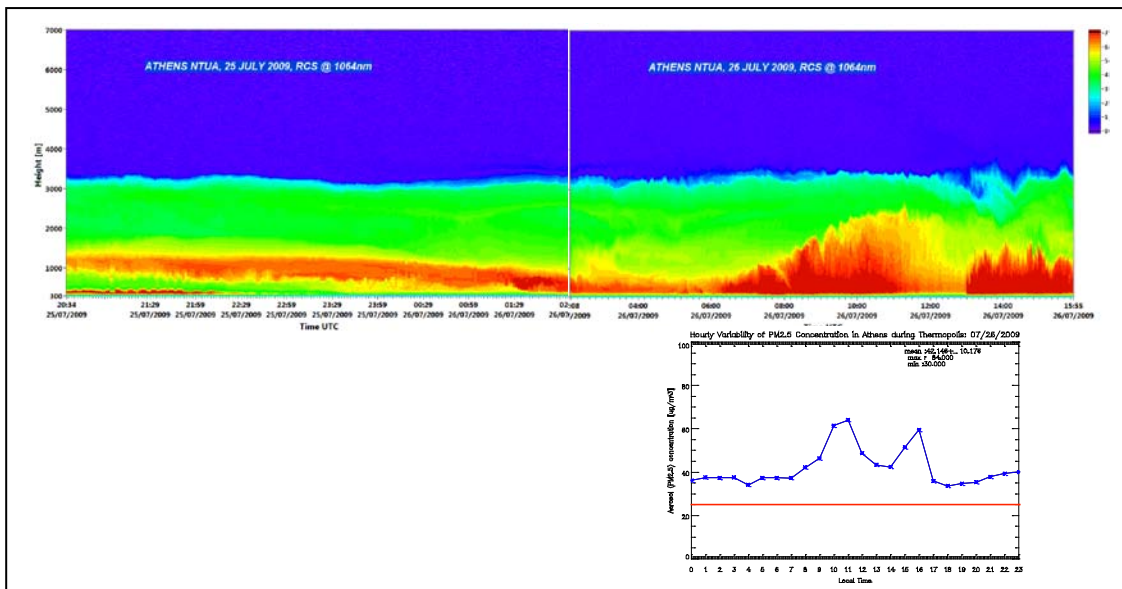


Figure 120: Range-corrected lidar signals at 1064 nm (upper graphs) obtained during the time period 25-26 July, 2009 (Saharan dust intrusion) over the city of Athens, together with the aerosol $PM_{2.5}$ concentration measured 15 m above ground level (215 m above mean sea level: asl.).

To verify the origin of the aerosols detected over Athens for the period 24-26 July 2009 we run the HYSPLIT back-trajectory code (lower left graph) and used the output of the

DREAM dust model (upper left graph) provided by Pérez et al., (2006). In fact, as shown in Fig. 10, left-hand side graphs the air masses arriving over Athens on 24 July (19:00 UTC) and 25 July (00:00 UTC) 2009, originated from the Saharan dust desert. This is corroborated by the SeaWiFS satellite image of 24 July, 2009, shown in the right-hand side panel of Fig. 10, where a strong dust layer is observed sweeping Greece from South to North, overpassing Athens.

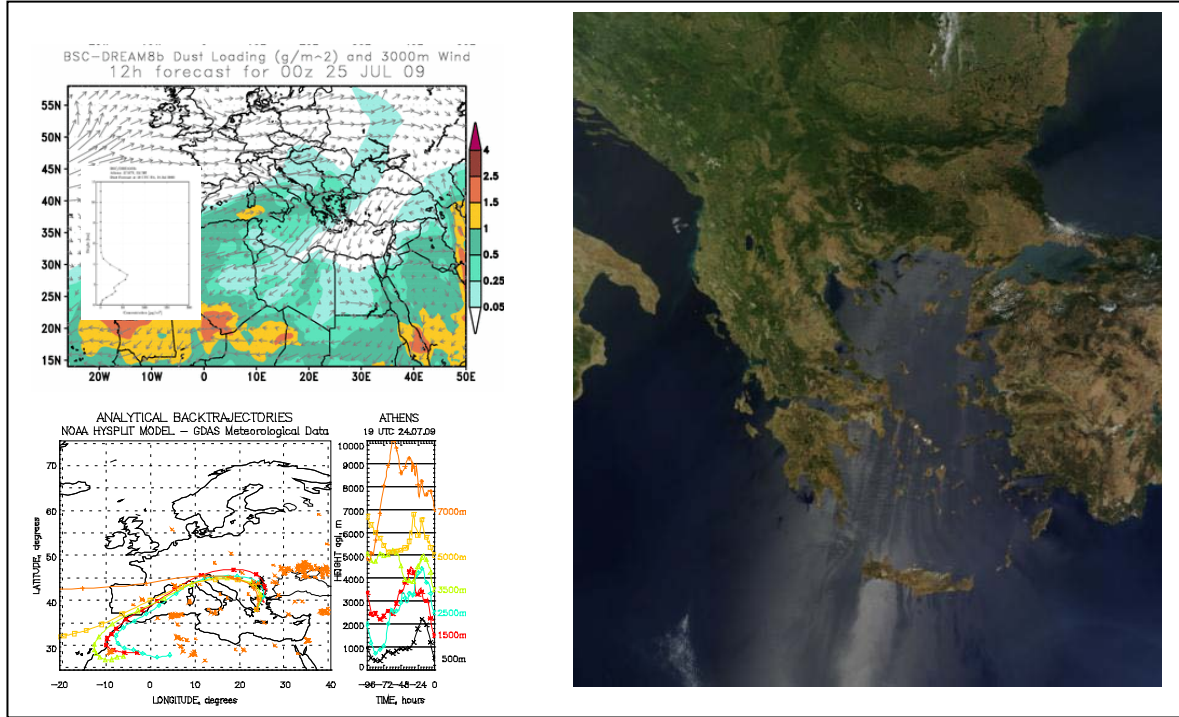


Figure 121. Left: HYSPLIT back-trajectory code (lower graph) and output of the DREAM dust model (upper graph) for air masses arriving over Athens on 24 July (19:00 UTC) and 25 July (00:00 UTC) 2009, respectively. Right: SeaWiFS satellite image obtained for 24 July, 2009.

Figure 122 shows the retrieved aerosol backscatter coefficients for 24 July 2009 at 355-532-1064 nm, as well as the Ångström backscatter-related exponent obtained by the NTUA lidar between 09:01 and 11:00 UTC. The intense Saharan dust aerosol layer is clearly visible around 2.3 and 4 km height.

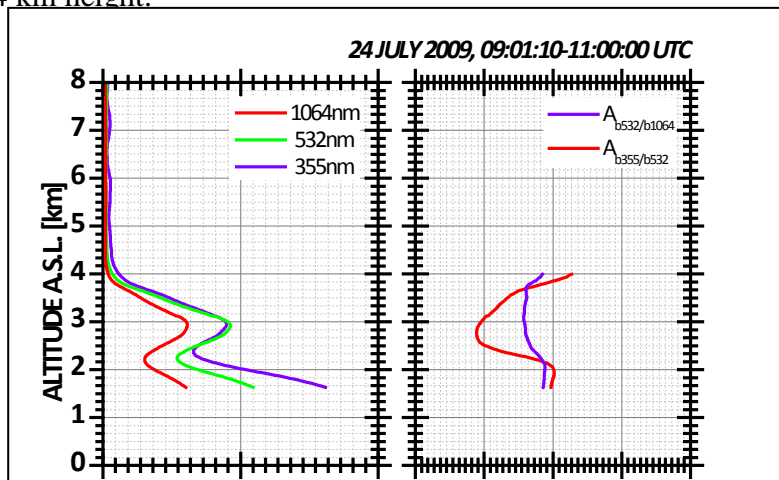


Figure 122. Retrieved aerosol backscatter coefficients for 24 July 2009 at 355-532-1064 nm, as well as the Ångström backscatter-related exponent obtained by the NTUA lidar between 09:01 and 11:00 UTC.

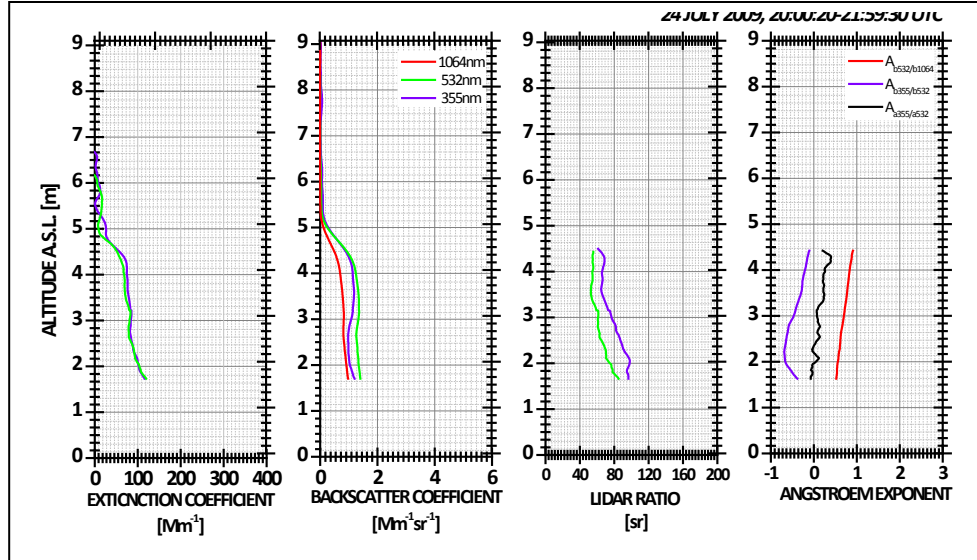


Figure 123. Retrieved nighttime aerosol optical properties (extinction, backscatter, lidar ratio, Ångström backscatter-related exponent) at 355-532-1064 nm, obtained by the NTUA lidar on 24 July 2009 between 20:00 and 21:59 UTC.

Fig. 123 shows the retrieved nighttime aerosol optical properties (extinction, backscatter, lidar ratio, Ångström backscatter-related exponent) at 355-532-1064 nm, obtained by the NTUA lidar on 24 July 2009 between 20:00 and 21:59 UTC. During nighttime a homogenous aerosol dust layer is observed between 1.5 and 5 km height, where the dust particles are well mixed inside the PBL mixing layer and extending up to 5 km height. In Table 2 we compare the aerosol microphysical properties (effective radius, refractive index, and single scattering albedo) derived by inverse modeling (from NTUA Raman lidar data) and in situ airborne measurements performed at selected heights by the Democretian University of Thrace (DUTH). In fact we can see that the retrieved aerosol radius (3 cases) and the SSA values (1 case) agree quite well. The non-available aerosol microphysical values could not be retrieved due to technical problems.

5.3.8 Correlated ground-based and space-borne aerosol lidar measurements

During THERMOPOLIS campaign in total 4 inter-comparisons between the aerosol backscatter profiles obtained by the CALIPSO satellite (Winker et al., 2007; Mamouri et al., 2008) and the NTUA Raman lidar over Athens were performed: daytime/nighttime 17 July 2009 and daytime/nighttime on 26-27 July 2009. A typical ground-track of the CALIPSO satellite over Greece is presented in Fig. 13. The corresponding aerosol attenuated backscatter profile along the satellite's path is also presented on the left side of the image.

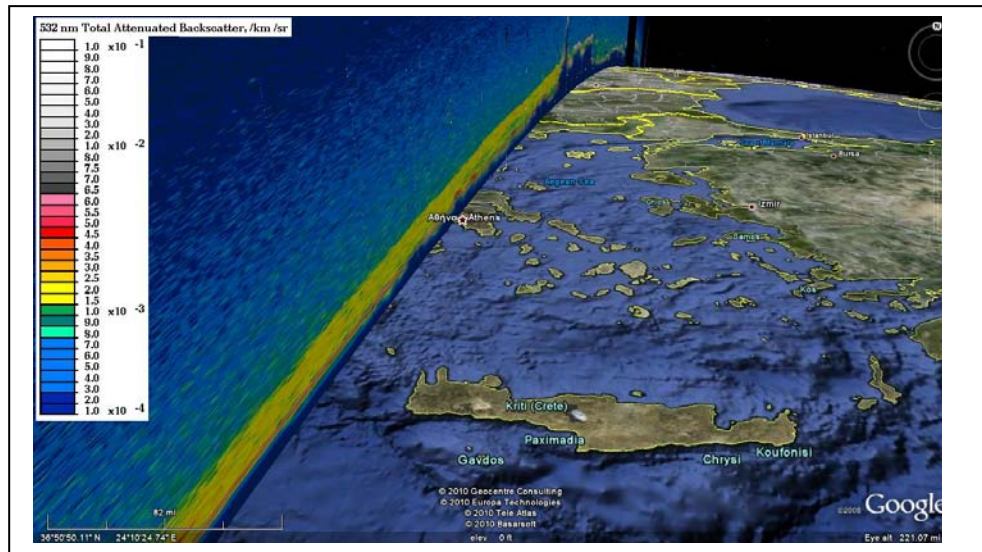


Figure 124. Typical ground-track of the CALIPSO satellite over Greece. The corresponding aerosol attenuated backscatter profile along the satellite's path is also presented on the left side of the image.

Table 66. Aerosol microphysical properties derived by inverse modeling (from NTUA Raman lidar data) and in situ measurements performed by the Democritus University of Thrace (DUTH).

Date	Time (local)	Alt (ft)	Alt (km)	Effective radius (μm) (reff) NTUA Fine/Total	Mean radius (μm) (reff) DUTH Fine/Total	SSA (ω) NTUA (532 nm)	SSA (ω) DUTH (532 nm)	Refractive index NTUA Real part	Refractive index NTUA Imag. part	Remarks
20/7/2009	2:23 PM	8592	2.62	N/A	0.25/0.357	N/A	0.654	N/A	N/A	Fires/ photoch
20/7/2009	3:07 PM	3167	0.96	N/A	0.25/0.379	N/A	0.965	N/A	N/A	Fires/ photoch
21/7/2009	5:05 AM	9228	2.81	$0.19 \pm 0.04 / 0.4 \pm 0.14$	0.25/ 0.370	0.63 ± 0.11	0.698	1.56 ± 0.13	0.051 ± 0.03	Haze/ Photoc-USA
21/7/2009	5:18 AM	11055	3.37	$0.14 \pm 0.03 / 0.14 \pm 0.03$	0.25/0.337	0.87 ± 0.08	N/A	1.43 ± 0.07	0.028 ± 0.02	Haze/ Photoc-USA
21/7/2009	11:54 PM	8612	2.63	$0.11 \pm 0.043 / 0.35 \pm 0.2$	0.25/0.3695	0.61 ± 0.1	N/A	1.376 ± 0.05	0.065 ± 0.01	NW Flow-clear
22/7/2009	12:16 AM	4539	1.38	N/A	0.25/0.391	N/A	0.513	N/A	N/A	NW Flow-clear

The CALIPSO level 2 data comparison with the ground-based retrievals of the aerosol optical properties (extinction and backscatter coefficients and lidar ratio) as shown in Fig. 14, shows a quite good agreement between the two instruments. The minimum horizontal distance between NTUA Raman lidar and the CALIPSO ground track during the nighttime measurements on 26-27 July, 2009 was of the order of 12 km.

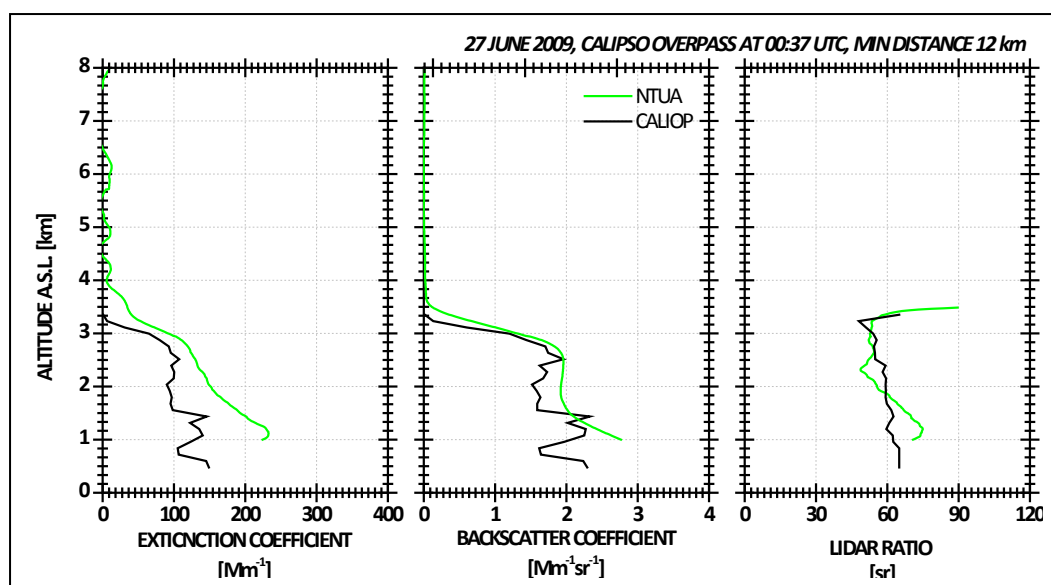


Figure 125. CALIPSO level 2 data comparison with the ground based retrievals of the aerosol optical properties. The minimum horizontal distance between NTUA Raman lidar and the CALIPSO ground track during the nighttime measurements on 26-27 July, 2009 was of the order of 12 km.

CONCLUSIONS

The NTUA group performed daily daytime and nighttime Raman lidar measurements of the aerosol optical properties (backscatter, extinction, lidar ratio and Ångström backscatter-related exponent) during the THERMOPOLIS field campaign 15 and 31 July, 2009. In addition, continuous $PM_{2.5}$ aerosol concentration and meteorological measurements (with 10 min temporal resolution) were performed at 15 m above ground level (215 m asl.). Thus, in the THERMOPOLIS database the following data were provided:

- Time series of the Range corrected lidar signals
- Mean vertical profiles of the aerosol optical properties

- Mean water vapor profiles for selected time periods and during the performed flights
- Aerosol Optical Depth (AOD) at 355-532 nm after sunset
- PM_{2.5} concentration measurements with 10-min temporal resolution and mean hourly values
- Continuous meteorological data (pressure, temperature, relative humidity, rain rate, dew point, wind speed/direction, solar radiation intensity, etc.) with 10-min temporal resolution and mean hourly values.

We classified our measurements into clusters using the air mass origin as criterion of the aerosol source region. Therefore, using the air mass backward trajectories ending over the sampling site (city of Athens at various heights in the lower troposphere) variable aerosol sources were identified for each measurement day. For instance, between 14 and 20 July 2009, anthropogenically produced particles were found over Athens; Saharan dust particles were observed between 24-26 July, whereas in the period 20-22 July a mixture of anthropogenic and smoke (biomass burning) aerosols occurred.

During the 14-23 July 2009 time period, the main conclusions derived are:

- 1) the AOD variations (14-20 July, 2009) were between 0.17 and 0.35 at 500 nm and of the Ångström exponent (440/870 nm) between 1.5 and 1.75 indicating the presence of rather small (anthropogenically produced) particles,
- 2) the AOD variations (20-22 July, 2009) were between 0.08 and 0.18 at 500 nm and of the Ångström exponent (440/870 nm) between 1.2 and 1.5 indicating the presence of rather small (biomass burning) particles,
- 3) the locally produced aerosols (14-20 July, 2009) were mostly confined between ground and the top of the PBL (around 2-2.5 km height around 12:00-13:00 UTC),
- 4) very high PM_{2.5} (exceeding EU standards) concentrations were observed during 20 July, 2009, due to local pollution sources,
- 5) distinct aerosol layers were observed during 20 and early 21 July, 2009 around 3 km height, which originated from the USA continent where they were

probably enriched with biomass burning aerosols and other anthropogenic emissions,

- 6) according to model retrievals, the aerosol effective radius remained lower than 0.4 ± 0.15 , the refractive index ranged between 1.35-1.55 (indicating the mixture of various types of aerosols) and the SSA showed strongly to moderate absorbing aerosols ranging between 0.88 (at 3 km height) and 0.62 (at 2.9 km height).

During the 24-26 July 2009 time period (Saharan dust intrusion), the main conclusions derived are:

- 1) the AOD variations were between 0.2 and 0.3 at 500 nm and of the Ångström exponent (440/870 nm) between 1.0 and 0.75 indicating the presence of rather big particles (desert origin),
- 2) very high $PM_{2.5}$ (exceeding EU standards) concentrations were observed on 26 July, 2009, due to Saharan dust particles,
- 3) the Saharan dust aerosols were mostly confined between ground and 4.5 km height.

Moreover, the comparison between the aerosol microphysical properties (effective radius and single scattering albedo) derived by inverse modeling (from NTUA Raman lidar data) and measured in situ by airborne instruments at selected heights by the Democretian University of Thrace (DUTH) showed that the retrieved aerosol radius (3 cases) and the SSA values (1 case) agreed quite well. Additionally, the CALIPSO level 2 data comparison with the ground-based retrievals of the aerosol optical properties (extinction and backscatter coefficients and lidar ratio) showed a quite good agreement between the two instruments (for a 12 km minimum horizontal distance between NTUA Raman lidar and the CALIPSO ground track).

References

1. Ansmann A., Riebesell, M., Wandinger, U., Weitkamp, C., Voss, C., Lahmann, W. and Michaelis, W.: Combined Raman Elastic-Backscatter lidar for vertical profiling of moisture, aerosol extinction, backscatter, and lidar ratio, *Applied Physics B*, 55, 18-28, 1992.
2. Bösenberg, *et al.*: EARLINET project: A European Aerosol Research Lidar Network, Max-Planck Institute (MPI), Final Report, 348, 1–250, 2003.
3. Chan L. Y., Lau, W. L., Lee, S. C., and Chan, C.Y.; Commuter exposure to particulate matter in public transportation modes in Hong Kong, *Atmos. Environ.*, 3363-3373, 2002.
4. Forster, P., *et al.*: Changes in Atmospheric Constituents and in Radiative Forcing. In: *Climate Change 2007: The Physical Science Basis. Contribution of Working Group I to the Fourth Assessment Report of the Intergovernmental Panel on Climate Change* (Solomon, S., *et al.*, (eds.). Cambridge University Press, Cambridge, U.K., 2007.
5. Mamouri, R.E., Amiridis, V., Papayannis, A., Giannakaki, E., Tsaknakis G., and Balis, D.S.: Validation of CALIPSO space-borne-derived attenuated backscatter coefficient profiles using a ground-based lidar in Athens, Greece, *Atmospheric Measurement Techniques*, 2, 513-522.
6. Müller, D. *et al.*: Microphysical particle parameters from extinction and backscatter lidar data by inversion with regularization: Theory, *Applied Optics*, 38, 2346-2357, 1999.
7. Müller, D., *et al.*: Comprehensive particle characterization from three wavelength Raman-lidar observation, *Applied Optics*, 40, 4863-4869, 2001.
8. Müller, D., Mattis, I., Wandinger, U., Ansmann, A., Althausen, D., and Stohl, A.: Raman lidar observations of aged Siberian and Canadian forest fire smoke in the free troposphere over Germany in 2003: Microphysical particle characterization, *Journal of Geophysical Research*, **110**, D17201, doi:10.1029/2004JD005756, 2005.
9. Pérez, C., Nickovic, S., Pejanovic, G., Baldasano, J. M., and Özsoy, E.: Interactive dust-radiation modeling: A step to improve weather forecasts, *J. Geophys. Res.*, doi:10.1029/2005JD006717, 2006.

10. Veselovskii, I., *et al.*: Inversion with regularization for the retrieval of tropospheric aerosol parameters from multiwavelength lidar sounding, *Applied Optics*, 41, 3685-3699, 2002.
11. Veselovskii, I., *et al.*: Retrieval of dust particle parameters from multi-wavelength lidar measurements using model randomly oriented spheroids, *Proceedings of ILRC25*, 5-9 July 2010, Saint Petersburg, Russia, 2010.
12. Winker D. M., Hunt, W. H., McGill, M. J., *et al.*: Initial performance assessment of CALIOP, *Geophysical Research Letters*, 34, L19803, doi:10.1029/2007GL030135, 2007.

5.4 Radiometric cal/val ground measurements (UVEG-GCU)

Measurement plan

A set of thermal radiometric measurements was carried out in the framework of the Thermopolis 2009 experimental field campaign. The retrieval of bio-geophysical parameters such as reflectivity, land surface emissivity and temperature was the main aim of these measurements. To this end, radiometric measurements were carried out in the solar and thermal infrared region with various instruments that included fixed FOV and single band or multi bands radiometers. In addition, black bodies (calibration sources) for calibration purposes were used (Sobrino et al, 2009).

Three different kinds of in situ measurements were carried out during the two weeks of the intensive period of measurement: i) radiometric measurements for calibration/validation of parameters extracted from the airborne (AHS) data and from the spaceborne data, ii) measurements for characterizing the urban heat island (UHI) effect, e.g. air temperature, which include transects, measurements in fixed masts and spectral characterization of urban surfaces and iii) measurements for survey urban thermography (UT).

Instrumentation

Thermal Radiometric Measurements:

The aim of these measurements was to obtain land surface emissivity and temperature over different test sites. These measurements were carried out in different ways: i) Making transects at regular steps in representative and extense surfaces for calibration and validation purposes during the flight overpasses, ii) By means of continuous measurements of ground radiometric temperature in fixed masts located in two points in Athens, iii) Carrying out emissivity measurements by applying the Temperature and Emissivity Separation (TES) algorithm (Sobrino et al., 2008) over the most representative samples in the site for spectral characterization purposes, and iv) Making thermal imagery for urban thermography purposes.

Various instruments were used to measure in the thermal infrared domain, including multiband and single-band radiometers with fixed fields-of-view (FOV). The CIMEL model CE312-2 is a radiance-based thermal-infrared radiometer composed of an optical head and a data storage unit.. The CE312-2 detector includes 6 bands, a wide one, 8-13 μm , and five narrower filters, 8.1 – 8.5 μm , 8.5 – 8.9 μm , 8.9 – 9.3 μm , 10.3 – 11 μm and 11 – 11.7 μm (see Figure 38). Temperature of an external blackbody can be measured with a temperature probe, especially for the estimation of emissivity.

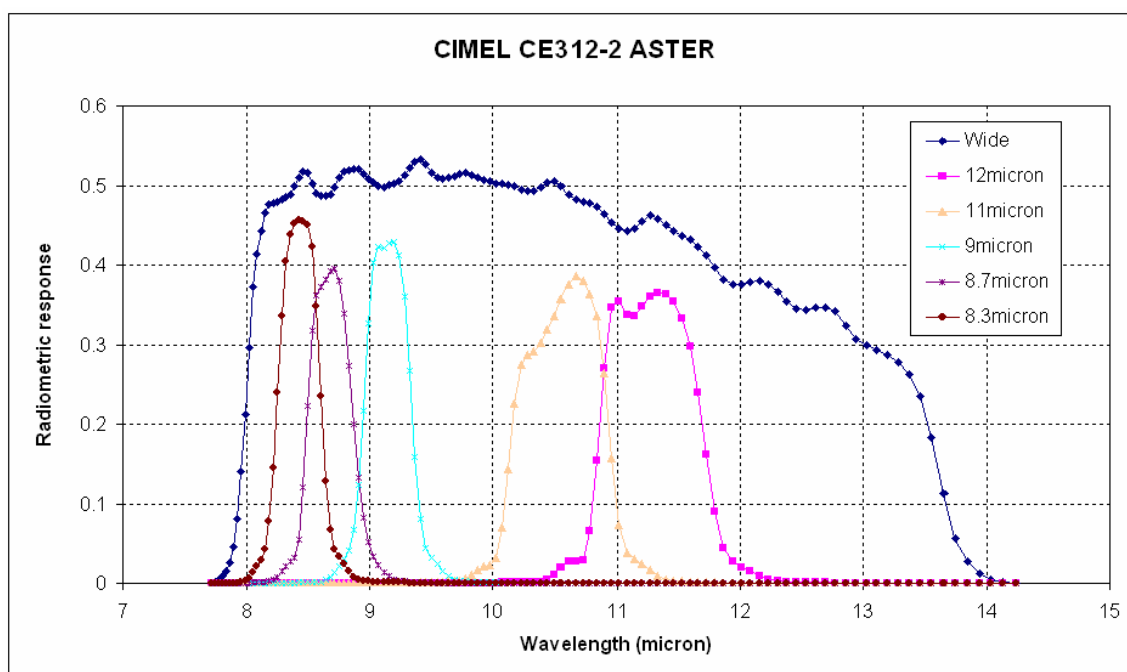


Figure 126. Radiometric response of the CIMEL CE312-2

The other thermal radiometers are single-band radiometers with spectral range from 8 to 14 μm (OPTRIS CT-LT15, Raytek ST6). They convert the infrared radiation from the sample into electrical signal. With the suitable calibration process, the electrical signal is converted to a signal in terms of temperature. These radiometers were used in the fixed masts and in the cal/val activities. Besides, one thermal camera acquired thermal imagery during the field campaign, NEC TH9100, for urban thermography and calibration/validation purposes. A visible image was also acquired simultaneously to the thermal image. A diffuse reflectance standard plate was used to estimate the downward radiance (Infragold from Labsphere Inc), and two calibration sources (LAND P80P and Everest 1000) to calibrate the radiometers. Table 12 shows the technical specifications of the instruments.

Table 66. Technical specifications of the thermal instruments

Instrument	Spectral Range (μm)	Temperature Range ($^{\circ}\text{C}$)	Accuracy (K)	Resolution	FOV
CIMEL CE312-2	8 – 13 11 – 11.7 10.3 – 11 8.9 – 9.3 8.5 – 8.9 8.1 – 8.5	-80 to 60	0.1	8 mK 50 mK 50 mK 50 mK 50 mK 50 mK	10 $^{\circ}$
OPTRIS CT-LT15	8 – 14	-40 to 600	0.3	0.1 K	4 $^{\circ}$
RAYTEK ST6	8 – 14	-32 to 400	0.5	0.1 K	2 $^{\circ}$
NEC TH9100	8 – 14	-40 to 120	2	0.1 K (320x240pxl)	22 $^{\circ}$ x16 $^{\circ}$

EVEREST 1000		Fixed to ambient	0.3	0.1 K	
LAND P80P		-10 to 80	0.1	0.01 K	

Figure 39 shows a picture of each thermal instrument used in the Thermopolis campaign and described in Table 12.



CIMEL
CE312-2



OPTRIS CT-LT15



RAYTEK ST6



NEC TH9100



EVEREST
1000



LAND P80P



INFRAGOLD

Figure 127. Instruments for thermal radiometric measurements

Air Temperature and Relative Humidity measurements: Continuous measurements were carried out during the field campaign by the GCU using HOBO-TMC6 HB Air temperature sensor located in two fixed masts and also by making car transects (AHLBORN FHA646-E1 Air temperature / Relative Humidity sensor). Table 13 shows the technical specifications of the sensors of air temperature and humidity.

Table 67. Technical specifications of air temperature and humidity sensors

Instrument	Operative Range	Temperature Accuracy	Temperature repeatability	Humidity Accuracy	Humidity Repeatability
AHLBORN FHA646-E1	-20 °C to +60 °C	0.1 °C	0.1 °C	± 2 %	< 1%
HOBO TMC6 HB	0 °C to +50 °C	0.25 °C	0.011 °C		

Besides, in Figure 40 we can observe a picture of each sensor used to measure air temperature (HOBO-TMC6 HB and AHLBORN FHA646-E1) and humidity (AHLBORN FHA646-E1)

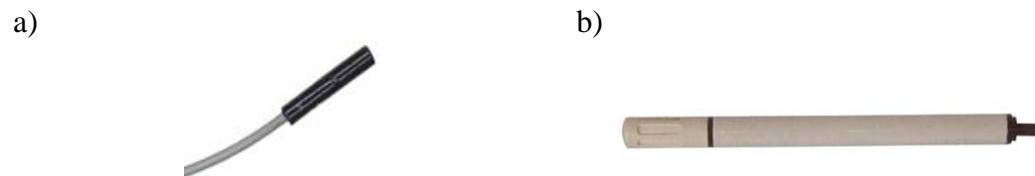


Figure 128. a) HOBOTMC6 HB air temperature sensor and b) AHLBORN FHA646-E1 sensor used for air temperature and relative humidity measurements.

Solar Range Measurements: Spectral reflectance signatures of different natural and artificial surfaces were acquired by GCU with the GER 1500 spectroradiometer to characterize urban surfaces and therefore produce a spectral library.

The GER 1500 is a very high resolution and fast spectroradiometer (scans in 5ms) with linear array technology and spectral range in the UV-VIS-NIR. Menu-driven programs control the set-up, acquisition, and data manipulation functions. Table 14 shows the technical specifications of the GER 1500 spectroradiometer.

Table 68. Technical specifications of GER 1500 spectroradiometer

Spectral range	350-1050 nm
Cannels	512
Bandwith	1.5 nm
Scan Time	≥ 5 ms
Field of view	Dependent on fore-optic
Wavelength Accuracy / Repeatability	± 1 nm / ± 0.1 nm
Spectrum Averaging	Selectable
Dark Current Correction	Automatic
Operating Environment	10 - 90 % Rel. Humidity, -10° to 50° C

Figure 129 shows a picture of the GER 1500.

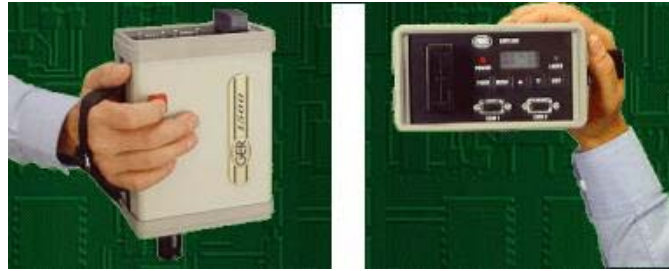


Figure 129. GER 1500 spectroradiometer

5.5.Ground measurements (UVEG-GCU)

MEASUREMENT PLAN

A set of thermal radiometric measurements was carried out in the framework of the Thermopolis 2009 experimental field campaign. The retrieval of bio-geophysical parameters such as reflectivity, land surface emissivity and temperature was the main aim of these measurements. To this end, radiometric measurements were carried out in the solar and thermal infrared region with various instruments that included fixed FOV and single band or multi bands radiometers. In addition, black bodies (calibration sources) for calibration purposes were used.

Three different kinds of in situ measurements were carried out during the two weeks of the intensive period of measurement:

- i) radiometric measurements for calibration/validation of parameters extracted from the airborne (AHS) data and from the spaceborne data,
- ii) measurements for characterizing the urban heat island (UHI) effect, e.g. air temperature, which include transects, measurements in fixed masts and spectral characterization of urban surfaces and
- iii) measurements for survey urban thermography (UT).

PROTOCOL OF MEASUREMENTS AND RESULTS

The calibration/validation measurements carried out with thermal and solar radiometers consisted of transects at regular steps, making 3 measurements with the instrument every time. The diffuse reflectance standard plate was used as target to measure the sky downward radiance every time the type of surface changed or every 20 minutes in order to correct from atmospheric effects. Figure 6 to 10 show different plots of the surface temperature obtained with thermal radiometers in the calibration/validation activities developed during the campaign. Additionally, Figure 11 shows the reflectance measured during this calibration/validation activities with the solar radiometer and Figure 12 shows the measurements of Air Temperature and

Humidity obtained in the roof of the Akropolis Museum while these activities were taking place.

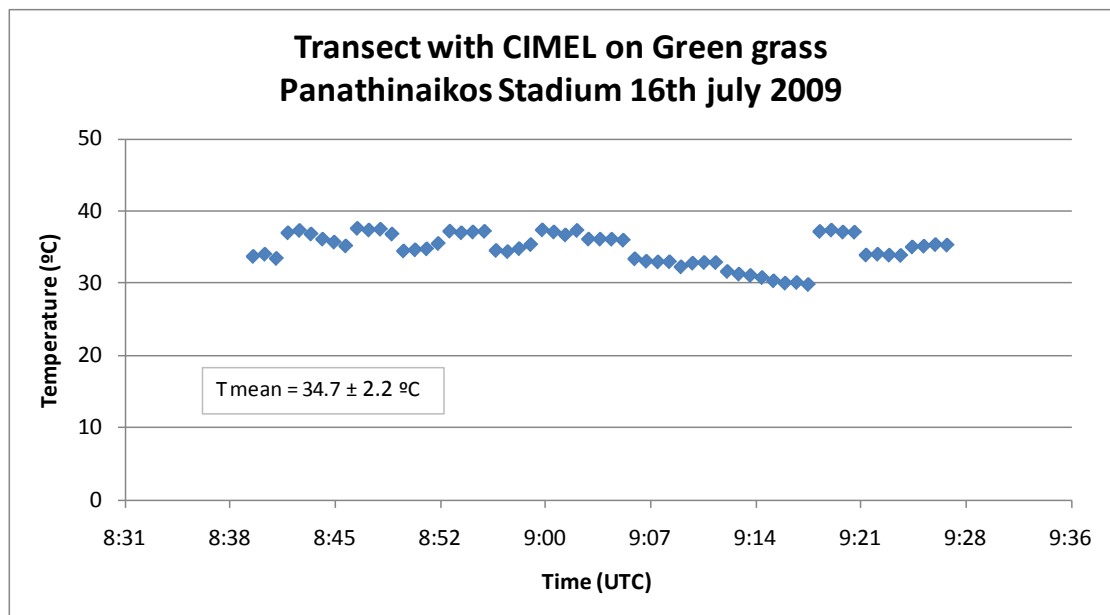


Figure 130.- Surface temperature of the green grass of Panathinaikos Stadium measured with CIMEL radiometer on 16th July 2009.

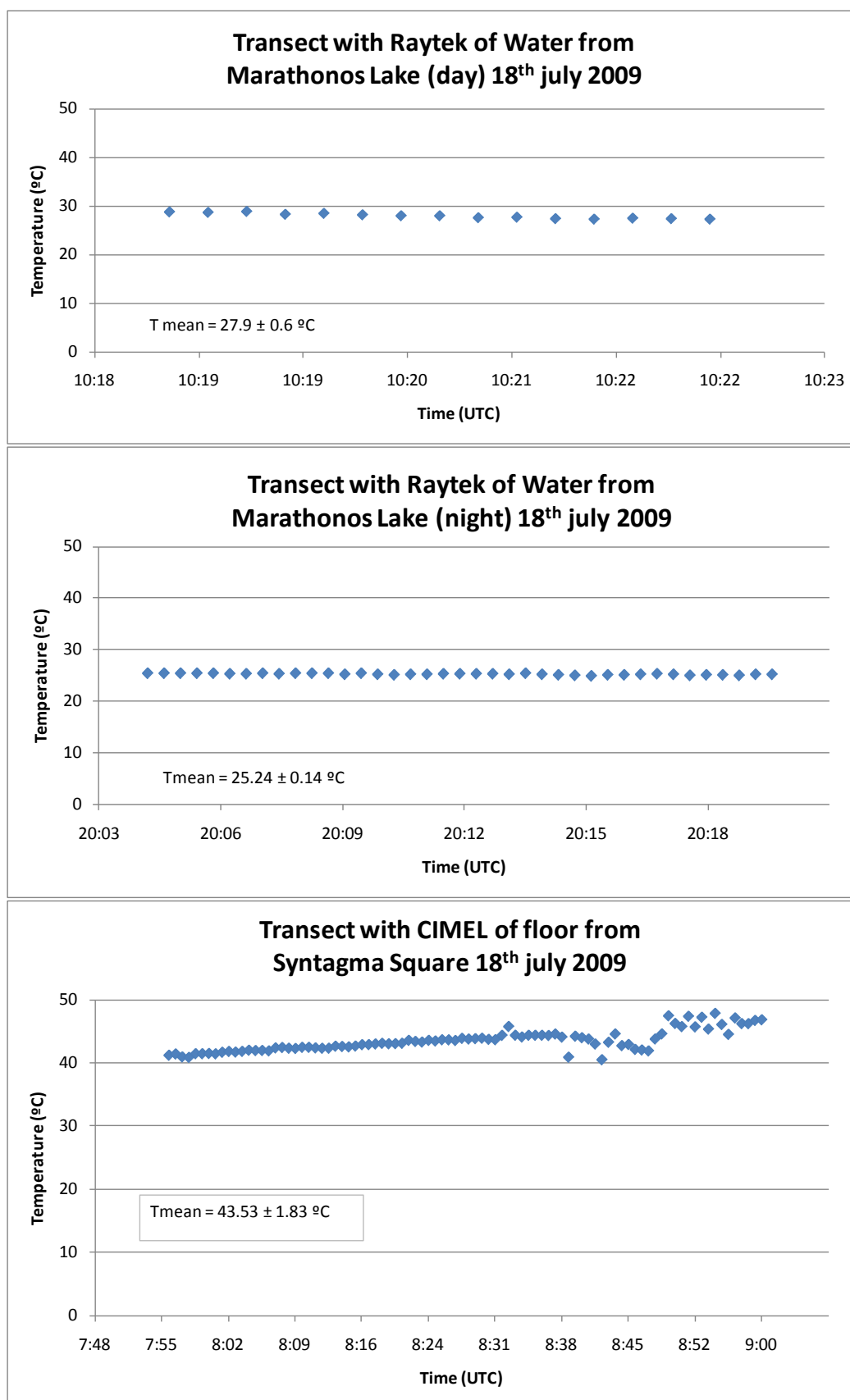
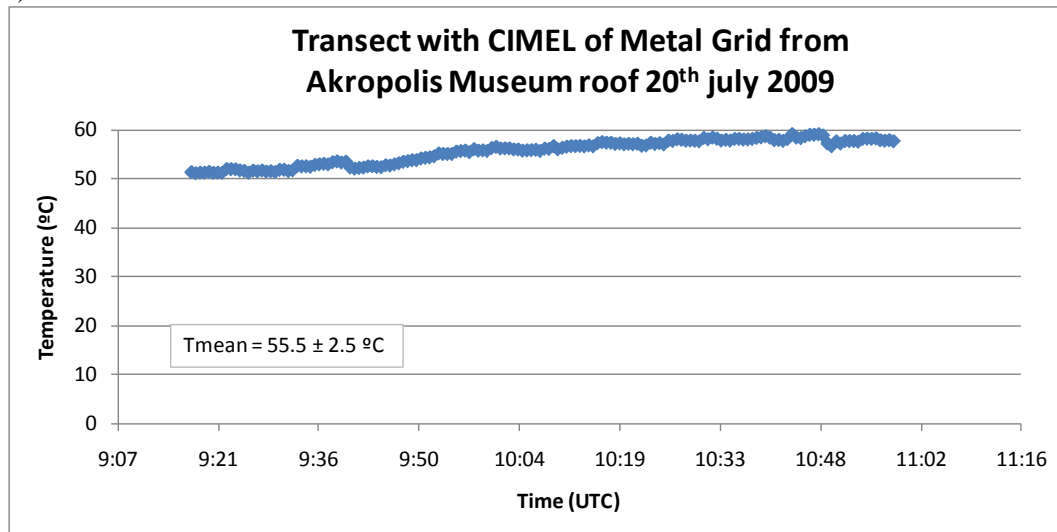


Figure 131.- Surface temperature of water of the Marathonos Lake (day and night), and an urban surface from the Syntagma Square measured with CIMEL radiometer on 18th July 2009.

a)



b)

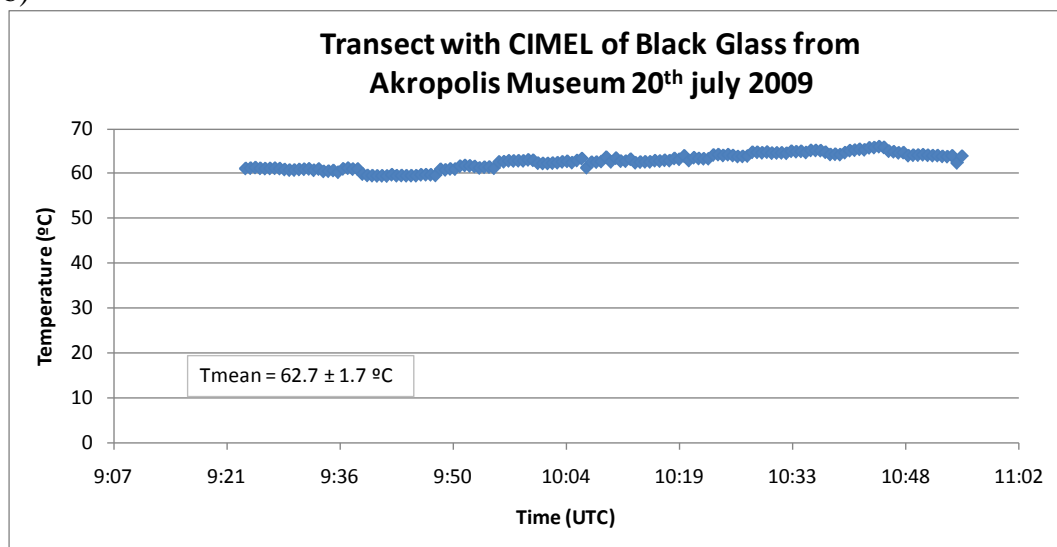
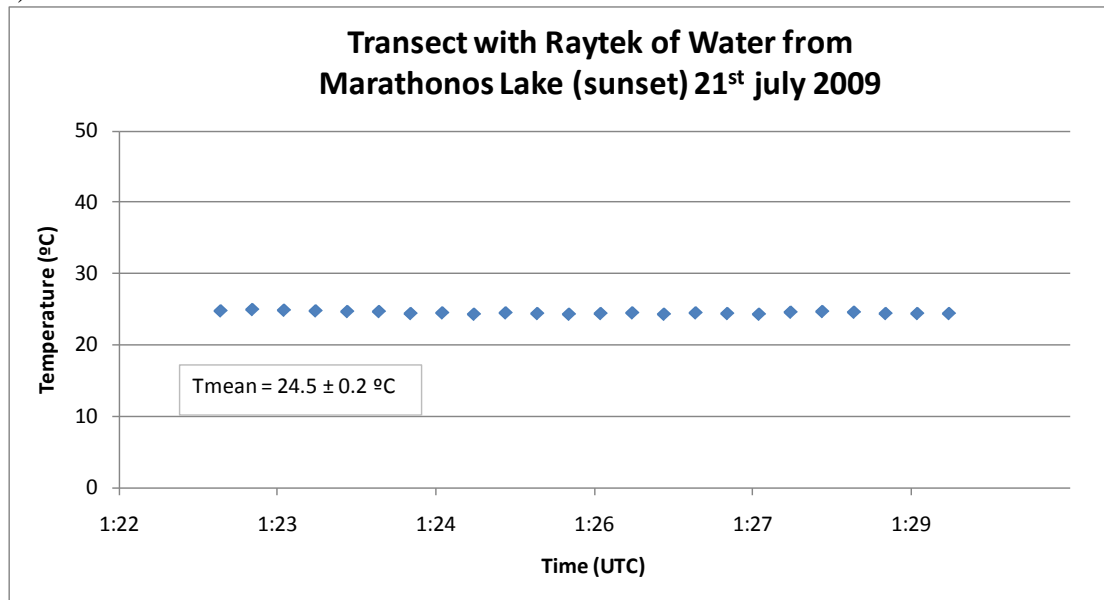


Figure 132.- Surface temperature of a) the Metal Grid and b) the Black Glass from the roof of the Akropolis Museum measured with CIMEL radiometer on 20th July 2009.

a)



b)

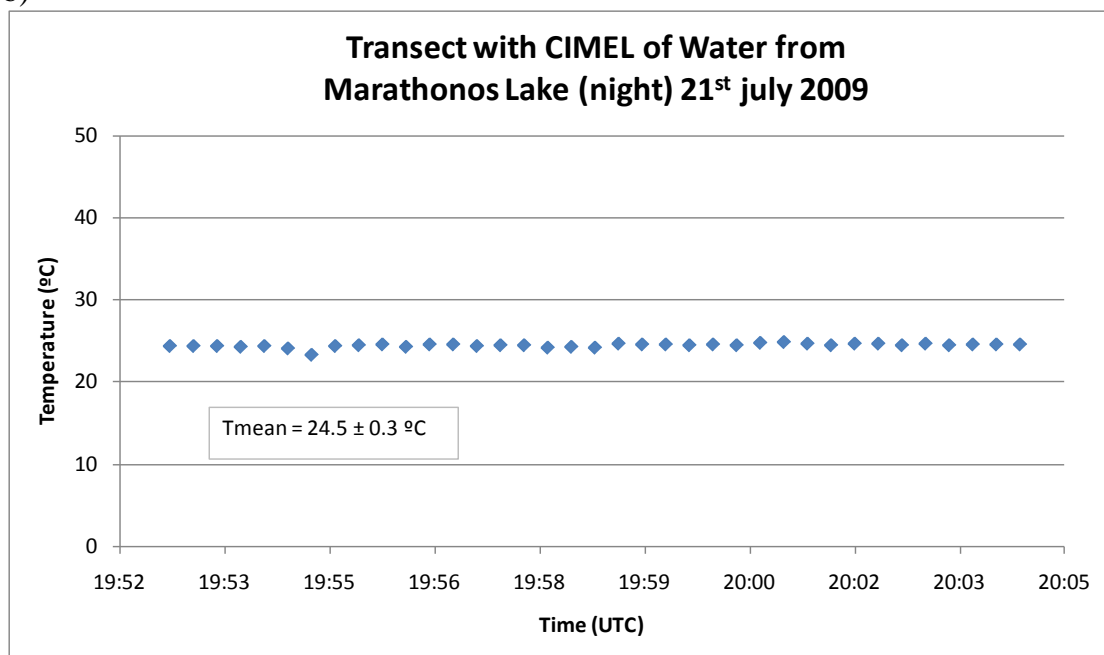
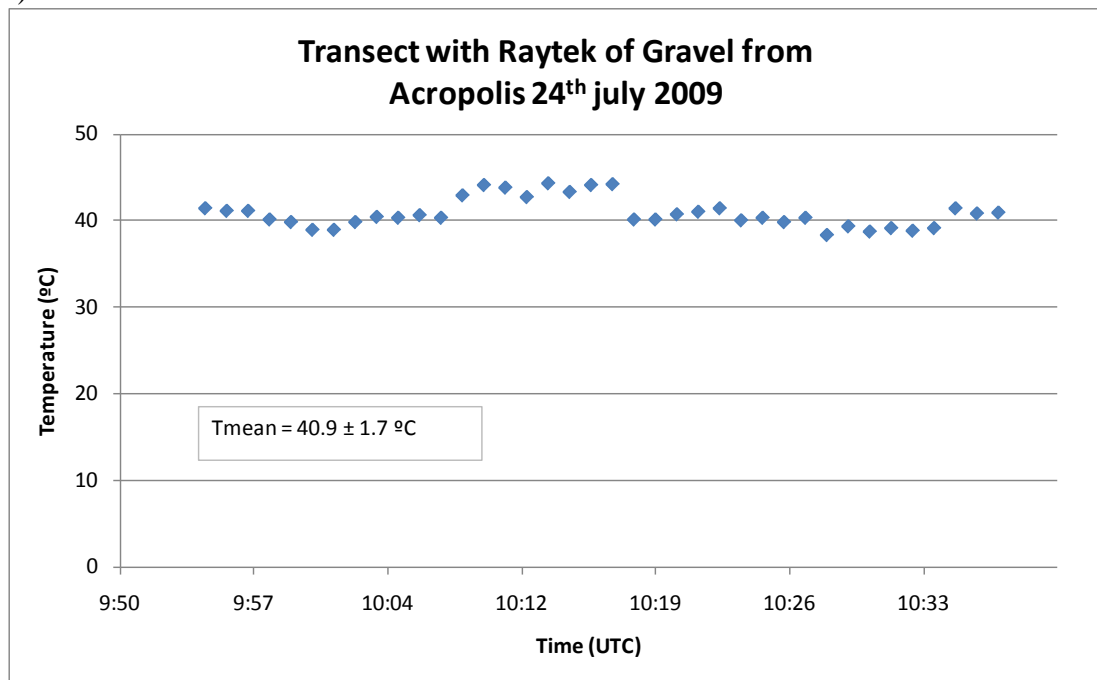


Figure 133.- Surface temperature of Water from Marathonos Lake in different day times a) at sunset and b) at night mesured with RAYTEK radiometer on 21st July 2009.

a)



b)

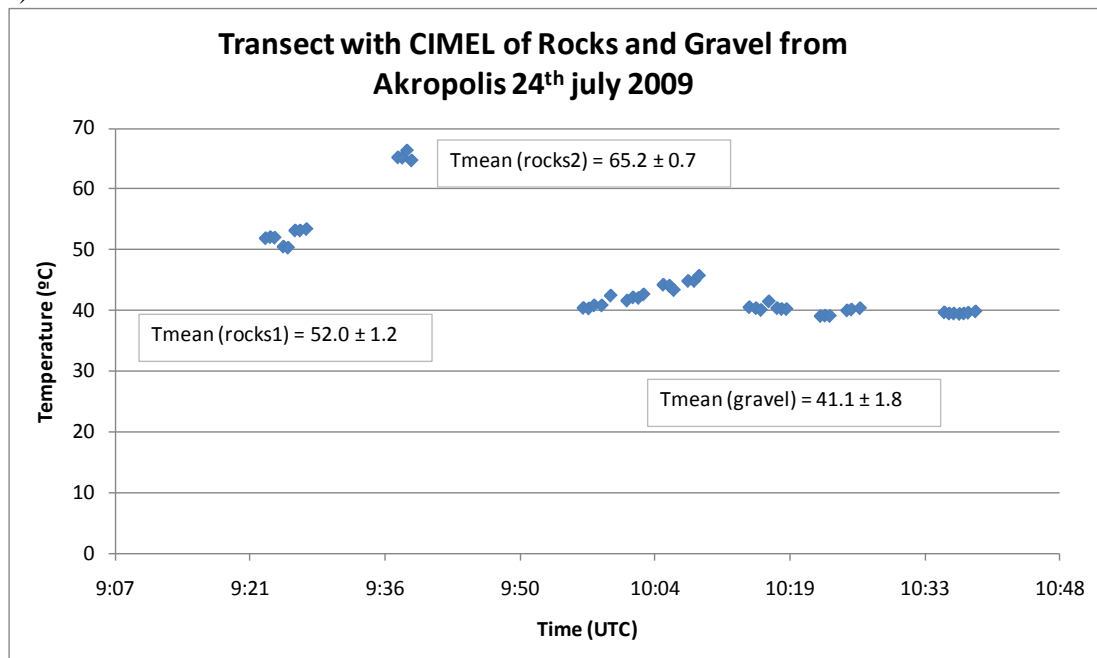
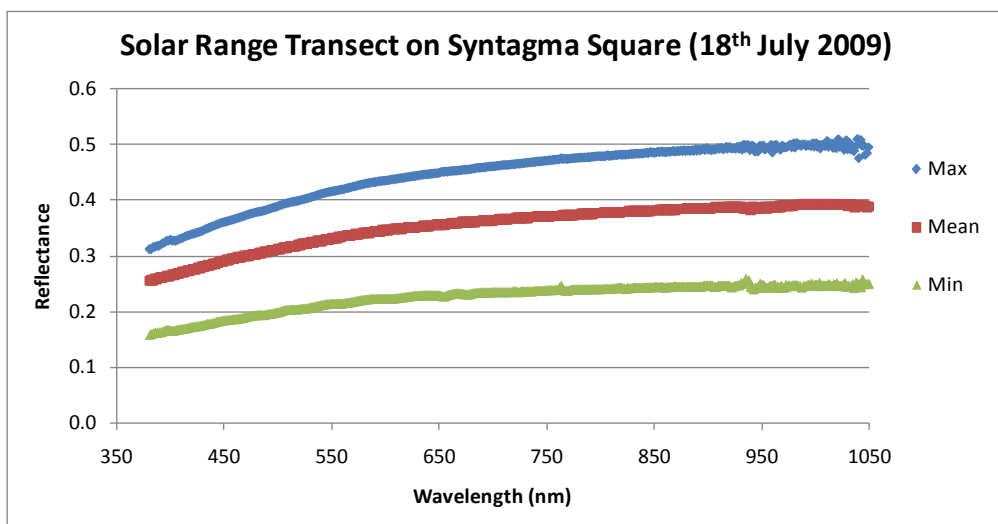
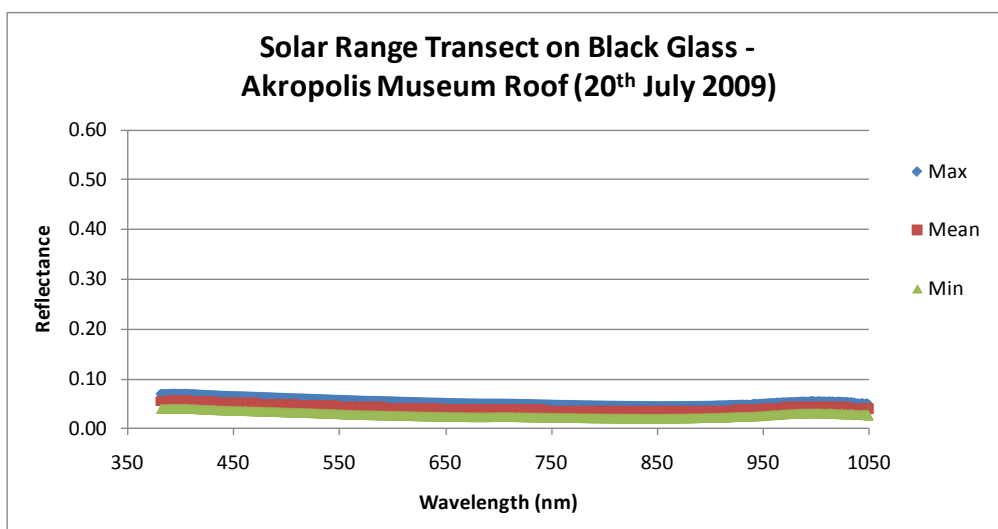


Figure 134.- Surface temperature of Gravel and Rocks from the Akropolis measured with RAYTEK and CIMEL radiometers on 24st July 2009.

a)



b)



c)

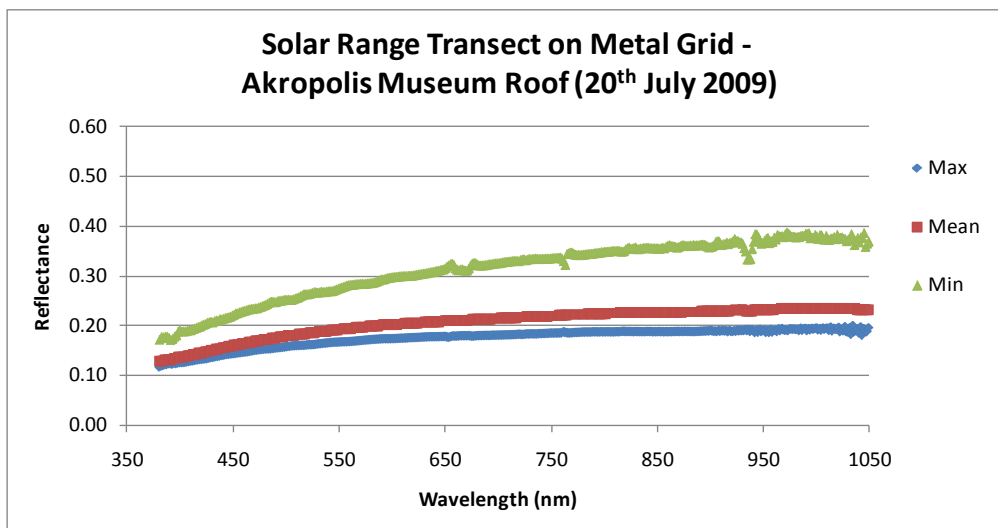


Figure 135.- Maximum, minimum and mean value of the reflectance spectra measured during transects on a) Syntagma Square (18th July

2010) and b) Black Glass and c) Metal Grid of the roof of the Akropolis musem (20th july 2010) measured with GER spectroradiometer.

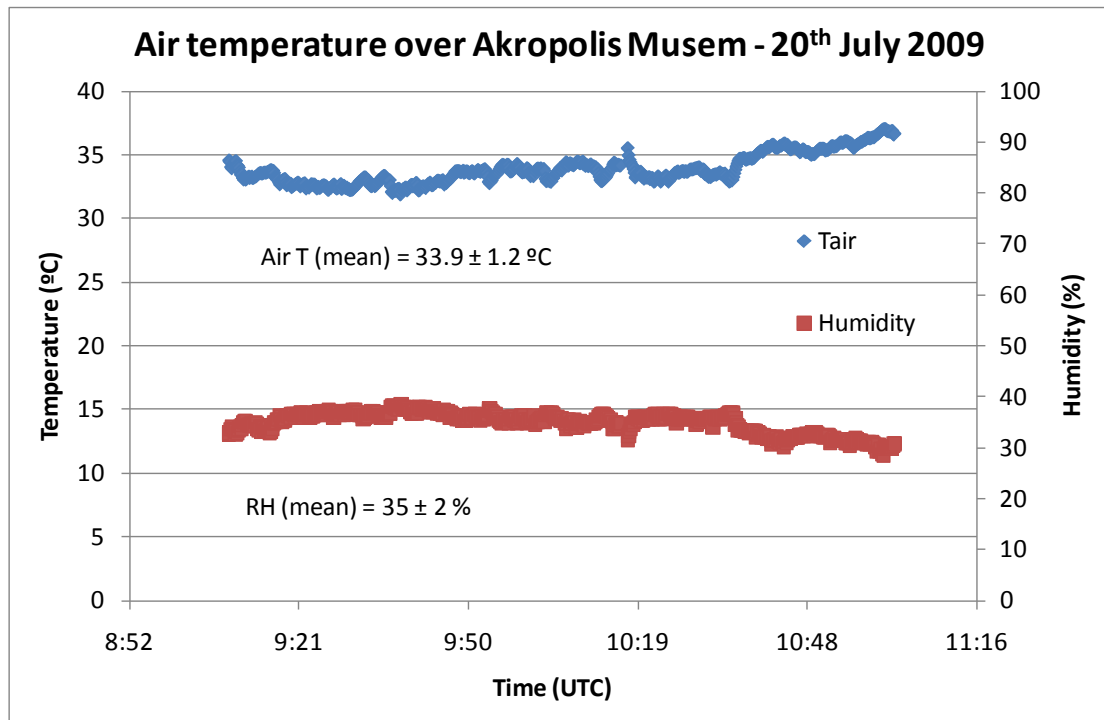


Figure 136.- Air temperature and Realtive Humidity measured during transects on the roof of the Akropolis musem (20th july 2010) measured with AHLBORN sensor.

Transects with cars

One route was defined by the GCU team in order to make transects driving a car along the city of Athens and surroundings with the purpose of characterize the Urban Heat Island during the AHS and ASTER overpass.

The transect runs along the North-South AHS overpass. It starts near the city centre and goes by wide streets going through the city of Athens. When it leaves the city it goes through suburban and rural, even forest, zones. Up to the Marathonos Lake. The way back goes through the same streets than the way out, in order to compare changes in the thermal structure of the city. Figure 13 shows the route of the transect.



Figure 137.- Route defined for the transects with car

Protocol of measurements:

The car was fit out with air temperature and humidity probe (AHLBORN FHA646-E1) with a frequency of data acquisition and storage of 10 seconds. These data was also georeferenced every 10 seconds. The probe was measuring at 3m high. Security distance was kept in front of the cars and the driving speed depended on the type of way and traffic, but was mainly centered at 50 km/h. GCU was in charge of driving the car. In Figures 14 to 19 we can observe the data measured for every transect obtained. Air temperature is plotted with the height measured by the GPS, in order to observe the relation between both magnitudes, when the altitude increases, the temperature decreases and viceversa.

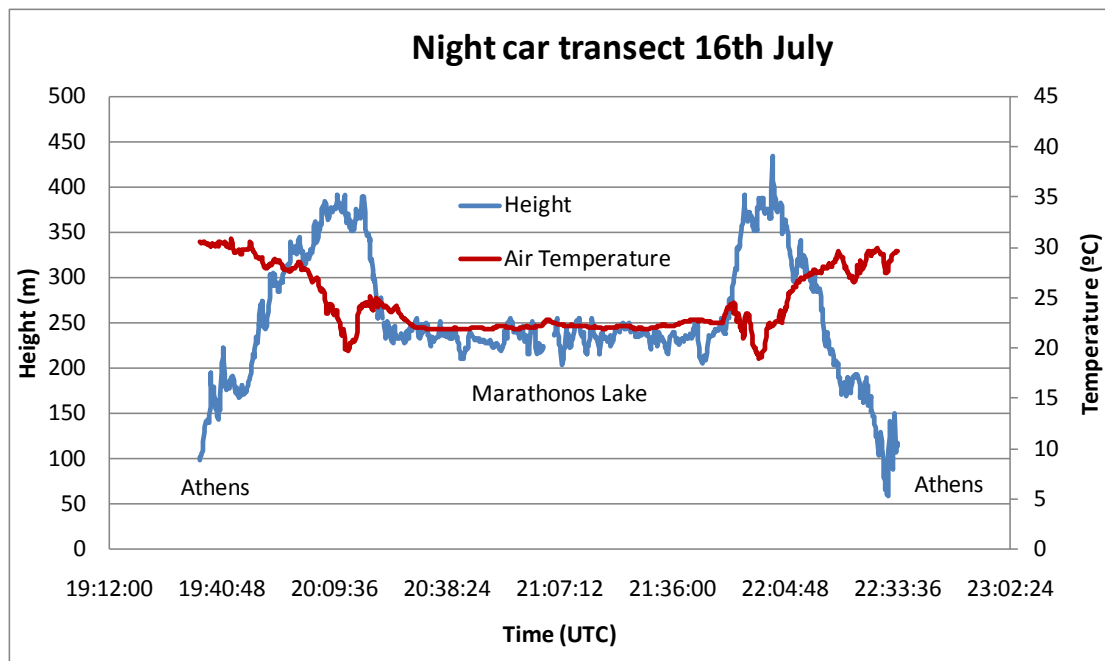


Figure 138.- Air temperature and height of the transect on 16th of July at night.

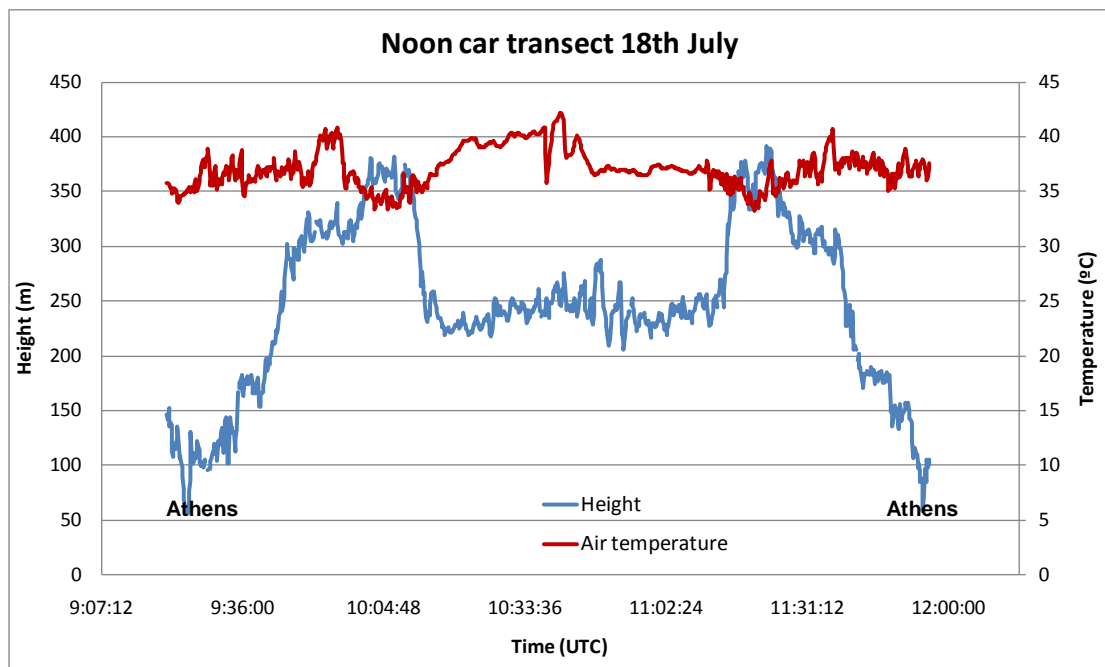


Figure 139.- Air temperature and height of the transect on 18th of July at noon.

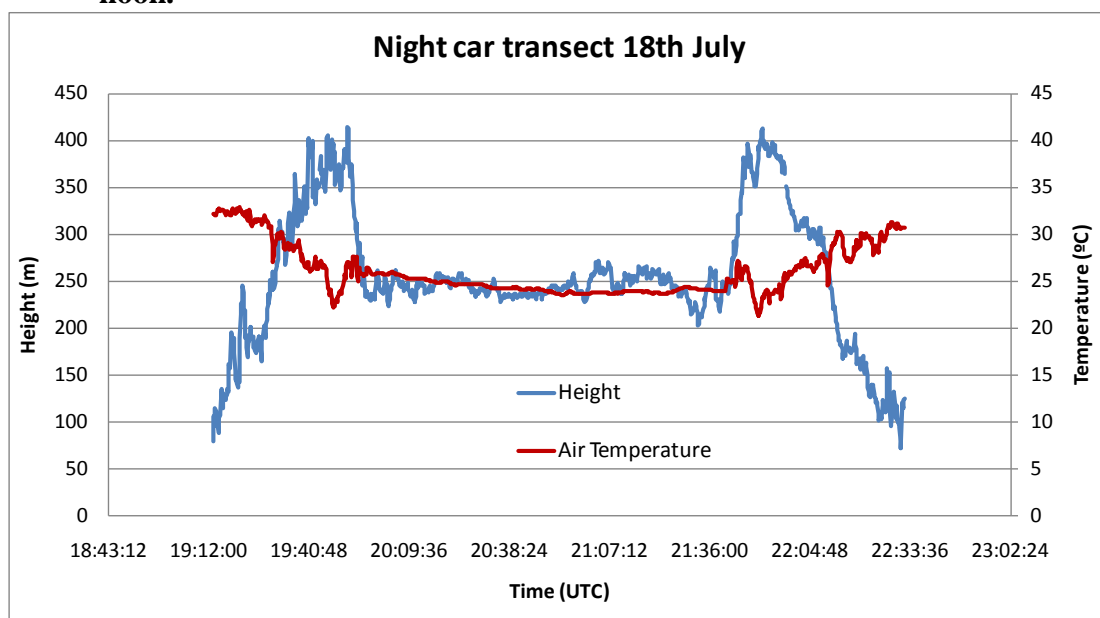


Figure 140.- Air temperature and height of the transect on 18th of July at night.

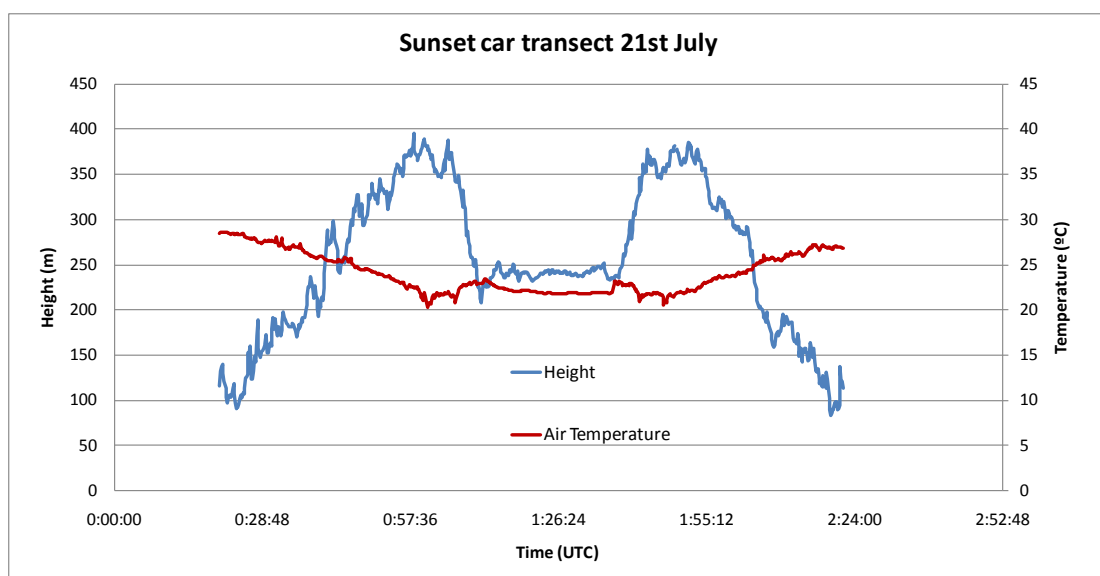


Figure 141.- Air temperature and height of the transect on 21st of July at sunset.

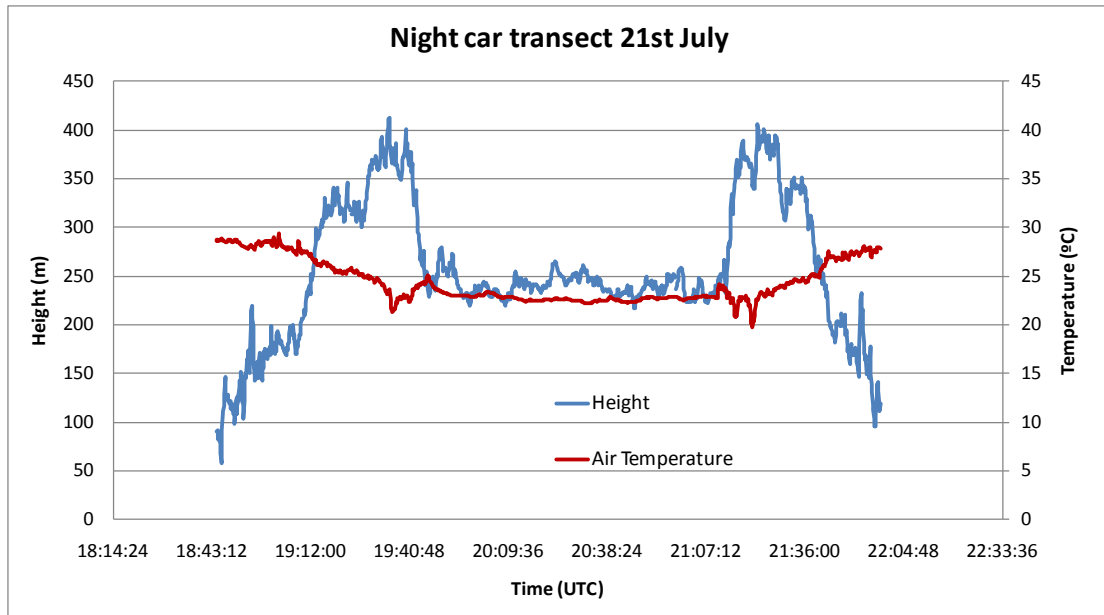


Figure 142.- Air temperature and height of the transect on 21st of July at night.

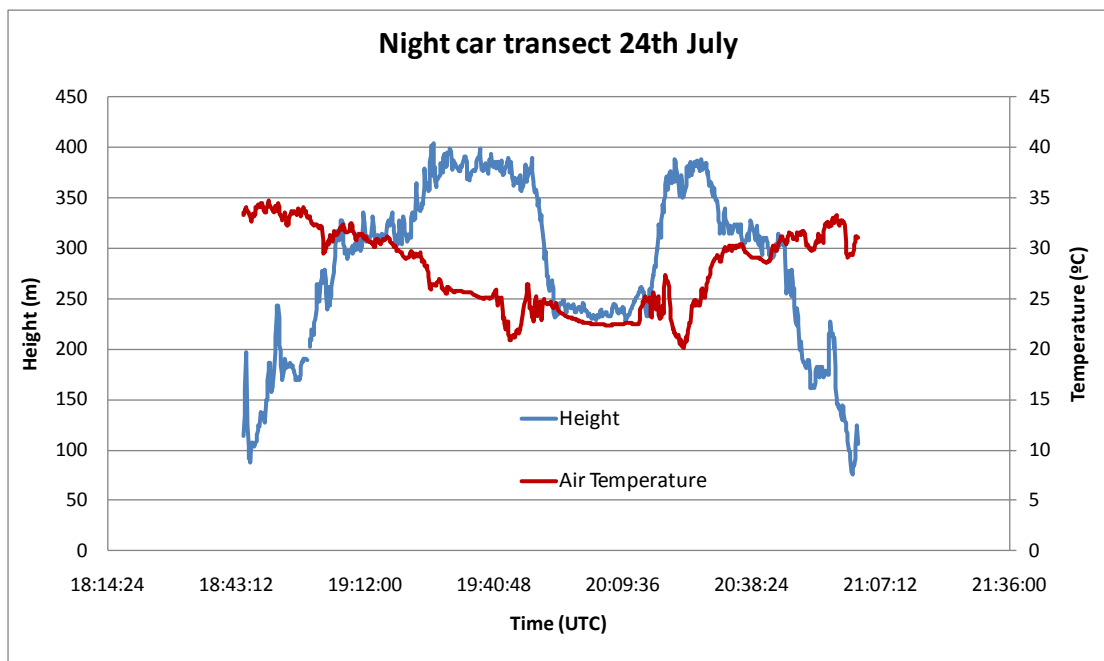


Figure 143.- Air temperature and height of the transect on 24th of July at night.

Measurements in fixed masts

Fixed masts were set up for continuous measurements stored every 5 minutes in two spots (one hot target and one cold target) in the city of Athens during Thermopolis campaign. Table 5 shows the location of the masts, the type of site, the parameters measured and the instrumentation used.

Table 69.- Fixed Masts description.

Site	Measured parameter	Instrument
Green Grass Panathinaikos Stadium (37° 59.226'N,23°45.216'E)	Air Temperature	HOBO TMC6-HB
	Radiometric Temperature	OPTRIS CT-LT15
Bare Soil NTUA Soccer Field (37° 58.886'N, 23°46.993'E)	Air Temperature	HOBO TMC6-HB
	Radiometric Temperature	OPTRIS CT-LT15

Figure 20 shows the setting up of the equipment in the different areas.



Green Grass - Panathinaikos Stadium

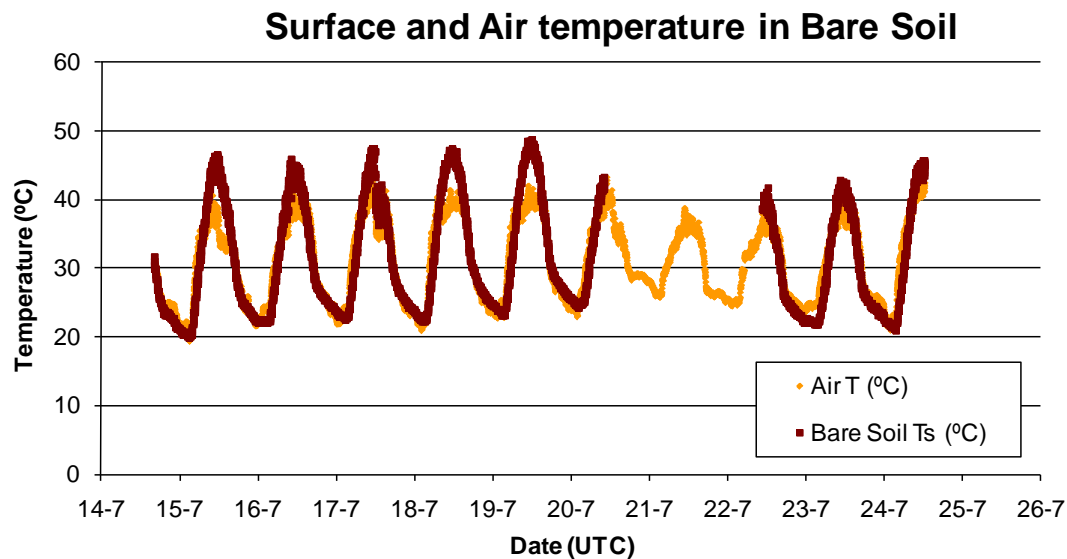


Bare Soil - NTUA Soccer Field

Figure 144.– Fixed masts in the Thermopolis field campaign.

Air temperature and ground radiometric temperature were acquired in both masts. Figure 21 shows the time serial acquired during Thermopolis Campaign. Not bare soil temperature was measured from 10h of 20/07/09 to 11h of 22/07/09 due to technical problems.

(a)



(b)

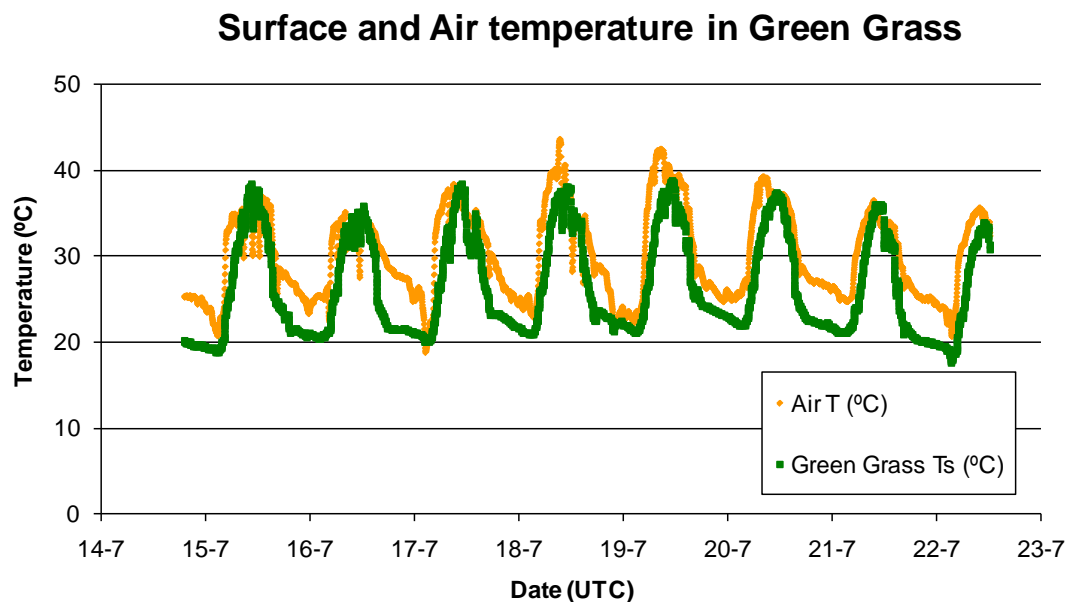


Figure 145.– Surface and Air Temperature measurements: (a) in the bare soil mast of NTUA and (b) in the green grass mast of Panathinaikos Stadium.

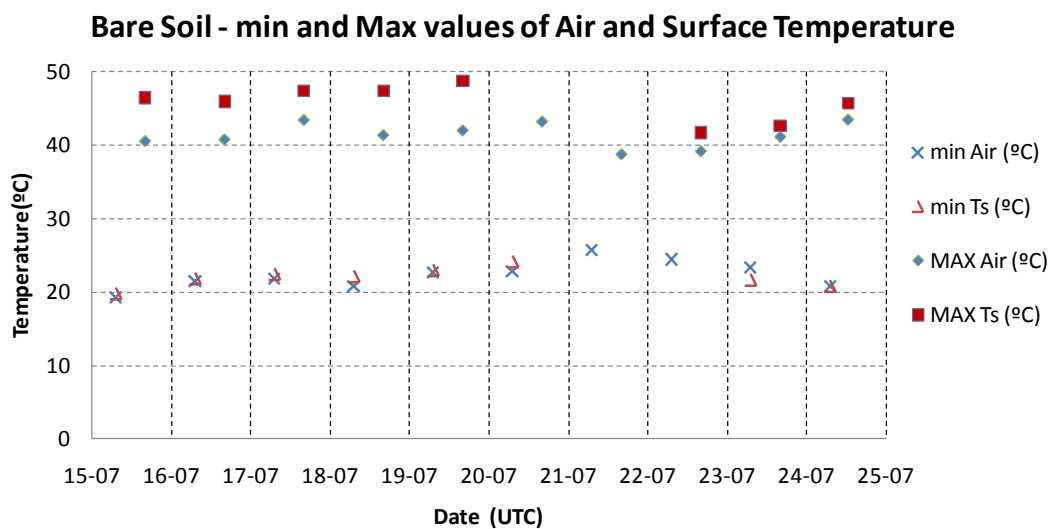
Figure 145 shows the maximum and minimum values of Air temperature and Surface Temperature registered for every day of measurement.

In bare soil, the higher difference between maximum and minimum was measured on the 15th (for Surface temperature a difference of 26.55°C) and 24th (for Air temperature a difference of 22.66°C); the lower difference was on the 23rd (a

difference of 20.9°C for Surface temperature) and 22nd (a difference of 14.7°C for Air temperature).

In green grass, the higher difference between maximum and minimum was measured on the 15th (for Surface temperature a difference of 19.6°C) and 19th (for Air temperature a difference of 21.1 °C); the lower difference was on the 21st (a difference of 15.0°C for Surface temperature and 11.8°C for Air temperature).

a)



b)

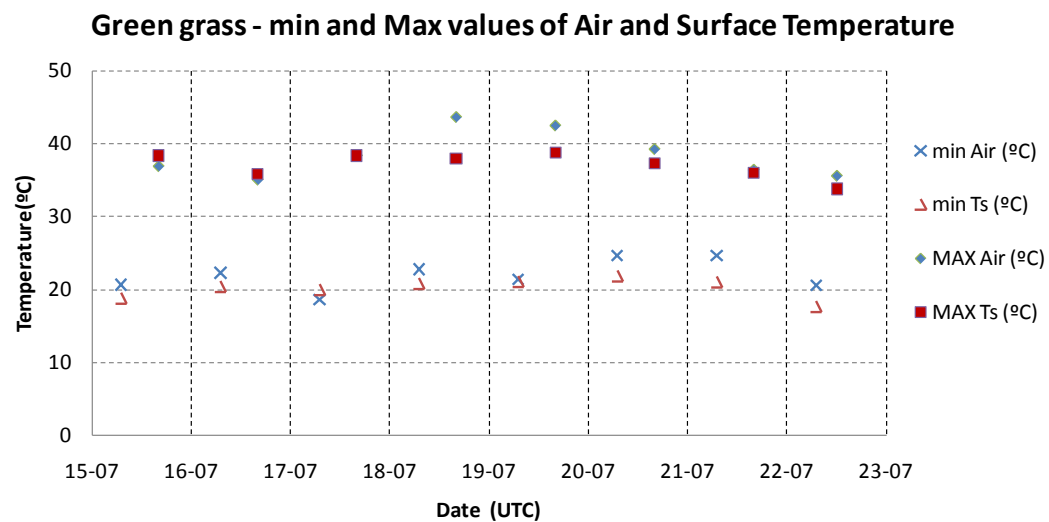


Figure 146.- Maximum and minimum values of Air temperature and Surface Temperature registered for every day of measurement in Bare Soil and Green grass masts.

Spectral characterization of urban surfaces

During the Thermopolis 2009 campaign, a spectral library of urban materials was built by the GCU. Reflectances and emissivities were obtained in visible and thermal infrared domain. Reflectances were obtained with GER 1500 spectroradiometer. Emissivities were obtained using the TES (Temperature and Emissivity Separation) algorithm. Although it was originally designed for ASTER data, TES algorithm can be also applied to *in situ* measurements collected with multiband radiometers, such as the CIMEL CE-312-2 with five TIR narrow bands (Payan and Royer, 2004; Jiménez-Muñoz and Sobrino, 2006). Figure 23 shows the kind of surfaces that were characterized: green grass, bare soil, rocks, asphalt, and different urban surfaces.



Green Grass - Panathinaikos Stadium



Bare Soil - NTUA Soccer Field



Floor 1



Floor 2



Floor 3



Floor 4

Urban surfaces – Ancient Library



Acropolis



Floor 1



Floor 2



Floor 3



Floor 4

Urban surfaces – Syntagma Square



Metal Grid



Black glass

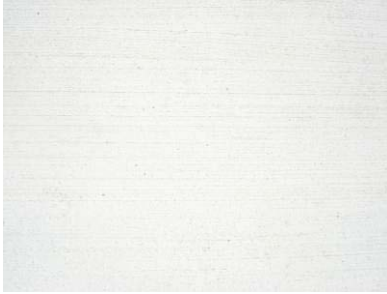
Urban surfaces – Acropolis Museum



Asphalt



Terrace



Grey floor 1



Grey Floor 2



Grey Floor 3



Red Floor 1



Red Floor 2



Red Floor 3

Urban surfaces – NTUA

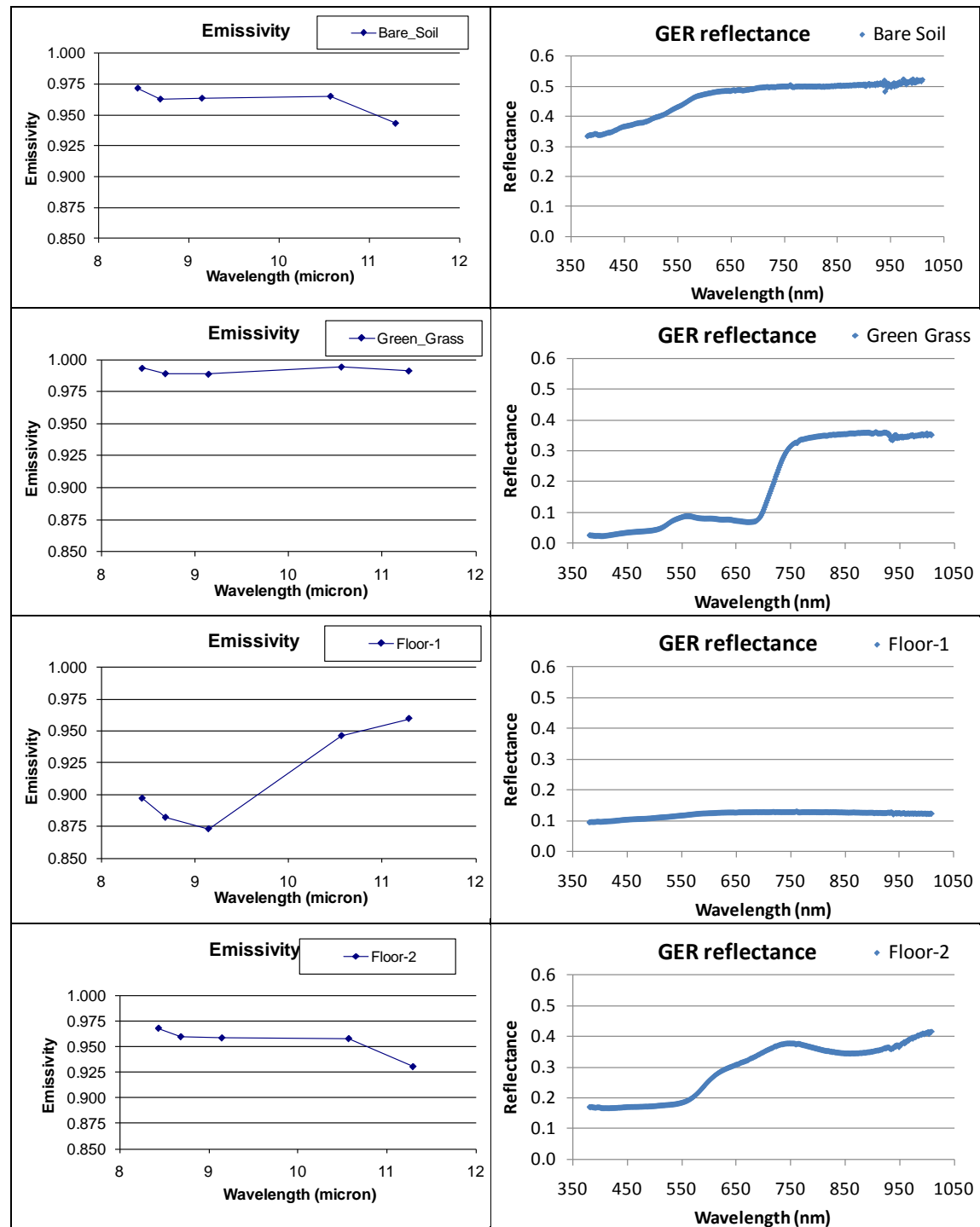


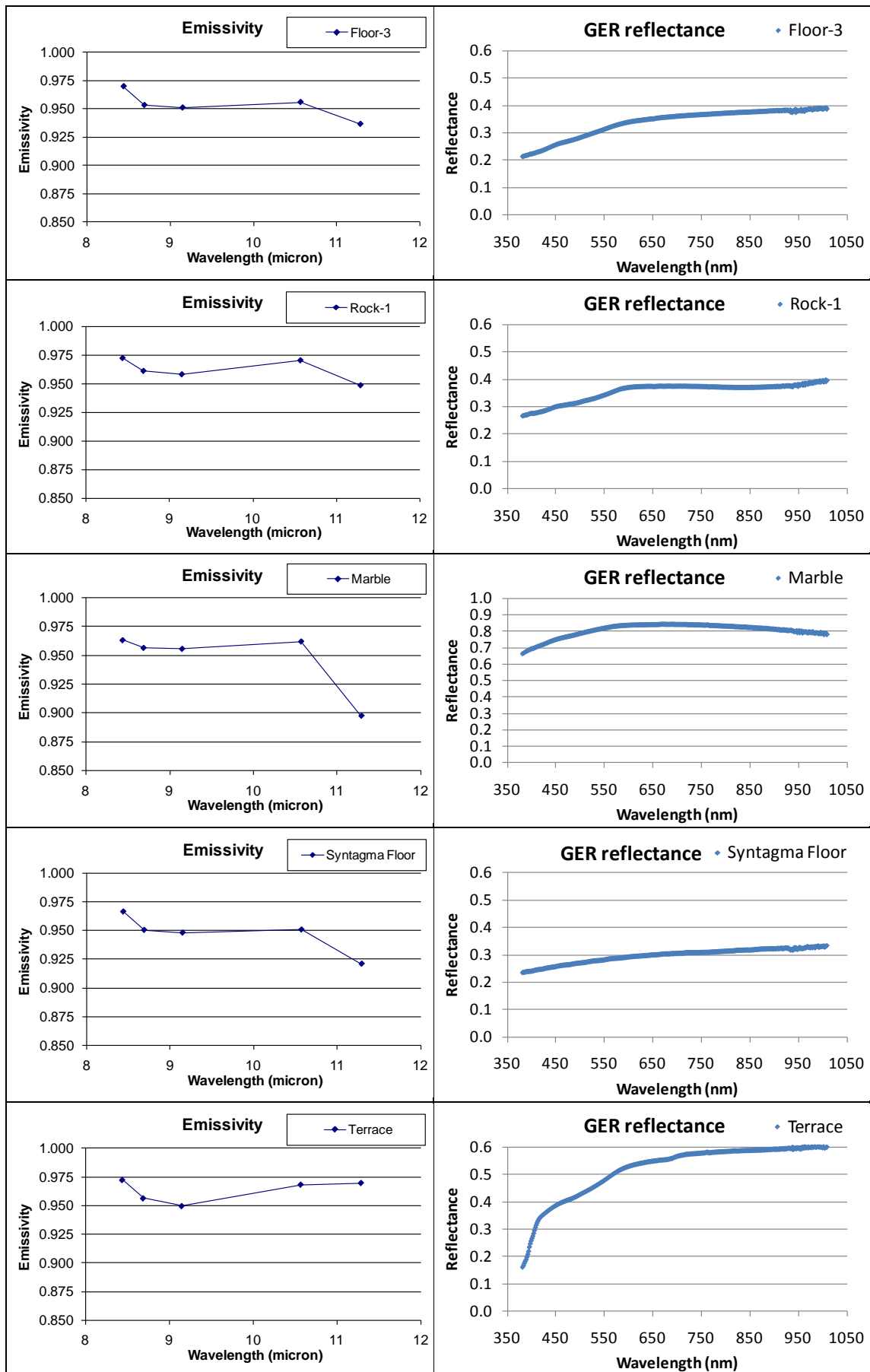
Terrace

Urban surfaces – Ministry of Environment

Figure 147.- Panoramic view and detail of the urban surfaces characterized with reflectivity and emissivity during the Thermopolis campaign.

Figure 148 shows some of the emissivity and reflectance obtained for the different measurements of spectral characterization of natural and urban surfaces.





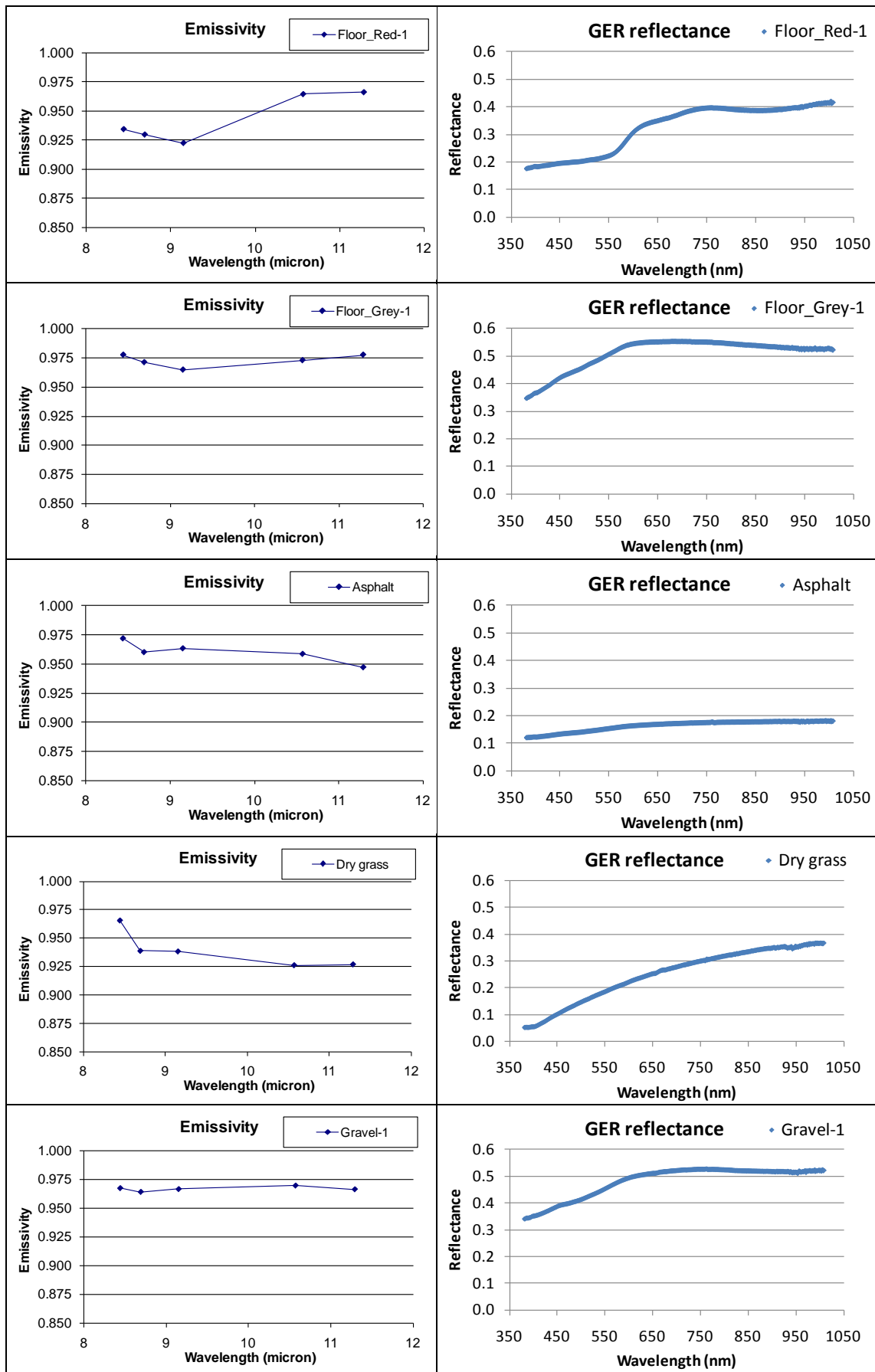


Figure 148.- Emissivity and reflectance of natural and urban surfaces.

Figure 149 shows the reflectance spectra of some of the most representative urban surfaces measured with the GER 1500.

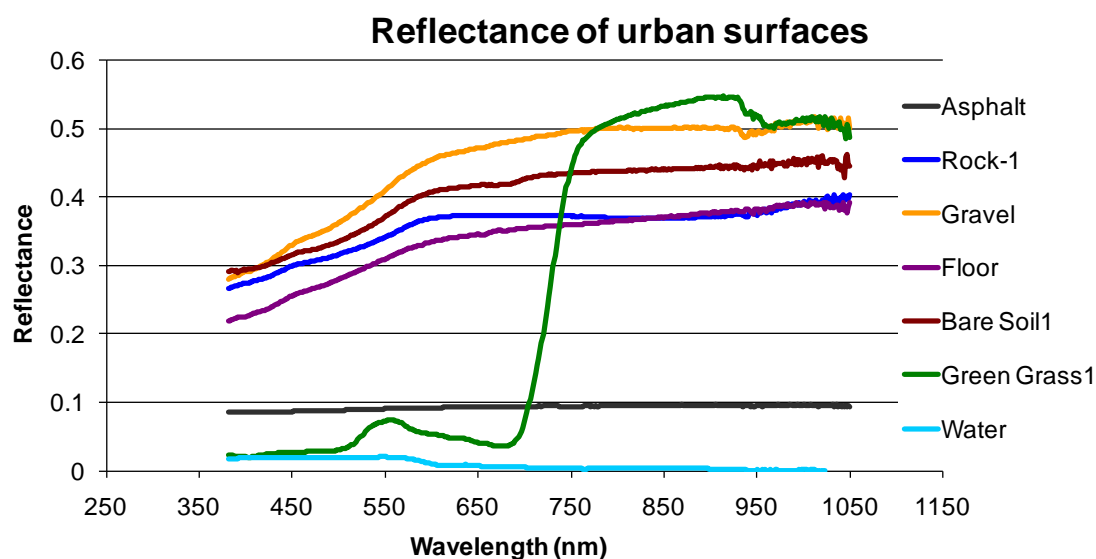


Figure 149.- Example of reflectance spectra of different surfaces measured with the GER 1500 spectroradiometer

Figure 150 shows the emissivity spectra of some of the most representative urban surfaces obtained by applying the TES algorithm to the measures of the CIMEL-CE312 radiometer.

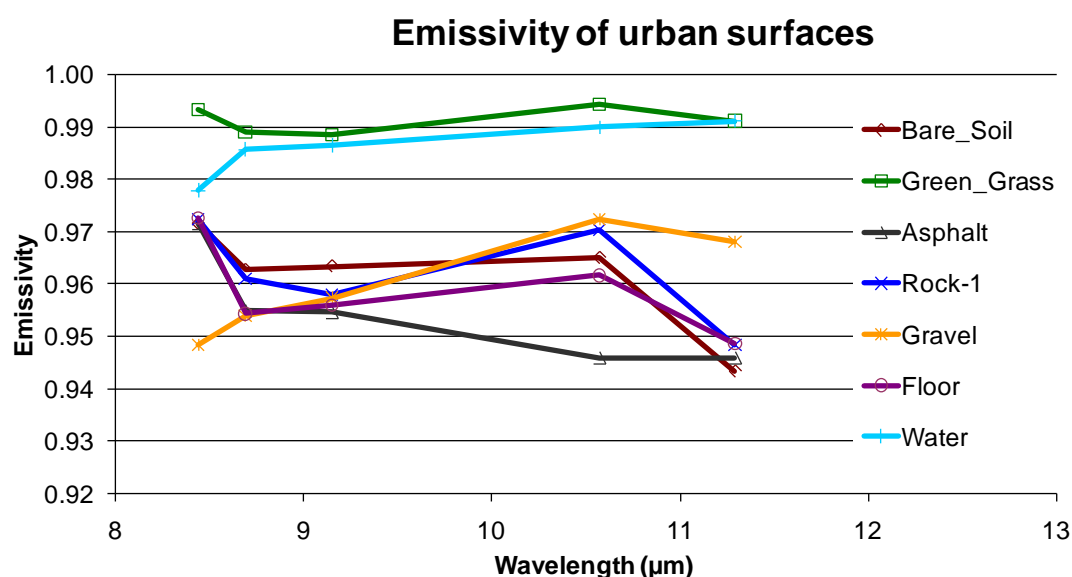


Figure 150.- Example of the some emissivity spectra for different urban surfaces measured with CIMEL thermal radiometer

Additionally, Table 6 shows the values of reflectance in two channels. These values have been obtained by filtering the data with AVHRR channels 1 and 2 response functions. These channels have effective wavelengths in the red and near infrared, and may be used for example for the calculation of vegetation indexes such as NDVI (Normalized Difference Vegetation Index). Emissivity values are also summarized in the table, where 10.54 μm corresponds to the broad band of the CIMEL CE-312 radiometer.

Table70.- Emissivity for the 6 bands of the CIMEL radiometer and effective reflectance for the AVHRR bands 1 and 2 of different natural and urban surfaces of the spectral characterization measurements database.

		Effective wavelength (micron)							
		8.44	8.69	9.15	10.57	11.29	Broad 10.54	0.630	0.910
Place	Sample	Emissivity						Reflectance	
NTUA	Bare_Soil	0.972	0.963	0.963	0.965	0.943	0.965	0.480	0.502
Panathinaikos Soccer Field	Green_Grass	0.993	0.989	0.989	0.994	0.991	0.987	0.097	0.339
Ancient Library	Floor-1	0.897	0.882	0.873	0.946	0.960	0.935	0.126	0.126
Ancient Library	Floor-2	0.968	0.960	0.958	0.958	0.931	0.963	0.297	0.367
Ancient Library	Floor-3	0.970	0.953	0.951	0.956	0.937	0.958	0.349	0.375
Acropolis	Rock-1	0.972	0.961	0.958	0.970	0.948	0.969	0.371	0.374
Acropolis	Marble	0.963	0.957	0.956	0.962	0.897	0.953	0.835	0.815
Syntagma Square	Syntagma Floor	0.966	0.950	0.948	0.951	0.921	0.945	0.298	0.317
NTUA	Terrace	0.972	0.956	0.950	0.968	0.970	0.965	0.545	0.587
NTUA	Floor_Red-1	0.934	0.930	0.922	0.965	0.966	0.952	0.339	0.395
NTUA	Floor_Grey-1	0.978	0.971	0.965	0.973	0.978	0.975	0.545	0.536
NTUA	Asphalt	0.972	0.960	0.963	0.959	0.947	0.966	0.168	0.177
Acropolis	Dry grass	0.966	0.939	0.938	0.926	0.927	0.936	0.252	0.334
Acropolis	Gravel-1	0.967	0.964	0.966	0.970	0.966	0.974	0.505	0.520

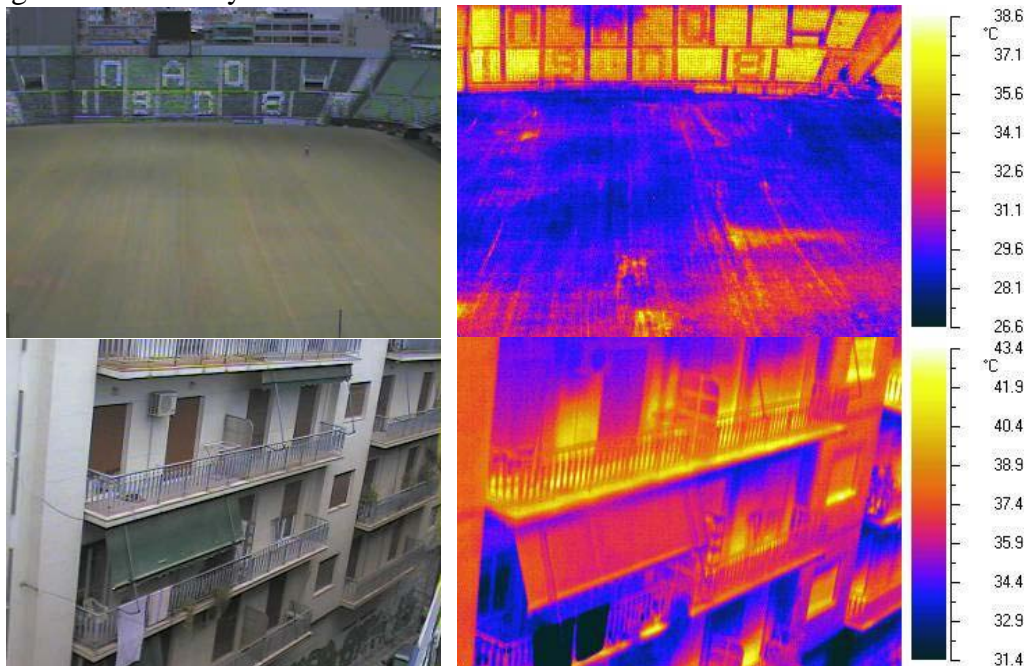
Urban Thermography

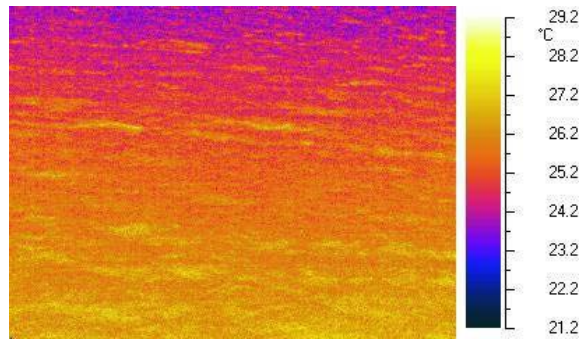
Thermal images were acquired simultaneously with the AHS flights for Urban Thermography (UT). Other imagery was acquired out of the flight time in order to support the data analysis and processing. Additionally, the front of important buildings and monuments was also measured by the thermal cameras (Parthenon, Acropolis museum, etc.), as well as some avenues in the city. Visible images of the field of view were also obtained by the cameras. The following pages show a summary of the thermal images taken for every day of the campaign:

Table 71: Summary of the thermal images taken for every day of the campaign:

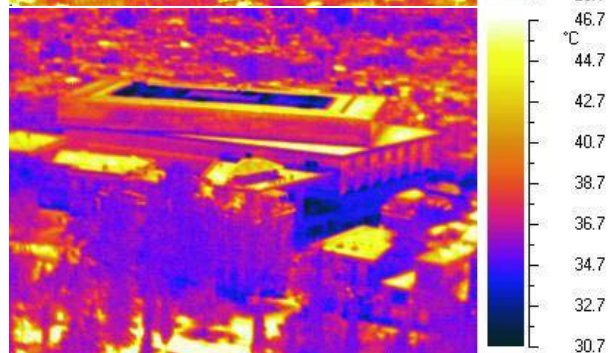
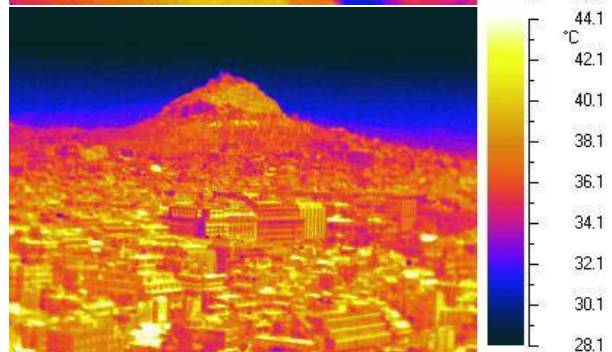
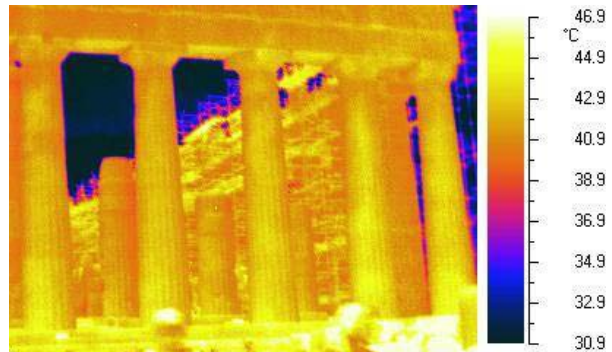
Day	Places where thermal images were taken
16 th july 2010	Panathinaikos Stadium (37° 59.226'N, 23°45.216'E) and Marathonos Lake (38°10.59'N, 23°54.352'E)
17 th july 2010	top of Acropolis (37° 58.312'N, 23°43.629'E)
18 th july 2010	during the day from Syntagma square (37° 58.54'N, 23°44.063'E) and during the night from Marathonos Lake
19 th july 2010	Acropolis
20 th july 2010	roof of the Acropolis museum (37° 58.122'N, 23°43.732'E)
21 st july 2010	Marathonos Lake
23 rd july 2010	Ministry of Environment (37°59.98'N, 23°43.982'W)
24 th july 2010	Acropolis and Marathonos Lake

Images from 16th July 2010:

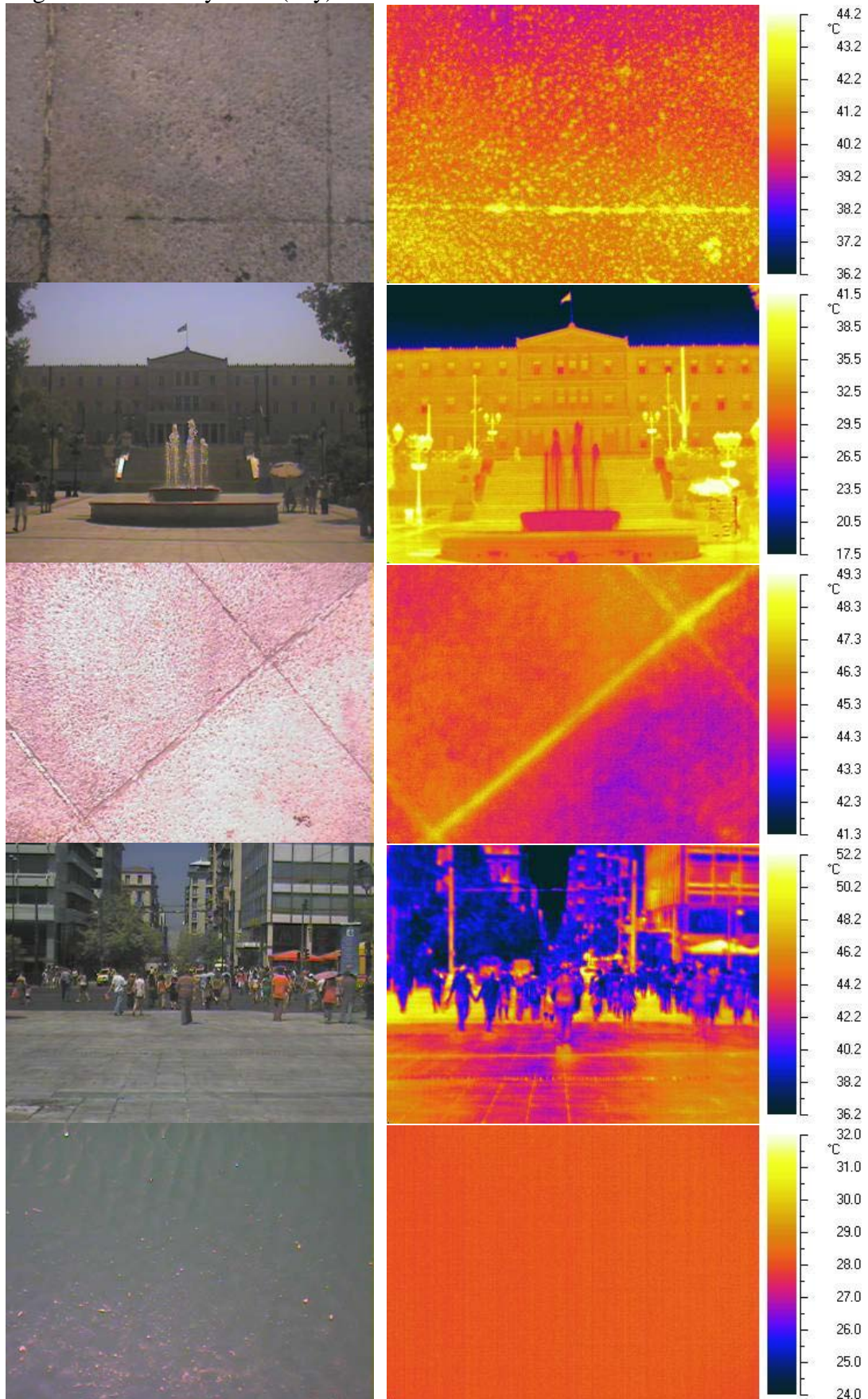




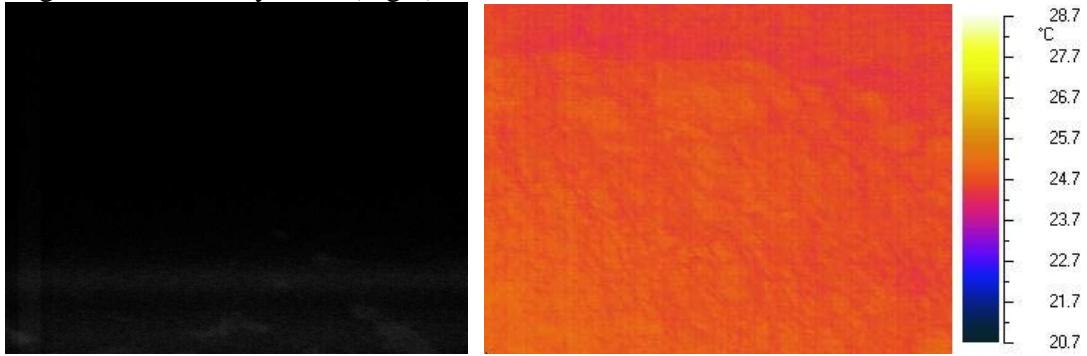
Images from 17th July 2010:



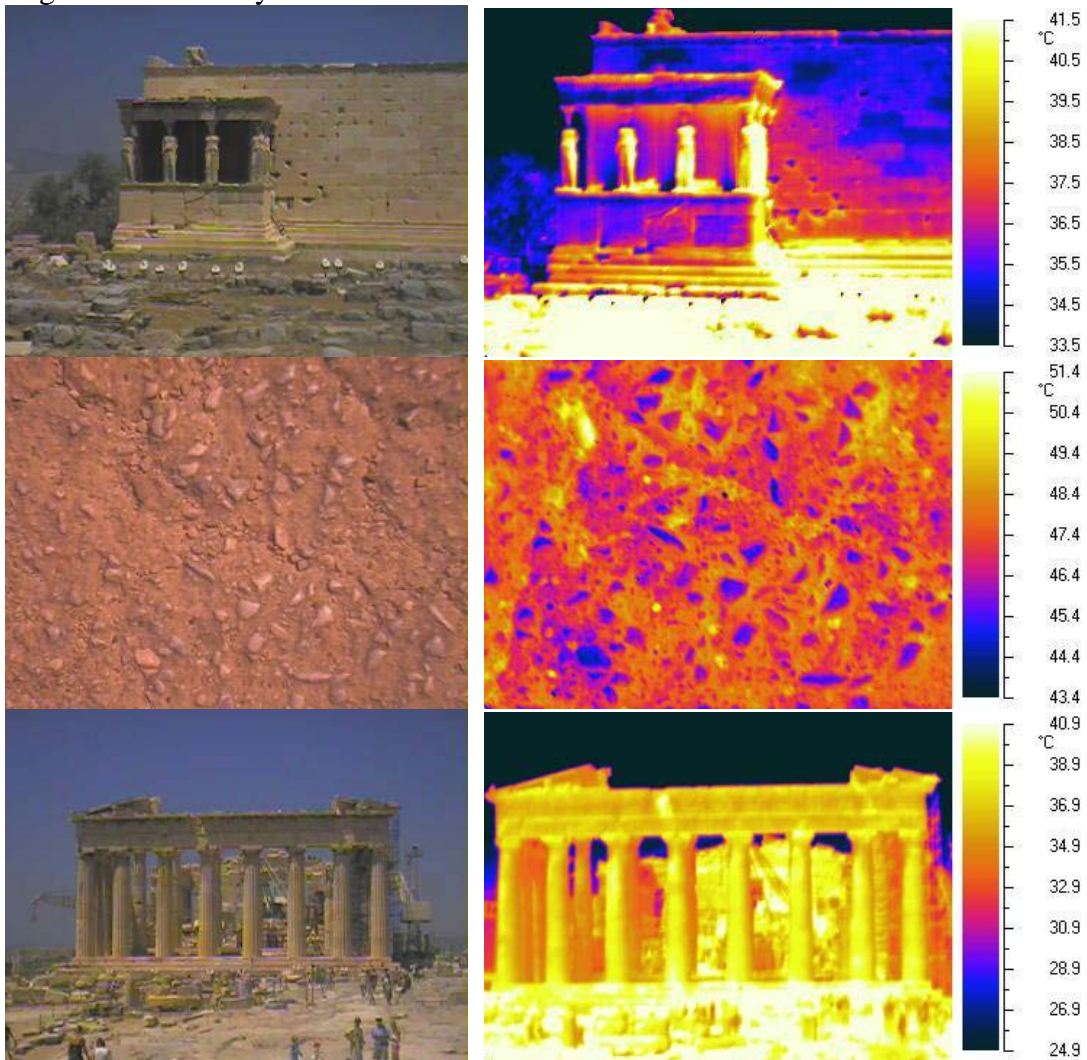
Images from 18th July 2010 (day):



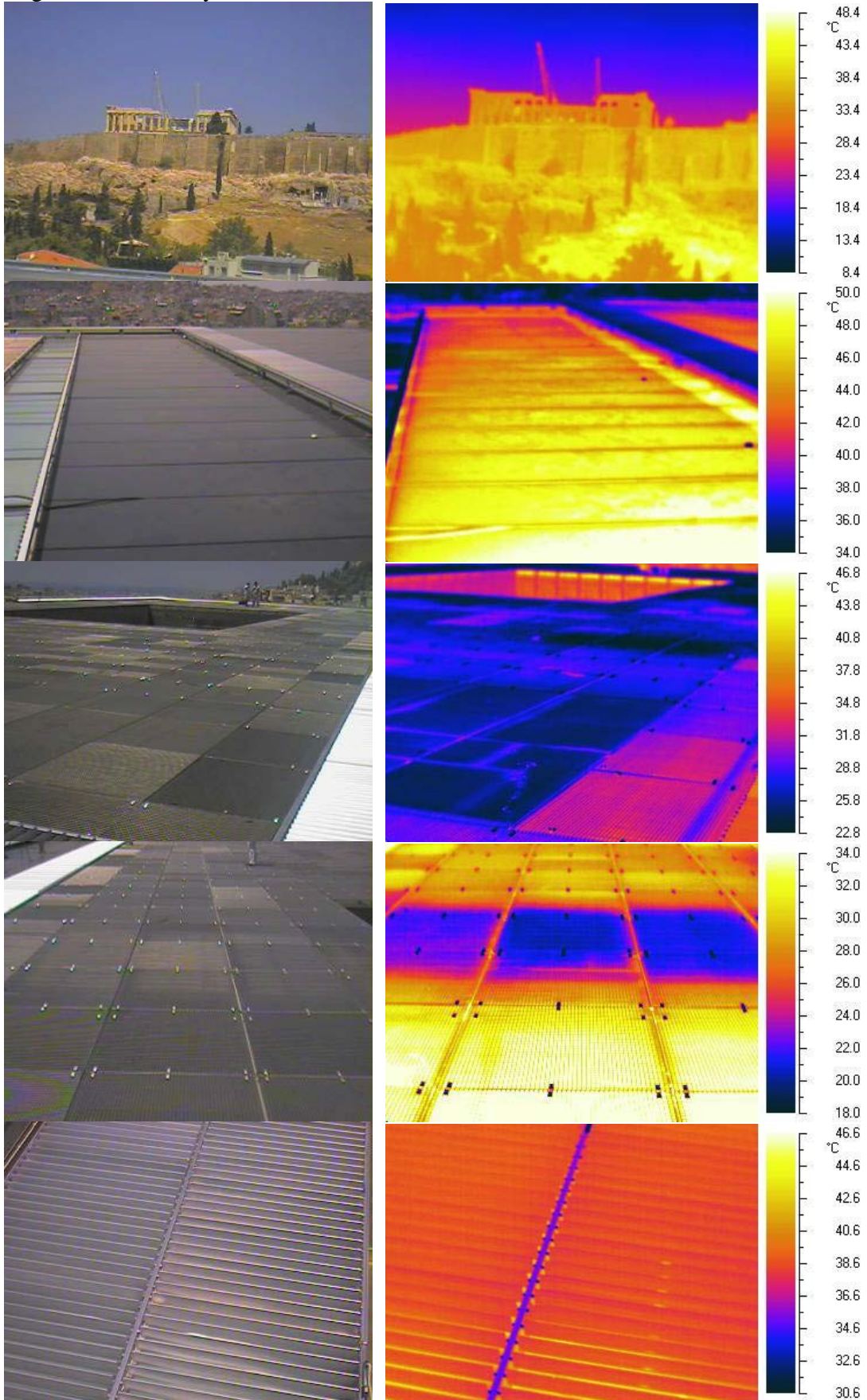
Images from 18th July 2010 (night):



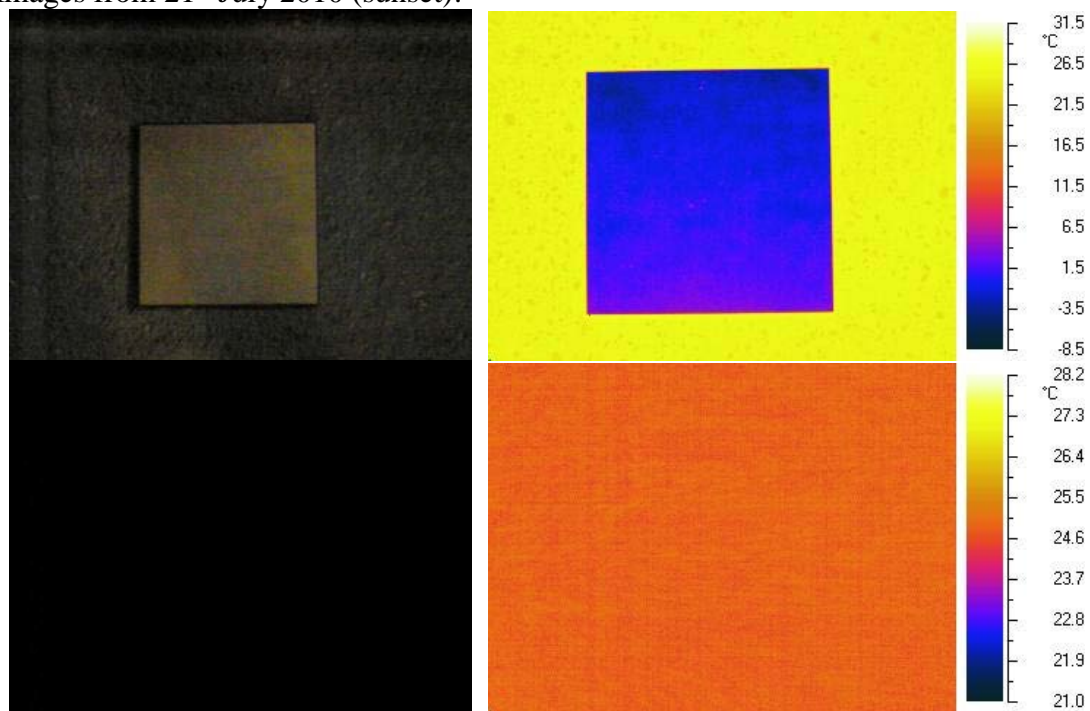
Images from 19th July 2010:



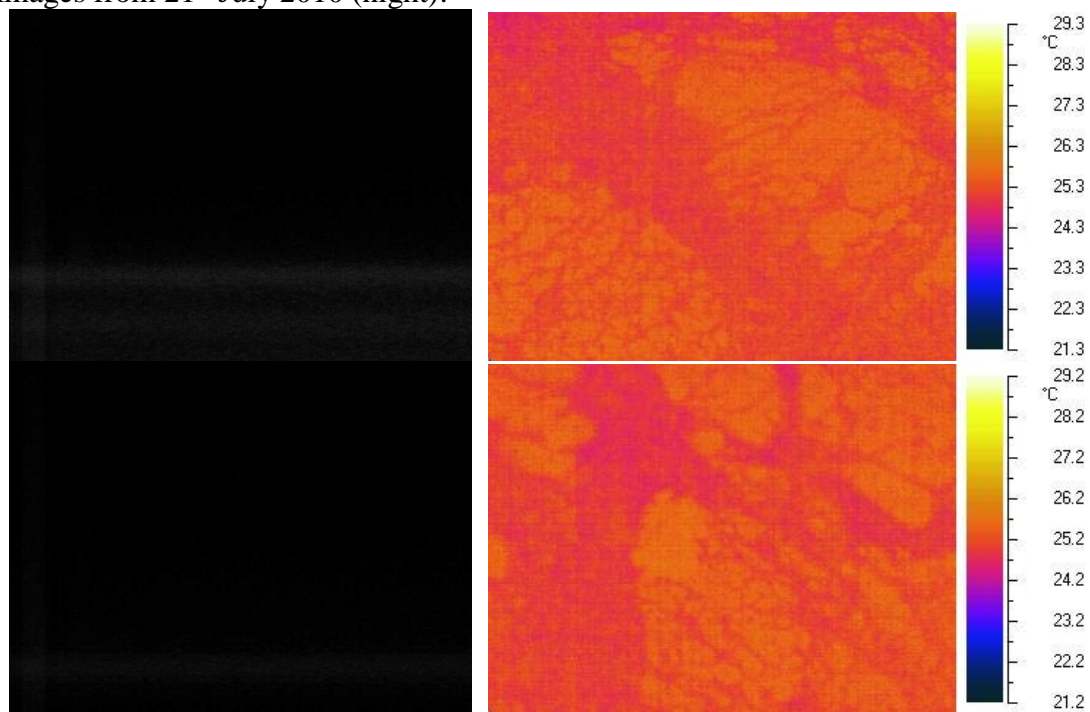
Images from 20th July 2010:



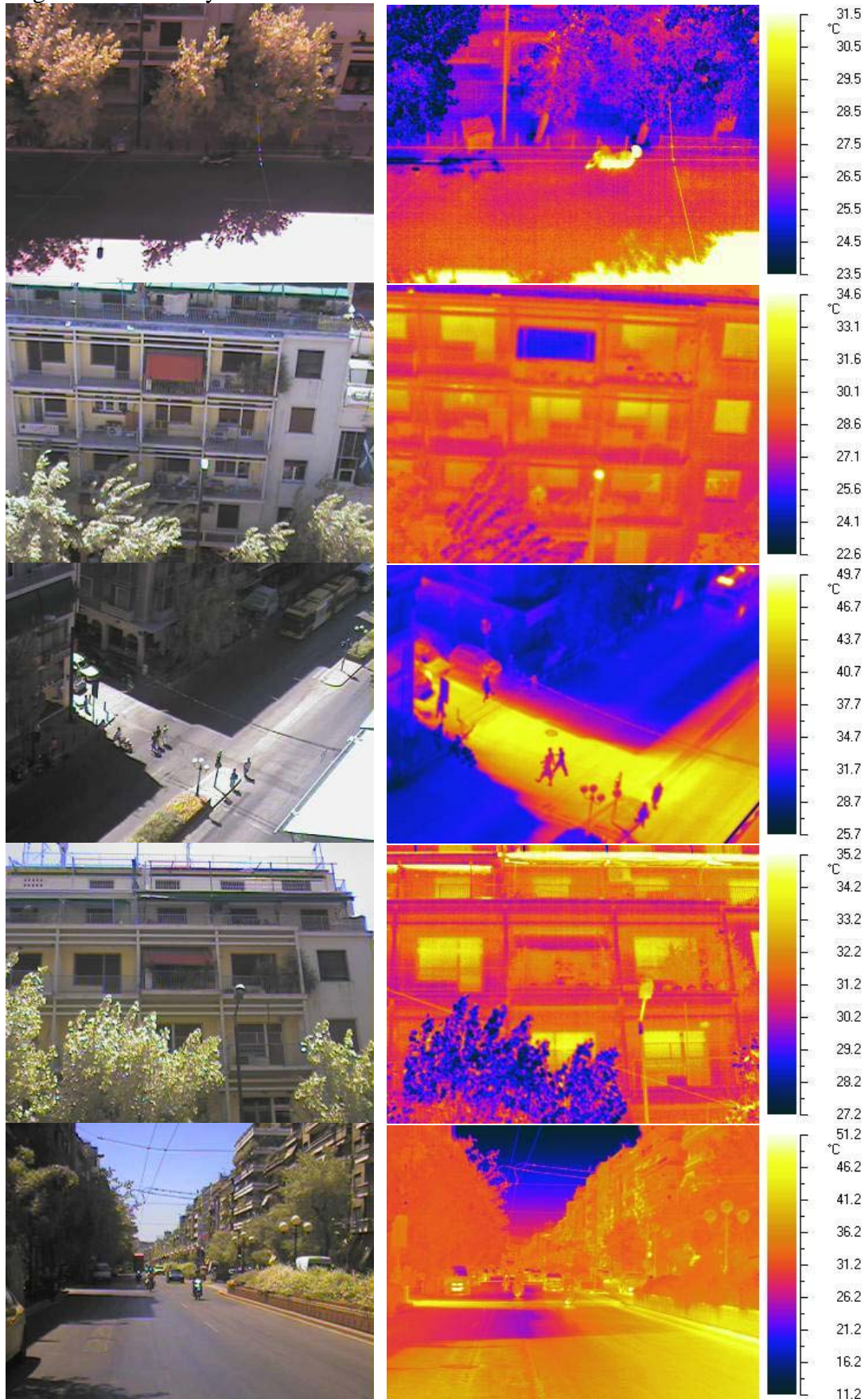
Images from 21st July 2010 (sunset):



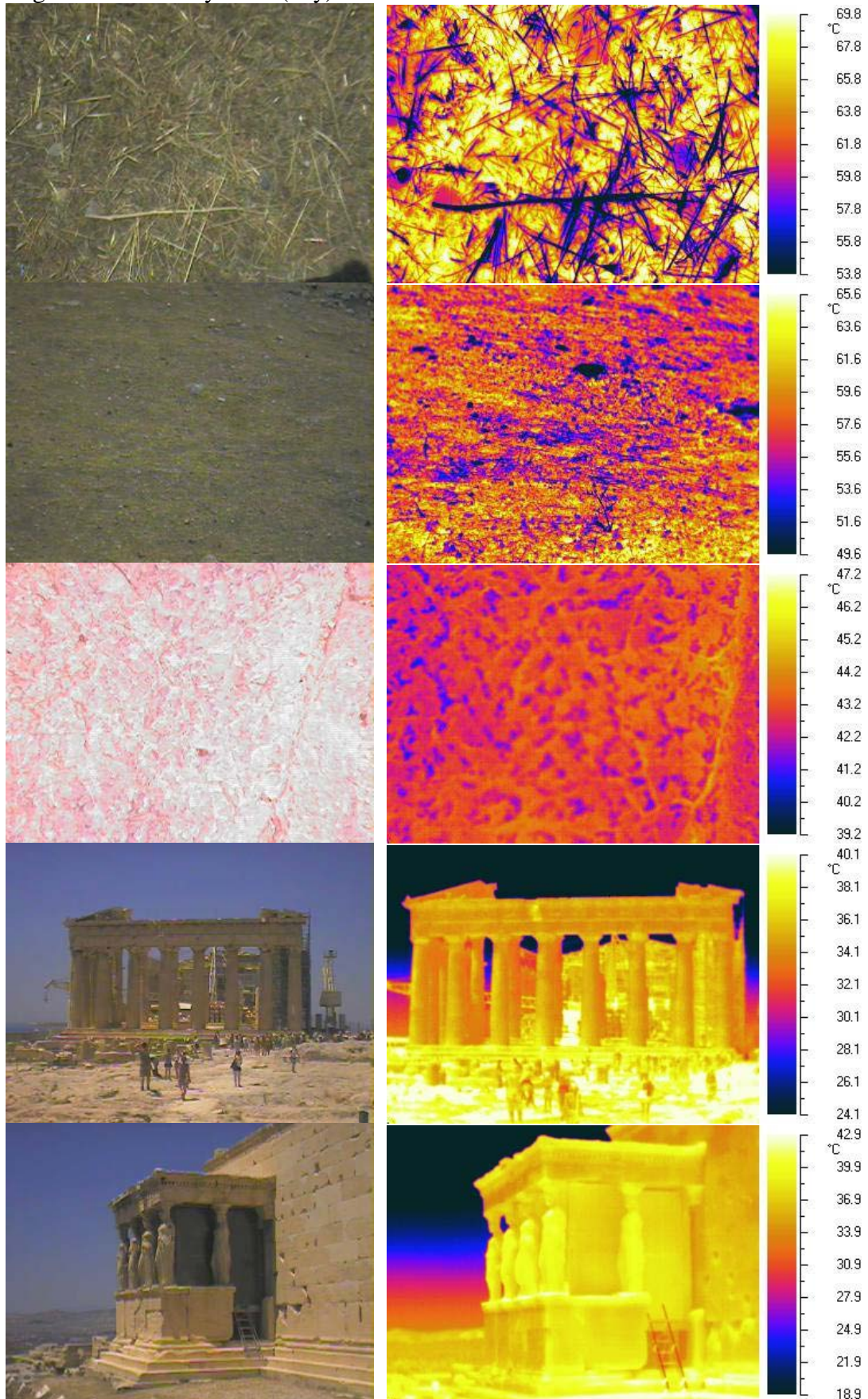
Images from 21st July 2010 (night):

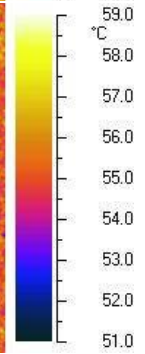
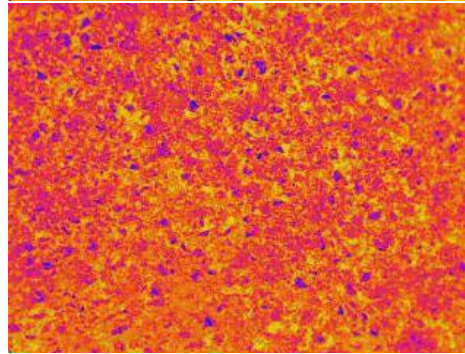
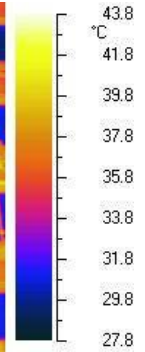
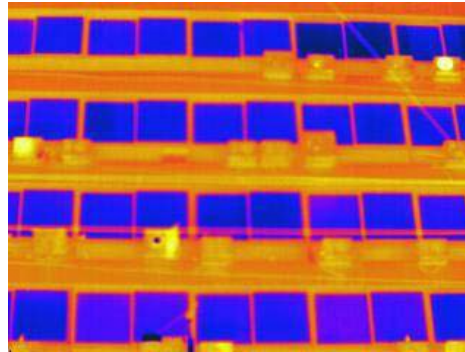
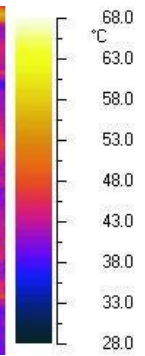
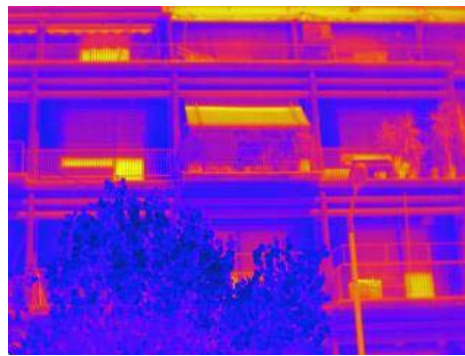


Images from 23rd July 2010:

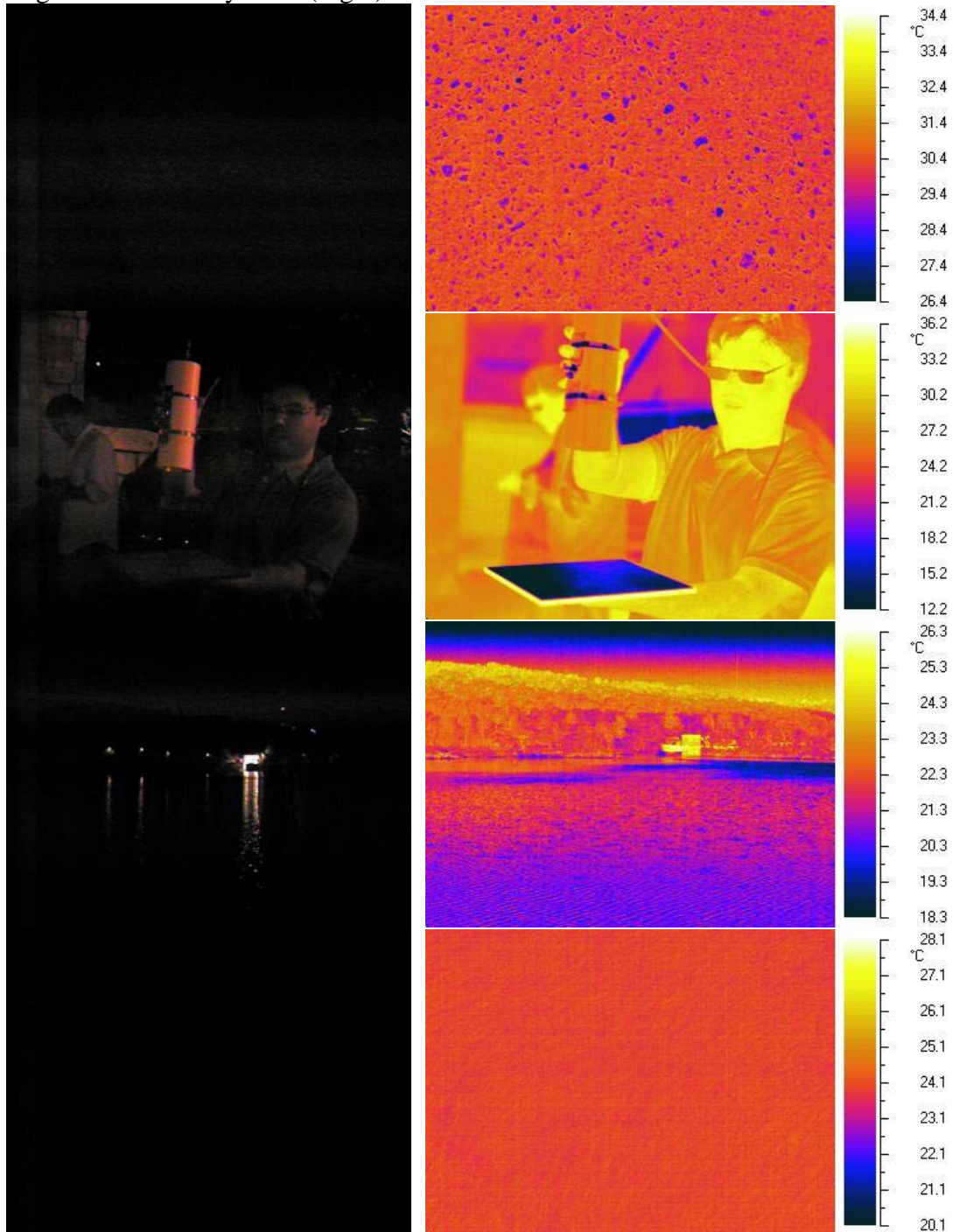


Images from 24th July 2010 (day):





Images from 24th July 2010 (night)



Conclusions

All the thermal and solar data measured during the Thermopolis 2009 are included into the data base. The data base is organized with folders by activities, and each sub-folder is delivered with a readme explaining the data in there.

To sum up, the experimental work of the Global Change Unit of the University of Valencia was the measurement of reflectivity, thermal radiometric temperatures, emissivities, atmospheric radiances, air temperature and temperature transects within the city of Athens area. Table 7 shows the work plan carried out by the GCU, explaining the activity carried out each day of the campaign and the instrument used. Underline that transects with car and transects for cal/val activities were performed concurrently to the flight overpasses (AHS).

Table 72.- Work Plan carried out by GCU in the framework of Thermopolis 2009.

DATE	CIMEL CE 312-2	GER 1500	RAYTEK ST6	NEC TH9100	OPTRIS CT-LT15	HOBO	AHLBORN
14/072009					2 fixed masts on Bare Soil (NTUA) and on Green Grass (Panathinaikos Stadium)	2 fixed masts on Bare Soil (NTUA) and on Green Grass (Panathinaikos Stadium)	
15/072009					2 fixed masts on Bare Soil (NTUA) and on Green Grass (Panathinaikos Stadium)	2 fixed masts on Bare Soil (NTUA) and on Green Grass (Panathinaikos Stadium)	
16/07/2009	Characterization on Bare Soil (NTUA) Cal/Val activities on Green Grass (Panathinaikos) and Water (Marathonos Lake)	Cal/Val activities on Green Grass (Panathinaikos) and Water (Marathonos Lake)	Cal/Val activities on Green Grass (Panathinaikos) and Water (Marathonos Lake)	Cal/Val activities Water (Marathonos Lake)	2 fixed masts on Bare Soil (NTUA) and on Green Grass (Panathinaikos Stadium)	2 fixed masts on Bare Soil (NTUA) and on Green Grass (Panathinaikos Stadium)	Car transect
17/07/2009	Characterization of urban surfaces (Ancient Library) Characterization of Acropolis Materials	Characterization of urban surfaces (Ancient Library) Characterization of Acropolis Materials	Characterization of urban surfaces (Ancient Library) Characterization of Acropolis Materials	Characterization of Acropolis Materials	2 fixed masts on Bare Soil (NTUA) and on Green Grass (Panathinaikos Stadium)	2 fixed masts on Bare Soil (NTUA) and on Green Grass (Panathinaikos Stadium)	
18/07/2009	Characterization	Characterization	Characterization	Characterization	2 fixed masts on	2 fixed masts on	Car transects

9	and Cal/Val activities on urban surfaces (Syntagma Square) Cal/Val activities on Water (Marathonos Lake)	and Cal/Val activities on urban surfaces (Syntagma Square) Cal/Val activities on Water (Marathonos Lake)	and Cal/Val activities on urban surfaces (Syntagma Square) Cal/Val activities on Water (Marathonos Lake)	and Cal/Val activities on urban surfaces (Syntagma Square) Cal/Val activities on Water (Marathonos Lake)	Bare Soil (NTUA) and on Green Grass (Panathinaikos Stadium)	Bare Soil (NTUA) and on Green Grass (Panathinaikos Stadium)	
19/07/2009				Characterization of Acropolis Materials	2 fixed masts on Bare Soil (NTUA) and on Green Grass (Panathinaikos Stadium)	2 fixed masts on Bare Soil (NTUA) and on Green Grass (Panathinaikos Stadium)	

DATE	CIMEL CE 312-2	GER 1500	RAYTEK ST6	NEC TH9100	OPTRIS CT-LT15	HOBO	AHLBORN
20/07/2009	Characterization and Cal/Val activities on urban surfaces (Acropolis Museum)	Characterization and Cal/Val activities on urban surfaces (Acropolis Museum)	Characterization and Cal/Val activities on urban surfaces (Acropolis Museum)	Characterization and Cal/Val activities on urban surfaces (Acropolis Museum)	2 fixed masts on Bare Soil (NTUA) and on Green Grass (Panathinaikos Stadium)	2 fixed masts on Bare Soil (NTUA) and on Green Grass (Panathinaikos Stadium)	Cal/Val activities on urban surfaces (Acropolis Museum)
21/07/2009	Cal/Val activities on Water (Marathonos Lake)		Cal/Val activities on Water (Marathonos Lake)	Cal/Val activities on Water (Marathonos Lake)	2 fixed masts on Bare Soil (NTUA) and on Green Grass (Panathinaikos Stadium)	2 fixed masts on Bare Soil (NTUA) and on Green Grass (Panathinaikos Stadium)	Car transects

					Stadium)	Stadium)	
22/07/2009	Characterization and Cal/Val activities on urban surfaces (NTUA)	Characterization and Cal/Val activities on urban surfaces (NTUA)	Characterization and Cal/Val activities on urban surfaces (NTUA)		2 fixed masts on Bare Soil (NTUA) and on Green Grass (Panathinaikos Stadium)	2 fixed masts on Bare Soil (NTUA) and on Green Grass (Panathinaikos Stadium)	
23/07/2009	Characterization and Cal/Val activities on urban surfaces (Ministry of Environment)	Characterization and Cal/Val activities on urban surfaces (Ministry of Environment)	Characterization and Cal/Val activities on urban surfaces (Ministry of Environment)	Characterization and Cal/Val activities on urban surfaces (Ministry of Environment)	Fixed in a mast on Bare Soil (NTUA)	Fixed in a mast on Bare Soil (NTUA)	
24/07/2009	Characterization and Cal/Val activities on the Acropolis ⇒ Cal/Val activities on Water (Marathonos Lake)	Characterization and Cal/Val activities on the Acropolis	Characterization and Cal/Val activities on the Acropolis Cal/Val activities on Water (Marathonos Lake)	Characterization and Cal/Val activities on the Acropolis Cal/Val activities on Water (Marathonos Lake)	Fixed in a mast on Bare Soil (NTUA)	Fixed in a mast on Bare Soil (NTUA)	Car transect

9. References

Gillespie, A., Rokugawa, S., Matsunaga, T., Cothorn, J. S., Hook, S., and Kahle, A. B., 1998 “A temperature and emissivity separation algorithm for advanced spaceborne thermal emission and reflection radiometer (ASTER) images”. *IEEE Transactions on Geoscience and Remote Sensing*, 36, 1113-1126.

Jiménez-Muñoz, J. C., and Sobrino, J. A., 2006. “Emissivity spectra obtained from field and laboratory measurements using the temperature and emissivity separation algorithm”. *Applied Optics*, 45(27), 7104-7109.

Payan, V. and Royer, A., 2004. “Analysis of Temperature Emissivity Separation (TES) algorithm applicability and sensitivity”. *International Journal of Remote Sensing*, 25(1), 15-37.

6. HEAT FLUXES MEASUREMENTS AND MODELING (CERTH).

6.1 Overview

Fig. 151 summarises the main components of the experimental work conducted during the experiment in Athens for the calculation of and the modeling of heat fluxes.

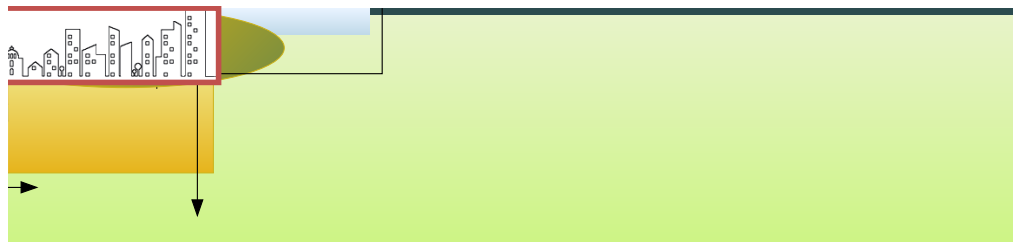


Figure 151. Overview

6.2. Introduction.

The alteration of the land surface and atmosphere by urban development leads to the creation of distinct urban climates. Ultimately, these urban climate effects are due to differences in the exchanges of heat, mass, and momentum between the city and its pre-existing landscape (Christen and Vogt 2004). Thus the understanding, prediction, and mitigation of urban climate effects are intricately tied to knowledge of surface-atmosphere exchanges in urban environments (Grimmond et al., 2004). The urban energy fluxes affect the whole boundary layer, its stability, thermodynamic properties, and the mixing layer height. Furthermore, the modified urban energy balance

compared to the rural areas results in typical urban climate phenomena like the urban heat island (Grimmond et al., 2004).

An effort has been made to investigate the energy exchange and partitioning over highly populated central-city surfaces in different campaigns all over the world. In recent years, studies in European cities add new aspects and results because of these cities have a distinct architectural styles, specific building materials, distinct climatic settings and energy use/emission patterns (Christen et al., 2002; Nemitz et al., 2002; Grimmond et al., 2004; Offerle et al., 2005). There are also examples of longer-term studies encompassing at least the full seasonal cycle and even multiple years (Grimmond et al., 2004; Offerle et al., 2005). All these studies document the temporal and spatial variability of flux partitioning, both within and between urban areas. However they are still limited.

Surface characteristics like albedo α , emissivity ϵ , complete aspect ratio λ_C , roughness length z_0 , or moisture availability significantly control the energy balance partitioning of any surface. Therefore, it is not only important to have accurate and representative measurements, but also detailed information on the characteristics of the surface and their spatial variability, i.e. on the urban two or three-dimensional structure, land cover, and typical materials. Also, the characteristics of the rural surroundings (e.g. surface cover and water availability) vary widely between cities and, therefore, can dramatically affect the urban modification of the surface energy balance Oke and Grimmond (2002).

When characterizing the structure of the urban atmosphere (Fig. 162), a fundamental distinction is made between the micro-scale effects that dominate the urban canopy layer (UCL), and the more homogenous urban boundary layer (UBL) climate above the buildings (Arnfield 2003). However, the influence of individual urban elements in fact extends above roof level into a roughness sub-layer (RSL), whose thickness depends on the nature of the underlying surface and where measurement difficulties over actual cities are emphasized (Rotach 1999).

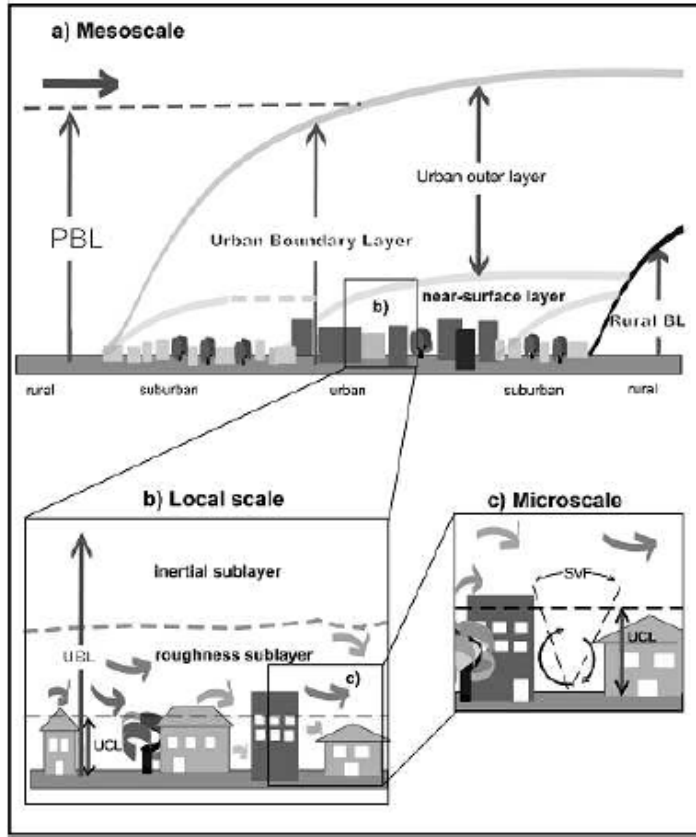


Figure 152: Sketch of the urban boundary layer structure indicating the various (sub) layers and their names (from Rotach et al., 2004a; modified after Oke, 1987).

If the upwind urban terrain is sufficiently homogenous, then above the canopy and RSL lies an inertial sub-layer (ISL), in which flow characteristics are fully adapted to the rough urban surface at the local land-use scale but are not disturbed by individual buildings (Roth 2000). Because vertical fluxes measured at any point within the ISL are conditioned by the spatially averaged properties of the underlying surface, an energy balance accounting of these fluxes provides a useful reference against which microscale variations within the canopy can be compared. Measurement of fluxes within the ISL also allows the problematic net horizontal advection term to be neglected in the urban surface energy balance equation, given in watts per meter squared as (Masson et al., 2002):

$$Q^* + Q_F + Q_H + Q_E + \Delta Q_s = 0 \quad (1)$$

where Q^* is net all-wave radiation, Q_F is anthropogenic heat, Q_H and Q_E are the respective turbulent fluxes of sensible and latent heat, and ΔQ_s is the net change in heat storage within the buildings, air, and ground down to a level where heat exchanges become negligible.

In this report, upward-directed turbulent flux densities are negative because they represent an energy loss from the surface. This has the advantage that all terms have a consistent sign convention, which defines whether a term is currently an energy gain (+) to or loss (−) from the surface.

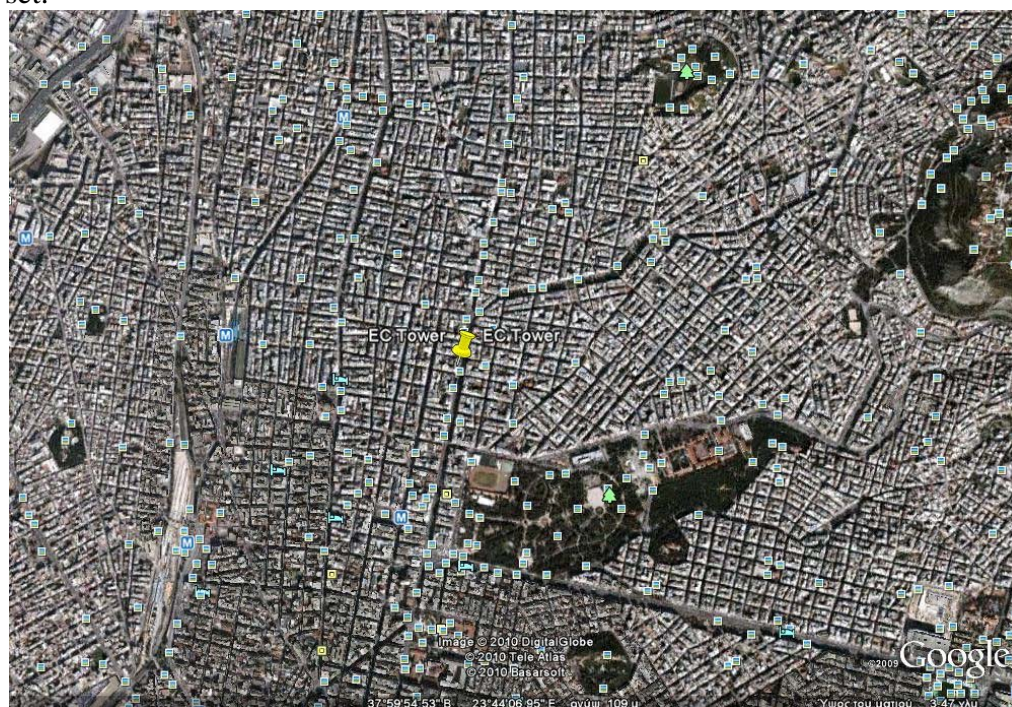
Anthropogenic heat is often omitted from the measured urban energy balance, both because of its small magnitude in residential settings, and because it is assumed to be embedded in other fluxes (Grimmond and Oke 2002). The latent heat flux (Q_E) may be substantial in vegetated areas, but for those dominated by “dry” surfaces, this component can be marginalized as well (Masson et al. 2002).

During the Thermopolis 2009 campaign local scale heat fluxes were measured at the city centre. Also, with the aid of the data from aircraft flights heat fluxes were modelled spatially. These flux data provide information on the summertime surface energy balance in a densely built-up area (sparse vegetation, tall buildings and deep street canyons) under a range of wind conditions. Aircraft measured heat fluxes provide independent data against which to evaluate and interpret the local-scale flux data.

6.3. Methods

6.3.1. Measurement site and instrumentation

The observation site in the urban area was on the rooftop of a building of the Ministry of Environment. The height of the building is 23.8 m. The observation yard is the flat rooftop made of cement concrete materials, the area of which is 20 m × 15 m. In the middle of the rooftop there is a small room of 2 m height where the 10 m mast was set.



Picture 153. Aerial photograph of the study area. EC tower is shown in yellow.

The selected site is representative of the city center and ensures a very large homogeneous fetch as depicted in the following figure:



Figure 154. Ten-meter flux tower in the roof of a 7-storey building and the respective fetch.

Details on instrumentation used, are depicted in the following Table 73 and 74:

Table 73 Measurement site description

Site	N	E	Height ASL	Comments (e.g. site type etc)
Patision	37° 59' 57.37"	23° 43' 58.78"	in the roof of a 7-storey building	the surrounding is buildings and the building, where the 10 m mast was installed, is higher than the others

Table 74: Parameters and frequency of measurements

Period and type of measurement (e.g. continuous with 5-min resolution, etc)	Measured parameter	Instrument
Period: 17/7/2009 noon– 28/7/2009 morning	WS (m/s) in 1 st height	3-cup wind sentry anemometer 03102VM
Type: Continuous with 1-sec resolution		(0-5V output), YOUNG
the same as above	WS (m/s) in 2 nd height	3-cup wind sentry anemometer 03102VM
		(0-5V output), YOUNG
the same as above	WS (m/s) in 3 rd height	3-cup wind sentry anemometer 03102VM
		(0-5V output), YOUNG
the same as above	Temperature (°C) in 1 st height	Thermo-sensor-Compact 2.1280.00.161,Thies Clima
the same as above	Temperature (°C) in 2 nd height	Thermo-sensor-Compact 2.1280.00.161,Thies Clima
the same as above	Temperature (°C) in 3 rd height	Thermo-sensor-Compact 2.1280.00.161,Thies Clima
the same as above	RH (%) and Temperature (°C) in 1 st height	Hygroclip S3C03, ROTRONIC
the same as above	RH (%) and Temperature (°C) in 2 nd height	Vaisala Probe HMP45A
the same as above	1) u (m/s) 2) v (m/s) 3) w (m/s) 4) Temperature (°C)	Sonic anemometer – CSAT3, Campbell Scientific
the same as above	Pressure (mb)	Barometer CS100, Setra
the same as above	WS (m/s) and WD (degrees) in the top of the tower	Wind sentry anemometer 03002LM (4-20mA outputs), YOUNG

6.3.2. Calibration, validation, data acquisition

For all the instruments it was the first times that were used in a field experiment, except of Vaisala which was used before for a six month period of measurements; all were factory-calibrated.

6.3.3. Protocol of measurements, results and discussion

The instruments were installed in the 9-meter tower in certain heights as follows:

1m	Hygroclip (RH+Temp)
2m	3-cup anemometer (1 st)
2.05m	Thermometer Thies Clima (1 st)
2.75m	Vaisala (RH+Temp)
3.45m	Thermometer Thies Clima (2 nd)
3.60m	3-cup anemometer (2 nd)
3.80m	Sonic anemometer
4m	Barometer
4.60m	Thermometer Thies Clima (3 rd)
5.30m	3-cup anemometer (3 rd)
9m	Wind sentry anemometer (wind speed and wind direction)

All the instruments were connected to two CR10X dataloggers (Campbell Scientific) as follows. The storage of data was achieved in these two dataloggers. The dataloggers were placed in the same box.

1st datalogger

Instruments
3-cup anemometer (1 st)
3-cup anemometer (2 nd)
3-cup anemometer (3 rd)
Thermometer Thies Clima (1 st)
Thermometer Thies Clima (2 nd)
Thermometer Thies Clima (3 rd)
Sonic anemometer
Barometer

2nd datalogger

Instruments
Wind sentry anemometer (wind speed and wind direction)
Hygroclip (Temp+RH)
Vaisala (Temp+RH)

The dataloggers were connected to a PC with 2 20m RS232 cables accordingly. Two SC32B communication interfaces were used in the dataloggers in order to communicate with a portable PC.

The LoggerNet (3.4.1 version) software was used in a laptop, which was placed in an office of the 6th floor of the building and was open all the period of measurements. The appropriate programs were sent to the dataloggers in order to storage and collect the data. There was a scheduled collection every 10 seconds for both the dataloggers in separate files.

In summary, data that were collected from 18/7/2009 to 29/7/2009 included:

- CSAT3 data
- Wind speed at 4 heights
- Temperature at 5 heights
- RH at 2 heights
- Wind direction
- Atmospheric Pressure

There are about 925,200 rows of data for 17 parameters.

6.3.4. Data Processing

Processing of the raw data form CSAT3 included the following steps:

- (1) removing spikes using an iterative two-sided filter that removed outliers outside the local 30-min average, until the change in average value was less than 0.01ms^{-1} (this criterion was always met within less than 10 iteration passes);
- (2) quality check of 1-minute averaged values of mean quantities and fluxes;
- (3) coordinate rotation of u, v and w wind components to align the coordinate system with the stream lines of the 30-min averages;
- (4) Based on wind direction data, sonic anemometer reading that correspond to 60° - 300° were excluded from calculations. If more than 60% data were eliminated this time interval was excluded from further analysis.

Processing of the raw data from the other sensors:

- (1) When horizontal mean wind speed was $<1.5\text{ m s}^{-1}$, the data from all sensors was excluded for further calculations.
- (2) quality check of 1-minute averaged values of mean quantities.

6.4. Results

6.4.1. Some indicative graphs from the EC tower data.

Example of 1-min data recorded on 23/7/09, in the tower. A 30 min set (15:30 h-16:00 h) is presented in the following graphs:

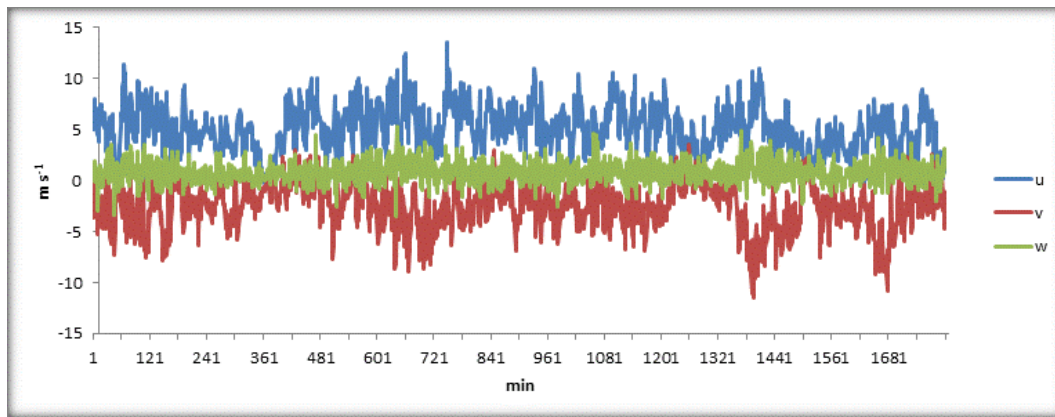


Figure 155. Wind velocities from sonic anemometer

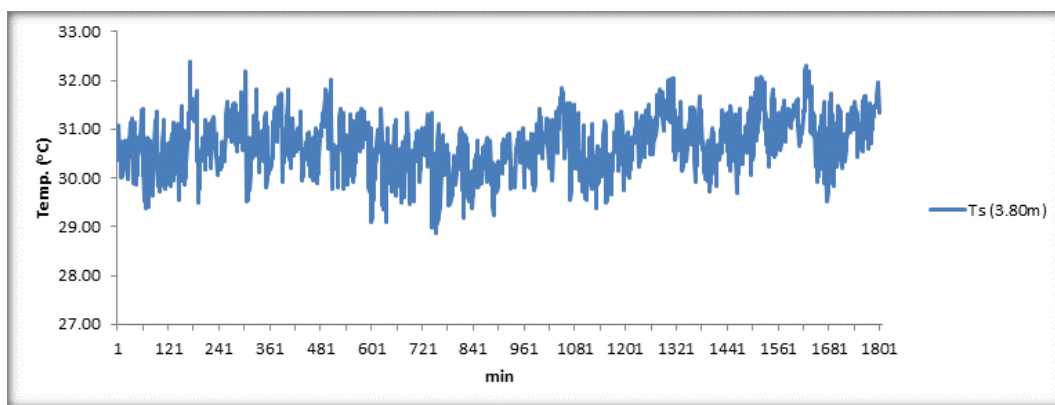


Figure 156. Temperature from sonic anemometer

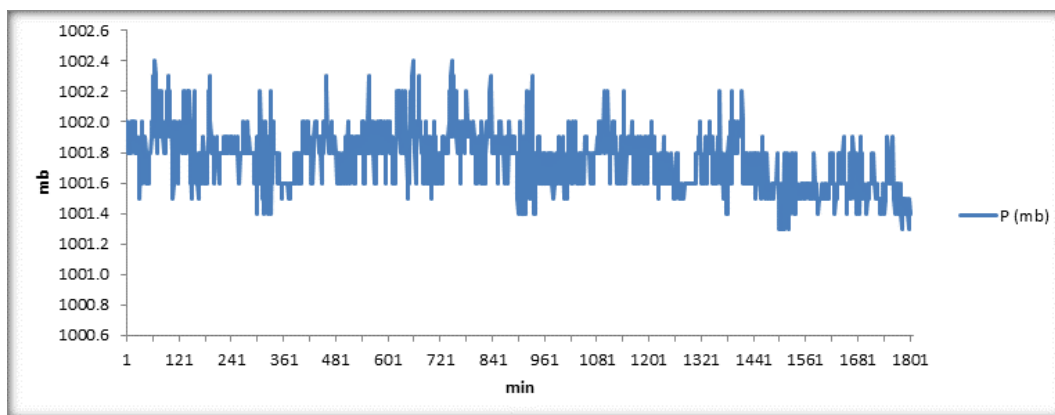


Figure 157. Atm. Pressure

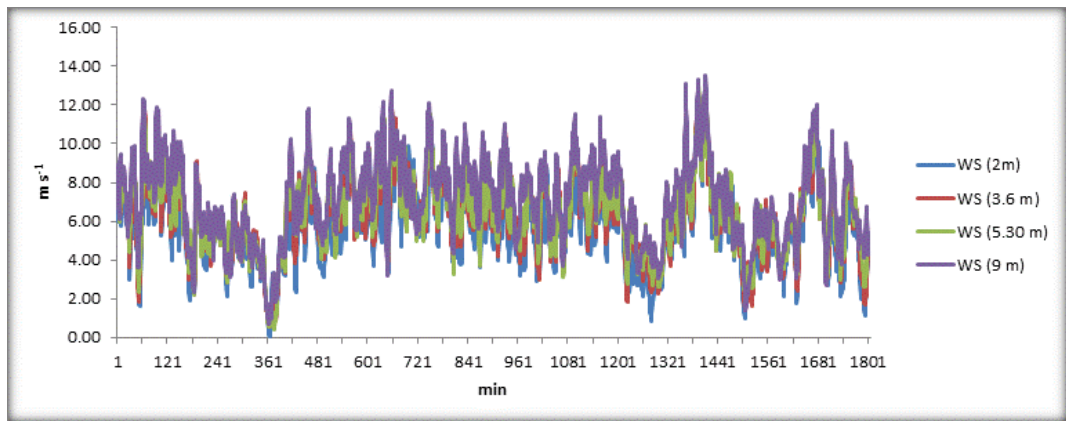


Figure 158. Wind speed at 4 heights



Figure 159. Wind direction at 9m

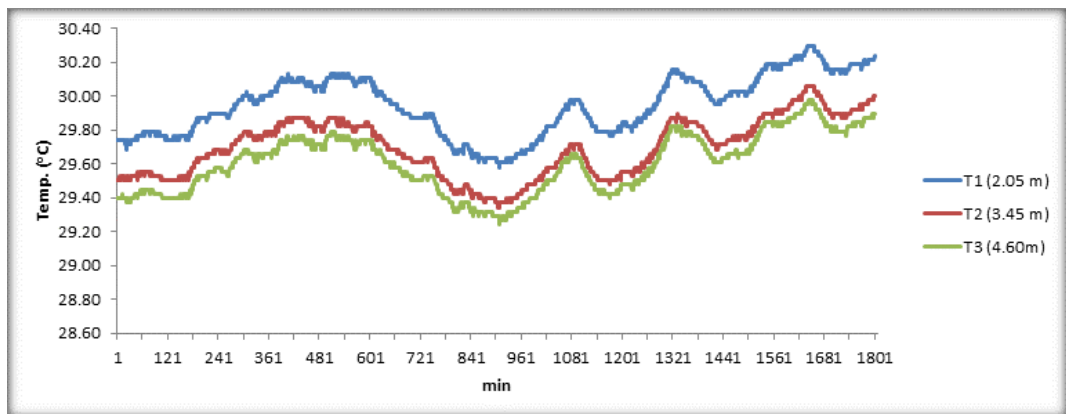


Figure 160. Temperature at 3 heights

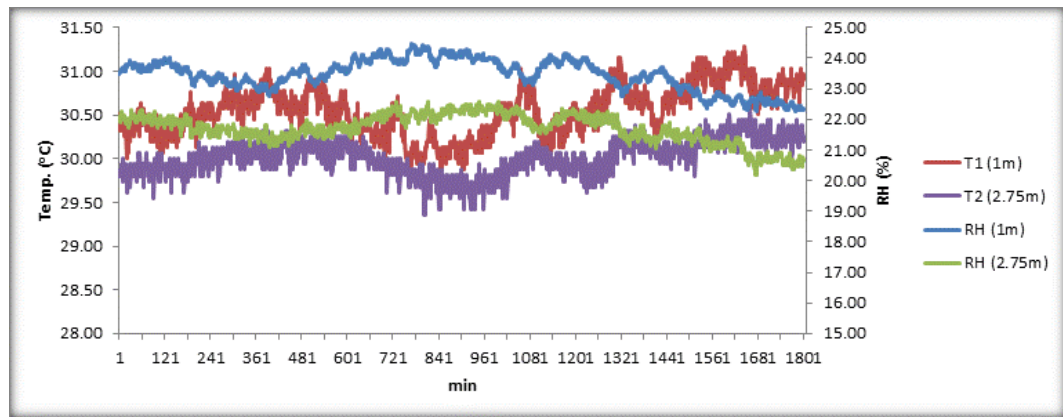


Figure 161. Relative humidity and temperature at 2 heights

6.4.2. Aerodynamic parameters at the observation site.

Accurate knowledge of the aerodynamic characteristics (the roughness length for momentum and the zero-plane displacement) of cities is vital to describe, model, and forecast the behaviour of urban winds and turbulence at all scales.

Methods to determine and can be generalized into two classes of approaches (Grimmond and Oke, 1999):

- 1) Morphological methods that relate aerodynamic parameters to measures of surface morphology, and
- 2) Anemometric methods that use field observations of wind and turbulence to solve for aerodynamic parameters included in theoretical relations derived from logarithmic wind profile (namely, the Monin-Obukhov similarity theory, hereinafter the MOST).

The MOST were applied at the anemometric data from the EC tower to calculate the roughness length for momentum z_0 and the zero-plane displacement d . The height of EC tower was on the limit between roughness sub layer and inertial sub layer where MOST is valid. Around the observation site, there are typical residences and business districts within the radius of 6 km, at least. Buildings stand densely in the districts. Some vegetation is contained within the urban canyons or in few parks.

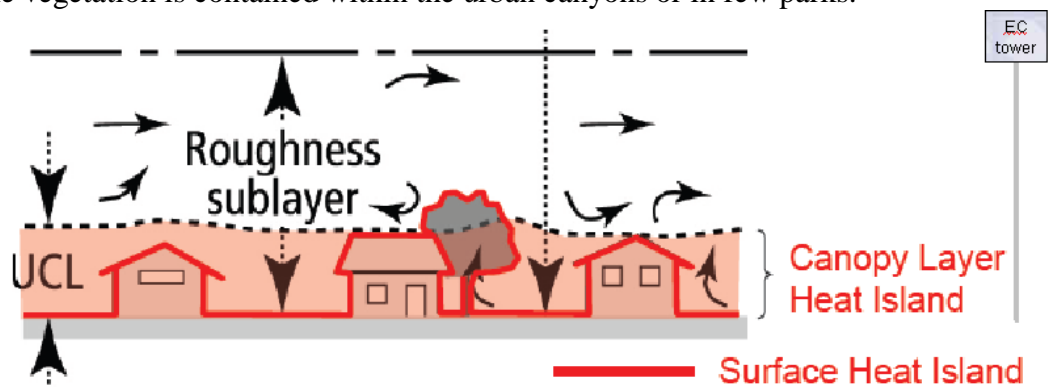


Figure 162. The height of EC tower lied above the roughness sub-layer.

Times when prevailed near neutral conditions ($-0.01 \leq Ri \leq 0$) were selected to apply the log law for the wind velocities:

$$u_z = \frac{u_*}{k} \left[\ln \left(\frac{z-d}{z_0} \right) - \Psi_m \right] \quad (2)$$

Where $\Psi_m \cong 0$ for near neutral conditions. Hence,

$$\frac{u_i - u_{i+1}}{u_{i+1} - u_{i+2}} = \frac{\ln(z_i - d) - \ln(z_{i+1} - d)}{\ln(z_{i+1} - d) - \ln(z_{i+2} - d)} \quad (3)$$

where $i=1, 2, 3$

Using observed wind speeds at the five heights (u_1, u_2, u_3, u_4, u_5 at z_1, z_2, z_3, z_4, z_5 respectively) we increase the value of d until Eq . 2 is valid, for each wind speed combination. This procedure identifies the value for the zero plane displacement for each 30-min time interval.

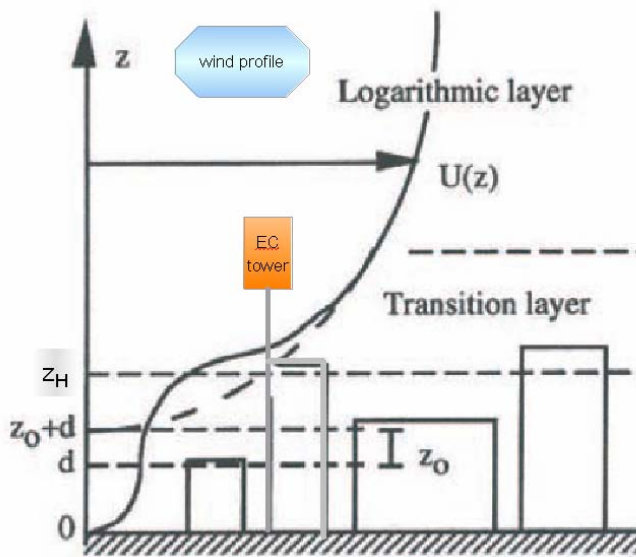


Figure 163. Wind profile and aerodynamic parameters.

In situ investigations were carried out to collect information about the height and orientation of each building in the study area. The mean building height in the vicinity of the EC tower was $z_H=17.01$ m. The zero plane displacement was calculated to be, on average, $d=13.2$ m (hence $d=0.78 z_H$), and according to the log law the mean roughness length for momentum was estimated to be $z_0=1.82$ m ($z_0=0.14 z_H$).

For the whole city of Athens, the fraction of the surface occupied by each surface type has been provided by land cover maps from the City Planning Authority, provided by DRAXIS. The city was divided into different areas according to the main type of the buildings in the area. For each type of buildings a mean building height was assigned. This value was verified by *in situ* measurements. The buildings occupy about 52% of the total surface area and streets with the pavements the 44%.

6.4.3. Heat fluxes calculations

Two methods were applied to calculate sensible (Q_H) and latent (Q_E) heat fluxes temporal variations from the data recorded on the EC tower:

- Eddy covariance
- Monin–Obukhov similarity theory (MOST)

The eddy covariance (eddy correlation, eddy flux) technique is a prime atmospheric flux measurement technique to measure and calculate vertical turbulent fluxes within atmospheric boundary layers. It is a statistical method used in meteorology and other applications that analyzes high-frequency wind and scalar atmospheric data series, and yields values of fluxes of these properties.

Monin–Obukhov similarity theory (MOST), which is established for smooth and homogeneous surface layers, is also used in modelling of turbulent transfer statistics in urban boundary layers. It is applicable above a certain height.

6.4.5. Heat fluxes modeling

The two modelling approaches adopted here are the Local-scale-Urban Meteorological Parameterization Scheme (LUMPS; Grimmond & Oke, 2002), and an aerodynamic resistance approach (ARM) (Voogt & Grimmond, 2000).

The models were firstly applied for the EC tower heat fluxes source area (the tower footprint). Secondly, the ARM model was applied for all the areas of the city covered from the INTA aircraft swath.

The Local-scale Urban Meteorological Parameterization Scheme (LUMPS) (Grimmond and Oke 2002).

LUMPS is designed for heat-flux calculations in the urban environment. Although it is a relatively simple scheme, it offers the considerable advantage of being dependent only on relatively easily identifiable surface characteristics, yet it still offers an acceptable level of accuracy compared to more sophisticated models. The LUMPS scheme, illustrated in Fig. 166, makes use of parameterizations based on standard meteorological observations and surface parameters of the target area, such as the fractional cover of vegetation, buildings, and other impervious surfaces. LUMPS also requires estimates of surface kinetic temperature and the net all wave radiation. Using the fractional cover of the three sub-pixel land cover components including roof, vegetation, road (including pavements) within each grid cell, LUMPS first determines the partitioning of the net all wave radiation (Q^*) using the methods outlined in Offerle et al. (2003), then computes the storage heat flux (ΔQ_s) via the Objective Hysteresis Model (OHM) and finally partitions the net available energy ($Q^* - \Delta Q_s$) into the turbulent fluxes of sensible (Q_H) and latent (Q_E) heat flux. The method has relatively limited data requirements yet is sophisticated enough to predict the spatial and temporal variability of heat fluxes known to occur within, and between, urban areas.

Net radiation data are needed to describe the heat fluxes of an urban or rural surface. This is the sum of all incoming and outgoing radiation fluxes and thus a key factor for the energy available for heat fluxes. If net radiation is positive, as is mostly the case during the day, energy can be transferred into turbulent heat fluxes (sensible and latent) and/or into the ground heat flux. If net radiation is negative, as is usual at night, it has to be compensated for by the heat fluxes (Eq. 1).

A flow chart of the structure of LUMPS (Fig. 166) shows that it is driven by relatively easily obtained meteorological and surface data. In the following, each sub-model is described briefly. LUMPS is formulated in the framework of the surface energy balance (SEB) described in Eq. 1.

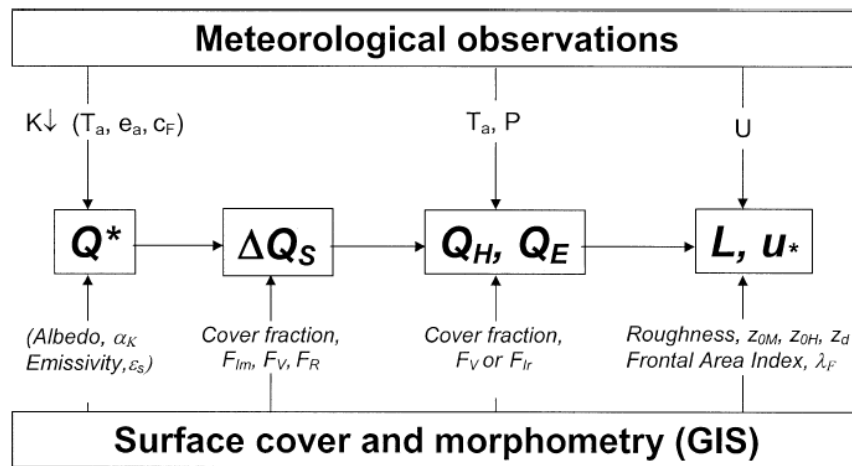


Figure 164. Flow chart of the structure of LUMPS. Quantities in parentheses are needed only if net all-wave radiation Q^* or incoming shortwave radiation $K\downarrow$ are not measured: T_a is air temperature, e_a is actual vapor pressure, c_F is cloud fraction, P is pressure, U is wind speed, ΔQ_S is storage heat flux, Q_H is turbulent sensible heat flux density, Q_E is latent heat flux density, L is Obukhov length, and u^* is friction velocity.

The anthropogenic heat flux is usually incorporated in the ΔQ_S . The ‘‘surface’’ here is the top of a ‘‘box,’’ the height of which extends from a measurement level above the city down to a depth in the ground where the diurnal conductive heat flux ceases. By ‘‘local scale’’ we refer to horizontal areas of approximately 10^2 – 10^4 m on a side and to measurement heights in the inertial sub-layer above the urban canopy and its roughness sub-layer (Fig. 167). At this height and scale, we expect the microscale variability of atmospheric effects generated by individual houses and other surfaces to be integrated into a characteristic neighbourhood response.

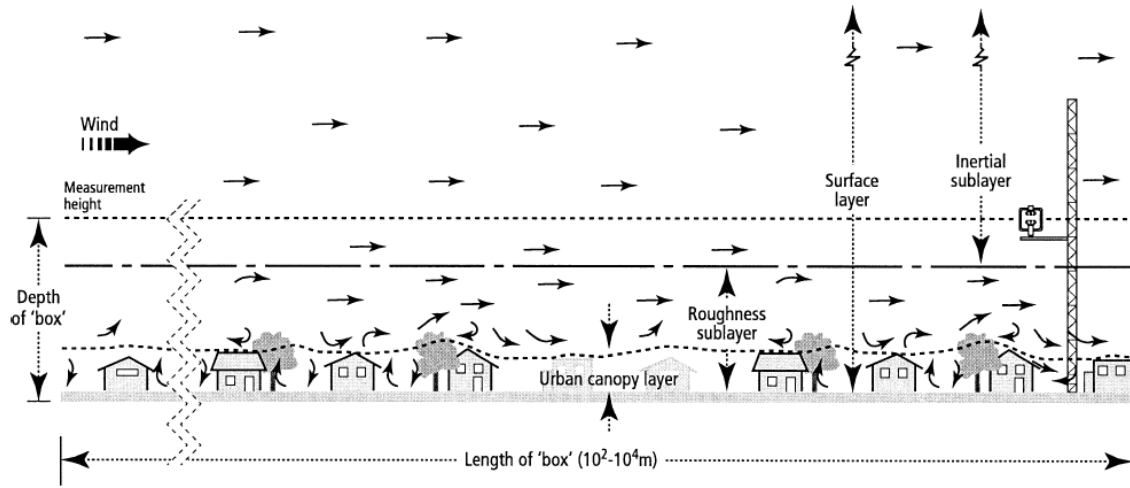


Figure 165. Definition of layers involved in the study of urban climates at the local scale (modified after Oke 1997) relative to the box modeled by LUMPS. The lateral (or third) dimension of the box (not shown) is 10^2 – 10^4 m. Within the roughness sublayer (RSL) there is greater spatial variability of temporally averaged fluxes than within the inertial sublayer; i.e., these fluxes are chaotic in the urban canopy layer and RSL but become invariant in the inertial sublayer. The top of the box is within the inertial sublayer, and the bottom is at the depth at which there is no net heat exchange over the time period of interest.

Storage heat flux

The storage heat flux in this urban SEB refers to the combined heat uptake and release from all substances (air, soil, biomass, and building materials) in the box, referred to as the equivalent surface flux through its top (Fig. 5). To capture the magnitude and diurnal hysteresis pattern of changes of the storage heat flux, the objective hysteresis model (OHM) will be used:

$$\Delta Q_s = \sum_{i=1}^n (f_i a_{1i}) Q^* + \sum_{i=1}^n (f_i a_{2i}) \frac{\partial Q^*}{\partial t} + \sum_{i=1}^n (f_i a_{3i}) \quad (4)$$

or simply:

$$\Delta Q_s = a_1 Q^* + a_2 \frac{\partial Q^*}{\partial t} + a_3 \quad (4a)$$

This requires knowledge of the local-scale Q^* , the fraction f_i of each of the n surface components within each grid cell, and the corresponding three coefficients (a_1 – a_3) for each surface component type (roof, road and vegetation). The fraction of the surface occupied by each surface type has been provided by land cover maps (DRAXIS).

EC tower source area (footprint)

The measured turbulent flux densities by the EC method are an area-averaged response of the surface, where the flux source areas depend on wind direction and stability (Schmid and Oke, 1990). The instruments at any urban site measure an integrated flux from an array of buildings, streets, backyards, and vegetation, which are representative of the local scale ('urban neighbourhood'). The source areas of the

downward looking radiation instruments and the variable-source areas of the eddy correlation instrumentation usually do not refer to the same area.

Source areas for the convective flux measurements were calculated using the footprint tool of Neftel et al, 2008. The FSAM model of Schmid (1994) was also applied, but it appeared that it underestimated the source area of heat fluxes.

The 95% source areas reached approximately 400 to 1600 m upwind (depending on the wind direction) under typical summertime conditions that prevailed, when flux densities were significant.

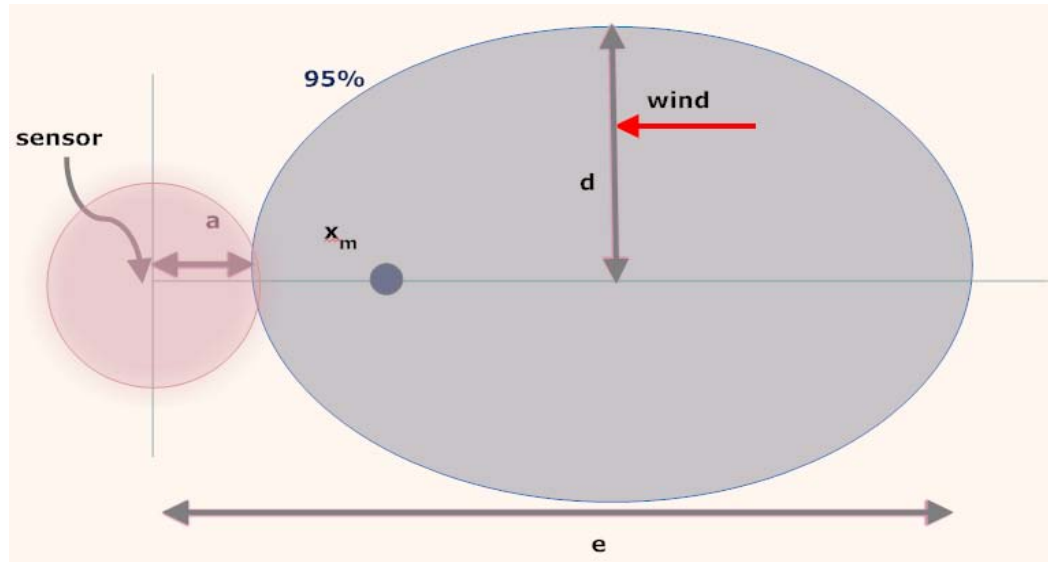


Figure 166. Radiometers source area and heat fluxes source area at the EC tower.

Parameterization and modelling of the net all wave radiation

The Q^* at each pixel of the source areas of heat fluxes was derived according to Offerle et al, 2003. The radiation budget for a horizontal surface is:

$$Q^* = K^* + L^* = K_{\downarrow} - K_{\uparrow} + L_{\downarrow} - L_{\uparrow} \quad (5)$$

where K and L represent the short- and longwave components, respectively, the arrows give the direction of the flux, and Q^* is a net flux.

The net shortwave term is a function of incoming solar radiation and the bulk surface albedo α_0 :

$$K^* = K_{\downarrow}(1 - \alpha_0) \quad (6)$$

Upwelling longwave radiation was calculated as:

$$L_{\uparrow} = \varepsilon_0 \sigma T_0^4 + (1 - \varepsilon_0)L_{\downarrow} \quad (7)$$

where ϵ_0 is surface broad band emissivity and T_o is the land surface temperature (LST).

Incoming short- and longwave components were provided by WRC measurements. Surface broadband albedo, surface broadband emissivity and LST parameters were derived from INTA data at a resolution 5 m x 5 m. Then the calculated Q^* for each pixel were averaged to derive the Q^* for each source area. The LUMPS was run for a time step of an hour and the rate of change of Q^* (in $W\ m^{-2}\ h^{-1}$) at each hour was calculated as:

$$\frac{\partial Q^*}{\partial t} = 0.5 (Q_{t+1}^* - Q_{t-1}^*) \quad (8)$$

Sensible and latent heat flux

The parameterizations of the turbulent sensible and latent heat fluxes (Q_H and Q_E , respectively) described by Grimmond and Oke (2002) were used. When written in a form appropriate for an urban environment, these are:

$$Q_H = \frac{(1-\alpha) + (\gamma/s)}{1 + (\gamma/s)} (Q^* - \Delta Q_s) - \beta \quad (9)$$

$$Q_E = \frac{\alpha}{1 + (\gamma/s)} (Q^* - \Delta Q_s) + \beta \quad (10)$$

where s is the slope of the saturation vapor pressure– versus-temperature curve, γ is the psychrometric “constant,” and α and β are empirical parameters. The RMSE (root mean square error) and the MBE (mean bias error) was calculated between the modelled heat fluxes with the LUMPS and the *in situ* eddy covariance flux observations. Hence, the values of the parameters α and β that minimized the errors were estimated:

Table 75. Empirical parameters α and β estimated for Athens.

	Estimate	Standard Error	t-value	p-level	Lo. Conf. Limit	Up. Conf. Limit
α	0.67	0.09	7.23	0.00	0.48	0.85
β ($W\ m^{-2}$)	-0.33	2.37	-0.14	0.89	-5.01	4.36

Net storage heat flux.

The Q_H and Q_E fluxes were measured directly from atmospheric data obtained in the EC tower at a height of at least 1.5 times the mean height of the roughness elements. Hence, the heat storage change in the urban fabric, expressed as a heat flux density through a horizontal plane (Fig. 167), was found as the residual in the surface energy balance in an **hourly** basis, as suggested by Grimmond and Oke (2002). Also, ΔQ was calculated through Eq. (4). Hence it was possible to estimate the “average” parameters α_1 - α_3 in Eq.4a through statistical analysis:

Table 76. Parameters in the OHM model (For hourly average heat fluxes)

	Estimate	Standard Error	t-value	p-level	Lo. Conf. Limit	Up. Conf. Limit
α_1	0.75	0.01	80.88	0.00	0.73	0.76
α_2 (h)	0.35	0.06	5.61	0.00	0.23	0.48
α_3 (W m ⁻²)	-50.26	1.95	-25.81	0.00	-54.11	-46.40

The Fig. 169 below presents the average energy fluxes that were modeled for the whole campaign.

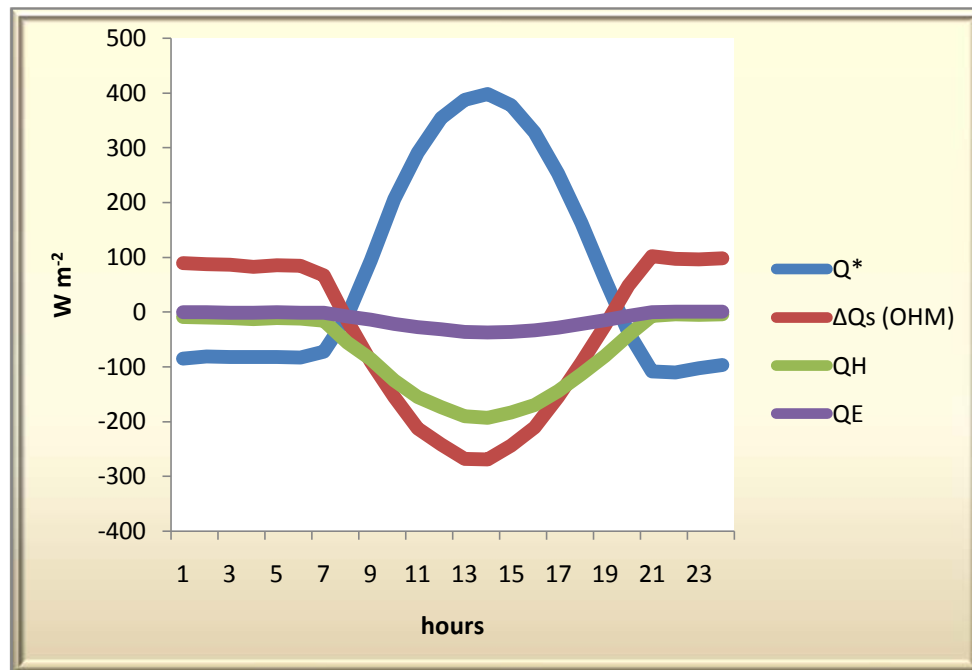


Figure 167. Average modelled energy fluxes around the EC tower.

Aerodynamic Resistance Method (ARM)

An alternative method (Voogt & Grimmond, 2000) to estimate the sensible heat fluxes uses the simple relation (bulk aerodynamic resistance equation):

$$Q_H = \rho C_p \frac{T_o - T_a}{r_{ah}} \quad (11)$$

where ρ is the density of air (kg m⁻³), C_p the specific heat of air at constant pressure (J kg⁻¹ K⁻¹), T_o is the remotely sensed radiometric land surface temperature (K) (provided by INTA aircraft, satellite data and WRC in the tower), T_a is the air temperature (K) recorded by the meteorological stations (provided by K. Kourtidis), and r_{ah} is the aerodynamic resistance (s m⁻¹). C_p will be corrected based on air pressure and vapour pressure in order to adjust for the effect of atmospheric humidity variations.

The r_{ah} is calculated as follows:

$$r_{ah} = \frac{1}{ku^*} \left[\ln \left(\frac{z-d}{z_{om}} \right) + \ln \left(\frac{z_{om}}{z_{oh}} \right) - \psi_h \left(\frac{z-d}{L} \right) \right] \quad (12)$$

z is the measurement height (m) of the sonic anemometer, the wind speed u is measured by the sonic anemometer, d is the zero plane displacement height (m), and z_{om} and z_{oh} are the roughness lengths (m) for momentum and heat transport, respectively. ψ_m and ψ_h are stability correction functions for momentum and heat (Businger et al., 1971 in the form of Högström 1988), which depend on the Richardson number (R_i) and k is von Karman's constant (0.4).

Friction velocity was calculated from sonic anemometer data as:

$$u^* = \left[(\overline{u'w'})^2 + (\overline{v'w'})^2 \right]^{1/4} \quad (13)$$

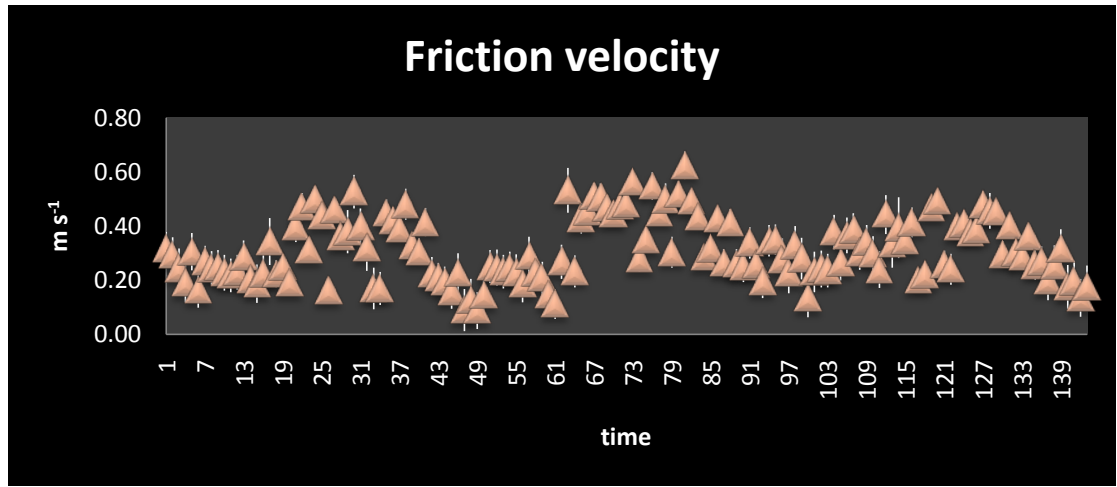


Figure 168. An example of friction velocity calculations

The gradient Richardson number (R_i):

$$R_i = \frac{g}{\theta} z \frac{\left(\frac{d\theta}{dz} \right)}{\left(\frac{du}{dz} \right)} \quad (14)$$

where z is the geometric mean height from all the measurement points at the tower.

The Monin–Obukhov length (L) was calculated as:

$$L = - \frac{u_*^3}{k \frac{g}{\theta_v} \overline{w'\theta'_v}} \quad (15)$$

Where θ_v is the virtual potential temperature calculated from sonic anemometer recorded temperature.

Most commonly in the literature the values for excess resistance are reported in the form of the parameter kB^{-1} where:

$$kB^{-1} = \ln \left(\frac{z_{om}}{z_{oh}} \right) \quad (16)$$

z_{oh} was calculated with the following method (Voogt & Grimmond, 2000):

$$z_{oh} = z_{om} [7.4 \exp (-1.8R_{e*}^{0.25})] \quad (17)$$

where $Re^* = z_{om} \mu^* / \nu$ is the roughness Reynolds number, with a kinematic molecular viscosity ν of $1.46 \times 10^{-5} \text{ m}^2 \text{ s}^{-1}$ (Brutsaert, 1982). The z_{om} was found from the wind profile, as described above.

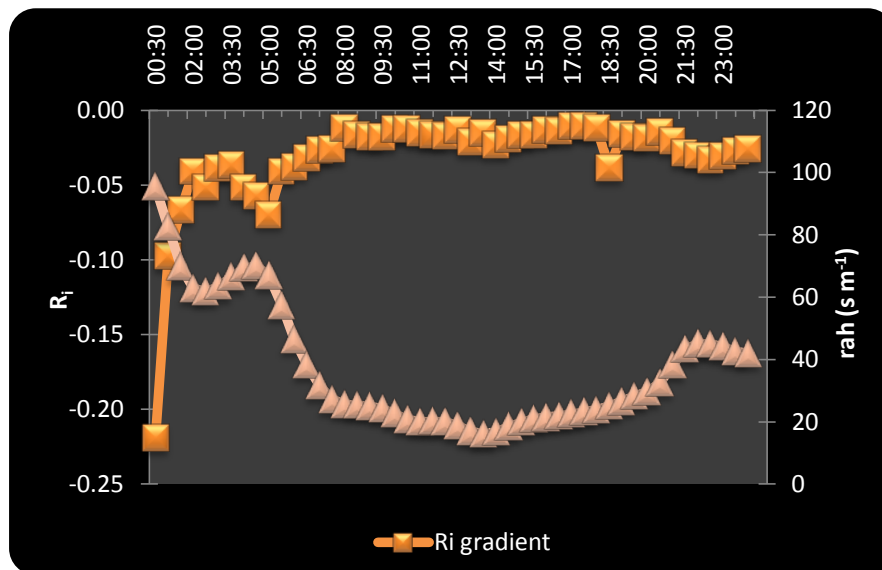


Figure 169. An example of R_i and r_{ah} calculation results

The ARM model was applied to calculated heat fluxes from each source area of the EC tower, which results were compared with the measured fluxes.

Measured and modeled heat fluxes comparisons

The following Figures 172, 173, 174 present the measured and modelled heat fluxes comparison as well as the calculated Bowen ratio.

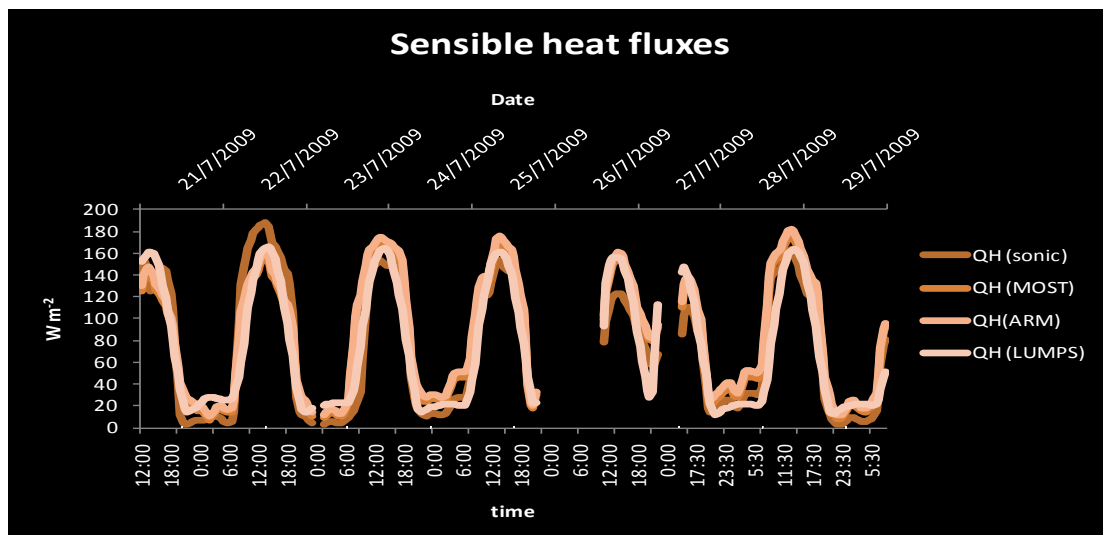


Figure 170. Sensible heat flux comparisons.

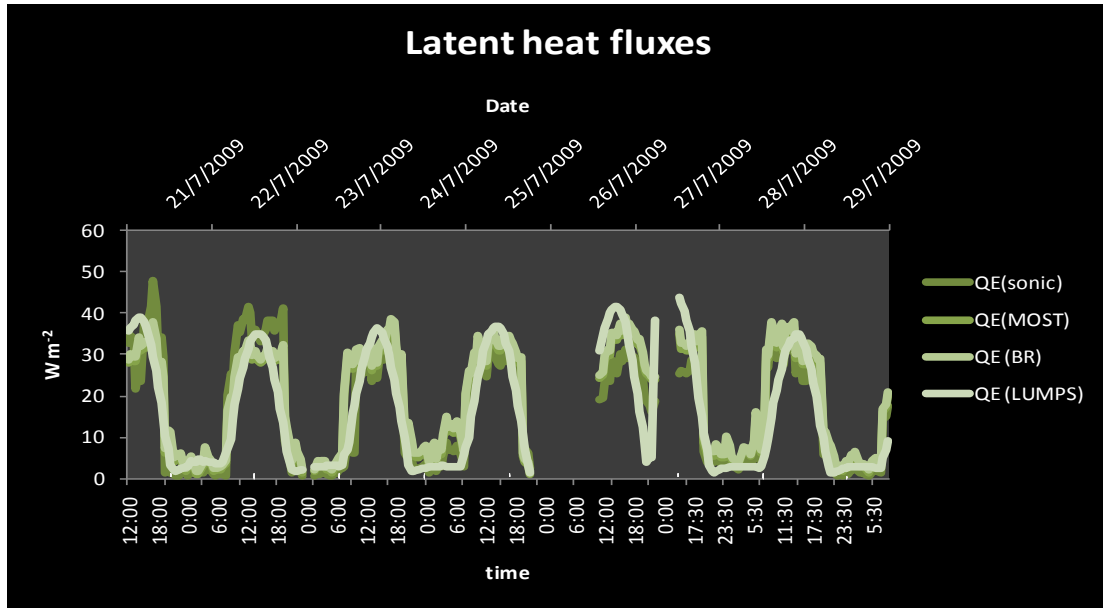


Figure 171. Latent heat flux comparisons.

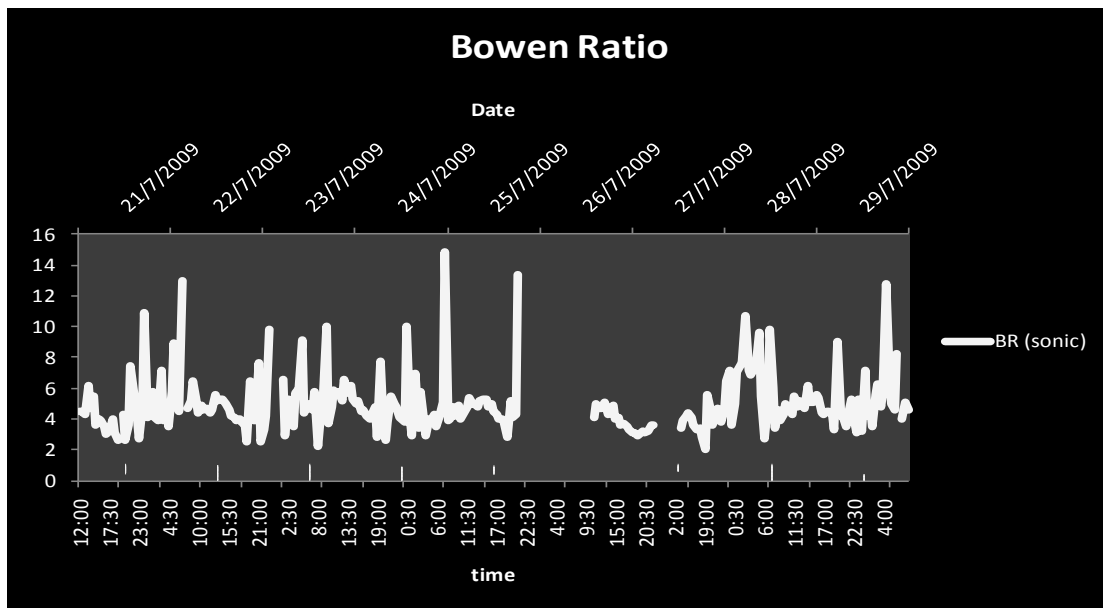


Figure 172. Bowen ratio.

6.4.6. The ARM application for the whole city (INTA aircraft swath)

The Eq. 11 was applied for each of the 5 m spatial resolution pixels of the land cover map in the areas corresponding to the aircraft's swath. The model was applied during times that aircraft have flight above the city. Hence, LST was available (provided by INTA), air temperature also available from interpolation of the ground data (kriging method) provided by K. Kourtidis.

It was found that $z_{oh}=0.14 \times z_H$ and $d=0.78 \times z_H$ on average, from the data acquired in the EC tower. It was assumed that L and u^* during the half an hour flight of the aircraft were the same at any pixel. Hence, knowing the mean building height at any

pixel, the r_{ah} could be calculated. The algorithms were applied to the land cover map to assign an aerodynamic resistance value for each pixel.

From the calculated at each pixel sensible heat flux, the latent heat flux was derived from the value of Bowen ratio, measured at the tower, during each flight time.

The figures below depict the heat fluxes calculated during a daytime and a night time flight.

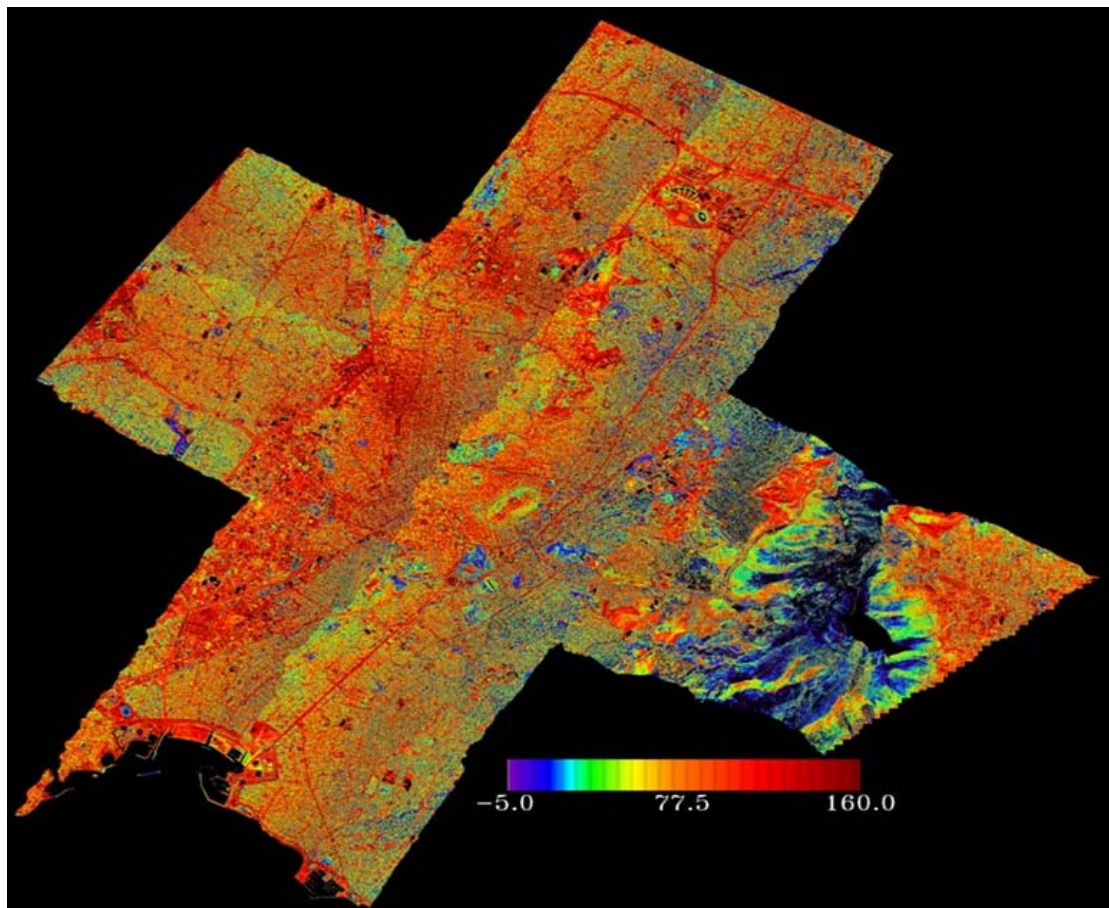


Figure 173. Sensible heat flux over Athens (daytime flight)

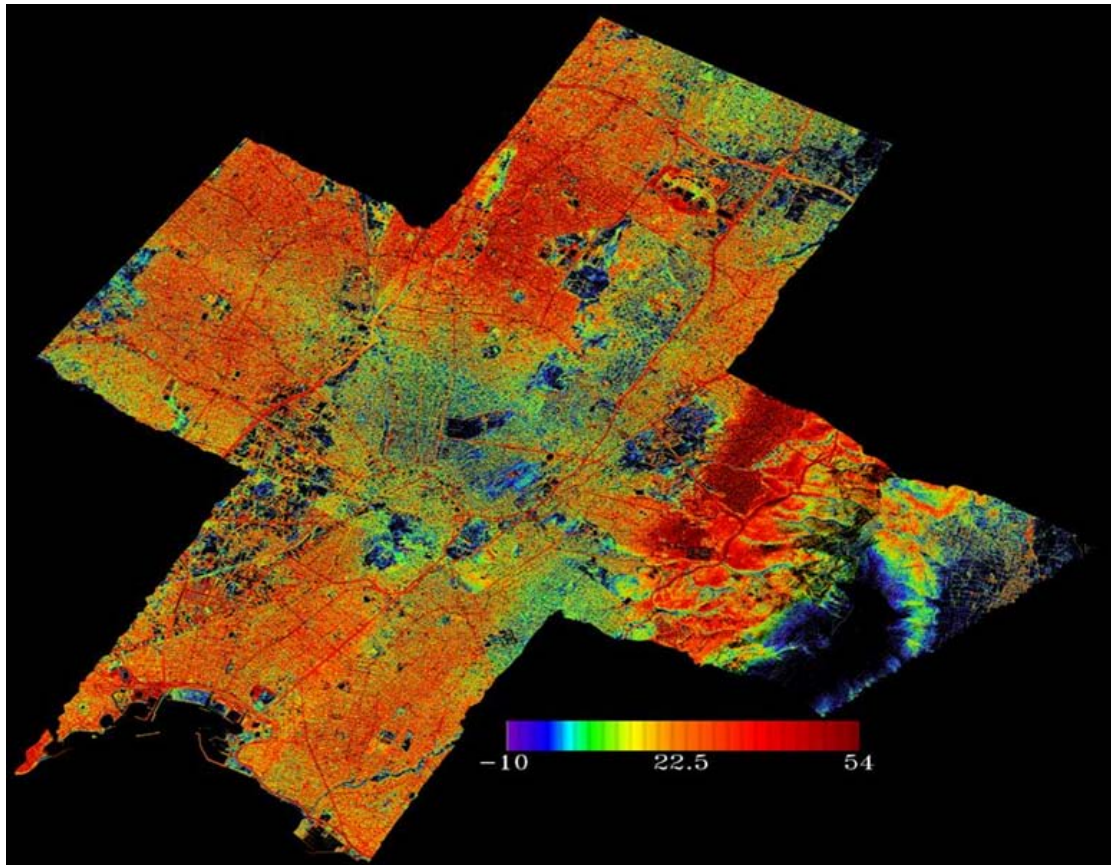


Figure 174. Sensible heat flux over Athens (night time flight)

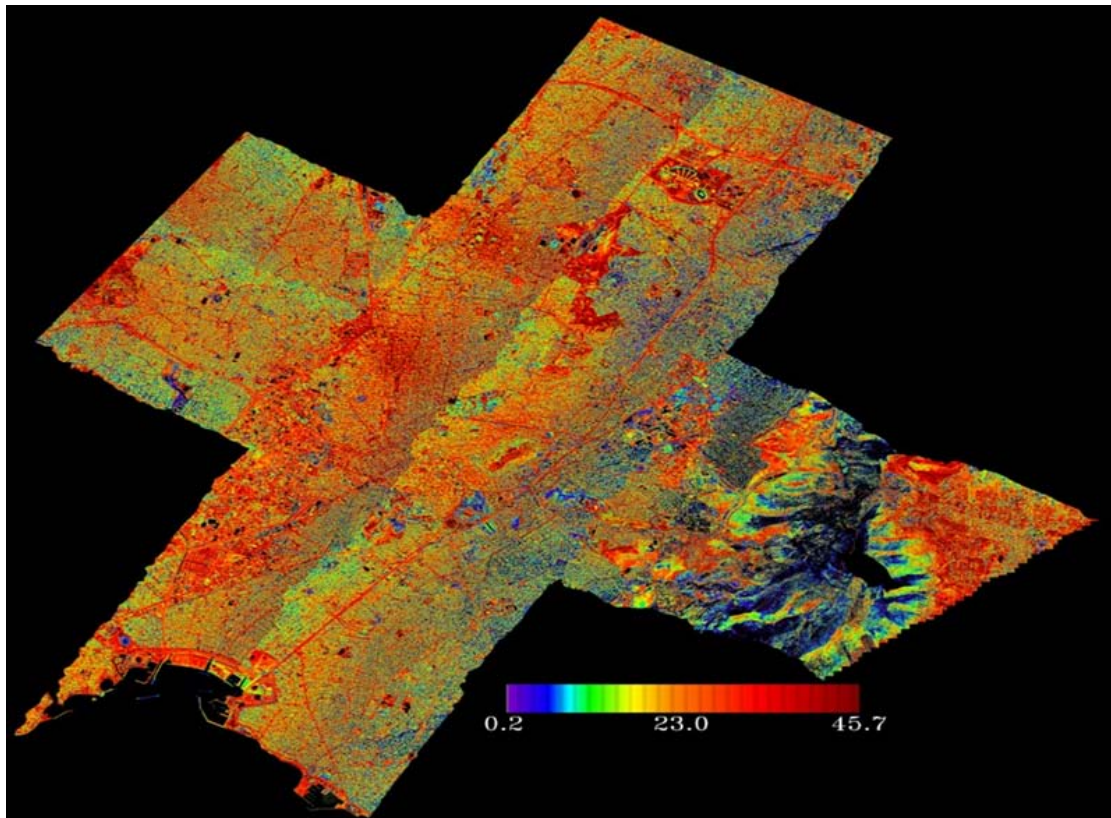


Figure 175. Latent heat flux over Athens (daytime flight)

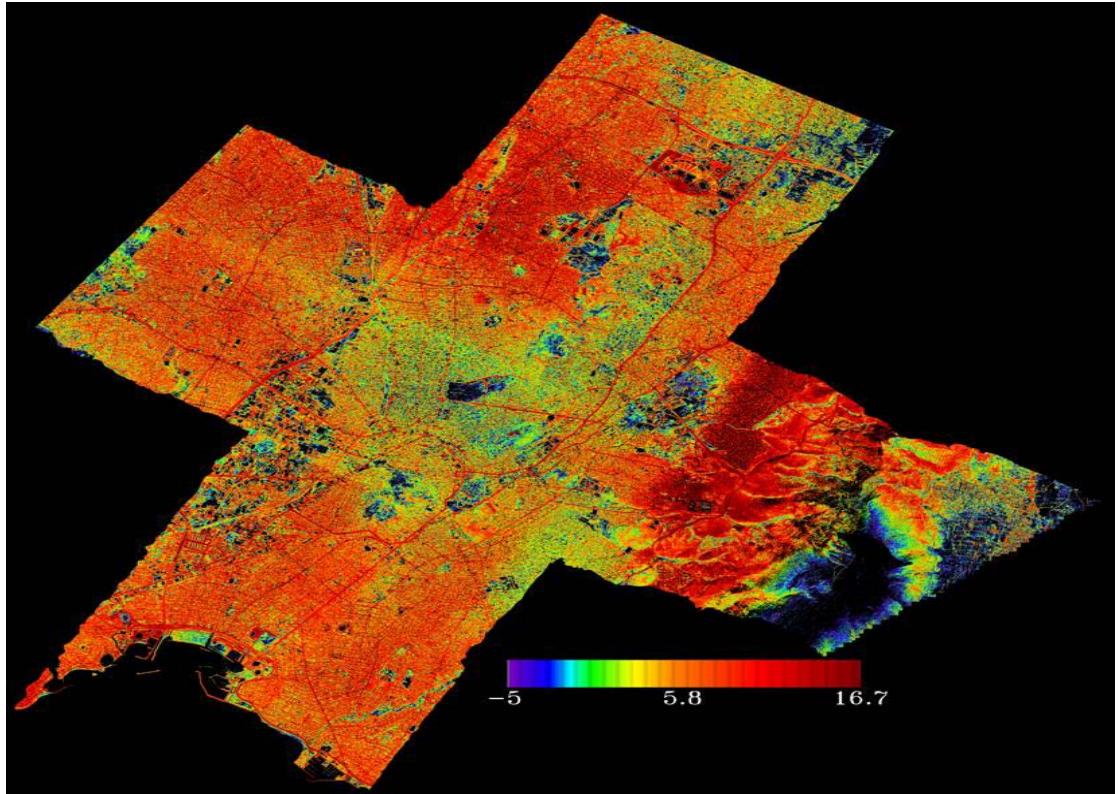


Figure 176. Latent heat flux over Athens (night time flight)

6.4.7. Statistical analysis

The estimation of the several empirical parameters used in the LUMPS was carried out comparing the mean bias error (MBE) and root-mean square error (RMSE) between measured with the EC method and modelled fluxes. These are the mean and standard deviation errors, respectively. Their definitions are the followings:

$$MBE = \frac{1}{n} \sum_{i=1}^n (Xm_i - Xo_i) \quad (16)$$

where n is the number of pairs compared, Xm_i is the modeled (estimated) value, and Xo_i is the observed or measured value. A positive MBE means that the model overestimated the reference value;

$$RMSE = \sqrt{\frac{1}{n-1} \sum_{i=1}^n [(Xm_i - Xo_i)] - MBE]^2} \quad (17)$$

The Figures 179, 180 present the mean energy flux densities as measured at the EC tower, as well as heat flux percentages of net all wave radiation.

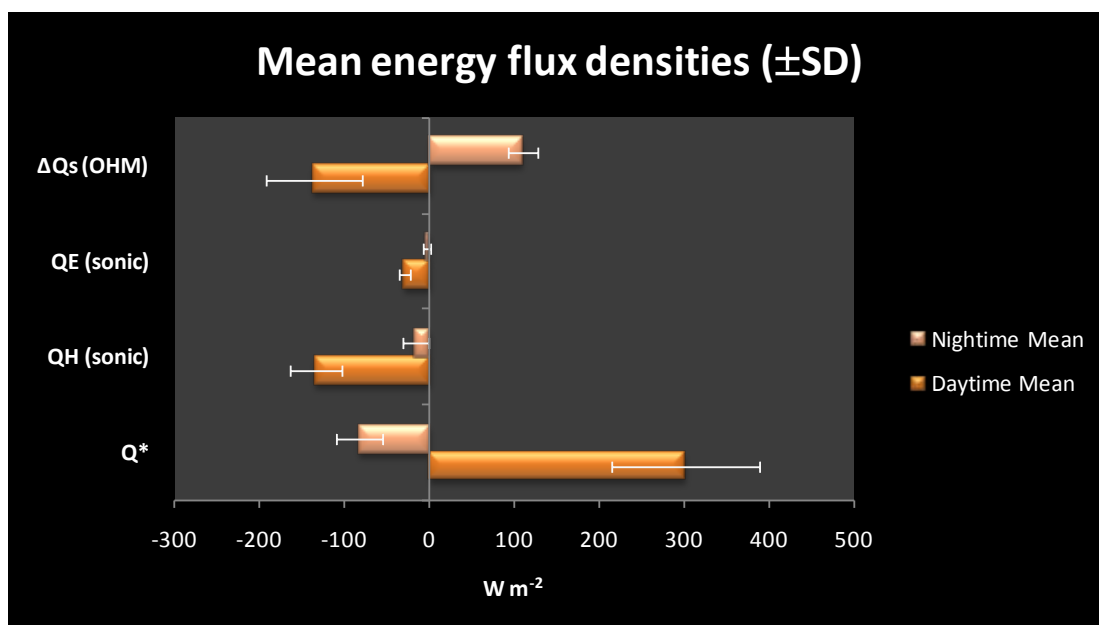


Figure 177. Mean energy flux densities (\pm SD) at the EC tower footprints.

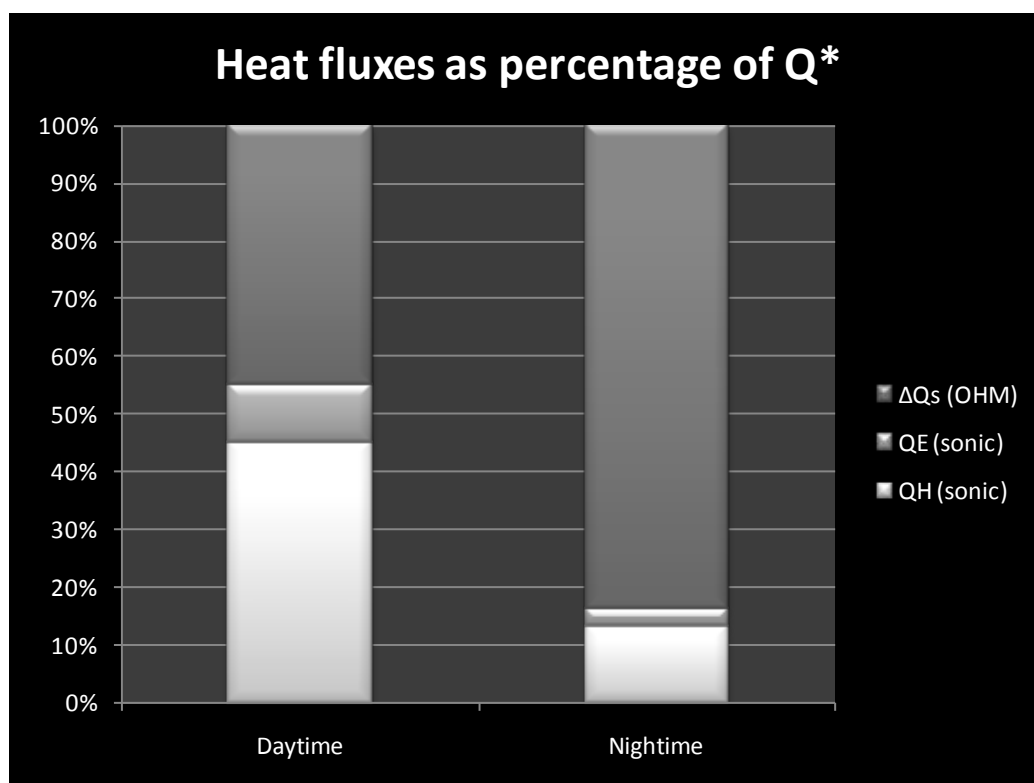


Figure 178. Heat flux as percentages of net all wave radiation.

The storage heat flux (Fig. 179, 180) was determined as residual term in the case of EC method. It includes all heat uptake and release of the urban surface materials. The rate of change of sensible heat storage of the air column between the surface and the measurement level is included. However, the results must be treated carefully

because, whenever ΔQ_s is determined as residual term, it incorporates all instrumental and methodical uncertainties. Hence, it can only be considered as an upper limit.

6.5. References

1. Arnfield AJ (2003) Two decades of urban climate research: a review of turbulence, exchanges of energy and water, and the urban heat island. *International Journal of Climatology* 23(1):1-26.
2. Brutsaert, W. (1982) Evaporation in the atmosphere. Theory, history, and applications. D. Reidel, Higham, MT, USA.
3. Christen A & Roland V (2004) Energy and radiation balance of a central European city. *International Journal of Climatology* 24(11):1395-1421.
4. Christen, A., R. Vogt, M. W. Rotach, and E. Parlow (2002), First results from Bubble: Partitioning of turbulent heat fluxes and urban surfaces, paper presented at 4th Symposium on the Urban Environment, Am. Meteorol. Soc., Norfolk, Va. Extended Abstracts of an Expert Meeting, Antwerp, Belgium, April 2000, EUR 19447, European Commission.
5. Grimmond CSB & Oke TR (2002) Turbulent Heat Fluxes in Urban Areas: Observations and a Local-Scale Urban Meteorological Parameterization Scheme (LUMPS). *Journal of Applied Meteorology* 41(7):792-810.
6. Grimmond CSB, Salmond JA, Oke TR, Offerle B, & Lemonsu A (2004) Flux and turbulence measurements at a densely built-up site in Marseille: Heat, mass (water and carbon dioxide), and momentum. *J. Geophys. Res.* 109.
7. Masson V (2000) A Physically-Based Scheme For The Urban Energy Budget In Atmospheric Models. *Boundary-Layer Meteorology* 94(3):357-397.
8. Neftel A, Spirig C, & Ammann C (2008) Application and test of a simple tool for operational footprint evaluations. *Environmental Pollution* 152(3):644-652.
9. Nemitz E, Hargreaves KJ, McDonald AG, Dorsey JR, & Fowler D (2002) Micrometeorological measurements of the urban heat budget and CO₂ emissions on a city scale. *Environmental Science and Technology* 36(14):3139-3146.
10. Offerle B, Grimmond CSB, & Oke TR (2003) Parameterization of Net All-Wave Radiation for Urban Areas. *Journal of Applied Meteorology* 42(8):1157-1173.
11. Oke TR, Grimmond CSB. (2002) Urban–rural energy balance differences. In Surface Energy Balance in Urban Areas. Cost Action 715.
12. Oke, T. R., (1987) Boundary Layer Climates, 2nd edition, Routledge, London.
13. Rotach MW (1999) On the influence of the urban roughness sublayer on turbulence and dispersion. *Atmospheric Environment* 33(24-25):4001-4008.
14. Rotach MW, *et al.* (2005) BUBBLE – an Urban Boundary Layer Meteorology Project. *Theoretical and Applied Climatology* 81(3):231-261.
15. Roth M (2000) Review of atmospheric turbulence over cities. *Quarterly Journal of the Royal Meteorological Society* 126(564):941-990.
16. Schmid HP (1994) Source areas for scalars and scalar fluxes. *Boundary-Layer Meteorology* 67(3):293-318.
17. Schmid, H. P. and T. R. Oke, (1990) A model to estimate the source area contributing to surface layer turbulence at a point over patchy terrain. *Quarterly Journal Royal Meteorological Society*, **116**, 965-988

18. Voogt JA & Grimmond CSB (2000) Modeling Surface Sensible Heat Flux Using Surface Radiative Temperatures in a Simple Urban Area. *Journal of Applied Meteorology* 39(10):1679-1699.

7. Validation and Exploitation of AHS Data

7.1 Introduction

This report provides a description of tasks performed by the Global Change Unit (University of Valencia) related to Airborne Hyperspectral Scanner (AHS) imagery processing in order to provide land surface reflectance, emissivity and temperature products in the framework of the THERMOPOLIS project supported by European Space Agency (ESA) and carried out in Athens (Greece) in July 2010. Description of instrumentation and details on ground-based measurements carried out for calibration and validation purposes have been included.

The report includes the theoretical basis considered in order to perform the atmospheric correction in both the solar (Visible and Near-InfraRed – VNIR) and Thermal InfraRed (TIR) spectral ranges, which cover AHS bands from 1 to 20 and from 71 to 80, respectively. The algorithms and methodology employed to generate reflectance and temperature/emissivity products are also described. These products have been tested against in-situ measurements in order to assess its accuracy.

7.2. Atmospheric Correction in the Solar Range

BACKGROUND

When the atmospheric correction in the Visible and Near Infrared (VNIR) is performed it is necessary to consider the different contributions of the atmosphere and the surface to the solar irradiance. Figure 1 shows the contributions to the top of the atmosphere signal that have been taken into account in the VNIR spectral range. Four terms are considered: (1) the photons reflected by the atmosphere before reaching the surface, (2) the photons transmitted directly to the target and directly reflected to the sensor, (3) the photons that are scattered by the atmosphere before reaching the target and directly reflected to the sensor and finally (4) the photons that have at least two interactions with the atmosphere and one with the target.

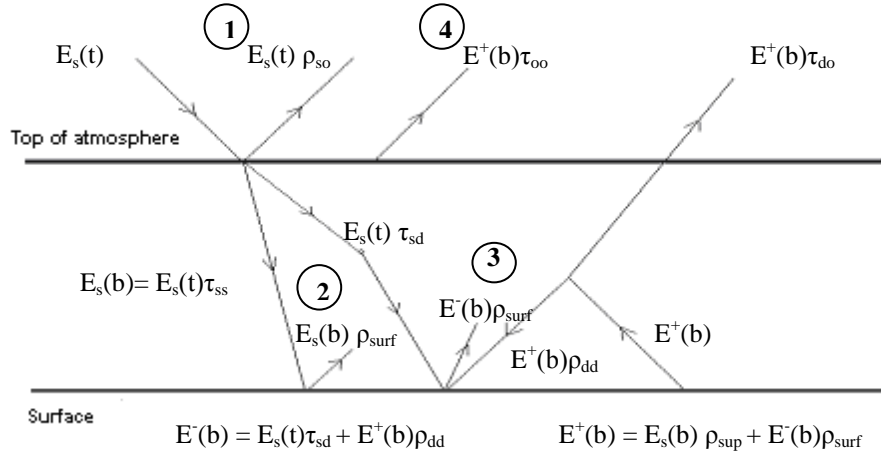


Figure 179. Different contributions of the atmosphere and the surface to the top of the atmosphere signal.

Taking these different contributions into account and considering the surface as uniform and Lambertian (Nicodemus 1977) the radiative transfer equations for the atmosphere can be written as (Verhoef 2003):

$$E_s(b) = \tau_{ss} E_s(t) \quad (1)$$

$$E^-(b) = \tau_{sd} E_s(t) + \rho_{dd} E^+(b) \quad (2)$$

$$E_o(t) = \rho_{so} E_s(t) + \tau_{do} E^+(b) + \tau_{oo} E_o(b) \quad (3)$$

$$E^+(b) = \rho_{surf} [E_s(b) + E^-(b)] \quad (4)$$

where (b) and (t) indicate the bottom and the top of the atmosphere irradiance respectively, ρ_{so} is the bi-directional reflectance of the atmospheric layer, τ_{ss} is the downwelling direct transmittance, τ_{sd} is the diffuse transmittance in the solar direction, τ_{do} is the diffuse transmittance in the viewing direction, ρ_{dd} is the atmospheric spherical albedo, τ_{oo} is the upwelling direct transmittance and ρ_{surf} is the surface reflectance.

In eq. (1) it is described the attenuation of direct sunlight by direct transmittance τ_{ss} through the whole atmospheric layer, Eq. (2) reflects the generation of diffuse downward flux (sky irradiance) by diffusely transmitted direct solar flux and upwelling diffuse flux from the surface that is reflected back by the atmosphere. Here, the term ρ_{dd} is the atmospheric spherical albedo. Eq. (3) describes how the top-of-atmosphere radiance is generated from atmospherically scattered direct sunlight via the term ρ_{so} (which can be considered a bi-directional reflectance of the atmospheric layer), diffuse upwelling flux that is scattered into the direction of view via the transmittance term τ_{do} , and directly transmitted radiance from the target via the direct

transmittance τ_{oo} . Finally, Eq. (4) describes the reflection of radiance by a Lambertian surface.

7.2.1 Surface Reflectance Retrieval

Assuming a Lambertian surface we can apply the approximation $E_o(b) = E^+(b)$ and using radiance units ($L_{TOA}(t) = E_o(t)/\pi$) it can be derived the expression

$$L_{TOA} = \left(\rho_{so} + \frac{(\tau_{ss} + \tau_{sd})\rho_{surf}\tau_{do}}{1 - \rho_{surf}\rho_{dd}} \right) \frac{E_s}{\pi} + \frac{(\tau_{ss} + \tau_{sd})}{1 - \rho_{surf}\rho_{dd}} \frac{E_s}{\pi} \rho_{surf}\tau_{oo} \quad (5)$$

where L_{TOA} is the radiance measured at the top of the atmosphere that must be corrected atmospherically. Using equation (5) but in reflectance terms, ρ_{TOA} :

$$\rho_{surf} = \frac{\rho_{TOA} - \rho_{so}}{(\tau_{do} + \tau_{oo})(\tau_{ss} + \tau_{sd}) + \rho_{dd}(\rho_{TOA} - \rho_{so})} \quad (6)$$

With the objective of obtaining surface reflectance images from the AHS sensor, it has been considered eq. (6) where the inputs are the AHS image (ρ_{TOA} in equation (6)) and the atmospheric parameters which have been obtained using the radiative transfer code MODTRAN 4 (Berk et al., 1999). Moreover, as our study is based on airborne data, depending on the atmospheric parameter we would have to decide whether to consider the entire atmosphere or only consider the atmosphere between the surface and the sensor altitude. Therefore, we only consider the entire atmosphere in the τ_{ss} (downwelling direct transmittance) and τ_{sd} (diffuse transmittance in the solar direction) estimation and the atmosphere between surface and the sensor in the other cases. In the THERMOPOLIS campaign atmospheric soundings were obtained from the MODIS water vapor product (MOD07) corresponding to each flight day and the Aerosol Optical Thickness (AOT) were considered from the database document “AOT550_A090715090803.dat”. Table 1 shows the Water Vapor Content and also the AOT values considered for each flight day. This methodology has been applied to airborne data and we have tested its accuracy making use of the ground-based measurements performed during the campaign simultaneously to the airborne overpass, as is explained bellow.

Table 77: Water vapor content and aerosol optical thickness values considered.

	18th July	20th July	24th July
WVC (g/cm²)	2.86	2.69	1.91
AOT	0.23	0.27	0.12

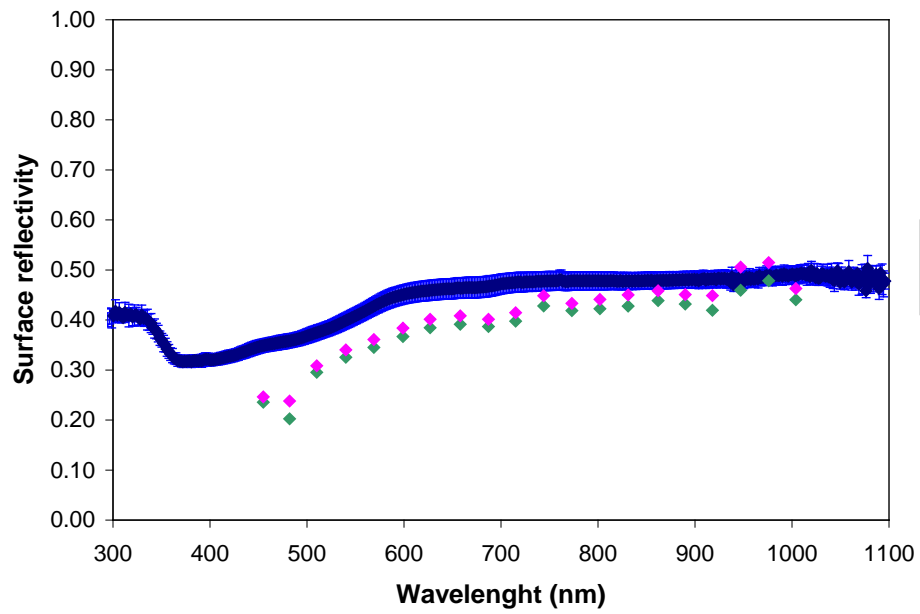
7.3 Validation

In order to estimate surface reflectance we have applied the methodology described to AHS images. Considering 18th of July, the spectrums of two plots are displayed in Figure 2, a bare soil and a green grass, measured in situ and also estimated from AHS images.

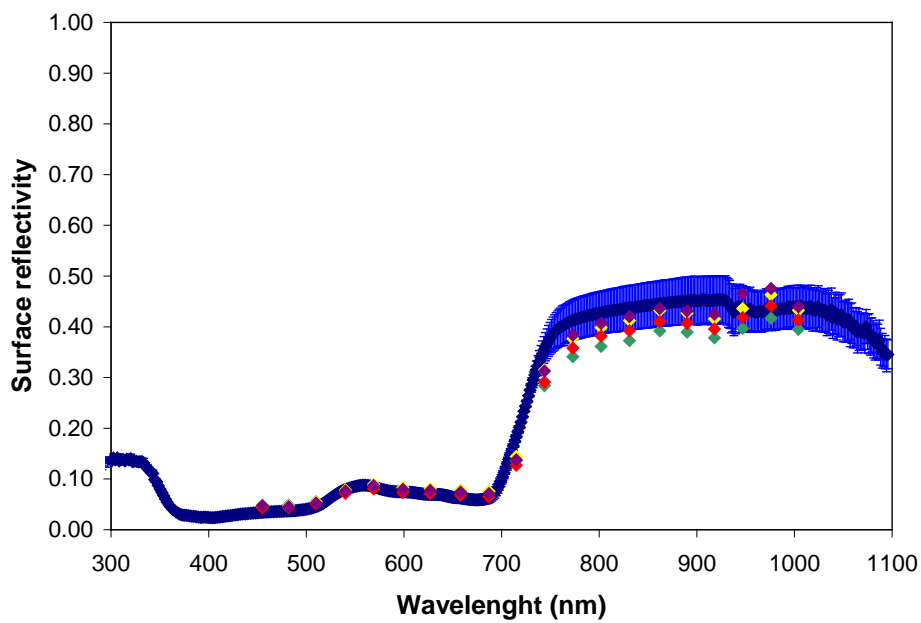
The surface reflectance test over every plot and considering every flight has been centered in two bands as a reference of the AHS atmospheric correction, one in the visible spectral range (Band 9 centered on 687 nm) and the other one in the near infrared spectral range (Band 12 centered on 773 nm). It is carried out by comparing the reflectance value of the in situ data with the corresponding pixel reflectance value of the corrected image as can be observed in Figure 3. In this graph each point corresponds to different plots measured in situ. At this date a total of three different plots were considered, two bare soils with high reflectance values in band 9 and low in band 12 and a green grass with low reflectance values. We can see that high reflectance values are more dispersed and differ from the diagonal line more than low reflectance values.

We have also tested the atmospheric correction comparing every flight's results. Figure 4 represents the surface reflectance of each plot considered in the validation of AHS images (differenced in the graph by colors). In each case the central line corresponds to the average of every flight surface reflectance and also it is shown the standard deviation in each band. The spectrums with the maximum positive (or negative) difference with reference to the mean are represented in this graph as the upper (or lower) line in each plot.

As an example, Figure 180 shows reflectance for AHS band 12 before (TOA) and after the atmospheric correction.



(a)



(b)

Figure180: Spectrum in the VNIR spectral range measured in situ and estimated from AHS of a) a bare soil and b) a green grass.

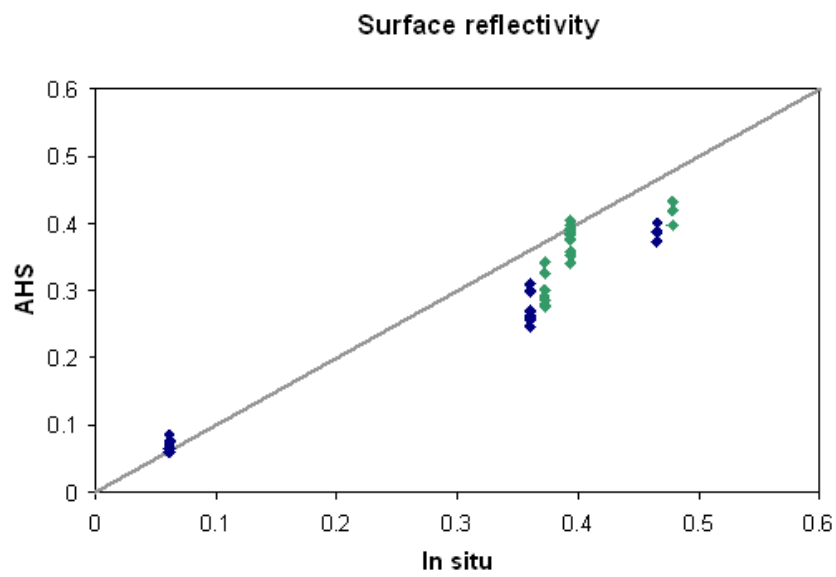


Figure 181. Band 9 and band 12 test over every flight.

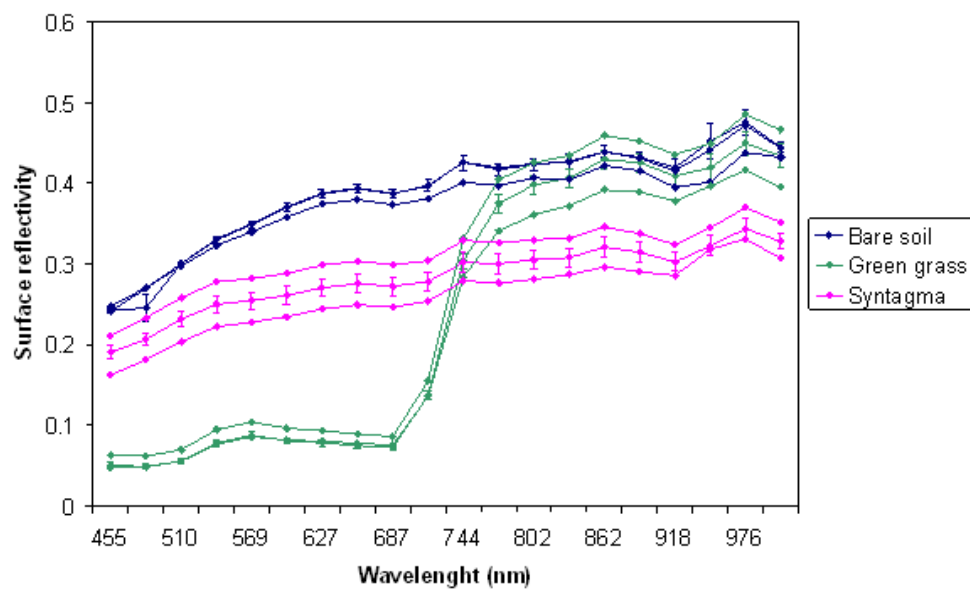


Figure 182. Comparison between every flight's surface reflectance.

AHS image P02I1 18th of July

AHS12 (760 nm) TOA reflectivity

AHS12 (760 nm) Surface reflectivity

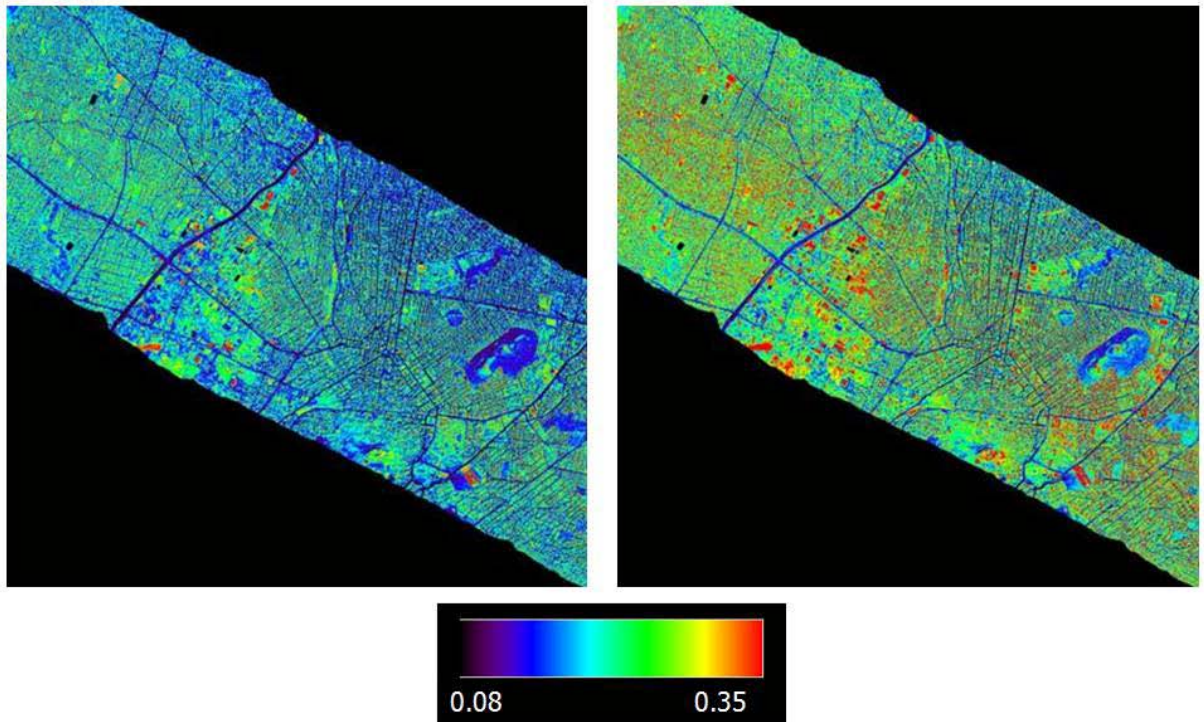


Figure 183. Atmospheric correction of AHS band 12.

7.4 Atmospheric Correction in the Thermal Infrared Range

BACKGROUND

Most of the Land Surface Temperature (LST) and Emissivity (LSE) retrieval algorithms are based on the Radiative Transfer Equation. When it is applied to a particular wavelength (λ) in the TIR region, it can be expressed as

$$L_{\lambda}^{sen} = \left[\varepsilon_{\lambda} B_{\lambda}(T_s) + (1 - \varepsilon_{\lambda}) L_{\lambda}^{\downarrow} \right] \tau_{\lambda} + L_{\lambda}^{\uparrow} \quad (7)$$

where L^{sen} is at-sensor registered radiance, B is the blackbody radiance, T_s is the LST, ε is the surface emissivity, τ is the atmospheric transmissivity, L^{\downarrow} is the down-welling atmospheric irradiance normalized by π sr, and L^{\uparrow} is the up-welling atmospheric path radiance. When applied to a certain sensor band, spectral magnitudes are averaged according to the spectral response function of that band. The term in brackets integrates all terms coming from the surface, so it is usually called Land-Leaving Radiance (LLR) :

$$LLR_{\lambda} = \varepsilon_{\lambda} B_{\lambda}(T_s) + (1 - \varepsilon_{\lambda}) L_{\lambda}^{\downarrow} \quad (8)$$

Atmospheric parameters (τ , L^{\uparrow} and L^{\downarrow}) involved in Eq. (7) are usually obtained from atmospheric profiles (radiosoundings) and radiative transfer codes such as MODTRAN 4 (Berk et al., 1999).

7.5 Land Surface Temperature and Emissivity Retrieval

7.5.1 Split-Window technique and emissivity from NDVI

Proposed split-window algorithm

The Two-Channel (TC) technique, also called Split-Window (SW) when working in 10-12 μ m, has been widely used by the scientific community (see for example Kerr et al., 2004). In this case we have considered the TC algorithm proposed by Sobrino and Raissouni (2000):

$$T_s = T_i + a_1(T_i - T_j) + a_2(T_i - T_j)^2 + a_0 + (a_3 + a_4 w)(1 - \varepsilon) + (a_5 + a_6 w)\Delta\varepsilon \quad (9)$$

being T_i and T_j the at-sensor brightness temperatures (in K) for two different AHS TIR bands, w the atmospheric water vapour content (in g/cm^2) and $\varepsilon=0.5(\varepsilon_i+\varepsilon_j)$ and $\Delta\varepsilon=(\varepsilon_i-\varepsilon_j)$ are respectively the mean emissivity and the emissivity difference for the two AHS bands considered. As it can be noticed, this method requires two TIR bands. Equation (9) can be theoretically obtained when Eq. (7) is applied to two TIR bands. The coefficients a_i ($i=0,6$) are obtained from simulated data (atmospheric soundings, MODTRAN-4 and emissivity spectra), as it is explained in Sobrino et al. (2006). In this case, 61 atmospheric soundings with five different surface temperatures ($T_0 - 5$ K, T_0 , $T_0 + 5$ K, $T_0 + 10$ K and $T_0 + 20$ K, where T_0 is the temperature at the first layer of the atmospheric profile) and 108 emissivity spectra extracted from the ASTER spectral library (soils, vegetation, water, ice and whole rock chips) have been used. Therefore, a total amount of $5 \times 61 \times 108 = 32,940$ simulated cases were considered. In Sobrino et al. (2006) simulations at different altitudes were made in order to provide specific coefficients for each flight altitude. However, for consistency, we provide in this case a single set of coefficients, which can be used for any flight altitude. The user only needs to take into account that water vapour (w) should be computed for the particular view angle (\square) and flight altitude (h), since this magnitude depends on both of them. Table 2 provides the results obtained for each AHS bands combinations, as well as the expected error on the LST retrieval according to the sensitivity analysis as presented for example in Jiménez-Muñoz & Sobrino (2009). The results show that best combination is obtained with AHS bands 76 ($10.5 \mu\text{m}$) and 79 ($12.3 \mu\text{m}$), so the final split-window algorithm is given by:

$$T_s = T_i + 0.747(T_i - T_j) + 0.108(T_i - T_j)^2 - 0.057 + (48.898 - 2.051w)(1 - \varepsilon) + (-86.311 + 11.470w)\Delta\varepsilon \quad (10)$$

Figure 6 shows a LST image retrieved from SW algorithm. The emissivity used to retrieve this LST map is the one obtained with the TES algorithm (see TES algorithm section). It is an image from the P01I2 AHS overpass on 18th July at 20:52 UTC.

Table 78. Errors on the Land Surface Temperature retrieved from Split-Window algorithms according to the sensitivity analysis and using different AHS bands combinations. ‘Std. Dev’ is the standard error of estimation, ‘r’ is the correlation coefficient, ‘e_noise’ is the error due to the NE \square T, ‘e_emis’ is the error due to the emissivity uncertainty, ‘e_vapor’ is the error due to the total water vapour content uncertainty and ‘e_total’ is the total error. Bands combinations providing total errors higher than 2 K have not been included.

Band ‘i’ (μm)	Band ‘j’ (μm)	Std. Dev. (K)	r	e_noise (K)	e_emis (K)	e_vapor (K)	e_total (K)
8.081	9.125	1.43	0.98	0.20	1.13	0.21	1.85
8.619	12.906	0.76	0.98	0.26	1.16	0.39	1.46
9.125	12.317	1.55	0.92	0.22	0.98	0.32	1.87
9.125	12.906	1.10	0.96	0.20	0.99	0.41	1.55

10.545	11.733	0.67	0.99	0.44	1.38	0.16	1.60
10.545	12.317	0.85	0.98	0.29	0.85	0.10	1.24
10.545	12.906	1.23	0.95	0.22	0.62	0.04	1.39
11.157	12.317	1.29	0.96	0.39	1.02	0.04	1.69
11.157	12.906	1.83	0.92	0.26	0.67	0.16	1.97

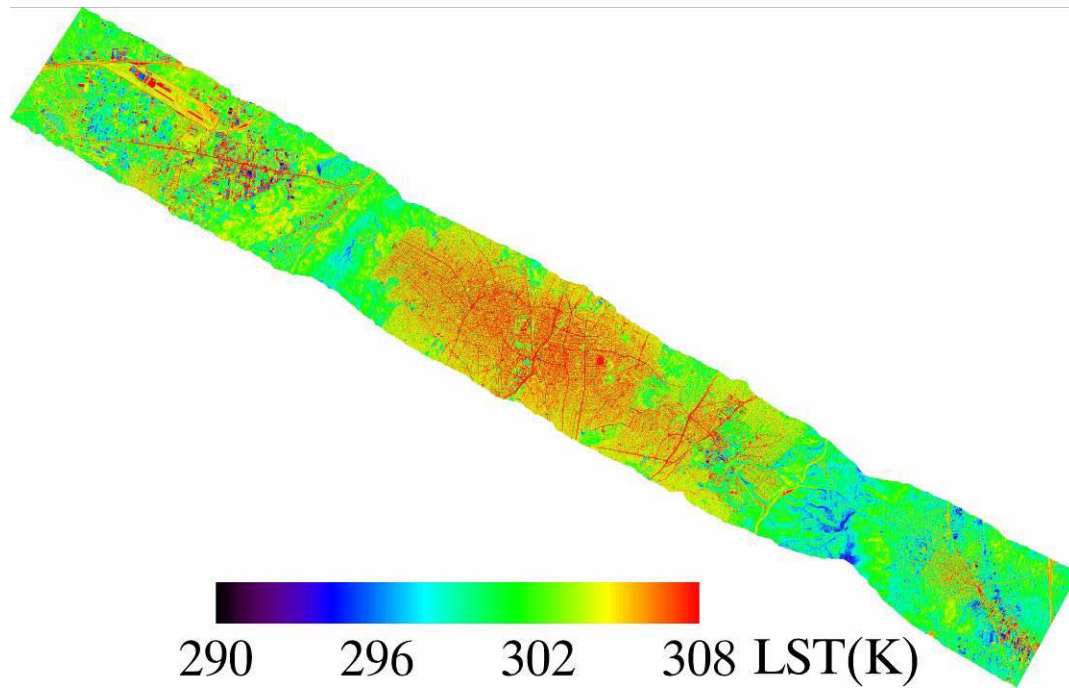


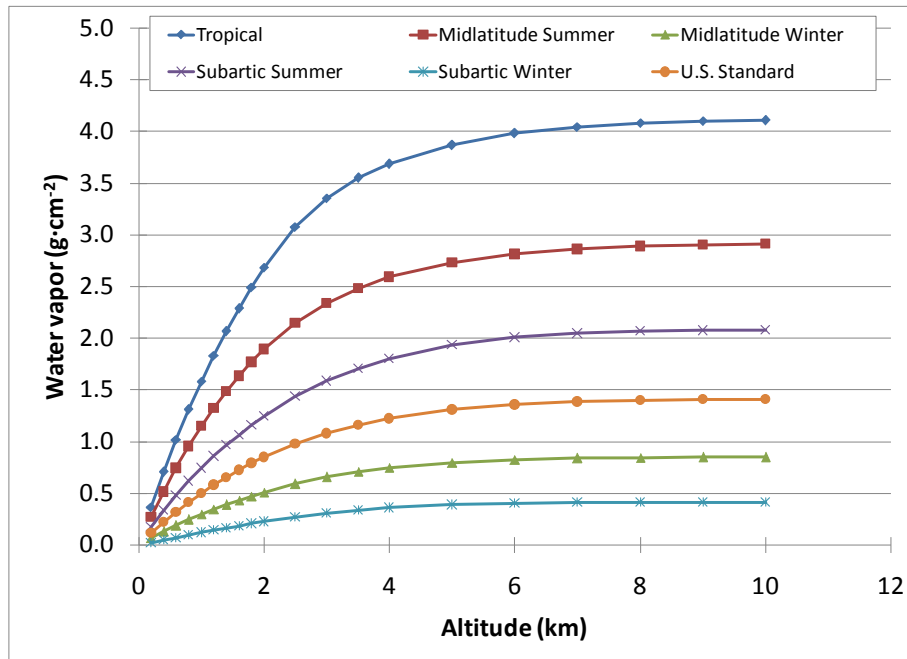
Figure 184. LST image retrieved from SW algorithm using emissivity from TES algorithm. P01I2 AHS overpass from 18th July 2009 at 20:52 UTC.

Atmospheric water vapour dependence on view angle and altitude

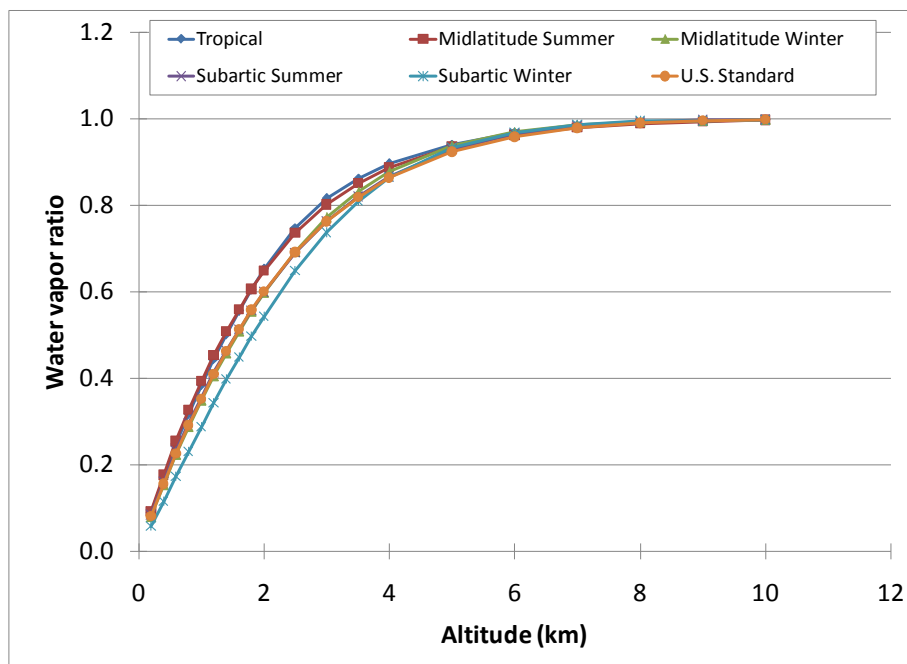
As stated before, water vapour should be computed for a given view angle and altitude. The relationship between at-nadir water vapour and the one for a given view angle is given by a cosine factor:

$$w(\theta) = \frac{w(0^\circ)}{\cos \theta} \quad (11)$$

The water vapour dependence on altitude is not so straightforward. Figure 7 shows water vapour values for different standard atmospheres versus the altitude (values obtained with MODTRAN 4 code). The ratio between water vapour at certain altitude and total water vapour (from 0 to 100 km) is also represented. Values of this ratio are also provided in Table 3. It can be observed that the ratio is equal to 1 from 10 km, and higher than 80% from 4 km. It is also observed that ratio values are similar for each standard atmosphere, so a mean value could be used to convert total water vapour contents to contents at a certain altitude (mean ratio values are also provided in Table 3).



(a)



(b)

Figure 185. (a) Atmospheric water vapor content versus the altitude for different standard atmospheres and (b) ratio between atmospheric water vapor content at a certain altitude and the total content.

Table 79. Values of ratio between atmospheric water vapor content at a certain altitude and the total content for different standard atmospheres. The mean ratio value is also given.

Altitude (km)	Tropical	Midlatitude summer	Midlatitude winter	Subartic summer	Subartic winter	U.S. Standard	Mean value
0.2	0.09	0.09	0.08	0.08	0.06	0.08	0.08
0.4	0.17	0.18	0.15	0.16	0.12	0.16	0.16
0.6	0.25	0.25	0.22	0.23	0.17	0.23	0.23
0.8	0.32	0.33	0.29	0.30	0.23	0.29	0.29
1.0	0.38	0.39	0.35	0.36	0.29	0.35	0.35
1.2	0.45	0.45	0.40	0.41	0.34	0.41	0.41
1.4	0.50	0.51	0.46	0.47	0.40	0.46	0.47
1.6	0.56	0.56	0.51	0.51	0.45	0.51	0.52
1.8	0.61	0.61	0.56	0.56	0.50	0.56	0.56
2.0	0.65	0.65	0.60	0.60	0.54	0.60	0.61
2.5	0.75	0.74	0.69	0.69	0.65	0.69	0.70
3.0	0.82	0.80	0.77	0.76	0.74	0.76	0.78
3.5	0.86	0.85	0.83	0.82	0.81	0.82	0.83
4.0	0.90	0.89	0.88	0.87	0.87	0.86	0.88
5.0	0.94	0.94	0.94	0.93	0.94	0.92	0.93
6.0	0.97	0.96	0.97	0.97	0.97	0.96	0.97
7.0	0.98	0.98	0.99	0.99	0.99	0.98	0.98
8.0	0.99	0.99	0.99	0.99	1.00	0.99	0.99
9.0	1.00	0.99	1.00	1.00	1.00	1.00	1.00
10.0	1.00	1.00	1.00	1.00	1.00	1.00	1.00

Emissivity from NDVI: the Thresholds Method

Land surface emissivity is a necessary parameter when LST is retrieved from the split-window algorithm given by Eq. (10). In this case the NDVI Thresholds Method (NDVI^{THM}) has been proposed for LSE retrieval (Sobrino & Raissouni, 2000; Sobrino et al., 2008).

The NDVI Thresholds method obtains emissivity values from the NDVI considering different cases

- NDVI < 0.2

In this case, the pixel is considered as bare soil and the emissivity is obtained from reflectivity values in the red region.

$$\varepsilon = a + b \rho_{red} \quad (12)$$

- NDVI > 0.5

In this case the pixel is considered as fully vegetated, and then a constant value for the emissivity is assumed, typically 0.99.

- 0.2 < NDVI < 0.5

In this case, the pixel is composed by a mixture of bare soil and vegetation, and the emissivity is calculated according to:

$$\varepsilon = mP_v + n \quad (13)$$

with

$$\begin{aligned} m &= \varepsilon_v - \varepsilon_s - (1 - \varepsilon_s) F \varepsilon_v \\ n &= \varepsilon_s + (1 - \varepsilon_s) F \varepsilon_v \end{aligned} \quad (14)$$

where ε_v is the vegetation emissivity and ε_s is the soil emissivity, P_v is the vegetation proportion obtained according to Carlson & Ripley (1997) and F is a shape factor, which mean value is 0.55 and has been obtained assuming different geometrical distributions (Sobrino et al., 1990).

7.5.2 Temperature and Emissivity Separation (TES) algorithm

Temperature and Emissivity Separation (TES) algorithm was developed by Gillespie et al. (1998) to produce the Standard Products of LST and LSE from the Advanced Spaceborne Thermal Emission and Reflection Radiometer (ASTER) data. It uses as input the land-leaving radiances (LLRs, Eq. 8) and the down-welling atmospheric radiance (L^\downarrow), and it is composed by three different modules: NEM (Normalized Emissivity Method), RATIO and MMD (Maximum-Minimum Difference). Basically, the NEM module provides a first guess of the surface temperature and emissivities using an iterative procedure, the RATIO module normalizes the surface emissivities

providing the so-called beta spectrum, and finally the MMD module recovers final surface emissivities and temperature using a semi-empirical relationship between minimum emissivity (ϵ_{\min}) and spectral contrast (MMD):

$$\epsilon_{\min} = a + b \times MMD^c \quad (15)$$

The relationship between ϵ_{\min} and MMD must be recalculated for each sensor, since it depends on bands spectral response functions and bands configuration. For this purpose, the 108 emissivity spectra used in the retrieval of the Two-Channel coefficients have been used. The result of the statistical fitting for the ten AHS TIR bands is the following:

$$\epsilon_{\min} = 1.001 - 0.787 MMD^{0.821} \quad [r = 0.998, \sigma = 0.004] \quad (16)$$

where r is the correlation coefficient and σ the standard error of estimation.

In Thermopolis campaign noisy signal is detected at the AHS band 78. Because of that, only nine bands are used to apply TES algorithm. The result of the statistical fitting for nine AHS TIR bands is the following:

$$\epsilon_{\min} = 1.000 - 0.784 MMD^{0.821} \quad [r = 0.997, \sigma = 0.004] \quad (8)$$

Figures 8, 9, 10 and 11 show images of LST retrieved by TES algorithm using nine TIR bands (71, 72, 73, 74, 75, 76, 77, 78, 79, 80). They correspond to all the AHS overpasses on the day 18th of July at night. In these images we can observe that the city is warmer than its surroundings without urban constructions.

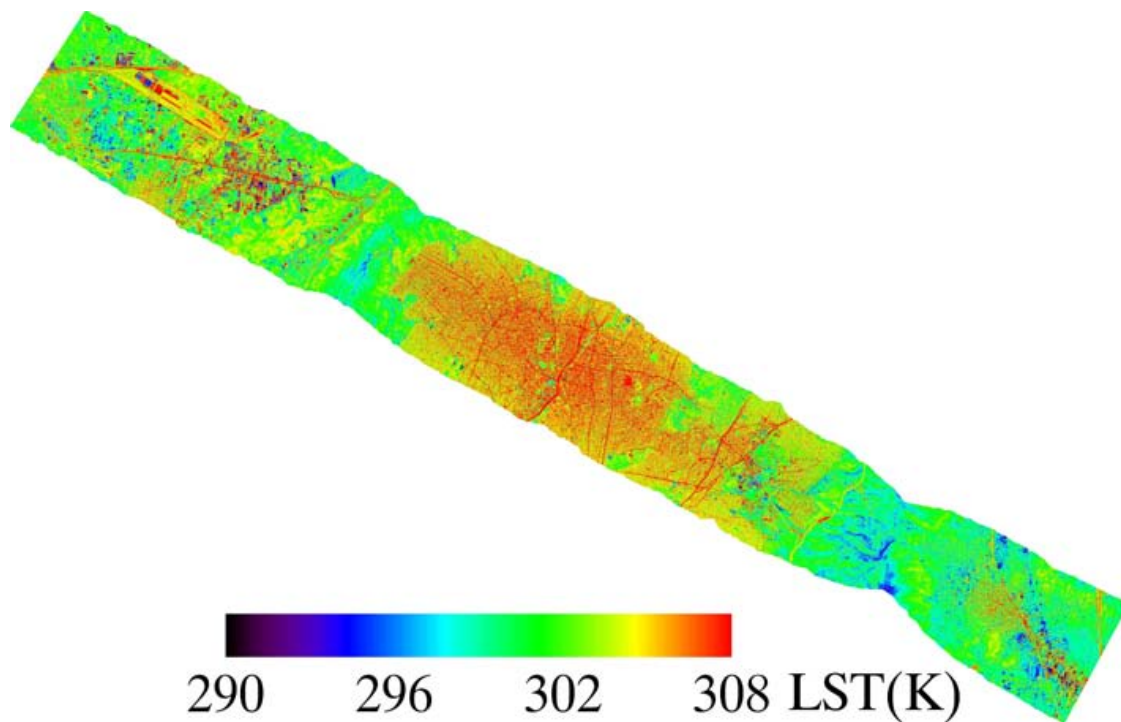


Figure 186. LST image retrieved from TES algorithm using 9 TIR bands. P01I2 AHS overpass from 18th July 2009 at 20:52 UTC.

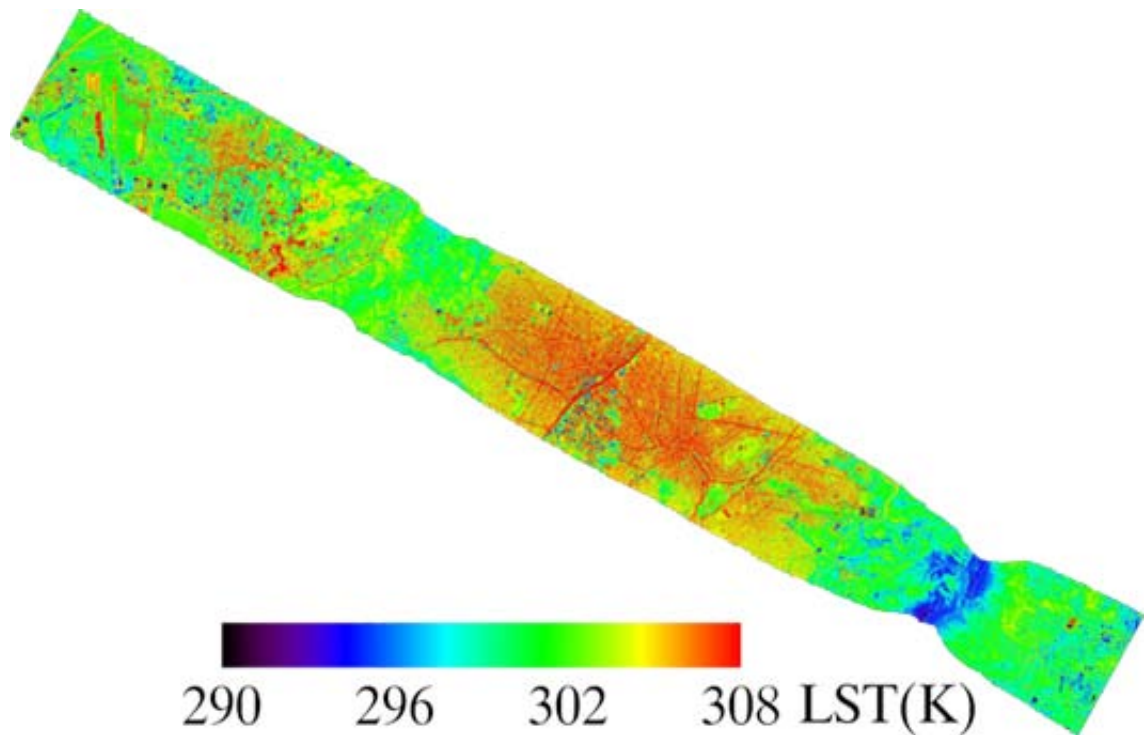


Figure 187. LST image retrieved from TES algorithm using 9 TIR bands. P02I2 AHS overpass from 18th July 2009 at 21:09 UTC.

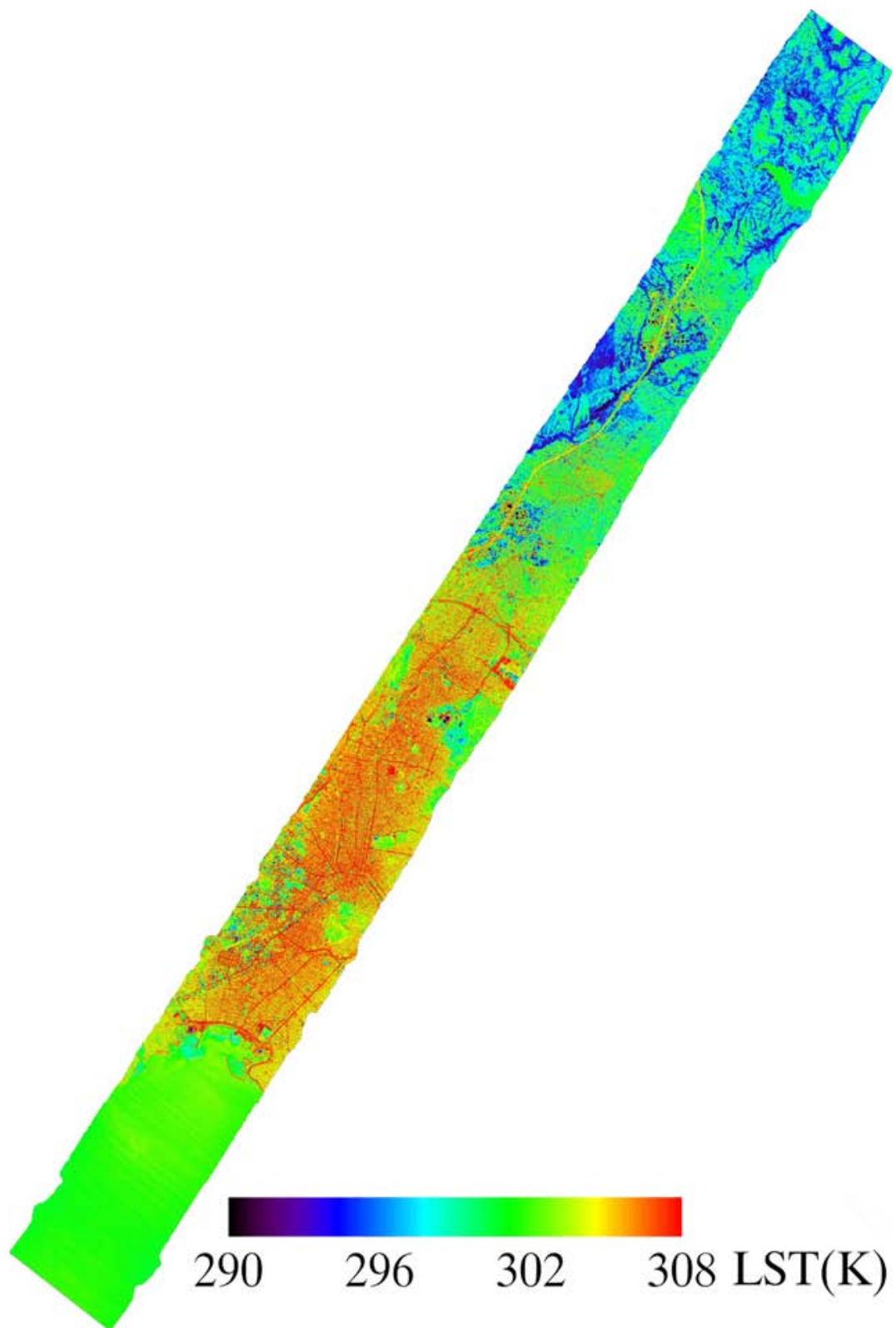


Figure 188. LST image retrieved from TES algorithm using 9 TIR bands. P03I2 AHS overpass from 18th July 2009 at 20:30 UTC.

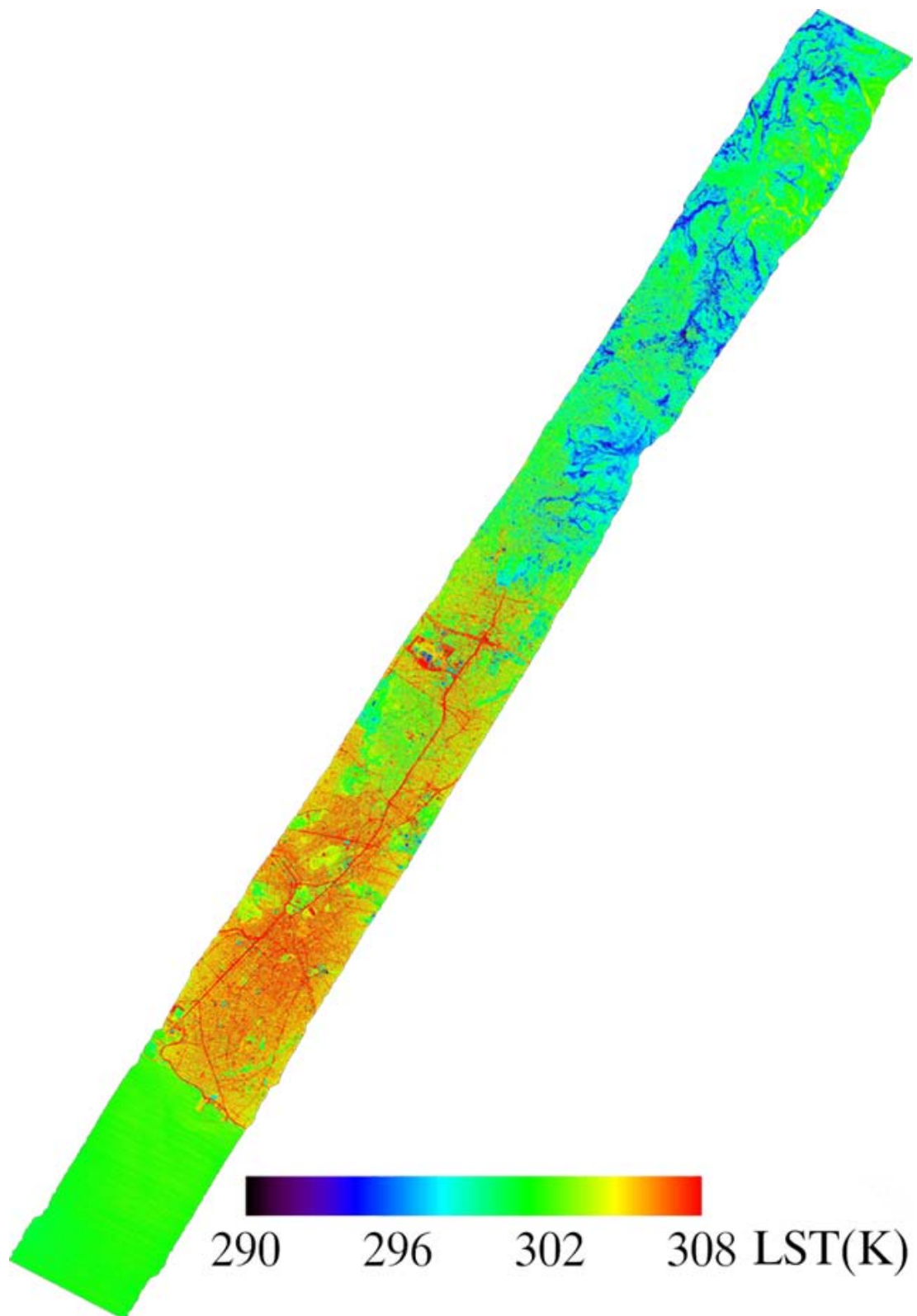


Figure 189. LST image retrieved from TES algorithm using 9 TIR bands. P03I2 AHS overpass from 18th July 2009 at 20:11 UTC.

As an example, Figure 12 shows the emissivity obtained from the TES algorithm on July 21st at 20:52 UTC.

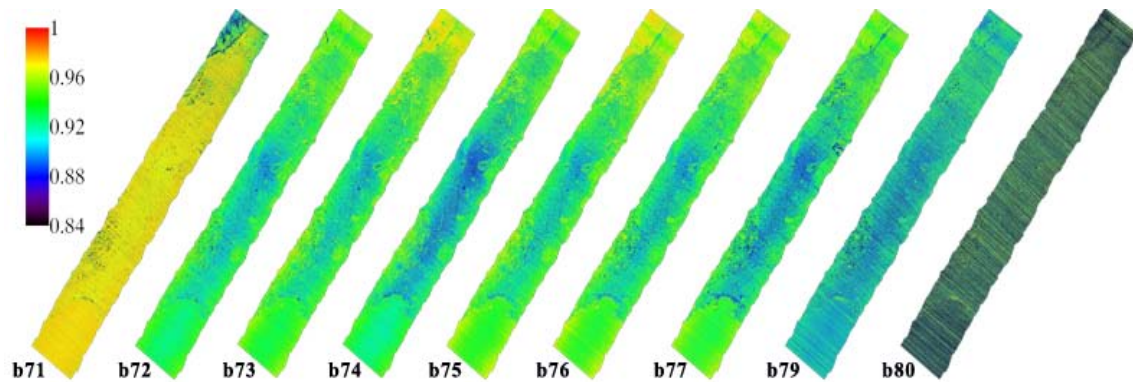


Figure 190. AHS emissivity image obtained with the TES algorithm on July 21st at 20:52, for the overpass number 3.

The emissivities obtained with the TES method provide similar results for all the images. This can be observed in Figure 13, where the difference between a daytime image and a nighttime image of day 18th of July is plotted as well as the histogram.

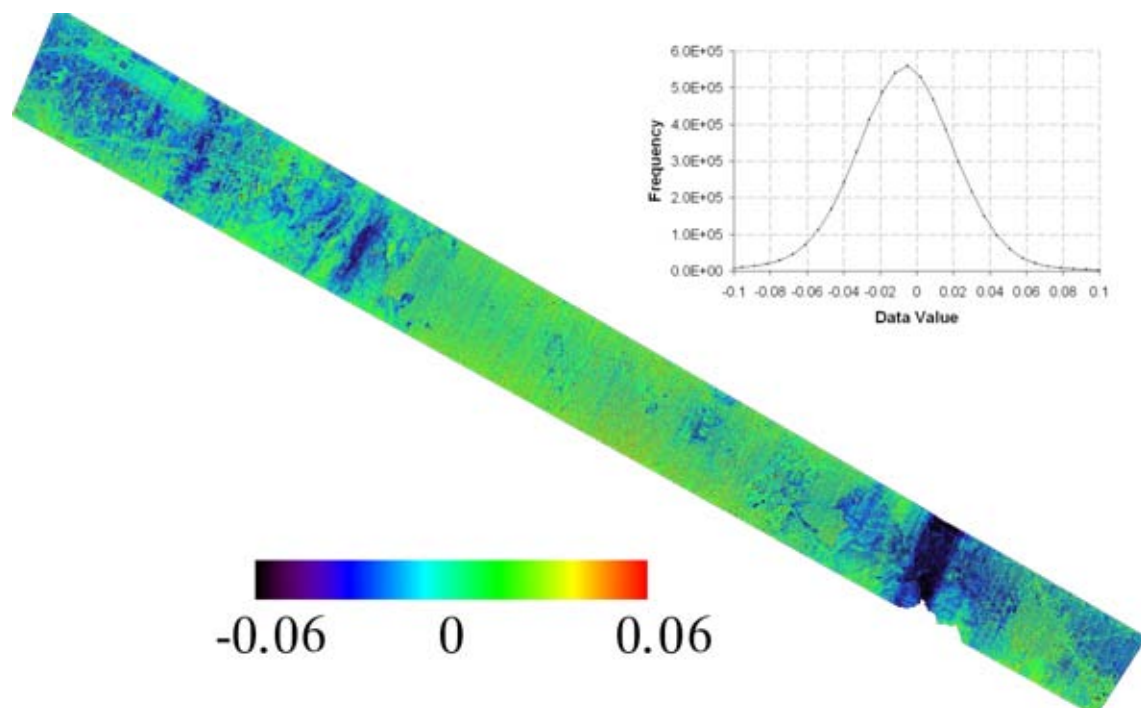


Figure 191. Difference on emissivity in AHS band 77 obtained with TES algorithm on July 18th at 09:21 and on July 18th at 20:07. And histogram of the difference image.

7.5.3 Vicarious Calibration

This section shows the analysis carried out to check the proper performance of the AHS TIR bands by means of in situ measurements.

The ideal conditions required for calibration sites are: i) the targets should be homogeneous in both surface temperature and emissivity, and ii) atmospheric conditions should be stable and cloud-free, with small total water vapour amounts. Therefore, the targets selected for the calibration of the AHS sensor include: water body (Marathonos Lake) and green grass (Soccer field at the Panathinaikos Stadium).

At-sensor radiances ($L_i^{\text{at-sensor}}$) for each AHS TIR bands ($i=71,80$) have been calculated from ground-based measurements using the radiative transfer equation given by (7). The emissivity has been obtained from spectral libraries, the atmospheric parameters (τ , L_i^\downarrow , L_i^\uparrow) have been estimated from the MODTRAN4 code and the atmospheric soundings from MODIS products (MOD07) for daytime images and from in situ atmospheric soundings for night time images. The at-sensor radiances reproduced from ground-based measurements have been compared with the ones extracted from the AHS images over regions of 3x3 pixels and for the 10 TIR bands of AHS.

Calibration measurements showed that all bands had a good performance. Nevertheless, band 78 had noisy signal.

Table 4 shows all the targets used to calibrate, it includes the date and time of the measures as well as the instrument used for the in situ measurement. There are also included the statistical values obtained from the comparison between in situ measurements and AHS images values for each target.

Figure 14 shows some examples of vicarious calibration for different flights over the green grass plot, whereas Figure 15 shows the results obtained over the water plot. Figure 16 displays the comparison between the at-sensor brightness temperature (obtained by inversion of the Planck's law applied to the at-sensor radiance) and the obtained from the AHS image. The comparison is made for each of the 10 AHS TIR bands and for all the targets included in Table 4. The result shows a RMSE deviation of around 1.4 K.

Table 80. Date, time, instrument, sample and statistical values from calibration measurements.

Date	Hour	Instrument	Surface	Bias (°)	σ (K)	RMSE (K)
18/07	08:10	Optris CT-LT15	GreenGrass	-0.6	0.6	0.9
18/07	08:45	Optris CT-LT15	GreenGrass	0.5	1.1	1.2
18/07	08:45	Cimel 6	Water	-1.1	0.4	1.2
18/07	08:45	Raytek	Water	-1.4	0.4	1.4
18/07	09:01	Cimel 6	Water	-1.2	0.5	1.3
18/07	09:01	Raytek	Water	-1.4	0.5	1.5
18/07	09:21	Optris CT-LT15	GreenGrass	-1.5	0.9	1.8
18/07	20:11	Optris CT-LT15	GreenGrass	0.8	0.7	1.1
18/07	20:11	Cimel 6	Water	-1.3	0.9	1.6
18/07	20:11	Raytek	Water	-0.4	0.9	1.0
18/07	20:30	Cimel 6	Water	-0.7	0.9	1.1
18/07	20:30	Raytek	Water	0.2	0.8	0.9
18/07	20:52	Optris CT-LT15	GreenGrass	-0.3	1.3	1.4
18/07	21:09	Optris CT-LT15	GreenGrass	0.8	0.6	1.0
20/07	10:16	Optris CT-LT15	GreenGrass	-1.4	1.2	1.9
20/07	10:32	Optris CT-LT15	GreenGrass	-1.8	1.2	2.2
20/07	10:51	Optris CT-LT15	GreenGrass	0.1	1.4	1.4
21/07	01:24	Optris CT-LT15	GreenGrass	-1.4	1.0	1.7
21/07	01:55	Cimel 6	Water	-1.0	0.9	1.4
21/07	01:55	Raytek	Water	1.0	1.5	1.9
21/07	01:55	Optris CT-LT15	GreenGrass	-1.2	1.1	1.7
21/07	02:05	Cimel 6	Water	-1.9	1.3	2.3
21/07	02:05	Raytek	Water	-1.1	1.4	1.8
21/07	20:07	Optris CT-LT15	GreenGrass	-1.1	0.5	1.2
21/07	20:22	Optris CT-LT15	GreenGrass	0.1	0.5	0.5
21/07	20:40	Optris CT-LT15	GreenGrass	-0.2	0.4	0.4
21/07	20:40	Cimel 6	Water	-1.0	0.4	1.1
21/07	20:40	Raytek	Water	0.0	0.5	0.5
24/07	21:03	Cimel 6	Water	-1.3	0.3	1.3
24/07	21:03	Raytek	Water	1.0	0.5	1.1

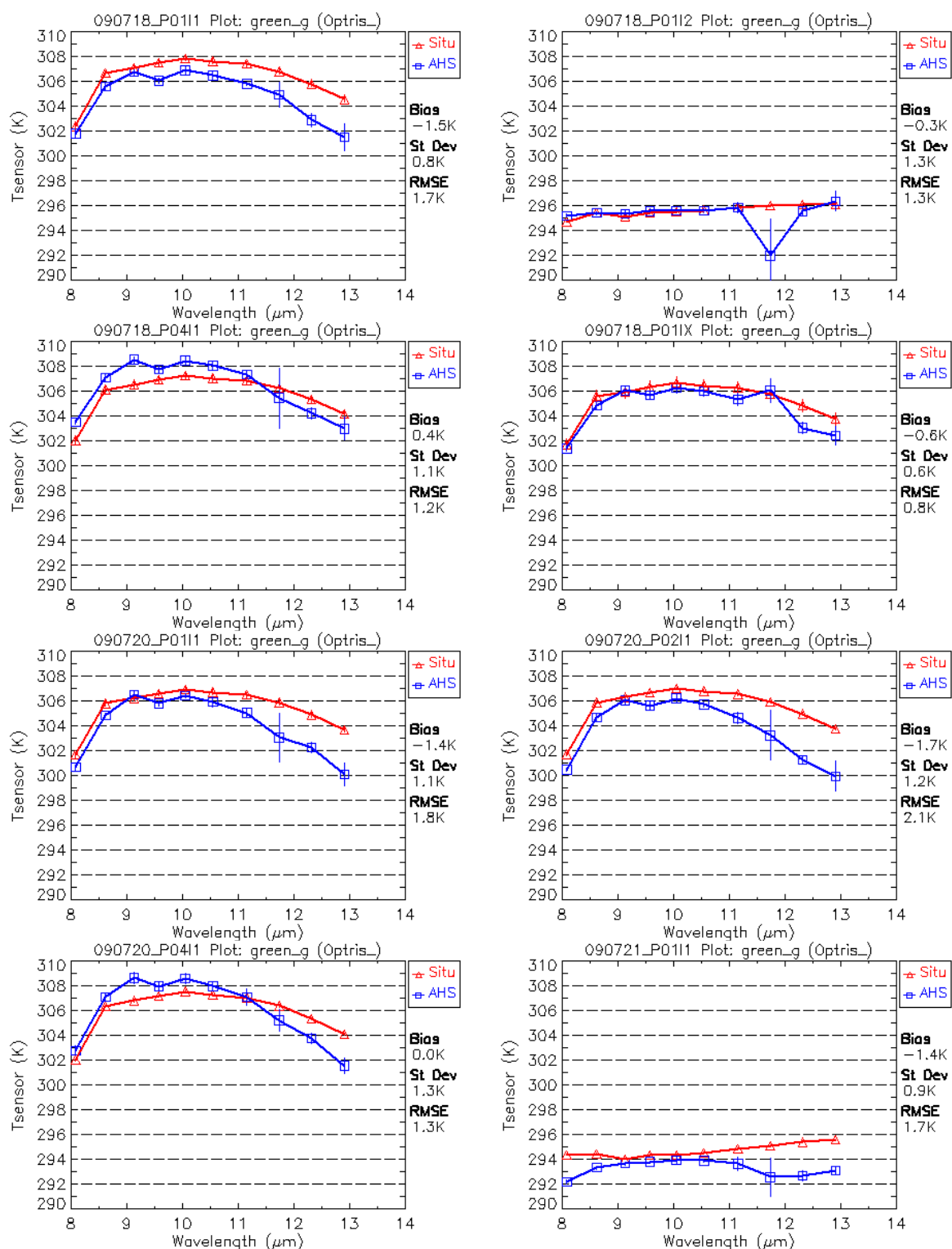


Figure 192. Vicarious calibration of AHS TIR bands for the green grass plot.

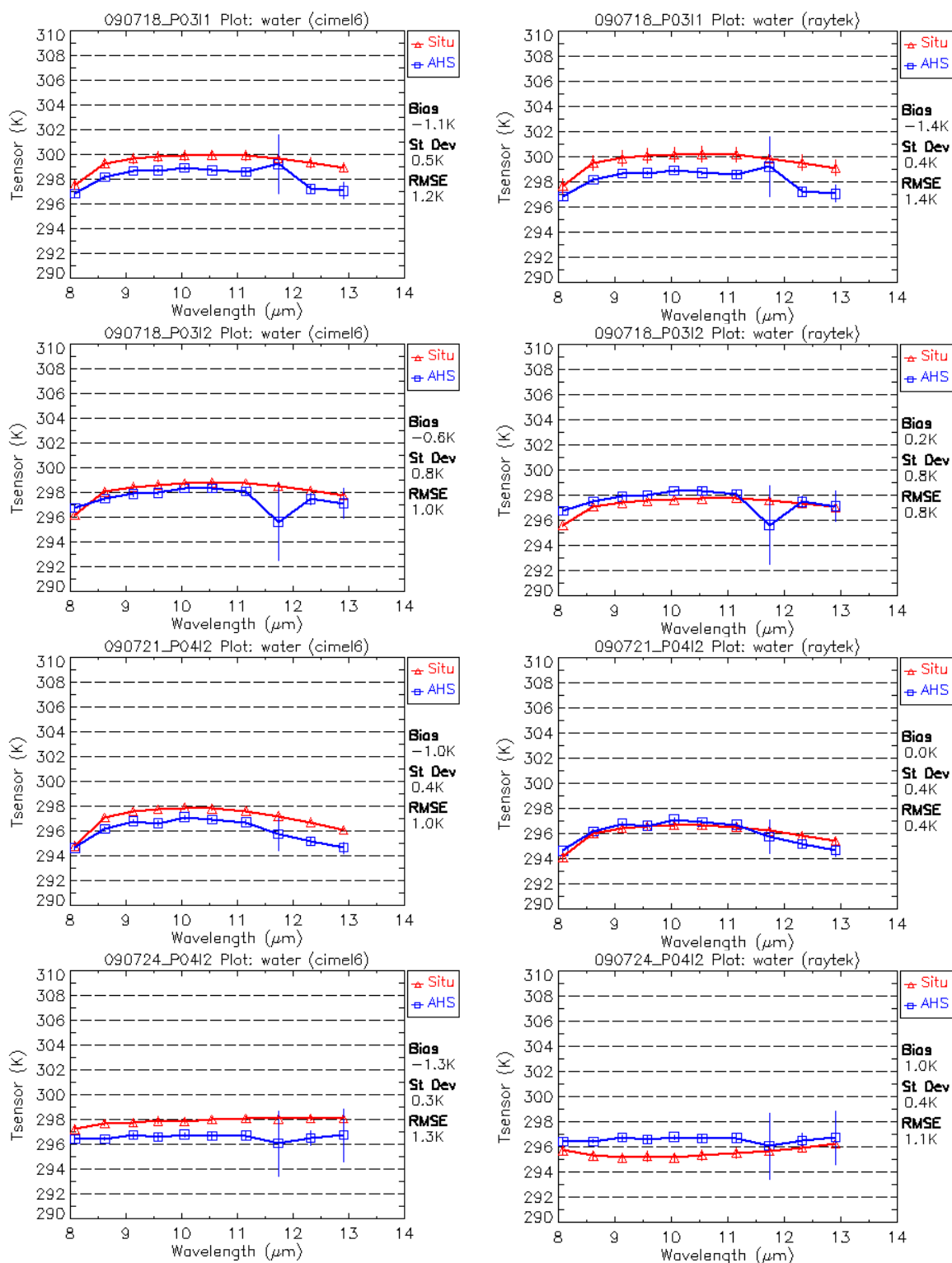


Figure 193. Vicarious calibration of AHS TIR bands for the water plot.

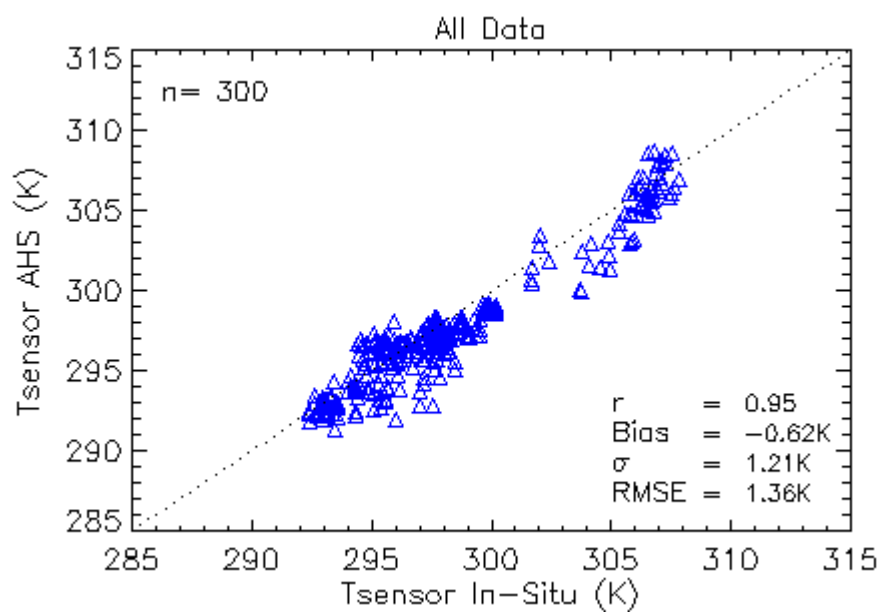


Figure 194. Comparison between the at-sensor brightness temperatures reproduced from ground-based measurements (Tsensor In-Situ) and the ones extracted from the AHS images (Tsensor AHS).

7.6 Validation

The LST values obtained from TES algorithm applied to the AHS images were compared with the LST obtained from in situ measurements. The radiative transfer equation, the surface emissivity and the sky downwelling radiance were taken into account for in situ LST retrieval. Validation sites were the same than calibration ones: AHS LST values were extracted over regions of 3x3 pixels from water (Marathonos Lake) and green grass (soccer field at the Panathinaikos Stadium). The test for each surface is presented in Figure 17. When the two surfaces are considered, the test gives a RMSE of 1.6 K.

The SW algorithm was applied using surface emissivities calculated with TES algorithm. SW validation is shown in Figure 18. To validate the algorithm the same ground-truth values used with the TES validation were used. The test using the two surfaces (water and green grass) gave a RMSE of 1.8 K.

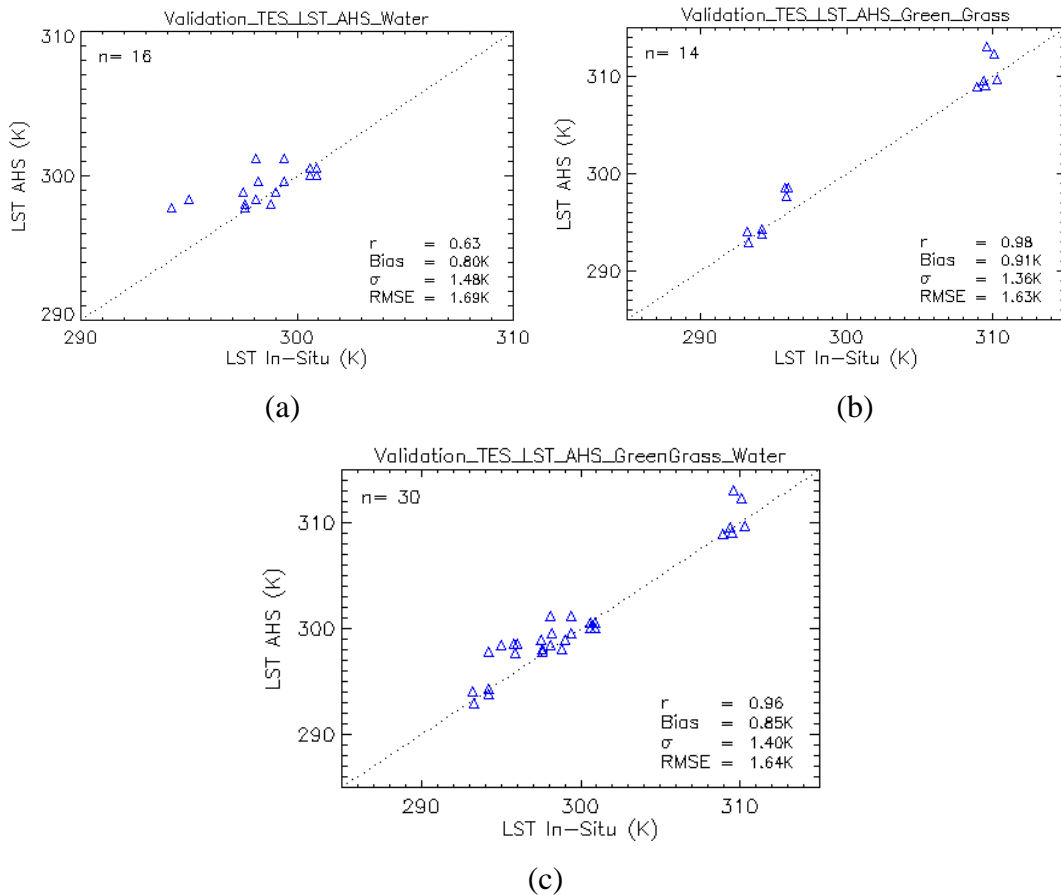


Figure 195. Validation of TES algorithm using 9 AHS TIR bands (LST AHS) with in situ measurements (LST In-Situ) using (a) only water points, (b) only green grass points and (c) water and green grass points.

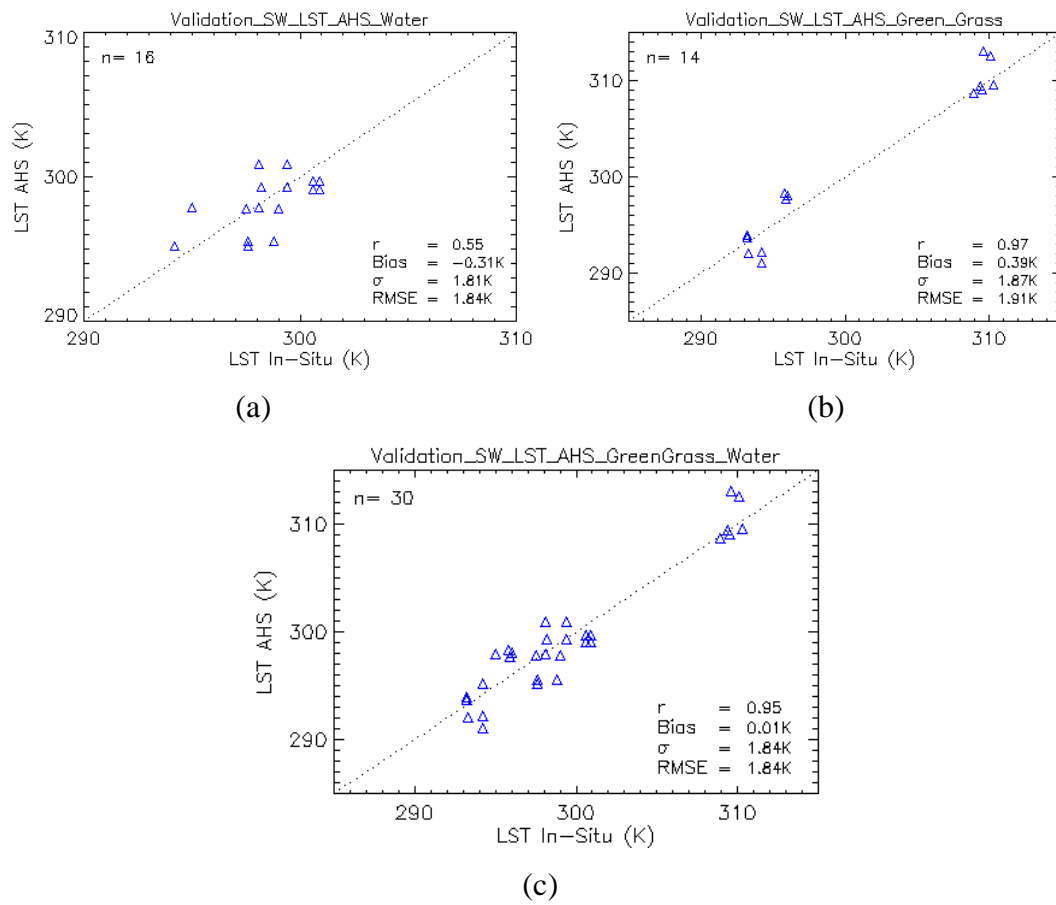


Figure 196. Validation of SW algorithm using 9 AHS TIR bands (LST AHS) with in situ measurements (LST In-Situ) using (a) only water points, (b) only green grass points and (c) water and green grass points.

7.7 Generation of Examples of Simulated Uhi Products at Different Spatial Sampling Distances

This section analyses the impact of changing the spatial resolution of the sensor in the estimation of LST over an urban area. To this end, the 4m resolution AHS images were resized to 10 m, 20 m, 30 m, 40 m, 50 m, 100 m, 200 m, 300 m, 400 m, 500 m and 1000 m resolution.

The resizing method consisted of averaging all the pixel values that contribute to the output pixel. This process was applied to the at-sensor radiance images, and after that LST was retrieved by applying the TES algorithm to the new resampled pixels. TES algorithm was applied as it is explained in the section “*Temperature and Emissivity Separation (TES) algorithm*”

Figure 19 shows an example of the results obtained at night for the overpass number 4 of the AHS of July 18th.

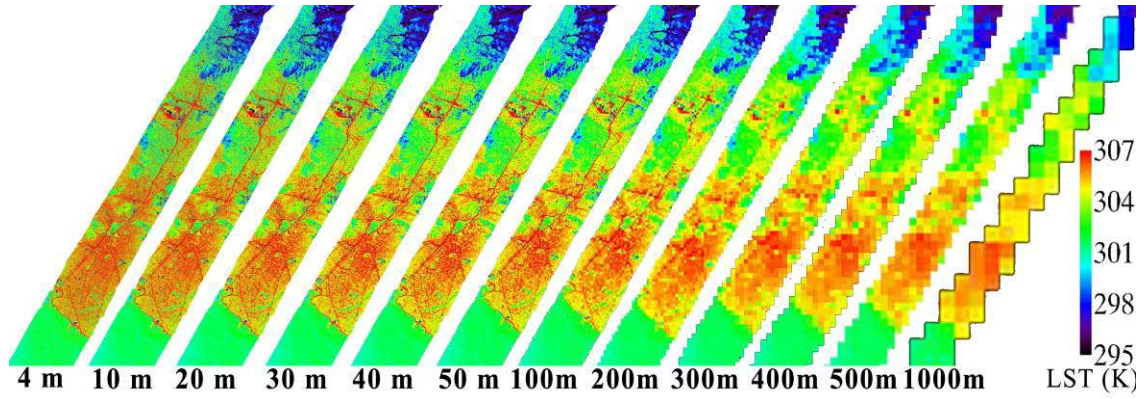


Figure 197. Resampling of the LST AHS image of July 18th at 20:11 UTC. Detail of the 4th AHS overpass.

7.8. Suhi Characterization By Means Of AHS Images

The Urban Heat Island (UHI) phenomenon is characterized by the warming of the urban zones in comparison with its surroundings not urbanized. The UHI is an atmospheric measurement, as the parameter studied is the air temperature. When we talk about Land Surface Temperature, the phenomenon studied is the Surface Urban Heat Island (SUHI) (Voogt et al. 2003) defined as:

$$SUHI = LST_{Urban} - LST_{Rural} \quad (6.35)$$

In order to calculate SUHI, AHS LST images have been divided into two different zones (see Figure 20), urban (into the black line) and rural (the rest of the image).

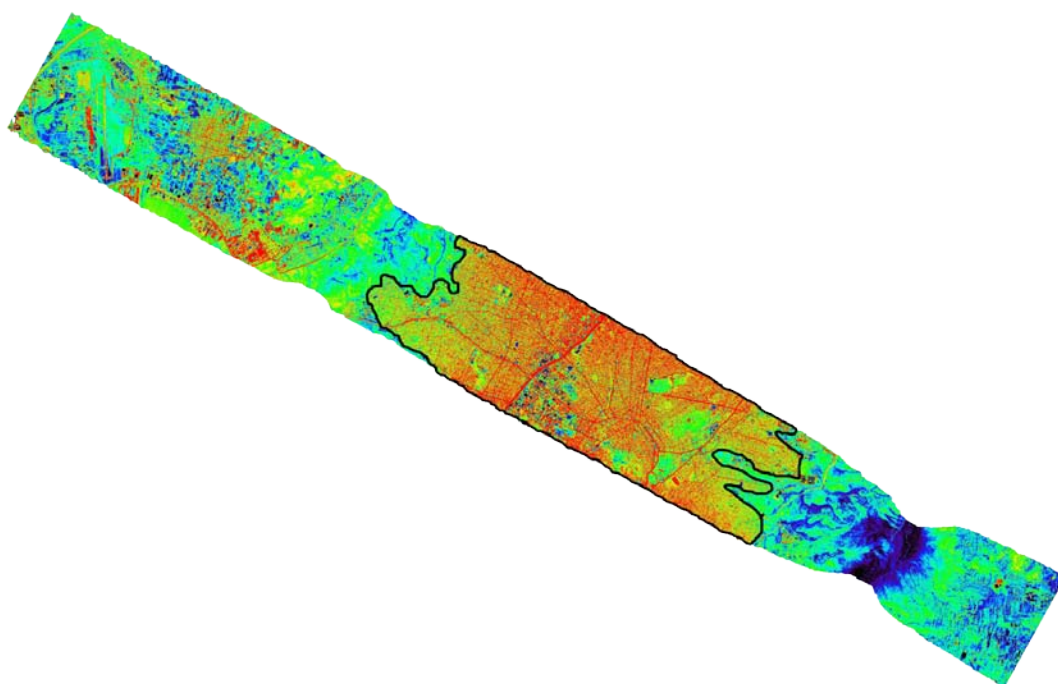


Figure 198. LST image with the urban zone considered delimited with a black line.

SUHI effect has been obtained by subtracting the average temperature of rural and urban zones and the results are shown in Figure 21.

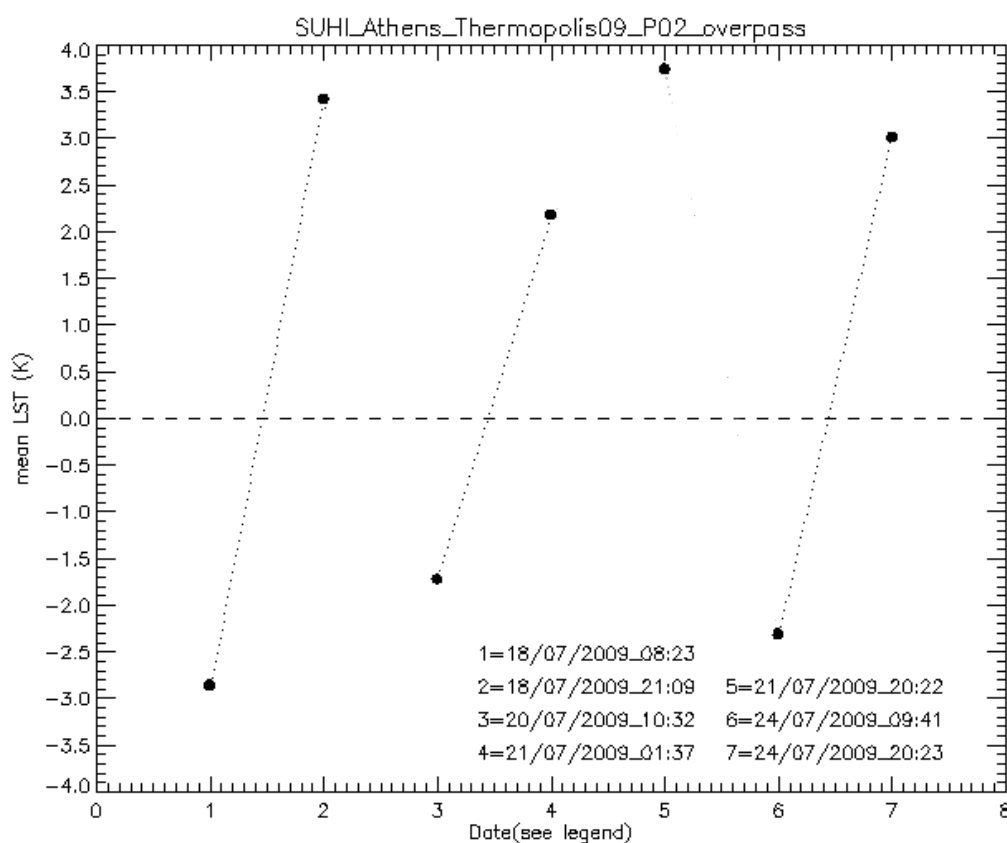


Figure 199. SUHI effect obtained using LST images from AHS overpass 2.

Figure 21 shows negative SUHI values for images at daytime, since the rural surfaces appear warmer than urban ones. For night time the city is warmer. The maximum values appears on the night of the 21st, when a SUHI of almost 4 K is reached.

Another approach to observe the SUHI effect is the analysis of the spatial profile of the AHS LST images. Figure 22 displays the AHS image with a black line which indicates the line of the profile considered. Relevant zones, where some big changes on LST are detected, are labeled with numbers.

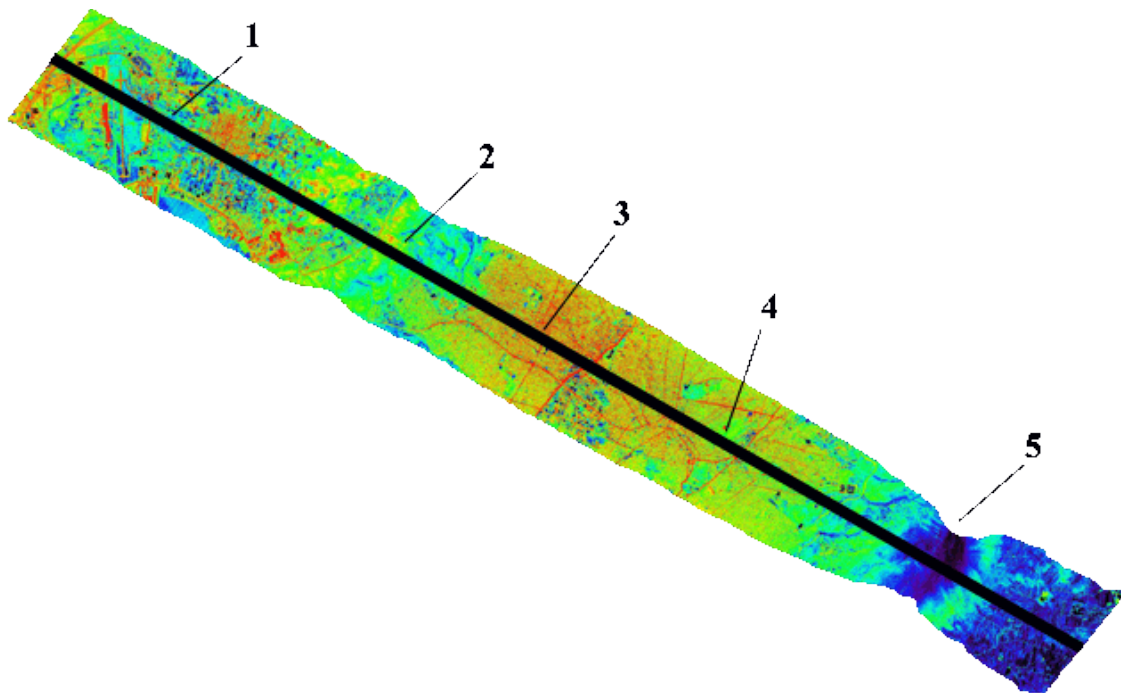


Figure 200. AHS image with a line indicating the profile. Numbers corresponds to the position indicated in next figure.

Figure 23 plots the profile of the AHS overpass 2, at night time. Red lines show two limits, the maximum and minimum LST achieved by the profile obtained by averaging all 4 profiles extracted from the images. The results define the thermal structure of the image. The numbers labeled stress the changes in temperature and they correspond to the position indicated in Figure 22 for each same number. Label 3 corresponds to a dense urban zone. And Label 4 corresponds to a green area inside Athens.

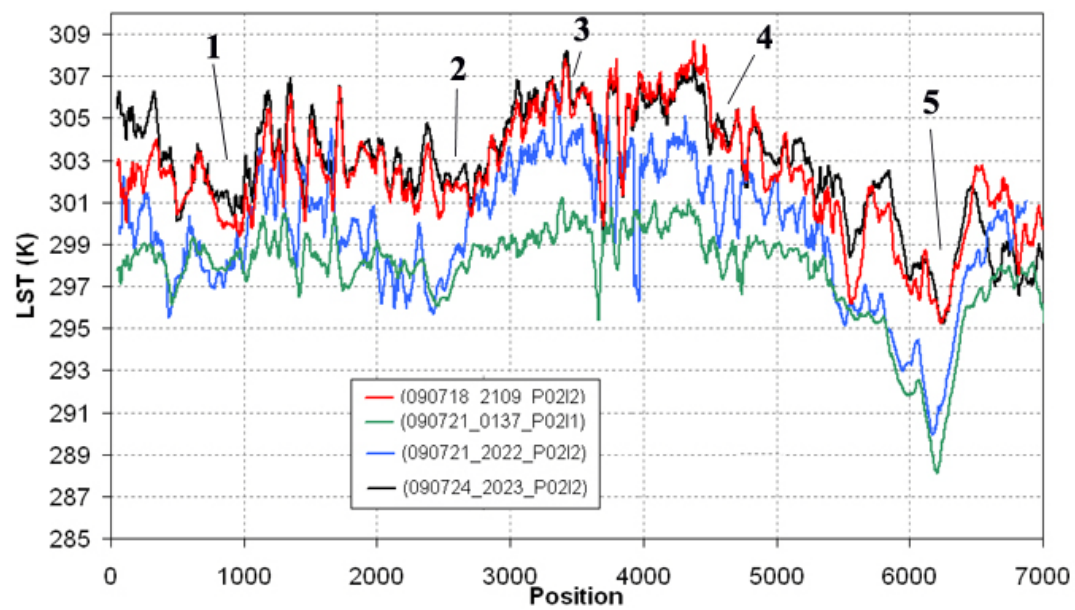


Figure 201. LST profiles in the AHS overpass 2 at night time. Position indicates number of pixels

7.9 Conclusions

AHS imagery acquired in the framework of the THERMOPLIS project has been atmospherically corrected in both VNIR and TIR spectral windows in order to retrieve land surface reflectance, emissivity and temperature. These retrievals were carefully tested against in-situ measurements collected with different instruments and over different plots.

Surface reflectances for AHS VNIR bands (from 1 to 20) were retrieved by inversion of the radiative transfer equation using atmospheric profiles and MODTRAN-4 radiative transfer code. Results were validated using in-situ reflectance spectra measured with GER-1500 spectroradiometer. As a reference, the Root Mean Square Error for AHS bands 9 and 12 over bare soil, green grass and concrete was 0.06 in reflectance units. When only green grass is considered in the test, RMSE decreases to 0.02.

Land surface temperature and emissivity was retrieved from AHS TIR bands using two different approaches: i) split-window algorithms and NDVI thresholds method, and ii) Temperature and Emissivity Separation (TES) algorithm. A new set of split-window coefficients was obtained from simulated data, providing a single split-window algorithm that can be applied to any flight altitude whenever the input atmospheric water vapour is rescaled to that flight altitude (and also for a given view angle). The lowest error was obtained for the combination between AHS bands 76 and 79, with a theoretical error of 1.2 K. The semi-empirical relationship between minimum emissivity (ϵ_{\min}) and spectral contrast (MMD) involved in the TES algorithms was also recomputed for AHS TIR bands. The standard error of estimation was 0.004 emissivity units.

A vicarious calibration was performed to AHS TIR bands in order to assess their performance. RMSE values for the ten AHS TIR bands (from 71 to 80) over water and green grass plots was below 1.4 K. A noisy signal was detected in AHS band 78, so this band was not considered in the surface temperature and emissivity retrieval. The validation of the split-window algorithm provided a RMSE of 1.8 K, whereas the TES algorithm provided a RMSE of 1.6 K.

Examples of simulated UHI products at resolution of 10 m, 20 m, 30 m, 40 m, 50 m, 100 m, 200 m, 300 m, 400 m, 500 m and 1 Km were produced, which showed the loss of detailed thermal information, and thus, the resolution required depends highly on the purpose of the study, depending on the scale of the phenomenon analyzed.

The analysis of the SUHI episode by means of AHS images showed that for daytime images the SUHI effect is negative and for night time is positive. The maximum SUHI value achieved was around 4 K the 21st of July at night.

References

1. Berk, A., Anderson, G. P., Acharya, P. K., Chetwynd, J. H., Bernstein, L. S., Shettle, E. P., Matthew, M. W., and Adler-Golden, S. M., "MODTRAN4 User's Manual," Air Force Research Laboratory, Hanscom AFB, MA, 1999.
2. Carlson, T. N., and Ripley, D. A., 1997. "On the relation between NDVI, fractional vegetation cover, and leaf area index". *Remote Sensing of Environment*, 62, 241-252.
3. Gillespie, A., Rokugawa, S., Matsunaga, T., Cothorn, J. S., Hook, S., and Kahle, A. B., 1998, "A temperature and emissivity separation algorithm for advanced spaceborne thermal emission and reflection radiometer (ASTER) images," *IEEE Trans. Geosci. Remote Sen.*, 36(4), 1113-1126.
1. Jiménez-Muñoz, J. C., and Sobrino, J. A., 2009, "Split-window coefficients for land surface temperature retrieval from low-resolution thermal infrared sensors", *IEEE Geoscience and Remote Sensing Letters*, 5(4), 806-809.
2. Kerr, Y. H., Lagouarde, J. P., Nerry, F., and Ottlé, C.: "Land surface temperature retrieval techniques and applications: case of the AVHRR". *Thermal Remote Sensing in Land Surface Processes*, D. A. Quattrochi and J. C. Luvall (eds), Ed. Florida: CRC Press, pp. 33–109, 2004.
3. Nicodemus, F. E., Richmond, J.C., Hsia, J.J., Ginsberg, I.W. and Limperis, T., 1977, Geometrical considerations and nomenclature for reflectance. *Tech. rep., National Bureau of Standards, US Department of Commerce, Washington, DC, USA*.
4. Sobrino, J. A., Caselles, V., and Becker, F., 1990, "Significance of the remotely sensed thermal infrared measurements obtained over a citrus orchard," *ISPRS-J. Photogram. Remote Sens.*, 44, 343-354.
5. Sobrino, J. A., and Raissouni, N., 2000, "Toward remote sensing methods for land cover dynamic monitoring: application to Morocco," *Int. J. Remote Sens.*, 21(2), 353-366.
6. Sobrino, J. A., Jiménez-Muñoz, J. C., Zarco-Tejada, P. J., Sepulcre-Cantó, G., and de Miguel, E., 2006, "Land surface temperature derived from airborne hyperspectral scanner thermal infrared data", *Remote Sensing of Environment*, 102, 99-115.
7. Sobrino, J. A., Jiménez-Muñoz, J. C., Sòria, G., Romaguera, M., Guanter, L., Moreno, J., Plaza, A., and Martínez, P., 2008, "Land surface emissivity retrieval from different VNIR and TIR sensors", *IEEE Trans. Geosci. Remote Sen.*, 46(2), 316-327.

8. Verhoef, W. and Bach H., 2003, “Simulation of hyperspectral and directional radiance images using coupled biophysical and atmospheric radiative transfer models”, *Remote Sensing of Environment*, 87, 23-41.
9. Voogt, J.A. and Oke, T.R., 2003. “Thermal remote sensing of urban climates”. *Remote Sensing of Environment*, 86, 370 – 384.

8. Thermopolis 2009 data base

An FTP server was set up to ensure fast, fair and constructive data exchange and joint analysis as well as providing a central repository for remotely sensed data acquired during the campaign.

Thermopolis FTP server offers access to quick-looks and supporting data (from local sources) including land use maps (cadastral), DEMs, atmospheric measurements (radio soundings, sun photometer data) and meteorological reports. In addition, copies of meeting minutes and slide presentations are held there.

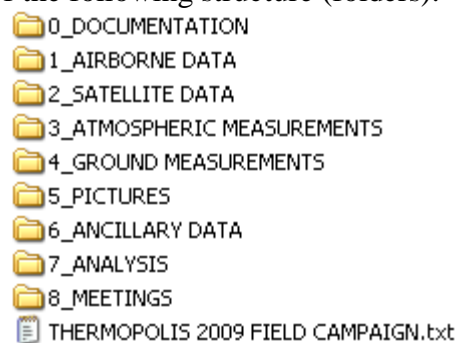
The directory is following the nomenclature below:

|-**Data**: to store raw data; within this directory, data is associated either with the measurement date or contained within a new subdirectory.

|-**Analyses**: to store processed data.

|-**Pictures**: self-explanatory

The data base consists of the following structure (folders):



0.-DOCUMENTATION: Documents from the project

1.-AIRBORNE DATA: Contains the images taken by AHS sensor.

2.-SATELLITE DATA: Contains folders with the different satellite/sensor acquisitions.

3.-ATMOSPHERIC MEASUREMENTS: Contains meteorological data, LIDAR data and Radiosoundings:

3.1- VERTICAL PROFILING: Contains 2 folders

- ceilometer backscatter profiles
- Radiosondes data

3.2- SUN PHOTOMETRIC MEASUREMENTS: Contains 5 folders

- CIMEL - CIMEL aerosol optical measurements

- MICROTOPS - aerosol, ozone and watervapor data and in-situ aerosol measurements
- PFR - PFR aerosol optical depth measurements at 4 wavelengths from UV to visible
- PGS - in-situ aerosol measurements with the PGS-100 spectrophotometer
- UVMFR - UV-MFR's aerosol optical depth measurements

3.3- LIDAR: Contains the LIDAR data

3.4- METEOROLOGICAL DATA: Meteorological data for Athens and surroundings provided by different organizations during the THERMOPOLIS campaign

3.5- RADIATION DATA: WRC - Data measured during the Thermopolis campaign by the PMOD/WRC in Athens

3.6- IN_SITU: in-situ aerosol measurements

4.-GROUND MEASUREMENTS: Contains 3 sub-folders:

- DATA EC tower
- GCU
- GROUNDBASED

5.-PICTURES: contains pictures of the field campaign sorted by activities.

6.-ANCILLARY DATA: includes

- ATTIKI MUNICIPALITIES
- CLUTTER_LANDUSE DATA
- DEM
- LANDUSE_MAP_Corine100m
- MORPHOMETRIC PARAMETERS

7.-ANALYSIS: contains calculated fluxes from DUTH

8.-MEETINGS: contains data from meetings

9. Conclusions

□ The reported work carried out by NOA, INTA and UVEG during the ATHENS THERMOPOLIS 2009 Campaign, resulted in data that support the UHI project objectives, via the analysis of comprehensive validated data sets and the data from the urban weather stations, concerning the quality assessment of the UHI information products. Data from AHS of INTA were compared with satellite derived LSTs, were validated and the differences between the two LSTs, with std deviations and RMSEs recorded and commented upon. The magnitude of the UHI phenomenon was also recorded via the intercomparison of LSTs for rural and urban areas in the Attica region. The ATs recorded at the weather stations run by CERTH across the conurbation of Athens for the period of the campaign, were interpolated to give spatial AT variability maps to match the satellite LST coverage. Hence, Land Surface Temperature and Air Temperature retrieval of urban and surrounding rural areas, at a high spatial resolution (5 to 90m) was achieved, in order to study in detail the spatial variability of UHI Athens. The feasibility of recording time series of AT and obtaining retrievals LST for the Athenian conurbation, together with weather forecasting, will, via the use of stochastic modeling, possibly effect prognostic and forecasting actions for Urban Heat Waves.

The secondary objective of providing additional datasets to perform a preliminary mission analysis for a dedicated TIR sensor that would feature the necessary higher spatial resolution and revisiting time for a more adequate provision of LST retrievals in the metropolitan areas of European cities, was also achieved.

The study of energy balance of the cities for a better response to the energy efficiency policies was achieved by determining heat fluxes from a micrometeorological tower, calibrating the heat flux measurements of the overflying DUTH-AEROPHOTO airplane and extrapolating the heat flux calculations to the swaths of the LST given by the AHS data. Hence, we do have a method to determine regional sensible heat fluxes from an aircraft platform, given the fact that this time the aircraft measurements were calibrated using an eddy-covariance tower. If the aircraft flies within the convective boundary layer, calculations are relatively simple. More complicated iterations are necessary for flights above the CBL.

The comparison between the aerosol microphysical properties (effective radius and single scattering albedo) derived by inverse modeling (from NTUA Raman lidar data) and measured in situ by airborne instruments at selected heights by the Democritus University of Thrace (DUTH)-AEROPHOTO aircraft, showed that the retrieved aerosol radius (3 cases) and the SSA values (1 case) agreed quite well. Additionally, the CALIPSO level 2 data comparison with the ground-based retrievals of the aerosol optical properties (extinction and backscatter coefficients and lidar ratio) showed a quite good agreement between the two instruments (for a 12 km minimum horizontal distance between NTUA Raman lidar and the CALIPSO ground track). The measurements were classified into clusters using the air mass origin as criterion of

the aerosol source region. Therefore, using the air mass backward trajectories ending over the sampling site (city of Athens at various heights in the lower troposphere) variable aerosol sources were identified for each measurement day. For instance, between 14 and 20 July 2009, anthropogenically produced particles were found over Athens; Saharan dust particles were observed between 24-26 July, whereas in the period 20-22 July a mixture of anthropogenic and smoke (biomass burning) aerosols occurred. The aerosol data were used to correct the satellite and INTA-AHS data.

AHS imagery acquired in the framework of the THERMOPLIS project has been atmospherically corrected in both VNIR and TIR spectral windows in order to retrieve land surface reflectance, emissivity and temperature. These retrievals were carefully tested against in-situ measurements collected with different instruments and over different plots. Surface reflectances for AHS VNIR bands (from 1 to 20) were retrieved by inversion of the radiative transfer equation using atmospheric profiles and MODTRAN-4 radiative transfer code. Results were validated using in-situ reflectance spectra measured with GER-1500 spectroradiometer. As a reference, the Root Mean Square Error for AHS bands 9 and 12 over bare soil, green grass and concrete was 0.06 in reflectance units. When only green grass is considered in the test, RMSE decreases to 0.02. Land surface temperature and emissivity was retrieved from AHS TIR bands using two different approaches: i) split-window algorithms and NDVI thresholds method, and ii) Temperature and Emissivity Separation (TES) algorithm. A new set of split-window coefficients was obtained from simulated data, providing a single split-window algorithm that can be applied to any flight altitude whenever the input atmospheric water vapour is rescaled to that flight altitude (and also for a given view angle). The lowest error was obtained for the combination between AHS bands 76 and 79, with a theoretical error of 1.2 K. The semi-empirical relationship between minimum emissivity (ϵ_{min}) and spectral contrast (MMD) involved in the TES algorithms was also recomputed for AHS TIR bands. The standard error of estimation was 0.004 emissivity units. A vicarious calibration was performed to AHS TIR bands in order to assess their performance. RMSE values for the ten AHS TIR bands (from 71 to 80) over water and green grass plots was below 1.4 K. A noisy signal was detected in AHS band 78, so this band was not considered in the surface temperature and emissivity retrieval. The validation of the split-window algorithm provided a RMSE of 1.8 K, whereas the TES algorithm provided a RMSE of 1.6 K. Examples of simulated UHI products at resolution of 10 m, 20 m, 30 m, 40 m, 50 m, 100 m, 200 m, 300 m, 400 m, 500 m and 1 Km were produced, which showed the loss of detailed thermal information, and thus, the resolution required depends highly on the purpose of the study, depending on the scale of the phenomenon analyzed.

The analysis of the SUHI episode by means of AHS images showed that for daytime images the SUHI effect is negative and for night time is positive. The maximum SUHI value achieved was around 4 K the 21st of July at night.

In the future we should be able to obtain daily or half daily heat fluxes of the conurbation, provided that we have satellite LSTs in situ ATs and occasional calibration of heat fluxes by aircraft measurements at very high spatial resolution. Again, stochastic and numerical modeling will support the forecasting of heat fluxes.

10. Relevant Documents and References

- [RD-1] ESA, Reorientation of the Fuegosat Consolidation Phase, 28 March 2008. ESA/PB-EO(2007)113, rev 1
- [RD-2] ESA, Urban Heat Islands and Urban Thermography Project, DUE-ITT May 2008
- Katsouyanni, K., et al., The 1987 Athens heatwave [letter], *Lancet*, 2(8610):573, 1988
- Stathopoulou, M. and K. Kartalis, Daytime urban heat islands from Landsat ETM+ and Corine land cover data: An application to major cities in Greece, *Solar Energy*, 81, 358-368, 2007
- Founda, D., et al., Analysis of mean, maximum, and minimum temperature in Athens from 1897 to 2001 with emphasis on the last decade: trends, warm events, and cold events, *Global and Planetary Change*, 44, 27-38, 2004
- J. A. Sobrino, J. C. Jiménez-Muñoz, G. Sòria, M. Gómez, A. Barella-Ortiz, M. Romaguera M. Zaragoza, Y. Julien y J. Cuenca, M. Atitar, V. Hidalgo, B. Franch, C. Mattar, A. Ruescas, L. Morales, A. Gillespie, L. Balick, Z. Su, F. Nerry, L. Peres, R. Libonati. Thermal Remote Sensing in the Framework of the SEN2FLEX Project: Field Measurements, Airborne Data and Applications. *International Journal of Remote Sensing* 29 (17-18), 4961-4991, 2008.
- J. A. Sobrino et al (49 co-authors). DESIREX-2008 Final Report. Contract No. 21717/08/I-LG. ESA Scientific Campaign Unit, ESTEC, 219 pp. ESA, Noordwijk, 2009.
- Böckmann, C., Wandinger, U., Ansmann, A., Bosenberg, J., Amiridis, V., Boselli, A., Delaval, A., De Tomasi, F., Frioud, M., Grigorov, I., Hagard, A., Horvat, M., Iarlori, M., Komguem, L., Kreipl, S., Larcheveque, G., Matthias, V., Papayannis, A., Pappalardo, G., Rocadenbosch, F., Rodrigues, J. A., Schneider, J., Shcherbakov, V., and Wiegner, M., Aerosol lidar intercomparisons in the frame of EARLINET: Part II - Aerosol backscatter algorithms, *Applied Optics*, **43**, 977-989, 2004.
- Matthias, V., D. Balis, J. Boesenberg, R. Eixmann, M. Iarlori, L. Komguen, I. Mattis, A. Papayannis, G. Pappalardo, M.R. Perrone and X. Wang, 'Vertical aerosol distribution over Europe: Statistical analysis of Raman lidar data from 10 European Aerosol Research Lidar Network (EARLINET) stations', *Journal of Geophysical Research*, **109**, D18201, doi:10.1029/2004JD004638, 2004.
- Pappalardo, G., A. Amodeo, U. Wandinger, V. Matthias, J. Bösenberg, M. Alpers, V. Amiridis, F. de Tomasi, M. Frioux, M. Iarlori, L. Komguen, G. Larcheveque, A. Papayannis, R. Schumacher, X. Wang, 'Aerosol lidar intercomparison in the frame of EARLINET: Part III: Aerosol extinction Raman lidar algorithm intercomparison', *Applied Optics*, **43**, 5370-5385, 2004.